



HAL
open science

Hemicryptophanes and Beyond: Synthesis, Recognition, Molecular Machines and Supramolecular Catalysis

Dawei Zhang

► **To cite this version:**

Dawei Zhang. Hemicryptophanes and Beyond: Synthesis, Recognition, Molecular Machines and Supramolecular Catalysis. Organic chemistry. Université de Lyon; East China normal university (Shanghai), 2017. English. NNT: 2017LYSEN011 . tel-01545415

HAL Id: tel-01545415

<https://theses.hal.science/tel-01545415>

Submitted on 22 Jun 2017

HAL is a multi-disciplinary open access archive for the deposit and dissemination of scientific research documents, whether they are published or not. The documents may come from teaching and research institutions in France or abroad, or from public or private research centers.

L'archive ouverte pluridisciplinaire **HAL**, est destinée au dépôt et à la diffusion de documents scientifiques de niveau recherche, publiés ou non, émanant des établissements d'enseignement et de recherche français ou étrangers, des laboratoires publics ou privés.



Numéro National de Thèse : 2017LYSEN011

THESE de DOCTORAT DE L'UNIVERSITE DE LYON
opérée par
l'Ecole Normale Supérieure de Lyon

Ecole Doctorale N° 206
Ecole Doctorale de Chimie

Discipline : Chimie

Soutenue publiquement le 23/05/2017, par :
M. Dawei ZHANG

**Hemicryptophanes and Beyond : Synthesis,
Recognition, Molecular Machines and
Supramolecular Catalysis**

Les hémicryptophanes : Synthèse, Reconnaissance, Machines Moléculaires
et Catalyse Supramoléculaire

Directeur de thèse : M. Alexandre MARTINEZ

Co-Directeur de thèse : M. Guohua GAO

Devant le jury composé de :

Mme Jeanne CRASSOUS, <i>Directrice de Recherche, Université de Rennes</i>	Rapporteure
M. Rinaldo POLI, <i>Professeur, Université de Toulouse</i>	Rapporteur
M. Mingyuan HE, <i>Professeur, East China Normal University</i>	Examineur
Mme Estelle METAY, <i>Chargée de Recherche, Université de Lyon 1</i>	Examinatrice
M. Julien LECLAIRE, <i>Professeur, Université de Lyon 1</i>	Examineur
M. Jean-Pierre DUTASTA, <i>Directeur de Recherche Emérite, ENS de Lyon</i>	Membre Invité
Mme Laure GUY, <i>Ingénieure de Recherche, ENS de Lyon</i>	Co-encadrante
M. Alexandre MARTINEZ, <i>Professeur, Ecole Centrale de Maresille</i>	Directeur
M. Guohua GAO, <i>Professeur, East China Normal University</i>	Co-directeur

Acknowledgements

I wish to express my sincere appreciation to those who have contributed to this thesis and supported me during this amazing PhD journey. This thesis is the result of four years of work whereby I have been accompanied and supported by many people.

First of all, I am extremely grateful to my PhD supervisor at the ENS-Lyon, Prof. Alexandre Martinez, who introduced me to the field of supramolecular chemistry and gave me constant direction. I appreciate so much that he recognized my potential as a first-year master's student when he taught at the ECNU and gave me the opportunity to carry out my doctoral research after my master's study. I was enlightened significantly by his wide knowledge, guidance, useful discussions and brainstorming sessions. His deep insights helped me at various stages of my PhD study, including the periods of time I studied at the University of Ottawa and University of Cambridge. He is always so kind and very considerate of his students. He treats my future career as very important, and always does his best to provide assistance with this.

I am also deeply grateful to Dr. Laure Guy, who is my co-supervisor at the ENS-Lyon. I have greatly benefited from her wide knowledge and logical way of thinking. I appreciate so much the frequent discussions with her and also the significant technical support in experiments, which has greatly advanced the progress of my research. She's always so helpful in both research and life, and is also one of the very few people who has carefully read this thesis letter by letter. I would also like to thank Dr. Jean-Pierre Dutasta, an emeritus CNRS research director in my group. I have obtained invaluable insights and suggestions, and learned a lot of experiences from him. His enthusiasm and passion for research has made a deep impression on me.

My sincere thanks also goes to my Chinese PhD supervisor, Prof. Guohua Gao, at the ECNU. I appreciate that he supported my idea to come to Lyon to start my PhD study one year in advance, during my master study, which is extremely important to my academic career. Although I fully conducted my PhD in France, I should emphasize that I have learned and been trained systematically under his supervision during my two years' masters' study, which is greatly helpful to both my PhD and future research.

In the past four years, I have also been to the University of Ottawa for one month and the University of Cambridge for five months, working with Prof. R. Tom Baker and Prof. Jonathan R. Nitschke, respectively. I am grateful to my supervisors in the two universities for providing me with these chances to learn new knowledge and skills. I thank them so much for their invaluable guidance, discussions and direction. In particular, a very special thanks to Prof. Jonathan R. Nitschke for offering me the opportunity of a post-doc position at the University of Cambridge after my PhD study, which I greatly look forward to taking up in July this year.

The research described in this thesis could not be accomplished without a lot of people's help, and they are mostly listed as contributors in each chapter. At the ENS-Lyon, I would like to thank Jean-Christophe and Delphine for their technical help in experiments; Dr. James

Cochrane and Sandrine for NMR support; Dr. Thierry Brotin and Dr. Yann Bretonniere for the discussions on cryptophanes and fluorescence, Christian for solving computer problems; Damien, Edwige and Marie-Francoise for the administrative affairs of the lab. I would also like to thank Dr. Christian Díaz-Urrutia and Dr. Kaitie Giffin at the University of Ottawa for their help in both research and life in Canada, and Dr. Tanya Ronson and Dr. Jesús Mosquera at the University of Cambridge for their great help, advice and direction in research while I was in the UK.

I would like to express my sincere gratitude to my PhD committee members Prof. Mingyuan He, Prof. Julien Leclaire, Prof. Rinaldo Poli, Prof. Jeanne Crassous, and Prof. Estelle Metay for their contributions and witness of my professional development during my graduate education.

I gratefully acknowledge the collaboration program between ENS-Lyon and ECNU, so that I could have this chance to study here four years ago. This is a very successful program, which has cultivated hundreds of PhD students who currently work across academia and industries spread all over the world. I would like to specially show my thanks to Mme Yunhua Qian, a respected woman who established this program and was in charge of it for more than ten years. She has greatly promoted the development of the collaboration between ENS and ECNU and cultural communication between France and China, which has benefited hundreds of students including myself. Without her, I couldn't have come to ENS-Lyon successfully, especially one year ahead, due to several serious barriers I met including the problem of funding.

Definitely, I would also like to acknowledge grants from the *China Scholarship Council* (four years), *Accueil Doc Bursary* from France Rhône-Alpes Region (six months) and *Enveloppe Attractivité Fellowship* from ENS-Lyon (four years) for my PhD study. With their financial support, I could not only complete my PhD research, but also enjoy my life. Besides China and France, I have travelled to many cities and countries, such as Switzerland, Italy, Spain, Germany, Belgium, Luxembourg, Netherlands, UK, Canada and Korea, which has greatly broadened my horizon and become the wealth of my life.

My time in Lyon was enjoyable in large part due to the many friends and group members that became a part of my life. I am grateful for time spent with all of them, they are from all over the world, Zheng, Jinping, Nanan, Jingyun, Chongzhi, Qingyi, Shuai, Kaiheng, Xiaopeng, Lianke, Ling, Wenyue, Xin, Xinnan, Laure-Lise, Maelle, Sara, Estelle, Orsola, Aline, Bastien, Nicolas, and all the members in the Laboratory of Chemistry. I cherish all the wonderful moments that we spent together.

Lastly, I would like to thank my family for all their love and encouragement. I have obtained constant unconditional support from my parents and my older sister – both emotionally and financially. Thank you!

Table of Contents

ACKNOWLEDGEMENTS.....	I
TABLE OF CONTENTS.....	III
ABSTRACT.....	VII
RESUME.....	XI
摘要.....	XIII
PART I. INTRODUCTION	1
Preface	3
Chapter 1. Emergence of Hemicryptophanes: From Synthesis to Applications for Recognition, Molecular Machines and Supramolecular Catalysis	5
1.1 Abstract.....	6
1.2 Introduction	6
1.3 Synthesis of hemicryptophanes.....	8
1.4 Host-guest chemistry of hemicryptophanes.....	36
1.5 Hemicryptophanes in motion: towards molecular machines	50
1.6 Hemicryptophanes: supramolecular catalysts	53
1.7 Conclusions and perspectives	60
1.8 References.....	62
Chapter 2. Objectives of This Thesis	71
PART II. HOST-GUEST CHEMISTRY OF HEMICRYPTOPHANES.....	73
Preface	75
Chapter 3. A Fluorescent Heteroditopic Hemicryptophane Cage for the Selective Recognition of Choline Phosphate	77
3.1 Abstract.....	78
3.2 Introduction	78
3.3 Results and discussion.....	79
3.4 Conclusion.....	83
3.5 Experimental section.....	83
3.6 References.....	89
Chapter 4. Insights into the Complexity of Weak Intermolecular Interactions Interfering in Host–Guest Systems	91

4.1 Abstract.....	92
4.2 Introduction	92
4.3 Results and discussion.....	93
4.4 Conclusion.....	98
4.5 Experimental section.....	99
4.6 References.....	104
Chapter 5. Synthesis, Resolution and Absolute Configuration of Chiral TPA-Based Hemicryptophane Molecular Cages.....	107
5.1 Abstract.....	108
5.2 Introduction	108
5.3 Results and discussion.....	109
5.4 Conclusion.....	112
5.5 Experimental section.....	112
5.6 References.....	121
Chapter 6. Helical, Axial and Central Chirality Combined in a Single Cage: Synthesis, Absolute Configuration and Recognition Properties	123
6.1 Abstract.....	124
6.2 Introduction	124
6.3 Results and discussion.....	125
6.4 Conclusion.....	130
6.5 Experimental section.....	130
6.6 References.....	140
PART III. HEMICRYPTOPHANES IN MOTION: TOWARDS MOLECULAR MACHINES	143
Preface	145
Chapter 7. Breathing Motion of a Modulable Molecular Cavity	147
7.1 Abstract.....	148
7.2 Introduction	148
7.3 Results and discussion.....	148
7.4 Conclusion.....	152
7.5 Experimental section.....	152

7.6	References.....	173
PART IV. HEMICRYPTOPHANES AS SUPRAMOLECULAR CATALYSTS.....		175
	Preface	177
	Chapter 8. Tailored Oxido-Vanadium(V) Cage Complexes for Selective Sulfoxidation in Confined Spaces	179
8.1	Abstract.....	180
8.2	Introduction	180
8.3	Results and discussion.....	182
8.4	Conclusion.....	187
8.5	Experimental section.....	188
8.6	References.....	197
	Chapter 9. Merging Aerobic Oxidation of Lignin Model Compounds with Supramolecular Catalysis	199
9.1	Abstract.....	200
9.2	Introduction	200
9.3	Results and discussion.....	201
9.4	Conclusion.....	203
9.5	Experimental section.....	203
9.6	References.....	206
	Chapter 10. Azaphosphatranes as Hydrogen-Bonding Organocatalysts for the Activation of Carbonyl Groups: Investigation of Lactide Ring-Opening Polymerization	207
10.1	Abstract.....	208
10.2	Introduction	208
10.3	Results and discussion.....	209
10.4	Conclusion	214
10.5	Experimental section.....	214
10.6	References	216
PART V. BEYOND HEMICRYPTOPHANES: CAGES CONSTRUCTED BY SELF-ASSEMBLY		219
	Preface	221
	Chapter 11. Anion Binding in Water Drives Structural Adaptation in an Azaphosphatrane-Functionalized Fe^{II}₄L₄ Tetrahedron	223

11.1 Abstract.....	224
11.2 Introduction	224
11.3 Results and discussion.....	225
11.4 Conclusion	229
11.5 Experimental section.....	230
11.6 References	272
PART VI. CONCLUSION	275

Abstract

In the wide area of host-guest chemistry, hemicryptophanes, a type of molecular cages, combining a cyclotrimeratrylene (CTV) unit with another different C_3 symmetrical moiety, have received increasing attention.

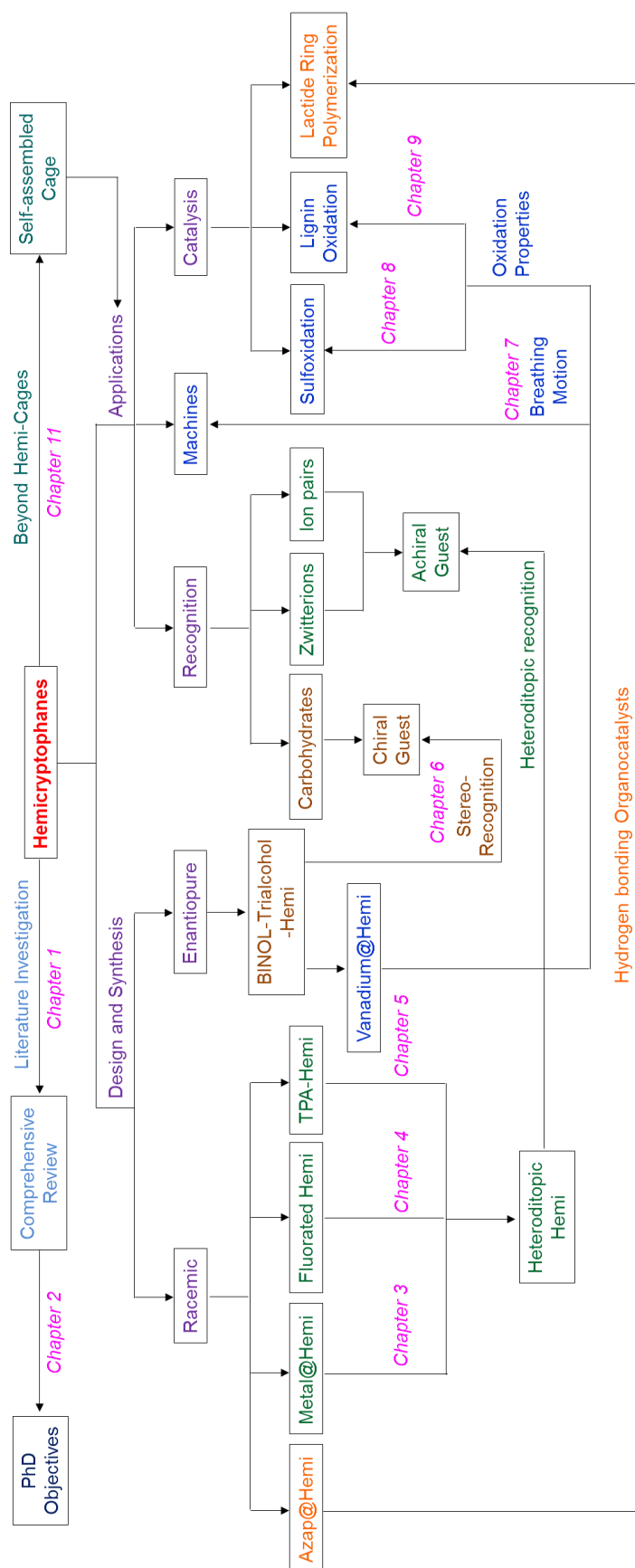
In the first part of this PhD thesis (**Part I**), the advances in hemicryptophane chemistry have been thoroughly reviewed in **Chapter 1**. This includes a brief history of its development, the synthetic methods, and applications in recognition, molecular machines and supramolecular catalysis. In **Chapter 2**, the objectives of this thesis have been postulated. This PhD work outlines my efforts to design and synthesize new hemicryptophanes for more efficient molecular recognition and supramolecular catalysis.

The works in **Part II** mainly describe the targeted molecular recognition by rational design of hemicryptophanes. Hence in each chapter, the synthesis has been included. In **Chapter 3**, a fluorescent hemicryptophane cage combining a CTV unit, three naphthalene rings, and a Zn(II) metal center has been developed as the first fluorescent sensor for choline phosphate in competitive media. The heteroditopic character of the host that leads to strong guest encapsulation has been systematically investigated by both fluorescence and NMR spectroscopy. In **Chapter 4**, two new hemicryptophanes bearing fluorinated aromatic linkers have been synthesized, and their complexation properties toward ion pairs have been investigated and compared to that of the host without fluorine atoms. We anticipate that the introducing of fluorine atoms around the aromatic linkers could improve the anion binding abilities of the host due to the enhanced anion- π interactions, therefore affecting their ion pair binding performance. **Chapter 5** has introduced the synthesis of two new heteroditopic hemicryptophanes bearing tris(2-pyridylmethyl)amine (TPA) units, one with phenyl rings as linkers and the other with naphthalene rings. The racemate of each hemicryptophane can be resolved by chiral HPLC to obtain their enantiopure forms. These enantiopure cages are expected to show interesting stereorecognition properties after metal complexation of TPA. In **Chapter 6**, we have designed and synthesized eight enantiopure cages combining three classes of chirality on seven stereogenic units. A chemical correlation strategy has been used to determine the absolute configuration of the eight hemicryptophane stereoisomers. The stereoselective recognition properties toward carbohydrates have been investigated.

In **Part III**, the only chapter, **Chapter 7**, describes the breathing motion of a series of enantiopure cages obtained in **Chapter 6**, complementing the rare application of hemicryptophanes in molecular machines. The breathing motion is initiated by vanadium coordination to a series of imploded cages, which inflates the cages to globular forms. The resulting vanadium cores can also be removed from the inner cavity according to external coordination with triethanolamine. Thus, the system is capable of switching between the imploded and expanded bistable states via external inputs, simulating breathing molecules.

In **Part IV**, three works related to hemicryptophanes for supramolecular catalysis have been discussed. In **Chapter 8**, the hemicryptophane vanadium(V) complexes, obtained in **Chapter 7**, have been developed as efficient supramolecular catalysts for sulfoxidation. The specific shape of the confined hydrophobic space above the metal center induced by the

PhD Thesis Network



* Azap = Azaphosphatrane; Hemi = Hemicryptophane; TPA = tris(2-pyridylmethyl)amine; BINOL = Binaphthol

bulky binaphthol linkers leads to strong improvement of the yield, the selectivity and also the catalytic activity. **Chapter 9** deals with the catalytic lignin oxidation by these vanadium(V)

hemicycrophane catalysts. Compared to the model catalyst with an open structure, an improvement of the catalytic activity associated with a diastereoselective conversion of substrates has been observed. In **Chapter 10**, we have attempted to develop the azaphosphatane-functionalized hemicycrophanes as hydrogen-bonding organocatalysts for the ring-opening polymerization of lactide. However, a low reactivity has been observed. Nevertheless, the model catalysts have shown satisfactory catalytic behavior.

In **Part V**, my attention has opened to a more prospective view focusing on cages constructed by self-assembly. In **Chapter 11**, we have demonstrated the feasibility of introducing azaphosphatanes, the units mentioned in **Chapter 10**, into tetrahedron capsules using subcomponent self-assembly, and also proved for the first time the utility of azaphosphatanes as anion binding moieties.

Except **Chapter 2**, which outlines the objectives of this thesis, all the other chapters have been prepared as manuscripts for journals, in which **Chapters 1, 3, 4, 5, 6, 7, 8, 10** and **11** have been published, and **Chapter 9** is being prepared. Therefore, each chapter is based partially on the corresponding publication.

Résumé

Les hémicryptophanes, molécules constituées d'une unité cyclotrimeratrylène (CTV) reliée à une autre groupement de symétrie C_3 sont des molécules cages qui trouvent de nombreuses applications dans le domaine de la chimie hôte-invité.

La première partie de ce manuscrit (**Part I**) présente une revue des développements récents de la chimie des hémicryptophanes (**Chapter 1**). Plus précisément, sont abordés un bref historique, les voies de synthèse connues ainsi que les applications dans les domaines de la reconnaissance moléculaire, des machines moléculaires et de la catalyse supramoléculaire. Le deuxième chapitre (**Chapter 2**) définit les objectifs de ce travail de thèse dans le développement et la synthèse de nouveaux hémicryptophanes pour améliorer les propriétés de reconnaissance et de catalyse de type supramoléculaire.

La deuxième partie (**Part II**) s'intéresse particulièrement aux hémicryptophanes conçus pour la reconnaissance moléculaire. Chaque chapitre de la partie II inclue donc la synthèse et les propriétés de nouvelles molécules cages. Ainsi, le chapitre 3 (**Chapter 3**) décrit la synthèse d'un hémicryptophane fluorescent composé d'une unité CTV, de groupes naphthyle dans les trois bras et d'un site coordinant un atome de Zn (II). Une telle molécule s'est avérée être un capteur très efficace de la choline phosphate dans un milieu compétitif pour la complexation. Le caractère hétéroditopique de l'association a été étudié à la fois par fluorescence et par RMN. Dans le chapitre 4 (**Chapter 4**) nous comparons l'effet de la fluoration des groupements aromatiques portés par les trois bras d'un hémicryptophane sur la reconnaissance de paires d'ions. Comme nous l'avions anticipé, la fluoration conduit à des constantes d'associations plus fortes grâce à une augmentation des interactions anion- π . Deux cages portant une sous-unité tris(2-pyridylmethyl)amine (TPA) sont font l'objet du chapitre 5 (**Chapter 5**). Elles se distinguent par des bras phényle ou naphthyle et leurs énantiomères ont pu être séparés par HPLC chirale. Enfin le chapitre 6 (**Chapter 6**) présente la synthèse en version énantiopure de huit stéréoisomères d'un nouvel hémicryptophane possédant sept centres stéréogènes de trois types différents. L'attribution de leurs configurations absolues ont pu être déterminées par corrélation chimique et leurs propriétés de reconnaissance des sucres a été examinée.

La troisième partie (**Part III**) est composée du chapitre 7 (**Chapter 7**) et s'intéresse à l'application des cages énantiopures décrites dans le chapitre 6 (**Chapter 6**) dans le domaine des machines moléculaires. Nous y décrivons le mouvement de „respiration“ initié par la coordination/décoordination d'un atome de vanadium s'accompagnant du passage d'une cavité à volume réduit (implosée) à une cage déployée (gonflée).

Dans la quatrième partie (**Part IV**), nous présentons trois études dans le domaine de la catalyse supramoléculaire. Les résultats présentés dans le chapitre 8 (**Chapter 8**) montrent que les complexes de vanadium(V) des cages obtenues dans le chapitre 7 (**Chapter 7**) sont des catalyseurs efficaces de la réaction de sulfoxydation. L'effet de confinement a été démontré par comparaison entre l'activité du catalyseur supramoléculaire et celle de son homologue ouvert ne comportant pas le CTV. En comparaison avec des résultats précédents, la présence des binaphthyle dans les bras permet une amélioration des rendements, de la sélectivité et de

l'activité catalytique. Ces mêmes complexes de vanadium (V) dérivés d'hémicryptophanes se sont avérés capable de catalyser l'oxydation de la lignine avec une activité catalytique une disatéréosélectivité bien supérieure aux catalyseurs modèles ouverts. Ces résultats font l'objet du chapitre 9 (**Chapter 9**). Comme nous le montrons dans le chapitre 10 (**Chapter 10**), nous avons tenté d'utiliser des dérivés azaphosphatrane d'hémicryptophanes comme organo-catalyseurs de la réaction de polymérisation par ouverture du lactide. Dans ce cas, une inhibition du catalyseur supramoléculaire a été observée alors que le catalyseur modèle ouvert s'est avéré plus performant et nous a permis de proposer un mécanisme pour cette réaction.

La cinquième partie (**Part V**) de ce manuscrit est consacrée à des développements nouveaux dans le domaine de la formation de cages par auto-assemblage. Elle est composée du chapitre 11 (**Chapter 11**) qui montre que nous avons réussi à former par coordination, des tétraèdres dont les quatre faces comportent une sous-unité azaphosphatrane. Et pour la première fois, dans ce type de cage, l'unité azaphosphatrane joue un rôle prépondérant dans la complexation d'anions.

A l'exception du chapitre 2 (**Chapter 2**) qui aborde les objectifs de ce travail de thèse, tous les chapitres ont été rédigés comme des articles scientifiques dont les chapitres 1, 3, 4, 5, 6, 7, 8, 10 et 11 (**Chapters 1, 3, 4, 5, 6, 7, 8, 10 and 11**) sont publiés et les chapitre 9 (**Chapter 9**) vont être soumis pour publication.

摘要

在主客体化学研究领域，hemicryptophane 是一类结合了环三亚藜芦基和另一种 C_3 对称结构单元的笼状化合物，近年来受到了人们广泛的关注。

论文第一部分的**第 1 章**，概述了 hemicryptophane 化学的研究进展，其中包括了该类笼状化合物的发展简史、合成方法、以及它们在分子识别、分子机器及超分子催化领域的应用。第一部分的**第 2 章**，提出了本论文的设想。本研究论文的目标是设计合成出新型的 hemicryptophane 化合物以达到更高效的分子识别和超分子催化性能。

论文的第二部分主要研究了如何合理的设计、合成 hemicryptophane 化合物，以实现目标分子的选择性识别。第二部分共四章，编号分别为第 3、4、5、6 章。**第 3 章**设计合成了一个含萘荧光团和 Zn(II)金属配位中心的 hemicryptophane 笼状化合物，并研究了它作为荧光探针对磷酸胆碱两性离子在含水溶剂中的分子识别性能。因主体分子一端的环三亚藜芦基可结合铵根阳离子，而另一端的金属配位中心对阴离子具有结合作用，因此该主体化合物具有明显的两性分子识别特性。核磁和荧光光谱等分析测试表明该主体分子对磷酸胆碱两性分子具有选择性包结作用。**第 4 章**合成了两个以氟代苯环作为连接链的 hemicryptophane 主体化合物，并研究了它们对离子对客体的识别性能。该实验的设计目的是期望通过在苯环侧链上引入氟原子，提高其阴离子- π 的结合力，进而提高主体分子一端对阴离子的结合能力。主体对阴离子结合性能的改变会导致其对离子对客体协同识别作用的调节，因此这些含氟主体对离子对的识别性能均与未含氟主体的识别性能进行了对比和结果分析。**第 5 章**合成了两个含三(2-吡啶基甲基)胺单元、具有两性识别特性的 hemicryptophane 笼状化合物。其中一主体以苯环作为环三亚藜芦基团和三(2-吡啶基甲基)胺单元的连接链；另一主体以萘环作为连接链，因此该主体具有荧光性能。由于环三亚藜芦基具有内在的螺旋手性，通过手性高效液相色谱仪成功的将合成的 hemicryptophane 外消旋混合物进行了手性拆分，分别获得了 hemicryptophane 化合物的每个对映异构体。这些对映异构体在通过三(2-吡啶基甲基)胺单元络合金属离子之后，将会被进一步研究其对手性的两性离子的立体识别性能。**第 6 章**设计合成了 8 个光学纯的 hemicryptophane 立体异构体。这些立体异构体含 3 种手性单元，分别为具有螺旋手性的环三亚藜芦基单元、具有轴手性的联萘基团和具有中心手性的三齿氨基三醇单元。通过化学交联的策略成功地归属了 8 个立体异构体的绝对构型，并研究了该系列主体对糖类客体的立体选择性识别性能。

第三部分唯一的一章，**第 7 章**，研究了一系列光学纯 hemicryptophane 化合物（第 6 章合成所得）分子的呼吸运动性能，弥补了 hemicryptophane 在分子机器领域应用较少的现状。核磁和 X-ray 单晶衍射等分析手段表明这一系列化合物具有内凹的空间构型。而氧化钒与分子笼一端的三齿氨基三醇单元的配位使得内凹的分子笼充分的膨胀鼓起，分子笼内络合形成的氧化钒中心又可以被外来的三乙醇胺配体移除。因此通过外在因素，这些分子笼的空腔可以在内凹和鼓起两种稳定构型中循环往复多次，这种分子构型上的往复转换可被看作分子的呼吸运动。

第四部分共三章，分别为第 8、9、10 章，研究了 hemicryptophane 在超分子催化领域的应用。**第 8 章**报道了一系列氧化钒 hemicryptophane 络合物（第 7 章合成所得）在硫醚催化氧化反应中作为超分子催化剂的应用。结果表明，在钒催化活性中心上侧由联萘侧链和环三亚藜芦基单元

所围成的疏水性空腔可极大提高硫醚氧化反应的产率、选择性和催化活性。**第 9 章**进一步将这些超分子钒催化剂应用于木质素模型化合物的催化氧化反应。与未含分子空腔的钒催化剂相比，超分子催化剂表现出明显的催化活性的提高，同时伴随着底物的非对映选择性转化的现象。**第 10 章**尝试性的研究了将氮磷川功能化的 hemicryptophane 化合物作为氢键供体有机催化剂用于交酯的开环聚合反应。结果表明，由于分子空腔内的空间位阻，这类笼状催化剂表现出极低的催化活性。相反，未含分子空腔的氮磷川催化剂表现出令人满意的催化性能，同时我们提出了对应的催化反应机理。

论文的第五部分仅一章，**第 11 章**，将研究的重点由 hemicryptophane 分子笼扩展到了自组装分子笼。通过多组分自组装策略，成功的将第 10 章介绍的氮磷川模块作为配体自组装成四面体金属胶囊；并且首次利用了氮磷川的氢键供体功能将氮磷川作为阴离子识别的受体；同时研究了氮磷川组装的四面体笼对阴离子的识别性能。

除了介绍论文研究目的的第 2 章，其他所有章节的研究内容均已发表或已整理好发表论文的形式准备发表。其中第 1、3、4、5、6、7、8、10、11 章已经正式发表，而第 9 章已整理好准备发表。因此本论文的每章均保持了原发表文章的内容和书写逻辑，只对其进行了部分修改和补充。

Part I. Introduction

Preface

Part I Network



As this thesis is focused on my efforts to develop hemicryptophane cages, **Chapter 1** chronicles the previous development of hemicryptophane chemistry and highlights their syntheses and applications in recognition, molecular machines and supramolecular catalysis. In **Chapter 2**, the objectives of this thesis are postulated. The aim I try to achieve is to forward hemicryptophanes moving toward targeted functions by the rational design.

It should be noted that **Chapter 1** is based partially on our review article published on *Chemical Reviews* (2017, 117, 4900–4942). The numbers of compounds, figures, schemes and tables have been renumbered in each chapter from the beginning, and the numbers of compounds between chapters have no relationship. The Table of Contents in **Chapter 1** has been presented in the chapter cover. The cited references are listed at the end of the corresponding chapter.

Chapter 1. Emergence of Hemicryptophanes: From Synthesis to Applications for Recognition, Molecular Machines and Supramolecular Catalysis

This Chapter is based partially on the following manuscript—

Dawei Zhang, Alexandre Martinez, Jean-Pierre Dutasta

Chem. Rev. **2017**, *117*, 4900–4942.

The work in this chapter was carried out at the ENS-Lyon.

Contents

1.1 Abstract	6
1.2 Introduction.....	6
1.3 Synthesis of hemicryptophanes	8
1.4 Host-guest chemistry of hemicryptophanes	36
1.5 Hemicryptophanes in motion: towards molecular machines	50
1.6 Hemicryptophanes: supramolecular catalysts	53
1.7 Conclusions and perspectives.....	60
1.8 References.....	62

1.1 Abstract

In the wide area of host-guest chemistry, hemicryptophanes, combining a cyclotribenzylene (or cyclotrimeratrylene CTV) unit with another different C_3 symmetrical moiety, appears as a recent family of molecular cages. The synthesis and recognition properties of the first hemicryptophane was reported in 1982 by Collet and Lehn; but the very little attention received by this class of host compounds in the twenty years following this first promising result can account for their apparently novelty. Indeed, in the last ten years hemicryptophanes have aroused a growing interest and new aspects have been developed. Thanks to the rigid shaping unit of the *north* part (CTV), and also the variable and easily functionalized *south* moiety, hemicryptophanes reveal to be inherently chiral ditopic host compounds, able to encapsulate various guests, including charged and neutral species. They also enter the field of stimuli-responsive supramolecular systems exhibiting controlled functions. Moreover, endohedral functionalization of their inner cavity leads to supramolecular catalysts. The confinement of the catalytic center affords nanoreactors with improved catalytic activities or selectivities when compared to model systems without cavity. The current trend shows that reactions in the confined space of synthetic hosts, mimicking enzyme behavior, will expand rapidly in the near future.

1.2 Introduction

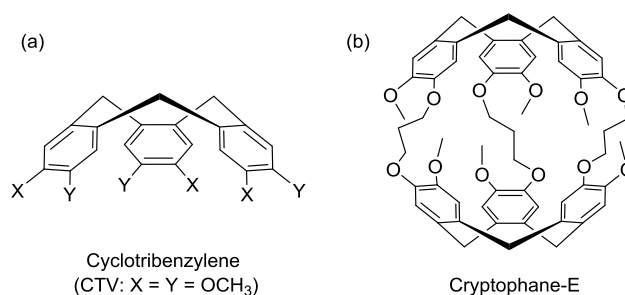


Figure 1.1 Cyclotribenzylene and cyclotrimeratrylene (CTV, X = Y = OCH₃); (b) Cryptophane-E.²⁴

Molecular cages, defined as hollow structures delineating a three-dimensional cavity, are attracting considerable attention in modern supramolecular chemistry due to their possible applications in molecular recognition, catalysis, drug delivery, biosensing, separation and storage.¹⁻⁸ Among the classes of molecular containers, such as crown-ethers,^{9,10} cryptands,¹⁰ calixarenes,¹¹⁻¹³ resorcinarenes,^{14,15} cucurbiturils,¹⁶⁻¹⁸ cyclodextrins,^{19,20} or pillararenes,²¹⁻²³ cryptophanes and hemicryptophanes based on a cyclotribenzylene core, most of the time identified to a derivative of the cyclotrimeratrylene (CTV) unit (Figure 1.1), recently received a growing interest. Cryptophanes, are homotopic host compounds built from two CTV units, which can efficiently encapsulate small molecules such as methane or epoxides, cations, anions, and xenon or radon noble gases.^{24,25} A previous comprehensive review on cryptophanes by Brotin and Dutasta has highlighted the synthesis methods, their binding and chiroptical properties, and their potential applications as biosensors and chiral agents.²⁴ In contrast, the related hemicryptophanes combining a CTV unit with another C_3 symmetrical

moiety via covalent bonds or non-covalent interactions are heteroditopic hosts able to recognize various charged or neutral guests, such as ion pairs, zwitterions, ammoniums, carbohydrates, and fullerenes. Currently, hemicryptophanes are mainly used as molecular receptors, supramolecular catalysts and as functional molecules anticipating molecular machines.

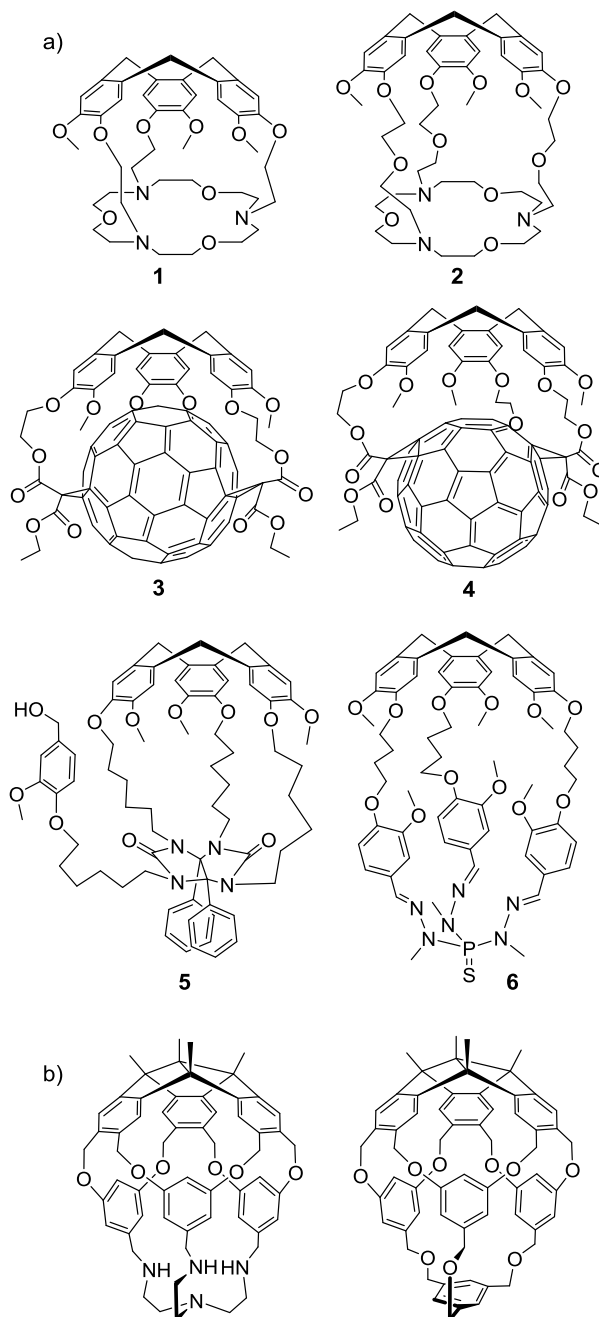


Figure 1.2 (a) Hemicryptophanes **1-6** synthesized between 1982 and 2005. (b) Structures of Kuck's hemicryptophanes based on the TBTQ unit.

The chemistry of hemicryptophane was developed quite slowly before 2005.²⁶ In 1982, Lehn and Collet described the first two members of a new type of molecular cages called *speleands* (**1** and **2** in Figure 1.2a), which associated a CTV and a crown ether unit, showing potential recognition properties toward methylammonium cations.²⁷ Then in 1989, Nolte *et al.* reported

the synthesis of a molecular host derived from CTV and diphenylglycoluril units presenting potential catalytic properties related to its easily functionalized arm (**5** in Figure 1.2a).²⁸ Ten years later, Diederich and Echegoyen described the synthesis of the two covalent CTV-C₆₀ adducts **3** and **4** (Figure 1.2a) prepared by the tether-directed Bingel reaction.²⁹ The C₃-symmetry of the two cage adducts was evidenced by NMR spectroscopy. Nevertheless, it is obvious that the free space in the cavity of the two compounds is quite restricted due to the interactions between the electron rich aromatic rings of the CTV and the electron poor C₆₀, limiting their applications as receptors. The same year, Dutasta and co-workers reported the synthesis and crystal structure of the thiophosphorylated molecular cage **6** (Figure 1.2a) based on the CTV unit, and proposed the term hemicryptophane for this type of molecular cages, which has been widely used thereafter.³⁰ At last, based on suitably functionalized CTVs, metal complexes were obtained that possess the hemicryptophane structure. In some specific cases, the CTV cap was used as ligand platform for iron(II) and iron(III) coordination.³¹ Hence, it can be seen that this class of host compounds has received little attention before 2005 since only few relevant papers were reported during this period, and even less have really focused on their applications. Unexpectedly, after 2005, this chemistry received a growing interest leading to a blossoming field of research, particularly for molecular recognition. For instance, a series of sophisticated enantiopure hemicryptophanes has been synthesized benefiting from the inherent chirality of the CTV unit and used for the stereoselective recognition of chiral guest molecules. They have also entered the field of controlled molecular motions, exhibiting solvent-responsive properties. Moreover, confinement of catalytic sites in the inner space of the cavity of hemicryptophanes resulted in supramolecular organic and organometallic catalysts, with remarkable properties. We should mention herein the important contribution of Kuck *et al.* who synthesized cryptophane and hemicryptophane-like molecular cages based on the tribenzotriquinacene (TBTQ) scaffold. Recently, they reported the synthesis of hemicryptophanes where the CTV part is replaced by the TBTQ unit. This type of molecular receptors does not strictly belong to the CTV-based derivatives, but their closely related structures deserve to be pointed out in this review (Figure 1.2b).³²

In this review article, we will first introduce the general synthetic methods (Section 1.3), to obtain racemic, enantiopure, water-soluble and metallated hemicryptophane hosts. Next, the applications of hemicryptophanes in molecular recognition (Section 1.4), as molecules with controllable motions (Section 1.5), and as supramolecular catalysts (Section 1.6), will be presented. Finally we will conclude and present the perspectives on the future development of hemicryptophanes, and highlight the key challenges in this emerging area of research (Section 1.7).

1.3 Synthesis of hemicryptophanes

Hemicryptophane hosts can be classified into two main families according to the method of preparation used: covalent hemicryptophanes and self-assembled hemicryptophane capsules. Covalent hemicryptophanes refer to compounds, where the two main C₃ symmetrical units defining the ditopic character of these hosts are connected by covalent bonds. The access to covalent cages most of time needs multi-step syntheses and often the main drawback of these

syntheses is a low overall yield. Although some cage compounds are only accessible on a milligram scale, a range of laboratory-scale synthesis schemes has been developed to afford hemicryptophanes with various functionalities that can be obtained easily on gram scale, allowing wider applications. The different approaches to the syntheses of covalent hemicryptophane hosts will be presented in Section 1.3.1. The formation of self-assembled hemicryptophane capsules is currently attracting great attention due to the developments in self-assembling strategies and will be described in Section 1.3.2. For instance, hemicryptophanes formed of two interacting molecular subunits have been reported using reversible dynamic covalent interactions such as the reversible formation of boronate esters, or supramolecular ionic interactions between charged moieties. Finally, Section 1.3.3 of this review is devoted to the functionalization of hemicryptophanes to develop specific properties and to investigate their applications in catalysis and sensing in organic or aqueous media.

An important aspect of hemicryptophanes is their inherent chirality arising from the CTV unit. A greatly growing demand for chiral hosts exists and consequently, the production of enantiopure hemicryptophanes should be considered as a significant breakthrough for applications in chiral recognition or catalysis. Particular attention will be paid to this aspect throughout this chapter. The C_3 symmetry of the CTV moiety confers to the hemicryptophanes an inherent chirality with *P* or *M* configuration.³³ When associated to other stereogenic centers the hemicryptophane molecules exist as diastereomers. Thus, the synthesis of enantiopure compounds either leads to enantiomers or diastereomers and it is essential to determine their absolute configuration. A convenient method relies on the determination of the X-ray crystal structure of the enantiopure compounds. However, obtaining crystals suitable for X-ray analysis is not always easy and successful.³⁴ The use of electronic circular dichroism (ECD) spectroscopy has been widely described in the literature, and is particularly suitable to determine the absolute configuration of compounds bearing the CTV unit.³⁵ Indeed, the spectra can be interpreted as the result of the excitonic coupling of the three aromatic rings of the CTV unit, which gives a specific ECD signature.³⁵⁻³⁸ This method is relatively easy and reliable, but may also fail in some specific cases, when the ECD signals of the CTV overlap with those of other aromatic groups. In such cases, chemical correlation methods were developed and successfully applied to hemicryptophane molecules.

When compared to racemic hemicryptophanes, enantiopure cages are more useful since chirality plays a crucial role in most of the biological events, and chiral synthetic bio-inspired supramolecular systems can be designed to mimic and understand these processes.³⁹⁻⁴¹ However, the easy synthesis of this type of enantiopure molecular cages is a difficult challenge because of the high complexity of such molecules. Two main strategies can be followed to prepare enantiopure hemicryptophanes. (i) The resolution of racemic mixtures using chiral semi-preparative high-performance liquid chromatography (HPLC). The major drawbacks of this method are the necessity of a chiral HPLC and the difficulty in providing sizable amounts of compounds. (ii) The introduction of additional stereocenters to form diastereomers. This second strategy needs more complex synthesis pathways, and in most cases the separation of two diastereomers reveals tedious, but affords more sizeable amounts of enantiopure cages. Both methods appeared in the literature and will be precised in the following sections. Throughout this review article, without specific indications, the chiral

compounds described are racemates.

1.3.1 Synthesis of covalent hemicryptophanes

Covalent hemicryptophanes can be obtained by three main pathways. The first one is a cage-closing reaction to form the CTV unit (arbitrary named *north* part) and is related to the "template method" used for the synthesis of cryptophanes (Figure 1.3a).²⁴ The Friedel-Crafts condensation of the veratryl precursors is a convenient and common approach for the synthesis of cryptophanes and hemicryptophanes. The acid catalyzed cyclization reaction, using mainly HCOOH or Sc(OTf)₃, gives rise to the CTV moiety leading to the desired hemicryptophanes. The performances of this intramolecular cyclodehydration to generate the CTV in the last step, in terms of yield and difficulties in their purification, usually depend on the structures of the hemicryptophane precursors.

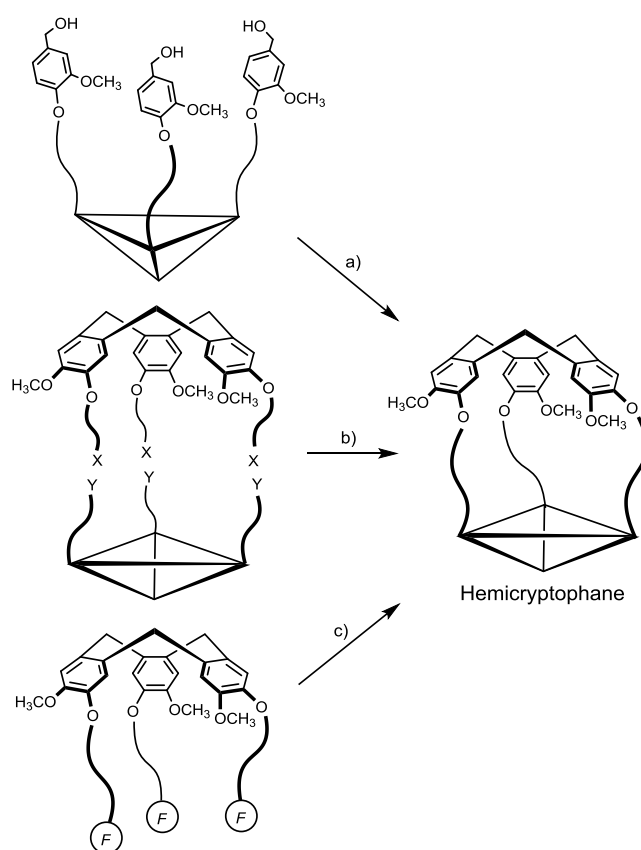


Figure 1.3 Synthesis strategies for the preparation of hemicryptophane hosts: (a) by formation of the CTV unit; (b) by [1+1] coupling of *north* and *south* parts; (c) by closure reaction at the *south* part (X, Y and F are suitable functions).

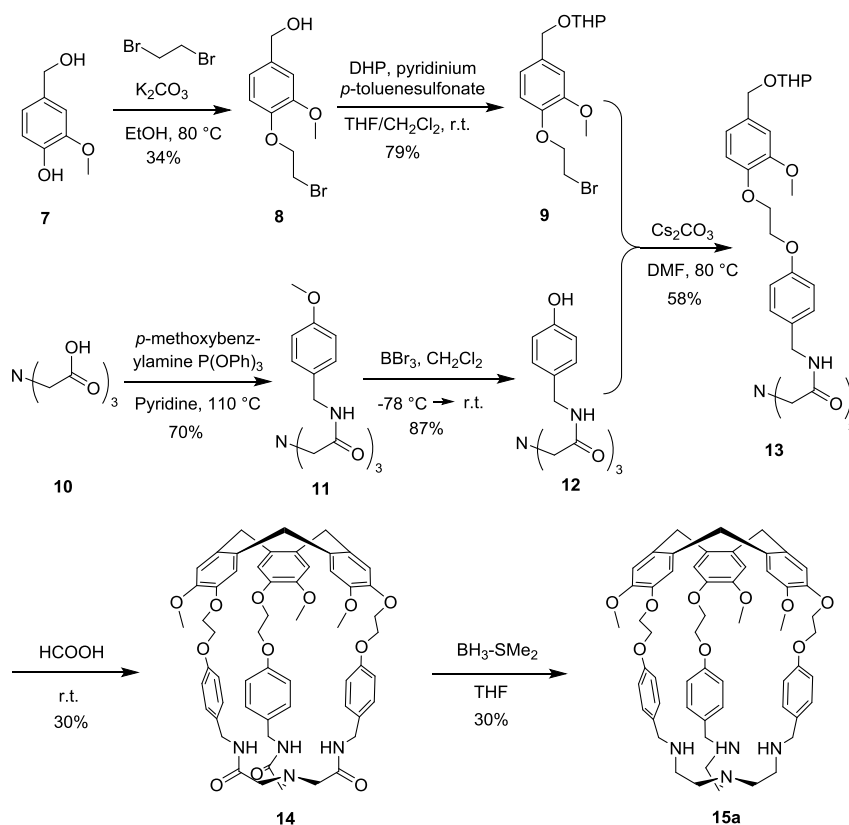
The second way is the [1+1] coupling between the *north* part and the other C₃ unit (arbitrary named *south* part), which is very effective in many cases and is particularly well suited for the preparation of enantiopure hemicryptophanes (Figure 1.3b). Moreover, this strategy allows the preparation of a wide range of ditopic molecules thanks to the numerous and versatile available *southern* moieties, and involve different approaches like the reactions of acyl chloride with primary or secondary amine, carboxyl with primary amine, Ugi reaction-type,

and disulfide-bond formation, for the most common. For instance, sophisticated structures such as crown-ethers, calixarenes and cyclodextrines were combined with the CTV cap to afford ditopic hosts with fairly good yields. This method usually requires high dilution conditions to avoid the formation of polymeric compounds.

The third way is to introduce the *southern* C₃ unit from the suitably functionalized CTV scaffold (Figure 1.3c). By this way, hemicryptophanes are formed by appending on the CTV three linkages bearing suitable functions for an intramolecular reaction that leads to the cage structure. This approach has been seldom used compared to the strategies based on the cage closure reaction at the *north* part or the [1+1] coupling presented above.

For a given compound, the authors often used either of the methods described above to increase the yields and/or to produce sizable amounts of enantiopure compounds. For instance, the [1+1] coupling between two modules has been often advantageously applied to the synthesis of hemicryptophanes already obtained by the formation of the CTV cap according to the first synthetic pathway. In the following subsections we will thus emphasize the various approaches reported in the literature for the synthesis of racemic and enantiomerically pure hemicryptophanes according to the nature of the *southern* units.

1.3.1.1 Triamide- and tren-hemicryptophanes

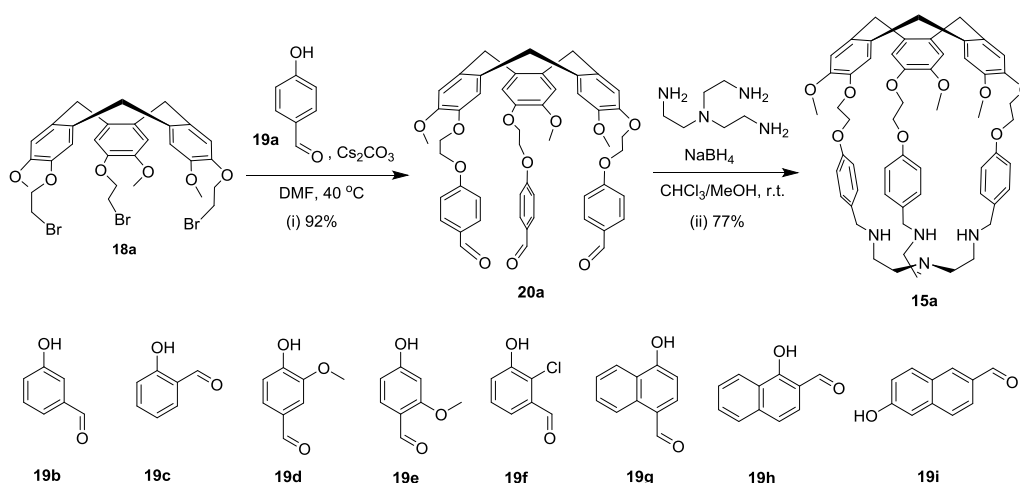


Scheme 1.1 Synthesis of Hemicryptophanes **14** and **15a**.

The triamide and the tris(2-aminoethyl)amine (*tren*) structures have been used to build receptors for the complexation of anionic^{42,43} and cationic species.⁴⁴ In particular, transition metal ions such as cobalt, zinc⁴⁵ and copper,⁴⁶ form complexes with these ligands, presenting interesting catalytic or recognition properties. Different hetero-elements have been also

trapped into a *tren* moiety, leading, in the case of phosphorus, to pro-azaphosphatrane compounds, which constitute a remarkable class of basic and nucleophilic organo-catalysts.⁴⁷

The racemic triamide- and *tren*-hemicryptophanes **14** and **15a** were first synthesized following the first method (Figure 1.3a) as depicted in Scheme 1.1.⁴⁸ The reaction of vanillyl alcohol **7** with dibromoethane in EtOH at 80 °C affords compound **8**, which is protected with THP to give **9** with an overall yield of 27%.⁴⁹ The C₃ symmetry precursor of the *south* part of the host is obtained from the nitrilotriacetic acid **10** that reacts with 3 equiv. of *p*-methoxy benzylamine in the presence of P(OPh)₃ to give the tripodal triamidoamine derivative **11**. The methoxy groups in **11** are then removed using BBr₃ to give the triphenol derivative **12**. Reacting **9** and **12** in DMF in the presence of Cs₂CO₃ affords the hemicryptophane precursor **13**. The cyclization is then performed in HCOOH to give the desired hemicryptophane **14** in 30% yield. Finally, the reduction of the amide functions is achieved with BH₃ in THF to give the *tren*-hemicryptophanes **15a** in 30% yield. The racemic triamide-hemicryptophane *rac*-**14** was resolved by chiral semi-preparative HPLC, leading to the enantiopure compounds *M*-**14** and *P*-**14**.⁵⁰ Applied to *rac*-**15a** the resolution reveals unsuccessful, underlining the limitation of the method.



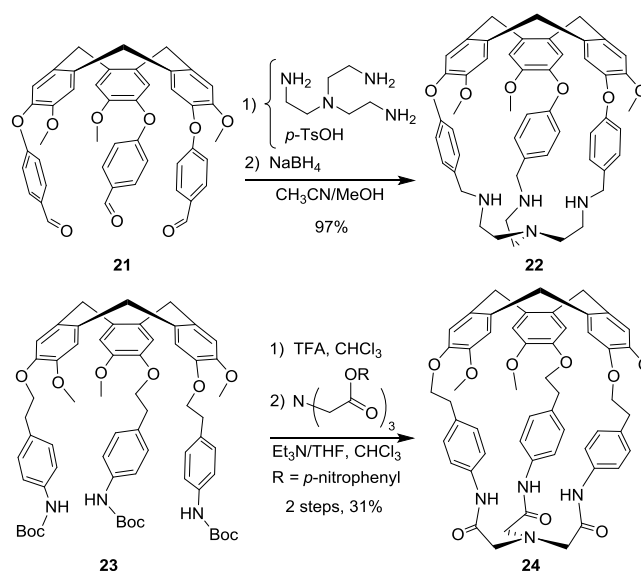
Scheme 1.2 Synthesis of Hemicryptophanes **15a-i**.

The convenient and efficient modular approach of the [1+1] coupling reaction (Figure 1.3b) was developed for the synthesis of the *tren*-based hemicryptophanes **15a-i** (Scheme 1.2).⁵¹ The alkyl-brominated CTV **18a** is first synthesized in two steps from vanillyl alcohol and dibromoethane according to the procedure described by Dmochowski *et al.*⁵² The preparation of the hemicryptophane precursor **20a** is then conducted under standard conditions by reacting **18a** with 4-hydroxybenzaldehyde (**19a**) in DMF in the presence of Cs₂CO₃ with excellent yields and without purification by column chromatography. The condensation of **20a** with tris(2-aminoethyl)-amine in CHCl₃/CH₃OH mixture, followed by a reduction step with NaBH₄, affords **15a** in 77% yield. Hemicryptophane **15a** is thus obtained in 8% overall yield via a four-step synthetic route, which improves the previous seven-step procedure (3% overall yield; Scheme 1.1) and allows the synthesis of **15a** on the gram scale. Moreover, the size, shape, and functionalities of the molecular cavity are easily modified by changing the nature of the aromatic linkages (Scheme 1.2). For instance, the cavity size was modified by changing the relative position of the aldehyde and the hydroxy groups on the aromatic rings

(hemicryptophanes **15b** and **15c**). An electron-donating group was also incorporated in the aromatic part of the linkages at different positions, leading to hemicryptophanes **15d** and **15e**, and the chlorine electron-withdrawing group was successfully integrated in the aromatic wall of the hemicryptophane **15f**. Hemicryptophanes **15g-i** with larger aromatic walls (naphthyl moieties) were obtained and showed fluorescent properties. Thus, this synthetic pathway constituted an important step in the chemistry of hemicryptophanes as it allowed production of larger amounts of compounds, which helped further applications as receptors or supramolecular catalysts.

Dutasta, Martinez *et al.* followed the pathway shown in Scheme 1.2 to develop the gram-scale preparation of enantiopure hemicryptophanes *M*-**15a** and *P*-**15a**.⁵³ The synthesis starts from the enantiopure CTV-**18a** obtained by the resolution of its racemates by chiral HPLC. To prevent the racemization of the enantiopure **18a** and **20a**, the two subsequent steps were performed at 25°C, affording the expected product with good yields and excellent enantiomeric excess for the final cages (*ee* ≥ 98%). Moreover, the enantiopure hemicryptophanes **15d**, **15f** and **15i** were also prepared from the corresponding phenols **19d**, **19f** and **19i**, respectively, highlighting the modularity of this strategy.

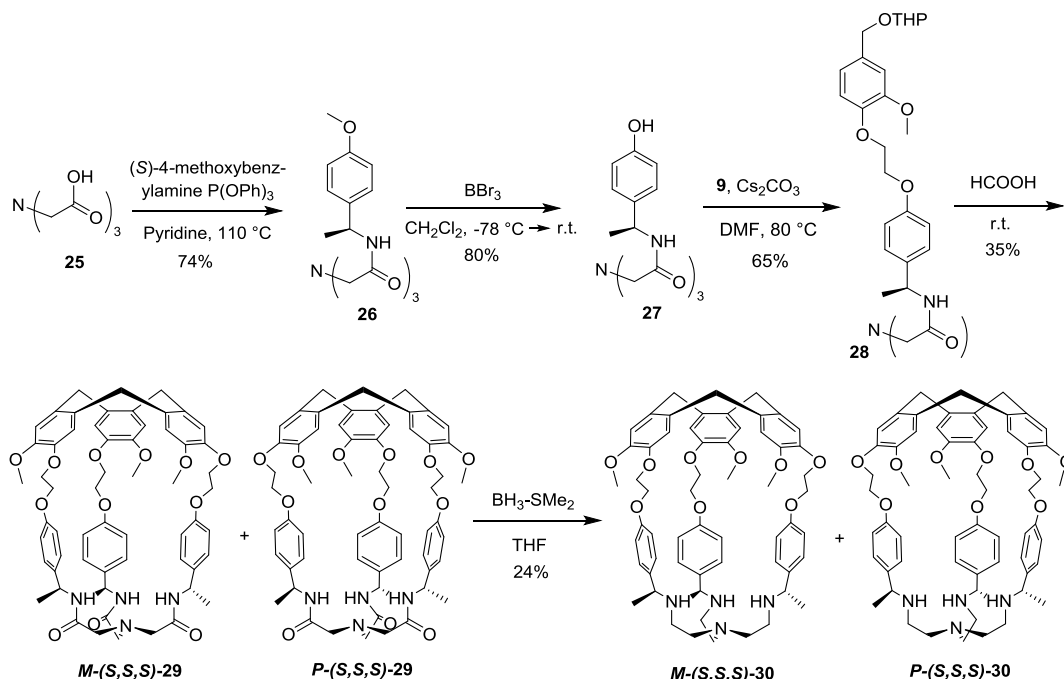
Makita and co-workers followed a similar strategy to synthesize the *tren*-hemicryptophane *rac*-**22** and triamide-hemicryptophane *rac*-**24** having smaller cavities (Scheme 1.3).^{54,55} It is noteworthy that hemicryptophane **22** was obtained in 97% yield from the precursor **21**,⁵⁴ demonstrating the high efficiency of this synthetic method. The triamide derivative **24** was obtained in a two-step synthesis. Removal the tri-*tert*-butoxycarbonyl (Boc) protecting groups from precursor **23**, and subsequent coupling with nitrilotriacetic acid tris(*p*-nitrophenyl ester) afforded hemicryptophane **24** in 31% overall yield. Hemicryptophane **24** was able to bind tetraalkylammonium salts and exhibited a strong affinity for acetylcholine neurotransmitter.



Scheme 1.3 Synthesis of Hemicryptophanes **22** and **24**.

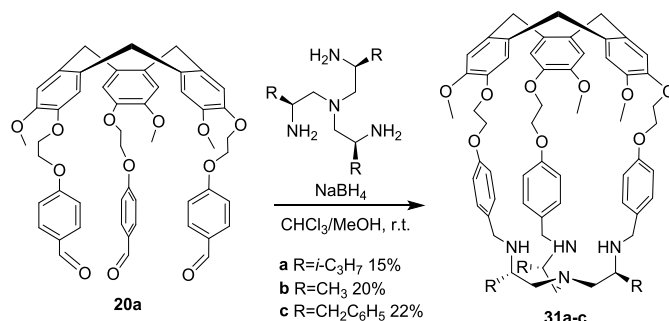
Compared to respectively **14** and **15a**, hemicryptophane stereoisomers *M*-(*S,S,S*)-**29/30**, *P*-(*S,S,S*)-**29/30**, *M*-(*R,R,R*)-**29/30** and *P*-(*R,R,R*)-**29/30**, possess three additional stereogenic centers (Scheme 1.4).^{56,57} Interestingly, by introducing these new chiral centers in **29** avoids

chiral HPLC to separate the enantiomers, and also makes this class of hosts more promising for stereoselective recognition experiments. A synthetic pathway similar to that used for **14** afforded hemicryptophanes **29** starting from the chiral (*S/R*)-4-methoxy- α -benzylamine. The two diastereomers *M*-(*S,S,S*)-**29** and *P*-(*S,S,S*)-**29** were separated by preparative achiral TLC. Direct reduction of the amides of the mixture of the two diastereomers **29** gives the two stereoisomers of **30**, which are readily separated by column chromatography on silica gel.⁵⁷



Scheme 1.4 Synthesis of Hemicryptophanes *M*-(*S,S,S*)-**29/30** and *P*-(*S,S,S*)-**29/30**.

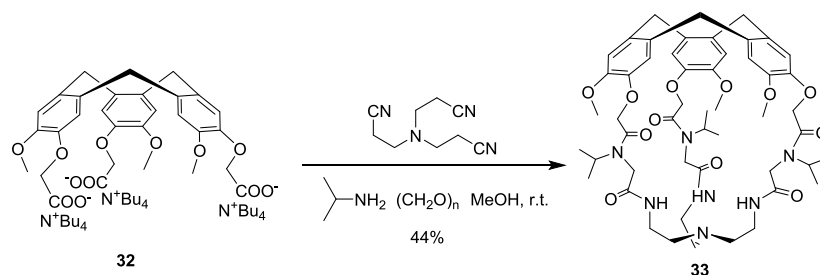
An easy synthesis of enantiopure hemicryptophanes **31a-c** via the thermodynamic resolution of the racemic CTV **20a** (Scheme 1.2), leading to enantiomerically pure compounds, was reported (Scheme 1.5).⁵⁸ It was found that when using enantiopure *tren* derivative as the other modular compound, only one diastereomeric cage was formed whatever the nature of the substituents located on the *tren*'s stereogenic centers. This route provides an original access to enantiopure hemicryptophanes avoiding the separation of two diastereomers.



Scheme 1.5 Synthesis of Hemicryptophanes **31a-c**.

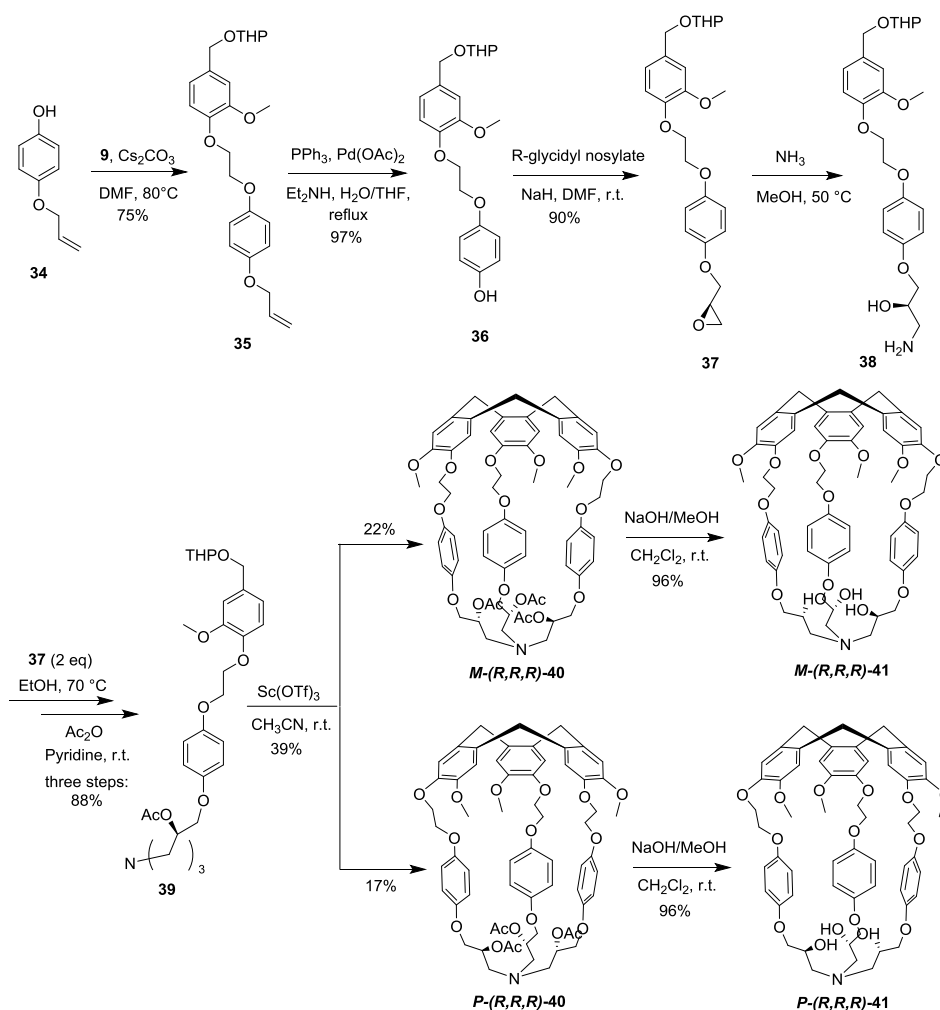
Rivera *et al.* developed a very efficient and straightforward method, featuring the one-pot assembly of molecular architectures by Ugi-type multiple multicomponent macrocyclization of trifunctional building blocks, for the synthesis of the hemicryptophane **33** bearing

Ugi-peptoid backbones.⁵⁹ In this approach, four components, *i.e.* CTV-tricarboxylic acid **32**, a primary amine, an oxo compound, and an isocyanide are required for the three-fold Ugi-reaction (Scheme 1.6). A methanol solution of tetra-*n*-butyl ammonium salt of CTV-tricarboxylic acid **32** is gradually added to a solution of paraformaldehyde and amine, followed by the slow addition of tris(2-isocyanoethyl)amine. The hemicryptophane **33** is thus obtained with acceptable yields after purification by flash column chromatography. Apart from the simplicity for constructing complex molecules, another key feature is the variability of the tris-functionalized scaffolds with defined geometries to build various molecular cages.



Scheme 1.6 Synthesis of Hemicryptophane **33**.

1.3.1.2 Trialkanolamine hemicryptophanes



Scheme 1.7 Synthesis of Hemicryptophanes *M*-(*R,R,R*)-**41** and *P*-(*R,R,R*)-**41**.

Hemicryptophanes combining CTV and triethanolamine groups such as compound **41** (Scheme 1.7), are particularly interesting for their potential as ligands for endohedral metal coordination. The synthesis of the enantiopure hemicryptophanes **41** was reported in 2005 and was facilitated by the introduction of additional stereocenters to form diastereomers.⁶⁰ As shown in Scheme 1.7, allyloxyphenol **34** reacts with compound **9** in the presence of Cs_2CO_3 in DMF to give **35**, which is subsequently deprotected to generate the phenol derivative **36**. The epoxide **37** is synthesized by a regioselective nucleophilic substitution reaction of **36** on (*R*)-(-)-glycidyl nosylate in DMF. Then an excess of ammonia is added to the methanol solution of **37** to give the primary amine **38**. The hemicryptophane precursor **39** is obtained by a trimerization reaction of **38** with 2 equiv. of the epoxide **37** in methanol followed by an acetylation reaction to decrease the polarity and facilitate the purification. An intramolecular cyclization of **39** is then accomplished using $\text{Sc}(\text{OTf})_3$ as Lewis acid in CH_3CN to produce hemicryptophanes *M*-(*R,R,R*)-**40** and *P*-(*R,R,R*)-**40** in their diastereomerically pure form with yields of 22% and 17%, respectively after separation by column chromatography. Finally, the synthesis of hemicryptophanes *M*-(*R,R,R*)-**41** and *P*-(*R,R,R*)-**41** is achieved quantitatively from the corresponding hemicryptophane **40** by hydrolysis with methanolic NaOH. Starting from the (*S*)-(+)-enantiomer of glycidyl nosylate, the other diastereoisomeric pair, *P*-(*S,S,S*)-**41** and *M*-(*S,S,S*)-**41**, were also successfully prepared using the same synthetic pathway.

The determination of the absolute configuration of the four stereoisomers of **41** was achieved using ECD spectroscopy. The *P*-configuration of the enantiopure hemicryptophane gave rise to a characteristic positive-negative bisignate (from low to high energies, 270-230 nm). In turn, the *M*-configuration is assigned to the hemicryptophane that gives a negative-positive bisignate, as observed in Figure 1.4.⁶⁰

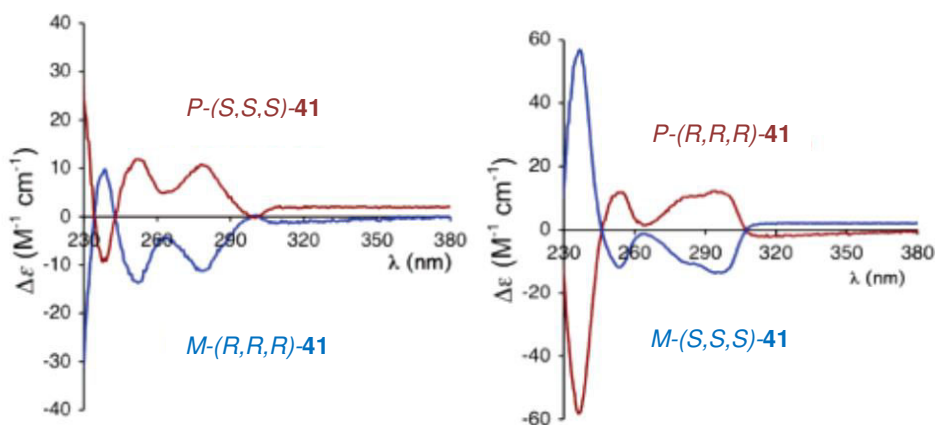
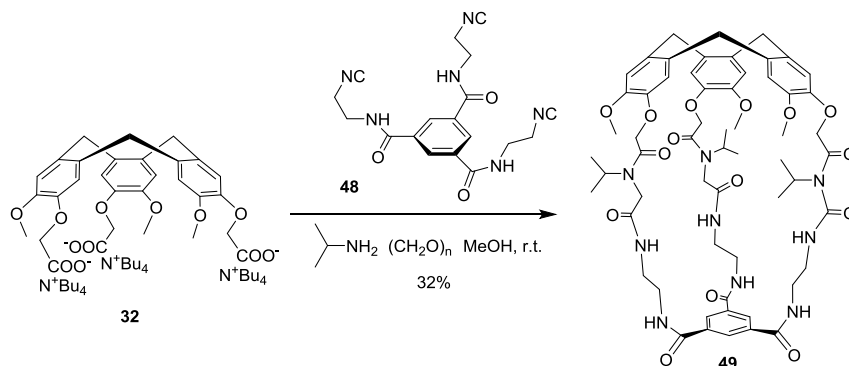


Figure 1.4 ECD spectra of the four stereoisomers of hemicryptophane **41** in CH_2Cl_2 at 20 °C.

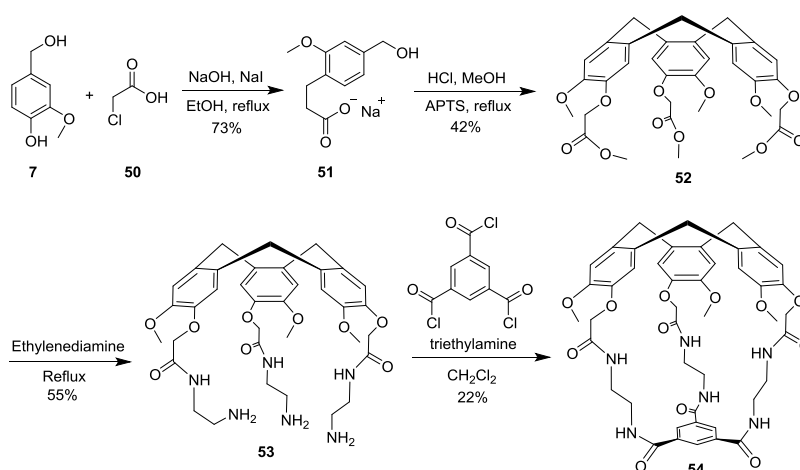
1.3.1.3 Hemicryptophanes based on a tripodal benzenic-platform

The benzenic ring is a simple and attractive unit to close a covalent cage because of its high modularity. Indeed, depending on the nature of the substituents attached to this moiety (withdrawing or electro-donating groups), it can either interact with anions, cations or neutral guests by anion- π , cation- π or CH- π interactions, respectively. The following examples are representative of the variety of strategies used for the construction of hemicryptophanes from a tripodal benzenic platform.

Rivera *et al.* applied the Ugi-type multiple multicomponent macrocyclization to the synthesis of hemicryptophane **49**.⁵⁹ Following the same synthesis pathway described for hemicryptophane **33** (Scheme 1.6) and adding the trisocyanide **48** to CTV **32**, they obtained the cage compound **49** bearing a C₃ symmetry tricarboxamide platform (Scheme 1.8).



Scheme 1.8 Synthesis of Hemicryptophane **49**.

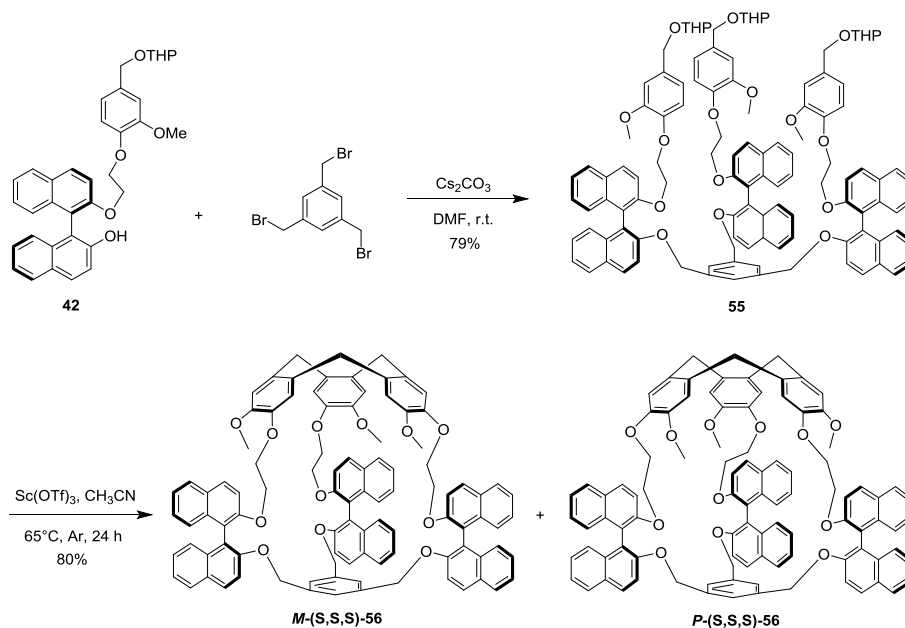


Scheme 1.9 Synthesis of hemicryptophane **54**.

Another example of tris amido-aromatic hemicryptophane was also synthesized from CTV derivative **53** and benzene-1,3,5-tricarbonyl trichloride, still using the [1+1] coupling reaction, to give compound **54** (Scheme 1.9).⁶³ Vanillyl alcohol **7** reacts with chloroacetic acid **50** in the presence of NaI and NaOH in EtOH to give compound **51**. The formation of the CTV **52** is performed by a one-pot synthesis by first adding one equivalent of HCl to **51** and then a catalytic amount of *p*-toluenesulfonic acid in MeOH. The resulting compound **52** is then condensed in pure ethylenediamine to give **53**. Finally, the [1+1] coupling between **53** and 1,3,5-benzenetricarbonyl trichloride generates the hemicryptophane **54** in four steps and with 4% overall yield from vanillyl alcohol without any chromatography.

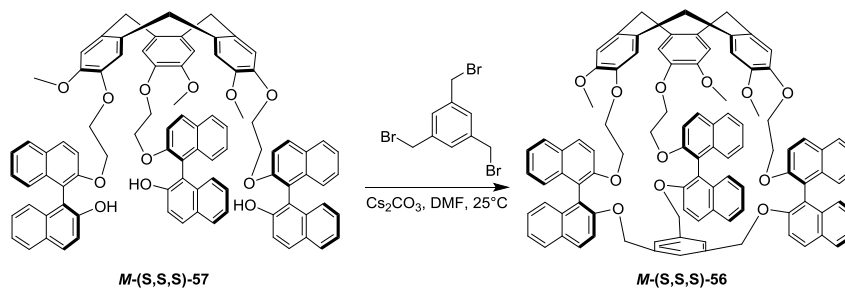
Hemicryptophanes bearing three BINOL groups in the linkages and a 1,3,5-trisubstituted aromatic ring at the *south* part, were also synthesized and afforded the four hemicryptophane stereoisomers of **56** (Scheme 1.10).⁶⁴ Starting from the (*S*)-BINOL derivative **42**, the hemicryptophane precursor **55** was obtained in one step by the reaction of **42** with tris(bromomethyl)benzene in DMF using Cs₂CO₃ as base. The macrocyclization of the precursor **55** in CH₃CN catalyzed by Sc(OTf)₃ gave the first pair of diastereomers of

hemicryptophane **56** with a moderate diastereoselectivity. The other pair of stereoisomers was synthesized using the same way starting from the (*R*)-BINOL derivative.



Scheme 1.10 Synthesis of Hemicryptophanes *M*-(*S,S,S*)-**56** and *P*-(*S,S,S*)-**56**.

The absolute configurations of the stereoisomers *M*-(*S,S,S*)-**56**, *P*-(*S,S,S*)-**56**, *M*-(*R,R,R*)-**56** and *P*-(*R,R,R*)-**56** were assigned using the chemical correlation method. For this, the authors synthesized the stereoisomers of **56** by the [1+1] coupling of diastereomerically and enantiomerically pure CTV **57** suitably substituted with BINOL arms, with 1,3,5-tris(bromomethyl)benzene as shown in Scheme 1.11 for *M*-(*S,S,S*)-**56**.⁶⁴



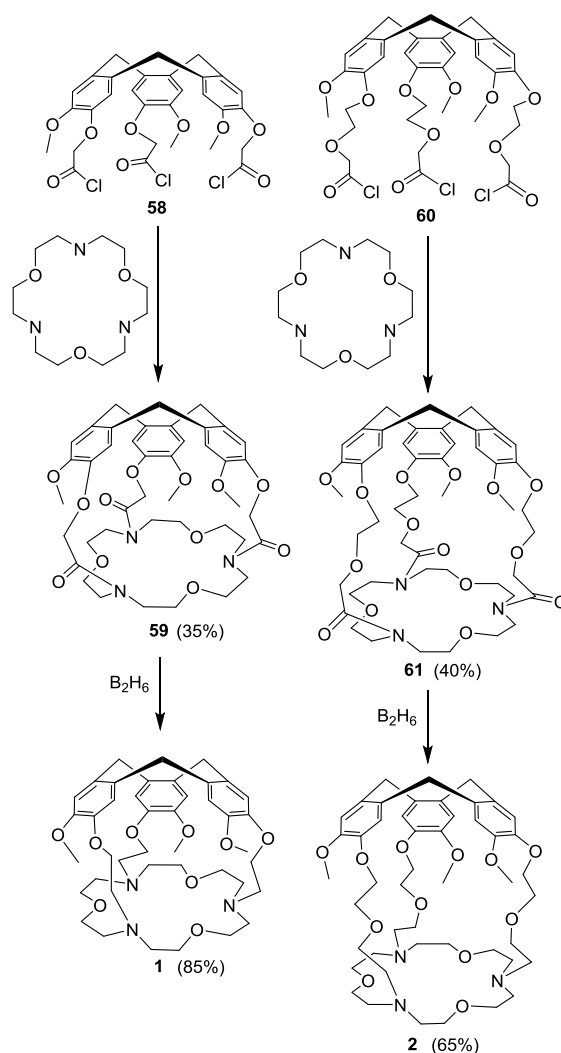
Scheme 1.11 Synthesis of Hemicryptophane *M*-(*S,S,S*)-**56** using the [1+1] Coupling Reaction.

1.3.1.4 Hemicryptophanes based on a macrocyclic platform

Macrocyclic units like calixarenes or cyclodextrines have been linked to CTV units, in order to combine in a single hemicryptophane molecule the recognition properties of both compounds. The syntheses of the resulting heteroditopic hosts are presented below.

Hemicryptophanes based on an aza-crown ether: speleands. The synthesis of the first two hemicryptophane derivatives (speleands **1** and **2**) developed by Collet and Lehn were achieved using the [1+1] coupling method.²⁷ As shown in Scheme 1.12, condensation of the trichloride **58** with the azacrown ether [18]-N₃O₃ under high dilution conditions afforded the tricarboxamide hemicryptophane **59** in 35% yield. Then, reduction of **59** with diborane gave

the hemicryptophane **1** in 85% yield. Starting from the trichloride **60** and following the same reaction sequence, the hemicryptophane **2** with a larger cavity was synthesized with an overall yield of 26%.

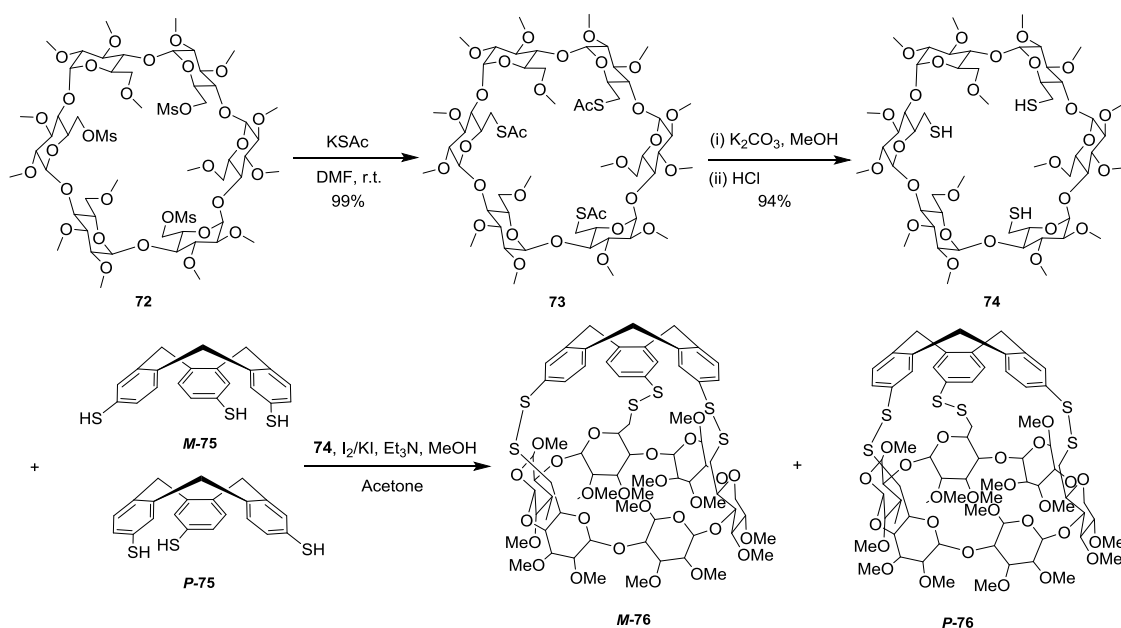


Scheme 1.12 Synthesis of Speleands **1** and **2**.

Hemicryptophanes based on a cyclopeptide platform. Hutton *et al.* synthesized a new class of enantiopure cyclic peptide-containing hemicryptophanes *PL-67* and *ML-67* (Scheme 1.13) able to recognize the biologically relevant carnitine zwitterion.⁶⁵ Three tyrosine residues provide hydrophobic ‘wall’ to the cavity, and glycine was chosen for the alternate residues to facilitate the synthesis of the cyclic peptide and to minimize steric bulk within the cage. Firstly, cleavage of the hexapeptide from the resin with 5% TFA gives the unprotected linear peptide **63**. The cyclization of compound **63** generates the cyclic peptide **65** in quantitative yield after 1 h. Compound **65** can also be prepared starting from the cleavage of the hexapeptide from the resin with 1% TFA, however, an additional deprotection step is required (see Scheme 1.13). The cyclic hexapeptide **65** is then triply alkylated with bromoethyl vanillyl alcohol **9** to give hemicryptophane precursor **66** in 55% yield. Finally the CTV unit was generated by treatment of **66** with HCOOH, providing **67** in good yields (64%) as a mixture of two diastereomers. The *P*- and *M*-isomers were formed in a 2:1 ratio and were separated by column chromatography.

hemicyptophane precursor has been tested with HCOOH or Sc(OTf)₃ as catalysts, however, both of them gave very low yields for the mixture of the two diastereomers of **71**, 8% and 5%, respectively. The separation by column chromatography of the two diastereomers obtained in a 6:1 ratio allowed the authors to isolate the main diastereomer in pure form. Interestingly, hemicyptophane **71** acts as a solvent sensitive NMR and ECD probe. Inclusion of a solvent molecule in the α -CD component of the hemicyptophane induces conformational changes that result in the shielding of the primary methoxy (6'-OMe) protons of the α -CD unit, which increases with the size of the chloroalkane solvent.⁶⁷

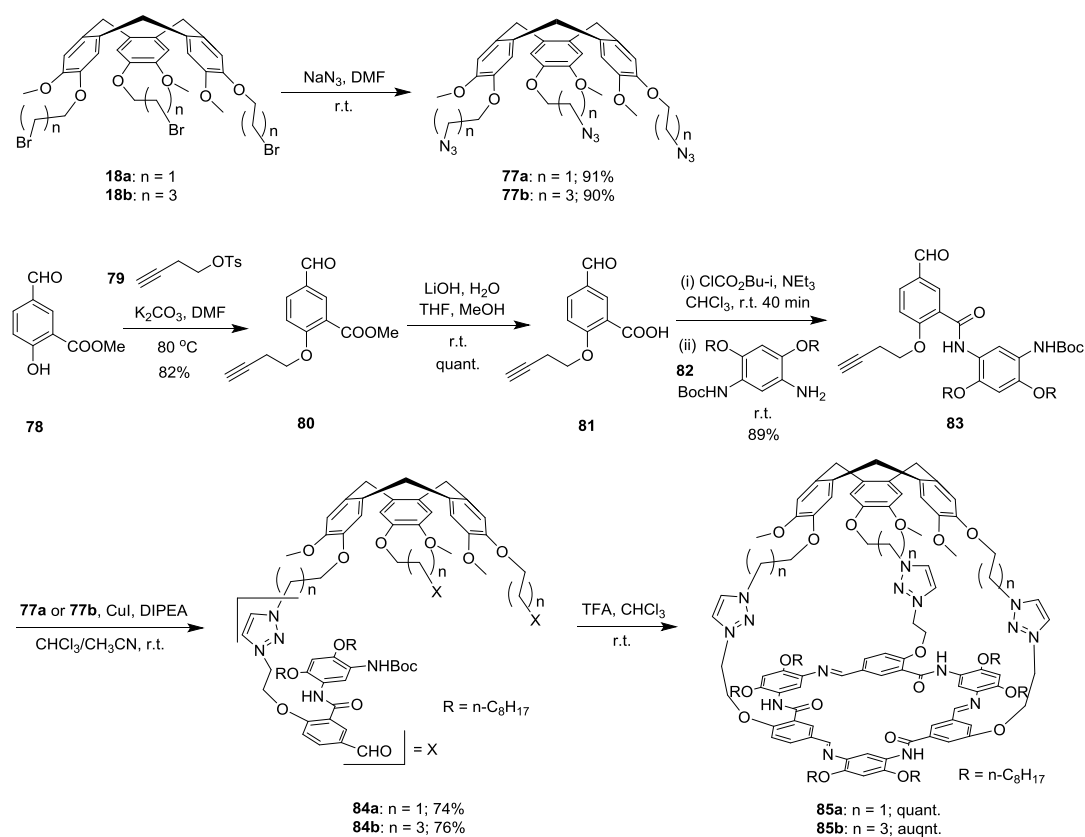
The formation of disulfide bonds was also used for constructing hemicyptophanes based on a α -cyclodextrine scaffold following the [1+1] coupling strategy (Scheme 1.15).⁶⁸ The trimesylate α -cyclodextrine **72** reacts with potassium thioacetate in DMF to give compound **73** in quantitative yield after column chromatography. Subsequently, methanolysis of **73** in the presence of K₂CO₃ in MeOH followed by acidification of the mixture with HCl, affords the tris-methylthiol α -cyclodextrine **74**. The addition of a solution of I₂ in MeOH to a methanol solution of **74** and racemic cyclotrithiophenolene **75** in the presence of KI and triethylamine, generates the final hemicyptophane **76** in 11% yield as a 5:3 mixture of two diastereomers that could not be separated.



Scheme 1.15 Synthesis of Hemicryptophanes *M-76* and *P-76*.

Hemicryptophanes based on a macrocyclic arylamide platform. Wang *et al.* synthesized hemicryptophanes **85a** and **85b** starting from the CTV tribromides **18a** and **18b** (Scheme 1.16).⁶⁹ This synthesis follows the seldom-used strategy consisting in preparing a cyclotriphenylene bearing suitably functionalized pendant arms that react together to form the hemicryptophane derivative (Figure 1.3c). The authors first treated **18a** or **18b** with an excess of NaN₃ in DMF to form the triazide derivatives **77a** and **77b**, respectively. Then, the alkynyl-methylbenzoate derivative **80** was prepared from **78** and **79** in DMF in the presence of K₂CO₃ at 80°C and was further hydrolyzed with LiOH to give **81** quantitatively. The acid **81** was then coupled with **82** in CHCl₃ to generate the compound **83**, which then reacts with **77a**

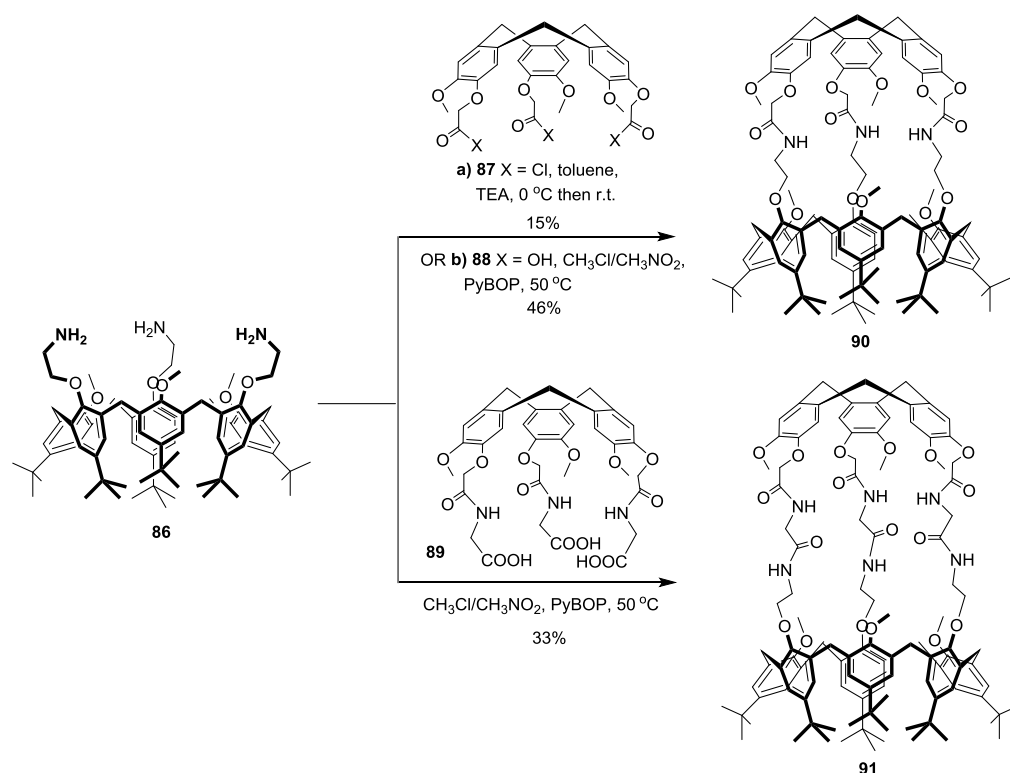
or **77b** in the presence of CuI to give the hemicryptophane precursors **84a** or **84b**. Finally, the hemicryptophanes **85a** and **85b** are assembled quantitatively by forming three imine bonds from arylamide-derived foldamer segments after adding TFA to the CHCl_3 solution of **84a** and **84b**. In principle, each of the two hemicryptophanes should have four stereoisomers, two pair of enantiomers, because of the relative orientation of the CTV and triimine macrocyclic units. However, only one set of signal is observed in the ^1H NMR spectra, suggesting that only one isomer (or a pair of enantiomers) was formed in the final step. Molecular dynamic simulations demonstrated that isomers, where the methoxy of the CTV moiety and the imine groups are arranged in *anti* with respect to one another located on either side of the related linkages, are more energetically favorable and are probably the observed products in solution. Hemicryptophanes **85a** and **85b** turned out to be good receptors for C_{60} and C_{70} fullerenes (see Section 1.4.2.5).



Scheme 1.16 Synthesis of Hemicryptophanes **85a** and **85b**.

Hemicryptophanes based on calixarene. Based on the reaction between tris-acyl chloride and tris-amino compounds, Jabin and coworkers synthesized hemicryptophane **90** with a calix[6]arene platform (Scheme 1.17).⁷⁰ The [1+1] macrocyclization reaction between calix[6]arene **86** and CTV **87** was first performed under high dilution conditions giving the hemicryptophane **90** in 15% yield after flash chromatography purification. With the aim of improving the yield, they also tested and optimized the reaction between calix[6]trisamine **86** and CTV tris-acid **88** in the presence of peptide-coupling reagents such as PyBOP (benzotriazol-1-yloxy)tripyrrolidinophosphonium hexafluorophosphate), to produce **90** with a much better yield (46%). Under the same reaction conditions, they also obtained the hemicryptophane **91** containing a wider cavity and a larger number of hydrogen bond donors,

in 33% yield (Scheme 1.17).

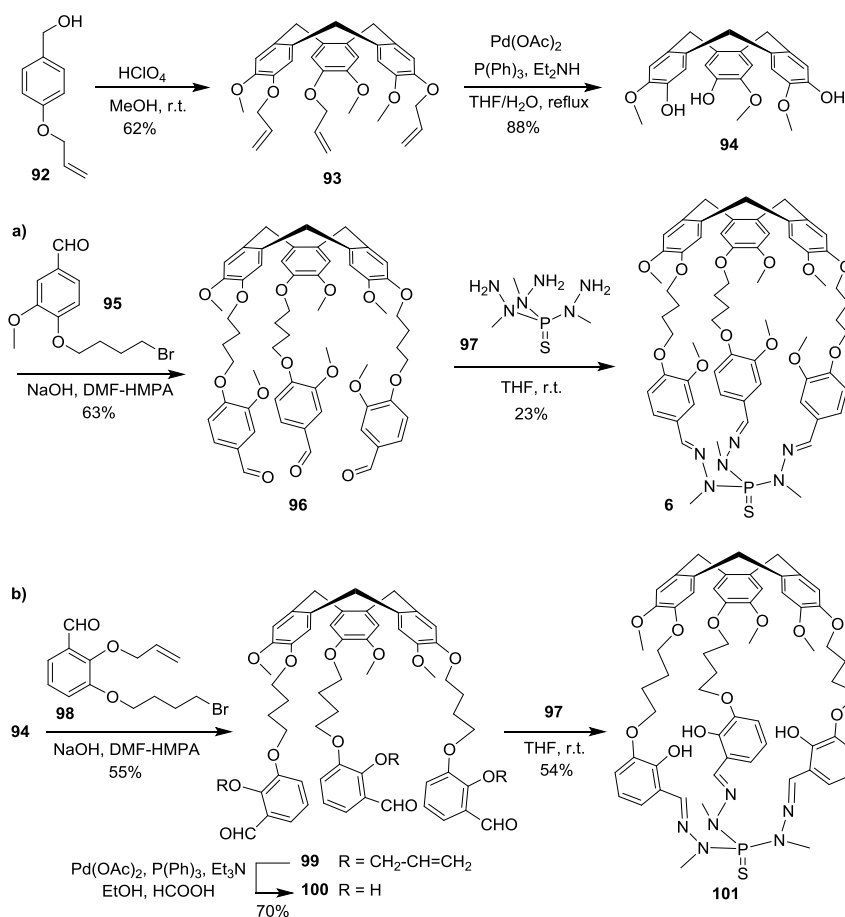


Scheme 1.17 Synthesis of Hemicryptophanes **90** and **91**.

1.3.1.5 Hemicryptophanes based on heteroatomic pivot

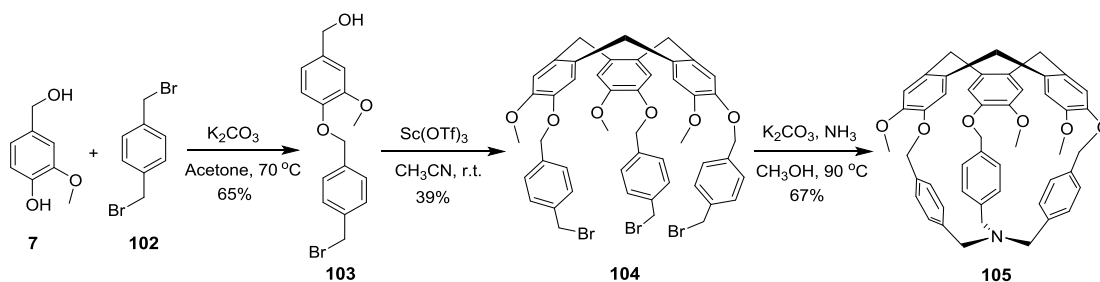
Hemicryptophanes with a phosphotrihydrazone core. Following the [1+1] strategy, the racemic hemicryptophane **6** was successfully obtained (Scheme 1.18a).³⁰ The trisallyl CTV **93** was first prepared from the allyl-protected vanillyl alcohol **92** in perchloric acid and methanol. The Pd-catalyzed deprotection of **93** in the presence of Et₂NH in THF/H₂O led to the cyclotriguaiacylene **94**, which reacted with the brominated derivative **95** in the presence of aqueous NaOH in DMF-HMPA to give the precursor **96** bearing three benzaldehyde moieties. Finally, **96** reacted with phosphotrihydrazide **97** in THF under high dilution conditions affording the hemicryptophane **6** in 23% yield. It was proposed that the success of the last reaction is partly attributed to the rather rigid conformation of the phosphorus derivative.

A similar synthetic scheme led to hemicryptophane **101**, which was specifically designed to complex iron and gallium ions (Section 1.3.3.2). The reaction of the cyclotriguaiacylene platform **94** with allyl-protected benzaldehyde **98** afforded the precursor **99**. Subsequent deprotection step led to compound **100** that was allowed to react with phosphotrihydrazide **97** to give hemicryptophane **101**(Scheme 1.18b).⁷¹



Scheme 1.18 Synthesis of Hemicryptophanes **6** (a) and **101** (b).

Hemicryptophanes with an amine core. The synthesis of hemicryptophane **105** was reported by Dmochowsky *et al.*,⁵² where vanillyl alcohol **7** reacted with dibromo-*p*-xylene **102** in the presence of K_2CO_3 to form compound **103**, which was treated with a catalytic amount of $\text{Sc}(\text{OTf})_3$ in CH_3CN to afford the hemicryptophane precursor **104** (Scheme 1.19). In the last step, compound **104** reacted with 7N NH_3 in MeOH at high temperature to give the hemicryptophane **105** in 67% yield. It can be noted that this short streamlined synthetic scheme utilizes mild conditions and results in a fairly good overall yield (13%).

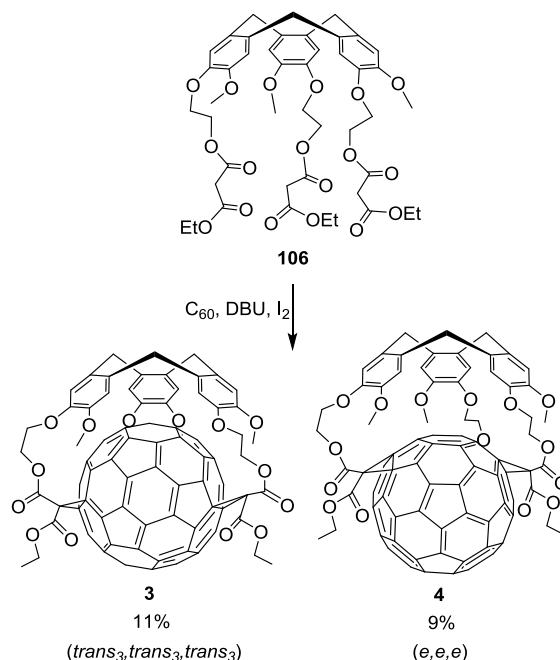


Scheme 1.19 Synthesis of Hemicryptophane **105**.

1.3.1.6 Hemicryptophanes formed from a covalent CTV-C60 adduct

The concave electron-donor aromatic surface of the CTV scaffold is known to interact favorably with electron-acceptor fullerenes C_{60} or C_{70} .⁷²⁻⁷⁴ Diederich *et coll.* used this property to build a covalent CTV- C_{60} assembly that led to a hemicryptophane-like architecture. The

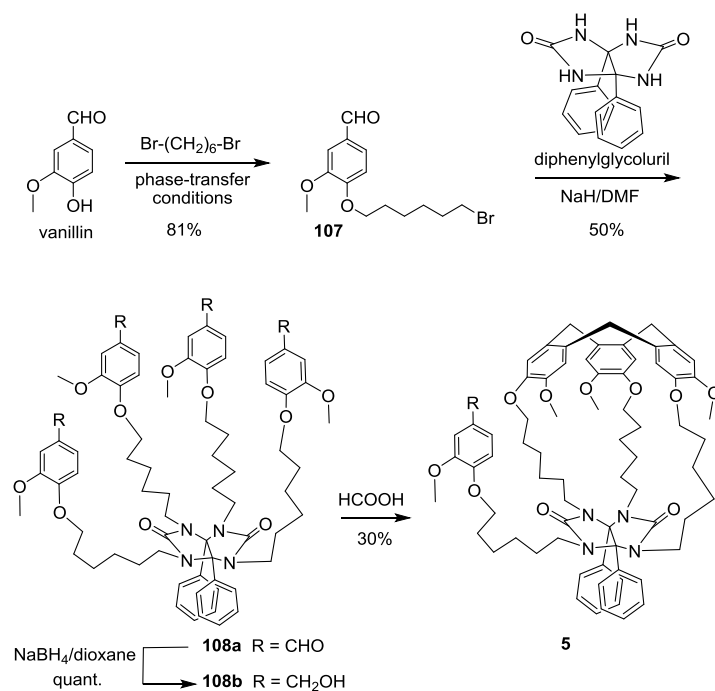
tether-directed Bingel reaction of C_{60} with the tris-malonate CTV derivative **106** led in one step to C_3 -symmetrical CTV- C_{60} tris-adducts **3** and **4** (Scheme 1.20).^{29,75} Although no available cavity is observed in **3** and **4**, these adducts can be considered as hemicryptophane structures. Many regioisomers are expected that complicate the determination of the stereochemistry of the isolated compounds.⁷⁶ In their former work, Diederich and colleagues isolated the *trans*-3,*trans*-3,*trans*-3 and *e,e,e* regioisomers, which were characterized by their FAB-Mass spectra, UV-vis and NMR spectroscopies. Later on, the authors performed a new synthesis from the enantiomerically pure CTV units *P*-**106** and *M*-**106** to get more insights into the structure and configuration of the CTV- C_{60} adducts. In this work, they observed the exclusive formation of only four CTV- C_{60} adducts among the $2^3 = 8$ expected ones, according to the combination of *trans*-3,*trans*-3,*trans*-3 or *e,e,e* with the (*P*) or (*M*) configurations of the CTV units. The ECD and VCD spectra allowed the assignment of the tris-adducts and their absolute configuration based on the known absolute configuration of the enantiopure CTV units *P*-**106** and *M*-**106**. These results revealed that only the *trans*-3,*trans*-3,*trans*-3 tris-adducts were formed underlining the complete regioselectivity of the addition of **106** with C_{60} .⁷⁷



Scheme 1.20 Synthesis of C_{60} -CTV tris-adducts **3** and **4**.

1.3.1.7 Hemicryptophanes constructed from a diphenylglycoluril unit

Nolte *et al.* reported in 1989 the preparation of one of the first hemicryptophane structures. The cage molecule (**5**) was constructed from the CTV scaffold and a diphenylglycoluril *southern* unit that did not satisfy the expected C_3 symmetry, giving rise to a molecular cage with a free functionalized arm. The strategy used is depicted in Scheme 1.21: vanillin reacts first with 1,6-dibromohexane to give **107**, which then reacts with diphenylglycoluril to give the precursor **108a** with four *n*-hexyl arms terminated with vanillyl groups. Reduction with $NaBH_4$ affords the corresponding benzylic alcohol derivative **108b**, which is treated in formic acid to produce the expected hemicryptophane **5**.²⁸



Scheme 1.21 Synthesis of Hemicryptophane 5.

1.3.1.8 Hemicryptophanes obtained by metal coordination

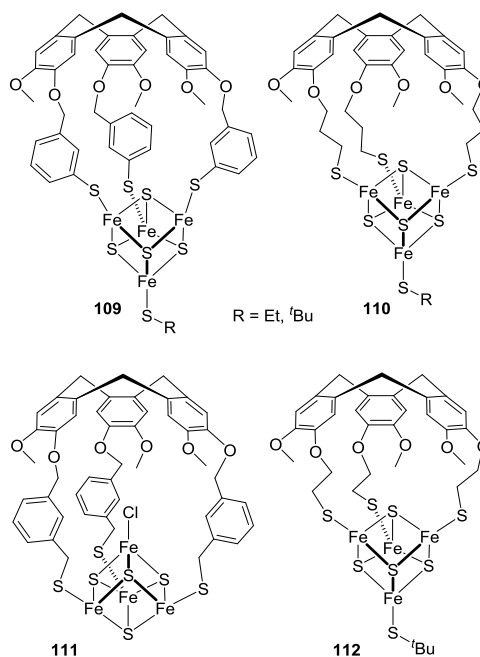


Figure 1.5 Structures of hemicryptophanes built on [4Fe-4S] clusters.

Although they are not strictly covalent hemicryptophane hosts, several CTV metal complexes gave rise to original hemicryptophane structures. Functionalized CTVs with three pendant arms have been prepared as new C_3 symmetrical ligands for metal coordination. For example, by incorporating thiol groups on the arms, the cyclotriveratrylene derivatives thus obtained were able to complex iron-sulfur clusters. Collet *et al.* reported in 1994 the formation of complexes **109** and **110** (Figure 1.5).⁷⁸ The same year, the group of Nolte synthesized very similar ligands, which reacted with various [4Fe-4S] clusters affording complexes such as **111**

and **112** presented in Figure 1.5. It was shown that for hemicryptophane **111** with Fe-Cl bond, the chloro ligand was pointing toward the cavity, whereas the Fe-SR group in **112** is oriented outside the cavity.⁷⁹

Several C_3 cyclotrimeratrylene ligands featuring three arms ending with catecholate, hydroxamate, bipyridine or iminopyridine moieties were synthesized for the octahedral coordination of iron(II) and iron(III) (Figure 1.6). Ligands bearing various pendant arms (a-h in Figure 1.6) were generally obtained by reaction of CTV precursors such as **52**, **53** or **88** with the corresponding suitable reagents.³¹ Magnetic and electrochemical properties of iron(II) complexes **113e-h** were investigated. As an example, compound **113g** was characterized by X-ray diffraction and Mössbauer spectroscopy, and it has been shown that both low-spin and high-spin states coexist in the solid. These iron complexes contains two stereogenic elements possibly leading to the two diastereomeric racemates ($M\Delta/P\Lambda$) and ($M\Lambda/P\Delta$). Interestingly, in the X-ray molecular structure of **113g** only the ($M\Delta/P\Lambda$) pair of enantiomers was found.⁸⁰

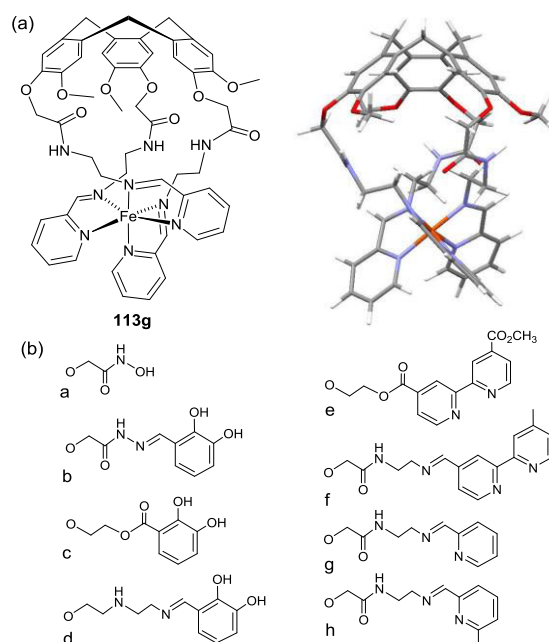


Figure 1.6 Hemicryptophane **113g** obtained by complexation of iron ion: (a) X-ray molecular structure, (b) different linkages used in the construction of complexes **113a-h**.

In 1995 Nolte and co-workers published also a rhodium complex of a CTV ligand bearing three arms terminated by triphenyl phosphite functions. The hemicryptophane complex thus obtained is quite flexible and the cavity occupied by the spacer arms.⁸¹

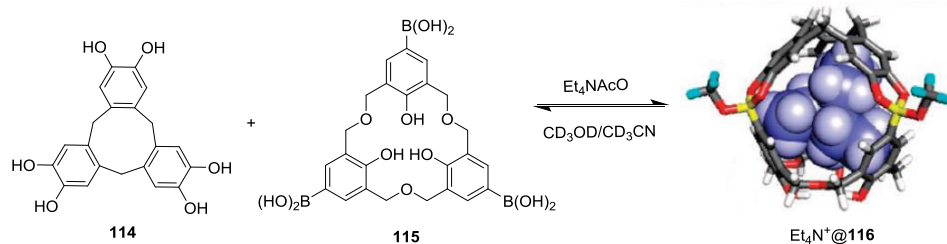
1.3.2 Formation of hemicryptophane capsules by reversible bonds/interactions

Association of two or more CTV units has led to interesting self-assembled supramolecular systems, which present a molecular cavity. We will not report on these cage structures, which are out of the scope of this review article. They are more like reversible capsules with C_3 symmetry when two cyclotribenzylene caps self arranged to form a cryptophane like

structure.⁸²⁻⁸⁵ Some can also form MOF-type structures,⁸⁶ when several cyclotribenzylene units are held together through metal coordination.⁸⁷⁻⁹² However, besides the covalent synthesis of hemicryptophane cages, reversible covalent bonds, such as dynamic boronate esterification,^{93,94} and reversible supramolecular interactions, such as ionic interaction,⁹⁵ have also been developed for the construction of hemicryptophane capsules. Compared to the covalent synthesis, the self-assembling is straightforward and can avoid tedious purification procedures. However, the lower stability of the resulting cages can be a main drawback, as mentioned for self-assembled architectures using reversible bonds/interactions.⁹⁶⁻⁹⁹ Furthermore, the assemblies are usually driven by external template molecules, which may go inside the cavity of the hemicryptophane capsules, preventing the access to their inner cavities to other guest molecules.¹⁰⁰

1.3.2.1 Formation by boronate esterification

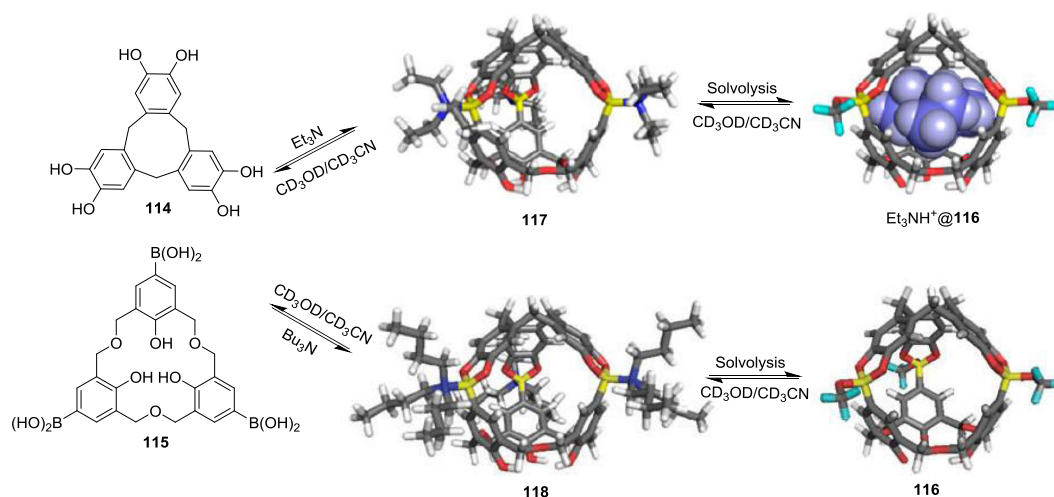
Boronic acids can rapidly and reversibly form cyclic boronate esters with diols showing great promise for developing self-assembled hemicryptophane capsules.^{101,102} For example, Kataoka *et al.* described the ion pair-driven hemicryptophane self-assembled capsule **116** using cyclotriatechylene **114** and boronic acid-appended hexahomotrioxacalix[3]arene **115** via boronate esterification (Scheme 1.22).⁹³ Individually, **114** exhibits a bowl-shaped structure, whereas **115** presents a flexible conformation. No assembled capsule is formed when mixing **114** and **115** in CD₃OD/CD₃CN since no change of the ¹H NMR chemical shifts of **114** and **115** is observed. However, when 3 equiv. of Et₄N⁺AcO⁻ are added to this solution, the ¹H NMR spectrum changed significantly, especially the ethereal protons in **115** become a doublet, suggesting that the conformation of **115** is frozen into a cone conformation. In addition, the encapsulated Et₄N⁺ species is also detected at low chemical shift, demonstrating the formation of molecular capsule induced by Et₄N⁺AcO⁻. The authors also use ROESY, DOSY and ESI-MS to investigate the Et₄N⁺AcO⁻-triggered self-organization. The decomposition-reconstruction process of **116** is reversible and could be controlled by the pH. Nevertheless, it cannot be neglected that Et₄N⁺ plays an important role as template in the formation of the cage, preventing the exploration of the recognition capacities of the inner space.



Scheme 1.22 Formation of Hemicryptophane capsule Et₄N⁺@116.

Subsequently, the authors reported the assembled hemicryptophane capsule **116** with the same modules **114** and **115** triggered by amine using dynamic boronate esterification.⁹⁴ As shown in Scheme 1.23, upon addition of Et₃N to the CD₃OD/CD₃CN solution of **114** and **115**, the N–B bonds are first formed together with the association of two modular compounds to generate the intermediate **117**. Then, the cage **117** is subjected to a solvolysis reaction to produce the CD₃O-attached **116** with the encapsulation of Et₃NH⁺. The addition of Bu₃N also

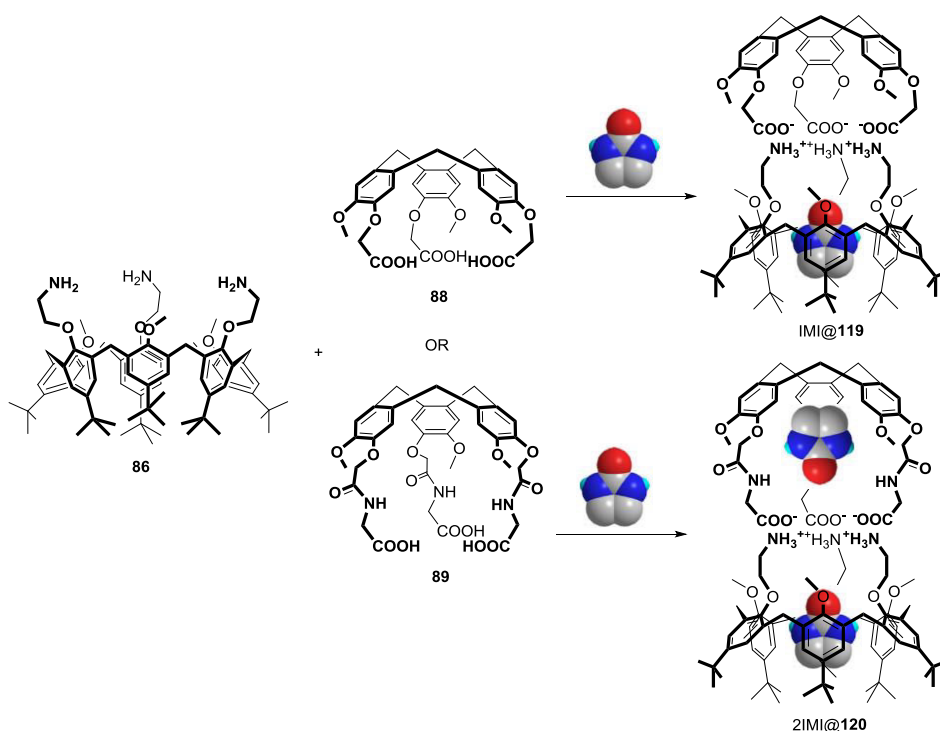
follows the same sequence first giving the intermediate **118**. However, only the capsule **116** with empty cavity is obtained in the solvolysis reaction because of the larger size of Bu_3NH^+ compared with Et_3NH^+ . This result is quite appealing since an empty assembled hemicryptophane capsule is obtained, of which properties and applications, such as molecular recognition, could be investigated.



Scheme 1.23 Formation of Hemicryptophane Capsules **116** and $\text{Et}_3\text{NH}^+@116$.

1.3.2.2 Formation by ionic interactions

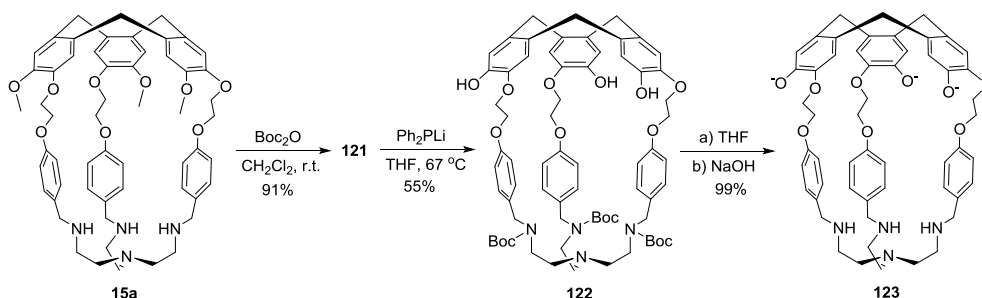
Ionic interactions between anion and cation have also been utilized for constructing self-assembled hemicryptophane cages.⁹⁵ Jabin *et al.* combined the trisamine-calix[6]arene **86** with the CTV-tricarboxylic acids **88** or **89** to generate [1+1] hemicryptophanes (Scheme 1.24). In a first experiment the addition of 1 equiv. of calix[6]trisamine **86** to a suspension of CTV-tricarboxylic acid **88** in CDCl_3 did not generate [1+1] hemicryptophane capsule, and instead, various aggregated species were formed probably because of the flexibility of the calix[6]arene structure. However, subsequent addition of 3 equiv. of neutral polar molecules, such as imidazolidin-2-one (IMI) to this 1:1 mixture led to a discrete [1+1+1] self-assembled ternary hemicryptophane capsule $\text{IMI}@119$ composed of **86**, **88** and encapsulated IMI. Furthermore, other polar molecules, such as imides, alcohols, amides, sulfoxides, carbamates, or ureas could also induce the formation of the hemicryptophane capsules through an induced-fit process. These polar molecules can go inside the cavity of the calix[6]tris-ammonium via hydrogen bonding, $\text{CH}-\pi$ interactions with the aromatic walls, and charge-dipole interactions, leading both to the expulsion of the methoxy groups from the calix cavity, the rigidification of the calixarene core, and the preorganization of the ammonium arms, which are necessary for the assembly of the [1+1] ion-paired complex. Interestingly, when using the CTV building block **89**, a new self-assembled ditopic hemicryptophane capsule $2\text{IMI}@120$ including simultaneously two IMI molecules, one in the calixarene cavity and one in the CTV cavity, was formed thanks to the larger size of the building block **89** and the flexibility of **86**.



Scheme 1.24 Formation of Hemicryptophane Capsules IMI@119 and 2IMI@120.

1.3.3 Functionalization of hemicryptophanes

1.3.3.1 Water-soluble hemicryptophanes

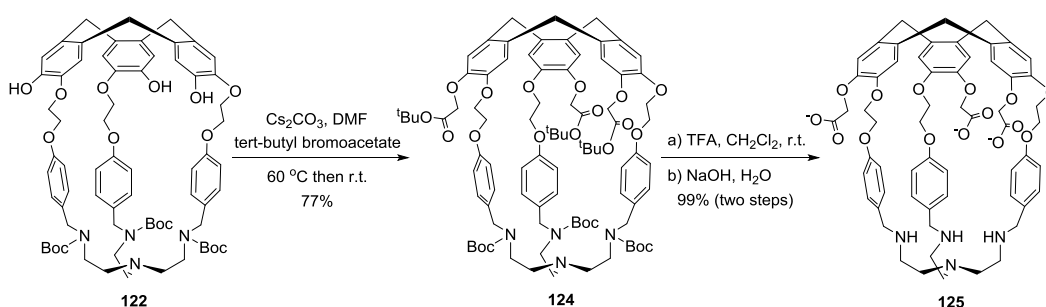


Scheme 1.25 Synthesis of the Water-soluble Hemicryptophane 123.

Effective molecular recognition or catalysis in water is especially meaningful and attractive since it can mimic more accurately biological systems.^{103,104} Accordingly, supramolecular events should take place in water at physiological pH without the addition of organic solvent, requiring water-soluble molecular hosts. The design of water-soluble hemicryptophanes is a real challenging task that mainly relies on the introduction of hydrosoluble functions on the CTV unit. Two strategies that address this issue have been reported, where hydrosoluble groups allow the solubilization of the host in strong basic aqueous solution,¹⁰⁵ or in water at physiological pH.¹⁰⁶ The two strategies that either introduce phenol functions or incorporate carboxylate groups on the CTV units originate from the synthesis of water-soluble cryptophanes.¹⁰⁷⁻¹⁰⁹ The *tren*-hemicryptophane **123** bearing three phenol functions on the CTV cap was synthesized from hemicryptophane **15a** (Scheme 1.25).¹⁰⁵ The *tren* unit in **15a** was first

protected by *tert*-butyloxycarbonyl groups (BOC) to give compound **121** avoiding the difficult and tedious purification of compounds presenting simultaneously amine and phenol functions. Then, the methoxy groups of **121** are removed using Ph₂PLi to afford the trihydroxy-*N*-Boc protected derivative **122**. Finally, deprotection of the amine functions in **122** using trifluoroacetic acid led quantitatively to the hexaphenolate hemicryptophane **123** soluble in water at pH = 12.

Hemicryptophane **123** is only soluble in water at strong basic pH, which does not allow its use in biological environment at physiological pH. To overcome this problem the hemicryptophane **125** was synthesized based on the above intermediate **122** (Scheme 1.26).¹⁰⁶ The first step involves the reaction of **122** with *tert*-butyl-bromoacetate in DMF in the presence of Cs₂CO₃ to yield the protected tri-ester derivative **124**. Deprotection of the amine and the ester functions with trifluoroacetic acid, affords quantitatively the desired hemicryptophane **125** bearing three carboxylate groups and soluble in water at physiological pH (pH ≈ 7).



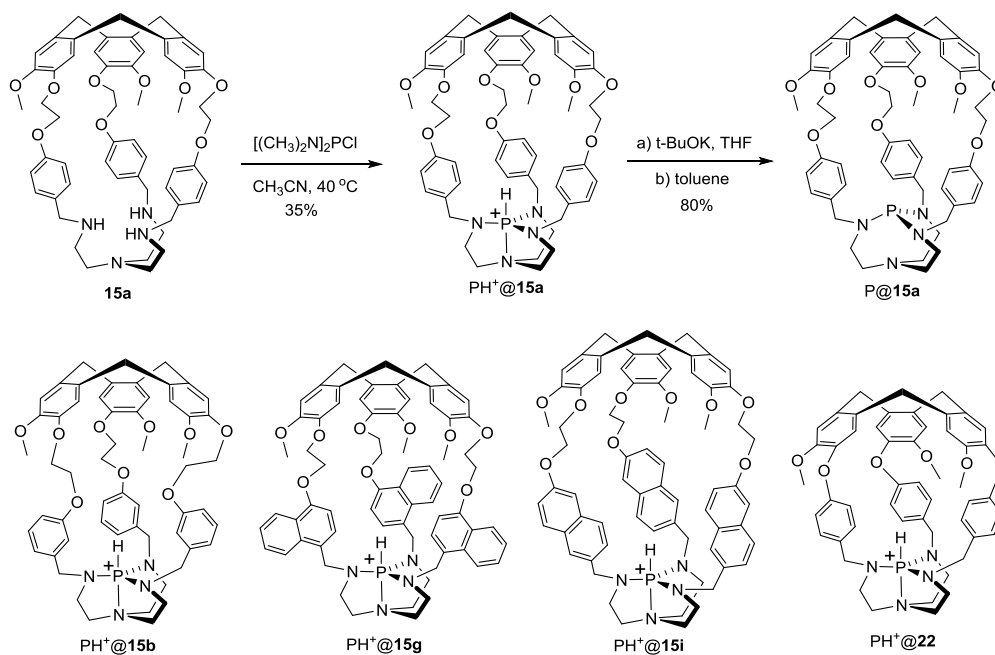
Scheme 1.26 Synthesis of the Water-soluble Hemicryptophane **125**.

1.3.3.2 Endohedral functionalization of hemicryptophanes

Endohedral functionalization of a molecular cavity is a highly challenging topic, arousing a growing interest from the international community.¹¹⁰⁻¹¹⁵ Endohedral non-metal or metal functional groups inside the molecular cavity can participate as binding sites to enhance the host-guest interactions or can act as reactive centers to promote catalytic reactions in the confined space of the inner cavity, mimicking biological entities such as enzymes.¹¹³⁻¹¹⁷ The endohedral functionalization of the hemicryptophane cages reported so far are mainly concerned with (pro)azaphosphatranes derivatives, and the vanadium (V(V)), zinc (Zn(II)), copper (Cu(II)) and ruthenium (Ru(II)) hemicryptophane complexes, the crucial role of which as supramolecular catalysts has been investigated.

Encaged (pro)azaphosphatranes: synthesis and cage effect. Proazaphosphatranes, also known as Verkade's superbases, and their azaphosphatranes protonated counterparts, exhibit catalytic properties in a wide range of reactions.^{47,118-122} In 2011, Dutasta, Martinez *et al.* synthesized the first hemicryptophane-Verkade's superbase P@**15a** and its conjugated acid PH⁺@**15a** from their precursor **15a** using the experimental conditions reported for other azaphosphatranes (Scheme 1.27). The addition of hemicryptophane **15a** to a solution of [(CH₃)₂N]₂PCl in CH₃CN afforded PH⁺@**15a** in 35% yield, which was then deprotonated using potassium *t*-butoxide (*t*-BuOK) in THF to give the encaged superbase P@**15a** in 80% yield.^{123,124} The azaphosphatranes-hemicryptophanes PH⁺@**15a** was optically resolved by chiral

semi-preparative HPLC, leading to the enantiopure compounds $\text{PH}^+@M\text{-15a}$ and $\text{PH}^+@P\text{-15a}$.¹²⁵ Likewise, hemicryptophane-superbases P@15b , P@15g , P@15i and their corresponding protonated forms were also obtained using the same synthetic pathway. Makita *et al.* also prepared the encaged azaphosphatrane $\text{PH}^+@22$,¹²⁶ but the deprotonation of the PH^+ failed even with an excess of *t*-BuOK or sodium hexamethyldisilazide (Scheme 1.27). This was attributed to the smaller size of the molecular cavity that protects the endohedral proton. Most of the encaged azaphosphatranes display a characteristic single ^{31}P NMR signal, which is about 20 ppm downfield shifted compared to non-encaged azaphosphatranes.¹²⁵



Scheme 1.27 Synthesis of (pro)Azaphosphatrane Encaged Hemicryptophane Complexes.

Then, Martinez *et al.* investigated the cage effect on the basicity and reactivity of the superbases.¹²³ Indeed the kinetics and thermodynamics of proton transfer in biological systems can be strongly modified by the surrounding medium.¹²⁷ Changes in the reactivity in such confined biological entities have led to the design of bio-inspired supramolecular structures.^{128,129} These investigations are likely to provide valuable information for a better understanding of enzymes or other complex biological systems. For that purpose, the model compounds P@126 and P@126a were prepared (Figure 1.7), and competition experiments were run for the determination of $\text{p}K_a$ of P@15a and P@126a relative to P@126 in CD_3CN using ^{31}P and ^1H NMR spectroscopy. This afforded a value of $K_a = 1.03 \times 10^{-33}$ for P@15a , 7 times smaller than that of its model superbase P@126a ($K_a = 7.25 \times 10^{-33}$), making the encaged superbase P@15a 7 times more basic than the model molecule P@126a . In addition, the deprotonation rate constant is more than 500-fold lower with the encaged $\text{PH}^+@15\text{a}$ than with the model $\text{PH}^+@126\text{a}$. In spite of the higher basicity of the superbase P@15a , the rate constant for its protonation is nearly 2 orders of magnitude lower than that for the model superbase P@126a , meaning that the rate constant is unrelated to the thermodynamics of proton transfer. These observations indicate that the encapsulation of phosphorus moiety inside the cage affects the basicity of the superbase, and strongly decreases the rate of proton transfer.

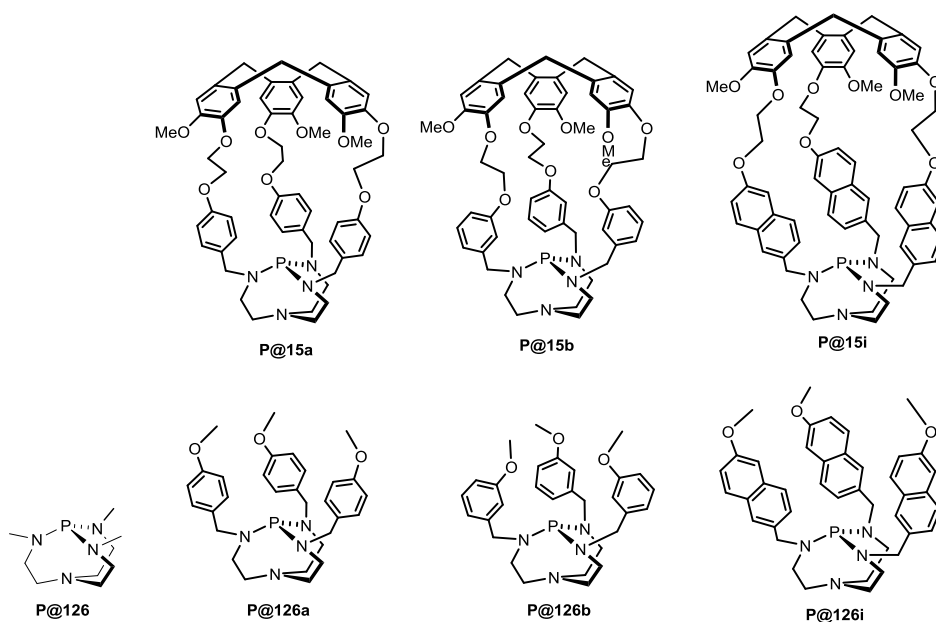


Figure 1.7 Structures of hemicryptophane superbases and the non-caged models.

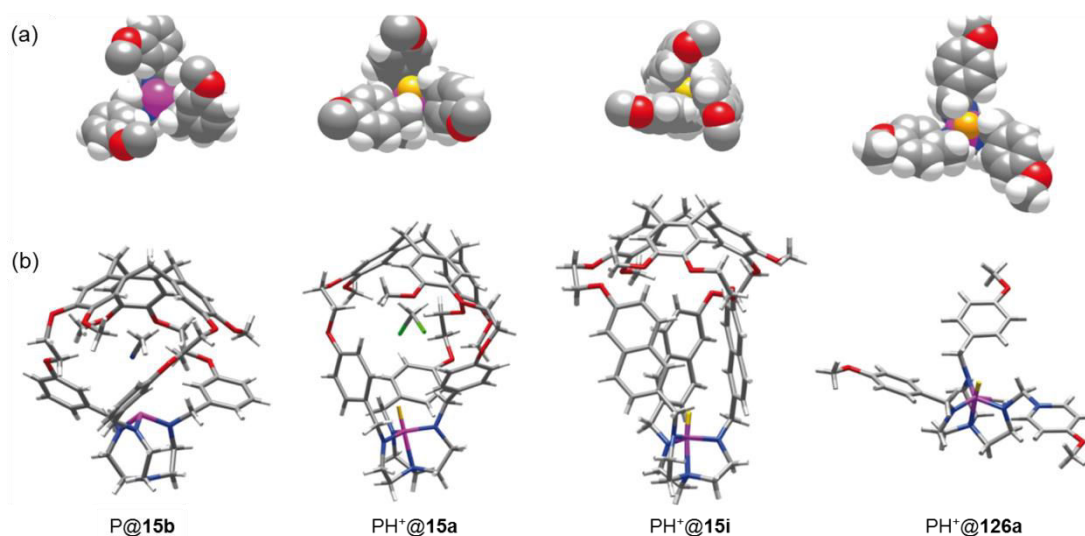


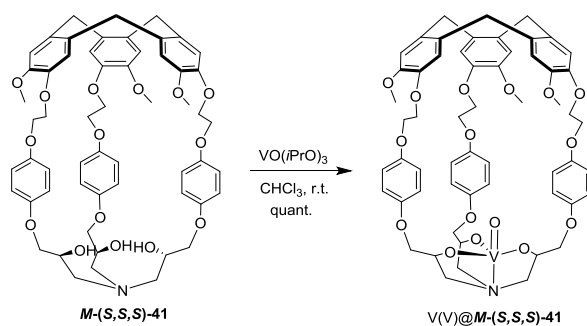
Figure 1.8 X-ray crystal structures of the encapsulated Verkade's superbase **P@15b** and the azaphosphatranes cations **PH⁺@15a**, **PH⁺@15i** and **PH⁺@126a**: (a) space filling top views of the phosphorus centers (for **P@15b**, **PH⁺@15a** and **PH⁺@15i**, the CTV units have been removed for clarity); (b) stick views.

In order to further investigate how the size and the shape of the nanospace around this highly reactive center can control the basicity and the rate of the proton transfer, the authors prepared a series of engaged proazaphosphatranes superbases having a molecular cavity with different volumes and shapes, and also their corresponding model compounds without cavity (Figure 1.7).¹²⁴ The X-ray crystal structures reveal that from **P@15b** to **PH⁺@15a** and **PH⁺@15i**, the molecular cavity grows along the pseudo C_3 axis of the molecule but also becomes narrower (Figure 1.8). It has been shown that the encapsulation greatly affects the basicity of the superbase. For example, according to the pK_a values, the engaged superbase **P@15a** is 7 times more basic than its model **P@126a**, whereas **P@15b** is more than 30 times less basic than its model **P@126b**, and **P@15i** was found to be over 100 times more basic than its model

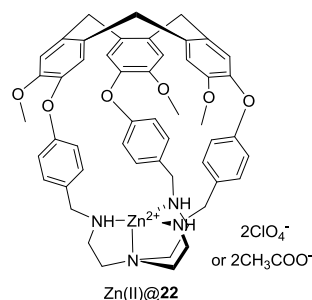
P@126i. These results were closely related to the geometry of the environment around the P-H site, and the congestion of the inner space around the phosphorus center corresponds to an increase of the basicity of the superbases P@15a and P@15i compared to their respective models P@126a and P@126i. In addition, the kinetic data show that the rates of the proton transfer for these superbases are in the order of $\text{PH}^+\text{@126a} > \text{PH}^+\text{@15b} > \text{PH}^+\text{@15a} > \text{PH}^+\text{@15i}$, which is consistent with the accessibility of the reactive phosphorus center also observed from the crystal structures.

Synthesis of endohedral metal@hemicryptophane complexes. Metal complexes possess a variety of coordination topologies, thermodynamic stabilities and kinetics, and have found wide applications in molecular recognition and catalysis. They can serve both as binding and catalytic sites in the development of sensors and catalysts, similar to the function of metalloenzymes in bioinorganic chemistry.¹³⁰⁻¹³⁵ The hemicryptophane cages including *tren* and trialkanolamine units, such as **15a** and **41**, can easily coordinate a metal ion such as Zn(II), Cu(II), Ru(II), Al(III) or V(V), to form atrane structures, which are an interesting class of compounds well represented across the periodic table and widely studied.^{44,136-138}

The oxidovanadium hemicryptophane complexes, such as the two diastereomers V(V)@M-(S,S,S)-**41** and V(V)@P-(S,S,S)-**41**, were synthesized in one step from their precursors bearing trialkanolamine moieties (Scheme 1.28).^{60,139} Hemicryptophane M-(S,S,S)-**41** reacted with 1 equiv. of vanadium oxytriisopropoxide to give the corresponding complex quantitatively. Noteworthy that these vanadium complexes present potential catalytic sites in chiral environments, which may find applications in asymmetric catalysis.¹⁴⁰ Another point is that besides vanadium(V), titanium(IV) and zirconium(IV) are also known to form stable complexes with trialkanolamine ligands.¹⁴¹⁻¹⁴³



Scheme 1.28 Synthesis of the Oxidovanadium Hemicryptophane Complex.

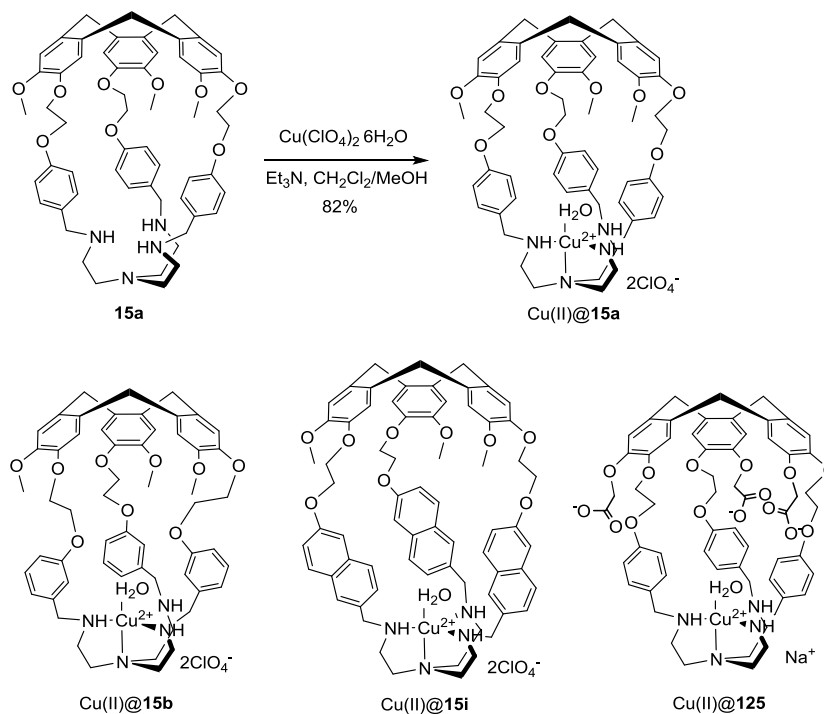


Scheme 1.29 Synthesis of Zn(II) Hemicryptophane Complexes.

Tren-hemicryptophane **22** reacted with $\text{Zn}(\text{ClO}_4)_2(\text{H}_2\text{O})_6$ to yield the Zn(II)@**22** complex

(Scheme 1.29). Following this method, Makita *et al.* also synthesized Zn(II)@**22** with CH₃COO⁻ as counterion,^{54,144} and the RuCl₂@**22** hemicryptophane complexes.¹⁴⁵

The *tren* unit easily binds Cu(II) ions, and a series of Cu(II)@hemicryptophane complexes have been described. Different tren-hemicryptophane ligands reacted with stoichiometric amounts of Cu(ClO₄)₂ in a CH₂Cl₂/MeOH mixture to produce Cu(II)@**15a**, Cu(II)@**15b**, Cu(II)@**15i** and Cu(II)@**125** complexes with high yields (Scheme 1.30).¹⁴⁶ It is important to point out that Cu(II)@**125** constitutes the first water-soluble Cu(II)@hemicryptophane complex.¹⁰⁶



Scheme 1.30 Synthesis of Cu(II) Hemicryptophane Complexes.

Recently, Dutasta *et al.* reported the preparation of Ga(III)@**101** and Fe(III)@**101** hemicryptophane complexes presenting an octahedral coordination site inside the molecular cavity of the host molecule.⁷¹ The complexes were obtained by addition of Ga(acac)₃ or Fe(acac)₃ to a solution of **101** in 1,1,2,2-tetrachloroethane and were characterized by ¹H, ¹³C and ³¹P NMR spectroscopy. The EPR spectrum of the iron complex Fe(III)@**101** indicated a high-spin Fe(III) ion in an octahedral environment. The isostructural X-ray molecular structures of both complexes showed the metal ions nested in the phosphorylated part of the ligand (Figure 1.9). It is interesting to note that the chiral CTV cap induces a helical arrangement of the three linkers of the host molecule, whose configuration is related to that of the CTV unit. Moreover, the complexes present two stereogenic centers, the CTV unit with *P* or *M* configuration, and the octahedral coordination site with Δ or Λ configuration, that should lead to two diastomeric racemates (*P* Δ /*M* Λ and *M* Δ /*P* Λ). In the present case the authors only observed the (*P* Δ /*M* Λ) racemate. This seems to be a general feature observed with other hemicryptophane structures where the CTV imposes the right or left-handed conformation of the linkers and also the stereochemistry of other stereogenic elements present in the host molecule.

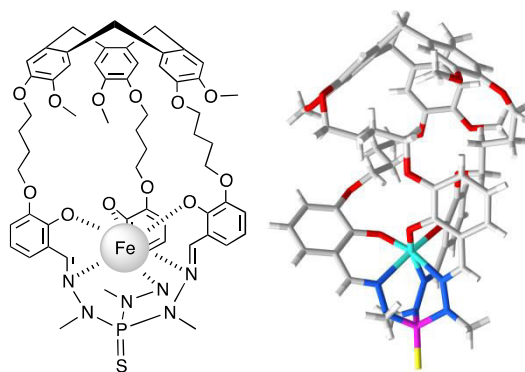


Figure 1.9 X-ray molecular structure of Fe(III)@101 complex.

1.4 Host-guest chemistry of hemicryptophanes

The use of molecular containers for the complexation and recognition of neutral or charged guests is of increasing interest as they can lead to a better understanding of recognition phenomena in biological systems.^{12,24,147-150} In particular, hemicryptophane molecular receptors present several advantages. (i) The rigid CTV scaffold results in a preorganized cavity, in terms of shape and size, enhancing guest binding. Furthermore, the size of the cavity can be controlled and adjusted by changing the linkages between CTV and *south* units. (ii) The versatile *south* unit is easily modified to specifically recognize cations, anions or neutral molecules depending on its interacting sites, thus, various homoditopic and heteroditopic hosts can be designed when combined with the electron-rich CTV moiety. (iii) Signaling groups, for instance fluorophore, can be incorporated into the cages to provide fast responses with low detection limit for the host-guest complexation. The position of the signaling groups is relatively flexible as they can be tethered to the *north* or *south* units, or included in the three linkages. (iv) Taking advantage of the chirality of the CTV unit, enantio- and dia-stereoselective recognition properties are expected.

The first complexation experiment was described in 1982 with hemicryptophane **1**,²⁷ followed 26 years later by a second example reported by Le Gac and Jabin.⁷⁰ Only recently, hemicryptophanes have been investigated as complexing agents for various chiral or achiral guests such as ammoniums,^{94,105,151,152} ion pairs,^{49,70,153} zwitterions,^{63,65,143,154} carbohydrates,^{56,57,61,155} and C₆₀ or C₇₀ fullerenes.⁶⁹ This section aims at reporting the complexation properties in the solid state and in solution of hemicryptophane hosts, emphasizing the enantioselective recognition with enantiopure receptors.

1.4.1 Guest inclusion in the solid state: X-ray structures

Dutasta *et al.* reported in 1999 the first structure of a guest imprisoned in the lipophilic cavity of a hemicryptophane host.³⁰ The crystal structure of hemicryptophane **6**, recrystallized from toluene, shows a well-preorganized cavity defined by the CTV and phosphotrihydrazide moieties, with the S=P bond oriented outward of the cavity (Figure 1.10). One toluene guest is totally encapsulated in the cavity of the host to form a host-guest complex stabilized by van der Waals and C-H \cdots π interactions. In the solid, host **101**

encapsulates a toluene molecule and displays the two *P* and *M* configurations of the CTV unit.⁷¹ Interestingly, the linkers adopt an α or β helical conformation and only the *P*- α -helix or *M*- β -helix enantiomers coexist in the crystal (Figure 1.10). Single crystals of hemicryptophane **14** were also obtained by slow evaporation from a CH_2Cl_2 solution (Figure 1.10).⁴⁸ Hemicryptophane **14** exhibits an asymmetric structure with respect to the C_3 axis of the CTV cap, introduced by the inward orientation of one C=O amide bond stabilized by H-bonds with the adjacent NH groups. The two other C=O groups are oriented outward and participate in the crystalline cohesion through intermolecular hydrogen bonding. One CH_2Cl_2 guest molecule is fully encapsulated in the host cavity and localized close to the CTV unit in the more lipophilic environment of the cavity. This important feature indicates the possible ditopic character of the hemicryptophane host towards guest compounds. Slow diffusion of pentane in a solution of **15a** in CH_2Cl_2 gave crystals suitable for X-ray analysis (Figure 1.10).⁴⁸ The structure presents a C_3 symmetrical axis with a well-preorganized cavity encapsulating a molecule of *n*-pentane. In the complex, C-H $\cdots\pi$ interactions between CH_3 groups of the guest and aromatic groups of the linkers are observed. Interestingly, water molecules can also be included into the cavity of hemicryptophanes. In the X-ray structure of **54**, crystallized from $\text{CH}_3\text{CN}/\text{H}_2\text{O}$, three water molecules are engaged inside the hemicryptophane cavity.⁶³ Two of them interact with an amide group of the host through hydrogen bonding and one is in the proximity of the electron-deficient aromatic ring. This anticipates the recognition properties of this host towards hydrophilic species.

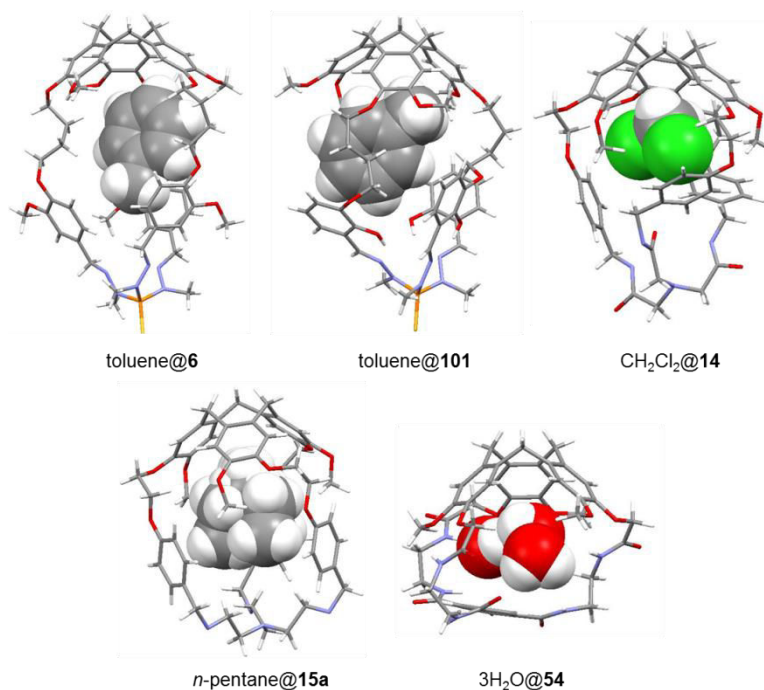


Figure 1.10 Crystal structures of toluene@**6**, toluene @**101**, $3\text{H}_2\text{O}$ @**54**, *n*-pentane@**15a** and CH_2Cl_2 @**14**.

Makita *et al.* also described a series of crystal structures of inclusion complexes with hemicryptophane hosts. For example, the X-ray crystal structure of hemicryptophane **22** (Figure 1.11), obtained by slow evaporation from a CH_3CN solution, exhibited a preorganized cavity constructed by the CTV and the *tren* moieties.¹⁴⁴ A molecule of CH_3CN is entrapped

inside the molecular cavity stabilized by hydrogen bonding and $\text{CH}\cdots\pi$ interactions.⁵⁴ Interestingly, the Zn(II) coordinated complex of **22** (ClO_4^- as counterion) also bound a CH_3CN molecule as observed from its crystal structure prepared by slow diffusion of THF into a CH_3CN solution.¹⁴⁴ In this case, the cage maintains the C_3 symmetry and includes a CH_3CN molecule through $\text{CH}\cdots\pi$ interactions. In addition, the CH_3CN N atom also loosely coordinates to the Zn(II) ion, which indicates the binding ability of this metal center. However, when AcO^- was used as the counterion, the $\text{Zn(II)}@22$ complex does not include a CH_3CN molecule despite the crystals were obtained by slow diffusion of Et_2O into a CH_3CN solution.⁵⁴ Instead, an AcO^- counterion was embedded inside the molecular cavity according to the coordination bond between the O atom in AcO^- and Zn(II). This inclusion behavior of $\text{Zn(II)}@22$ towards AcO^- was also observed in solution. These results underline the strong binding ability and heteroditopic character of the $\text{Zn(II)}@22$ host.

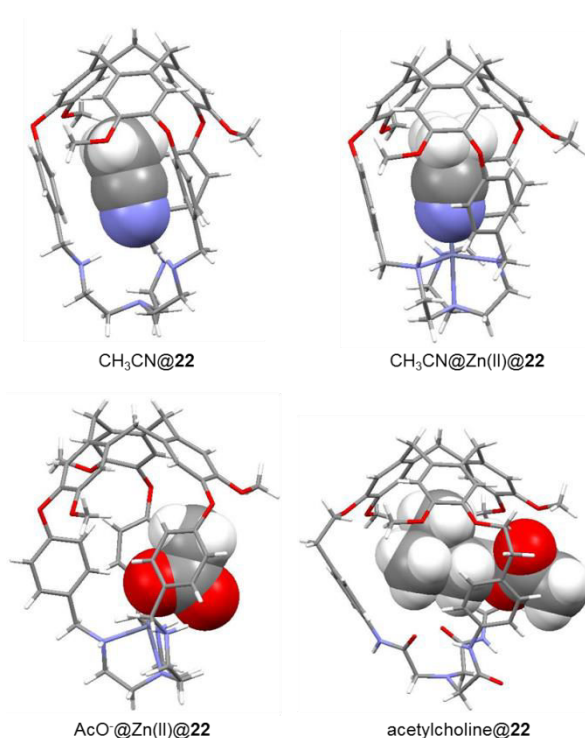


Figure 1.11 Crystal structures of $\text{CH}_3\text{CN}@22$, $\text{CH}_3\text{CN}@Zn(II)@22$, $\text{AcO}^-@Zn(II)@22$ and $\text{acetylcholine}@22$.

Most of the X-ray structures of guest inclusion in hemicryptophane hosts reported so far are restricted to solvent@hemicryptophane complexes. However, in 2016 Makita *et al.* reported the solid-state structure of an acetylcholine molecule engaged in the cavity of hemicryptophane **24**.⁵⁵ A partial encapsulation of the neurotransmitter was observed: indeed the ammonium head of acetylcholine is trapped inside the cavity whereas the acetyl group is located outside, leading to an original pseudo-rotaxane structure (Figure 1.11). This important result highlights the ability of hemicryptophane to tolerate partial encapsulation and thus to complex only a part of large guest molecules.

X-ray molecular structures of free hosts, without guest molecules in the molecular cavity have also been reported, and result from two main factors. (i) The cavity is too small to accommodate any guest molecules as for instance in the crystal structure of hemicryptophane

105 described by Dmochowski *et al.*⁵² or in hemicryptophane **15b** where hydrogen bonds involving the three linkages induce a twisted structure, giving rise to very small available space inside the cavity (Figure 1.12).⁵¹ (ii) The hemicryptophane structure collapses and the molecule adopts a compact structure with the molecular cavity occupied by one of the linkages or the *south* moieties such as the crystal structures of V(V)@P-(S,S,S)-**41**.¹⁵⁶ Therefore, when designing a hemicryptophane host with the purpose of complexing molecules, these factors, that may induce no guest encapsulation, should be taken into account.

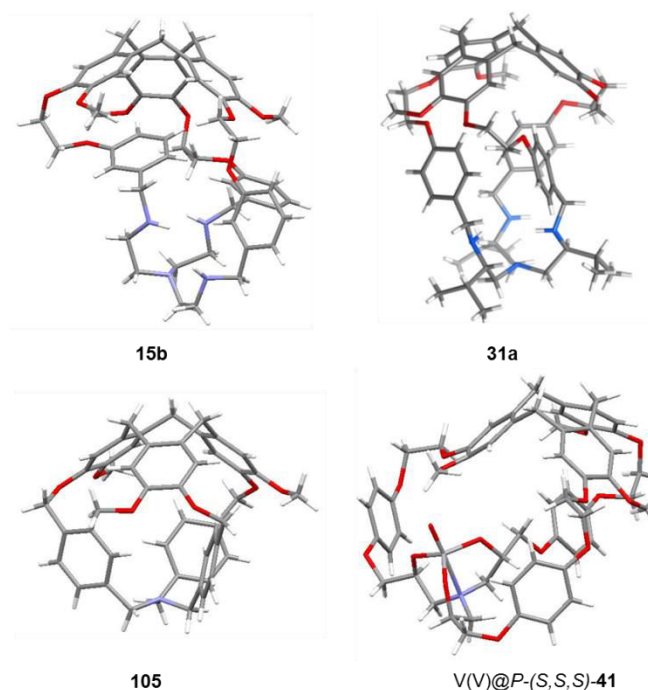


Figure 1.12 Crystal structures of **15b**, **31a**, **105** and V(V)@P-(S,S,S)-**41**.

Interestingly, the X-ray molecular structures can be used to assign the absolute configuration of the chiral CTV unit. For instance, in the solid-state structure of hemicryptophane **31a**, recrystallized from a dichloromethane solution, a well-defined molecular cavity was observed (Figure 1.12). Because the *S* configuration of the three stereogenic carbons of the *tren* moiety was controlled during the synthetic pathway, it has been possible to assign the *M* configuration of the CTV unit (Flack parameter = 0.00(1)).⁵⁸

1.4.2 Complexation in solution

Most of host-guest systems with hemicryptophane hosts have been investigated in solution. The binding affinities rely on the lipophilic and electron-donor properties of the CTV moiety, which can be associated to various *southern* units leading to a wide range of suitable guests. Thus, the peculiar properties of the hemicryptophanes are strongly related to their hetero-ditopic character with modulable cavity size and shape, polarity, hydrophilicity and hydrophobicity. Among the various noncovalent interactions that can take place with hemicryptophane hosts, hydrogen-bonding and cation- π or anion- π interactions prevail due to the aromatic environment of the receptors built from the CTV platform. This review will cover the most encountered hemicryptophane-guest complexes reported in the literature

including charged species (ammonium, ion pairs, zwitterions) and neutral guests such as fullerenes and carbohydrates.

Because of the chirality of the CTV unit, the recognition of achiral molecules by hemicryptophane hosts usually involves racemic mixtures. Conversely, the complexation of chiral guests uses enantiopure hemicryptophane hosts. The enantioselective recognition of chiral molecules with C_3 symmetrical hosts is highly challenging. Indeed, the first enantioselective recognition of chiral primary ammonium ions with C_3 symmetric tripodal receptors was reported by Ahn *et al.* only in 2002,¹⁵⁷ followed by few other examples.^{158,159} Then, Moberg *et al.* were able to rationalize the enantioselectivity observed with C_3 symmetric hosts, putting an end to an old scientific controversy.^{160,161} This highlights that enantioselective recognition of chiral molecules with C_3 symmetrical hosts remains a difficult task. The access to enantiomerically pure hemicryptophanes as described in the preceding sections, allowed important investigations in the field of chiral recognition in solution that will be underlined in the following sub-sections.

1.4.2.1 Recognition of ammonium guests

The first hemicryptophane, speleand **1**, developed by Collet and Lehn, was shown to be an efficient binding receptor for primary ammonium.²⁷ A schematic representation of the inclusion complex is shown in Figure 1.13: the NH_3^+ group interacts with the azacrown ether by hydrogen bonding, and the CH_3 head is located inside the molecular cavity. A host-guest complex with the CH_3 group located outside of the cavity below the azacrown ether is also detected, and a 2:1 ratio between the *exo*- and *endo*-complexes is observed.

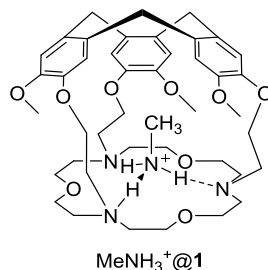


Figure 1.13 A proposed binding mode between hemicryptophane **1** and MeNH_3^+ .

The second example of encapsulation of ammoniums was reported in 2009 using the *n*- Bu_3N -triggered hemicryptophane capsule **118** in $\text{CD}_3\text{OD}/\text{CD}_3\text{CN}$.⁹⁴ The *n*- Bu_3NH^+ cannot go inside the cavity because of its too large size. However, the addition of ammoniums Et_4N^+ and Me_4N^+ , or phosphonium Me_4P^+ , to a solution of the empty capsule **116** gave rise to new signals in the range of 0.3-0.7 ppm on the ^1H NMR spectra, indicating the formation of encapsulated species. The authors then used competition experiments to investigate the relative binding affinities of the hemicryptophane capsule towards these three guests. For instance, when a 1:1 mixture of Et_4NI and Me_4NI was added to **116**, two kinds of guest-filled capsules $\text{Et}_4\text{N}^+@116$ and $\text{Me}_4\text{N}^+@116$ appeared in a 2.3:1 ratio. In this way, the relative binding abilities were determined in the following order: $\text{Et}_4\text{N}^+ > \text{Me}_4\text{N}^+ > \text{Me}_4\text{P}^+$. Interestingly, the authors also characterized the encapsulation of the Cs^+ cation by host **116**. However, for the two above cases no binding constants are reported.

Tren-hemicryptophanes were also used for the recognition of primary ammonium. For example, host **15a** was demonstrated to be an efficient primary alkylammonium receptor in CDCl₃/MeOD solution.¹⁵² Upon addition of the host **15a** to the solution of picrate salts of ammoniums, such as BnNH₃⁺, MeNH₃⁺, *t*-BuNH₃⁺ and *n*-PrNH₃⁺, the guest's protons displayed significant highfield shifts due to the shielding effect of the aromatic cavity, in agreement with the formation of inclusion complexes. The binding constants were thus determined based on the 1:1 stoichiometry indicated by Job's plot, and showed relatively high values (10⁴-10⁵ M⁻¹) with an order BnNH₃⁺ > MeNH₃⁺ > *t*-BuNH₃⁺ > *n*-PrNH₃⁺. A combination of a stabilizing hydrogen bonding network between the encapsulated ammonium and the tren moiety, and a good fit allowing both favourable CH...π interactions within the aromatic cavity and minimization of steric repulsions, can account for these results. In addition, the ability of hemicryptophane **15a** to complex ammonium neurotransmitters was also investigated. A binding constant of 2.5 × 10⁴ M⁻¹ was measured with dopamine as guest molecule, highlighting the potential use of hemicryptophane hosts for the recognition of neurotransmitters. A binding mode between **15a** and dopamine has been proposed by DFT calculations (Figure 1.14a).

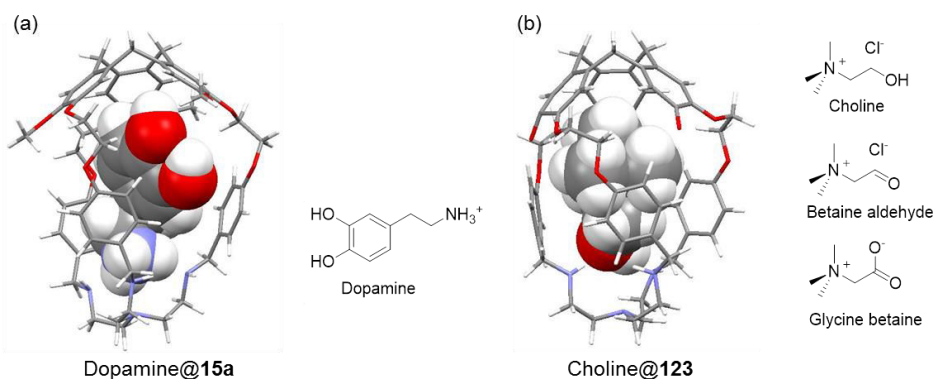


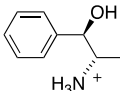
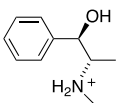
Figure 1.14 (a) DFT optimized structure of dopamine@**15a**, and the structure of dopamine. (b) DFT optimized structure of choline@**123**, and the structures of choline, betaine aldehyde and glycine betaine.

The efficient complexation of choline neurotransmitter in water using the water-soluble hemicryptophane **123**, was reported, constituting a real advance in host-guest recognition, rarely described in aqueous medium.¹⁰⁵ ¹H NMR titration was first used for characterizing the host-guest association, where significant high-field shifts of the guest's protons were observed attributed to the shielding effect of the aromatic environment. At lower temperature (270 K), under slow exchange conditions on the NMR time-scale, a new signal appeared in the high-field region corresponding to the included choline ammonium. In addition, DFT calculations are consistent with the ¹H NMR data and confirm the location of the ammonium part of the guest in the vicinity of the CTV unit (Figure 1.14b). A binding constant of 2300 M⁻¹ was determined by isothermal titration calorimetry (ITC). Surprisingly, no association was observed by ITC for betaine aldehyde and glycine betaine guest molecules, highlighting the high specificity and selectivity of hemicryptophane **123** towards choline.

The complexation of choline emphasized the use of hemicryptophanes for the recognition of compounds of biological interest in water. More importantly, the recognition of neurotransmitters is very meaningful since many of them are involved in important

biological processes.¹⁶² However, most of them are chiral amine derivatives that lead to the formation of diastereomeric host-guest complexes in the recognition experiments run with racemic host compounds. To this end, enantiopure hemicryptophanes have been synthesized and used successfully in the recognition of chiral ammonium guests. Enantiopure tren-hemicryptophanes, *M*-(*S,S,S*)-**30**, *P*-(*S,S,S*)-**30**, *M*-(*R,R,R*)-**30** and *P*-(*R,R,R*)-**30**, were tested in the stereoselective recognition of norephedrine and ephedrine in CDCl₃/CD₃OD solution.¹⁵¹ ¹H NMR titration experiments were performed showing the formation of 1:1 and 1:2 host-guest complexes. The authors explained the 1:2 stoichiometry with the fact that both the tren and CTV moieties are able to bind ammonium guests according to hydrogen bonding and cation- π interactions, as previously observed in the recognition of dopamine and choline with **15a** and **123** respectively. Examination of the binding constants reported in Table 1.1 shows that these hosts are able to complex ephedrine and norephedrine with high binding constants, and in addition, most of the host diastereomers discriminate norephedrine from ephedrine, exhibiting larger affinity towards the former. Furthermore, remarkable enantioselectivities in favour of the *P*-(*S,S,S*) enantiomer over *M*-(*R,R,R*) are displayed for both guests.

Table 1.1 Association Constants of Enantiopure Receptors **30** with Ephedrine or Norephedrine ^a

				
	Norephedrine		Ephedrine	
	β_1 (M ⁻¹) ^b	β_2 (M ⁻¹) ^b	β_1 (M ⁻¹) ^b	β_2 (M ⁻¹) ^b
	1:1 host-guest	1:2 host-guest	1:1 host-guest	1:2 host-guest
<i>M</i> -(<i>R,R,R</i>)- 30	– ^c	1.39 10 ⁷	– ^c	4.60 10 ⁶
<i>M</i> -(<i>S,S,S</i>)- 30	1.52 10 ⁵	2.64 10 ⁹	4.71 10 ⁴	2.18 10 ⁸
<i>P</i> -(<i>S,S,S</i>)- 30	3.99 10 ³	2.18 10 ⁷	8.06 10 ³	2.52 10 ⁷
<i>P</i> -(<i>R,R,R</i>)- 30	2.50 10 ⁵	1.95 10 ⁹	1.65 10 ⁴	7.92 10 ⁷

^a β_1 and β_2 values were determined by fitting the ¹H NMR titration curves of the methyl protons of the guests using *hypNMR2008* software¹⁶³ (CDCl₃/CD₃OD 95/5, 500 MHz, 298 K). ^b Estimated error: 10%. ^c No 1:1 complex observed after fitting the titration curves.

The large scale and easy synthesis of enantiopure hemicryptophanes *M*-**15a** and *P*-**15a**, allowed the authors to investigate their stereoselective recognition properties towards norephedrine in CDCl₃/CD₃OD solution.⁵³ ¹H NMR titration experiments and binding stoichiometry similar to those for enantiopure **30** were observed for hosts *M*-**15a** and *P*-**15a**. Interestingly, compared with **30**, the two simplest hosts exhibited higher enantioselectivity towards norephedrine (91:9), indicating the important role of the inherently chiral CTV and highlighting the high potentiality of such simple and easy accessible enantiopure hemicryptophane hosts.

Makita *et al.* reported the formation of the 1:1 complex between acetylcholine and hemicryptophane **24** in a 20/1 CDCl₃/CD₃OD solution.⁵⁵ A binding constant of 1.3 x 10⁴ M⁻¹

was obtained by fitting the curve obtained from the NMR titration experiment. Interestingly, the ^1H NMR signals of the NCH_2CH_2 and $\text{N}(\text{CH}_3)_3$ protons of acetylcholine are broadened in the presence of host **24**, whereas those of the acetyl CH_3 remain sharp, suggesting that the formers are encapsulated inside the cavity of the hemicryptophane and the latter are outside the cavity, as observed in the solid state (Figure 1.11). Recognition of ammonium-chloride salts was also achieved using hemicryptophane **24**. In the ^1H NMR spectra, the protons of the guests display downfield shifts upon progressive addition of the ammonium salts to the host solutions. The binding constants were measured for Me_4NCl ($6.5 \times 10^4 \text{ M}^{-1}$), $\text{Et}_2\text{Me}_2\text{NCl}$ ($9.8 \times 10^3 \text{ M}^{-1}$) and Et_3MeNCl ($5.5 \times 10^2 \text{ M}^{-1}$) and showed that the decrease of the affinity of **24** for the guests is related to the size of the cation, the highest the size the lowest the affinity.⁵⁵

1.4.2.2 Recognition of ion pairs

In 2008, Jabin *et al.* reported a heteroditopic hemicryptophane cage that displays versatile host-guest properties towards organic associated ion pair salts (Figure 1.15).⁷⁰ Upon the addition of an excess of RNH_3Cl ($\text{R} = \text{Et}$ or Pr) to a solution of **91** in CDCl_3 , high-field shifted signals of the alkyl chain of the ammonium ions were observed, indicating that the ammonium ions are located inside the cavity of the calixarene. In addition, the amide protons close to the calixarene subunit also show a significant downfield shift, suggesting a strong hydrogen bonding interaction with the Cl^- anion. Hence, hemicryptophane **91** behaves as a heteroditopic receptor because of the simultaneous *endo*-complexation of cation and anion. Concerning the ammonium cation, in addition to the electrostatic interaction with its counterion, it is also probably stabilized through a combination of $\text{CH}\cdots\pi$ interactions and hydrogen bonding to the ethereal oxygen atoms of the amide arms. Furthermore, by using $n\text{Bu}_4\text{NCl}$ and RNH_3Pic salts, the authors demonstrated that the complexation of the Cl^- anion might only occur when an ammonium cation is present in the calixarene cavity, and corollary efficient binding of ammonium needs the presence of the Cl^- anion. This remarkable positive cooperativity benefits from a combination of polarization and induced-fit effects.

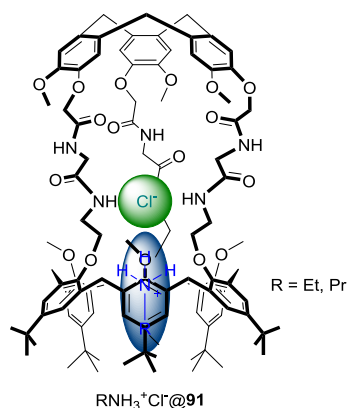


Figure 1.15 A proposed binding mode between hemicryptophane **91** and RNH_3Cl .

Hemicryptophane **14**, which bears a tripodal anion binding site (triamide moiety) and a cation recognition site (CTV unit) is an efficient ion-pair receptor in CDCl_3 .¹⁵³ Firstly, anion binding properties of **14** were evaluated by ^1H NMR titration and showed binding constants in with the order of $K_a(\text{F}^-) > K_a(\text{Cl}^-) > K_a(\text{Br}^-) > K_a(\text{AcO}^-)$, which is related with the hydrogen-bond-accepting ability and symmetry factors. Then the complexation of

ammonium cations was investigated and showed that the affinity of hemicryptophane **14** decreases from Me_4N^+ ($K = 380 \text{ M}^{-1}$) to Et_4N^+ ($K = 97 \text{ M}^{-1}$) in accord with an increase of the steric hindrance. Finally, the ability of **14** to accommodate associated organic ion pairs was achieved by measuring the apparent anion binding constants K'_a of **14** in the presence of 1 equiv. of Me_4N^+ . As shown in Figure 1.16a, host **14** binds anions more strongly in the presence of 1 equiv. of Me_4N^+ emphasizing the heteroditopic character of receptor **14**. Especially, a cooperativity factor, defined by the ratio $K'_a/K_a = 15$, was observed for the complexation of Cl^- , which also exhibits the largest binding constant. DFT calculations demonstrated that efficient hydrogen bonding between Cl^- and triamide, and $\text{CH}\cdots\pi$ interactions between Me_4N^+ and CTV, together with maximized electrostatic interactions between the bound Me_4N^+ and Cl^- account for this high positive cooperativity (Figure 1.16b).

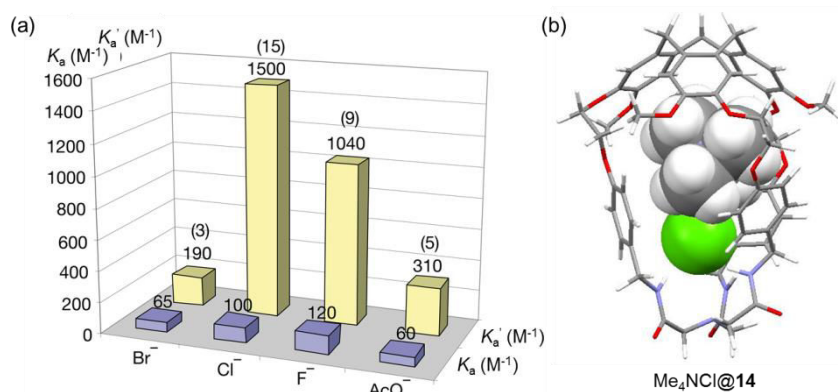


Figure 1.16 (a) Anion binding constants of hemicryptophane **14** in the absence or presence of 1 equiv. of Me_4N^+ . Cooperativity factors are given in parentheses. (b) DFT-optimized structure of $\text{Me}_4\text{NCl}@14$.

1.4.2.3 Recognition of zwitterions

Zwitterions, such as those shown in Figure 1.17, play an important role in the transfer of neuronal information, which is the subject of studies involving chemical, biochemical and clinical approaches.^{165,166} As these guests are strongly solvated species in aqueous media, their biomimetic encapsulation through endohedral weak interactions in a hydrophobic neutral molecular pocket is still a challenge. The principle of complexation of zwitterions using heteroditopic hemicryptophane hosts is almost similar to that of ion pairs, *i.e.* stabilizing the cation part of zwitterions with the CTV unit via $\text{CH}\cdots\pi/\text{cation}\cdots\pi$ interactions and binding the anion part with the *south* moiety using other supramolecular interactions.

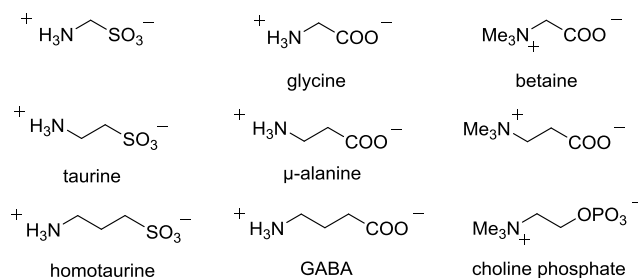


Figure 1.17 Structures of zwitterionic guests.

Hemicryptophane **14**, used for the recognition of ion pairs, is also an efficient heteroditopic hosts for the recognition of zwitterions since, as mentioned above, the CTV unit can stabilize

the ammonium part and the triamide subunit can form hydrogen bonds with the anionic part.¹⁵⁴ The binding constants determined by NMR experiments in CD₃CN/D₂O are shown in Table 1.2. These results indicate that the encapsulation of guests by hemicryptophane **14** relies on three main criteria: (i) the zwitterionic character of the guest, (ii) its van der Waals volume since the packing coefficient has to be close to 55%, in agreement with the Rebek's criteria,^{167,168} and (iii) its shape. Indeed, two CH₂ groups, between the anionic and cationic parts, are necessary to have an optimal recognition process. Only the simultaneous existence of these three factors allows optimum complexation with this receptor. As a consequence, host **14** is highly selective towards taurine. DFT calculations emphasize that only weak intermolecular interactions stabilize the host-guest association (Figure 1.18a).

Table 1.2 Association Constants K_a of hemicryptophane **14** with neurotransmitters and related guests (CD₃CN/D₂O 9:1)

Guest ^a	K_a (M ⁻¹) ^b	V_{vdw} (Å ³)	pc (%) ^c
H ₃ N ⁺ CH ₂ SO ₃ ⁻	–	82	48
Taurine	14000	99	59
Homotaurine	530	116	69
Glycine	–	69	41
β-Alanine	8500	86	51
GABA	510	104	61
Betaine	80	121	78
(CH ₃) ₃ N ⁺ CH ₂ CH ₂ COO ⁻	–	138	82
Choline phosphate	–	160	94

^a Picrate salts. ^b K_a values were determined by DOSY NMR experiments except for (CH₃)₃N⁺CH₂CH₂COO⁻ for which K_a was determined by ¹H NMR titration using WinEQNMR2 software¹⁶⁹ (estimated error 10%). ^c Packing coefficient based on a cavity volume of 169 Å³.

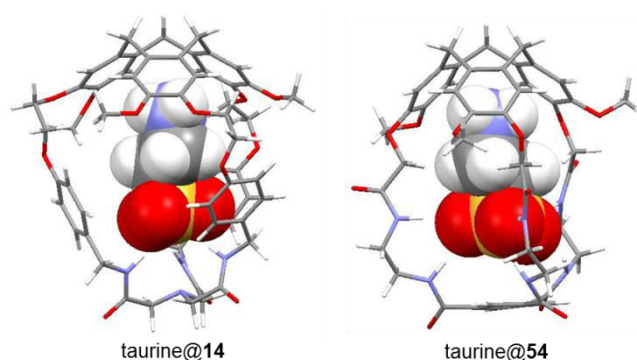


Figure 1.18 DFT-optimized structures of (a) taurine@**14**, and (b) taurine@**54**.

The authors noted that the structure of **14** revealed one major drawback as the three linkages are formed of electron-rich aromatic rings, which can induce electrostatic repulsions with the guest anion located inside the cavity. To tackle this problem, aromatic rings were

replaced by an electron-deficient system in hemicryptophane **54**, which improved the stability of the host-guest complex by favorable anion- π interactions.⁶³ Adding three amide functions also increased the number of hydrogen bond donors, and the binding abilities of host **54** towards zwitterions have been significantly improved compared to host **14** (Table 1.3). For some guests, binding constants are up to three orders of magnitude larger than those previously reported for host **14**, whereas the solvent is even more competitive (20% of water in CD₃CN vs. 10% initially). In particular, the binding constant for taurine reaches $5 \times 10^5 \text{ M}^{-1}$, which was attributed to the good complementarity in size and shape between the host and guest, as demonstrated by DFT calculations (Figure 1.18b). In order to investigate whether this recognition process was driven by both hydrogen bonding and ion- π interactions (cation- π in the *north* part and anion- π in the *south* part) or the contribution of these latter could be neglected in the formation of the complex, multireference wavefunction-based calculations¹⁶⁴ were carried out to have a deeper insight on ion- π interactions. The results showed that the two ion- π interactions (cation- π and anion- π interaction) play a crucial role in the recognition process and could be combined in a synergistic manner.

Table 1.3 Association Constants K_a and Complexation Induced Shifts (CIS) $\Delta\delta_{\text{max}}$ Measured by ¹H NMR Titration of Guests with Host **54** (CD₃CN/D₂O 8:2; 500 MHz; 298 K)

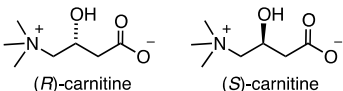
Guest	$K_a \text{ (M}^{-1}\text{)}^a$	$V_{\text{vdw}} \text{ (Å}^3\text{)}^b$	$\Delta\delta_{\text{max}} \text{ NCH}_2^+$ (ppm)	$\Delta\delta_{\text{max}} \text{ CH}_2\text{X}^-$ (ppm)
β -Alanine	$1.5 \pm 0.1 \cdot 10^4$	86	-0.41	-0.25
Taurine	$5.0 \pm 0.4 \cdot 10^5$	99	-0.39	-0.20
GABA	$2.3 \pm 0.1 \cdot 10^5$	103	-0.41	-0.20
Homotaurine	$1.1 \pm 0.2 \cdot 10^5$	116	-0.31	-0.07

^a K_a values were determined by fitting ¹H NMR titration curves using WinEQNMR2 software¹⁶⁹. ^b Van der Waals volume were calculated according to the method of Abraham *et al.*¹⁷⁰

Benefiting from the heteroditopicity of the hemicryptophane hosts, stereoselective recognition of chiral zwitterions was also achieved. For instance, Hutton *et al.* synthesized the enantiopure hemicryptophanes *ML-67* and *PL-67* (Section 1.3.1.4), which associate a CTV and a cyclic peptide (Scheme 1.15), for the enantioselective binding of (*R/S*)-carnitine in CD₃CN.⁶⁵ During ¹H NMR titration experiments, significant downfield shifts were observed for the glycy and tyrosyl NH protons of the cyclic peptide, indicating the encapsulation of the guest within the cavity to form 1:1 host-guest complex in accord with Job's plot and ESI-MS. Binding of carnitine with *PL-67* was found to be enantioselective with (*R*)-carnitine with a 1.5-fold greater K_a than with (*S*)-carnitine (Table 1.4). With *ML-67*, a 1.3-fold larger K_a was observed for (*R*)-carnitine compared to the (*S*)-enantiomer. In addition, considering that the association constant for the d-tyrosine-glycine hemicryptophane complex of (*R*)-carnitine (*PDR*-complex) is identical to the known enantiomeric l-tyrosine-glycine hemicryptophane complex of (*S*)-carnitine (*MLS*-complex), the authors determined a 5.9-fold difference in

association constants of (*R*)-carnitine with the *PL-67* and *PD-67* hosts. In contrast, switching from *PL-67* to *ML-67* results in a 4.5-fold drop in binding affinity for (*R*)-carnitine. These results suggest that the *PL-67* stereoisomer is the best matched to bind (*R*)-carnitine with a modest chiral discrimination. DFT calculations indicate that carnitine was bound to the host in a ditopic mode exploiting hydrogen bond interactions between the cyclic peptide and the carnitine carboxylate group, together with the cation- π /CH $\cdots\pi$ interactions between the CTV and the carnitine ammonium moieties (Figure 1.19)

Table 1.4 Association Constants K_a of Host **67** with (*R*)- and (*S*)-Carnitine



(*R*)-carnitine (*S*)-carnitine

Host	Guest	K_a (M^{-1}) ^a	δ_{\max} (ppm) ^b
<i>PL-67</i>	<i>R</i> -Carnitine	$4.1 \pm 0.3 \cdot 10^3$	-0.8945
<i>PL-67</i>	<i>S</i> -Carnitine	$2.7 \pm 0.2 \cdot 10^3$	-0.5937
<i>ML-67</i>	<i>R</i> -Carnitine	$9.1 \pm 0.1 \cdot 10^2$	-0.7194
<i>ML-67</i>	<i>S</i> -Carnitine	$6.9 \pm 0.5 \cdot 10^2$	-0.4791

^a K_a values were determined by fitting 1H NMR titration curves using WinEQNMR2 software¹⁶⁹. ^b δ from Gly-NH protons of host **67**.

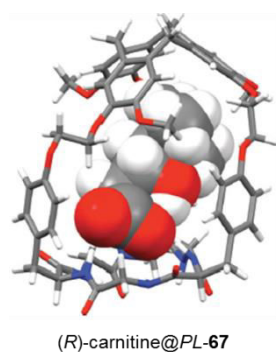


Figure 1.19 DFT-optimized structure of (*R*)-carnitine@*PL-67*.

1.4.2.4 Recognition of carbohydrates

The recognition of carbohydrates, such as those in Figure 1.20, is involved in numerous biological processes such as protein folding, cell-cell recognition, infection by pathogens or tumour metastasis.¹⁷¹ Thus, there is a great interest in mimicking biological receptors of carbohydrates.¹⁷²⁻¹⁷⁷ However, these guests are challenging for supramolecular chemists as they possess complex three-dimensional structures, which often present subtle changes, so that a large selectivity is difficult to achieve. In this regard, hemicyptophane hosts appears as potential carbohydrate recognition receptors, since they can provide appropriate matches for both polar functionalities (through hydrogen bonding in the *south* part with the OH group of

carbohydrates) and apolar surfaces (through C-H $\cdots\pi$ interactions with the aromatic rings of the host molecule).

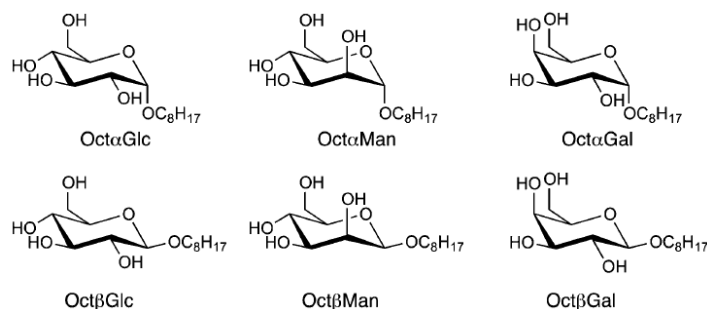


Figure 1.20 Structures of carbohydrate guests.

In 2011, the first octyl- β -D-glucopyranoside (Oct β Glc) and octyl- α -D-glucopyranoside (Oct α Glc) recognition using enantiopure hemicryptophanes **M-14** and **P-14** (Scheme 1.1) was reported.¹⁵⁵ The binding constants, measured in CDCl₃ solution reveal two main features (Table 1.5). Firstly, a good diastereo-discrimination is observed for host **M-14**, with a factor of *ca.* 3 between the binding constants with Oct α Glc and Oct β Glc, and exclusive diastereoselective recognition of Oct α Glc is achieved with **P-14**. Secondly, a 7:1 enantioselectivity for Oct α Glc and exclusive enantioselective recognition for Oct β Glc are respectively observed, indicating the perfect enantio-discrimination induced by the inherent chirality of the *M*-enantiomer. Next, the authors also tested the recognition of the same sugar derivatives with the four stereoisomers of hemicryptophane **41** (Scheme 1.7) to investigate more accurately the control of the inherent chirality of the CTV on the enantioselective recognition. In this case, modest to high diastereoselectivity in favor of Oct β Glc over Oct α Glc for the four isomers of **41** is reported. In addition, in most cases the exclusive binding of the *M*-enantiomers is observed, in accord with the above results, demonstrating the crucial role of the inherent chirality of the CTV, by comparison with the central chirality of the trialkanol amine moiety.

The four stereoisomers of hemicryptophane **29**, which bear four stereogenic centers, (three asymmetric carbons and the CTV unit, Scheme 1.4), were also tested for the stereoselective recognition of glucopyranoside in CDCl₃.⁵⁶ As shown in Table 1.5, the binding abilities of **29** have been improved compared to the previous hosts, with *K_a* values up to one order of magnitude larger. For example, host *M*-(*S,S,S*)-**29** shows the largest binding constant for Oct α Glc (595 M⁻¹) and Oct β Glc (1660 M⁻¹). The trend in diastereoselectivity is opposite to that of host **14**, since for all the isomers of **29** Oct β Glc shows larger binding constants than its α -anomer with a diastereoselective ratio of 2.8 for *M*-(*S,S,S*)-**29**, and exclusive binding for *P*-(*S,S,S*)-**29**. According to the authors, the binding sites being similar in hosts **14** and **29**, conformational changes induced by the addition of the methyl groups account for both the improvement of the binding affinity and the change in selectivity. A marked, or even exclusive, enantioselectivity in favor of the *M*-configured hosts is also observed, such as the binding of Oct α Glc with *P*-(*S,S,S*)-**29** and *M*-(*R,R,R*)-**29**, which is consistent with the results obtained with **14**.

Remarkable diastereoselective recognition of α -mannoside in CDCl₃ was achieved using

the four stereoisomers of hemicryptophane **30** (Scheme 1.4).⁵⁷ An overall trend of the selectivity, defined from the binding constants towards the different guests with the four hosts, was observed with the following order (Table 1.5): Oct α Man > Oct β Man > Oct β Glc > Oct α Glc > Oct α Gal > Oct β Gal, which is in good agreement with the different abilities of the guest to be involved in intermolecular hydrogen bonds.^{178,179} The more the saccharide can make hydrogen bonds with other molecules, the higher is the binding constant. This also highlights that hydrogen-bonding interactions are crucial for the recognition process. For instance, receptor *M*-(*R,R,R*)-**30** can complex almost exclusively Oct α Man facing to Oct β Gal with the higher binding constant $K_a = 2511 \text{ M}^{-1}$. However, the authors report an excellent diastereoselectivity for the four stereoisomers of **30** with the carbohydrate guests, but a moderate enantioselectivity.

Table 1.5 Binding Constants K_a (M^{-1}) for the 1:1 Complexes Formed Between Different Enantiopure Hemicryptophane Hosts and Carbohydrate Guests^{a,b}

Host	Oct α Glc	Oct β Glc	Oct α Man	Oct β Man	Oct α Gal	Oct β Gal	Ref.
<i>M</i> - 14	216	64					155
<i>P</i> - 14	31	— ^c					155
<i>M</i> -(<i>R,R,R</i>)- 41	123	226	— ^c	— ^c			155
<i>P</i> -(<i>R,R,R</i>)- 41	— ^c	115	— ^c	— ^c			155
<i>M</i> -(<i>S,S,S</i>)- 41	155	184	— ^c	— ^c			155
<i>P</i> -(<i>S,S,S</i>)- 41	— ^c	— ^c	— ^c	— ^c			155
<i>M</i> -(<i>S,S,S</i>)- 29	595	1660					56
<i>P</i> -(<i>S,S,S</i>)- 29	— ^c	183					56
<i>P</i> -(<i>R,R,R</i>)- 29	34	384					56
<i>M</i> -(<i>R,R,R</i>)- 29	56	192					56
<i>M</i> -(<i>S,S,S</i>)- 30	213	378	1410	804	29	13	57
<i>P</i> -(<i>S,S,S</i>)- 30	141	400	1648	387	112	68	57
<i>P</i> -(<i>R,R,R</i>)- 30	95	722	1544	967	142	59	57
<i>M</i> -(<i>R,R,R</i>)- 30	83	270	2511	641	22	— ^c	57
<i>M</i> -(<i>S,S,S</i>)- 56	41	— ^c	— ^c	61			64
<i>P</i> -(<i>S,S,S</i>)- 56	174	— ^c	— ^c	118			64
<i>P</i> -(<i>R,R,R</i>)- 56	29	72	182	458			64
<i>M</i> -(<i>R,R,R</i>)- 56	223	287	55	40			64
<i>P</i> -(<i>R,R,R</i>)- 57	177	359	616	204			64
<i>M</i> -(<i>R,R,R</i>)- 57	122	457	1174	375			64
<i>M</i> -(<i>S,S,S</i>)- 57	161	403	393	288			64
<i>P</i> -(<i>S,S,S</i>)- 57	98	334	749	197			64

^a K_a was determined by fitting ¹H NMR titration curves (CDCl_3 , 500 MHz, 298 K) with HypNMR2008; estimated error 10%. ^b The blank cells indicate no measurement for this host and guest.

^c No complexation detected.

The binding properties of the stereoisomers of hemicryptophane **56** were compared to those of the model open-shell compounds **57** (Scheme 1.11).⁶⁴ The cage derivatives **56** exhibit lower binding constants than **57**, probably because of the lack of OH groups able to induce hydrogen bonding with the alcohol functions of the carbohydrate guests. The affinity towards carbohydrates follows the same order with hemicryptophane **56** and model host **57**: Oct α Man > Oct β Glc > Oct β Man \approx Oct α Glc. Nevertheless, a better stereoselectivity was achieved with the cage compounds, probably due to a better preorganization. For instance, excellent enantioselectivities were observed with *P*-(*R,R,R*)-**56** and *M*-(*R,R,R*)-**56** with binding constants of 182 M⁻¹ and 287 M⁻¹ toward Oct α Man and Oct β Glc, respectively, whereas no complexation occurred with the enantiomer hosts (Table 1.5). Furthermore, the role played by the inherent chirality of the CTV unit of the hemicryptophanes in the recognition process is highlighted by the fact that the affinity for Oct β Man guest is ten times higher with the host *P*-(*R,R,R*)-**2** than with its diastereomer *M*-(*R,R,R*)-**2**. A good 1:16 diastereoselectivity ratio was also reached in the recognition of Oct β Glc over Oct α Man using hemicryptophane *P*-(*R,R,R*)-**1** as receptor.

1.4.2.5 Recognition of fullerenes

Hemicryptophanes **85a** and **85b** (Scheme 1.16) are good receptors for C₆₀ and C₇₀ fullerenes.⁶⁹ The ¹H NMR NOESY experiments of **85b** in CDCl₃/CS₂ revealed the existence of NOE cross-peaks between some protons in CTV and cyclic triimine, indicating the close contact between the two cyclic units. Addition of 1 equiv. of C₆₀ or C₇₀ caused the disappearance of these NOE signals, suggesting the encapsulation of the fullerenes in the molecular cavity of **85b**. DOSY experiments performed with **85b** showed a significant decrease of the diffusion coefficients of the host molecule in the presence of C₆₀ or C₇₀, in accord with the increase of the apparent size of **85b** resulting in an extended conformation of the linkers after fullerene binding. Vapor pressure osmometry (VPO) experiments in toluene were also performed and the number-average molecular weights of **85b**, C₆₀@**85b** and C₇₀@**85b** were determined to be 2500, 3200 and 3500 u, respectively, in agreement with the corresponding calculated values. Finally, UV-vis titrations were used for determining the binding constants of **85a** and **85b** towards C₆₀ and C₇₀, giving values up to 10⁵ M⁻¹.

1.5 Hemicryptophanes in motion: towards molecular machines

There is an increased interest in the synthesis and development of complex systems capable of performing a well-defined function at the molecular level like brakes, gears, propellers, ratchets, turnstiles, rotors, scissors, gyroscopes, and molecular springs.¹⁸⁰⁻¹⁸⁹ Most supramolecular assemblies are particularly concerned with those novel approaches of functional intelligent molecules and materials. We may assume that changes in the molecular cage conformational space can affect not only thermodynamic properties, such as binding affinity, but also dynamic properties, such as molecular motions, on different time scales and rates, due to conformational changes. In this section we would like to report recent works involving hemicryptophane structures, which have been investigated for their reversible and

controllable conformational changes, foreseeing molecular machines and switches.

1.5.1 Molecular gyroscope

Molecular gyroscopes are chemical compounds or supramolecular complexes containing a rotor that moves freely relative to a stator.¹⁹⁰ Generally, the following three criteria are required for the design of molecular gyroscopic systems: (i) rotary elements (rotators) should be attached to a static framework (stator); (ii) steric contacts, internal rotation barriers, and interaction with solvent should be minimized to allow low-barrier rotary motion; and (iii) rotating groups should be isolated and/or well-separated from each other.

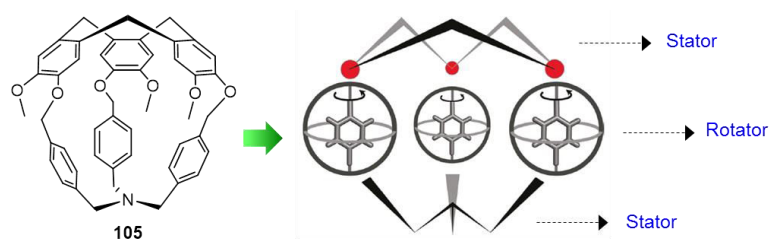


Figure 1.21 Gyroscope-inspired hemicryptophane **105** possessing two rigid stator and three rotator groups.

Dmochowski *et al.* reported the gyroscope-inspired scaffold shown in Figure 1.21, in which the CTV and trisbenzylamine units of hemicryptophane **105** serve as the two-component stator bridged by three *p*-phenylenes, which are rotators.⁵² The X-ray molecular structure of **105** showed an empty tribenzylamine hemicryptophane cavity because of the compact size of the cage. This absence of encapsulated solvent molecules that could hinder *p*-phenylene rotation, suggests a high freedom degree of rotation for the three rotators. The ¹H NMR experiments performed in the 180-300 K temperature range allowed determining the energy barrier of 9.2 kcal mol⁻¹ for the rotation of the *p*-phenylene groups at the coalescence temperature (203 K). To investigate the conformational fluctuations of the rotators and stator, molecular dynamic simulations were carried out, which reveal the existence of weak steric hindrance between neighboring *p*-phenylenes, accounting for the measured energy barrier for rotation. Hence, this work presents a rigid hemicryptophane framework bearing close multiple rotators, which constitutes a molecular gyroscopic system. It should be noted that in spite of the fact that the correlated despite rotation of the aromatic rings was not observed and the control of the direction of the motion was not achieved, this gyroscope-inspired hemicryptophane is an important step towards the control of the direction and the coupling of rotators within molecular systems.

1.5.2 Molecular propeller

Atrane structures are an interesting class of compounds, which adopt a right- or left-handed propeller-like geometry defining a helical chirality with Δ or Λ configuration, respectively.^{138,191,192} For instance, the vanatrane derivatives obtained from the triethanolamine core and oxidovanadium compounds provide Δ/Λ enantiomers (Figure 1.22). If an additional chiral element, for example with *S*-configuration, is introduced to the framework, the two *S*- Δ

and S - Λ diastereomers combining the new stereocenter with the helical chirality of the atrane structure are formed. If the two diastereomers are rigid so that the stereoconversion of the clockwise and anticlockwise orientations of the propeller-like arrangement is slow on the NMR time scale, the Δ or Λ forms corresponding to the two species could be observed on the ^1H NMR spectra. More importantly, if the Δ and Λ configuration of the atrane structure can be controlled by external stimuli, such as chemical, electrochemical, photochemical or thermal input, a real molecular propeller system with molecular switch function could be developed.

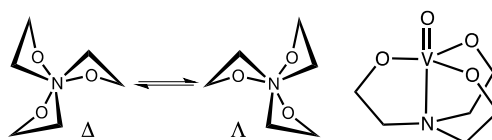


Figure 1.22 Vanatrane structure and its Δ and Λ forms viewed down the N-V bond.

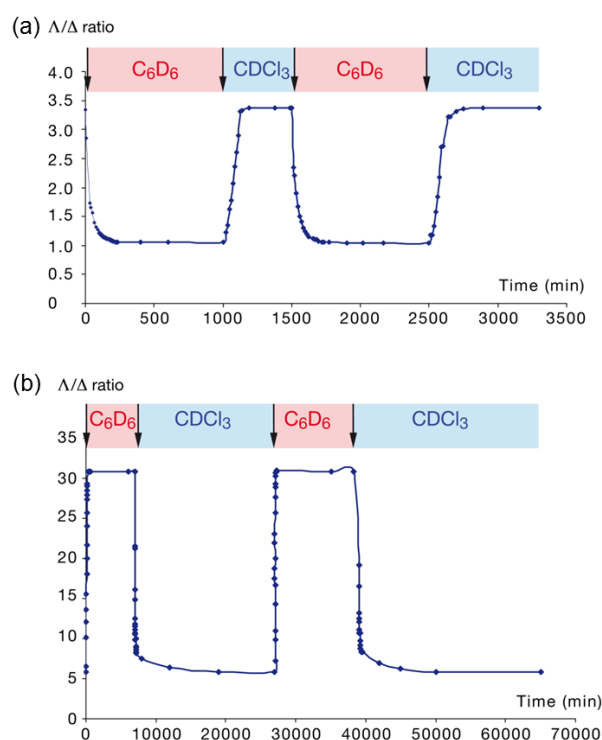


Figure 1.23 Plot of the Λ/Δ ratio (from ^1H NMR data) vs. time for the $\Delta \rightleftharpoons \Lambda$ stereoconversion of (a) V(V)@M-(S,S,S)-41 and (b) V(V)@P-(S,S,S)-41 , after alternating dissolution in C_6D_6 and CDCl_3 .

Martinez *et al.* investigated the oxidovanadium hemicryptophane complex V(V)@41 including the vanatrane structure (Scheme 1.28). Because of the atrane structure of the vanadyl moiety, they identified in the ^1H NMR spectra the two diastereomers $\text{V(V)@M-(S,S,S)-\Lambda-41}$ and $\text{V(V)@M-(S,S,S)-\Delta-41}$ in the 1:0.35 ratio in CDCl_3 , respectively.^{139,156} Similarly, the $\text{V(V)@P-(S,S,S)-\Lambda-41}$ and $\text{V(V)@P-(S,S,S)-\Delta-41}$ diastereomers were obtained in the 1:0.17 ratio. The molecular structures obtained from DFT calculations and from X-ray diffraction demonstrate that the major species in each complex adopts the Λ configuration, more stable than the Δ one. Interestingly, it was found that the nature of the solvent strongly affects the Δ/Λ ratio (solvent driven process). For instance, when the solid of V(V)@M-(S,S,S)-41 , obtained by evaporation from a CHCl_3 solution, is dissolved in C_6D_6 , the Δ/Λ ratio gradually decreased from 1/0.35 to 1/1 as a result of interconversion between the

two diastereomers. Afterwards, evaporation and re-dissolution of the solid in CDCl_3 resulted in the slow increase of the Δ/Λ ratio from 1/1 to 1/0.35. Therefore, alternating change of the solvent could give rise to a diastereoselective interconversion between the two stable states having Λ -**41**/ Δ -**41** ratios of 74/26 and 50/50 respectively (Figure 1.23a). At least, six switching cycles in the reversible bistable system were performed. Alternating change of the solvent for $V(V)@P$ -(*S,S,S*)-**41** also led to a diastereoselective interconversion (Figure 1.23b). These results show that not only the motion of the hemicryptophane molecular propellers can be controlled, but they could also be developed as molecular chiral switches by means of the solvent as an external stimulus. The energy barriers for the $\Delta \rightleftharpoons \Lambda$ equilibrium were determined by NMR experiments, and gave high values (around 100 $\text{kJ}\cdot\text{mol}^{-1}$ for both complexes). This class of atrane propellers can be considered as a novel mode of chiral switching that is worth of being explored for potential applications.¹⁹³⁻¹⁹⁶

1.6 Hemicryptophanes: supramolecular catalysts

Because of their high activity and selectivity, enzymes have been a source of inspiration for supramolecular catalysis.^{111,116,117} The peculiar confined environment induced by the cavity around the substrate should provide a structural preorganization that can stabilize a transition state and ensure the desolvation of the guest molecules. Thus, catalysts, involving host-guest complexes, have been synthesized to mimic such properties of enzymes. To avoid any misunderstanding, by supramolecular catalysis we mean here a catalysis for “reactions that involve supramolecular interactions that do not form part of the basic catalytic reaction”.¹¹⁰ Therefore, hemicryptophanes, presenting a well-defined cavity just above a reactive center, constitute a class of supramolecular catalysts. From the above sections, it has been shown that hemicryptophane cages can encapsulate various guests, including both charged and neutral species. It is thus expected that endohedral location of highly reactive species in such artificially protected and confined space of hemicryptophanes will lead to new catalytic activities and selectivities because of the specific size, shape and chemical environment that may impose specific orientation and conformation of the guest substrates. Moreover, the rigid framework of the host molecule may also protect the catalytic site inside the cavity from degradation during the reaction, improving the stability of the catalyst. In this section, we will report on the use of hemicryptophane complexes that possess endohedral functions acting as supramolecular catalysts. A peculiar attention is paid to the comparison with the corresponding model catalyst, which lacks cavity, in order to highlight the key role of the confinement on the catalytic activity. Two main topics have been investigated: organocatalysis with (pro)azaphosphatranes derivatives (Section 1.6.1) and catalysis using metal-hemicryptophane complexes (Section 1.6.2).

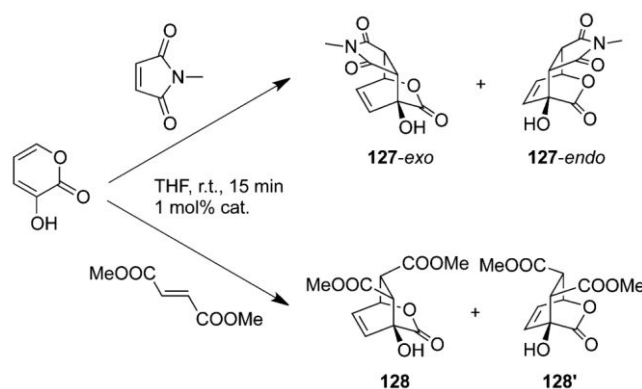
1.6.1 Hemicryptophanes as organocatalysts

Pro-azaphosphatranes, often named Verkade’s superbases ($\text{pK}_a \approx 32$), display remarkable properties as basic or nucleophilic catalysts in numerous reactions, such as transesterification, allylation, silylation and elimination.^{118,122,197} In contrast, their conjugated acid azaphosphatranes, resulting from the protonation of the phosphorous atom of the

proazaphosphatrane, have received less attention. In this section, the use of engaged azaphosphatrane and Verkade's superbase hemicryptophane complexes as organocatalysts is described.

1.6.1.1 Encaged Verkade's superbases for Diels-Alder reactions

Table 1.6 Diels-Alder Reaction Between 3-Hydroxy-2-pyrone and *N*-Methylmaleimide or Dimethylfumarate with Catalysts P@**15a** and P@**126a**.



dienophile	catalyst	compound (%) ^a	de (%) ^b
<i>N</i> -methylmaleimide	P@ 126a	127 (99)	43 ^c
<i>N</i> -methylmaleimide	P@ 15a	127 (100)	77 ^c
dimethylfumarate	P@ 126a	128 (95)	20
dimethylfumarate	P@ 15a	128 (<1)	-

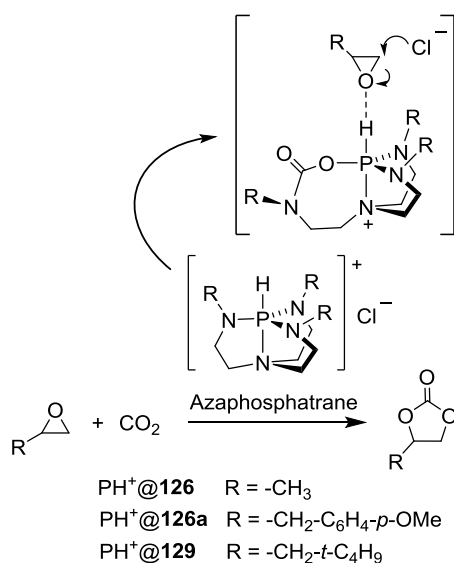
^a Yields were determined from NMR spectra using 2,4-dibromomesitylene as internal reference. ^b Diastereomeric excesses were determined by NMR. ^c The major product is **127-endo**.

A first example concerns the use of pro-azaphosphatranes in Diels-Alder reactions. Despite Verkade's superbases display remarkable properties as basic or nucleophilic catalysts in numerous reactions, their use in Diels-Alder reaction was only reported in 2014. The encaged Verkade's superbase P@**15a** and the model one P@**126a**, which lacks a cavity (Figure 1.7), were used as organocatalyst for the base-catalyzed Diels-Alder reactions (Table 1.6).¹⁹⁸ The model catalyst P@**126a** is able to perform this reaction efficiently for both substrates with high yields, while the supramolecular catalyst P@**15a** displays a catalytic activity that is substrate-dependent. For instance, a quantitative yield is achieved with *N*-methylmaleimide as dienophile, whereas no reaction occurs with dimethylfumarate (Table 1.6). According to the authors, the confinement of the organocatalyst in a deep and narrow cavity combined with steric hindrance of the *trans*-dimethylfumarate can account for this result. In addition, it could be noticed that both catalysts exhibit quantitative yields for the reaction between 3-hydroxy-2-pyrone and *N*-methylmaleimide, but the caged catalyst P@**15a** displays much higher diastereomeric excess than the model P@**126a** (77% and 43%, respectively, both in favor of the **127-endo** product). It is suggested that large active sites allow various transition-state geometries, whereas a catalyst engaged in a tight space can limit them, thus favoring the most compact ones and leading to an overall improvement of the selectivity. These results indicate

that not only the yields and catalytic activities are altered by the confinement of the active site, but the encapsulation of the organocatalyst also improves the stereoselectivity of the Diels-Alder reaction. This case constitutes an important step in the development of stereoselective catalysis based on active sites confined in a hemicryptophane cavity.

1.6.1.2 Encaged azaphosphatrane catalysts for CO₂ conversion

The use of azaphosphatranes as organocatalysts for CO₂ conversion was developed recently. The conversion of carbon dioxide (CO₂) into cyclic carbonate has emerged as a powerful tool to produce renewable chemical feedstocks for organic synthesis from this greenhouse effect gas, since this carbon source is abundant, cheap and non-toxic.¹⁹⁹⁻²⁰¹ In 2013, Dufaud, Martinez *et al.* found that azaphosphatranes, such as those in Scheme 1.31, can be used as efficient catalysts for the synthesis of cyclic carbonates from CO₂ and epoxides.²⁰² They demonstrated that the catalytic reaction was first-order rate dependent on epoxide, catalyst and CO₂, and proposed a mechanism where both the epoxide and the CO₂ were simultaneously activated at a single molecule of catalyst. They also found that the substitution pattern on the catalyst greatly affects activity and stability; for instance, catalysts PH⁺@**126a** and PH⁺@**129** are much more efficient and stable than PH⁺@**126**, because of the steric protection of the ⁺P-H site in the former catalysts.



Scheme 1.31 Synthesis of Cyclic Carbonates from Epoxide and Carbon Dioxide Catalyzed by Azaphosphatranes PH⁺@**126**, PH⁺@**126a** and PH⁺@**129**.

In order to further improve the efficiency and stability of the catalyst, azaphosphatrane@hemicryptophane catalysts, such as PH⁺@**15a**, PH⁺@**15b** and PH⁺@**15i** (Scheme 1.27), were engaged in CO₂ conversion into cyclic carbonates.²⁰³ The caged catalyst PH⁺@**15a** was found to be much more efficient than the corresponding model catalyst PH⁺@**126a**, as shown in Figure 1.24. Firstly, regarding the turnover number (TON) after 24 h, the caged PH⁺@**15a** was twice as active as its model PH⁺@**126a** when a ratio of 1000:1 was inputted between the epoxide (styrene oxide) and catalyst (1 bar, 373 K). In addition, no noticeable alteration of activity for PH⁺@**15a** was observed, whereas a steady decline in activity occurred for model catalyst PH⁺@**126a**. Hence, these results indicate that the P-H

active site of $\text{PH}^+\text{@15a}$ is protected from degradation. The preorganization of the molecular cage likely reinforces the ability of the catalytic core to maintain its atrane structure during the catalytic cycle, thus improving the stability. Interestingly, it was also found that the reactivity of the caged catalyst $\text{PH}^+\text{@15i}$, which has a narrower cavity, was much lower than $\text{PH}^+\text{@15a}$. These observations suggest that the size and shape of the nanospace for the caged catalysts significantly affect their reactivity in the conversion of CO_2 to cyclic carbonates.

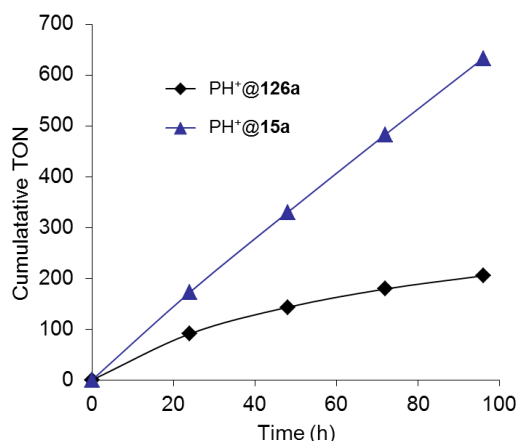


Figure 1.24 Changes of the cumulative TON for catalysts $\text{PH}^+\text{@15a}$ and $\text{PH}^+\text{@126a}$ as a function of time. Reaction conditions: styrene oxide (50.0 mmol), catalyst (0.05 mmol), CO_2 (1 bar) and 100 °C.

1.6.2 Metal-hemicryptophane complexes as catalysts

It is widely recognized that metal ion embedded in the proteic cavity has key roles not only in the recognition events but also in catalysis for generating transient species and directing their reactivity.^{111,112,116} Thus the design of biomimetic cage complexes for the modelling of these metallo-enzyme active sites is very meaningful. Although most of the supramolecular systems designed for catalysis are not so active either because they are too rigid, or they should be used in stoichiometric amounts since the reaction product remains in the cavity preventing the next catalytic cycle, the metal-hemicryptophane complexes have proved to be very efficient in catalysis achieving usually very high turnover number (TON). In this section, the organometallic hemicryptophane complexes bearing metal active sites, such as vanadium(V), zinc(II), copper(II) and ruthenium(II) for supramolecular catalysis will be presented.

1.6.2.1 Encaged Vanadium(V) catalysts for sulfoxidation

In 2009, the first metal-hemicryptophane complex used for catalysis was reported.²⁰⁴ The diastereomeric hemicryptophane-oxidovanadium(V) complexes, V(V)@M-(S,S,S)-41 and V(V)@P-(S,S,S)-41 succeeded in efficient oxidation of sulfide to sulfoxide. With a 10 mol% catalyst and cumene hydroperoxyde (CHP) as oxygen source, the oxidation of thioanisole is much faster with the encaged catalyst V(V)@M-(S,S,S)-41 than with the model catalyst $\text{V(V)@M-(S,S,S)-126a}$, which lacks a cavity (Figure 1.25). Within 90 min, the yield reaches 95% with high selectivity (98%). In addition, when decreasing the amount of catalyst to 0.5 mol% and performing the catalysis at r.t., TON up to 180 was obtained, indicating the high efficiency of these supramolecular catalysts.

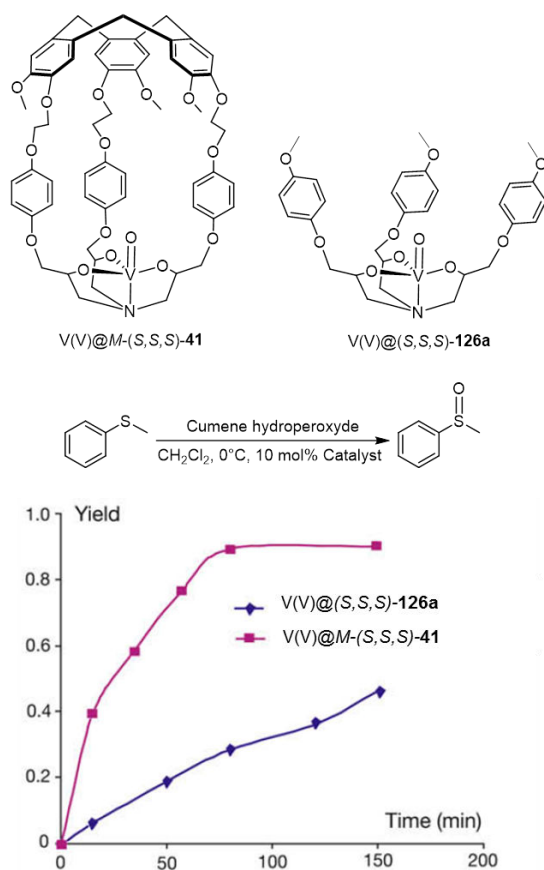


Figure 1.25 Time course of oxidation of thioanisole catalyzed by catalysts **V(V)@M-(S,S,S)-41** and **V(V)@(S,S,S)-126a**. Conditions: 10 mol% catalyst, 1.0 equiv. of CHP, CH_2Cl_2 , 0°C .

The catalysis is also very efficient when *t*-butyl hydroperoxide (TBHP) is used as oxidant. Almost the same catalytic performance is achieved using catalyst **V(V)@P-(S,S,S)-41**. The kinetic constants for the reaction are estimated up to 6-fold higher with the hemicryptophane complex **41** than with the model complex **V(V)@126**. The improvement in the reaction rate by the cage was attributed to the guest activation via molecular encapsulation, and also by the relative flexibility of this cage that can allow fast responsiveness.

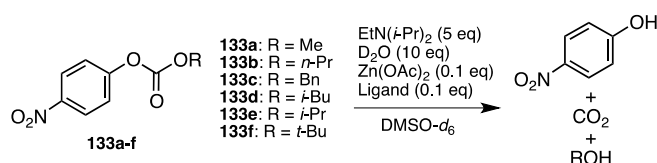
1.6.2.2 Encaged Zinc (II) catalysts for carbonate hydrolysis

The Zn(II)-coordinated hemicryptophane complex **Zn(II)@22** and the **Zn(II)@132** model catalyst were used for the hydrolysis of alkyl carbonates.^{54,205} The Zn-catalysts were generated in situ by adding $\text{Zn}(\text{OAc})_2$ to a solution of the corresponding ligand. The reaction conditions and kinetic data for the hydrolysis of alkyl carbonate **133a-f** are shown in Table 1.7. $\text{DMSO-}d_6$ was used as the solvent because it was found that the reaction rates are much faster in $\text{DMSO-}d_6$ than in other solvent, such as CDCl_3 or CD_3CN . From Table 1.7 it can be seen that for all the substrates, except **133f**, the reaction rates with hemicryptophane catalyst **Zn(II)@22** are much higher than with the model catalyst **Zn(II)@132** with a ratio ranging from 1.8 to 3.5. In addition, different reactivities are also observed for different substrates with the hemicryptophane catalyst.

For example, the hydrolysis of substrate **133a** bearing a methyl group gives the highest rate constant and a 2.2 ratio for $k_{\text{Zn(II)@22}}/k_{\text{Zn(II)@132}}$. Despite the large size of benzyl and

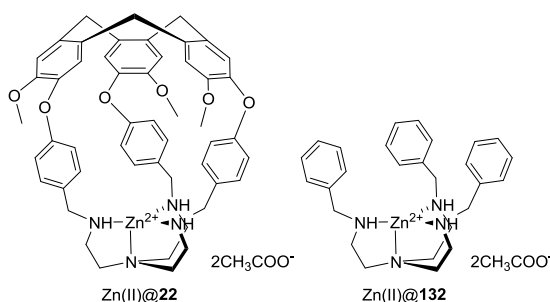
p-nitrophenoxy groups in **133c**, the rate constant is still acceptable, suggesting that part of the substrate goes inside the cavity. The hydrolysis of **133d** and **133e** gives rise to the largest value of $k_{\text{Zn(II)@22}}/k_{\text{Zn(II)@132}}$ between hemicryptophane and model catalysts. Surprisingly, the hydrolysis of **133f** with the hemicryptophane catalyst is slower than the model compound, indicating that the *t*-Bu group has fully hindered the access to the inner zinc site. Hence, all these results demonstrate that the higher catalytic reactivity of the hemicryptophane catalyst is due not only to the proximity thanks to the substrate encapsulation within the cavity, but also to the control of the solvent access, inhibiting DMSO coordination with the zinc site into the cavity.

Table 1.7 Zinc-Catalyzed Hydrolysis of Alkyl Carbonates **133a-f**.^a



Substrate	Ligand	k_{obs} (10^{-3} h^{-1})	$k(\mathbf{22})/k(\mathbf{120})$
133a	22	35	2.2
133a	132	16	
133b	22	18	1.8
133b	132	10	
133c	22	27	1.8
133c	132	15	
133d	22	6.2	2.6
133d	132	2.4	
133e	22	9.2	3.5
133e	132	2.6	
133f	22	4.4	0.8
133f	132	5.4	

^a Conditions: 85 μM substrate, 5.0 equivalents EtN(*i*-Pr)₂, 10 equivalents D₂O and 0.1 equivalent catalyst in DMSO-*d*₆ at 295 K.



1.6.2.3 Encaged Ru (II) catalysts for the oxidation of alcohols

RuCl₂@**22** was tested as catalyst in the oxidation of alcohols into aldehyde and carboxylic acid, using cerium(IV) ammonium nitrate (Ce(NH₄)₂(NO₃)₆) as stoichiometric oxidant (Table

1.8).¹⁴⁵ The cage catalyst was found to be much more selective than the model compound based on the tris(2-benzylaminoethyl)amine ligand **132** (RuCl₂@**132**). Indeed, a complex mixture of aldehyde and carboxylic acid was obtained when catalyst RuCl₂@**132** was used for the oxidation of primary alcohols, whereas the hemicryptophane complex RuCl₂@**22** strongly favored the formation of the aldehyde and suppressed the over-oxidation to the carboxylic acid. Moreover, using the electro-deficient 4-nitrobenzyl alcohol substrate, the cage complex was found to be both more efficient and selective than the model one. However, with the 2-dodecanol secondary alcohol, the model catalyst RuCl₂@**132** displayed a better activity: the higher steric hindrance of the secondary alcohol could prevent its access to the encaged catalytic site, accounting for this experimental result.

Table 1.8 Ruthenium Catalyzed Oxidation Reactions.^a

Catalyst	Substrate	Aldehyde Yield (%)	Carboxylic acid Yield (%)
RuCl ₂ @ 132	1-octanol	18	82
RuCl ₂ @ 22	1-octanol	90	0
RuCl ₂ @ 132	benzyl alcohol	52	48
RuCl ₂ @ 22	benzyl alcohol	91	9
RuCl ₂ @ 132	4-methoxybenzyl alcohol	55	41
RuCl ₂ @ 22	4-methoxybenzyl alcohol	94	6
RuCl ₂ @ 132	4-nitrobenzyl alcohol	27	10
RuCl ₂ @ 22	4-nitrobenzyl alcohol	88	12
RuCl ₂ @ 132	2-dodecanol	68 ^b	-
RuCl ₂ @ 22	2-dodecanol	26 ^b	-

^a Conditions: alcohol (0.1 mmol), catalyst (5 mol%), Ce(NH₄)₂(NO₃)₆ (4eq.), in CH₃CN/H₂O (1/0.3). ^b Product is 2-dodecanone.

1.6.2.4 Encaged Copper (II) catalysts for cycloalkane oxidation

The direct conversion of largely available alkanes into more valuable products is a subject of great interest.²⁰⁶⁻²⁰⁹ An example with industrial significance concerns the oxidation products of cyclohexane, cyclohexanol and cyclohexanone, since they are used for the production of adipic acid and caprolactame involved in the manufacture of nylon-6,6' and nylon-6 respectively.²¹⁰⁻²¹³ The industrial process uses homogeneous cobalt(III)-naphthalenate as catalyst and dioxygen as oxidant at high temperature (150°C) forming cyclohexanone in low yield (4%) to achieve good selectivity (85%). Hence, alternative approaches to transform alkane efficiently and selectively under relatively mild conditions are necessary.

Efficient alkane C-H bond oxidation with H₂O₂ as a clean oxidant under mild conditions was achieved using the Cu(II)-hemicryptophane complex Cu(II)@**15a**.²¹⁴ As shown in Figure 1.26, when using 1 mol% catalyst for the oxidation of cyclohexane (CyH) by H₂O₂ in MeCN at r.t., a much higher yield is obtained after two hours with the hemicryptophane catalyst Cu(II)@**15a** than with the model catalysts Cu(II)@**126** or Cu(ClO₄(H₂O))₆, indicating the important role of the cage structure. The time course also shows similar initial reaction rates for Cu(II)@**15a** and Cu(II)@**126**, however, the reaction stopped after 1 hour with Cu(II)@**126**

(14% yield), whereas it still proceeded using Cu(II)@**15a** until 2-fold higher yield was displayed. These observations suggest that the improved catalytic performance of the hemicryptophane catalyst is attributed to the prevention of active site degradation protected by the cage, rather than the direct increase of reactivity of the catalytic center. Self-oxidation reactions between two molecules of the hemicryptophane catalysts should be avoided because of the location of the active site in the inner cavity. When decreasing the catalyst amount to 0.1 mol%, a TON of about 110-130 was achieved, indicating the high efficiency of the Cu(II)@**15a** for CyH oxidation. Furthermore, competition experiments between the closely related CyH and cyclooctane or adamantane were performed and show that Cu(II)@**15a** is able to discriminate more efficiently CyH from cyclooctane or adamantane than its model, emphasizing that the oxidation occurs inside the catalyst cavity similar to enzyme catalysis.

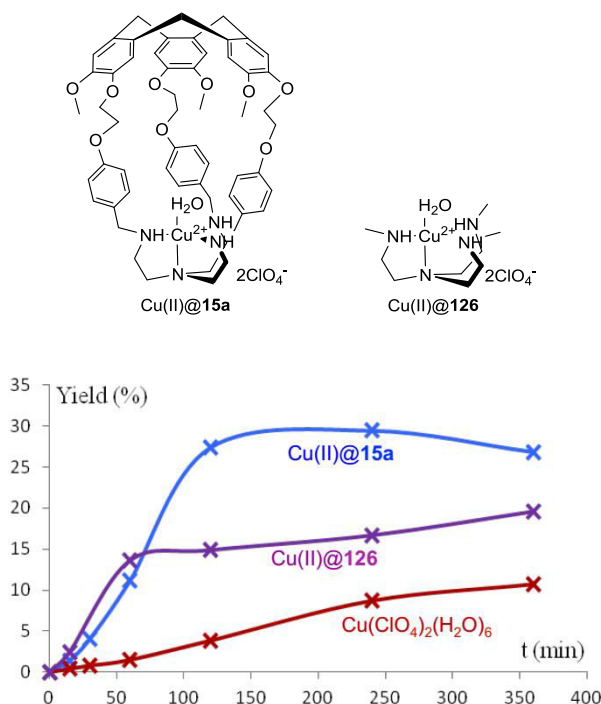


Figure 1.26 Time course of oxygenation of CyH catalyzed by Cu(II)@**15a**, Cu(II)@**126** and Cu(ClO₄)₂(H₂O)₆. Conditions: MeCN (250 μ L), CyH (3.2 μ L, 30 μ mol), H₂O₂ (300 μ mol), catalyst (0.3 μ mol), 35 $^{\circ}$ C).

1.7 Conclusions and perspectives

In this article, advances in hemicryptophane chemistry have been thoroughly reviewed. A brief history about its development is first given in the introduction part. Then synthetic methods and applications in recognition, molecular machines and supramolecular catalysis are respectively described. When compared to other molecular containers such as cryptophanes, hemicryptophanes appear as a young family of molecular cages, which were only gradually recognized within the last decade. It cannot be neglected that they bear plenty of inborn advantages that have greatly promoted their development.

(1) With respect to the synthesis, their synthetic strategies are quite flexible. The cage-closure could be end up with the reaction at the *north* or *south* part, or [1+1] coupling

between the *north* and *south* moieties. Sometimes, high overall yield could be obtained starting from commercial available materials. In addition, hemicryptophanes are chiral cages because of the inherent chirality of the CTV, and many enantiopure hemicryptophanes have been successfully obtained. Furthermore, water-soluble compounds, capsules constructed by dynamic reversible bonds/interactions, and metal/non-metal functionalized cages represent also important developments in the synthesis of hemicryptophanes.

(2) In terms of their application in recognition, the hemicryptophanes are a versatile class of host molecules that can encapsulate various substrates, including neutral or charged guests, chiral or achiral molecules. The rigid CTV scaffold provides a well-preorganized cavity, of which size and shape can be adjusted by changing the linkages between the CTV and *south* units. The *south* moiety is also modulable and can lead to cage molecules with ditopic recognition properties. Thus, elegant heteroditopic recognition of ion pairs and zwitterions has been successfully achieved. Other exciting progresses include the use of water-soluble cages for the recognition of choline in pure water and the exclusive enantioselective complexation of carbohydrates.

(3) Despite the hemicryptophane enters the field of molecular machinery very recently, some appealing results have been achieved. For instance, hemicryptophane oxidovanadium complexes exhibit a reversible change in its propeller motion of the vanatrane structure uniquely controlled by the solvent, establishing an atrane-based molecular chiral switch displaying stimuli-responsive properties. The relatively rigid scaffold of the CTV and the multiple functionalizations of the linkages and *south* moieties imply that hemicryptophanes frequently display unexpected molecular mechanical properties.

(4) With regard to the catalysis, the endohedral location of highly reactive sites in this special class of hemicryptophane cages has offered a lifelike biomimetic modeling of enzymes. Benefiting from the easy functionalization of the *south* part with active species and their guest encapsulation properties, various efficient organo- and organometallic-hemicryptophane catalysts have been prepared. A stimulating step is the Verkade's encaged hemicryptophane catalysts, whose basicity and reactivity can be controlled by designing the size and shape of the cavity. Another one is that hemicryptophane complexes have proven to be superior catalysts usually exhibiting high TONs, because of their relatively flexible structure compared with other macrocycles. The high stability of the catalysts protected by the cage structure, for instance, observed from the case of CO₂ conversion, is also a key feature that can greatly improve their catalytic performance.

Albeit hemicryptophane chemistry has made great progress during the last decade, their potential in synthesis and applications are still waiting for being further explored. (i) More synthetic strategies can be involved for more efficient and greener cage constructions, such as combinatorial dynamic chemistry.²¹⁵⁻²¹⁷ (ii) The characterization of the guest recognition mainly relies on NMR spectroscopy, which has a high detection limit and slow analysis speed. More effective signaling groups can be incorporated into the cage allowing their use in living systems,²¹⁸⁻²²⁰ such as fluorescent bio-imaging or magnetic resonance imaging (MRI). (iii) The exploration of their molecular mechanical properties is relatively poor. Indeed, these cages may be able to build various stimuli-responsive host-guest systems based on self-assembly,

similar to what has been studied with rotaxanes, pseudorotaxanes, catenanes or even supramolecular polymers.^{96,98,185-189,221} (iv) Although a few elegant enantiopure hemicryptophanes have been obtained, their application in enantioselective asymmetric catalysis has never been reported, underlining the interest of this challenging task. (v) The major challenge for chemists in supramolecular chemistry is always to run experiments in aqueous medium.^{103,104} Especially, the results can be very exciting if the water-soluble hemicryptophanes achieved the above-mentioned outlook of applications in biological media. (vi) The hemicryptophane cages may also be immobilized on various solid materials, such as zeolite, SiO₂ or polymer, via covalent bonds or non-covalent interactions, which will open new research domains.²²² Therefore, we can confidently anticipate that the chemistry of hemicryptophanes will go far beyond from what has been reported herein and will be an increasingly active field further contributing to the progresses of supramolecular chemistry.

1.8 References

1. Zarra, S.; Wood, D. M.; Roberts, D. A.; Nitschke, J. R. *Chem. Soc. Rev.* **2015**, *44*, 419-432.
2. Ajami, D.; Liu, L.; Rebek, J., Jr. *Chem. Soc. Rev.* **2015**, *44*, 490-499.
3. Qi, Z.; Schalley, C. A. *Acc. Chem. Res.* **2014**, *47*, 2222-2233.
4. Liu, F.; Helgeson, R. C.; Houk, K. N. *Acc. Chem. Res.* **2014**, *47*, 2168-2176.
5. Jin, Y.; Wang, Q.; Taynton, P.; Zhang, W. *Acc. Chem. Res.* **2014**, *47*, 1575-1586.
6. Durot, S.; Taesch, J.; Heitz, V. *Chem. Rev.* **2014**, *114*, 8542-8578.
7. McKee, V.; Nelson, J.; Town, R. M. *Chem. Soc. Rev.* **2003**, *32*, 309-325.
8. Yu, G.; Jie, K.; Huang, F. *Chem. Rev.*, **2015**, *115*, 7240-7303.
9. Zheng, B.; Wang, F.; Dong, S.; Huang, F. *Chem. Soc. Rev.*, **2012**, *41*, 1621-1636.
10. Gokel, G. W. Crown ethers and cryptands. *Monographs in Supramolecular Chemistry*, Stoddart, J. F. Ed., **1991**, The Royal Society of Chemistry.
11. Rebilly, J. N.; Colasson, B.; Bistri, O.; Over, D.; Reinaud, O. *Chem. Soc. Rev.* **2015**, *44*, 467-489.
12. Guo, D. S.; Liu, Y. *Acc. Chem. Res.* **2014**, *47*, 1925-1934.
13. Mokhtari, B.; Pourabdollah, K.; Dalali, N. *J. Coord. Chem.* **2011**, *64*, 743-794.
14. Kobayashi, K.; Yamanaka, M. *Chem. Soc. Rev.* **2015**, *44*, 449-466.
15. Pochorovski, I.; Diederich, F. *Acc. Chem. Res.* **2014**, *47*, 2096-2105.
16. Assaf, K. I.; Nau, W. M. *Chem. Soc. Rev.* **2015**, *44*, 394-418.
17. Kaifer, A. E. *Acc. Chem. Res.* **2014**, *47*, 2160-2167.
18. Isaacs, L. *Acc. Chem. Res.* **2014**, *47*, 2052-2062.
19. Crini, G. *Chem. Rev.* **2014**, *114*, 10940-10975.
20. Engeldinger, E.; Armspach, D.; Matt, D. *Chem. Rev.* **2003**, *103*, 4147-4173.
21. Xue, M.; Yang, Y.; Chi, X.; Zhang, Z.; Huang, F. *Acc. Chem. Res.*, **2012**, *45*, 1294-1308.
22. Ogoshi, T. *J. Incl. Phenom. Macrocycl. Chem.*, **2012**, *72*, 247-262.
23. Ogoshi, T. Pillararenes. *Monographs in Supramolecular Chemistry*, vol. 18, P. Gale, J. Steed, Eds., **2016**, The Royal Society of Chemistry.
24. Brotin, T.; Dutasta, J.-P. *Chem. Rev.* **2009**, *109*, 88-130.
25. Collet, A. *Tetrahedron* **1987**, *43*, 5725-5759.
26. Collet, A. *Comprehensive Supramolecular Chemistry*; Atwood, J. L.; Davies, J. E. D.;

- MacNicol, D. D.; Vogtle F. (Eds.); Elsevier: Oxford, 1996; vol. 2, p 325.
27. Canceill, J.; Collet, A.; Gabard, J.; Kotzyba-Hiber, F.; Lehn, J. M. *Speleands. Helv. Chim. Acta* **1982**, *65*, 1894-1897.
 28. Smeets, J. W. H.; Coolent, H. K. A. C.; Zwikker, J. W.; Nolte, R. J. M. *Recl. Trav. Chim. Pays-Bas* **1989**, *108*, 215-218.
 29. Rapenne, G.; Crassous, J.; Collet, A.; Echegoyen, L.; Diederich, F. *Chem. Commun.* **1999**, 1121-1122.
 30. Gosse, I.; Dutasta, J.-P.; Perrin, M.; Thozet, A. *New J. Chem.* **1999**, *23*, 545-548.
 31. Vériot, G.; Dutasta, J.-P.; Matouzenko, G.; Collet, *Tetrahedron* **1995**, *51*, 389-400.
 32. Wei, J.; Li, Z.-M.; Jin, X.-J.; Yao, X.-J.; Cao, X.-P.; Chow, H.-F.; Kuck, D. *Chem. Asian J.* **2015**, *10*, 1150-1158.
 33. Szumna, A. *Chem. Soc. Rev.* **2010**, *39*, 4274-4285.
 34. Zhang, W.-Z.; Yang, K.; Li, S.-Z.; Ma, H.; Luo, J.; Wang, K.-P.; Chung, W.-S. *Eur. J. Org. Chem.* **2015**, 765-774.
 35. Canceill, J.; Collet, A.; Gabard, J.; Gottarelli, G.; Spada, G. *J. Am. Chem. Soc.* **1985**, *107*, 1299-1308.
 36. Freedman, T. B.; Cao, X.; Dukor, R. K.; Nafie, L. A. *Chirality* **2003**, *15*, 743-758.
 37. Stephens, P. J.; Devlin, F. J. *Chirality* **2000**, *12*, 172-179.
 38. Collet, A.; Gottarelli, G. *J. Am. Chem. Soc.* **1981**, *103*, 5912-5913.
 39. Hembury, G. A.; Borovkov, V. V.; Inoue, Y. *Chem. Rev.* **2008**, *108*, 1-73.
 40. Hamilton, T. D.; MacGillivray, L. R. *Cryst. Growth. Des.* **2004**, *4*, 419-430.
 41. Brotin, T.; Guy, L.; Martinez, A.; Dutasta, J.-P. *Top. Curr. Chem.* **2013**, *341*, 177-230.
 42. Valiyaveetil, S.; Engbersen, J. F. J.; Verboom, W.; Reinhoudt, D. N. *Angew. Chem., Int. Ed.* **1993**, *32*, 900-901.
 43. Voloshin, Y. Z.; Belov, A. S. *Russ. Chem. Rev.* **2008**, *77*, 161-175.
 44. Verkade, J. G. *Coord. Chem. Rev.* **1994**, *137*, 233-295.
 45. Hammes, B. S.; Ramos-Maldonado, D.; Yap, G. P. A.; Liable-Sands, L.; Rheingold, A. L.; Young, V. G., Jr.; Borovik, A. S. *Inorg. Chem.* **1997**, *36*, 3210-3211.
 46. Tobey, S. L.; Jones, B. D.; Anslyn, E. V. *J. Am. Chem. Soc.* **2003**, *125*, 4026-4027.
 47. Verkade, J. G.; Kisanga, P. B. *Tetrahedron* **2003**, *59*, 7819-7858.
 48. Raytchev, P. D.; Perraud, O.; Aronica, C.; Martinez, A.; Dutasta, J.-P. *J. Org. Chem.* **2010**, *75*, 2099-2102.
 49. Brotin, T.; Devic, T.; Lesage, A.; Emsley, L.; Collet, A. *Chem. Eur. J.* **2001**, *7*, 1561-1573.
 50. Perraud, O.; Raytchev, P. D.; Martinez, A.; Dutasta, J.-P. *Chirality* **2010**, *22*, 885-888.
 51. Chatelet, B.; Payet, E.; Perraud, O.; Dimitrov-Raytchev, P.; Chapellet, L.-L.; Dufaud, V.; Martinez, A.; Dutasta, J.-P. *Org. Lett.* **2011**, *13*, 3706-3709.
 52. Khan, N. S.; Perez-Aguilar, J. M.; Kaufmann, T.; Hill, P. A.; Taratula, O.; Lee, O. S.; Carroll, P. J.; Saven, J. G.; Dmochowski, I. J. *J. Org. Chem.* **2011**, *76*, 1418-1424.
 53. Lefevre, S.; Zhang, D.; Godart, E.; Jean, M.; Vanthuyne, N.; Mulatier, J.-C.; Dutasta, J.-P.; Guy, L.; Martinez, A. *Chem. Eur. J.* **2016**, *22*, 2068-2074.
 54. Makita, Y.; Sugimoto, K.; Furuyoshi, K.; Ikeda, K.; Fujiwara, S.-i.; Shin-ike, T.; Ogawa, A. *Inorg. Chem.* **2010**, *49*, 7220-7222.
 55. Makita, Y.; Katayama, N.; Lee, H.-H.; Abe, T.; Sogawa, K.; Nomoto, A.; Fujiwara, S.-I.; Ogawa, A. *Tetrahedron Lett.* **2016**, *57*, 5112-5115.

56. Schmitt, A.; Perraud, O.; Payet, E.; Chatelet, B.; Bousquet, B.; Valls, M.; Padula, D.; Di Bari, L.; Dutasta, J.-P.; Martinez, A. *Org. Biomol. Chem.* **2014**, *12*, 4211-4217.
57. Schmitt, A.; Chatelet, B.; Padula, D.; Di Bari, L.; Dutasta, J.-P.; Martinez, A. *New J. Chem.* **2015**, *39*, 1749-1753.
58. Chatelet, B.; Joucla, L.; Padula, D.; Bari, L. D.; Pilet, G.; Robert, V.; Dufaud, V.; Dutasta, J.-P.; Martinez, A. *Org. Lett.* **2015**, *17*, 500-503.
59. Rivera, D. G.; Wessjohann, L. A. *J. Am. Chem. Soc.* **2006**, *128*, 7122-7123.
60. Gautier, A.; Mulatier, J.-C.; Crassous, J.; Dutasta, J.-P. *Org. Lett.* **2005**, *7*, 1207-1210.
61. Brotin, T.; Montserret, R.; Bouchet, A.; Cavagnat, D.; Linares, M.; Buffeteau, T. *J. Org. Chem.* **2012**, *77*, 1198-1201.
62. Brotin, T.; Goncalves, S.; Berthault, P.; Cavagnat, D.; Buffeteau, T. *J. Phys. Chem. B* **2013**, *117*, 12593-12601.
63. Perraud, O.; Robert, V.; Gornitzka, H.; Martinez, A.; Dutasta, J.-P. *Angew. Chem., Int. Ed.* **2012**, *51*, 504-508.
64. Lefevre, S.; Simonet, R.; Pitrat, D.; Mulatier, J.-C.; Vanthuyne, N.; Jean, M.; Dutasta, J.-P.; Guy, L.; Martinez, *ChemistrySelect* **2016**, *1*, 6316-6320.
65. Cochrane, J. R.; Schmitt, A.; Wille, U.; Hutton, C. A. *Chem. Commun.* **2013**, *49*, 8504-8506.
66. Brégier, F.; Karuppanan, S.; Chambron, J.-C. *Eur. J. Org. Chem.* **2012**, 1920-1925.
67. Brégier, F.; Aubert, E.; Espinosa, E.; Chambron, J.-C. *ChemistrySelect* **2016**, *1*, 2389-2395.
68. Brégier, F.; Lavalle, J.; Chambron, J.-C. *Eur. J. Org. Chem.* **2013**, 2666-2671.
69. Wang, L.; Wang, G.-T.; Zhao, X.; Jiang, X.-K.; Li, Z.-T. *J. Org. Chem.* **2011**, *76*, 3531-3535.
70. Le Gac, S.; Jabin, I. *Chem. Eur. J.* **2008**, *14*, 548-557.
71. Gosse, I.; Robeyns, K.; Bougault, C.; Martinez, A.; Tinant, B.; Dutasta, J.-P. *Inorg. Chem.* **2016**, *55*, 1011-1013
72. Steed, J. W.; Junk, P. C.; Atwood, J. L. *J. Am. Chem. Soc.* **1994**, *116*, 10346-10347.
73. Matsubara, H.; Oguri, S.; Asano, K.; Yamamoto, K. *Chem. Lett.* **1999**, 431-432.
74. Huerta, E.; Isla, E.; Perez, E. M.; Bo, C.; Martin, N.; de Mandoza, J. *J. Am. Chem. Soc.* **2010**, *132*, 5351-5353.
75. Rapenne, G.; Crassous, J.; Echegoyen, L. E.; Echegoyen, L.; Flapan, E.; Diederich, F. *Helv. Chim. Acta* **2000**, *83*, 1209-1223.
76. Hirsch, A.; Lamparth, I.; Karfunkel, H. R. *Angew. Chem., Int. Ed.* **1994**, *33*, 437-438.
77. Kraszewska, A.; Rivera-Fuentes, P.; Rapenne, G.; Crassous, J.; Petrovic, A. G.; Alonso-Gómez, J. L.; Huerta, E.; Diederich, F.; Thilgen, C. *Eur. J. Org. Chem.* **2010**, 4402-4411.
78. Bougault, C.; Bardet, M.; Laugier, J.; Jordanov, J.; Dutasta, J.-P.; Collet, A. *Supramol. Chem.* **1994**, *4*, 139-146.
79. Van Strijdonck, G. P. F.; van Haare, J. A. E. H.; van der Linden, J. G. M.; Steggerda, J. J.; Nolte, R. J. M. *Inorg. Chem.* **1994**, *33*, 999-1000.
80. Matouzenko, G.; Vériot, G.; Dutasta, J.-P.; Collet, A.; Jordanov, J.; Varret, F.; Perrin, M.; Lecocq, S. *New J. Chem.* **1995**, *19*, 881-885.
81. Coolen, H. K. A. C.; Reek, J. N. H.; Ernsting, J. M.; van Leeuwen, P. W. N. M.; Nolte, R. J. M. *Recl. Trav. Chim. Pays-Bas* **1995**, *114*, 381-386.
82. Sumby, C. J.; Hardie, M. J. *Angew. Chem., Int. Ed.* **2005**, *44*, 2945-2959.
83. Sumby, C. J.; Fisher, J.; Prior, T. J.; Hardie, M. J. *Chem. Eur. J.* **2006**, *12*, 6395-6399.

84. Rue, N. M.; Sun, J.; Warmuth, R. *Isr. J. Chem.* **2011**, *51*, 743-768.
85. Makita, Y.; Danno, T.; Fujita, T.; Ikeda, K.; Fujiwara, S.; Ogawa, A. *J. Chem. Crystallogr.* **2012**, *42*, 1075-1079.
86. Cook, T. R.; Zheng, Y.; Stang, P. J. *Chem. Rev.* **2013**, *113*, 734-777.
87. Carruthers, C.; Ronson, T. K.; Sumby, C. J.; Westcott, A.; Harding, L. P.; Prior, T. J.; Rizkallah, P.; Hardie, M. J. *Chem. Eur. J.* **2008**, *14*, 10286-10296.
88. Hardie, M. J. *Isr. J. Chem.* **2011**, *51*, 807-816.
89. Abrahams, B. F.; Boughton, B. A.; FitzGerald, N. J.; Holmes, J. L.; Robson, R. *Chem. Commun.* **2011**, *47*, 7404-7406.
90. Abrahams, B. F.; FitzGerald, N. J.; Robson, R. *Angew. Chem., Int. Ed.* **2010**, *49*, 2896-2899.
91. Henkelis, J. J.; Carruthers, C. J.; Chambers, S. E.; Clowes, R.; Cooper, A. I.; Fisher, J.; Hardie, M. J. *J. Am. Chem. Soc.* **2014**, *136*, 14393-14396.
92. Schaly, A.; Rousselin, Y.; Chambron, J.-C.; Aubert, E.; Espinosa, E. *Eur. J. Inorg. Chem.* **2016**, 832-843.
93. Kataoka, K.; James, T. D.; Kubo, Y. *J. Am. Chem. Soc.* **2007**, *129*, 15126-15127.
94. Kataoka, K.; Okuyama, S.; Minami, T.; James, T. D.; Kubo, Y. *Chem. Commun.* **2009**, *13*, 1682-1684.
95. Le Gac, S.; Luhmer, M.; Reinaud, O.; Jabin, I. *Tetrahedron* **2007**, *63*, 10721-10730.
96. Dong, S.; Zheng, B.; Wang, F.; Huang, F. *Acc. Chem. Res.* **2014**, *47*, 1982-1994.
97. Hu, X. Y.; Xiao, T.; Lin, C.; Huang, F.; Wang, L. *Acc. Chem. Res.* **2014**, *47*, 2041-2051.
98. Ma, X.; Tian, H. *Acc. Chem. Res.* **2014**, *47*, 1971-1981.
99. Schmidt, A.; Casini, A.; Kühn, F. E. *Coord. Chem. Rev.* **2014**, *275*, 19-36.
100. Castilla, A. M.; Ramsay, W. J.; Nitschke, J. R. *Acc. Chem. Res.* **2014**, *47*, 2063-2073.
101. Nishiyabu, R.; Kubo, Y.; James, T. D.; Fossey, J. S. *Chem. Commun.* **2011**, *47*, 1124-1150.
102. Wu, X.; Li, Z.; Chen, X. X.; Fossey, J. S.; James, T. D.; Jiang, Y. B. *Chem. Soc. Rev.* **2013**, *42*, 8032-8048.
103. Kubik, S. *Chem. Soc. Rev.* **2010**, *39*, 3648-3663.
104. Bistri, O.; Reinaud, O. *Org. Biomol. Chem.* **2015**, *13*, 2849-2865.
105. Schmitt, A.; Robert, V.; Dutasta, J.-P.; Martinez, A. *Org. Lett.* **2014**, *16*, 2374-2377.
106. Schmitt, A.; Collin, S.; Bucher, C.; Maurel, V.; Dutasta, J.-P.; Martinez, A. *Org. Biomol. Chem.* **2015**, *13*, 2157-2161.
107. Brotin, T.; Cavagnat, D.; Berthault, P.; Montserret, R.; Buffeteau, T. *J. Phys. Chem. B* **2012**, *116*, 10905-10914.
108. Dubost, E.; Kotera, N.; Garcia-Argote, S.; Boulard, Y.; Leonce, E.; Boutin, C.; Berthault, P.; Dugave, C.; Rousseau, B. *Org. Lett.* **2013**, *15*, 2866-2868.
109. Bai, Y.; Hill, P. A.; Dmochowski, I. J. *Anal. Chem.* **2012**, *84*, 9935-9941.
110. Raynal, M.; Ballester, P.; Vidal-Ferran, A.; van Leeuwen, P. W. *Chem. Soc. Rev.* **2014**, *43*, 1660-1733.
111. Raynal, M.; Ballester, P.; Vidal-Ferran, A.; van Leeuwen, P. W. *Chem. Soc. Rev.* **2014**, *43*, 1734-1787.
112. Brown, C. J.; Toste, F. D.; Bergman, R. G.; Raymond, K. N. *Chem. Rev.* **2015**, *115*, 3012-3035.
113. Pluth, M. D.; Bergman, R. G.; Raymond, K. N. *Science* **2007**, *316*, 85-88.
114. Yoshizawa, M.; Tamura, M.; Fujita, M. *Science* **2006**, *312*, 251-254.

115. Kang, J.; Rebek, J. J. *Nature* **1997**, *385*, 50-52.
116. Homden, D. M.; Redshaw, C. *Chem. Rev.* **2008**, *108*, 5086-5130.
117. Pemberton, B. C.; Raghunathan, R.; Volla, S.; Sivaguru, J. *Chem. Eur. J.* **2012**, *18*, 12178-12190.
118. Wadhwa, K.; Verkade, J. G. *Tetrahedron Lett.* **2009**, *50*, 4307-4309.
119. Wadhwa, K.; Verkade, J. G. *J. Org. Chem.* **2009**, *74*, 5683-5686.
120. Wadhwa, K.; Chintareddy, V. R.; Verkade, J. G. *J. Org. Chem.* **2009**, *74*, 6681-6690.
121. Raders, S. M.; Verkade, J. G. *J. Org. Chem.* **2010**, *75*, 5308-5311.
122. Chintareddy, V. R.; Wadhwa, K.; Verkade, J. G. *J. Org. Chem.* **2009**, *74*, 8118-8132.
123. Raytchev, P. D.; Martinez, A.; Gornitzka, H.; Dutasta, J.-P. *J. Am. Chem. Soc.* **2011**, *133*, 2157-2159.
124. Chatelet, B.; Gornitzka, H.; Dufaud, V.; Jeanneau, E.; Dutasta, J.-P.; Martinez, A. *J. Am. Chem. Soc.* **2013**, *135*, 18659-18664.
125. Payet, E.; Dimitrov-Raytchev, P.; Chatelet, B.; Guy, L.; Grass, S.; Lacour, J.; Dutasta, J.-P.; Martinez, A. *Chirality* **2012**, *24*, 1077-1081.
126. Makita, Y.; Furuyoshi, K.; Ikeda, K.; Fujita, T.; Fujiwara, S.-i.; Ehara, M.; Ogawa, A. *Tetrahedron Lett.* **2011**, *52*, 4129-4131.
127. Wilcox, J. L.; Bevilacqua, P. C. *J. Am. Chem. Soc.* **2013**, *135*, 7390-7393.
128. Wiestner, M. J.; Ulmann, P. A.; Mirkin, C. A. *Angew. Chem., Int. Ed.* **2011**, *50*, 114-137.
129. Yoshizawa, M.; Klosterman, J. K.; Fujita, M. *Angew. Chem., Int. Ed.* **2009**, *48*, 3418-3438.
130. Shinoda, S. *Chem. Soc. Rev.* **2013**, *42*, 1825-1835.
131. Fabbrizzi, L.; Poggi, A. *Chem. Soc. Rev.* **2013**, *42*, 1681-1699.
132. Ngo, H. T.; Liu, X.; Jolliffe, K. A. *Chem. Soc. Rev.* **2012**, *41*, 4928-4965.
133. Mercer, D. J.; Loeb, S. J. *Chem. Soc. Rev.* **2010**, *39*, 3612-3620.
134. Steed, J. W. *Chem. Soc. Rev.* **2009**, *38*, 506-519.
135. Beer, P. D.; Hayes, E. J. *Coord. Chem. Rev.* **2003**, *240*, 167-189.
136. Verkade, J. G. *Acc. Chem. Res.* **1993**, *26*, 483-489.
137. Kim, Y.; Verkade, J. G. *Inorg. Chem.* **2003**, *42*, 4804-4806.
138. Schrock, R. R. *Acc. Chem. Res.* **1997**, *30*, 9-16.
139. Martinez, A.; Guy, L.; Dutasta, J.-P. *J. Am. Chem. Soc.* **2010**, *123*, 16733-16734.
140. Drago, C.; Caggiano, L.; Jackson, R. F. *Angew. Chem., Int. Ed.* **2005**, *117*, 7387-7389.
141. Santoni, G.; Mba, M.; Bonchio, M.; Nugent, W. A.; Zonta, C.; Licini, G. *Chem. Eur. J.* **2010**, *16*, 645-654.
142. Bonchio, M.; Licini, G.; Furia, F. D.; Mantovani, S.; Modena, G.; Nugent, W. A. *J. Org. Chem.* **1999**, *64*, 1326-1330.
143. Bonchio, M.; Licini, G.; Modena, G.; Bortolini, O.; Moro, S.; Nugent, W. A. *J. Am. Chem. Soc.* **1999**, *121*, 6258-6268.
144. Makita, Y.; Sugimoto, K.; Furuyoshi, K.; Ikeda, K.; Fujita, T.; Fujiwara, S.-I.; Ogawa, A. *Supramol. Chem.* **2011**, *23*, 269-272.
145. Makita, Y.; Fujita, T.; Danno, T.; Inoue, M.; Ueshima, M.; Fujiwara, S.; Ogawa, A. *Supramol. Catal.* **2012**, *1*, 9-11.
146. Perraud, O.; Tommasino, J.-B.; Robert, V.; Albela, B.; Khrouz, L.; Bonneviot, L.; Dutasta, J.-P.; Martinez, A. *Dalton Trans.* **2013**, *42*, 1530-1535.
147. Uhlenheuer, D. A.; Petkau, K.; Brunsveld, L. *Chem. Soc. Rev.*, **2010**, *39*, 2817-2826.

148. Ma, X.; Yanli Zhao, Y. *Chem. Rev.*, **2015**, *115*, 7794–7839.
149. Yu, G.; Zhou, J.; Shen, J.; Tang, G.; Feihe Huang, F. *Chem. Sci.*, **2016**, *7*, 4073–4078.
150. Yu, G.; Zhao, R.; Wu, D.; Zhang, F.; Shao, L.; Zhou, J.; Yang, J.; Tang, G.; Chen, X.; Huang, F. *Polym. Chem.*, **2016**, *7*, 6178–6188.
151. Schmitt, A.; Chatelet, B.; Collin, S.; Dutasta, J. P.; Martinez, A. *Chirality* **2013**, *25*, 475–479.
152. Perraud, O.; Lefevre, S.; Robert, V.; Martinez, A.; Dutasta, J.-P. *Org. Biomol. Chem.* **2012**, *10*, 1056–1059.
153. Perraud, O.; Robert, V.; Martinez, A.; Dutasta, J.-P. *Chem. Eur. J.* **2011**, *17*, 4177–4182.
154. Perraud, O.; Robert, V.; Martinez, A.; Dutasta, J.-P. *Chem. Eur. J.* **2011**, *17*, 13405–13408.
155. Perraud, O.; Martinez, A.; Dutasta, J.-P. *Chem. Commun.* **2011**, *47*, 5861.
156. Martinez, A.; Robert, V.; Gornitzka, H.; Dutasta, J.-P. *Chem. Eur. J.* **2010**, *16*, 520–527.
157. Kim, S.-G.; Kim, K.-H.; Jung, J.; Shin, S. K.; Ahn, K. H. *J. Am. Chem. Soc.* **2002**, *124*, 591–596.
158. Schnopp, M.; Haberhauer, G. *Eur. J. Org. Chem.* **2009**, 4458–4467.
159. Haberhauer, G.; Oeser, T.; Rominger, F. *Chem. Eur. J.* **2005**, *11*, 6718–6726.
160. Lohr, H.-G.; Vogtle, F. *Acc. Chemical Res.* **1985**, *18*, 65–72.
161. Moberg, C. *Angew. Chem., Int. Ed.* **2006**, *45*, 4721–4723.
162. Pradhan, T.; Jung, H. S.; Jang, J. H.; Kim, T. W.; Kang, C.; Kim, J. S. *Chem. Soc. Rev.* **2014**, *43*, 4684–4713.
163. Frassinetti, C.; Ghelli, S.; Gans, P.; Sabatini, A.; Moruzzi, M. S.; Vacca, A. *Anal. Biochem.* **1995**, *231*, 374–382.
164. Alkorta, I.; Rozas, I.; Elguero, J. *J. Org. Chem.* **1997**, *62*, 4687–4691.
165. Hibbs, D. E.; Austin-Woods, C. J.; Platts, J. A.; Overgaard, J.; Turner, P. *Chem Eur. J.* **2003**, *9*, 1075–1084.
166. Zajac, M.; Peters, R. *Chem Eur. J.* **2009**, *15*, 8204–8222.
167. Mecozzi, S.; Rebek Jr J. *Chem. Eur. J.* **1998**, *4*, 1016–1022.
168. Pluth, M. D.; Johnson, D. W.; Szigethy, G.; Davis, A. V.; Teat, S. J.; Oliver, A. G.; Bergman, R. G.; Raymond K. N. *Inorg. Chem.* **2009**, *48*, 111–120.
169. Hynes, M. J. *J. Chem. Soc. Dalton Trans.* **1993**, 311–312.
170. Zhao, Y. H.; Abraham, M. H.; Zissimos, A. M. *J. Org. Chem.* **2003**, *68*, 7368–7373.
171. Davis, A. P. *Org. Biomol. Chem.* **2009**, *7*, 3629–3638.
172. Dong, J.; Zhou, Y.; Zhang, F.; Cui, Y. *Chem. Eur. J.* **2014**, *20*, 6455–6461.
173. Sookcharoenpinyo, B.; Klein, E.; Ferrand, Y.; Walker, D. B.; Brotherhood, P. R.; Ke, C.; Crump, M. P.; Davis, A. P. *Angew. Chem., Int. Ed.* **2012**, *51*, 4586–4590.
174. Ke, C.; Destecroix, H.; Crump, M. P.; Davis, A. P. *Nat. Chem.* **2012**, *4*, 718–723.
175. Ferrand, Y.; Klein, E.; Barwell, N. P.; Crump, M. P.; Jimenez-Barbero, J.; Vicent, C.; Boons, G. J.; Ingale, S.; Davis, A. P. *Angew. Chem., Int. Ed.* **2009**, *48*, 1775–1779.
176. Barwell, N. P.; Crump, M. P.; Davis, A. P. *Angew. Chem., Int. Ed.* **2009**, *48*, 7673–7676.
177. Ferrand, Y.; Crump, M. P.; Davis, A. P. *Science* **2007**, *318*, 619–622.
178. Bonar-Law, R. P.; Sanders, J. K. M. *J. Am. Chem. Soc.* **1995**, *117*, 259–271.
179. López de la Paz M.; Ellis, G.; Perez, M.; Perkins, J.; Jimenez-Barbero, J.; Vicent, C. *Eur. J. Org. Chem.* **2002**, 840–855.
180. Erbas-Cakmak, S.; Leigh, D. A.; McTernan, C. T.; Nussbaumer, A. L. *Chem. Rev.* **2015**, *115*, 10081–10206.

181. Mavroidis, C.; Dubey, A.; Yarmush, M. L. *Annu. Rev. Biomed. Eng.* **2004**, *6*, 363-395.
182. Harvey, E. C.; Feringa, B. L.; Vos, J. G.; Browne, W. R.; Pryce, M. T. *Coord. Chem. Rev.* **2015**, *282*, 77-86.
183. Collin, J.-P.; Dietrich-Buchecker, C.; Gavin, P.; Jimenez-Molero, M. C.; Sauvage, J.-P. *Acc. Chem. Res.*, **2001**, *34*, 477-487.
184. Marsella, M. J.; Rahbarnia, S.; Wilmot, N. *Org. Biomol. Chem.*, **2007**, *5*, 391-400.
185. Bruns, C. J.; Stoddart, J. F. *Acc. Chem. Res.* **2014**, *47*, 2186-2199.
186. Zhang, Z.; Han, C.; Yu, G.; Huang, F. *Chem. Sci.*, **2012**, *3*, 3026-3031.
187. Gao, L.; Zhang, Z.; Zheng, B.; Huang, F. *Polym. Chem.*, **2014**, *5*, 5734-5739.
188. Niess, F.; Duplan, V.; Sauvage, J.-P. *Chem. Lett.*, **2014**, *43*, 964-974.
189. Xue, M.; Yang, Y.; Chi, X. Yan, X.; Huang, F. *Chem. Rev.* **2015**, *115*, 7398-7501.
190. Karlen, S. D.; Garcia-Garibay, M. A. *Top. Curr. Chem.* **2005**, *262*, 179-227.
191. Canary, J. W. *Chem. Soc. Rev.* **2009**, *38*, 747-756.
192. Canary, J. W.; Mortezaei, S.; Liang, J. *Coord. Chem. Rev.* **2010**, *254*, 2249-2266.
193. Barboiu, M.; Stadler, A.-M.; Lehn, J.-M. *Angew. Chem., Int. Ed.* **2016**, *55*, 4130-4154.
194. Wang, S.; Sawada, T.; Ohara, K.; Yamaguchi, K.; Fujita, M. *Angew. Chem., Int. Ed.* **2016**, *55*, 2063-2066.
195. Arroyave, F. A.; Ballester, P. J. *Org. Chem.* **2015**, *80*, 10866-10873.
196. Mough, S. T.; Goeltz, J. C.; Holman, K. T. *Angew. Chem. Int. Ed.* **2004**, *43*, 5631-5635.
197. Wadhwa, K.; Verkade, J. G. J. *Org. Chem.* **2009**, *74*, 4368-4371.
198. Chatelet, B.; Dufaud, V.; Dutasta, J. P.; Martinez, A. J. *Org. Chem.* **2014**, *79*, 8684-8688.
199. Aresta, M. Ed, *Carbon dioxide as chemical feedstock*. Wiley-VCH: Weinheim, Germany, 2010.
200. Sakakura, T.; Choi, J. C.; Yasuda, H. *Chem. Rev.* **2007**, *107*, 2365-2387.
201. Omae, I. *Catal. Today* **2006**, *115*, 33-52.
202. Chatelet, B.; Joucla, L.; Dutasta, J.-P.; Martinez, A.; Szeto, K. C.; Dufaud, V. *J. Am. Chem. Soc.* **2013**, *135*, 5348-5351.
203. Chatelet, B.; Joucla, L.; Dutasta, J.-P.; Martinez, A.; Dufaud, V. *Chem. Eur. J.* **2014**, *20*, 8571-8574.
204. Martinez, A.; Dutasta, J.-P. *J. Catal.* **2009**, *267*, 188-192.
205. Makita, Y.; Ikeda, K.; Sugimoto, K.; Fujita, T.; Danno, T.; Bobuatong, K.; Ehara, M.; Fujiwara, S.-i.; Ogawa, A. *J. Organomet. Chem.* **2012**, *706*, 26-29.
206. Shul'pin, G. B. In *Transition metals for organic synthesis*. 2nd ed.; Beller, M.; Bolm, C., Eds.; Wiley-VCH: Weinheim/New York, 2004, vol. 2, pp. 215-242.
207. Olah G. A.; Molnár, Á. *Hydrocarbon Chemistry*, Wiley, Hoboken, NJ, 2003.
208. Crabtree, R. H. *J. Organomet. Chem.* **2004**, *689*, 4083-4091.
209. Shilov, A. E.; Shul'pin G B. *Chem. Rev.* **1997**, *97*, 2879-2932.
210. Schuchardt, U.; Cardoso, D.; Sercheli, R.; Pereira, R.; da Cruz, R. S.; Guerreiro, M.C.; Mandelli, D.; Spinace E. V.; Pires, E. L. *Appl. Catal. A* **2001**, *211*, 1-17.
211. Whyman, R. In *Applied Organometallic Chemistry and Catalysis*; Oxford University Press: Oxford, 2001.
212. Mears D. E.; Eastman, A. D. In *Kirk-Othmer Encyclopedia of Chemical Technology*. 5th ed.; Seidel, A. Ed.; Wiley, 2004, vol. 13, p. 706.
213. Ullmann's, *Encyclopedia of Industrial Chemistry*, 6th ed.; Wiley-VCH: Weinheim, 2002.
214. Perraud, O.; Sorokin, A. B.; Dutasta, J.-P.; Martinez, A. *Chem. Commun.* **2013**, *49*,

- 1288-1290.
215. Cougnon, F. B. L.; Sanders, J. K. M. *Acc. Chem. Res.* **2011**, *45*, 2211-2221.
216. Lehn, J. M. *Angew. Chem., Int. Ed.* **2015**, *54*, 3276-3289.
217. Otto, S. *Acc. Chem. Res.* **2012**, *45*, 2200-2210.
218. Yin, J.; Hu, Y.; Yoon, J. *Chem. Soc. Rev.* **2015**, *44*, 4619-4644.
219. Guo, Z.; Park, S.; Yoon, J.; Shin, I. *Chem. Soc. Rev.* **2014**, *43*, 16-29.
220. Yang, Y.; Zhao, Q.; Feng, W.; Li, F. *Chem. Rev.* **2013**, *113*, 192-270.
221. Zhang, M.; Yan, X.; Huang, F.; Niu, Z.; Gibson, H. W. *Acc. Chem. Res.* **2014**, *47*, 1995-2005.
222. Chatelet, B.; Joucla, L.; Dutasta, J.-P.; Martinez, A.; Dufaud, V. J. *Mater. Chem. A* **2014**, *2*, 14164-14172.

Chapter 2. Objectives of This Thesis

As reviewed in **Chapter 1**, hemicryptophanes are a type of molecular cages that are useful in various applications, such as recognition, molecular machines and supramolecular catalysis. Despite the great progress during the last decade in hemicryptophane chemistry, their potential in synthesis and applications are still waiting for further exploration. Therefore, the major mission of this PhD thesis is to design and synthesize new hemicryptophane cages to either broaden their applications or to make the existing utilization more efficient. The final goal is to enhance the fundamental knowledge of hemicryptophanes in order to realize the targeted-function-directed molecular design, and apply them to other relevant cage hosts used in supramolecular chemistry.

(i) A targeted function: molecular recognition

Hemicryptophanes are able to encapsulate zwitterions or ion pairs due to their heteroditopicity (Sections 1.4.2.2 and 1.4.2.3). To this end, additional factors that contribute to their binding performances can be incorporated, for instance the preparation of fluorescent cages, the introducing of additional weak binding interactions, and construction of cages by new building blocks. As enantiopure hemicryptophanes can stereoselectively complex carbohydrates (Section 1.4.2.4), more sophisticated structures bearing multiple types of chirality can be designed and prepared.

(ii) A targeted function: molecular machines

Although it is not obvious to design molecular machines by cage molecules and only two cases were reported with hemicryptophanes (Section 1.5), one can expect that the cage is behaving as a type of molecular machines if it is able to switch between bistable states according to molecular motion.

(iii) A targeted function: supramolecular catalysis

The vanadium(V)@hemicryptophane complexes were reported as supramolecular catalysts for sulfoxidation (Section 1.6.2.1). The bulky aromatic binaphthol groups can be introduced into the cages to increase the hydrophobicity of the cavities leading to efficient supramolecular catalyst with high turnover numbers. These supramolecular vanadium(V) catalysts might be further used for catalytic lignin models oxidation. Azaphosphatane-based hemicryptophanes were developed as organocatalysts for CO₂ activation previously due to the hydrogen-bonding donor ability of +P–H group (Section 1.6.1.2). They might be developed as hydrogen-bonding catalysts for the activation of carbonyl groups.

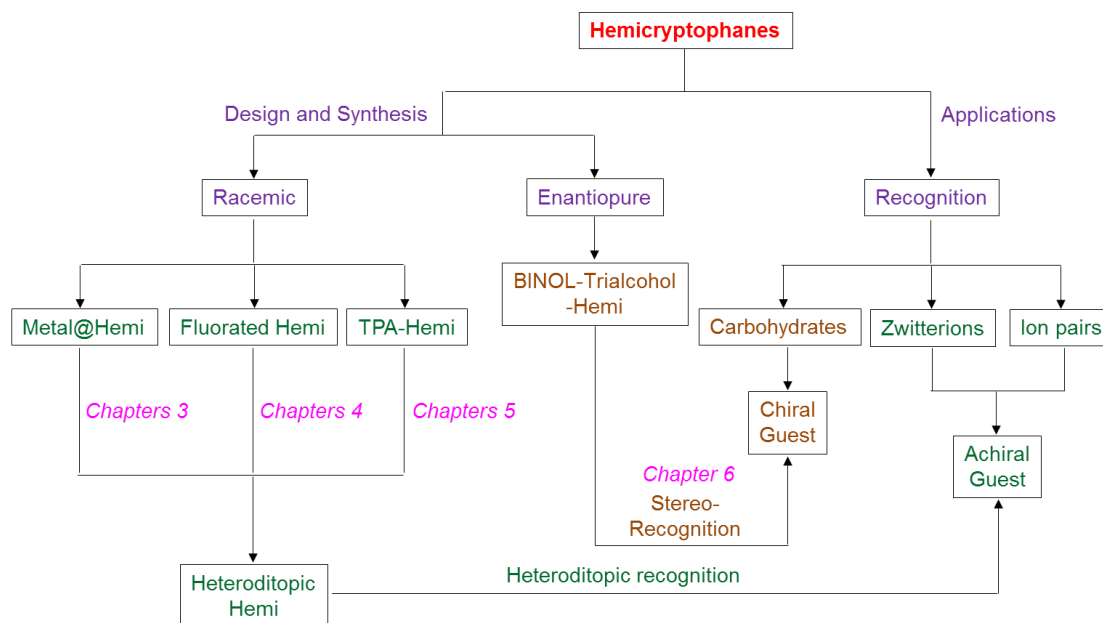
(iv) Beyond hemicryptophanes: cages constructed by self-assembly

The final stage of this thesis is to apply the fundamental knowledge achieved from hemicryptophanes to more general cages constructed by self-assembly. The building blocks for self-assembly will be selected from those moieties of the reported hemicryptophanes, for instance, azaphosphatane units.

Part II. Host-Guest Chemistry of Hemicryptophanes

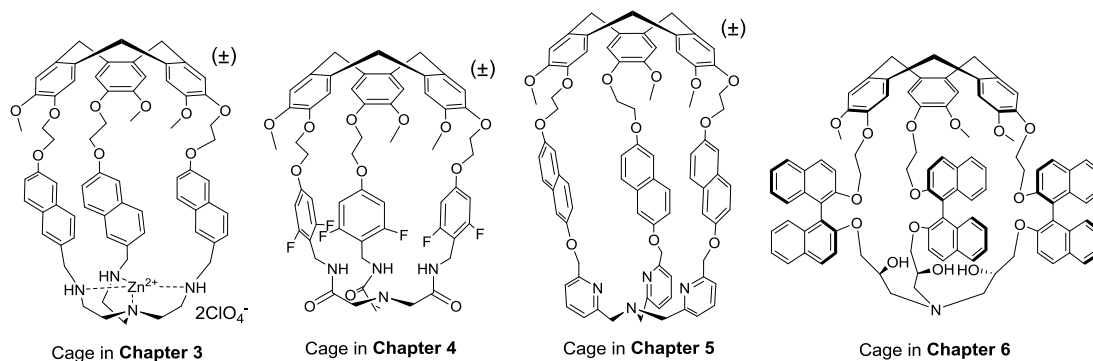
Preface

Part II Network



* Hemi = Hemicryptophane; TPA = tris(2-pyridylmethyl)amine; BINOL = Binaphthol

Following the advances of hemicryptophane chemistry and presentation of the objectives of this thesis in **Part I**, **Part II** is mainly focused on the host-guest chemistry of hemicryptophanes. As shown in the scheme above, for a targeted application in molecular recognition for both achiral and chiral guests, a series of hemicryptophane cages have been designed and synthesized, including both the racemic and enantiopure versions (see the figure below). One common feature among the obtained racemic cages is that they all show heteroditopic properties, which are promising in the complexation of achiral zwitterions or ion pairs, as described in **Chapters 3, 4 and 5**. The enantiopure cages have been used for stereorecognition of carbohydrates, as discussed in **Chapter 6**.



It should be noted that **Chapters 3, 4 and 6** are respectively based partially on my following publications: *Chemical Communications* (2015, 51, 2679–2682), *ChemPhysChem* (2015, 16, 293–2935), *The Journal of Organic Chemistry* (DOI: 10.1021/acs.joc.7b00559) and *Chemistry -*

A European Journal (2016, 22, 8038–8042). The numbers of compounds, figures, schemes and tables have been renumbered in each chapter from the beginning, and the numbers of compounds between chapters have no relationship. Table of Contents in each chapter has been presented in the corresponding chapter cover. The cited references are listed at the end of each chapter.

Chapter 3. A Fluorescent Heteroditopic Hemicryptophane Cage for the Selective Recognition of Choline Phosphate

This Chapter is based partially on the following manuscript—

Dawei Zhang, Guohua Gao, Laure Guy, Vincent Robert, Alexandre Martinez,
Jean-Pierre Dutasta

Chem. Commun. **2015**, 51, 2679–2682.

The work in this chapter was carried out at the ENS-Lyon.

Contents

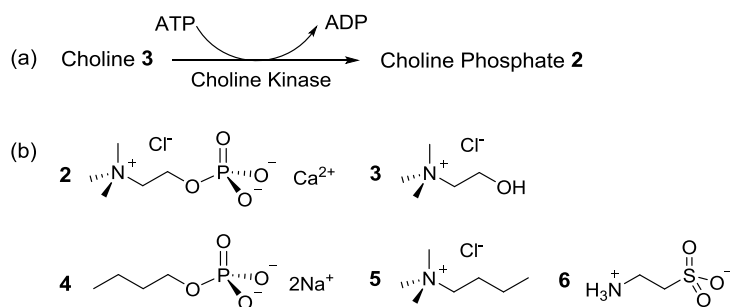
3.1 Abstract	78
3.2 Introduction.....	78
3.3 Results and discussion	79
3.4 Conclusion.....	83
3.5 Experimental section.....	83
3.6 References.....	89

3.1 Abstract

The first fluorescent hemicryptophane cage was synthesized and developed as an efficient and selective sensor for choline phosphate. The heteroditopic character of the host in the recognition process was evidenced. NMR experiments highlight a full encapsulation of the guest, inducing the chiralisation-like behavior of the achiral choline phosphate.

3.2 Introduction

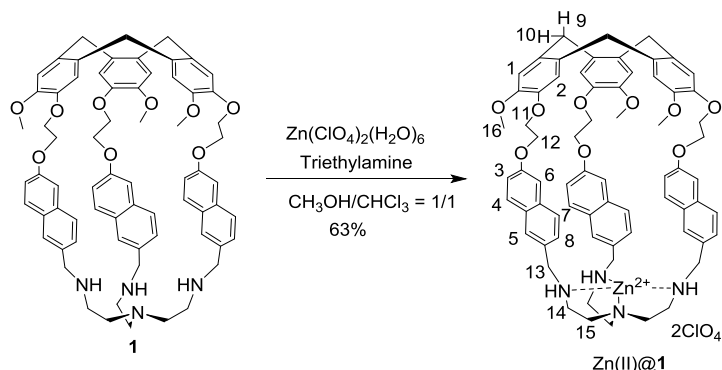
The design of artificial molecular receptors is very attractive as they can mimic biological systems such as enzymes.¹⁻⁵ A large number of bio-inspired compounds have been designed and their recognition properties towards guests of biological interest have been studied. Among the classes of molecular containers, such as calixarenes, resorcinarenes, cucurbiturils, or cyclodextrines,⁶ cryptophanes and hemicryptophanes both based on cyclotrimeratrylene (CTV) unit have recently received a growing interest.^{7,8} Cryptophanes are homotopic host compounds and have been shown to efficiently complex small molecules like methane or epoxides, or atoms like xenon. The related hemicryptophanes combining a CTV unit with another C_3 symmetrical moiety are ditopic hosts presenting recognition properties towards biological molecules like carbohydrates, ammonium and zwitterionic neurotransmitters.⁹ For example, we have recently demonstrated that using ^1H NMR and ITC techniques, a water-soluble hemicryptophane host is able to selectively recognize choline.^{9h} Despite the high efficiency and good selectivity of hemicryptophanes as receptors, the development of fluorescent hemicryptophanes for molecular recognition studies has never been described to date. However, it should be noted that fluorescence spectroscopy appears as an efficient method for the detection of biological molecules due to its high sensitivity, simple manipulation and facile visualization of bio-processes.



Scheme 3.1 The biological process involved in the generation of choline phosphate (a) and the guests studied in this work (b).

It is known that phosphorylated molecules play a crucial role in many biological processes.^{10,11} In particular choline phosphate, generated by the conversion of choline and ATP under the choline kinase along with the production of ADP (Scheme 3.1a), is an important biological phosphorylated compound. It is an essential intermediate in the biosynthetic pathway of phosphatidylcholine, a major component of the membrane of all eukaryotic cells.^{12,13} Thus, both effective complexation and optical detection of choline phosphate may have application as inhibitor or indicator in biological environment, allowing

therefore a better understanding of this biosynthetic pathway. Moreover, the selective sensing of choline phosphate among choline may be developed as a method to monitor choline kinase activity in real time. Nevertheless, to the best of our knowledge, there is no fluorescent sensor capable of selective recognition of choline phosphate.



Scheme 3.2 Synthesis of the fluorescent Zn(II)@1 complex.

As literatures have revealed that metal-based sensors are particularly relevant for the sensing of phosphorylated molecules,¹⁴ we decided to combine the recognition properties of hemicryptophanes with those of Zn(II) complexes to design a heteroditopic host for the recognition of zwitterionic choline phosphate (Scheme 3.2). It is anticipated that (i) the CTV unit of Zn(II)@1 will bind the ammonium part of choline phosphate, (ii) the Zn(II) center will stabilize the phosphate part and (iii) the naphthalene fluorophores which are used as hydrophobic “walls” connecting the Zn(II) binding moiety to the CTV unit, will confer fluorescent properties of the host structure.

3.3 Results and discussion

Ligand **1** was first synthesized in four steps, from vanillic alcohol, with 4% overall yield, according to a previous procedure.¹⁵ Then the Zn(II) cation was coordinated by the tris(2-aminoethyl)amine (tren) unit via a reaction between ligand **1** and Zn(ClO₄)₂ in a CHCl₃/CH₃OH mixture (1/1, v/v) (Scheme 3.2). The ¹H NMR spectrum of the Zn(II)@1 exhibits broad signals at room temperature (298 K), probably because of the conformational rigidification of the whole structure induced by the metal complexation (Figure 3.1). Variable temperature ¹H NMR experiments in the range of 298–373 K were then performed, and they show that the signals became increasingly narrow and well defined as the temperature raised. In particular, at 373 K, a set of expected sharp peaks with a C_{3v} symmetrical conformation was well displayed.

The complexation of choline phosphate **2** by Zn(II)@1 was studied by evaluating the fluorescent changes of a 5 μM solution of Zn(II)@1 upon progressive addition of the guest in DMSO containing 2% water. As shown in Figure 3.2a, addition of choline phosphate **2** resulted in significant fluorescence quenching of the host at 350 nm with 5 equivalents reaching the end of titration. A binding constant of 4.2×10⁵ M⁻¹ was obtained according to a 1:1 model confirmed by Job plot (Figure S3.1a). Choline **3** could also give rise to obvious fluorescence quenching of Zn(II)@1 while 90 equiv. of **3** were needed to reach the end of titration (Figure S3.1b and S3.2). In addition, a much smaller binding constant compared with

choline phosphate **2** was achieved ($7.0 \times 10^3 \text{ M}^{-1}$). The fluorescence quenching of the host induced by guest **2** or **3** could be attributed to the promotion of the photo-induced electron transfer (PET) process from the tren nitrogens to the naphthalene fluorophores because of the weakening of the tren-Zn(II) bonds after guest coordination.^{14f} It should be noted that in spite of a moderate binding between Zn(II)@**1** and choline **3**, the host could fully distinguish choline phosphate from choline since as shown in Figure 3.2b, 2 equiv. of choline phosphate **2** lead to remarkable fluorescence quenching of the host (75%), while only 9% quenching is generated by 2 equiv. of choline **3**. This high selectivity of Zn(II)@**1** towards **2** over **3** is very meaningful since the two biologically important compounds simultaneously participate in one crucial process of metabolism (Scheme 3.1a). Moreover, this selectivity was also maintained in a more competitive solvent. In DMSO/H₂O (80/20, v/v), the marked fluorescence quenching of the host induced by choline phosphate **2** also occurred and a binding constant of $4.1 \times 10^3 \text{ M}^{-1}$, larger than that with choline ($1.2 \times 10^2 \text{ M}^{-1}$), was presented (Figure S3.3). This result also underlines that the Zn(II)@**1** cage is very efficient for the sensing of choline phosphate even in competitive media.

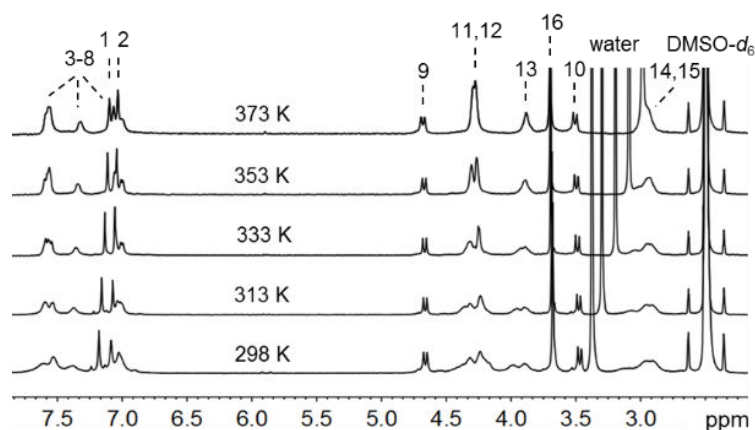


Figure 3.1 ¹H NMR spectra of Zn(II)@**1** at different temperature in DMSO-*d*₆. For the proton assignment, see Scheme 3.2.

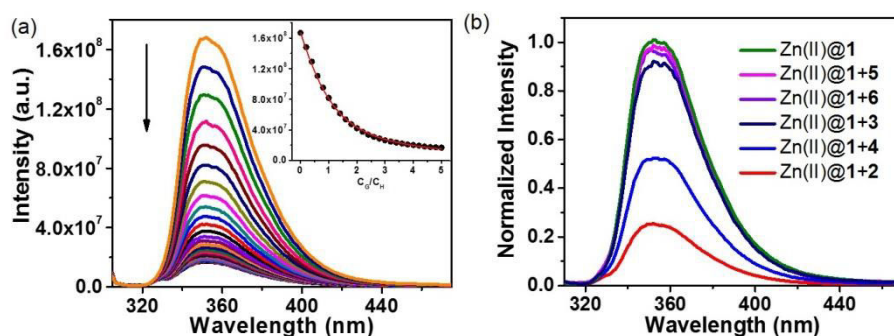


Figure 3.2 (a) Fluorescence titrations of 5 μM Zn(II)@**1** excited at 300 nm with choline phosphate **2** in DMSO containing 2% water. Inset: the fluorescence intensity at 350 nm as a function of the equivalents of added choline phosphate **2**. (b) Normalized spectra of 5 μM Zn(II)@**1** upon addition of 2 equiv. of different guests in DMSO containing 2% water.

We then decided to investigate whether the heteroditopicity of the host played a crucial role in the recognition process or if the complexation was only driven by either phosphate-zinc or cation- π interaction. Thus, the binding experiments of Zn(II)@**1** with

butylphosphate **4** and butyl-trimethylammonium **5**, which only contain one kind of the recognized units, were carried out. As shown in Figure 3.2b, when in the presence of 2 equiv. of whatever **4** or **5**, a much smaller fluorescence quenching of Zn(II)@**1** was observed (75%, 48% and 3% quenching induced by guests **2**, **4** and **5**, respectively), indicating that only the guest bearing both the phosphate and ammonium parts allows an efficient fluorescence quenching. The corresponding titration experiments of host **1** with **4** and **5** were also performed and binding constants of $6.3 \times 10^4 \text{ M}^{-1}$ and $2.2 \times 10^3 \text{ M}^{-1}$ were respectively achieved, which are distinctly smaller than that obtained with the zwitterionic choline phosphate **2** ($4.2 \times 10^5 \text{ M}^{-1}$), again emphasizing the synergistic effects of both the CTV and Zn(II) moieties in the complexation (Figure S3.4).

Previously, our group also reported two other heteroditopic hemicryptophane hosts for the recognition of zwitterions.^{9d,9e} Both of the two previous receptors showed the largest binding constant for taurine **6**, up to $5.0 \times 10^5 \text{ M}^{-1}$ (Scheme 3.1b).^{9e} Hence, we decided to study the fluorescent response of the present cage Zn(II)@**1** for this competitive zwitterion. It was found that taurine **6** only gave rise to negligible fluorescence quenching of Zn(II)@**1** in DMSO containing 2% water (Figure 3.2b and Figure S3.5), highlighting (i) the high sensing selectivity of this new host for choline phosphate **2** and (ii) the possibility to tune the structure of hemicryptophane hosts in order to complex selectively a zwitterionic guest of biological interest. In this case, the specificity probably arise from the high binding affinity of Zn(II) moiety towards phosphorylated molecules.^{14b,14d} Indeed, the fluorescent sensing of choline phosphate using the ligand **1** was also investigated, and only very small fluorescent changes were observed (Figure S3.6), emphasizing the crucial role of Zn(II) moiety in this recognition process.

More insights into the interaction mechanism were obtained from a series of NMR experiments. Progressive additions of choline phosphate **2** to a solution of Zn(II)@**1** in DMSO-*d*₆/D₂O (80/20, v/v) at room temperature lead to more complicated signals for aromatic protons (down-field region) and to new peaks (up-field region) that cannot be assigned to the free choline phosphate **2**, indicating the existence of multiple conformers in solution for the host-guest complex (Figure 3.3a and Figure S3.7). Heating the host-guest mixture up to 353 K resulted in the disappearance of these additional signals and the appearance of sharp and well defined peaks for the whole spectrum (Figure 3.3b and Figure S3.8). A subsequent return to room temperature for the mixture restored the initial spectrum (Figure S3.8). These results imply that the exchange between the free and complexed choline phosphate appears slow on the NMR time scale at room temperature while it is fast at high temperature (353 K). It is interesting to note that the four new peaks respectively at -0.50, 0.61, 1.32 and 1.79 ppm display almost the same integration ratio (1:1:1:1). Indeed, these four new peaks in the up-field region of the spectrum can be attributed to the four diastereotopic protons of methylene group of the encaged choline phosphate which suffer from a shielding effect by the naphthalene linkers. The complexed choline phosphate is encapsulated in a chiral environment, hence any points of the cavity are chirotopic.¹⁶ As a consequence, methylene groups of choline phosphate also become diastereotopic after inclusion giving rise to the four new peaks. Even though the latter are quite weak and broad, some clear cross-peaks between the four diastereotopic hydrogens were also observed in the COSY NMR spectrum (Figure

S3.9). Thus, both the low chemical shifts of these shielded protons and the chiralisation-like behavior¹⁷ of the guest strongly suggest that the choline phosphate is fully encaged inside the molecular cavity of Zn(II)@1. Interestingly, a similar but less extent NMR titration behavior also occurred with choline 3. At room temperature, progressive addition of choline to Zn(II)@1 in DMSO-*d*₆/D₂O (80/20, v/v) gave rise to new peaks in the up-field region of the ¹H NMR spectra (0.5-2.0 ppm), indicating a slow complexation exchange on the NMR time scale (Figure S3.10), whereas at higher temperature (353 K), the gradual shifts of the initial signals and the absence of new peaks during titrations suggest a fast exchange on the NMR time scale (Figure S3.11).

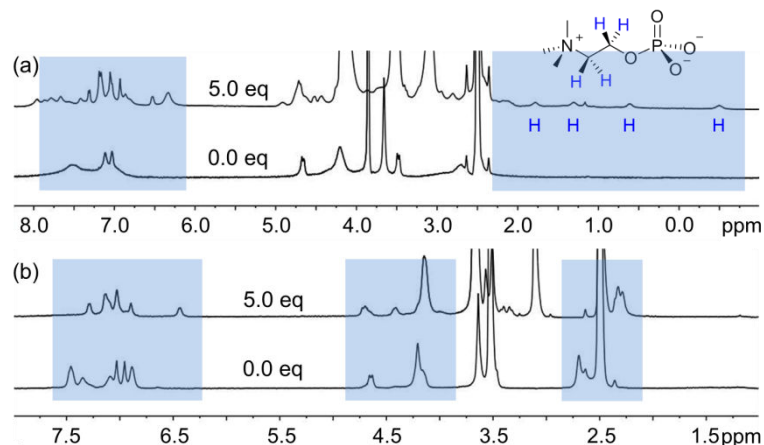


Figure 3.3 ¹H NMR spectra of 1 mM Zn(II)@1 in the absence and presence of 5.0 equiv. of choline phosphate 2 in DMSO-*d*₆/D₂O (80/20, v/v) at 298 K (a) and at 353 K (b). The four new peaks respectively at -0.50, 0.61, 1.32 and 1.79 ppm in Figure 3.3a are attributed to the four diastereotopic protons of the methylene groups of the encaged choline phosphate 2.

³¹P NMR titration experiments were also carried out to investigate the interaction mechanism. After addition of Zn(II)@1 to choline phosphate 2 in DMSO-*d*₆/D₂O (80/20, v/v), the signal composed initially of only one sharp peak splits into two peaks with opposite direction of chemical shifts: one narrow down-field shifted peak and a broad up-field shifted signal (Figure S3.12). The former strongly favored after addition of 0.5 equiv. of host was attributed to the encapsulated choline phosphate, whereas the latter whose intensity decreased was assigned to the free guest. These results support the encapsulation event between the host and guest and the slow complexation process on the NMR time scale at room temperature, which are in good agreement with those obtained from ¹H NMR titrations.

Finally, we examined the interactions involved in the recognition process by Density Functional Theory (DFT) calculations. In the fully optimized geometry of the complex, choline phosphate is encapsulated inside the Zn(II)@1 cavity (Figure 3.4).¹⁸ The phosphate unit of the guest is linked to the zinc atom through a coordination bond (Zn...O distance: 1.9 Å). The distances between the aromatic rings of both the CTV unit and the naphthalene linkers of the host, and the ammonium moiety of the guest suggest that they interact through several CH... π interactions (several distances between 2.8 and 3.3 Å). Thus, both the CTV and Zn(II) units contribute to the efficient and selective binding of choline phosphate, emphasizing the heteroditopic character of the host. Interestingly, C-H... π interactions also occur between the methylene groups of the guest and the naphthalene linkers (several

distances between 2.8 and 3.3 Å), accounting for the high-field shifts of these protons observed in ^1H NMR titrations, and also highlighting their diastereotopic behavior.

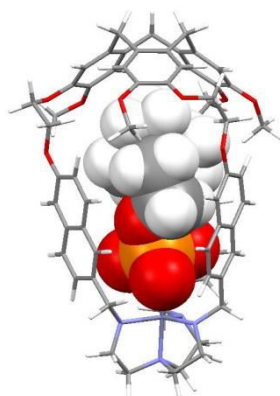


Figure 3.4 DFT optimized structure of the complex between Zn(II)@**1** and choline phosphate **2**.

3.4 Conclusion

We have described a hemicryptophane cage combining a CTV unit and a Zn(II) metal center holding fluorescent properties. This fluorescent hemicryptophane has been developed as the first fluorescent sensor for zwitterionic choline phosphate in competitive media. The heteroditopic character of the host towards the guest was evidenced since the guest bearing both the ammonium and phosphate parts can give rise to the most significant fluorescence quenching and largest binding constant. Moreover, it was found that the exchange between the free and complexed guest is slow on the NMR time scale at room temperature while it is fast at higher temperature (353 K). NMR experiments also indicate the formation of an inclusion complex between the cage and the guest, and a chiralisation-like behavior of the achiral choline phosphate occurs inside the cavity. The exact binding mode has been examined by DFT calculations. Studies of stereoselective recognition properties of chiral zwitterions using enantiopure fluorescent metal-based hemicryptophanes are in progress.

3.5 Experimental section

3.5.1 Materials and instrumentation

All solvents used were of commercial grade. ^1H NMR and ^{13}C NMR spectra were recorded on a Bruker Avance spectrometer operating at 500.10 MHz and 125.76 MHz for ^1H NMR and ^{13}C NMR spectra, respectively. ^1H NMR chemical shifts (δ) are reported in ppm. Fluorescence spectra were carried out with a Horiba-Jobin Yvon spectrofluorimeter. Mass spectra were recorded by the Centre de Spectrométrie de Masse, Institute of Chemistry, Lyon. DFT calculations were performed by Vincent Robert.

3.5.2 Synthesis and characterization

Hemicryptophane **1** was synthesized according to our previously reported procedure.^{15a}

Zn(II)@1 complex was prepared as follow: to a solution of **1** (90.3 mg, 0.082 mmol) in 6 mL CHCl₃, 20 μ L triethylamine was added under argon followed by addition of the solution of Zn(ClO₄)₂(H₂O)₆ (30.5 mg, 0.082 mmol, 1.0 equivalent) in 6 mL CH₃OH. After stirring the reaction mixture at room temperature for 2 hours, a large amount of precipitate appeared. The precipitate was collected, washed thoroughly with Et₂O and dried under vacuum to give the final product as a white solid (70.8 mg, yield 63%). The ligand **1** is soluble in most of the common solvents, for example CH₂Cl₂, CHCl₃, acetone and DMSO. However, the Zn(II)@1 complex is only soluble in DMSO, and moderate soluble in acetone.

Ligand 1: ¹H NMR (500.1 MHz, 298 K, CDCl₃) δ 7.33 (d, 3H, *J* = 8.4 Hz); 7.16 (d, 3H, *J* = 8.3 Hz); 7.13 (s, 3H); 7.07 (s, 3H); 7.00 (d, 3H, *J* = 9.0 Hz); 6.92 (s, 3H); 6.89 (s, 3H); 6.56 (d, 3H, *J* = 8.6 Hz); 4.84 (d, 3H, *J* = 13.8 Hz); 4.58-4.61 (m, 3H); 4.39-4.43 (m, 3H); 4.25 (t, 6H, *J* = 4.90 Hz); 3.69 (s, 9H); 3.65 (d, 3H, *J* = 13.3 Hz); 3.63 (d, 3H, *J* = 13.7 Hz); 3.53 (d, 3H, *J* = 13.3 Hz); 2.54-2.69 (m, 12H). ¹³C NMR (125.7 MHz, 298 K, CDCl₃) δ 156.8, 148.7, 146.5, 133.6, 133.2, 131.9, 129.3, 128.9, 127.2, 126.9, 126.5, 119.4, 116.7, 113.7, 107.3, 67.6, 67.5, 56.0, 52.9, 47.7, 36.7. ESI-MS *m/z*: found 1101.5350 [M+H]⁺; calcd for C₆₉H₇₃N₄O₉: 1101.5372. IR $\bar{\nu}$ = 2931, 1606, 1508, 1263 cm⁻¹. M.p. > 310 °C (decomp.).

Zn(II)@1 complex: ¹H NMR (500.1 MHz, 298 K, DMSO-*d*₆) δ 7.43-7.63 (broad, 12H); 7.20 (s, 3H); 7.05-7.11 (broad, 9H); 4.66 (d, 3H, *J* = 13.3 Hz); 4.21-4.43 (broad, 12H); 4.03 (broad, 3H); 3.93 (broad, 3H); 3.69 (s, 9H); 3.47 (d, 3H, *J* = 13.4 Hz); 2.96-3.18 (broad, 12H). ¹H NMR (500.1 MHz, 373 K, DMSO-*d*₆) δ 7.57 (bs, 9H); 7.32 (bs, 3H); 7.03-7.10 (m, 12H); 4.68 (d, 3H, *J* = 13.5 Hz); 4.28 (bs, 12H); 3.88 (bs, 6H); 3.70 (s, 9H); 3.50 (d, 3H, *J* = 13.5 Hz); 2.97 (bs, 12H). ¹³C NMR (125.7 MHz, 298 K, DMSO-*d*₆) δ 156.6, 148.4, 146.5, 133.9, 133.0, 132.0, 129.4, 128.4, 127.4, 119.3, 116.4, 107.4, 66.9, 66.3, 57.2, 54.6, 51.0, 49.4, 35.4. ESI-MS *m/z*: found 1199.4224 [M²⁺ + Cl]⁺; calcd for C₆₉H₇₃N₄O₉: 1199.4274. IR $\bar{\nu}$ = 3237, 2934, 1612, 1507, 1483, 1263, 1218, 1282, 1085 cm⁻¹. M.p. > 350 °C (decomp.).

3.5.3 Job plot

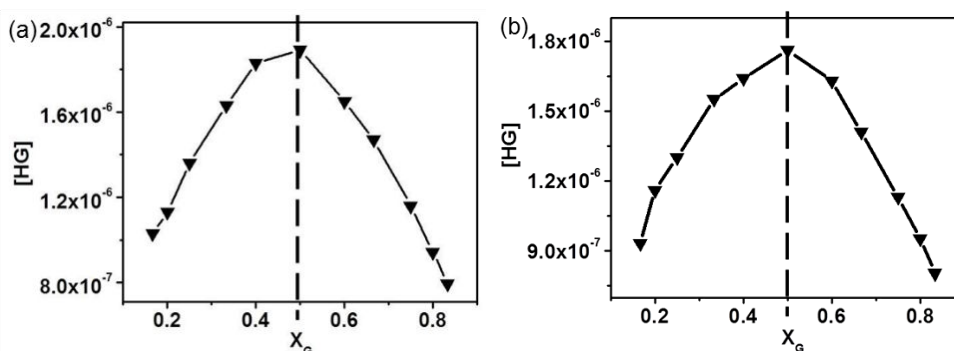


Figure S3.1 Fluorescence Job plot of Zn(II)@1 with choline phosphate **2** (a) and choline **3** (b).

In The continuous variation method was used for determining the binding stoichiometry.¹⁹ In this method, solutions of the host and guest at the same concentration (5 μ M) were prepared in DMSO containing 2% H₂O. Then the two solutions were mixed in different proportions maintaining a total volume of 3 mL and a total concentration of 5 μ M. After incubating the mixture for 30 s, the spectra of the solutions for different compositions were

recorded.

3.5.4 Fluorescence spectroscopic titration

2 mL Zn(II)@1 complex solution (5 μ M) was taken into the cuvette, and then certain equivalents of a concentrated guest solution (0.5 mM or 5 mM) were added stepwise with a syringe. As a very small volume of guest solution was added, the final amount of the solution was almost unchanged (2 mL). The mixed solution was incubated for 30 s and then irradiated at 300 nm. The corresponding emission values at 350 nm during titration were then recorded.

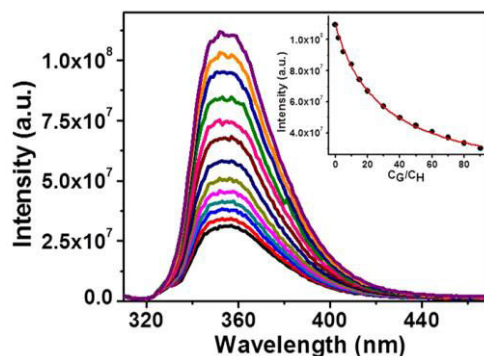


Figure S3.2 Fluorescence titrations of 5 μ M Zn(II)@1 with choline **3** excited at 300 nm in DMSO containing 2% water. Inset: the intensity at 350 nm as a function of the added choline **3**.

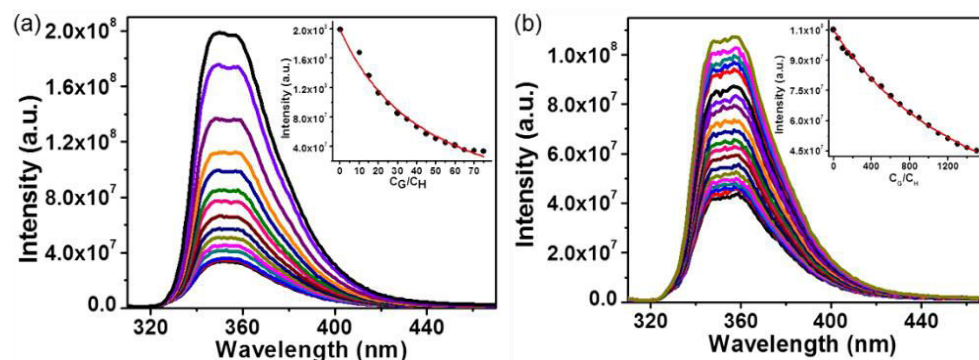


Figure S3.3 Fluorescence titrations of 5 μ M Zn(II)@1 with choline phosphate **2** (a) and choline **3** (b) excited at 300 nm in DMSO/H₂O (80/20, v/v). Inset: the intensity at 350 nm as a function of the guest.

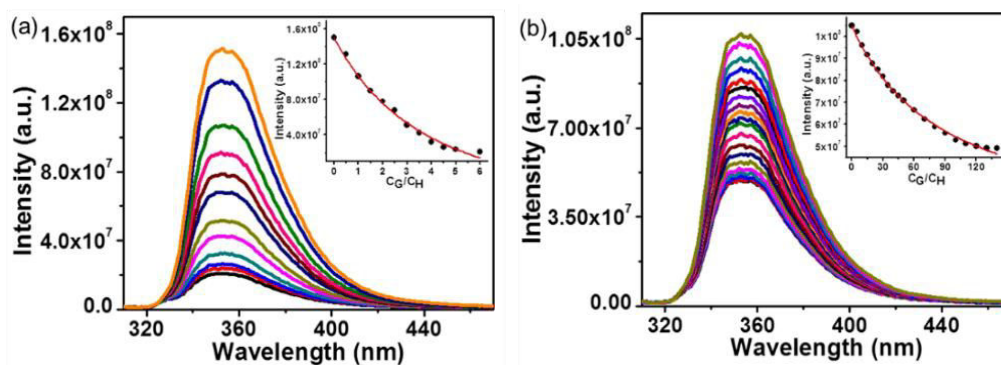


Figure S3.4 Fluorescence titrations of 5 μ M Zn(II)@1 excited at 300 nm with guest **4** (a) and guest **5** (b) in DMSO containing 2% water. Insets: the intensity at 350 nm as a function of the guest.

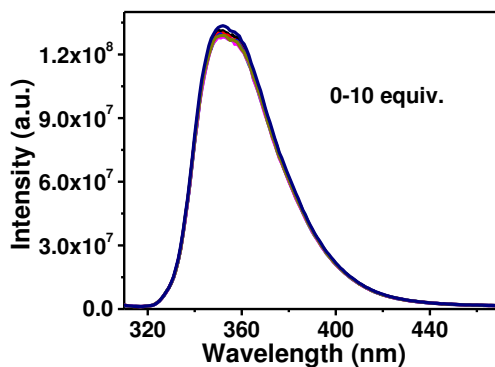


Figure S3.5 Fluorescence titrations of 5 μM $\text{Zn}(\text{II})@1$ excited at 300 nm with taurine **6** in DMSO containing 2% water.

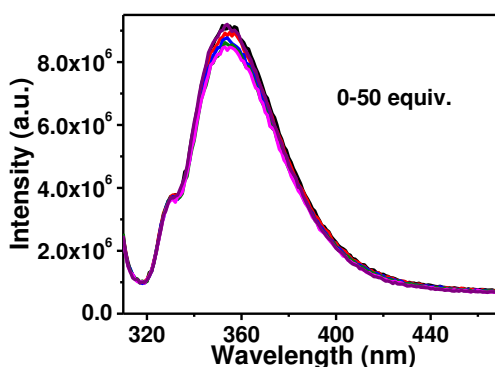


Figure S3.6 Fluorescence titrations of 5 μM ligand **1** excited at 300 nm with choline phosphate **2** in DMSO containing 2% water.

3.5.5 ^1H NMR spectroscopic titration

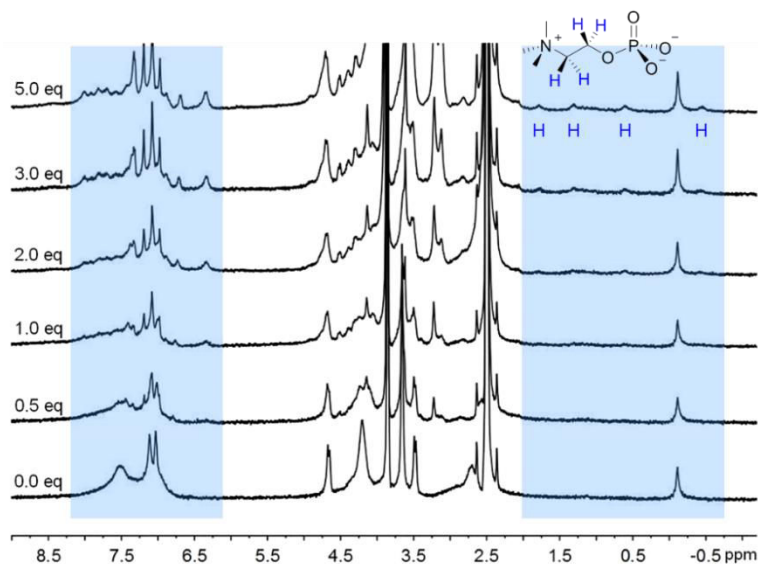


Figure S3.7 ^1H NMR titrations of 1 mM $\text{Zn}(\text{II})@1$ with choline phosphate **2** at 298 K in $\text{DMSO-}d_6/\text{D}_2\text{O}$ (80/20, v/v). H atoms in blue are the four diastereotopic protons of the engaged **2**.

0.5 mL $\text{Zn}(\text{II})@1$ complex solution was taken into the NMR spectroscopy tube, and then certain equivalents of a concentrated guest solution were added stepwise with a syringe. As a

very small volume of guest solution was added, the final amount of the solution was almost unchanged (0.5 mL). The mixed solution was incubated for 30 s and then the measurement of ^1H NMR spectroscopy of the solution was performed.

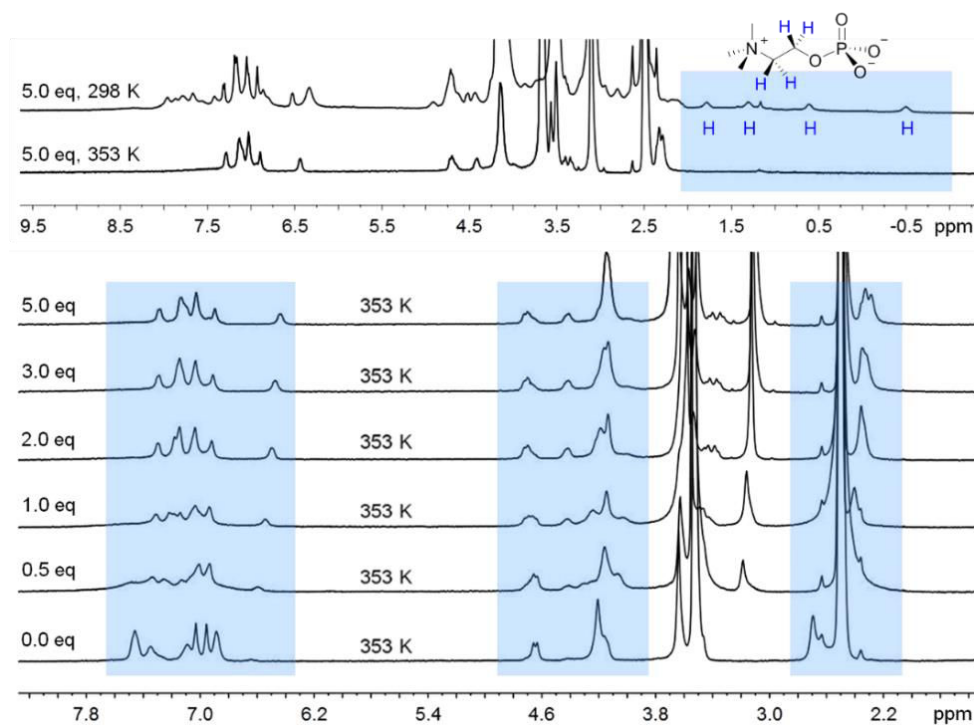


Figure S3.8 ^1H NMR titrations of 1 mM $\text{Zn(II)}@1$ with choline phosphate **2** at 353 K and then return to 298 K in $\text{DMSO-}d_6/\text{D}_2\text{O}$ (80/20, v/v).

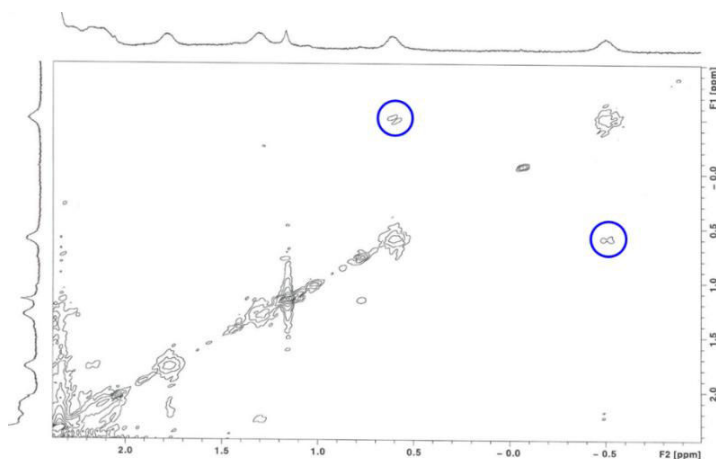


Figure S3.9 The up-field region of the COSY spectrum for the mixture of $\text{Zn(II)}@1$ and 5 equiv. of choline phosphate **2** in $\text{DMSO-}d_6/\text{D}_2\text{O}$ (80/20, v/v).

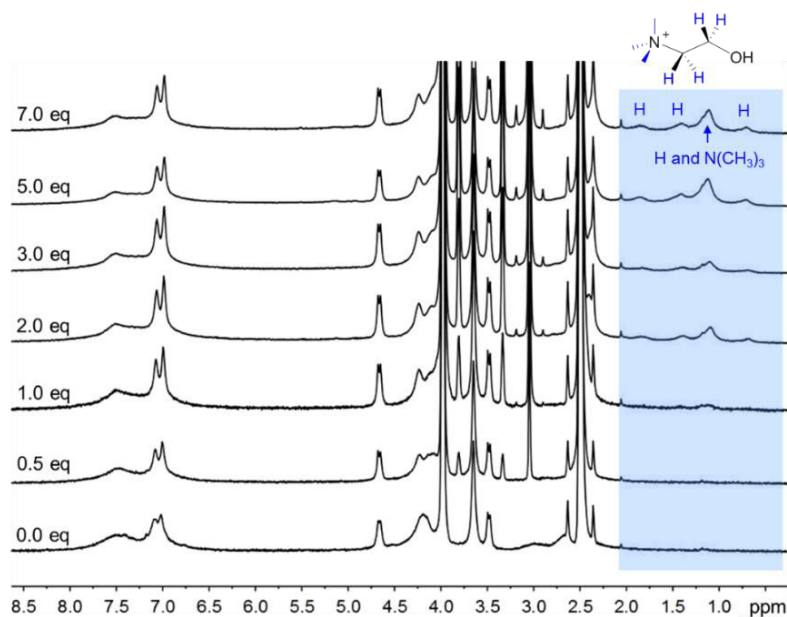


Figure S3.10 ^1H NMR titrations of 1 mM $\text{Zn(II)}@1$ with **3** at 298 K in $\text{DMSO-}d_6/\text{D}_2\text{O}$ (80/20, v/v). H atoms in blue are attributed to the diastereotopic protons of methylene and $\text{N}(\text{CH}_3)_3$ of the encaged **3**.

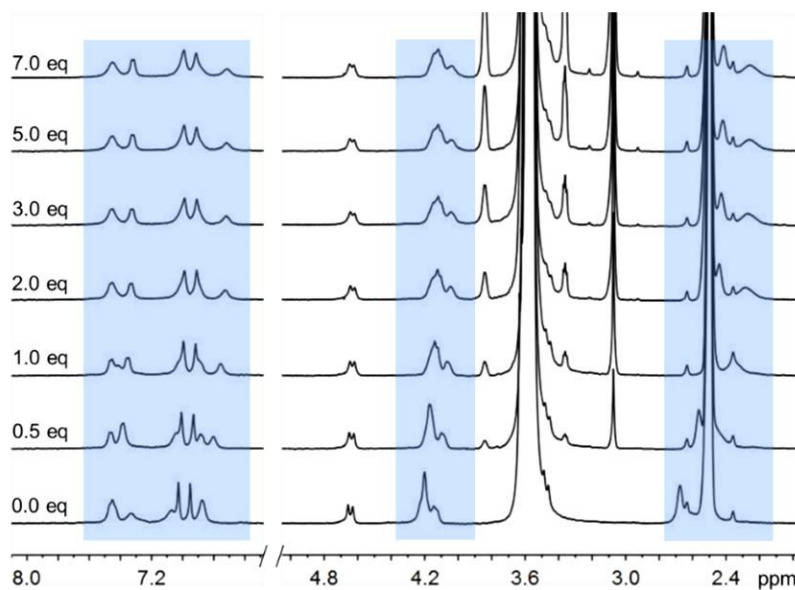


Figure S3.11 ^1H NMR titrations of 1 mM $\text{Zn(II)}@1$ with **3** at 353 K in $\text{DMSO-}d_6/\text{D}_2\text{O}$ (80/20, v/v).

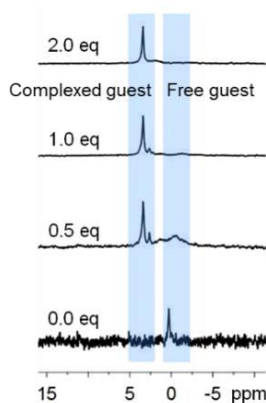


Figure S3.12 ^{31}P NMR titrations of 1 mM **2** with $\text{Zn(II)}@1$ at 298 K in $\text{DMSO-}d_6/\text{D}_2\text{O}$ (80/20, v/v).

3.5.6 Computational method

Ab initio evaluations were performed using the Gaussian 03 package¹⁷ within a restricted DFT framework.¹⁸ In order to access geometrical information upon the host-guest species, full geometry optimizations were performed using DFT calculations. A combination of BP86 function and an all electron 6-31G* basis set including polarization functions has proven to be very satisfactory for similar issues.¹⁴ We checked using the hybrid B3LYP function that our results do not suffer from the arbitrariness of the exchange correlation function.

3.6 References

1. A. J. Kirby, *Angew. Chem., Int. Ed.*, 1996, **35**, 707.
2. J. K. M. Sanders, *Chem. Eur. J.*, 1998, **4**, 1378.
3. J.-M. Lehn, *Rep. Prog. Phys.*, 2004, **67**, 245.
4. M. Raynal, P. Ballester, A. Visal-Ferran and P. W. N. M. Van Leeuwen, *Chem. Rev.*, 2014, **43**, 1660.
5. M. Raynal, P. Ballester, A. Visal-Ferran and P. W. N. M. Van Leeuwen, *Chem. Rev.*, 2014, **43**, 173.
6. (a) R. Breslow, *Acc. Chem. Res.*, 1995, **28**, 146; (b) E. Engeldinger, D. Armspach and D. Matt, *Chem. Rev.*, 2003, **103**, 4147; (c) D. M. Homden and C. Redshaw, *Chem. Rev.*, 2008, **108**, 5086.
7. T. Brotin and J.-P. Dutasta, *Chem. Rev.*, 2009, **109**, 88.
8. J. Canceill, A. Collet, J. Gabard, F. Kotzyba-Hibert and J.-M. Lehn, *Helv. Chim. Acta*, 1982, **65**, 1894.
9. (a) O. Perraud, V. Robert, A. Martinez and J.-P. Dutasta, *Chem. Eur. J.*, 2011, **17**, 4177; (b) L. Wang, G.-T. Wang, X. Zhao, X.-K. Jiang and Z.-T. Li, *J. Org. Chem.*, 2011, **76**, 3531; (c) O. Perraud, A. Martinez and J.-P. Dutasta, *Chem. Commun.*, 2011, **47**, 5861; (d) O. Perraud, V. Robert, A. Martinez and J.-P. Dutasta, *Chem. Eur. J.*, 2011, **17**, 13405; (e) O. Perraud, V. Robert, H. Gornitzka, A. Martinez and J.-P. Dutasta, *Angew. Chem., Int. Ed.*, 2012, **51**, 504; (f) O. Perraud, S. Lefevre, V. Robert, A. Martinez and J.-P. Dutasta, *Org. Biomol. Chem.*, 2012, **10**, 1056; (g) J. R. Cochrane, A. Schmitt, U. Wille and C. A. Hutton, *Chem. Commun.*, 2013, **49**, 8504; (h) A. Schmitt, V. Robert, J.-P. Dutasta and A. Martinez, *Org. Lett.*, 2014, **16**, 2374.
10. (a) T. Hunter, *Protein Phosphorylation*; Academic Press, New York, 1998; (b) T. Pawson and J. D. Scott, *Trends Biochem. Sci.*, 2005, **30**, 286.
11. (a) J. Götz and L. M. Ittner, *Nat. Rev. Neurosci.*, 2008, **9**, 532; (b) S. Chakraborti, S. Das, P. Kar, B. Ghosh, K. Samanta, S. Kolley, S. Ghosh, S. Roy and T. Chakraborti, *Mol. Cell. Biochem.*, 2007, **298**, 1; (c) S. Veeramani, T. C. Yuan, S. J. Chen, F. F. Lin, J. E. Petersen, S. Shaheduzzaman, S. Srivastava, R. G. MacDonald and M. F. Lin, *Endocr. Relat. Cancer*, 2005, **12**, 805.
12. (a) C. Sohlenkamp, I. M. López-Lara and O. Geiger, *Prog. Lipid Res.*, 2003, **42**, 115; (b) S. J. Singer and G. L. Nicolson, *Science*, 1972, **175**, 720; (c) G. J. Doherty and H. T. McMahon, *Annu. Rev. Biophys.*, 2008, **37**, 65; (d) X. Yu, Z. Liu, J. Janzen, I. Chafeeva, S. Horte, W. Chen, R. K. Kainthan, J. N. Kizhakkedathu and D. E. Brooks, *Nat. Mater.*, 2012,

- 11**, 468.
13. (a) H. Goldfine, *J. Lipid Res.*, 1984, **25**, 1501; (b) A. Peschel, *J. Exp. Med.*, 2001, **193**, 1067; (c) S. L. Hazen and G. Chisolm, *Proc. Natl Acad. Sci. USA*, 2002, **99**, 12515.
14. (a) J. W. Steed, *Chem. Soc. Rev.*, 2009, **38**, 506; (b) H. T. Ngo, X. Liu and K. A. Jolliffe, *Chem. Soc. Rev.*, 2012, **41**, 4928; (c) L. Fabbrizzi and A. Poggi, *Chem. Soc. Rev.*, 2013, **42**, 1681; (d) A. E. Hargrove, S. Nieto, T. Zhang, J. L. Sessler and E. V. Anslyn, *Chem. Rev.*, 2011, **111**, 6603; (e) Y. Kurishita, T. Kohira, A. Ojida and I. Hamachi, *J. Am. Chem. Soc.*, 2012, **134**, 18779; (f) V. Bhalla, V. Vij, M. Kumar, P. R. Sharma and T. Kaur, *Org. Lett.*, 2012, **14**, 1012.
15. (a) B. Chatelet, E. Payet, O. Perraud, P. Dimitrov-Raytchev, L.-L. Chapellet, V. Dufaud, A. Martinez and J.-P. Dutasta, *Org. Lett.*, 2011, **13**, 3706; (b) O. Perraud, J.-B. Tommasino, V. Robert, B. Albela, L. Khrouz, L. Bonneviot, J.-P. Dutasta and A. Martinez, *Dalton Trans.*, 2013, **42**, 1530.
16. (a) K. Bartik, M. Luhmer, A. Collet and J. Reisse, *Chirality*, 2001, **2**; (b) K. Bartik, M. El Haouaj, M. Luhmer, A. Collet and J. Reisse *ChemPhysChem*, 2000, **4**, 221; (c) E. Graf, R. Graf, M. W. Hosseini, C. Huguenard and F. Taubelle, *Chem. Commun.*, 1997, 1459; (d) C. Huguenard, F. Taubelle, E. Graf and M. W. Hosseini, *J. Chim. Phys.*, 1998, **95**, 341.
17. Although the concept of chiralisation must be restricted to cases where the chiralizing and the chiralized partners are not bonded by covalent bonds, ionic, H-bonds or any kind of coordination bonds (according to Bartik *et al.* see ref 16(a)), in our case the chiralisation of choline phosphate is induced by different interactions including for instance coordination bonds but also C-H $\cdots\pi$ interactions with the aromatic rings of both the naphthalene linkers and the chiral CTV unit, therefore we decide to use this term to describe this behavior.
18. Gaussian 03: M. J. Frisch, G. W. Trucks, H. B. Schlegel, G. E. Scuseria, M. A. Robb, J. R. Cheeseman, G. Scalmani, V. Barone, B. Mennucci, G. A. Petersson, H. Nakatsuji, M. Caricato, X. Li, H. P. Hratchian, A. F. Izmaylov, J. Bloino, G. Zheng, J. L. Sonnenberg, M. Hada, M. Ehara, K. Toyota, R. Fukuda, J. Hasegawa, M. Ishida, T. Nakajima, Y. Honda, O. Kitao, H. Nakai, T. Vreven, J. A. Jr. Montgomery, J. E. Peralta, F. Ogliaro, M. Bearpark, J. J. Heyd, E. Brothers, K. N. Kudin, V. N. Staroverov, R. Kobayashi, J. Normand, K. Raghavachari, A. Rendell, J. C. Burant, S. S. Iyengar, J. Tomasi, M. Cossi, N. Rega, J. M. Millam, M. Klene, J. E. Knox, J. B. Cross, V. Bakken, C. Adamo, J. Jaramillo, R. Gomperts, R. E. Stratmann, O. Yazyev, A. J. Austin, R. Cammi, C. Pomelli, J. W. Ochterski, R. L. Martin, K. Morokuma, V. G. Zakrzewski, G. A. Voth, P. Salvador, J. J. Dannenberg, S. Dapprich, A. D. Daniels, O. Farkas, J. B. Foresman, J. V. Ortiz, J. Cioslowski, D. J. Fox, *Gaussian*, Wallingford, CT, 2009.
19. Job, *P. Ann. Chim.*, 1928, **9**, 113.

Chapter 4. Insights into the Complexity of Weak Intermolecular Interactions Interfering in Host–Guest Systems

This Chapter is based partially on the following manuscript—

Dawei Zhang, Bastien Chatelet, Eloisa Serrano, Olivier Perraud, Jean-Pierre Dutasta, Vincent Robert, Alexandre Martinez

ChemPhysChem **2015**, *16*, 293–2935.

The work in this chapter was carried out at the ENS-Lyon.

Contents

4.1 Abstract	92
4.2 Introduction.....	92
4.3 Results and discussion	93
4.4 Conclusion.....	98
4.5 Experimental section.....	99
4.6 References.....	104

4.1 Abstract

The recognition properties of heteroditopic hemicryptophane hosts towards anions, cations, and neutral pairs, combining both cation- π and anion- π interaction sites, were investigated to probe the complexity of interfering weak intermolecular interactions. It is suggested from NMR experiments, and supported by CASSCF/CASPT2 calculations, that the binding constants of anions can be modulated by a factor of up to 100 by varying the fluorination sites on the electron-poor aromatic rings. Interestingly, this subtle chemical modification can also reverse the sign of cooperativity in ion-pair recognition. Wavefunction calculations highlight how short- and long-range interactions interfere in this recognition process, suggesting that a disruption of anion- π interactions can occur in the presence of a cobound cation. Such molecules can be viewed as prototypes for examining complex processes controlled by the competition of weak interactions.

4.2 Introduction

The Complex systems arouse great interest in physics, biology, and chemistry.¹ Nonlinearity of equations or responses to stimuli and inputs is one of the origins of complexity. In chemistry, heteroditopic molecular receptors that can simultaneously bind cationic and anionic guests appear as particularly interesting platforms to examine and ultimately control such complex processes; the response of a given host towards different guest molecules can differ from the linear combinations of the separate unit responses.²⁻¹² Such ion-pair receptors combine two different binding sites for the cation and the anion in a single molecular cavity, and one can anticipate a modulation of the cooperativity through chemical engineering. However, a delicate balance between long- and short-distance interactions must be established to achieve this goal. If the host has been carefully designed, a positive cooperative effect can be observed; an additional or enhanced long-range electrostatic interaction between ions is likely to improve affinity. Conversely, mismatched distances between the cationic and anionic binding sites can lead to negative cooperativity, possibly disrupting the short-range interactions. Among these noncovalent interactions, cation- π interactions have been extensively solicited.^{13,14} They allow for the recognition of cationic guests through attractive interactions with the electron-rich aromatic rings of the host. Anion- π interactions, which involve electron deficient aromatic rings, have received little attention in this context.¹⁵⁻²⁰ The combination of cation- π and anion- π interactions in the recognition of ion pairs by using a specifically designed molecular cavity would provide a playground to decipher the interfering weak interactions that control the sign of cooperativity in recognition processes. Hemicryptophanes appear to be a relevant class of host molecules for addressing this issue.²¹ These molecular receptors are able to complex various guest compounds such as zwitterions and ion pairs, taking advantage of the ditopic character of the host cavity.²²⁻³⁰ For instance, hemicryptophane **1** (Figure 4.1) was found to bind simultaneously to anionic and cationic species, exhibiting a strong positive cooperative effect.³⁰

To extend the series, starting with electron-rich aromatic rings as in compound **1**, we

decided to synthesize and investigate the recognition properties of two new hemicryptophane cages, **2** and **3**, bearing fluorinated aromatic rings close to the anionic binding site. This should allow 1) an increase in the anion- π attractive interactions, thus reinforcing the binding ability of anions, and 2) the assessment of the consequences on cooperativity. The recognition properties were found to largely depend on the position of the fluorine atoms in the aromatic linkers, that is, anion binding constants were significantly increased and decreased in **2** and **3**, respectively. Quantum chemistry [density functional theory (DFT) and complete active space self-consistent field (CASSCF and subsequent CASPT2)] calculations were performed to grasp the weak interactions involved in that recognition process and to rationalize the experimental results. For ion-pairs recognition, the cooperativity switched from positive to negative, that is, host **1** displayed high positive cooperativity, whereas that for host **2** was moderate, and a strong negative cooperative effect was observed with host **3**. Thus, depending on the nature of the guest and the location of the fluorine atoms, the cooperativity can be modulated, providing a unique platform to study the interfering short- and long-range interactions.

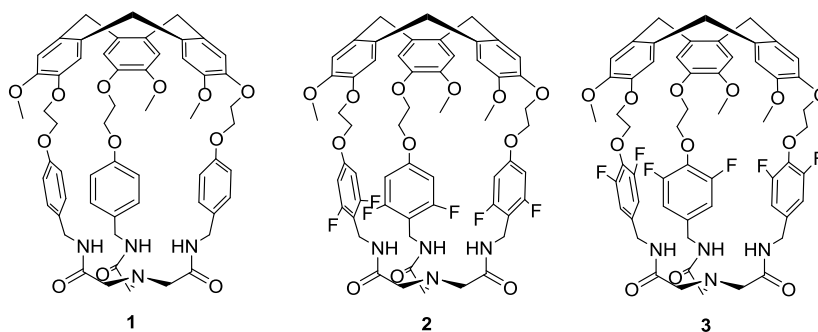
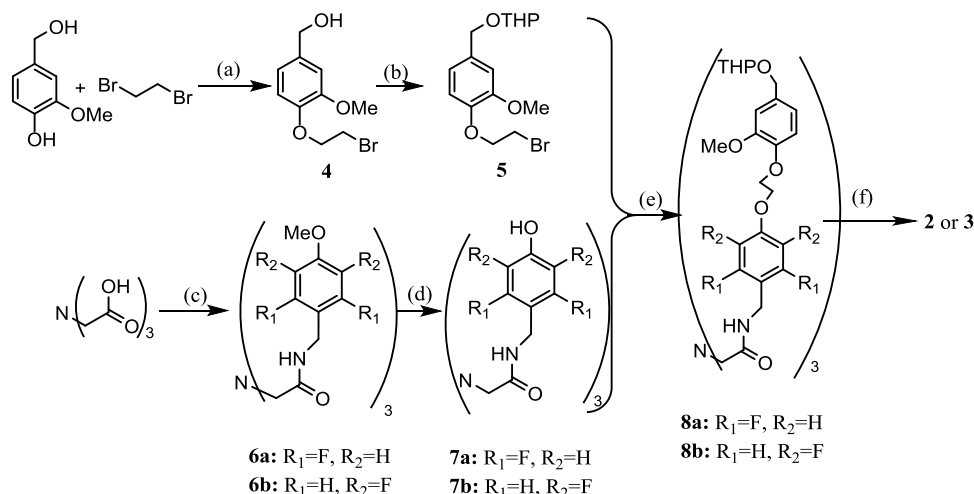


Figure 4.1. Structures of hemicryptophanes **1**, **2**, and **3**.

4.3 Results and discussion

Hemicryptophanes **2** and **3** with respective arbitrarily designed “down” and “up” fluorine atoms in the aromatic linkers, respectively (Figure 4.1), were synthesized following a procedure similar to that described for hemicryptophane **1** (Scheme 4.1).³¹

The reaction of vanillyl alcohol with 1,2-dibromoethane followed by protection with tetrahydropyranyl (THP) acetal afforded compound **5** in 46% overall yield. Nitrilotriacetic acid was activated by $P(O\text{Ph})_3$ and then condensed with 2,6-difluoro-4-methoxybenzylamine or 3,5-difluoro-4-methoxybenzylamine in pyridine to provide compounds **6a** and **6b**, respectively. Deprotection of **6a** and **6b** was performed by using BBr_3 , giving the trisphenol derivatives **7a** and **7b**, respectively. The hemicryptophane precursors **8a** and **8b** were then obtained by reacting **7a** and **7b**, respectively, with **5** in dimethylformamide (DMF) in the presence of Cs_2CO_3 . The cyclization step was then performed in formic acid, affording the desired hemicryptophane derivatives **2** and **3** in 12 and 15% overall yields, respectively, from nitrilotriacetic acid. The ^1H NMR spectra of **2** and **3** indicate that both molecules are, on average, of C_3 symmetry (Figure S4.1)



Scheme 4.1 Synthesis of hemicryptophanes **2** and **3**. (a) K_2CO_3 , EtOH, 50 °C, 6 h, 48%; (b) DHP, APTS, THF/ CH_2Cl_2 , r.t., 3 h, 96%; (c) 2,6-difluoro-4-methoxybenzylamine or 3,5-difluoro-4-methoxybenzylamine, $P(OPh)_3$, pyridine, 110 °C, 15 h, 100% and 75% for **6a** and **6b**, respectively; (d) BBr_3 , CH_2Cl_2 , -78 °C to r.t., 18 h, and 95% and 69% for **7a** and **7b**, respectively; (e) Cs_2CO_3 , DMF, 80 °C, 18 h, 46% and 56% for **8a** and **8b**, respectively; (f) $HCOOH$, [**8**] < 1mM, r.t., one week, 28% and 51% for **2** and **3**, respectively.

The complexation properties of **2** and **3** toward different anions were investigated in $CDCl_3$ by means of 1H NMR titrations, with *n*-tetrabutyl ammonium as the counter ion. In all cases, only one set of signals was observed for the guest and for the receptor, indicating fast exchange conditions on the NMR timescale. The 1H NMR experiments provide information on the geometry of the complexes in chloroform solutions (Figure S4.2): 1) the NH protons display a strong downfield shift upon progressive addition of the guest, evidencing hydrogen bonding between the anionic guest and the amide groups of the host; 2) the protons of the aromatic linkers are significantly shifted upfield (0.05 ppm), indicating that the anion faces the π system of the linkers; 3) no shift was observed for the *n*- Bu_4N^+ protons, thereby indicating that no host–guest interaction between hosts **2** or **3** and *n*- Bu_4N^+ occurs. Taken together, these chemical-shift changes indicate that the anion is bound to the *south* part of the receptor through both hydrogen bonding with the amide functional groups and anion– π interactions with the aromatic rings of the linkers.

Complexation-induced shifts of the aromatic protons of the linkers or those of the $C(O)-CH_2-N$ groups were plotted as a function of the guest/host ratio, and the resulting curves were fitted with WinEQNMR2 software, using a 1:1 model, in agreement with the results of the Job's plot experiments (Figures S4.3 and S4.4).³² The binding constants K_a are reported in Figure 4.2 (see also Table S4.1 in the Experimental Section). The three hosts display a similar trend; the spherical halide anions are bound with the following affinity $F^- > Cl^- > Br^- > I^-$, as expected from the hydrogen-bond-accepting ability of these guests. This is also consistent with the fact that $H_2PO_4^-$ is better coordinated than HSO_4^- . Compared to the less basic $H_2PO_4^-$ anion, the most basic anion AcO^- shows a slightly more complicated behavior, as expected from the hydrogen-bond-accepting ability, with host **3** and the acetate anion displaying a slightly higher binding constant than $H_2PO_4^-$. However, a weaker affinity is observed with

hosts **1** and **2**. Symmetry consideration can account for this weaker association constant; contrary to the V-shaped AcO^- anion, the tetrahedral H_2PO_4^- anion can bind simultaneously to the three hydrogen atoms of the amide functions in **1** and **2**. Nevertheless, the most striking feature is the remarkable change in the binding constant induced by the introduction of the two fluorine atoms in the aromatic linkers. If host **1**, lacking fluorine atoms, is chosen as a reference, a strong enhancement or decrease of the association constant is observed for a given anion, depending on the position of the two additional fluorine atoms. If the fluorine atoms are “down” (host **2**), binding constants are significantly lower than that obtained with host **1**. If the fluorine atoms are “up” (host **3**), the complexation properties toward anions are strongly increased, up to 20 times higher compared to the benchmark host **1**. Thus, it appears that the location of the fluorine atoms on the aromatic rings strongly affect the binding properties of the host. As their positions are modified, a dramatic change in the binding constant, up to a 100-fold increase (see for instance with AcO^- as the guest, Table S4.1), can be observed.

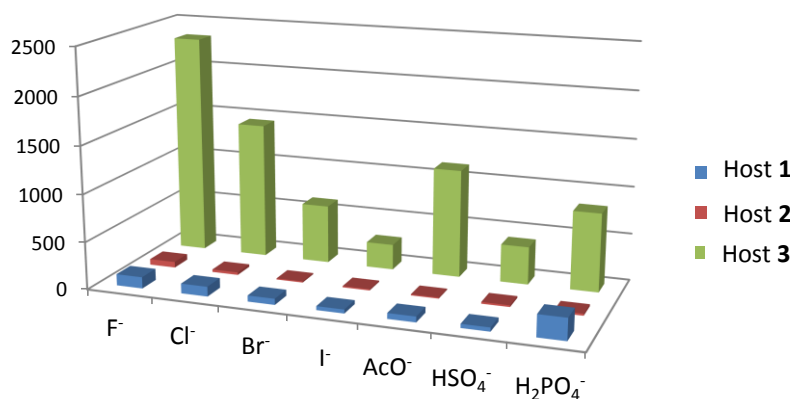


Figure 4.2 Comparison of association constants K_a for anion guests with hosts **1–3**, obtained by modeling the titration curves with WinEQNMR2.³¹

The crucial role played by the location of the fluorine atoms on the binding affinity of the anions prompted us to carefully investigate the role of the anion- π interactions in the recognition process. Indeed, we hypothesized that the free energy of binding corresponds to the sum of three different types of interactions: 1) the steric repulsion between the guest and the linkers, 2) hydrogen bonding between the anions and the amide groups, and 3) the anion- π interactions between the aromatic rings of the linkers and the anions. We considered that the steric hindrance related to the introduction of the fluorine atom can be neglected, because of the similar van der Waals radius of hydrogen and fluorine atoms. Thus, this first contribution is supposed to remain constant throughout the series, (*i.e.* for a given anion), the other interactions (hydrogen bonding and anion- π) should account for the observed differences in the binding affinities. Thus, a deeper inspection of these interactions was undertaken by means of combined DFT and multireference wavefunction-based calculations.

Starting from the DFT-optimized structures, the chlorine anion was displaced along the C_3 axis of the host by using simplified structures as the receptor. In this respect, CASSCF and subsequent CASPT2 calculations were performed to capture dispersion-origin and H-bond interactions (see the Experimental Section). Irrespective of the positions of the fluorine atoms,

the C_3 axis is maintained, which is a common feature with the naked host. Z stands for the guest position along the C_3 axis of the host and Z_{DFT} corresponds to the position in the DFT-optimized geometry. Starting from these geometries, the chlorine anion was displaced along the C_3 axis and the CAS[8,8]PT2 energy was calculated, setting a reference of $Z = 10 \text{ \AA}$. The CAS[8,8] molecular orbitals (MOs) are shown in Figure S4.5. They correspond to the six MOs that are mostly π - π^* in character on the benzyl ring and the $\delta_{\text{N-H}}-\delta_{\text{N-H}^*}$ pair on the N-H bond. Figure 4.3 shows the CASPT2 potential-energy curves for the three host-guest associations.

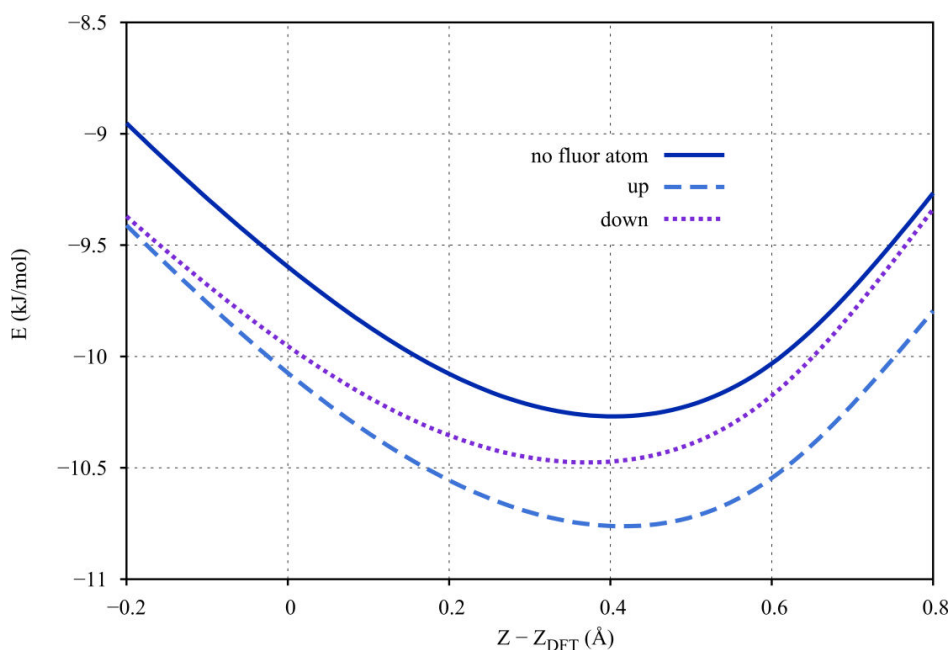


Figure 4.3 CASPT2 energies (kJ mol^{-1}) as a function of the $Z-Z_{\text{DFT}}$ (\AA) displacement of the Cl^- ion along the C_3 axis of the hemicryptophane cavities. The reference energy was chosen for $Z-Z_{\text{DFT}}=10 \text{ \AA}$, a distance for which the highlighted interactions are very small.

First, the minimum position is relatively insensitive ($Z-Z_{\text{DFT}} = -0.04 \text{ \AA}$) to the presence and positions of the fluorine atoms. This is to be contrasted with the interaction energies. At this stage, let us recall that our calculations recover only the gasphase enthalpic contribution of the Gibbs energy. For hosts **1** and **3**, the calculations are in good agreement with the experimental results and suggest the existence of a much stronger combination of anion- π and hydrogen-bond interactions with hemicryptophane **3** than with host **1**. Thus, our calculations reveal that the fluorinated aromatic linker should interact much more strongly with the anion than the “naked” linker, which is fully consistent with the higher binding constant observed with host **3**. Similar calculations indicate that anion- π interactions are stronger with host **3** than with host **2**, which is consistent with the experimental results. However, the experimental results unambiguously demonstrated that host **2** displays the worst binding properties towards anions of the three hosts. Therefore, our calculations fail to fully rationalize the low binding constants observed in that case. Nevertheless, all of the calculations were performed in the gas phase, and it has been shown that the energy of the anion- π interaction strongly differs in gas or solid phase from that in solution. A recent publication from Ballester *et al.* estimates their values as approximately 4 kJ mol^{-1} in solution,

whereas values up to 20 kJ mol⁻¹ are proposed in the solid or gas phases.¹⁶ Thus, solvation effects should be taken into account in the study of the controversial anion- π interaction. Besides, the Gibbs energy in the complexation process is more sensitive to the solvent reorganization, a contribution that has not been evaluated.³³ There is no doubt that upon anion- π interactions and H-bond formation, entropic changes are expected to compete with the enthalpic contribution arising from these weak interactions.

According to our previous study with host **1**, hosts **2** and **3** should be able to complex ion pairs; ammonium and anions are expected to bind respectively to the “north” (CTV, cyclotrimeratrylene) and “south” (triamide) parts of hemicryptophanes **2** and **3**.³⁰ We first investigated the binding properties of **2** and **3** towards cationic guests, without any anion trapped inside the cavity. The tetramethylammonium picrate salt M₄NPic was chosen because 1) the picrate anion cannot bind to the NH groups of host **1–3**, and 2) compared to other tetraalkyl ammonium, tetramethyl ammonium exhibits the highest binding constant with host **1** (380 M⁻¹).³⁰ In all cases, the Job’s plot evidences the formation of 1:1 host-guest complexes. Upon addition of hosts **2** or **3**, the protons of the tetramethyl ammonium display upfield shifts, suggesting the encapsulation of the M₄N⁺ cation in the CTV unit. Modeling of the titration curves with WinEQNMR2 afforded binding constants of 167±11 and 1600±120 M⁻¹ with hosts **2** and **3**, respectively. This trend is similar to that obtained for the recognition of anion.

As hosts **2** and **3** are able to complex anions and cations at the two ends of their cavity, we decided to examine their ability to complex ion pairs, and the nature (positive or negative) of the resulting cooperative effect. Owing to the low solubility of the Me₄N⁺ halide salts, we first prepared [2·Me₄N⁺] or [3·Me₄N⁺] complexes from the soluble Me₄NPic guest, and then *n*-Bu₄NX was added as the source of the halide anion guest. Picrate and tetra-*n*-butylammonium ions do not enter the hemicryptophane cavity (*vide infra*). Following this procedure, we obtained the apparent binding constants *K*_a′ for the complexation of the anions in the presence of a co-bound counter ion, Me₄N⁺, which allowed us to estimate a cooperativity effect (Figure 4.4 and Table S4.2). From the additional electrostatic interaction between the anion and the cation already trapped inside the cavity, one anticipates a positive cooperative effect. With host **2**, a moderate positive cooperative effect is observed, with a cooperativity factor (*K*_a′/*K*_a) lower than that obtained with host **1**. Indeed, host **2** exhibits lower affinities for cations than host **1**. Consequently, fewer cation@**2** species are present in solution when the anion is added, giving a lower positive cooperative effect. Surprisingly, a lower binding constant with host **3** is observed when one equivalent of the cation is already engaged; the binding constant of **3** for Cl⁻ decreases from 1440 to 640 M⁻¹. This observation is rather puzzling, as host **3** exhibits a much higher affinity for cations and anions when the recognition experiments are run independently. This unexpected observation is probably the manifestation of a destructive interference between two recognition processes. In the absence of a host, the Me₄N⁺⋯Cl⁻ distance was estimated by using DFT calculations to be 3.59 Å. To estimate the impact of the presence of a cation species, the energy changes at the optimal Z-ZDFT value (*ca.* 0.4 Å, see Figure 4.3) were quantified by placing a positive point charge on the C₃ axis at Z-ZDFT=3.59 Å. We felt that there was no need to further explore the anion-cation interaction, considering the aforementioned simplification of hosts **1** and **3**. As above,

CAS[8,8] was converged and the CASPT2 energies were evaluated. From these complementary calculations, the recognition ability for the chlorine anion is more affected with host **3** by approximately 1.1 kJ mol^{-1} than with host **1**. Host **3** suffers from a partial disruption of the anion– π interactions as soon as the chlorine atom gets involved in an electrostatic interaction with a cation, dragging the electronic density away from the π cloud. This study not only confirms the tremendous importance of such weak interactions, but also suggests the destructive nature of interfering mechanisms.

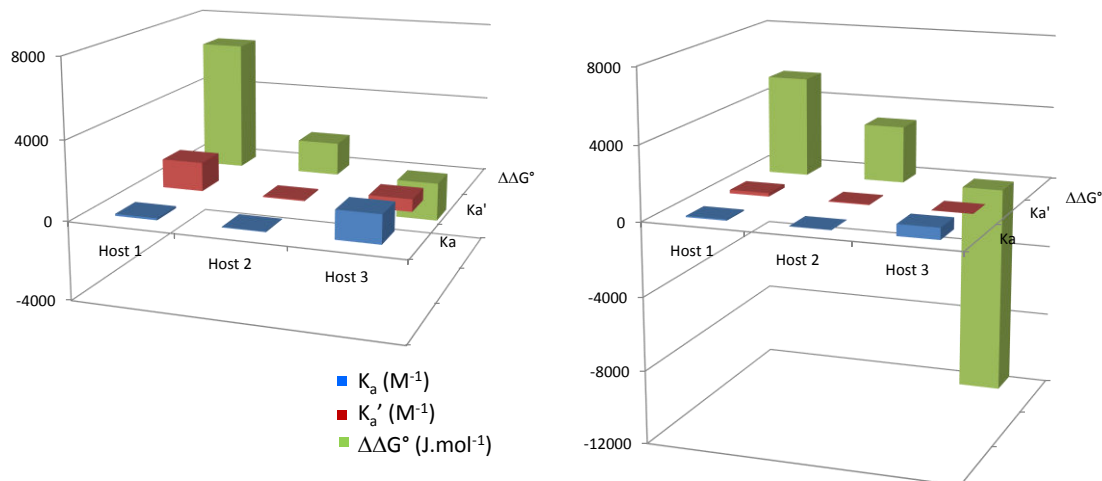


Figure 4.4 Association constants for a) Cl⁻ and b) Br⁻ with hosts **1**, **2**, and **3** without Me₄N⁺ inside the cavity (K_a , in blue) and with one equivalent of Me₄N⁺ inside (K_a' , in red). The cooperativity $\Delta\Delta G^\circ$ is also given (green).

Further experimental evidence for this intriguing observation supported by theoretical calculations was finally given by substituting chlorine for bromine. For host **3**, a stronger negative cooperative effect was observed (Figure 4.4b); the binding constant decreased from 620 to 5 M⁻¹. The enhanced polarizability results in stronger anion– π interactions, which, in turn, are expected to be affected to a greater extent by the presence of a cation species. These observations underline the complexity of cooperative effects in polytopic receptors. Depending on the balance of the main interactions (cation–anion, cation– π , anion– π , and hydrogen bonding) involved in the recognition process, the optimal position of the cation and anion can change slightly, inducing a dramatic switch in the nature of the cooperativity.

4.4 Conclusion

In conclusion, we have described the synthesis of two new hemicryptophane hosts, **2** and **3**, bearing fluorinated aromatic linkers. Their complexation properties were investigated and compared to host **1**, which lacked fluorine atoms in the aromatic linkers. The binding affinity toward anions was found to strongly rely on the location of the fluorine atoms on the linker, highlighting the difficulty in anticipating and understanding the complex role of anion– π and H-bond interactions in recognition processes. Furthermore, the nature of the cooperativity involved in the recognition of ion pairs can be modulated from positive to negative by chemical engineering. This switch in the cooperativity emphasizes the complexity of such polytopic receptors in which interfering interactions occur. We believe that the current

research can promote the better use and understanding of anion- π interactions and facilitate the design of more sophisticated systems bearing multiple weak interactions for cooperative molecular recognition.

4.5 Experimental section

4.5.1 Materials and instrumentation

All reactions were carried out under argon by means of an inert gas/vacuum double manifold and standard Schlenk techniques. Pyridine, DMF, chloroform and methanol were dried prior to use over molecular sieves. Dichloromethane was dried and degassed on a solvent station by passage through an activated alumina column followed by an argon flush. ^1H and ^{13}C spectra were recorded at 500.1 MHz and 125.7 MHz respectively, and are reported relative to the residual protonated solvent signal (^1H , ^{13}C). Mass spectra were recorded by the Centre de Spectrométrie de Masse, Institute of Chemistry, Lyon. Compound **5** was prepared according to the published procedure.³¹ DFT calculations were performed by Vincent Robert.

4.5.2 Synthesis and characterization

Synthesis of compound 2. Compound **8a** (2.51 g, 1.78 mmol) was dissolved in formic acid (2.5 L) and the reaction mixture was stirred at room temperature for one week. The solvent was removed under reduced pressure and the residue was partitioned between chloroform (100 mL) and 10% aq. K_2CO_3 solution. The aqueous phase was extracted 2 times with chloroform (100 mL) and the combined organic phases were dried over Na_2SO_4 , filtered and evaporated to give a brown oil. This procedure was carried out a second time with 2.89 g (2.05 mmol) compound **8a**. Both crude compounds were purified by column chromatography over silica gel (CHCl_3 :MeOH, 150:2 \rightarrow 150:10, v:v) to give **2** as a beige solid (1.20 g, 28% yield). ^1H NMR (CDCl_3 , 298K, 500.1 MHz): δ 7.13 (t, 3H, J = 5.9 Hz); 6.96 (s, 3H); 6.82 (s, 3H); 6.15 (d, 6H, J = 9.2 Hz); 4.76 (d, 3H, J = 13.8 Hz); 4.40-4.42 (m, 6H); 4.20-4.26 (m, 12H); 3.82 (s, 9H); 3.55 (d, 3H, J = 13.8 Hz); 3.17 (s, 6H). ^{13}C NMR (CDCl_3 , 298K, 125.7 MHz): δ 169.9, 161.6, 159.4, 148.6, 146.2, 133.3, 131.7, 117.1, 113.6, 106.0, 98.7, 68.4, 68.2, 60.7, 55.9, 36.4, 30.8. **ESI-HRMS** m/z : calcd for $\text{C}_{57}\text{H}_{55}\text{F}_6\text{N}_4\text{O}_{12}$ [$\text{M}+\text{H}$] $^+$ 1101.3715, found 1101.3673. **IR** (KBr) $\bar{\nu}$ = 3406, 3068, 2937, 1639, 1590, 1510, 1444, 1265 1149 cm^{-1} .

Synthesis of compound 3. The procedure is identical to the one followed for compound **2**. The reaction was carried out with 2.6 g (1.85 mmol) and then with 2.80 g (2.0 mmol) starting material **8b** but the reaction time is only 3 days. Both crude compounds were purified by column chromatography over silica gel (CHCl_3 :MeOH, 150:2 \rightarrow 150:108, v/v) to give **3** as a beige solid (1.03 g, 51% yield). ^1H NMR (CDCl_3 , 298K, 500.1 MHz): δ 7.60 (t, 3H, J = 5.9 Hz); 6.87 (s, 3H); 6.80 (s, 3H); 6.63 (d, 6H, J = 8.2 Hz); 4.71 (d, 3H, J = 13.8 Hz); 4.48 (m, 6H); 4.43-4.45 (m, 3H); 4.21-4.31 (m, 6H); 4.09-4.13 (m, 3H); 3.80 (s, 9H); 3.51 (d, 3H, J = 13.8 Hz); 3.44 (m, 6H). ^{13}C NMR (CDCl_3 , 298K, 125.7 MHz): δ 170.8, 155.7, 148.9, 146.4, 133.9, 133.6, 133.4, 131.8, 117.5, 114.0, 110.6, 72.0, 68.6, 61.3, 56.0, 42.0, 36.4. **ESI-HRMS** m/z : calcd for $\text{C}_{57}\text{H}_{55}\text{F}_6\text{N}_4\text{O}_{12}$ [$\text{M}+\text{H}$] $^+$ 1101.3715, found 1101.3669. **IR** (KBr) $\bar{\nu}$ = 3423, 3068, 2935, 1656, 1514,

1444, 1336, 1265 1039 cm⁻¹.

Synthesis of compound 6a. 2,6-difluoro-4-methoxybenzylamine (4.75 g, 27 mmol) and nitrilotriacetic acid (1.67 g, 8.8 mmol) were added to pyridine (60 mL) and then heated at 50°C for 20 minutes. Triphenylphosphite (8.5 mL, 32 mmol) was added dropwise and the solution is then stirred at 100°C for 17 h. Volatiles were evaporated. The residue was taken up with chloroform (75 mL) and washed with 10% aq. NaHCO₃ and 75 mL distilled water. The organic phase was dried over Na₂SO₄, filtered and evaporated. The crude compound was dissolved with acetone and precipitated with pentane leading to a pure white solid (5.93g, 99% yield). ¹H NMR (CDCl₃, 298K, 500.1 MHZ): δ 7.17 (bs, 3H); 6.46 (d, 6H, J = 9.5 Hz); 4.43 (d, 6H, J = 5.3 Hz); 3.81 (s, 9H); 3.29 (s, 6H). ¹³C NMR (CDCl₃, 298K, 125.7 MHZ): δ 169.8, 162.1, 160.7, 105.6, 98.0, 59.7, 55.8, 31.1. **ESI-HRMS** m/z: calcd for C₃₀H₃₁F₆N₄O₆ [M+H]⁺ 657.2142, found 657.2126. **IR** (KBr) $\bar{\nu}$ = 3302, 3074, 2948, 1643, 1591, 1549, 1506, 1143, 1070 cm⁻¹.

Synthesis of compound 6b. The procedure is identical to the one followed for the synthesis of **6a** with 3,5-difluoro-4-methoxybenzylamine (5.0 g, 29 mmol), nitrilotriacetic acid (1.76 g, 9.0 mmol) and triphenylphosphite (8.32 mL) and gave a white solid (4.48 g, 75% yield). ¹H NMR (CDCl₃, 298K, 500.1 MHZ): δ 7.53 (bs, 3H); 6.82 (d, 6H, J = 8.5 Hz); 4.34 (d, 6H, J = 5.9 Hz); 3.99 (s, 9H); 3.42 (s, 6H). ¹³C NMR (CDCl₃, 298K, 125.7 MHZ): δ 170.7, 155.6, 135.7, 133.3, 111.3, 61.8, 60.6, 42.3. **ESI-HRMS** m/z: calcd for C₃₀H₃₁F₆N₄O₆ [M+H]⁺ 657.2142, found 657.2126. **IR** (KBr) $\bar{\nu}$ = 3328, 3216, 3060, 2948, 2842, 1656, 1520, 1442, 1246, 1039 cm⁻¹.

Synthesis of compound 8a. Under argon, compound **6a** (5.87g, 8.94 mmol) was partially dissolved in dry dichloromethane (100 mL) and the solution was cooled to -78°C. A solution of 1M boron tribromide in dichloromethane (53 mL, 53 mmol) was added dropwise for 1 h and the solution was allowed to slowly warm up at room temperature over the night. Methanol was then added until the gas emission stopped, and the pH was adjusted to 8 with 10% aqueous NaHCO₃. The aqueous phase was then extracted with ethyl acetate (200 mL) for 3 times. The combined organic phases were dried over Na₂SO₄, filtered and concentrated under vacuum to give a beige solid **7a** which was then used without purification (5.21 g, 95% yield). Compound **7a** was placed with compound **5** (5.19 g, 8.41 mmol), cesium carbonate (12.2 g, 37.3 mmol) and 50 mL DMF. The reaction mixture was heated to 80°C for 17 h. After cooling to room temperature, water (200 mL) was added and the aqueous phase was extracted with ethyl acetate (200 mL) for 3 times. The combined organic phases were washed with 10% aq. NaOH (200 mL) and distilled water (200 mL), dried over Na₂SO₄, filtered and evaporated. Purification of the crude by column chromatography over silica gel (CH₂Cl₂ → CH₂Cl₂:MeOH, 95:5, v:v) gave compound **8a** as a brown oil (5.45 g, 46% yield). ¹H NMR (CDCl₃, 298K, 500.1 MHZ): δ 7.15 (t, 3H, J = 5.5 Hz); 6.91-6.95 (m, 9H); 6.53 (d, 6H, J = 9.3 Hz); 4.75 (d, 3H, J = 11.9 Hz); 4.71 (m, 3H); 4.47 (d, 3H, J = 11.9 Hz); 4.43 (d, 6H, J = 5.3 Hz); 4.35 (m, 12H); 3.93 (m, 3H); 3.88 (s, 9H); 3.57-3.59 (m, 3H); 3.27 (s, 6H); 1.64-1.90 (m, 18H). ¹³C NMR (CDCl₃, 298K, 125.7 MHZ): δ 169.9, 162.0, 159.7, 149.8, 147.4, 132.2, 120.5, 114.3, 112.1, 105.9, 98.9, 98.6, 97.7, 68.7, 67.7, 67.3, 62.3, 59.8, 55.9, 30.6, 25.5, 19.5. **ESI-HRMS** m/z: calcd for C₇₂H₈₅F₆N₄O₁₈ [M+H]⁺ 1407.5758, found 1407.5729. **IR** (KBr) $\bar{\nu}$ = 3309, 3066, 2940, 2871, 1639, 1591, 1510, 1265, 1151, 1072, 1036 cm⁻¹.

Synthesis of compound 8b. The procedure for the demethylation of compound **6b** was the

same as those used for compound **6a** with 3.78 g (5.76 mmol) starting material and 33 mL of a solution of BBr_3 in CH_2Cl_2 and gave 2.43 g beige compound **7b** (69% yield). This compound was then reacted with compound **5** (5.85 g, 17 mmol) and Cs_2CO_3 (5.66 g, 17 mmol) with the same procedure followed as those for compound **7a** leading to the formation of compound **8b** (3.04 g, 56% yield). $^1\text{H NMR}$ (CDCl_3 , 298K, 500.1 MHz): δ 7.62 (bs, 3H); 6.91-6.93 (m, 9H); 6.82 (d, 6H, $J = 8.2$ Hz); 4.74 (d, 3H, $J = 11.7$ Hz); 4.71 (m, 3H); 4.45-4.49 (m, 9H); 4.32-4.35 (m, 12H); 3.94 (m, 3H); 3.85 (s, 9H); 3.55-3.58 (m, 3H); 3.39 (s, 6H); 1.63-1.90 (m, 18H). $^{13}\text{C NMR}$ (CDCl_3 , 298K, 125.7 MHz): δ 170.8, 155.7, 149.9, 147.6, 134.5, 134.0, 132.1, 120.6, 114.6, 112.3, 111.3, 111.2, 97.8, 72.6, 68.8, 68.5, 62.4, 60.3, 56.0, 30.7, 25.5, 19.6. **ESI-HRMS** m/z : calcd for $\text{C}_{72}\text{H}_{85}\text{F}_6\text{N}_4\text{O}_{18}$ $[\text{M}+\text{H}]^+$ 1407.5758, found 1407.5729. **IR** (KBr) $\bar{\nu} = 3309, 3066, 2940, 2871, 1639, 1591, 1510, 1265, 1151, 1072, 1036$ cm^{-1} .

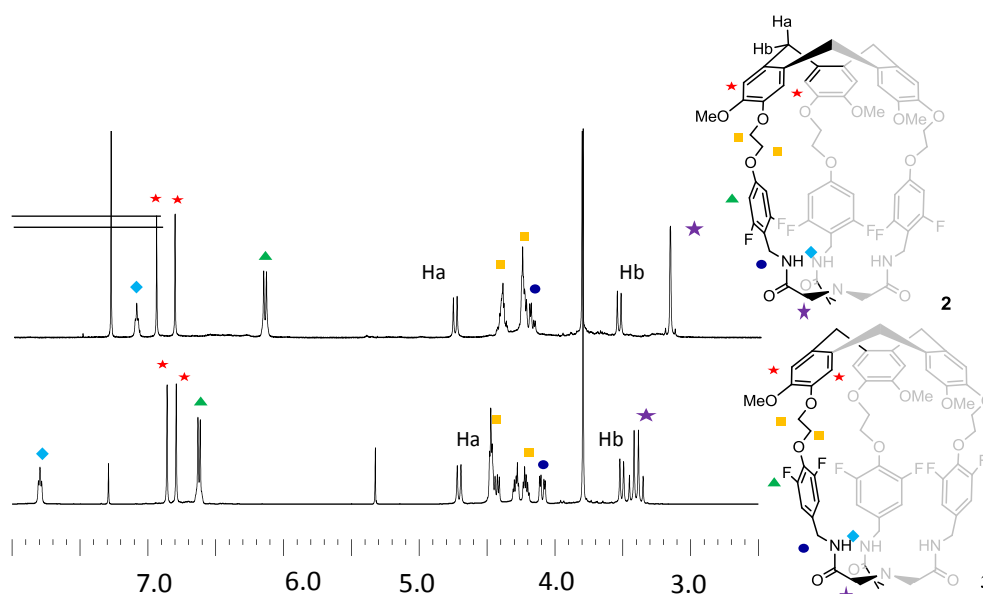


Figure S4.1 $^1\text{H NMR}$ spectra (500.1 MHz, CDCl_3 , 298 K) of hemicryptophanes **2** and **3**.

4.5.3 $^1\text{H NMR}$ titration

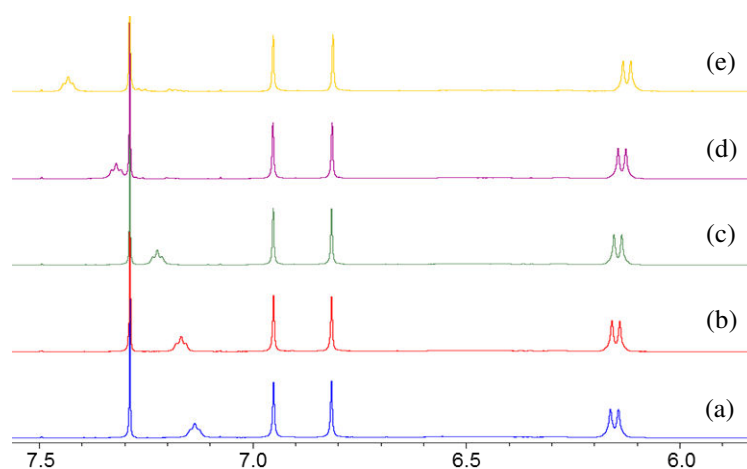


Figure S4.2 $^1\text{H NMR}$ (CDCl_3 , 298 K, 500 MHz) titration experiment of host **2** (3.7 mM) with Bu_4NCl : (a) 0 eq. of Bu_4NCl ; (b) 0.6 eq. of Bu_4NCl ; (c) 1.7 eq. of Bu_4NCl ; (d) 5.1 eq. of Bu_4NCl ; (e) 11.3 eq. of Bu_4NCl .

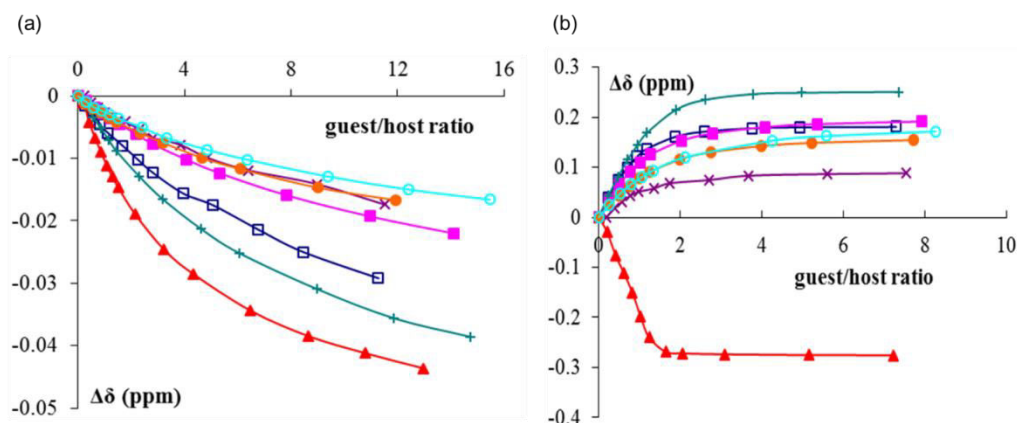


Figure S4.3 ^1H NMR (CDCl_3 , 500 MHz, 298 K) titration curves for different anions with 5.0 mM hosts **2** (a) and **3** (b) (+ : H_2PO_4^- , ■ : Br^- , □ : Cl^- , ● : HSO_4^- , ○ : I^- , × : Ac^- , ▲ : F^-).

Table S4.1. Association constants K_a of hosts **1-3** with anion guests obtained by modeling the titration curves with WinEQNMR2.³²

	K_a (M^{-1}) host 1	K_a (M^{-1}) host 2	K_a (M^{-1}) host 3
F^-	120 ± 5	61 ± 3	2330 ± 100
Cl^-	103 ± 4	27 ± 5	1440 ± 70
Br^-	64 ± 3	12 ± 2	620 ± 13
I^-	41 ± 3	13 ± 1	270 ± 8
AcO^-	60 ± 3	11 ± 1	1140 ± 60
HSO_4^-	42 ± 5	18 ± 1	400 ± 16
H_2PO_4^-	230 ± 20	21 ± 1	830 ± 110

Table S4.2. Association constants of hosts **2** and **3** with anions in the absence (K_a) and presence (K_a') of one equivalent of Me_4N^+ inside the cavity, and the cooperativity factors of hosts **1-3** with anion guests.

	K_a (M^{-1}) 2	K_a' (M^{-1}) 2	K_a'/K_a 2	K_a (M^{-1}) 3	K_a' (M^{-1}) 3	K_a'/K_a 3	K_a'/K_a 1
F^-	61 ± 3	-	-	2330 ± 100	-	-	3
Cl^-	27 ± 5	58 ± 1	2	1440 ± 70	640 ± 70	0.44	15
Br^-	12 ± 2	42 ± 1	3.5	620 ± 13	< 5	< 0.01	9
AcO^-	11 ± 1	27 ± 2	2.5	1140 ± 60	145 ± 15	0.13	5

4.5.4 Job plot

The continuous variation method was used for determining the binding stoichiometry.³⁴ In this method, solutions of the host and guest at the same concentration were prepared in CDCl_3 . Then the two solutions were mixed in different proportions maintaining a constant

volume and concentration. After incubating the mixture for 30 s, the spectra of the solutions for different compositions were recorded.

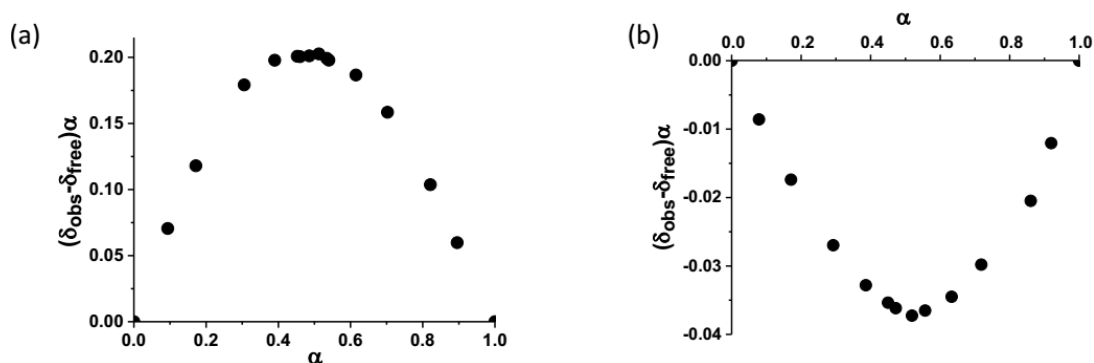


Figure S4.4 ^1H NMR Job plot of **3** with TBACl (a) and tetramethylammonium picrate (b).

4.5.5 Computational details

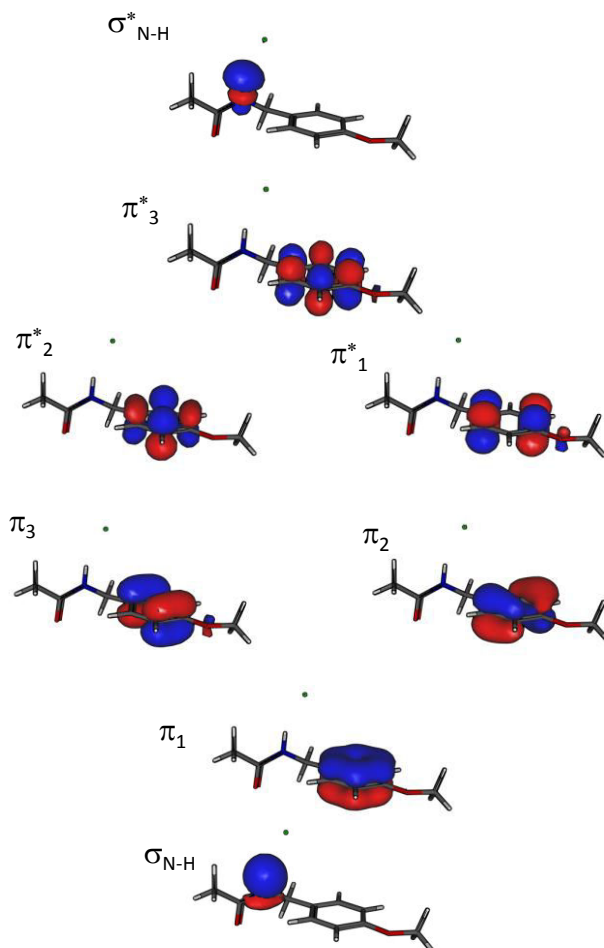


Figure S4.5 MOs: CAS[8,8]SCF MOs of a simplified structure of host **2** and Cl^- anion guest.

Similar pictures are obtained for hosts **1** and **3**.

Quantum chemistry calculations were performed to explore the origin of the binding association differences observed in the hemicryptophanes recognition. First, density functional theory (DFT) was used to generate optimal geometries of the 3 hosts and the

encapsulated chlorine guest.³⁵ Full geometry optimizations were performed using a combination of B3LYP functional and 6-31+G** basis set.

Ion- π interactions result from charge density fluctuations (*i.e.* dispersion interactions) within a given π system in the presence of charges. Besides, one would like to seize the importance of charge reorganization in the N-H bond involved in possible H-bond formation with the chlorine anion. Multi-reference calculations are particularly attractive since one can effectively account for these physical phenomena. Thus, complete active space self-consistent field (CASSCF) calculations were then performed including 8 electrons in 8 molecular orbitals (MOs) on simplified structures of hosts (CAS[8,8]). The active space was converged onto the 6 π MOs of the benzyl ring and the σ - σ^* pair of the NH bond. We checked that the mostly chlorine-localized MOs remain almost doubly occupied and need not to be included in the active space. Subsequent second-order perturbation theory treatment (CASPT2) was carried out to account for the so-called dynamical correlation effects. Using this strategy, one can accurately take into account the charge density fluctuations accounting for the H-bond and anion- π interactions. Assuming a fixed geometry of the host, the energetics was followed as a function of the chlorine ion position Z along the C_3 axis. Since our purpose was to concentrate the numerical effort on the π - π^* charge fluctuations and the hydrogen bond, extended basis set was used for the aromatic ring, namely ANO-RCC 4s3p2d1f for C and N, 2s1p for H, while the other atoms were depicted using ANO-RCC double-zeta+polarization (DZP) basis sets. This combination of basis sets has been recently used successfully in various weak interactions inspections (VR2, VR3). Finally, the Cl^- anion was depicted with a 4s3p1d ANO-RCC basis set. All our calculations were performed using the MOLCAS 7.2 suite of program (VR 4).

4.6 References

1. J. Ross, A. P. Arkin, *Proc. Natl. Acad. Sci. USA* **2009**, *106*, 6433.
2. M. Ciardi, A. Gal, P. Ballester, *J. Am. Chem. Soc.* **2015**, *137*, 2047.
3. E. N. W. Howe, M. Bhadbhade, P. Thordarson, *J. Am. Chem. Soc.* **2014**, *136*, 7505.
4. M. Ciardi, F. Tancini, G. Gil-Ramirez, E. C. E. Ad, C. Massera, E. Dalcanale, P. Ballester, *J. Am. Chem. Soc.* **2012**, *134*, 13121.
5. S. K. Kim, G. I. Vargas-Ziflig, B. P. Hay, N. J. Young, L. H. Delmau, C. Masselin, C.-H. Lee, J. S. Kim, V. M. Lynch, B. A. Moyer, J. L. Sessler, *J. Am. Chem. Soc.* **2012**, *134*, 1782.
6. S. K. Kim, J. L. Sessler, D. E. Gross, C.-H. Lee, J. S. Kim, V. M. Lynch, L. H. Delmau, B. P. A. Hay, *J. Am. Chem. Soc.* **2010**, *132*, 5827.
7. J. L. Sessler, S. K. Kim, D. E. Gross, C.-H. Lee, J. S. Kim, V. M. Lynch, *J. Am. Chem. Soc.* **2008**, *130*, 13162.
8. A. J. McConnell, P. D. Beer, *Angew. Chem., Int. Ed.* **2012**, *51*, 5052.
9. M. Cametti, M. Nissinen, A. Dalla Cort, L. Mandolini, K. Rissanen, *J. Am. Chem. Soc.* **2007**, *129*, 3641.
10. S. K. Kim, J. L. Sessler, *Acc. Chem. Res.* **2014**, *47*, 2525.
11. S. K. Kim, V. M. Lynch, N. J. Young, B. P. Hay, C.-H. Lee, J. S. Kim, B. A. Moyer, J. L. Sessler, *J. Am. Chem. Soc.* **2012**, *134*, 20837.
12. L. S. Tobey, E. V. Anslyn, *J. Am. Chem. Soc.* **2003**, *125*, 10963.

- 13 E. Persch, O. Dumele, F. Diederich, *Angew. Chem., Int. Ed.* **2015**, *54*, 3290.
- 14 D. A. Dougherty, *Acc. Chem. Res.* **2013**, *46*, 885.
- 15 H. T. Chifotides, K. R. Dunbar, *Acc. Chem. Res.* **2013**, *46*, 894.
- 16 L. Adriaenssens, G. Gil-Ramirez, A. Frontera, D. Quinonero, E. C. Escudero-Adan, P. Ballester, *J. Am. Chem. Soc.* **2014**, *136*, 3208.
- 17 P. Ballester, *Acc. Chem. Res.* **2013**, *46*, 874.
- 18 K. Fujisawa, C. Beuchat, M. Humbert-Droz, A. Wilson, T. A. Wesolowski, J. Mareda, N. Sakai, S. Matile, *Angew. Chem., Int. Ed.* **2014**, *53*, 11266.
- 19 A. Vargas Jentzsch, D. Emery, J. Mareda, P. Metrangolo, G. Resnati, S. Matile, *Angew. Chem., Int. Ed.* **2011**, *50*, 11675.
- 20 O. Perraud, V. Robert, H. Gornitzka, A. Martinez, J.-P. Dutasta, *Angew. Chem., Int. Ed.* **2012**, *51*, 504.
- 21 J. Canceill, A. Collet, J. Gabard, F. Kotzyba-Hibert, J.-M. Lehn, *Helv. Chim. Acta* **1982**, *65*, 1894.
- 22 L. Wang, G.-T. Wang, X. Zhao, X.-K. Jiang, Z.-T. Li, *J. Org. Chem.* **2011**, *76*, 3531.
- 23 O. Perraud, A. Martinez, J.-P. Dutasta, *Chem. Commun.* **2011**, *47*, 5861.
- 24 O. Perraud, V. Robert, A. Martinez, J.-P. Dutasta, *Chem. Eur. J.* **2011**, *17*, 13405.
- 25 O. Perraud, S. Lefevre, V. Robert, A. Martinez, J.-P. Dutasta, *Org. Biomol. Chem.* **2012**, *10*, 1056.
- 26 J. R. Cochrane, A. Schmitt, U. Wille, C. A. Hutton, *Chem. Commun.* **2013**, *49*, 8504.
- 27 A. Schmitt, V. Robert, J.-P. Dutasta, A. Martinez, *Org. Lett.* **2014**, *16*, 2374.
- 28 D. Zhang, G. Gao, L. Guy, V. Robert, J.-P. Dutasta, A. Martinez, *Chem. Commun.* **2015**, *51*, 2679.
- 29 A. Schmitt, B. Chatelet, D. Padula, L. Di Bari, J.-P. Dutasta, A. Martinez, *New J. Chem.* **2015**, *39*, 1749.
- 30 O. Perraud, V. Robert, A. Martinez, J.-P. Dutasta, *Chem. Eur. J.* **2011**, *17*, 4177.
- 31 P. Dimitrov Raytchev, O. Perraud, C. Aronica, A. Martinez, J.-P. Dutasta, *J. Org. Chem.* **2010**, *75*, 2099.
- 32 M. J. Hynes, *J. Chem. Soc. Dalton Trans.* **1993**, 311.
- 33 L. S. Tobey, E. V. Anslyn, *J. Am. Chem. Soc.* **2003**, *125*, 14807.
- 34 P. Job, *Ann. Chim.*, 1928, **9**, 113.
- 35 Gaussian 03: M. J. Frisch, G. W. Trucks, H. B. Schlegel, G. E. Scuseria, M. A. Robb, J. R. Cheeseman, G. Scalmani, V. Barone, B. Mennucci, G. A. Petersson, H. Nakatsuji, M. Caricato, X. Li, H. P. Hratchian, A. F. Izmaylov, J. Bloino, G. Zheng, J. L. Sonnenberg, M. Hada, M. Ehara, K. Toyota, R. Fukuda, J. Hasegawa, M. Ishida, T. Nakajima, Y. Honda, O. Kitao, H. Nakai, T. Vreven, J. A. Jr. Montgomery, J. E. Peralta, F. Ogliaro, M. Bearpark, J. J. Heyd, E. Brothers, K. N. Kudin, V. N. Staroverov, R. Kobayashi, J. Normand, K. Raghavachari, A. Rendell, J. C. Burant, S. S. Iyengar, J. Tomasi, M. Cossi, N. Rega, J. M. Millam, M. Klene, J. E. Knox, J. B. Cross, V. Bakken, C. Adamo, J. Jaramillo, R. Gomperts, R. E. Stratmann, O. Yazyev, A. J. Austin, R. Cammi, C. Pomelli, J. W. Ochterski, R. L. Martin, K. Morokuma, V. G. Zakrzewski, G. A. Voth, P. Salvador, J. J. Dannenberg, S. Dapprich, A. D. Daniels, O. Farkas, J. B. Foresman, J. V. Ortiz, J. Cioslowski, D. J. Fox, *Gaussian*, Wallingford, CT, 2009.

Chapter 5. Synthesis, Resolution and Absolute Configuration of Chiral TPA-Based Hemicryptophane Molecular Cages

This Chapter is based partially on the following manuscript—

Dawei Zhang, Benjamin Bousquet, Jean-Christophe Mulatier, Marion Jean, Nicolas Vanthuynne, Laure Guy, Jean-Pierre Dutasta, Alexandre Martinez

J. Org. Chem. Accepted, DOI: 10.1021/acs.joc.7b00559.

The work in this chapter was carried out at the ENS-Lyon.

Contents

5.1 Abstract	108
5.2 Introduction.....	108
5.3 Results and discussion	109
5.4 Conclusion.....	112
5.5 Experimental section.....	112
5.6 References.....	121

5.1 Abstract

The synthesis, characterization and chiroptical properties of a new class of hemicryptophane cages combining both a bowl shaped cyclotrimeratrylene (CTV) unit and a tris(2-pyridylmethyl)amine (TPA) moiety are reported. Interestingly, changing the linkers between these two units allows for the modification of the size and shape of the cavity. The synthesis is straightforward and efficient, providing gram-scale of cage compounds. The racemic mixture of each hemicryptophane can be readily resolved by chiral HPLC, giving an easy access to the enantiopure molecular cages of which absolute configurations have been assigned by ECD spectroscopy. These new hemicryptophanes represent available chemical platforms ready to use for various purposes due to the versatile metal complexation properties and applications of the TPA unit.

5.2 Introduction

Molecular cages have attracted considerable attention in the last two decades, leading to great applications in recognition, catalysis, separation and reactive species stabilization.¹ In particular, biomimetic chiral cages arouse a growing interest because of the important role of chirality in nature.² One prominent example is substrate binding and transformation by enzyme, displaying high chemoselectivity, regioselectivity and stereospecificity.³ Among the chiral cages, hemicryptophanes, which combine a cyclotrimeratrylene (CTV) unit with another C_3 -symmetric moiety, exhibit remarkable properties in molecular recognition and supramolecular catalysis.^{1a} The promising applications of hemicryptophanes benefit from the rigid bowl shape of the inherently chiral CTV unit as well as the feature of variability and easy functionalization of the other C_3 -symmetrical moiety.

To construct novel hemicryptophane scaffolds, typical tripodal building blocks, such as tris(2-aminoethyl)-amine (tren)⁴ and trialkanolamine units,⁵ have been introduced as the other moiety connected with the CTV unit. The usefulness and easy availability should be considered when choosing this C_3 -symmetric group. In this regard, tris(2-pyridylmethyl)amine (TPA) unit appears promising. Indeed, TPA is a very useful ligand in coordination chemistry, which can coordinate with various metals, such as Fe,⁶ Cu,⁷ Zn,⁸ Co,⁹ Mn,¹⁰ Ru,¹¹ Rh,¹² Ni,¹³ and Ln,¹⁴ and the resulting complexes have been extensively used in recognition,¹⁵ catalysis,^{6-7,10b,11b,12} chiroptical molecular switches,¹⁶ and enantiomeric excess (*ee*) determination.^{8a,8b,17} For instance, complex [Fe-(TPA)(MeCN)₂](ClO₄)₂ combined with photocatalyst riboflavin tetraacetate was used as a readily accessible and efficient catalyst system for the visible-light-driven aerobic C-H bond oxidation of alkyl benzene to ketones and carboxylic acids.^{6a} The copper complexes of TPA derivatives have widely catalyzed the reactions of atom transfer radical cyclization (ATRC),^{7a} atom transfer radical addition (ATRA),^{7b} and atom transfer radical polymerization (ATRP).^{7c} Moreover, Anslyn and Giulia *et al.* adopted Zn(II) or Cu(II) complexes of TPA derivatives for rapid determination of *ee* of alcohols, carboxylic acids, amines, and amino acids.^{8a,8b,17} This application originates from the propeller-like arrangement of TPA ligands around the metal center. The handedness of this helicity of the TPA analogues can also be controlled by the presence of a stereogenic

center in the ligand backbone which realizes redox-triggered chiroptical switches, as reported by the group of Canary.¹⁶

In line with the versatile nature of TPA complexes and their potential applications, we hereby report on the design and synthesis of a class of TPA-based hemicryptophanes (Figure 5.1). The obtained racemic mixture can also be readily resolved by chiral HPLC to give the enantiopure form in a relatively large-scale. Electronic circular dichroism (ECD) spectroscopy was used to determine the absolute configuration of each hemicryptophane enantiomer. To the best of our knowledge, the synthesis of enantiopure TPA-based cage molecules is unprecedented and these enantiopure hemicryptophanes are promising chemical platforms capable of complexation of various metals for different purposes and applications.

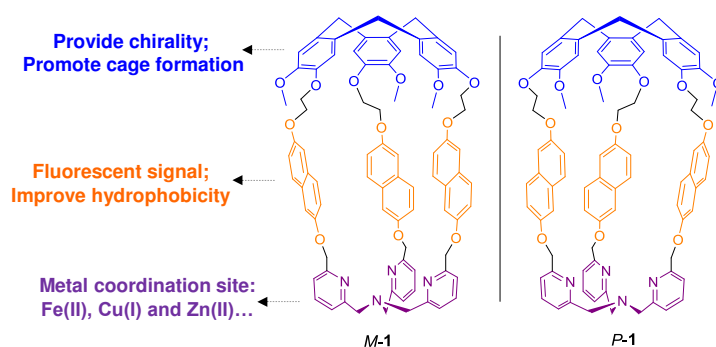


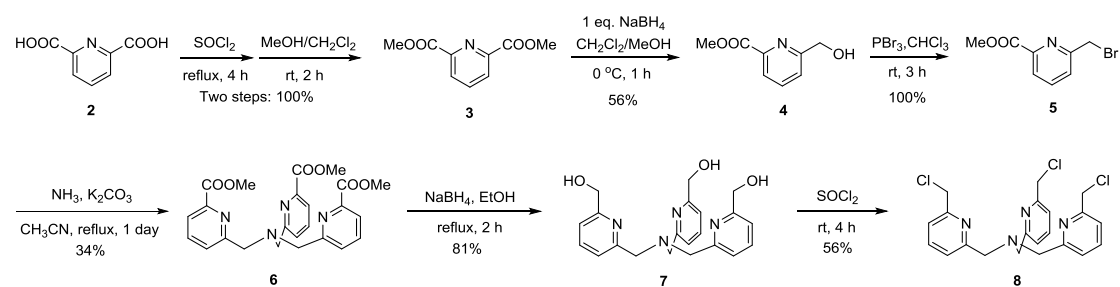
Figure 5.1 Design of the new enantiopure TPA-based hemicryptophanes which are available chemical platforms able to coordinate with various metals for different applications.

5.3 Results and discussion

The structures of the enantiomeric hemicryptophanes *M-1* and *P-1* (Figure 5.1) present the following features: (i) Firstly, the bowl-shaped CTV unit allows the formation of a well-defined chiral cavity; (ii) the naphthalene fluorophores, used as hydrophobic “walls” connecting the TPA and CTV units, confer fluorescence properties to the host; (iii) as mentioned above, the TPA moiety is able to coordinate with various metals giving rise to chemical platforms for further applications. Two routes can be followed to obtain hemicryptophane compounds: either a [1+1] coupling reaction between a CTV moiety and another C_3 symmetrical unit to afford the expected cage, or a triple macrocyclization reaction to build the CTV core in the last step of the synthesis.^{1a} We anticipated that the protonation of the TPA unit in formic acid could lead to some preorganization of the precursor for the cyclization, thus we decided to adopt the second strategy.^{1a,1b,5a} As the TPA constitutes the lower part of this precursor, the first aim was to prepare the TPA-trichloride **8** (Scheme 5.1).¹⁸

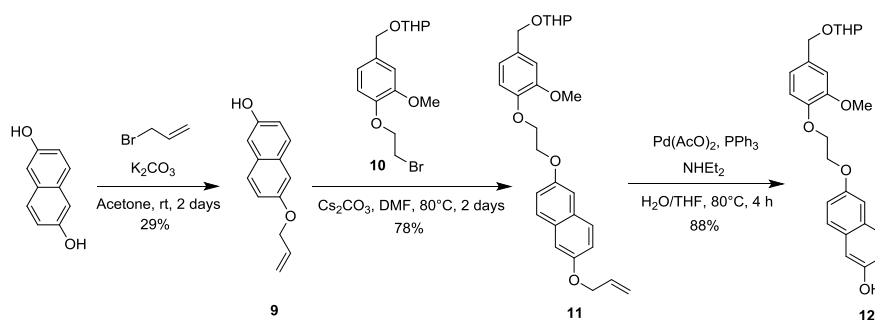
Starting from 2,6-pyridinedicarboxylic acid **2**, 2,6-pyridinedicarboxylate **3** was quantitatively prepared by two successive steps: chloroformylation with thionyl chloride under reflux and esterification with MeOH at room temperature (Scheme 5.1). The reduction of one ester group in **3** by 1.0 equiv. of NaBH₄ in CH₂Cl₂/MeOH gave alcohol **4** in 56% yield. Bromide **5** was then obtained quantitatively by bromination of **4** with PBr₃ at r.t. The addition of an ammonium solution to **5** in the presence of K₂CO₃ under reflux for 1 day, gave the TPA-triester **6** in 34% yield. The synthesis of **8** was achieved by reduction of **6** with an excess

of NaBH₄ followed by chlorination using thionyl chloride, with an overall yield of 45%.



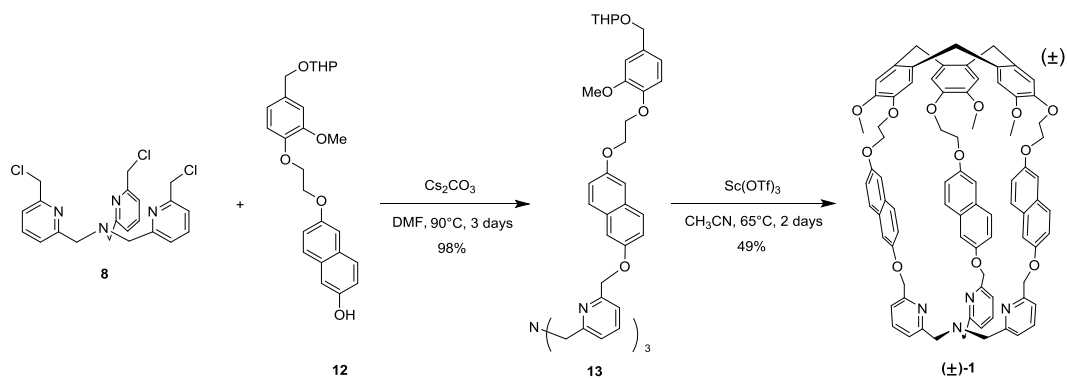
Scheme 5.1 Synthesis of TPA-trichloride **8**.

In order to achieve the hemicryptophane precursor **13**, the phenol **12** was synthesized according to the pathway described in Scheme 5.2. Firstly, 2,6-dihydroxynaphthalene was mono-protected with an allyl group via its reaction with 1.0 equiv. of allyl bromide in acetone in the presence of K₂CO₃ to give allyloxyphenol **9** in 29% yield. Then, phenol **9** reacted with compound **10**, obtained in 3 steps as described previously,^{5a} in the presence of Cs₂CO₃ in DMF at 80 °C to give **11** in 78% yield. Compound **11** was subsequently deprotected using Pd(II) complex in a H₂O/THF mixture at 80 °C to generate the phenol **12** in 88% Yield.



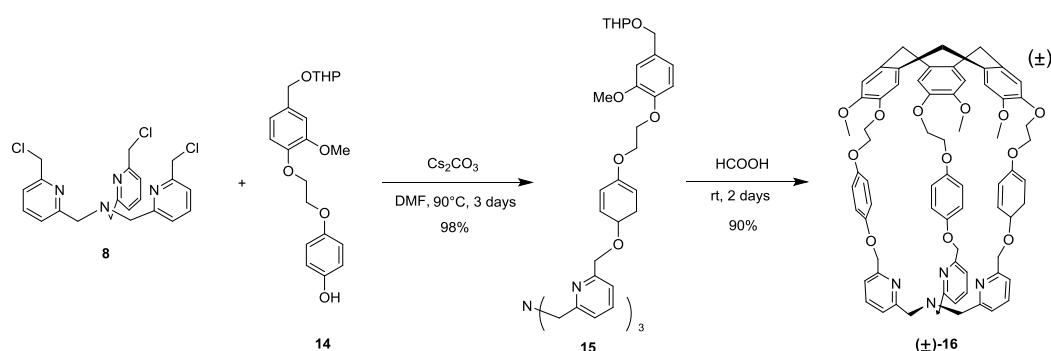
Scheme 5.2 Synthesis of the phenol derivative **12**.

With **8** and **12** in hand, hemicryptophane precursor **13** was prepared in one step (98% yield) by heating the two compounds in DMF at 90 °C for 3 days in the presence of Cs₂CO₃ as a base (Scheme 5.3). The intramolecular cyclization of **13** performed in formic acid led to low yields because of purification issues: several side products were very difficult to separate from the cage compounds. Finally, the use of stoichiometric amounts of Lewis acid Sc(OTf)₃ in CH₃CN at 65 °C provided rac-hemicryptophane (±)-**1** with a yield of 49%.



Scheme 5.3 Synthesis of the racemic mixture of hemicryptophane (±)-**1**.

Given the modular feature of this synthetic pathway, we decided to change the naphthyl linkers to phenyl ones in order to prepare the hemicryptophane analogue (\pm)-**16** presenting a smaller cavity (Scheme 5.4). Compound **14** was first obtained following the known procedure.^{5a} After achieving the hemicryptophane precursor **15** from **14**, we observed that the macrocyclization of **15** in formic acid gave the racemic mixture of **16** in an extremely high yield (90%). In particular, hemicryptophane **16** can be isolated by simple precipitation in CH₂Cl₂/Et₂O without the need of column chromatography purification. The preorganization of the precursor of cyclization in formic acid can account for the remarkable yield obtained. Moreover, as the yield of each previous step is relatively high, gram-scale synthesis of (\pm)-**16** was achieved. This constitute an important step for the future development of this class of host compounds as sensors or catalysts considering the common limitation related to the difficulty of accessing cage compounds on a large scale.^{1a}



Scheme 5.4 Synthesis of the racemic mixture of hemicryptophane (\pm)-**16**.

The ¹H NMR spectra of (\pm)-**1** and (\pm)-**16** indicate that the molecules are, on average, of C₃ symmetry in solution (Figure 5.2). They display the usual features of the structure of the CTV unit, *i.e.* two singlets for the aromatic protons, one singlet for the OCH₃ groups, and the characteristic AB system for the ArCH₂ bridges.^{1a,1b} The protons on aromatic TPA and linkers, and the multiplets for the OCH₂ linkers were carefully assigned by 2D NMR (see 5.5.3).

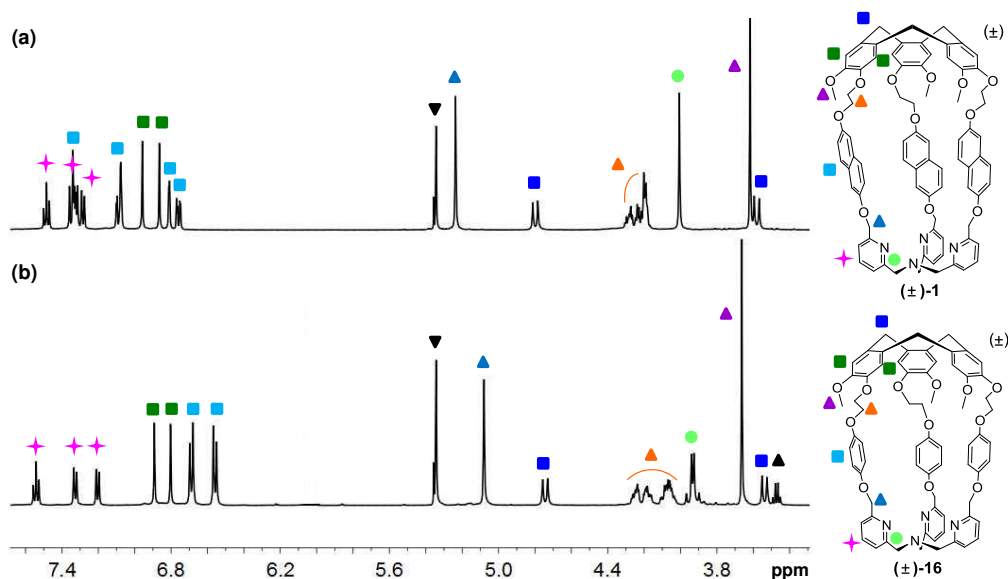


Figure 5.2 ¹H NMR spectra (500.1 MHz, CD₂Cl₂, 298 K) of hemicryptophanes (\pm)-**1** (a) and (\pm)-**16** (b) and their protons assignment. ▼ = CHDCl₂; ▲ = Et₂O.

As enantiopure host is very useful in chiral recognition, asymmetric catalysis, and chirality sensing,² we attempt the resolution of the racemate of hemicryptophanes **1** and **16** by chiral HPLC. In the case of (\pm)-**1**, the two enantiomers were separated on a Chiralpak IA column (250 \times 4.6 mm) with an enantioselectivity of 1.52 and a resolution of 2.3, using heptane/ethanol/CH₂Cl₂/triethylamine (20/40/40/0.1) as the mobile phase. At preparative scale, after multiple injections on a Chiralpak IA column (250 \times 10 mm), around 80 mg of each enantiomer were obtained in 12 h with *ee* values of 99% and 90% for the first and second eluted compounds, respectively. For (\pm)-**16**, with the same eluent on a Chiralpak ID column, the enantioselectivity is 1.51 and the resolution is 4.6 for the analytical separation, and around 50 mg of each enantiomer with both *ee* values > 99% were obtained in 3 h. The absolute configuration of each enantiopure hemicryptophane was determined by ECD spectroscopy recorded in CH₂Cl₂ at 298 K.¹⁹ As shown in Figure 5.3, in both cases, the spectra of the first eluted enantiomers exhibit a characteristic positive-negative bisignate curve from 230-250 nm corresponding to the *M*-configuration; The second eluted enantiomers show similar but inverted signals, thus allowing the assignment of the *P*-configuration.¹⁹

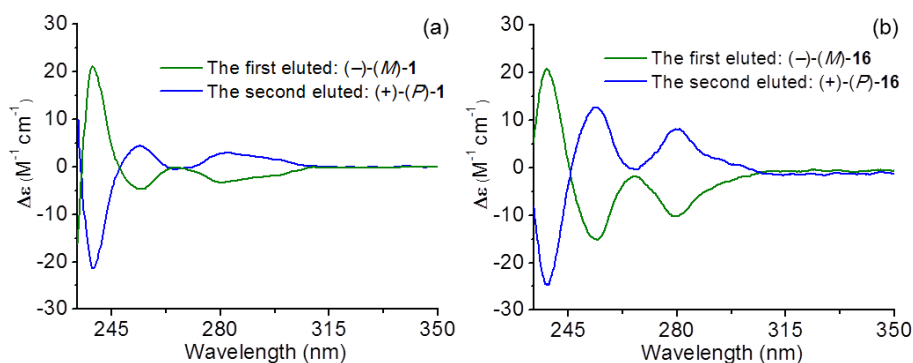


Figure 5.3 Experimental ECD spectra in CH₂Cl₂ at 298 K of: (a) (+)-(*P*)-**1** (blue) and (–)-*M*-**1** (green), and (b) (+)-(*P*)-**16** (blue) and (–)-*M*-**16** (green).

5.4 Conclusion

In summary, we have described the synthesis of two hemicryptophanes (**1** and **16**) belonging to a new class of TPA-based hemicryptophane cages. As TPA unit can complex various metals, these hemicryptophanes are chemical platforms available for various purposes and applications. Moreover, the naphthalene linkers in hemicryptophane **1** confer fluorescence properties to the host structure. Despite the 14 steps involved in the synthesis of each cage, all the reactions are quite straightforward with relatively high yields. In particular, benefiting from a remarkable 90% yield of a triple macrocyclization reaction, gram-scale synthesis of hemicryptophane **16** was achieved. The racemate of each hemicryptophane can be readily resolved by chiral HPLC to give the enantiopure cages of which absolute configurations have been assigned by ECD spectroscopy. Currently, the preparation of metal complexes for these new cages, such as Zn(II), Cu(I) and Fe(II), and their applications in molecular recognition and supramolecular catalysis are being investigated and will be reported in due course.

5.5 Experimental section

5.5.1 Materials and instrumentation

All reactions were carried out under argon by means of an inert gas/vacuum double manifold and standard Schlenk techniques. Dichloromethane was dried and degassed on a solvent station by passage through an activated alumina column followed by argon flush. Other solvents were dried prior to use over molecular sieves. ^1H and ^{13}C NMR spectra were recorded at 500.1 and 125.7 MHz, respectively. The HRMS-ESI mass spectra were recorded in positive-ion mode (or negative) on a hybrid quadrupole time-of-flight mass spectrometer with an electrospray ionization (ESI) ion source. Specific rotations (in $\text{deg cm}^2\text{g}^{-1}$) were measured in a 1 dm thermostated quartz cell on a Jasco-P1010 polarimeter. Circular dichroism spectra were recorded on a CD6 Jobin-Yvon dichrograph. Resolution of the racemic hemicyptophanes was performed by Marion Jean and Nicolas Vanthuyne.

5.5.2 Synthesis, resolution and characterization

Synthesis of 8 and 9. Compound **8** was prepared starting from 2,6-pyridinedicarboxylic acid **2** according to the reported procedures.^{18,20} Compound **9** was synthesized according to the published procedure.²¹

Synthesis of 11. A solution of **9** (100 mg, 0.500 mmol), **10** (172 mg, 0.500 mmol), and Cs_2CO_3 (244 mg, 0.750 mmol) in DMF (4 mL) was stirred for 2 days at 80 °C under argon. Then AcOEt (30 mL) and 10% aqueous NaOH (30 mL) were added. The organic layer was separated, and the aqueous phase was extracted with AcOEt (2 × 30 mL). The combined organic layers were washed with 10% aqueous NaOH (2 × 30 mL) and dried over Na_2SO_4 . After filtration, the organic solvent was removed under vacuum. The crude product was purified by column chromatography on silica gel with a 400 : 3 mixture of CH_2Cl_2 : MeOH as eluent to give compound **11** as a light yellow solid (180 mg, 0.39 mmol, 78% yield). ^1H NMR (CDCl_3 , 298K, 500.1 MHz): δ 7.65 (dd, J = 8.9, 1.9 Hz, 2H); 7.21-7.14 (m, 4H); 7.00-6.93 (m, 3H); 6.19-6.11 (m, 1H); 5.50 (dd, J = 17.3, 1.4 Hz, 1H); 5.35 (dd, J = 10.5, 1.2 Hz, 1H); 4.76 (d, J = 11.7 Hz, 1H); 4.72 (t, J = 3.6 Hz, 1H); 4.66 (d, J = 5.3 Hz, 1H); 4.50-4.47 (m, 5H); 3.98-3.91 (m, 1H); 3.90 (s, 3H); 3.60-3.56 (m, 1H); 1.93-1.62 (m, 6H) ppm. ^{13}C NMR (CDCl_3 , 298K, 125.7 MHz): δ 155.2(5), 155.1(9), 149.8, 147.7, 133.4, 131.9, 129.9, 129.8, 128.3, 128.2, 120.6, 119.3(1), 119.2(8), 117.7, 114.2, 112.1, 107.4, 107.3, 97.6, 69.0, 68.8, 68.0, 66.6, 62.4, 56.0, 30.7, 25.5, 19.5 ppm. ESI-HRMS m/z : found 487.2077, calcd for $\text{C}_{28}\text{H}_{32}\text{NaO}_6$ [**11**+Na] $^+$ 487.2091.

Synthesis of 12. In a 25 mL round bottom flask, **11** (750 mg, 1.62 mmol), $\text{Pd}(\text{OAc})_2$ (7.3 mg, 0.033 mmol), PPh_3 (28.5 mg, 0.110 mmol), NHEt_2 (25.1 mmol), H_2O (2 mL) and THF (8 mL) were mixed and stirred at 80 °C under argon for 4 h. Then the mixture was cooled to r.t., and the solvents were removed under vacuum. AcOEt (10 mL) was first added and then removed under vacuum twice. AcOEt (200 mL) and H_2O (100 mL) were then added. After thoroughly mixing, the organic layer was separated, and the aqueous phase was extracted with AcOEt (2 × 30 mL). The combined organic layers were dried over Na_2SO_4 , and the organic solvent was removed under vacuum. The crude product was purified by column chromatography on silica gel with a 20 : 3 mixture of CH_2Cl_2 : AcOEt as eluent to give compound **12** as a light yellow solid (600 mg, 1.41 mmol, 88% yield). ^1H NMR (CDCl_3 , 298K, 500.1 MHz): δ 7.60 (dd, J

= 15.1, 8.3 Hz, 2H); 7.18-7.08 (m, 4H); 7.00-6.93 (m, 3H); 5.10 (s, 1H); 4.76 (d, J = 11.7 Hz, 1H); 4.72 (t, J = 3.7 Hz, 1H); 4.50-4.43 (m, 5H); 3.99-3.94 (m, 1H); 3.90 (s, 3H); 3.61-3.57 (m, 1H); 1.93-1.63 (m, 6H) ppm. ^{13}C NMR (CDCl_3 , 298K, 125.7 MHz): δ 155.1, 152.0, 149.7, 147.7, 131.8, 130.0, 129.6, 128.5, 127.8, 120.6, 119.6, 118.1, 114.1, 112.1, 109.7, 107.2, 97.7, 68.8, 67.9, 66.5, 62.4, 56.0, 30.7, 25.5, 19.5 ppm. ESI-HRMS m/z : found 447.1763, calcd for $\text{C}_{25}\text{H}_{28}\text{NaO}_6$ [$\mathbf{12}+\text{Na}$] $^+$ 447.1778.

Synthesis of 13. In a 50 mL round bottom flask, **8** (100 mg, 0.230 mmol), **12** (321 mg, 0.757 mmol), Cs_2CO_3 (337 mg, 1.04 mmol), and DMF (10 mL) were mixed and stirred at 90 °C for 3 days. Then the mixture was cooled to r.t., and DMF was removed under vacuum. CH_2Cl_2 (200 mL) and H_2O (200 mL) were then added. After thoroughly mixing, the organic layer was separated, and the aqueous phase was extracted with CH_2Cl_2 (2×50 mL). The combined organic layers were dried over Na_2SO_4 , and the organic solvent was removed under vacuum. The crude product was purified by column chromatography on silica gel with a 18 : 1 mixture of CH_2Cl_2 : MeOH as eluent to give hemicyptophane precursor **13** as a yellow solid (330 mg, 0.207 mmol, 90% yield). ^1H NMR (CDCl_3 , 298K, 500.1 MHz): δ 7.72-7.65 (m, 6H); 7.61-7.56 (m, 6H); 7.46 (d, J = 7.7 Hz, 3H); 7.26 (dd, J = 8.9, 2.5 Hz, 3H); 7.20-7.16 (m, 9H); 6.99-6.92 (m, 9H); 5.31 (s, 6H); 4.75 (d, J = 11.7 Hz, 3H); 4.72 (t, J = 3.5 Hz, 3H); 4.49-4.44 (m, 15H); 4.01 (s, 6H); 3.98-3.93 (m, 3H); 3.89 (s, 9H); 3.59-3.56 (m, 3H); 1.90-1.54 (m, 18H) ppm. ^{13}C NMR (CDCl_3 , 298K, 125.7 MHz): δ 159.1, 156.7, 155.3, 155.0, 149.8, 147.7, 137.3, 131.9, 129.9, 129.8, 128.3, 121.8, 120.6, 119.6, 119.3, 119.1, 114.2, 112.1, 107.8, 107.3, 97.6, 70.8, 68.8, 67.9, 66.6, 62.4, 60.3, 56.0, 30.7, 25.5, 19.5 ppm. ESI-HRMS m/z : found 1621.7043, calcd for $\text{C}_96\text{H}_{102}\text{N}_4\text{NaO}_{18}$ [$\mathbf{13}+\text{Na}$] $^+$ 1621.7081.

Synthesis of hemicyptophane (\pm)-1. A solution of hemicyptophane precursor **13** (100 mg, 63.0 μmol) in CH_3CN (18 mL) was added dropwise (4 hours) under argon at 65 °C to a solution of $\text{Sc}(\text{OTf})_3$ (44 mg, 88 μmol) in CH_3CN (46 mL). The mixture was stirred under argon at 65 °C for 24 hours. The solvent was then evaporated. The crude product was purified by column chromatography on silica gel with a 200 : 5 : 1 mixture of CHCl_3 : MeOH : triethylamine as eluent to give hemicyptophane (\pm)-1 as a light yellow solid (40 mg, 88 μmol , 49% yield). The crude product could be also used directly for the following resolution procedure.

Chiral HPLC analysis for (\pm)-1. On a Chiralpak IA column (250 \times 4.6 mm), with 1 mL min^{-1} as flow-rate, heptane/EtOH/ CH_2Cl_2 /TEA (20/40/40/0.1) as mobile phase, UV detection at 254 nm, $R_t(M-1)$ = 4.7 min, $R_t(P-1)$ = 5.6 min, $k(M-1)$ = 0.59, $k(P-1)$ = 0.90, α = 1.52 and R_s = 2.3.

Resolution of hemicyptophane (\pm)-1. The crude product of (\pm)-1 (320 mg) was dissolved in 25 mL of CH_2Cl_2 . On a Chiralpak IA column (250 \times 10 mm), with 5 mL min^{-1} as flow-rate, hexane/EtOH/ CH_2Cl_2 /TEA (20/40/40/0.1) as mobile phase, UV detection at 254 nm, 210 injections of 120 μL were stacked every 3.5 minutes. Both enantiomers were collected and the solvent was then evaporated. The first eluted enantiomer ((-), *M*-1, 84 mg) was obtained with 99% *ee*, and the second one ((+), *P*-1, 73 mg) with 90% *ee*. *P*-1: $[\alpha]_D^{25}$: +38 (c = 0.114; CH_2Cl_2); *M*-1: $[\alpha]_D^{25}$: -35 (c = 0.114; CH_2Cl_2). ^1H NMR (CD_2Cl_2 , 298K, 500.1 MHz): δ 7.48 (t, J = 7.7 Hz, 3H); 7.36-7.28 (m, 12H); 7.10-7.08 (m, 6H); 6.96 (s, 3H); 6.86 (s, 3H); 6.81 (d, J = 2.3 Hz, 3H); 6.76 (dd, J = 8.9, 2.5 Hz, 3H); 5.24 (s, 6H); 4.80 (d, J = 13.7 Hz, 3H); 4.30-4.19 (m, 12H); 4.01 (s, 6H);

3.62 (s, 9H); 3.58 (d, $J = 13.7$ Hz, 3H) ppm. ^{13}C NMR (CD_2Cl_2 , 298K, 125.7 MHz): δ 158.8, 156.6, 154.9, 154.6, 148.7, 146.9, 136.8, 133.1, 132.0, 129.7, 129.6, 128.1, 128.0, 122.2, 119.5, 119.2, 118.9, 118.7, 116.6, 113.9, 108.4, 107.4, 70.9, 68.2, 66.7, 60.6, 56.0, 36.2 ppm. ESI-HRMS m/z : found 1293.5175, calcd for $\text{C}_{81}\text{H}_{73}\text{N}_4\text{O}_{12}$ [$\mathbf{1}+\text{H}$] $^+$ 1293.5220. M.p. > 250 °C (decomp.).

Synthesis of 15. In a 100 mL round bottom flask, **8** (225 mg, 0.516 mmol), **14** (638 mg, 1.70 mmol), Cs_2CO_3 (757 mg, 2.32 mmol), and DMF (22 mL) were mixed and stirred at 90 °C for 3 days. Then the mixture was cooled to r.t., and DMF was removed under vacuum. 300 mL CH_2Cl_2 and 300 mL H_2O were then added. After thoroughly mixing, the organic layer was separated, and the aqueous phase was extracted with CH_2Cl_2 (2×100 mL). The combined organic layers were dried over Na_2SO_4 , and the organic solvent was removed under vacuum. The crude product was purified by column chromatography on silica gel with a 25 : 1 mixture of CH_2Cl_2 : MeOH as eluent to give hemicryptophane precursor **15** as a white solid (728 mg, 0.504 mmol, 98% yield). ^1H NMR (CDCl_3 , 298K, 500.1 MHz): δ 7.70 (t, $J = 7.8$ Hz, 3H); 7.55 (d, $J = 7.7$ Hz, 3H); 7.40 (d, $J = 7.7$ Hz, 3H); 6.96-6.88 (m, 21H); 5.15 (s, 6H); 4.75 (d, $J = 11.8$ Hz, 3H); 4.71 (t, $J = 3.5$ Hz, 3H); 4.47 (d, $J = 11.8$ Hz, 3H); 4.36 (t, $J = 5.0$ Hz, 6H); 4.30 (t, $J = 5.0$ Hz, 6H); 3.98-3.89 (m, 9H); 3.88 (s, 9H); 3.60-3.55 (m, 3H); 1.91-1.54 (m, 18H) ppm. ^{13}C NMR (CDCl_3 , 298K, 125.7 MHz): δ 159.0, 156.9, 153.1, 152.9, 149.8, 147.7, 137.2, 131.8, 121.6, 120.6, 119.5, 116.1, 116.0, 115.8, 115.7, 114.1, 112.1, 97.6, 71.3, 68.8, 68.0, 67.2, 62.3, 56.0, 30.7, 25.5, 19.5. ESI-HRMS m/z : found 1449.6739, calcd for $\text{C}_{84}\text{H}_{97}\text{N}_4\text{O}_{18}$ [$\mathbf{15}+\text{H}$] $^+$ 1449.6792.

Synthesis of hemicryptophane (\pm)-16. In a 2 L round bottom flask, the hemicryptophane precursor **15** (1.45 g, 1.00 mmol), HCOOH (1 L) and CH_2Cl_2 (10 mL) were added. The mixture was stirred at r.t. for 2 days. Then HCOOH was removed under vacuum and yellow oil was obtained. CH_2Cl_2 (100 mL) and TEA (5 mL) were added and then evaporated. Finally CH_2Cl_2 (3 mL) was added to fully solubilize the crude product followed by the addition of Et_2O (300 mL) to precipitate the product. After filtration and washing with Et_2O , the pure (\pm)-**16** was obtained as a white solid (1.03 g, 0.90 mmol, 90% yield).

Chiral HPLC analysis for (\pm)-16. On Chiralpak ID column (250 \times 4.6 mm), with 1 mL min^{-1} as flow-rate, heptane/ $\text{EtOH}/\text{CH}_2\text{Cl}_2/\text{TEA}$ (20/40/40/0.1) as mobile phase, UV detection at 254 nm, $\text{Rt}(\text{M-16}) = 8.7$ min, $\text{Rt}(\text{P-16}) = 11.7$ min, $k(\text{M-16}) = 1.92$, $k(\text{P-16}) = 2.90$, $\alpha = 1.51$ and $\text{R}_s = 4.6$.

Resolution of hemicryptophane (\pm)-16. The pure product of (\pm)-**16** (100 mg) was dissolved in 5.2 mL of CH_2Cl_2 . On a Chiralpak ID column (250 \times 10 mm), with 5 mL min^{-1} as flow-rate, hexane/ $\text{EtOH}/\text{CH}_2\text{Cl}_2/\text{TEA}$ (20/40/40/0.1) as mobile phase, UV detection at 300 nm, 26 injections of 200 μL were stacked every 7.2 minutes. Both enantiomers were collected and the solvent was then evaporated. The first eluted enantiomer ((-), **M-16**, 46 mg) and the second one ((+), **P-16**, 48 mg) were obtained with both ee values > 99%. **P-16**: $[\alpha]_D^{25}$: +52 ($c = 0.27$; CH_2Cl_2); **M-16**: $[\alpha]_D^{25}$: -52 ($c = 0.25$; CH_2Cl_2). ^1H NMR (CD_2Cl_2 , 298K, 500.1 MHz): δ 7.56 (t, $J = 7.7$ Hz, 3H); 7.34 (d, $J = 7.4$ Hz, 3H); 7.22 (d, $J = 7.7$ Hz, 3H); 6.90 (s, 3H); 6.82 (s, 3H); 6.70 (d, $J = 9.0$ Hz, 6H); 6.56 (d, $J = 9.0$ Hz, 6H); 5.08 (s, 6H); 4.75 (d, $J = 13.7$ Hz, 3H); 4.27-4.23 (m, 3H); 4.19-4.15 (m, 3H); 4.09-4.03 (m, 6H); 3.97-3.90 (m, 6H); 3.66 (s, 9H); 3.54 (d, $J = 13.7$ Hz, 3H) ppm. ^{13}C NMR (CD_2Cl_2 , 298K, 125.7 MHz): δ 158.7, 156.8, 152.6, 148.8, 146.7, 136.8, 133.1, 131.9, 122.2, 119.4, 116.7, 115.7, 115.6, 113.8, 71.2, 68.2, 67.2, 60.5, 56.0, 36.1 ppm. ESI-HRMS

m/z: found 1143.4697, calcd for C₆₉H₆₇N₄O₁₂ [16+H]⁺ 1143.4750. M.p. = 260 °C.

5.5.3 Supplementary figures

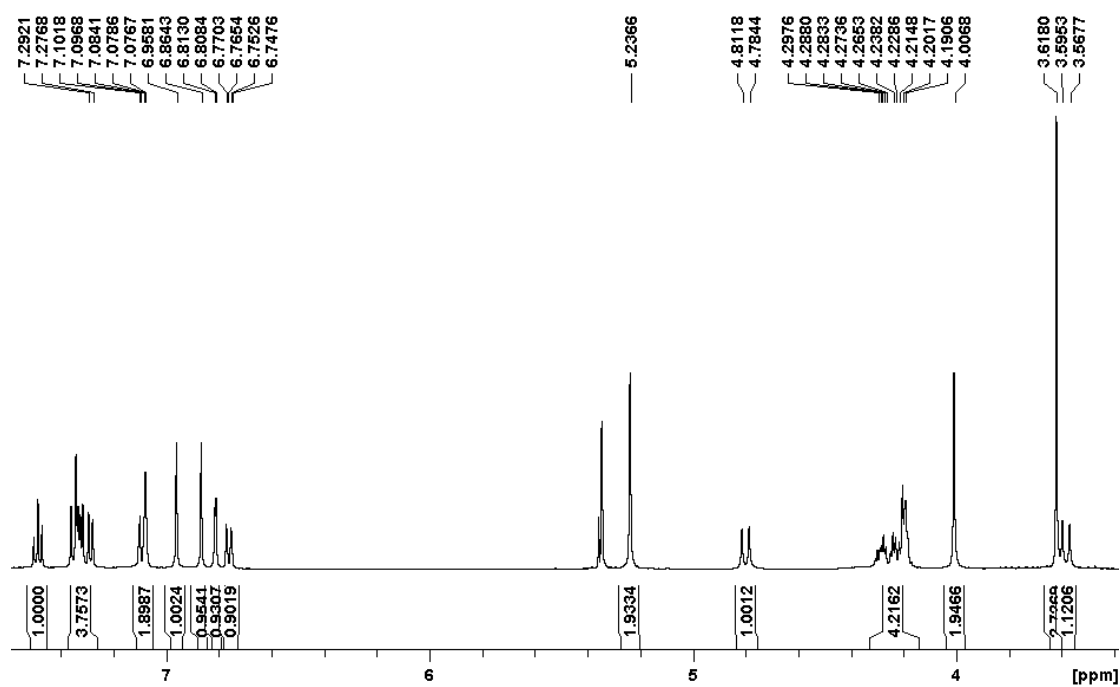


Figure S5.1 ¹H NMR spectrum (CD₂Cl₂, 500.1 MHz, 298K) of hemicryptophane **1**.

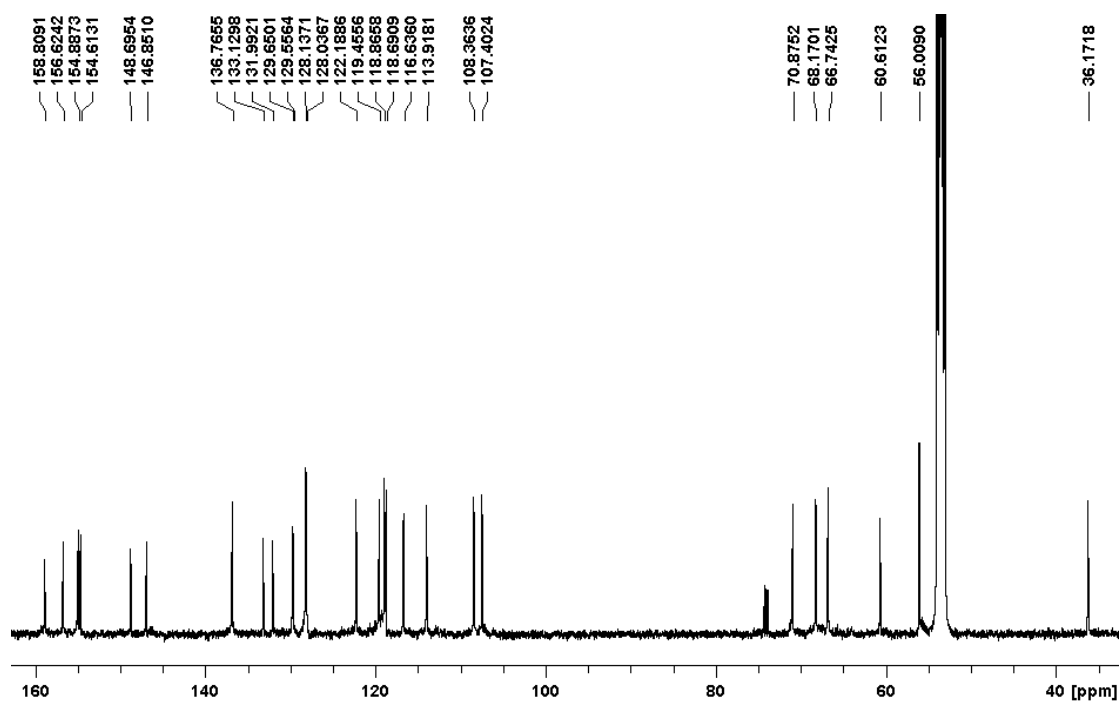


Figure S5.2 ¹³C NMR spectrum (CD₂Cl₂, 125.8 MHz, 298K) of hemicryptophane **1**.

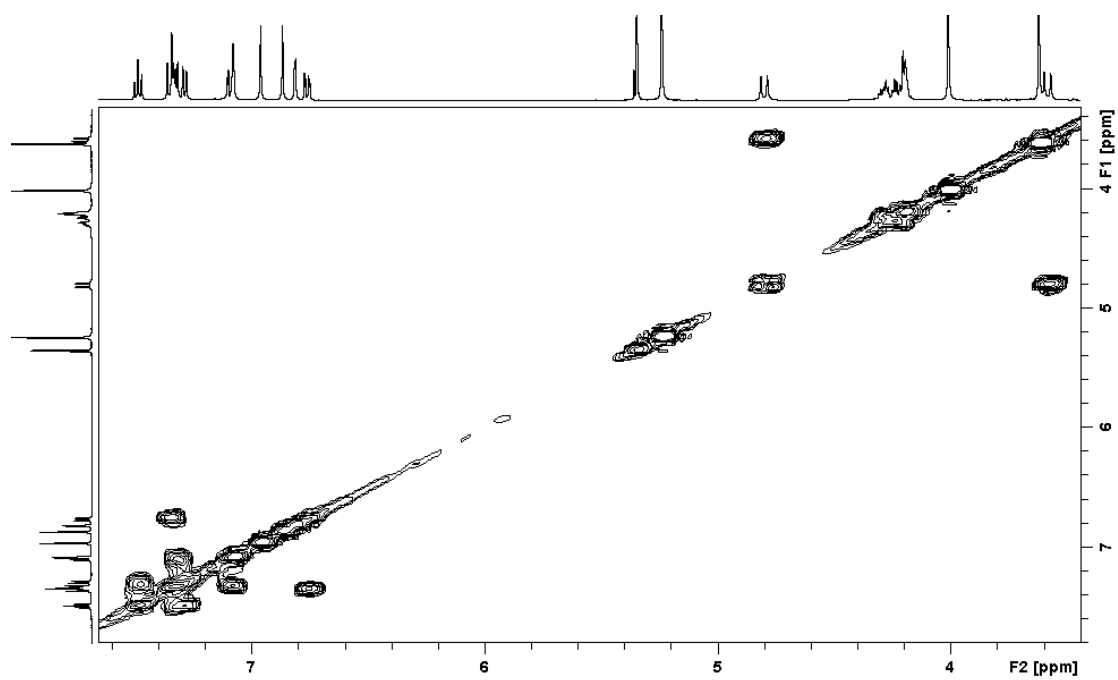


Figure S5.3 COSY spectrum (CD_2Cl_2 , 500.1 MHz, 298K) of hemicyptophane **1**.

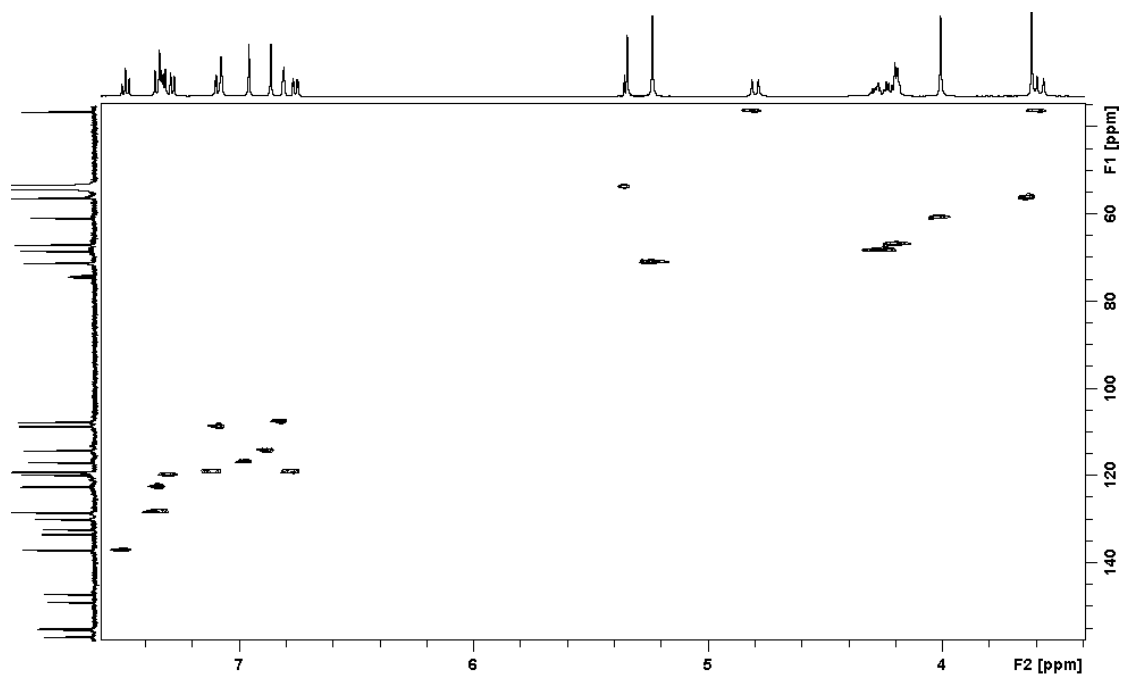
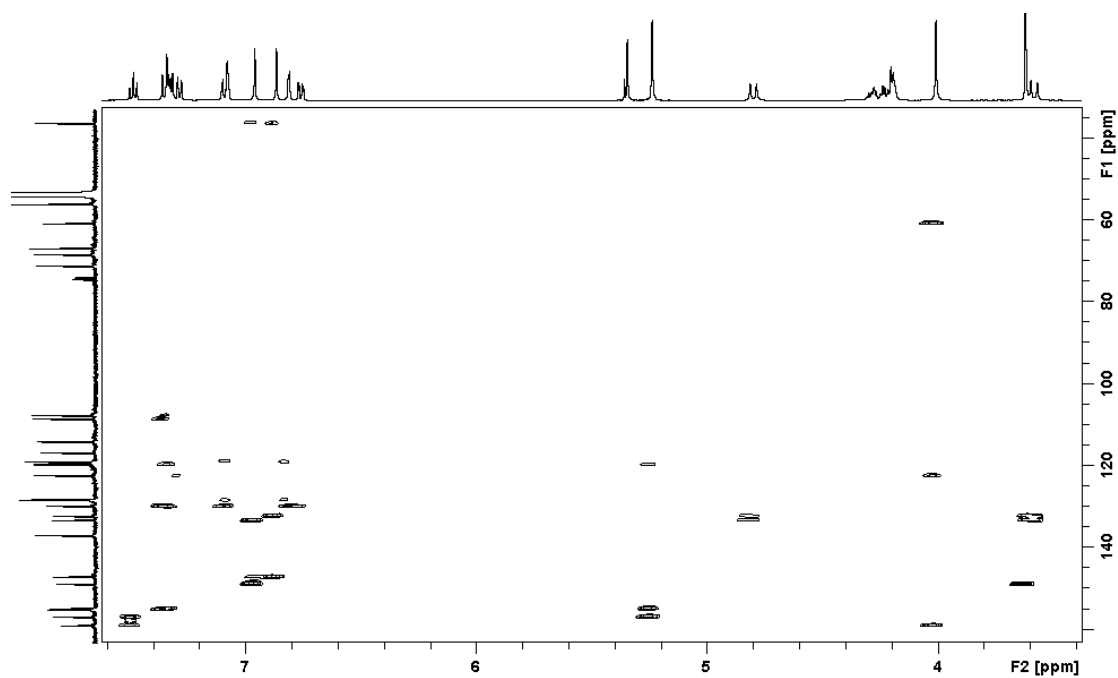
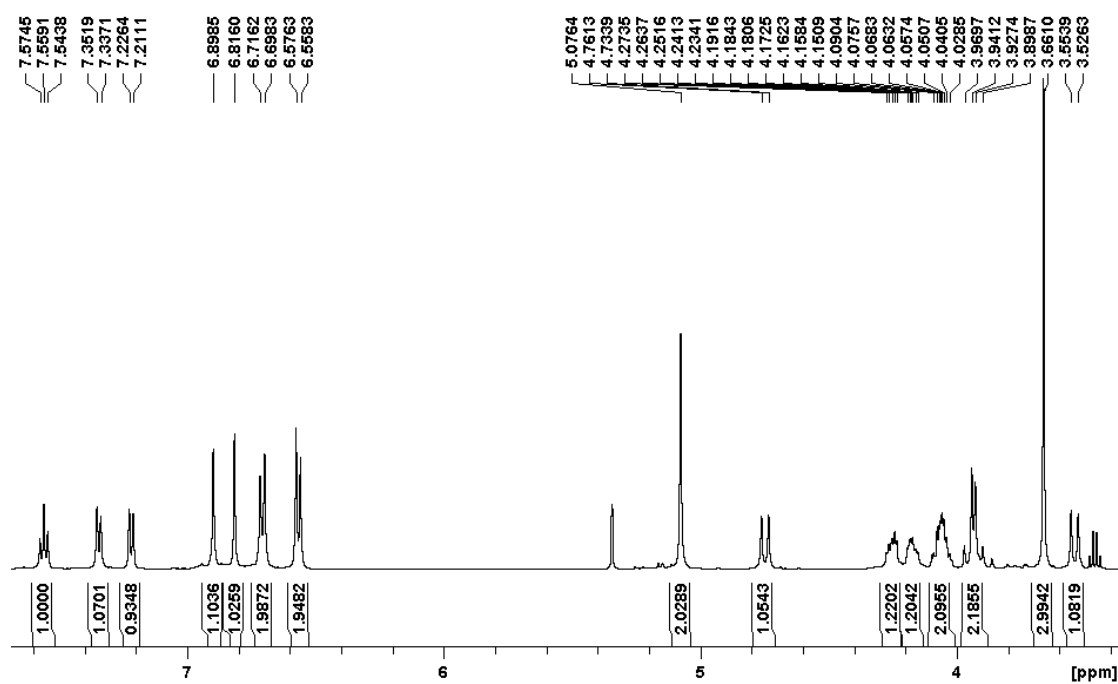


Figure S5.4 HSQC spectrum (CD_2Cl_2 , 500.1 MHz, 298K) of hemicyptophane **1**.

Figure S5.5 HMBC spectrum (CD_2Cl_2 , 500.1 MHz, 298K) of hemicyptophane **1**.Figure S5.6 ^1H NMR spectrum (CD_2Cl_2 , 500.1 MHz, 298K) of hemicyptophane **16**.

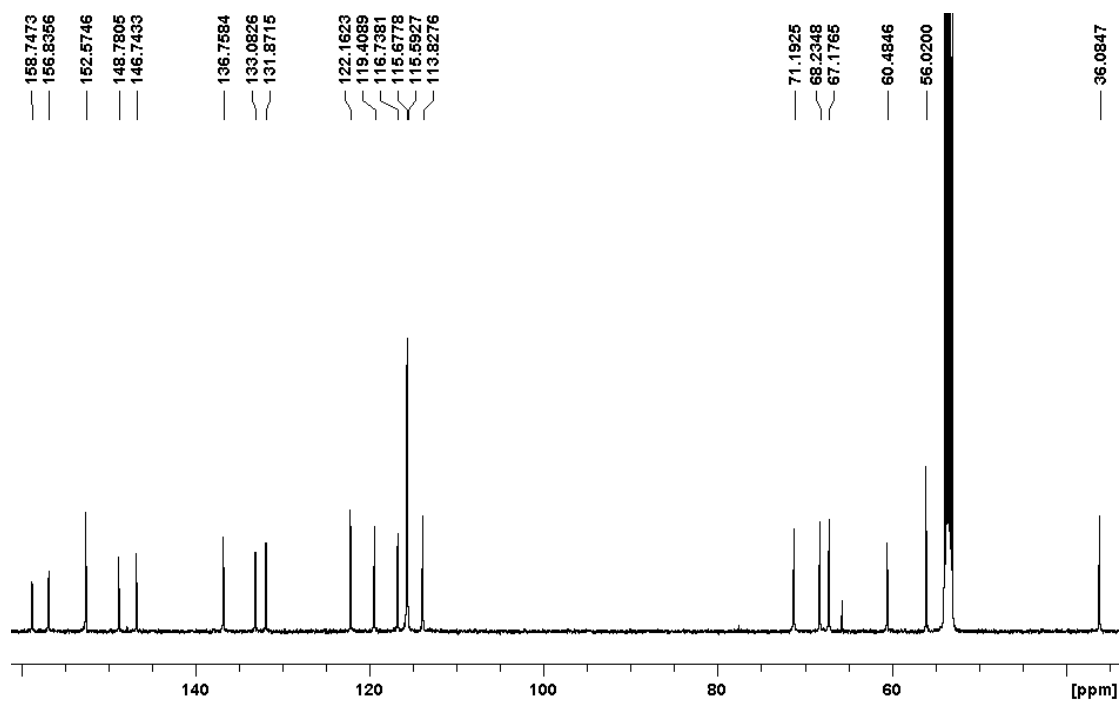


Figure S5.7 ^{13}C NMR spectrum (CD_2Cl_2 , 125.8 MHz, 298K) of hemicryptophane **16**.

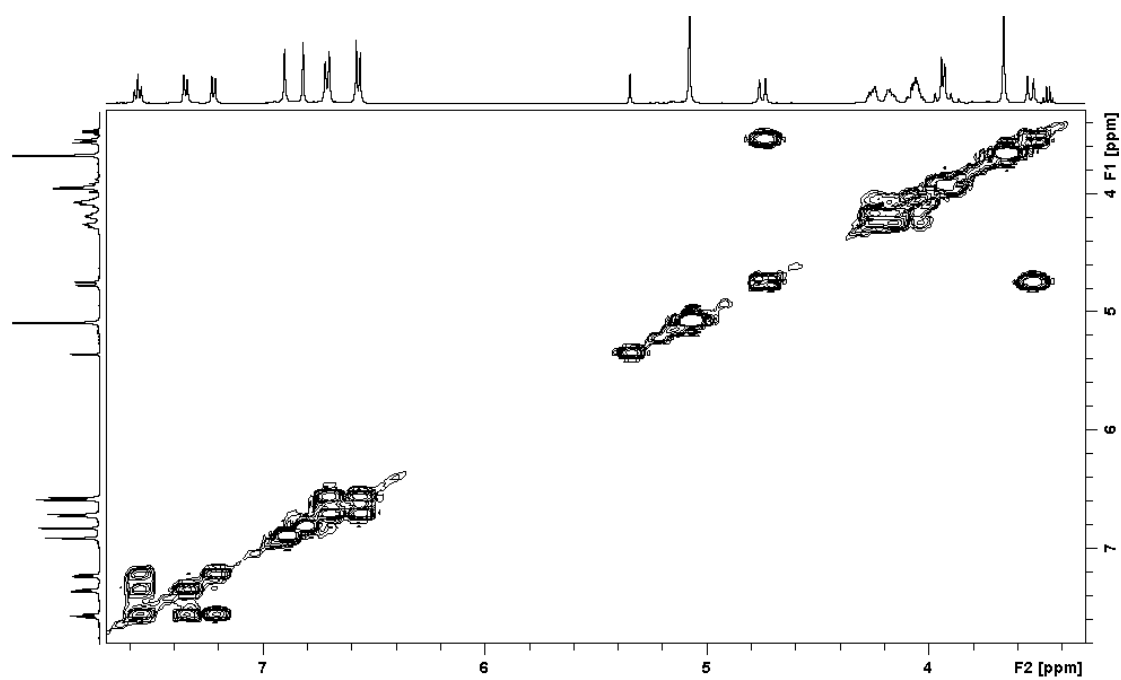


Figure S5.8 COSY spectrum (CD_2Cl_2 , 500.1 MHz, 298K) of hemicryptophane **16**.

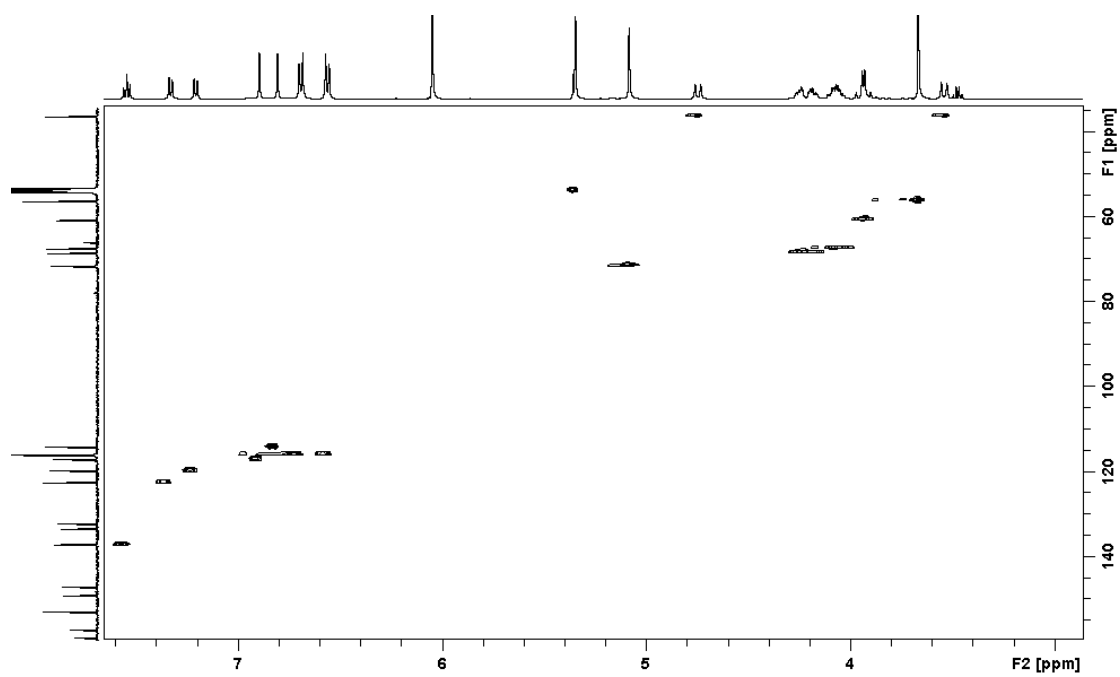


Figure S5.9 HSQC spectrum (CD_2Cl_2 , 500.1 MHz, 298K) of hemicryptophane **16**.

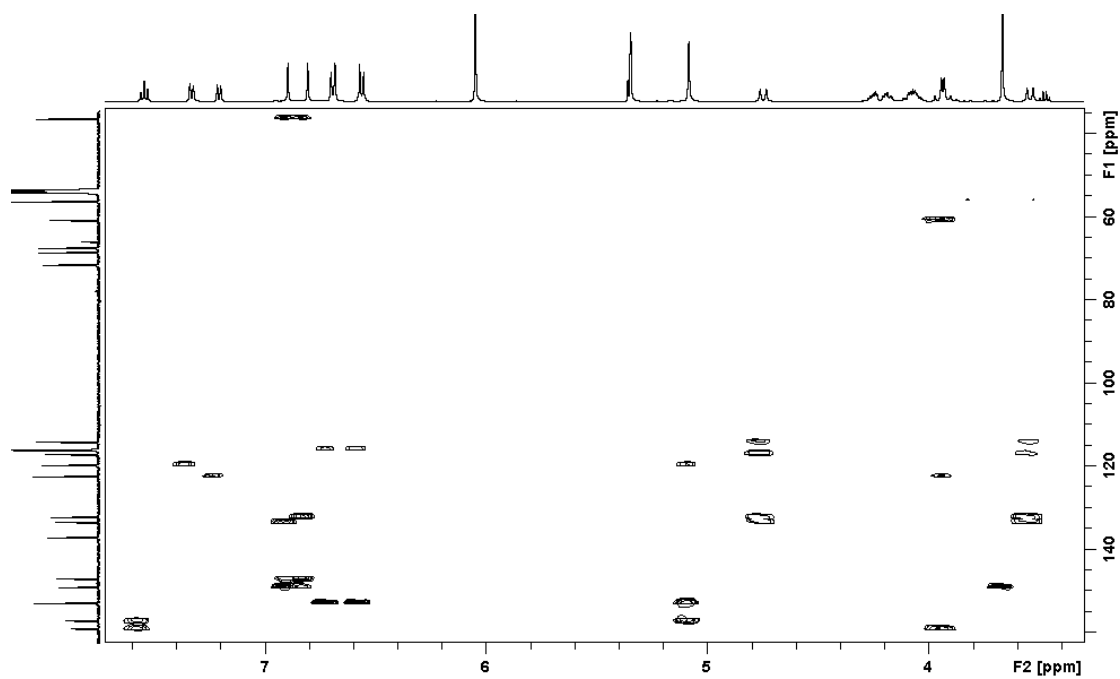


Figure S5.10 HMBC spectrum (CD_2Cl_2 , 500.1 MHz, 298K) of hemicryptophane **16**.

5.6 References

- (a) Zhang, D.; Matinez, A.; Dutasta, J.-P. *Chem. Rev.* **2017**, *Accepted*. (b) Brotin, T.; Dutasta, J. P. *Chem. Rev.* **2009**, *109*, 88. (c) Ajami, D.; Liu, L. J.; Rebek, J. *Chem. Soc. Rev.* **2015**, *44*, 490. (d) Assaf, K. I.; Nau, W. M. *Chem. Soc. Rev.* **2015**, *44*, 394. (e) Zarra, S.; Wood, D. M.; Roberts, D. A.; Nitschke, J. R. *Chem. Soc. Rev.* **2015**, *44*, 419. (f) Kobayashi, K.; Yamanaka, M. *Chem. Soc. Rev.* **2015**, *44*, 449. (g) Zhang, M. M.; Yan, X. Z.; Huang, F. H.; Niu, Z. B.; Gibson, H. W. *Acc. Chem. Res.* **2014**, *47*, 1995. (h) Liu, F.; Helgeson, R. C.; Houk, K. N. *Acc. Chem. Res.* **2014**, *47*, 2168. (i) Durot, S.; Taesch, J.; Heitz, V. *Chem. Rev.* **2014**, *114*, 8542. (j) Brown, C. J.; Toste, F. D.; Bergman, R. G.; Raymond, K. N. *Chem. Rev.* **2015**, *115*, 3012. (k) Raynal, M.; Ballester, P.; Vidal-Ferran, A.; van Leeuwen, P. W. N. M. *Chem. Soc. Rev.* **2014**, *43*, 1660. (l) Yoshizawa, M.; Klosterman, J. K.; Fujita, M. *Angew. Chem., Int. Edit.* **2009**, *48*, 3418.
- Hembury, G. A.; Borovkov, V. V.; Inoue, Y. *Chem. Rev.* **2008**, *108*, 1.
- Wiester, M. J.; Ulmann, P. A.; Mirkin, C. A. *Angew. Chem., Int. Edit.* **2011**, *50*, 114. (b) Jaeger, K. E.; Eggert, T. *Curr. Opin. Biotech.* **2004**, *15*, 305. (c) Raynal, M.; Ballester, P.; Vidal-Ferran, A.; van Leeuwen, P. W. N. M. *Chem. Soc. Rev.* **2014**, *43*, 1734.
- (a) Chatelet, B.; Payet, E.; Perraud, O.; Dimitrov-Raytchev, P.; Chapellet, L. L.; Dufaud, V.; Martinez, A.; Dutasta, J. P. *Org. Lett.* **2011**, *13*, 3706. (b) Zhang, D. W.; Gao, G. H.; Guy, L.; Robert, V.; Dutasta, J. P.; Martinez, A. *Chem. Commun.* **2015**, *51*, 2679.
- (a) Gautier, A.; Mulatier, J. C.; Crassous, J.; Dutasta, J. P. *Org. Lett.* **2005**, *7*, 1207. (b) Zhang, D. W.; Mulatier, J. C.; Cochrane, J. R.; Guy, L.; Gao, G. H.; Dutasta, J. P.; Martinez, A. *Chem. Eur. J.* **2016**, *22*, 8038.
- (a) Muhldorf, B.; Wolf, R. *Angew. Chem., Int. Edit.* **2016**, *55*, 427. (b) Oloo, W. N.; Fielding, A. J.; Que, L. J. *Am. Chem. Soc.* **2013**, *135*, 6438.
- (a) Isse, A. A.; Visona, G.; Ghelfi, F.; Roncaglia, F.; Gennaro, A. *Adv. Synth. Catal.* **2015**, *357*, 782. (b) Eckenhoff, W. T.; Biernesser, A. B.; Pintauer, T. *Inorg. Chem.* **2012**, *51*, 11917. (c) Pan, X. C.; Malhotra, N.; Simakova, A.; Wang, Z. Y.; Konkolewicz, D.; Matyjaszewski, K. *J. Am. Chem. Soc.* **2015**, *137*, 15430.
- (a) Badetti, E.; Wurst, K.; Licini, G.; Zonta, C. *Chem. Eur. J.* **2016**, *22*, 6515. (b) Scaramuzzo, F. A.; Licini, G.; Zonta, C. *Chem. Eur. J.* **2013**, *19*, 16809. (c) Lei, Z. Q.; Polen, S.; Hadad, C. M.; RajanBabu, T. V.; Badjic, J. D. *J. Am. Chem. Soc.* **2016**, *138*, 8253.
- (a) Wang, H. Y.; Mijangos, E.; Ott, S.; Thapper, A. *Angew. Chem., Int. Edit.* **2014**, *53*, 14499. (b) Woods, T. J.; Ballesteros-Rivas, M. F.; Ostrovsky, S. M.; Pali, A. V.; Reu, O. S.; Klokishner, S. I.; Dunbar, K. R. *Chem. Eur. J.* **2015**, *21*, 10302.
- (a) Chatelain, L.; Walsh, J. P. S.; Pecaut, J.; Tuna, F.; Mazzanti, M. *Angew. Chem., Int. Edit.* **2014**, *53*, 13434. (b) Aratani, Y.; Yamada, Y.; Fukuzumi, S. *Chem. Commun.* **2015**, *51*, 4662.
- (a) Sawaki, T.; Ishizuka, T.; Kawano, M.; Shiota, Y.; Yoshizawa, K.; Kojima, T. *Chem. Eur. J.* **2013**, *19*, 8978. (b) Weisser, F.; Stevens, H.; Klein, J.; van der Meer, M.; Hohloch, S.; Sarkar, B. *Chem. Eur. J.* **2015**, *21*, 8926.
- (a) Kotani, H.; Sugiyama, T.; Ishizuka, T.; Shiota, Y.; Yoshizawa, K.; Kojima, T. *J. Am. Chem. Soc.* **2015**, *137*, 11222. (b) Desnoyer, A. N.; Behyan, S.; Patrick, B. O.; Dauth, A.; Love, J. A.; Kennepohl, P. *Inorg. Chem.* **2016**, *55*, 13.
- Saad, F. A.; Knight, J. C.; Kariuki, B. M.; Amoroso, A. J. *Dalton Trans.* **2016**, *45*, 10280.

- 14 Andrez, J.; Bozoklu, G.; Nocton, G.; Pecaut, J.; Scopelliti, R.; Dubois, L.; Mazzanti, M. *Chem. Eur. J.* **2015**, *21*, 15188.
- 15 Ngo, H. T.; Liu, X. J.; Jolliffe, K. A. *Chem. Soc. Rev.* **2012**, *41*, 4928.
- 16 (a) Canary, J. W.; Mortezaei, S.; Liang, J. A. *Coordin. Chem. Rev.* **2010**, *254*, 2249. (b) Canary, J. W. *Chem. Soc. Rev.* **2009**, *38*, 747.
- 17 (a) You, L.; Berman, J. S.; Anslyn, E. V. *Nat. Chem.* **2011**, *3*, 943. (b) Joyce, L. A.; Maynor, M. S.; Dragna, J. M.; da Cruz, G. M.; Lynch, V. M.; Canary, J. W.; Anslyn, E. V. *J. Am. Chem. Soc.* **2011**, *133*, 13746. (c) Jo, H. H.; Edupuganti, R.; You, L.; Dalby, K. N.; Anslyn, E. V. *Chem. Sci.* **2015**, *6*, 158.
- 18 Zeng, X. S.; Coquiere, D.; Alenda, A.; Garrier, E.; Prange, T.; Li, Y.; Reinaud, O.; Jabin, I. *Chem. Eur. J.* **2006**, *12*, 6393.
- 19 Cochrane, J. R.; Schmitt, A.; Wille, U.; Hutton, C. A. *Chem. Commun.* **2013**, *49*, 8504.
- 20 Liu, X.; Bouwman, E. *Polyhedron* **2016**, *118*, 25.
- 21 Hau, S. C. K.; Cheng, P. S.; Mak, T. C. W. *Polyhedron* **2013**, *52*, 992.

Chapter 6. Helical, Axial and Central Chirality Combined in a Single Cage: Synthesis, Absolute Configuration and Recognition Properties

This Chapter is based partially on the following manuscript—

Dawei Zhang, Jean-Christophe Mulatier, James Robert Cochrane, Laure Guy,
Guohua Gao, Jean-Pierre Dutasta, Alexandre Martinez

Chem. Eur. J. **2016**, *22*, 8038–8042.

The work in this chapter was carried out at the ENS-Lyon.

Contents

6.1 Abstract	124
6.2 Introduction.....	124
6.3 Results and discussion	125
6.4 Conclusion.....	130
6.5 Experimental section.....	130
6.6 References.....	140

6.1 Abstract

The synthesis of eight enantiopure molecular cages (four diastereomeric pairs of enantiomers) comprising a helically chiral cyclotrimeratrylene (CTV) unit, three axially chiral binaphthol linkages and three centrally asymmetric carbons of a trialkanolamine core, is described. These new cages constitute a novel family of hemicryptophanes, which combine three classes of chirality. Their absolute configuration was successfully assigned by a chemical correlation method to overcome the signals overlap in the ECD spectra of the binaphthol and CTV units. Stereoselective recognition of glucose and mannose derivatives was investigated with these new chiral cages. Excellent enantio-selectivity and diastereo-selectivity were reached, since in some cases, both exclusive enantio- and diastereo-discrimination have been observed. In addition, compared with the most relevant hemicryptophanes, these new cages also exhibit improved binding affinities.

6.2 Introduction

Chirality plays an important role in living systems from the double helical strand of DNA to the confined chiral space of the enzyme cavities. Almost all natural products are chiral.¹ The application, control or monitoring of chirality via the principles of a supramolecular approach constitute a modern multidisciplinary field of research in chiral supramolecular science.² Various artificial and biomimetic compounds have been synthesized not only for fundamental purposes but also for a number of practical applications, such as asymmetric catalysis,³ material science,⁴ chiral recognition⁵ and absolute configuration assignment.⁶ To mimic more sophisticated chiral structures, bioinspired enantiopure cages have also been reported.⁷ However, the synthesis of such chiral architectures remains challenging, in particular for highly engineered cages bearing multiple classes of stereogenic elements, because of their high complexity.

Among the chiral cage derivatives, cryptophanes and hemicryptophanes, both based on the cyclotrimeratrylene (CTV) moiety have aroused a growing interest.⁸ Due to the bowl shape of the CTV unit, cryptophanes and hemicryptophanes are inherently chiral with helical chirality.⁹ Cryptophanes, which combine two CTV units, present complexation properties toward small molecules or atoms.^{8a,10} Hemicryptophanes, associating a CTV unit with another different C_3 symmetrical moiety, were found to act as selective molecular receptors or supramolecular catalysts. New stereocenters have also been incorporated into the hemicryptophane cages, giving rise to various efficient and stereoselective hosts, for instance, for chiral zwitterions,¹¹ ammoniums¹² and carbohydrates.¹³ Until now, the most sophisticated hemicryptophanes hold two types of chirality, helical and central chirality, leading to two diastereomeric pairs of enantiomers.¹⁴

Herein, we report on the design and synthesis of a family of enantiopure hemicryptophanes bearing three types of stereogenic elements (Figure 6.1), helical, axial and central chirality, which respectively results from the CTV, binaphthol and trialkanol moieties. Hence, four diastereomeric pairs of enantiomers are expected. We believe that the various stereogenic units as well as their different chirality should strongly affect the size and shape of the inner

space of the hemicryptophane cavity, and therefore, have a dramatic influence on their stereoselective recognition properties. However, it should be noted that besides the high synthetic challenge, the binaphthol linkages also make it difficult to determine the absolute configuration of the hemicryptophanes using conventional methods, such as electronic circular dichroism (ECD), because of the signal overlap between binaphthol and CTV moieties. Hence in the present work, we shall mainly address the following three issues: (i) to design a synthetic pathway to obtain the eight stereoisomers; (ii) to develop a method to assign the absolute configuration of each enantiopure hemicryptophane; (iii) to investigate their stereoselective recognition properties towards carbohydrates and compare their binding performance with those of the previously reported relevant hemicryptophanes.

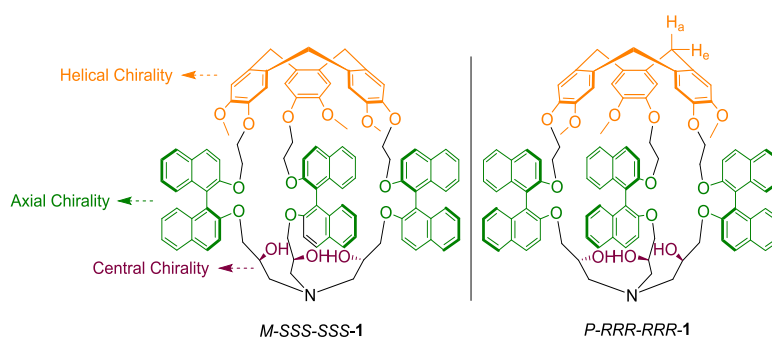
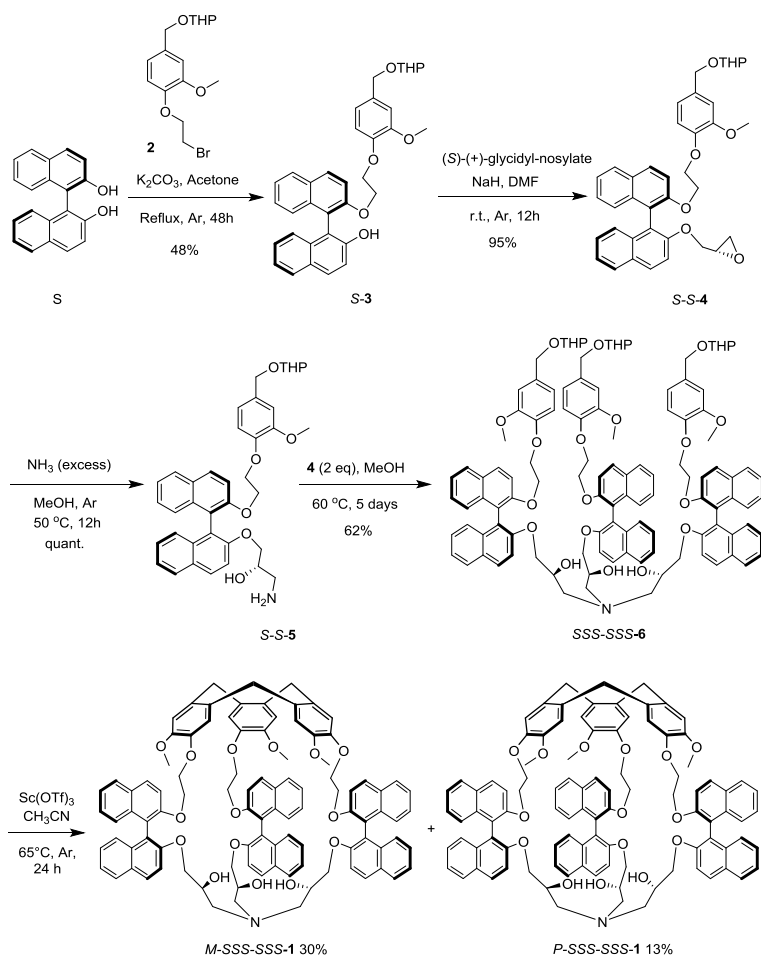


Figure 6.1 Structures of enantiomers *M*-SSS-SSS-1 and *P*-RRR-RRR-1. Varying the chirality of CTV, binaphthol or trialkanol moieties, gave rise to the other three pairs of enantiomers *P*-SSS-SSS-1/*M*-RRR-RRR-1, *M*-SSS-RRR-1/*P*-RRR-SSS-1 and *M*-RRR-SSS-1/*P*-SSS-RRR-1.

6.3 Results and discussion

The synthetic route for obtaining a pair of two diastereomers is shown in Scheme 6.1. Firstly, compound **2**, obtained via a previously reported two step procedure,^{14a} was reacted with (*S*)-binaphthol in acetone using K_2CO_3 as a base to give the mono-protected binaphthol **S-3**. The enantiopure epoxide **S-S-4** was synthesized by a regioselective nucleophilic substitution reaction of its phenol unit with commercially available (*S*)-(-)-glycidyl nosylate in DMF. Compound **S-S-4** was then treated with an excess of ammonia to give the primary amine **S-S-5**, followed by addition of 2 equiv. of **S-S-4** in methanol producing the trialkanolamine **SSS-SSS-6**. Finally, intramolecular cyclization of trialkanolamine **SSS-SSS-6** was achieved using a stoichiometric quantity of Lewis acid $Sc(OTf)_3$ in acetonitrile under moderate dilution conditions to afford the hemicryptophanes mixture. The diastereomeric pair *M*-SSS-SSS-1 and *P*-SSS-SSS-1 was separated by column chromatography on silica gel followed by preparative TLC and isolated in 30% and 13% yields, respectively. The yields of *M*- and *P*- isomers are not equal, and a diastereoselectivity around 2:1 was observed, indicating the stereocontrol induced by the binaphthol and trialkanol moieties.^{14b} A diastereomeric ratio higher than 99:1 was obtained after separation, since no signal corresponding to the other diastereomer could be detected on the 1H NMR spectra. Similar strategies were used to prepare and isolate *M*-RRR-RRR-1/*P*-RRR-RRR-1, *M*-SSS-RRR-1/*P*-SSS-RRR-1, and *M*-RRR-SSS-1/*P*-RRR-SSS-1 isomers by changing either the stereochemistry of the starting binaphthol or that of the reacting chiral glycidyl nosylate.



Scheme 6.1 Synthetic route for obtention of hemicryptophane diastereomers *M*-SSS-SSS-1 and *P*-SSS-SSS-1.

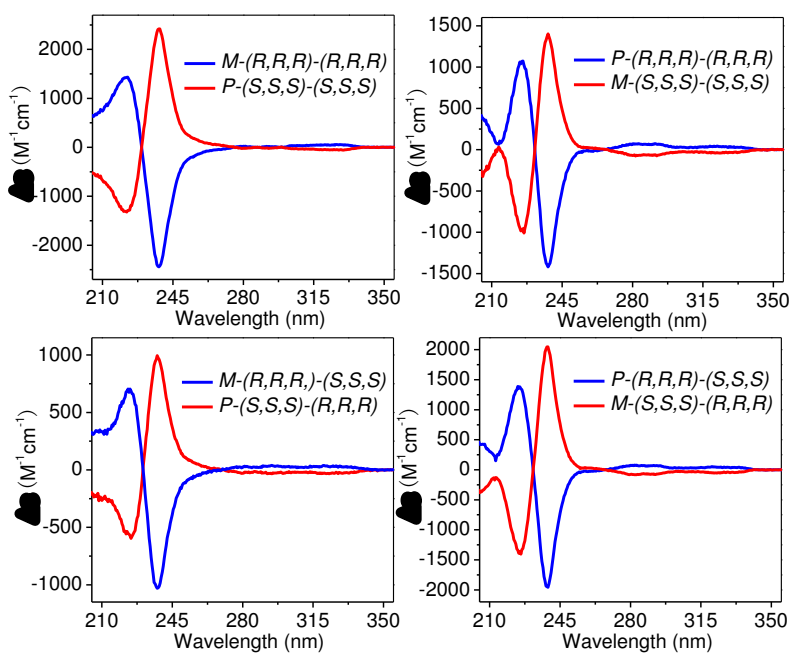
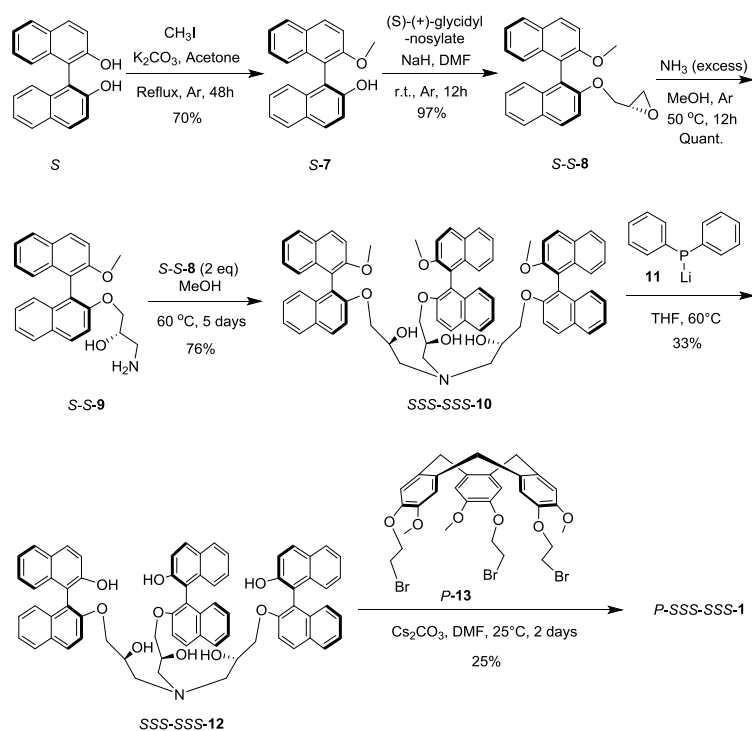


Figure 6.2 Experimental ECD spectra (CH_3CN , 298 K) of the four enantiomeric pairs of hemicryptophane **1**.

The assignment of the absolute configuration of enantiopure CTV derivatives is usually achieved by ECD thanks to the sign of the band around the 1L_A transition (240 nm). If the enantiopure hemicryptophane gives rise to a characteristic positive-negative bisignate from low to high energies (270-230 nm), a *P*-configuration is indicated, otherwise a *M*-configuration.^{14a} The ECD spectra of the eight stereoisomers were then recorded in CH_3CN at 298 K. As shown in Figure 6.2, the spectra of each pair of enantiomers exhibit a perfect mirror image. All of them present a similar behavior that consists of one main exciton pattern centered at 239 nm. However, it was found that the sign of this intense band was strictly determined by the configuration of the binaphthol moiety rather than the CTV. For instance, all the isomers bearing (*R*)-binaphthol give rise to a negative sign for this band, whereas (*S*)-binaphthol-based isomers correspond to a positive sign. Indeed, the signals of the binaphthol completely overlap that of the CTV, preventing any assignment of the configuration. Facing this failure, we then developed a novel chemical correlation method to determine the absolute configuration of these new compounds.



Scheme 6.2 Synthetic pathway to *P*-SSS-SSS-1 used for the assignment of the absolute configuration of the hemicryptophanes by chemical correlation.

Based on the retrosynthesis, we proposed that the enantiopure hemicryptophane **1** may also be obtained from the enantiopure tris-binaphthol **12** and CTV-tribromide **13**, via a [1+1] macrocyclization reaction (Scheme 6.2). The first key issue is to prepare the two important enantiomerically pure intermediates **12** and **13**. The racemate **13**, obtained by known procedures,¹⁵ was readily resolved by means of chiral HPLC in gram scale and the absolute configuration of the two enantiomers *P*-**13** and *M*-**13** has been successfully assigned by ECD spectra (Figure S6.1).¹⁶ We then devised a synthetic pathway to access the enantiopure compound **12**. As shown in Scheme 6.2, (*S*)-binaphthol was first mono-protected by reaction with iodomethane in acetone, in the presence of K_2CO_3 . The resulting mono-phenol *S*-7

reacted with (*S*)-(+)-glycidyl nosylate to give *S*-*S*-**8**. Ring opening of the epoxide by ammonia was then performed in MeOH, providing the primary amine *S*-*S*-**9** in quantitative yield. Heating **9** with 2 equiv. of **8** at 50°C for 5 days afforded *SSS*-*SSS*-**10**. Deprotection of the methoxy groups by an excess of a solution of lithium diphenylphosphide **11** in THF (1 M) at 60 °C gave rise to the triphenol *SSS*-*SSS*-**12**.

The subsequent [1+1] macrocyclization has to be performed at low temperature with reaction time no longer than two days to prevent the racemization of enantiopure **13**.¹⁶ In addition, the concentration of the reaction solution should be optimal to avoid polymerization or low reaction rate. Thus, the macrocyclization step between *SSS*-*SSS*-**12** and *P*-**13** was performed at 25°C, leading to hemicryptophane *P*-*SSS*-*SSS*-**1** in 25% yield (Scheme 6.2). Comparing the ¹H NMR spectra of enantiopure *P*-*SSS*-*SSS*-**1** with those of the diastereomeric pair *P*-*SSS*-*SSS*-**1**/*M*-*SSS*-*SSS*-**1** obtained in the last step of the synthesis in Scheme 6.1, the cage with the *P*-configuration was identified, and accordingly, the other is *M*-*SSS*-*SSS*-**1**. Moreover, as the NMR spectra and TLC migration properties of enantiomers are identical, this experiment also allows the assignment of the configuration of their mirror images *M*-*RRR*-*RRR*-**1** and *P*-*RRR*-*RRR*-**1**. Hence, a single chemical correlation experiment assigns the absolute configuration of four hemicryptophane cages (Figure S6.2). It can be noticed that no racemization of CTV-**13** occurred during the reaction as only one diastereomer is observed when the ¹H NMR spectra of the crude product and of the pure diastereomeric pair are compared (Figure S6.3). LCMS analyses further demonstrate the configuration assignment and the lack of racemization (Figure S6.4). The similar synthesis with enantiopure (*S*)-binaphthol, (*R*)-(-)-glycidyl nosylate and *P*-**13** was then carried out to produce *P*-*SSS*-*RRR*-**1**, which allows the assignment of the configuration of the other four enantiopure hemicryptophanes.

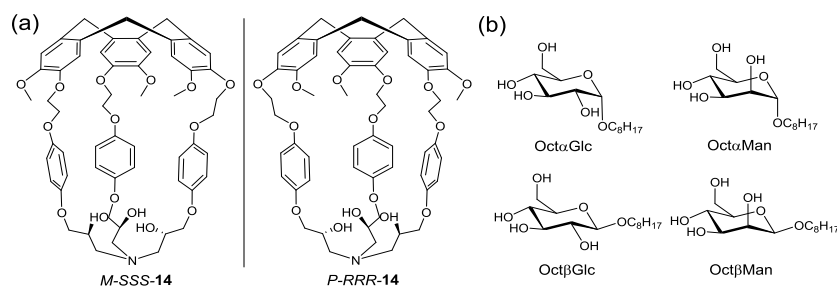


Figure 6.3 (a) Structures of hemicryptophane enantiomeric pair *M*-*SSS*-**14**/*P*-*RRR*-**14**. Varying the chirality of CTV or trialcohol moiety afforded the enantiomeric pair *P*-*SSS*-**14**/*M*-*RRR*-**14**. (b) Structures of carbohydrate guests.

We have previously reported the enantio- and diastereo-selective recognition of glucopyranosides by hemicryptophane **14** (Figure 6.3a), where the host-guest association relies on hydrogen bonding and C-H $\cdots\pi$ interactions.^{13a,17} As the introduction of the axially chiral binaphthol units should strongly modify the shape of the inner cavity, we thus decided to study the recognition properties of the enantiopure hemicryptophanes **1** toward carbohydrates. Binding constants with two *n*-octyl-pyranoside anomers of glucose (Oct α Glc and Oct β Glc), and mannose (Oct α Man and Oct β Man) (Figure 6.3b), were determined from ¹H NMR titrations in CDCl₃ at 298 K. Only one set of signals of the host was observed upon progressive addition of carbohydrate guests, evidencing that the recognition process is fast on

NMR time scale (Figure S6.5). During the titration, both the OMe and the aromatic protons of the CTV are shifted, underlining the interactions of this unit with the guest. The anomeric proton of the carbohydrate also exhibits slight highfield shift, which may be related with the vicinity of this proton with the aromatics of the host. In contrast, we did not observe any changes of the protons of the octyl-chain, suggesting that this moiety do not interact with the host. Complexation induced shifts of the CTV-OMe signal were plotted as a function of the guest/host ratio and modeled with the HypNMR2008 software,¹⁸ using a 1:1 model according to job's plot (Figure S6.6-6.8).¹⁹ The resulting binding constants K_a are reported in Table 6.1

Table 6.1 Binding constants K_a (M^{-1}) for the 1:1 complexes formed between the different isomers of hosts **1** or **14** and the carbohydrate guests.^a

Host	Oct α Glc	Oct β Glc	Oct α Man	Oct β Man
<i>M</i> -SSS-RRR- 1	105	83	58	— ^b
<i>P</i> -RRR-SSS- 1	89	537	135	48
<i>M</i> -RRR-SSS- 1	— ^b	— ^b	50	— ^b
<i>P</i> -SSS-RRR- 1	— ^b	— ^b	100	— ^b
<i>M</i> -RRR- 14 ^c	123	126	— ^b	— ^b
<i>P</i> -RRR- 14 ^c	— ^b	115	— ^b	— ^b
<i>M</i> -SSS- 14 ^c	155	184	— ^b	— ^b
<i>P</i> -SSS- 14 ^c	— ^b	— ^b	— ^b	— ^b

^a K_a was determined by fitting ¹H NMR titration curves (CDCl₃, 500 MHz, 298 K) on OMe protons with HypNMR2008; estimated error 10%. For hosts *M*-RRR-RRR-**1**, *P*-SSS-SSS-**1**, *M*-SSS-SSS-**1** and *P*-RRR-RRR-**1**, no complexation was detected. ^b No complexation detected. ^c From ref. 13a.

From Table 6.1, several trends can be observed. (i) Concerning the stereorecognition of glucose derivatives with **1**, excellent diastereoselectivity is obtained, since only the stereoisomers *M*-SSS-RRR-**1** and *P*-RRR-SSS-**1** exhibit binding properties. In addition, depending on the enantiomer of *M*-SSS-RRR-**1** or *P*-RRR-SSS-**1** used, the α/β selectivity can be reversed. Good enantioselectivity was also achieved in the recognition of the anomer Oct β Glc ($K_{a(P\text{-RRR-SSS-1})}/K_{a(M\text{-SSS-RRR-1})} = 6.0$), associated with an improvement of the binding constant compared to those of the previous hosts **14** (537 M^{-1} vs 184 M^{-1}). (ii) In contrast to hosts **14**, which showed no affinity for mannose derivatives, good α/β selectivity is reached with *M*-SSS-RRR-**1**, *M*-RRR-SSS-**1** and *P*-SSS-RRR-**1**, which only recognize Oct α Man. It is also interesting to note that only *P*-RRR-SSS-**1** binds Oct β Man with a binding constant of 48 M^{-1} , indicating an exclusive enantio-differentiation compared to *M*-SSS-RRR-**1**. (iii) these cages are able to discriminate glucose from mannose derivatives and the selectivity observed is not correlated to the different intrinsic abilities of the guests to be involved in intermolecular hydrogen bonds (Oct α Man > Oct β Man > Oct β Glc > Oct α Glc).²⁰ For instance,

with *P*-RRR-SSS-1, the binding constants decrease following the order Oct β Glc > Oct α Man > Oct α Glc > Oct β Man, highlighting the specific host-guest interactions involved in the recognition process.

6.4 Conclusion

In summary, we have described the synthesis of eight enantiomerically and diastereomerically pure cage compounds combining three classes of chirality on seven stereogenic units: the helical chirality of the CTV unit, the axial chirality of the binaphthol linkages and the central chirality of the asymmetric carbons on the triol unit. Albeit the multiple chirality in the engineered structure makes it difficult in the assignment of the absolute configuration of CTV with conventional methods, a chemical correlation strategy was developed, to successfully determine the configuration of the eight hemicryptophane stereoisomers. The stereoselective recognition properties toward glucose and mannose derivatives with these new enantiopure cages were investigated. It was found that the recognition behaviour strongly depends on the configuration of the cages, and from moderate to exclusive guest diastereo- and enantio-discrimination were observed. In particular, compared with the structurally relevant hemicryptophanes, these new cages exhibit an improved binding performance, such as the stereoselectivity and also binding affinity. Considering the sophisticated cage structures, the novel method of configuration assignment, and excellent stereorecognition properties, we do believe that the current research will contribute significantly to the burgeoning field of chiral supramolecular science.

6.5 Experimental section

6.5.1 Materials and instrumentation

All solvents used were of commercial grade and were dried prior to use over molecular sieves. ^1H NMR and ^{13}C NMR spectra were recorded on a Bruker Avance spectrometer operating at 500.10 MHz and 125.76 MHz for ^1H NMR and ^{13}C NMR spectra, respectively. ^1H NMR chemical shifts (δ) are reported in ppm and referenced to the protonated residual solvent signal. Mass spectra were recorded by the Centre de Spectrométrie de Masse, Institute of Chemistry, Lyon. Specific rotations (in $\text{deg cm}^2 \text{g}^{-1}$) were measured in a 1 dm thermostated quartz cell on a Jasco-P1010 polarimeter. Circular dichroism spectra were recorded on a CD6 Jobin-Yvon dichrograph.

6.5.2 Synthesis and Characterization

S-3/R-3: A solution of K_2CO_3 (0.75 g, 5.4 mmol) and (*S/R*)-(-/+)-1,1'-Bi(2-naphthol) (1.29 g, 4.5 mmol) in acetone (50 mL) was stirred at room temperature for 1 h under argon. Then 30 mL acetone solution of compound **2** (1.54 g, 4.5 mmol) was added in one portion. After reflux under argon for 48 h, the solvent was evaporated. The mixture was then dissolved in CH_2Cl_2 , and washed with distilled water for 3 times. The organic phase was dried over anhydrous Na_2SO_4 , filtrated and evaporated. After column chromatography over silica gel (first with

CH₂Cl₂ as eluent, then use CH₂Cl₂/AcOEt 95:5), 1.20 g (49%) *S-3/R-3* was obtained as a white solid. ¹H NMR (CD₂Cl₂, 298K, 500.1 MHz): δ 7.97 (dd, *J* = 4.3, 9.05 Hz, 1H); 7.94-7.91 (m, 2H); 7.88 (d, *J* = 8.2 Hz, 1H); 7.49 (dd, *J* = 1.5, 9.1 Hz, 1H); 7.41 (t, *J* = 7.1 Hz, 1H); 7.39-7.29 (m, 3H); 7.22-7.17 (m, 2H); 7.05 (d, *J* = 8.5 Hz, 1H); 6.79 (d, *J* = 8.2 Hz, 1H); 6.75 (s, 1H); 6.63 (dd, *J* = 1.5, 8.1 Hz, 1H); 5.95 (d, *J* = 5.4 Hz, 1H); 4.67-4.65 (m, 2H); 4.51-4.56 (m, 1H); 4.38 (d, *J* = 11.6 Hz, 1H); 4.28-4.32 (m, 1H); 4.16-4.19 (m, 1H); 4.06-4.11 (m, 1H); 3.93-3.88 (m, 1H); 3.51-3.55 (m, 1H); 3.34 (d, *J* = 3.7 Hz, 3H); 1.73-1.58 (m, 6H). ¹³C NMR (CD₂Cl₂, 298K, 125.7 MHz): δ 155.7, 151.9, 149.1, 146.7, 134.1, 134.0, 131.7, 130.4, 130.0, 129.6, 129.0, 128.1, 128.0, 126.9, 126.3, 124.9, 124.7, 124.3, 123.1, 120.3, 118.1, 117.8, 116.7, 115.4, 113.0, 111.6, 97.8, 68.7, 68.2, 67.9, 62.1, 55.1, 30.7, 25.6, 19.5. **ESI-HRMS** for *S-3* *m/z*: found 573.2236, calcd for C₃₅H₃₄NaO₆ [M+Na]⁺ 573.2248. **ESI-HRMS** for *R-3* *m/z*: found 573.2225, calcd for C₃₅H₃₄NaO₆ [M+Na]⁺ 573.2248.

S-S-4/R-R-4: To NaH (90 mg, 3.75 mmol) (60% suspension in oil), a solution of *S/R-3* (1.05 g, 1.91 mmol) in DMF (22 mL) was added at room temperature. After stirring under argon for 60 min, a solution of *S/R-(+/-)*-glycidyl nosylate (621 mg; 2.40 mmol) in DMF (8 mL) was added. The mixture was stirred at room temperature under argon for 24 h. Then the reaction was quenched by adding saturated NH₄Cl solution and the resulting mixture was diluted with water and extracted with ethyl acetate. The organic phase was washed with water, dried over anhydrous Na₂SO₄, filtrated and evaporated. After column chromatography over silica gel (CH₂Cl₂/AcOEt 100:7.5), 1.10 g (95%) *S-S-4/R-R-4* was obtained as a white solid. ¹H NMR (CD₂Cl₂, 298K, 500.1 MHz): δ 8.03 (d, *J* = 9.0 Hz, 1H); 7.99 (d, *J* = 9.0 Hz, 1H); 7.92 (t, *J* = 9.2 Hz, 2H); 7.59 (d, *J* = 9.1 Hz, 1H); 7.45 (d, *J* = 9.0 Hz, 1H); 7.39-7.33 (m, 2H); 7.26-7.20 (m, 2H); 7.13-7.09 (m, 2H); 7.85 (d, *J* = 1.8 Hz, 1H); 6.71 (dd, *J* = 1.8, 8.2 Hz, 1H); 6.50 (d, *J* = 8.2 Hz, 1H); 4.67-4.64 (m, 2H); 4.39-4.31 (m, 3H); 4.23 (dd, *J* = 2.9, 11.6 Hz, 1H); 3.99 (t, *J* = 5.0 Hz, 2H); 3.95-3.87 (m, 2H); 3.75 (s, 3H); 3.56-3.51 (m, 1H); 2.98-2.95 (m, 1H); 2.54 (t, *J* = 4.8 Hz, 1H); 2.31 (dd, *J* = 2.6, 5.1 Hz, 1H); 1.88-1.56 (m, 6H). ¹³C NMR (CD₂Cl₂, 298K, 125.7 MHz): δ 154.3, 154.0, 149.5, 147.6, 133.9, 131.8, 129.6, 129.6, 129.5, 129.4, 128.0, 126.3, 126.3, 125.2, 123.8, 120.4, 120.3, 120.3, 116.2, 115.8, 113.7, 112.0, 97.8, 70.2, 68.7, 68.7, 68.1, 62.1, 55.7, 50.2, 43.9, 30.7, 25.6, 19.5. **ESI-HRMS** for *S-S-4* *m/z*: found 629.2486, calcd for C₃₈H₃₈NaO₇ [M+Na]⁺ 629.2510. **ESI-HRMS** for *R-R-4* *m/z*: found 629.2485, calcd for C₃₈H₃₈NaO₇ [M+Na]⁺ 629.2510.

S-R-4/R-S-4: The procedure was similar as that of *S-S-4/R-R-4* using the starting materials with the corresponding chirality in 90% yield. ¹H NMR (CD₂Cl₂, 298K, 500.1 MHz): δ 8.04 (d, *J* = 9.0 Hz, 1H); 8.00 (d, *J* = 9.0 Hz, 1H); 7.93 (t, *J* = 8.6 Hz, 2H); 7.61 (d, *J* = 9.1 Hz, 1H); 7.46 (d, *J* = 9.0 Hz, 1H); 7.40-7.35 (m, 2H); 7.27-7.21 (m, 2H); 7.15-7.10 (m, 2H); 6.87 (d, *J* = 1.6 Hz, 1H); 6.72 (dd, *J* = 1.6, 8.2 Hz, 1H); 6.53 (d, *J* = 8.1 Hz, 1H); 4.69-4.66 (m, 2H); 4.41-4.35 (m, 3H); 4.20 (dd, *J* = 2.9, 11.5 Hz, 1H); 4.01 (t, *J* = 5.1 Hz, 2H); 3.98-3.90 (m, 2H); 3.76 (s, 3H); 3.57-3.53 (m, 1H); 2.97-2.95 (m, 1H); 2.57 (t, *J* = 4.7 Hz, 1H); 2.35 (dd, *J* = 2.6, 5.0 Hz, 1H); 1.89-1.55 (m, 6H). ¹³C NMR (CD₂Cl₂, 298K, 125.7 MHz): δ 154.4, 154.1, 149.5, 147.6, 134.0, 131.7, 129.6, 129.6, 129.5, 129.5, 128.0, 126.4, 126.3, 125.2, 125.2, 123.9, 123.8, 120.4, 120.4, 120.3, 116.2, 115.9, 113.7, 112.0, 97.8, 70.4, 68.8, 68.7, 68.1, 62.1, 55.8, 50.1, 44.1, 30.7, 25.6, 19.5. **ESI-HRMS** for *S-R-4* *m/z*: found 629.2480, calcd for C₃₈H₃₈NaO₇ [M+Na]⁺ 629.2510. **ESI-HRMS** for *R-S-4* *m/z*: found 629.2479, calcd for C₃₈H₃₈NaO₇ [M+Na]⁺ 629.2510.

SSS-SSS-6/RRR-RRR-6: To a solution of 7N NH₃ in methanol (36 mL, 252 mmol), compound **4** (350 mg, 0.58 mmol) was added. After stirring at 50 °C for 12 h under argon, the

solvent was evaporated. 10 mL pentane was added and evaporated for 3 times to fully remove the residue NH_3 . Then 2.0 equivalent of **6** (700 mg, 1.16 mmol) and 60 mL MeOH were added under argon. The solution was stirred at 60 °C for 5 days. After evaporation of the solvent, the crude product was purified by column chromatography over silica gel (first with $\text{CH}_2\text{Cl}_2/\text{AcOEt}$ 98:2, then use pure AcOEt), 660 mg (62%) *SSS-SSS-6/RRR-RRR-6* was obtained as a white solid. $^1\text{H NMR}$ (CD_2Cl_2 , 298K, 500.1 MHz): δ 8.00 (d, J = 9.0 Hz, 1H); 7.91 (d, J = 8.2 Hz, 1H); 7.80 (d, J = 9.0 Hz, 1H); 7.73 (d, J = 8.1 Hz, 1H); 7.40 (d, J = 9.0 Hz, 2H); 7.35 (t, J = 7.4 Hz, 1H); 7.25 (t, J = 7.3 Hz, 1H); 7.21 (t, J = 7.9 Hz, 1H); 7.16-7.11 (m, 2H); 7.03 (d, J = 8.5 Hz, 1H); 6.83 (s, 1H); 6.68 (d, J = 7.3 Hz, 1H); 6.44 (d, J = 8.1 Hz, 1H); 4.66-4.64 (m, 2H); 4.37 (d, J = 11.6 Hz, 1H); 4.27-4.20 (m, 2H); 3.95-3.88 (m, 4H); 3.69-3.67 (m, 4H); 3.54-3.51 (m, 1H); 2.98-2.97 (m, 1H); 2.89 (bs, 1H); 1.85-1.54 (m, 7H); 1.35 (d, J = 11.9 Hz, 1H). $^{13}\text{C NMR}$ (CD_2Cl_2 , 298K, 125.7 MHz): δ 154.2, 154.1, 149.5, 147.5, 133.9, 133.9, 131.7, 129.5, 129.5, 129.4, 128.0, 127.9, 126.3, 125.2, 125.1, 123.8, 123.6, 120.6, 120.3, 119.7, 116.4, 115.1, 113.8, 112.0, 97.8, 71.1, 68.8, 68.7, 68.0, 66.3, 62.1, 56.0, 55.7, 30.7, 25.6, 19.5. **ESI-HRMS** for *SSS-SSS-6* m/z: found 1836.8142, calcd for $\text{C}_{114}\text{H}_{118}\text{NO}_{21}$ $[\text{M}+\text{H}]^+$ 1836.8191. **ESI-HRMS** for *RRR-RRR-6* m/z: found 1836.8235, calcd for $\text{C}_{114}\text{H}_{118}\text{NO}_{21}$ $[\text{M}+\text{H}]^+$ 1836.8191.

SSS-RRR-6/RRR-SSS-6: The procedure was similar as that of *SSS-SSS-6/RRR-RRR-6* using the starting materials with the corresponding chirality in 56% yield. $^1\text{H NMR}$ (CD_2Cl_2 , 298K, 500.1 MHz): δ 7.98 (d, J = 9.0 Hz, 1H); 7.90 (d, J = 8.1 Hz, 1H); 7.83 (d, J = 9.1 Hz, 1H); 7.72 (d, J = 8.2 Hz, 1H); 7.43 (d, J = 9.1 Hz, 1H); 7.40 (d, J = 9.0 Hz, 1H); 7.37-7.34 (m, 1H); 7.23-7.17 (m, 2H); 7.14-7.03 (m, 3H); 6.83 (d, J = 1.8 Hz, 1H); 6.67 (dd, J = 1.8, 8.2 Hz, 1H); 6.40 (d, J = 8.1 Hz, 1H); 4.66-4.63 (m, 2H); 4.36 (d, J = 11.6 Hz, 1H); 4.29-4.22 (m, 2H); 3.91-3.89 (m, 3H); 3.76-3.75 (m, 2H); 3.68 (s, 3H); 3.55-3.50 (m, 1H); 3.08-3.07 (m, 1H); 2.77 (bs, 1H); 1.85-1.57 (m, 8H). $^{13}\text{C NMR}$ (CD_2Cl_2 , 298K, 125.7 MHz): δ 154.2, 154.1, 149.5, 147.5, 133.9, 133.9, 131.8, 129.6, 129.5, 128.0, 126.4, 126.3, 125.2, 125.1, 123.9, 123.7, 120.5, 120.3, 120.1, 116.2, 115.8, 113.8, 112.0, 97.8, 72.0, 68.7, 68.7, 68.0, 66.6, 62.1, 56.6, 55.7, 30.7, 25.6, 19.5. **ESI-HRMS** for *SSS-RRR-6* m/z: found 1836.8216, calcd for $\text{C}_{114}\text{H}_{118}\text{NO}_{21}$ $[\text{M}+\text{H}]^+$ 1836.8191. **ESI-HRMS** for *RRR-SSS-6* m/z: found 1836.8117, calcd for $\text{C}_{114}\text{H}_{118}\text{NO}_{21}$ $[\text{M}+\text{H}]^+$ 1836.8191.

Hemicryptophanes *P-SSS-SSS-1* and *M-SSS-SSS-1*: A solution of *SSS-SSS-6* (200 mg, 109 μmol) in CH_3CN (30 mL) was added dropwise (4 hours) under argon at 65 °C to a solution of $\text{Sc}(\text{OTf})_3$ (75 mg, 152.3 μmol) in CH_3CN (80 mL). The mixture was stirred under argon at 65 °C for 24 hours. The solvent was then evaporated. A column chromatography (SiO_2 , $\text{CHCl}_3/\text{MeOH}$ 20:0.1) for the crude product gave the pure product *P-SSS-SSS-1* (22 mg, 13%) and diastereomerically enriched *M-SSS-SSS-1*. Then a silica preparative TLC was performed for the crude *M-SSS-SSS-1* with $\text{CHCl}_3/\text{MeOH}$ (20:0.1) to give 50 mg enantiopure *M-SSS-SSS-1* in 30% yield. Both of the two enantiopure compounds are white solid after precipitation with MeOH.

Diastereomer *P-SSS-SSS-1*: $^1\text{H NMR}$ (CDCl_3 , 298K, 500.1 MHz): δ 8.65 (d, J = 9.2 Hz, 1H); 8.08 (d, J = 8.2 Hz, 1H); 8.04 (d, J = 9.2 Hz, 1H); 7.77 (d, J = 8.1 Hz, 1H); 7.69 (t, J = 7.2 Hz, 1H); 7.63 (d, J = 9.2 Hz, 1H); 7.23 (t, J = 8.1 Hz, 2H); 7.07 (t, J = 7.3 Hz, 1H); 6.91 (s, 1H); 6.81 (s, 1H); 6.77 (d, J = 8.6 Hz, 1H); 6.74 (d, J = 8.5 Hz, 1H); 5.64 (d, J = 9.3 Hz, 1H); 4.82 (d, J = 13.7 Hz, 1H); 4.64 (t, J = 11.3 Hz, 1H); 4.53 (t, J = 10.0 Hz, 1H); 4.17 (t, J = 13.3 Hz, 2H); 4.08 (s, 3H); 3.59 (d, J = 13.8 Hz, 1H); 3.01 (d, J = 11.5 Hz, 1H); 2.88 (d, J = 11.9, 8.2 Hz, 1H); 2.32-2.30 (m, 2H); 0.97 (t, J =

11.1 Hz, 1H); -0.19 (dd, $J = 5.0, 11.4$ Hz, 1H). ^{13}C NMR (CDCl_3 , 298K, 125.7 MHz): δ 155.7, 154.3, 147.2, 146.4, 134.1, 134.0, 131.7, 131.1, 130.1, 129.0(2), 129.0(0), 128.5, 127.9, 127.6, 126.6, 126.4, 126.0, 124.9, 123.9, 123.0, 120.7, 119.5, 117.3, 115.1, 112.1, 111.8, 71.3, 67.8, 66.7, 66.4, 55.7, 53.0. 36.5. **ESI-HRMS** m/z : found 1530.6080, calcd for $\text{C}_{99}\text{H}_{88}\text{NO}_{15}$ $[\text{M}+\text{H}]^+$ 1530.6148. $[\alpha]_D^{25}$: 547 ($c = 0.092$; CH_2Cl_2).

Diastereomer *M*-SSS-SSS-1: ^1H NMR (CDCl_3 , 298K, 500.1 MHz): δ 8.05 (d, $J = 9.0$ Hz, 1H); 7.97 (d, $J = 9.1$ Hz, 1H); 7.90 (t, $J = 8.2$ Hz, 2H); 7.59 (d, $J = 9.0$ Hz, 1H); 7.39-7.29 (m, 3H); 7.24-7.19 (m, 2H); 7.09 (d, $J = 8.5$ Hz, 1H); 6.99 (d, $J = 8.6$ Hz, 1H); 6.82 (s, 1H); 6.73 (s, 1H); 4.67 (d, $J = 13.9$ Hz, 1H); 4.44-4.41 (m, 2H); 4.11-4.02 (m, 2H); 3.92-3.90 (m, 1H); 3.61 (bs, 1H); 3.54 (t, $J = 7.3$ Hz, 1H); 3.48-3.45 (m, 4H); 3.07 (bs, 1H); 1.33 (t, $J = 12.6$ Hz, 1H); 0.31 (dd, $J = 4.8, 12$ Hz, 1H). ^{13}C NMR (CDCl_3 , 298K, 125.7 MHz): δ 152.7, 147.7, 146.3, 134.3, 134.3, 132.3, 131.8, 130.4, 129.6, 129.3, 129.2, 128.0, 127.9, 126.7, 126.4, 126.0, 125.1, 124.6, 123.6, 123.3, 119.1, 118.0, 115.2, 115.0, 71.7, 69.6, 67.1, 65.8, 56.5, 56.2, 36.4. **ESI-HRMS** m/z : found 1530.6079, calcd for $\text{C}_{99}\text{H}_{88}\text{NO}_{15}$ $[\text{M}+\text{H}]^+$ 1530.6148. $[\alpha]_D^{25}$: -35 ($c = 0.097$; CH_2Cl_2).

Hemicryptophanes *P*-RRR-RRR-1 and *M*-RRR-RRR-1: The procedure was similar as that of *M*-SSS-SSS-1/*P*-SSS-SSS-1 in the same yield except using the starting materials with the corresponding chirality. Because of the mirror image properties, the ^1H and ^{13}C NMR spectra are also exactly the same as those of *M*-SSS-SSS-1/*P*-SSS-SSS-1.

Diastereomer *P*-RRR-RRR-1: **ESI-HRMS** m/z : found 1530.6079, calcd for $\text{C}_{99}\text{H}_{88}\text{NO}_{15}$ $[\text{M}+\text{H}]^+$ 1530.6148. $[\alpha]_D^{25}$: 41 ($c = 0.087$; CH_2Cl_2).

Diastereomer *M*-RRR-RRR-1: **ESI-HRMS** m/z : found 1530.6095, calcd for $\text{C}_{99}\text{H}_{88}\text{NO}_{15}$ $[\text{M}+\text{H}]^+$ 1530.6148. $[\alpha]_D^{25}$: -516 ($c = 0.116$; CH_2Cl_2).

Hemicryptophanes *P*-SSS-RRR-1 and *M*-SSS-RRR-1: A solution of SSS-SSS-6 (200 mg, 109 μmol) in CH_3CN (30 mL) was added dropwise (4 hours) under argon at 65 $^\circ\text{C}$ to a solution of $\text{Sc}(\text{OTf})_3$ (75 mg, 152.3 μmol) in CH_3CN (80 mL). The mixture was stirred under argon at 65 $^\circ\text{C}$ for 24 hours. The solvent was then evaporated. A first silica preparative TLC ($\text{CHCl}_2/\text{MeOH}$ 20:1) for the crude product gave the diastereomeric pair mixture with no other impurities. Then a second silica preparative TLC was performed for the mixture with $\text{CHCl}_3/\text{MeOH}$ (20:1) to give 19 mg enantiopure *P*-SSS-RRR-1 in 11% yield and 40 mg *M*-SSS-RRR-1 in 24% yield. Both of the two compounds are white solid after precipitation with MeOH.

Diastereomer *P*-SSS-RRR-1: ^1H NMR (CDCl_3 , 298K, 500.1 MHz): δ 8.02 (d, $J = 9.0$ Hz, 1H); 7.92 (t, $J = 8.7$ Hz, 2H); 7.82 (d, $J = 8.9$ Hz, 2H); 7.46 (d, $J = 9.1$ Hz, 1H); 7.37 (t, $J = 7.1$ Hz, 1H); 7.30-7.24 (m, 2H); 7.17-7.13 (m, 2H); 7.03 (d, $J = 8.5$ Hz, 1H); 6.78 (s, 1H); 6.68 (s, 1H); 4.71 (d, $J = 13.8$ Hz, 1H); 4.60-4.55 (m, 1H); 4.22-4.19 (m, 1H); 4.06-4.05 (m, 2H); 3.75 (s, 3H); 3.61 (dd, $J = 3.7, 10.3$ Hz, 1H); 3.48 (d, $J = 13.9$ Hz, 1H); 3.03 (dd, $J = 5.7, 10.1$ Hz, 1H); 2.61-2.48 (m, 1H); 1.10 (dd, $J = 9.1, 13.4$ Hz, 1H). ^{13}C NMR (CDCl_3 , 298K, 125.7 MHz): δ 154.3, 147.7, 147.2, 134.1, 133.9, 132.2, 132.1, 129.5, 129.3, 129.1, 127.9, 127.6, 126.4(4), 126.4(0), 125.6, 125.4, 123.9, 123.7, 120.3, 120.0, 116.9, 115.5, 114.5, 113.7, 70.9, 68.4, 67.4, 56.9, 56.7, 36.4. **ESI-HRMS** m/z : found 1530.6094, calcd for $\text{C}_{99}\text{H}_{88}\text{NO}_{15}$ $[\text{M}+\text{H}]^+$ 1530.6148. $[\alpha]_D^{25}$: 5 ($c = 0.132$; CH_2Cl_2).

Diastereomer *M*-SSS-RRR-1: ^1H NMR (CDCl_3 , 298K, 500.1 MHz): δ 7.95 (dd, $J = 9.1, 14.4$

Hz, 2H); 7.88 (dd, $J = 8.3, 12.8$ Hz, 2H); 7.49 (d, $J = 9.0$ Hz, 1H); 7.39-7.33 (m, 3H); 7.24-7.20 (m, 2H); 7.08 (t, $J = 10.9$ Hz, 2H); 6.76 (s, 1H); 6.50 (s, 1H); 4.69 (d, $J = 13.7$ Hz, 1H); 4.37-4.33 (m, 1H); 4.19-4.17 (m, 1H); 4.08-4.04 (m, 2H); 3.70 (dd, $J = 5.9, 10.7$ Hz, 1H); 3.46 (d, $J = 13.8$ Hz, 1H); 3.41 (dd, $J = 4.4, 10.7$ Hz, 1H); 3.00 (s, 3H); 2.77 (bs, 1H); 0.96-0.87 (m, 2H). $^{13}\text{C NMR}$ (CDCl_3 , 298K, 125.7 MHz): δ 154.4, 153.5, 148.4, 146.3, 134.3, 133.9, 133.0, 131.5, 129.7(4), 129.7(1), 129.4, 129.1, 128.1, 127.7, 126.7, 126.4, 125.7, 125.1, 124.3, 123.7, 122.0, 119.4, 116.8, 116.7, 115.8, 113.1, 71.9, 68.5, 68.4, 58.0, 54.9, 36.5. **ESI-HRMS** m/z : found 1530.6099, calcd for $\text{C}_{99}\text{H}_{88}\text{NO}_{15}$ $[\text{M}+\text{H}]^+$ 1530.6148. $[\alpha]_D^{25}$: -14 ($c = 0.130$; CH_2Cl_2).

Hemicryptophanes *P*-RRR-SSS-1 and *M*-RRR-SSS-1: The procedure was similar as that of *M*-SSS-RRR-1/*P*-SSS-RRR-1 in the same yield except using the starting materials with the corresponding chirality. Because of the mirror image properties, the ^1H and ^{13}C NMR spectra are also exactly the same as those of *M*-SSS-RRR-1/*P*-SSS-RRR-1.

Diastereomer *P*-RRR-SSS-1: **ESI-HRMS** m/z : found 1530.6101, calcd for $\text{C}_{99}\text{H}_{88}\text{NO}_{15}$ $[\text{M}+\text{H}]^+$ 1530.6148. $[\alpha]_D^{25}$: 12 ($c = 0.077$; CH_2Cl_2).

Diastereomer *M*-RRR-SSS-1: **ESI-HRMS** m/z : found 1530.6083, calcd for $\text{C}_{99}\text{H}_{88}\text{NO}_{15}$ $[\text{M}+\text{H}]^+$ 1530.6148. $[\alpha]_D^{25}$: -4 ($c = 0.120$; CH_2Cl_2).

S-7: A solution of K_2CO_3 (0.75 g, 5.4 mmol) and (*S*)-(-)-1,1'-Bi(2-naphthol) (1.29 g, 4.5 mmol) in acetone (50 mL) was stirred at room temperature for 1 h under argon. Then 20 mL acetone solution of iodomethane (640 mg, 4.5 mmol) was added in one portion. After reflux under argon for 48 h, the solvent was evaporated. The mixture was then dissolved in CH_2Cl_2 , and washed with distilled water for 3 times. The organic phase was dried over anhydrous Na_2SO_4 , filtrated and evaporated. After column chromatography over silica gel (CH_2Cl_2 as eluent), 949 mg (70%) *S*-7 was obtained as a white solid. $^1\text{H NMR}$ (CD_2Cl_2 , 298K, 500.1 MHz): δ 8.12 (d, $J = 9.1$ Hz, 1H); 7.96-7.93 (m, 2H); 7.89 (d, $J = 8.2$ Hz, 1H); 7.55 (d, $J = 9.2$ Hz, 1H); 7.41-7.38 (m, 1H); 7.36-7.28 (m, 3H); 7.25-7.22 (m, 1H); 7.13 (d, $J = 8.5$ Hz, 1H); 7.03 (d, $J = 8.5$ Hz, 1H); 5.00 (s, 1H); 3.85 (s, 3H). $^{13}\text{C NMR}$ (CD_2Cl_2 , 298K, 125.7 MHz): δ 156.0, 151.3, 134.0, 133.8, 131.1, 129.7, 129.5, 129.1, 128.2, 128.1, 127.2, 126.4, 124.6, 124.5, 124.0, 123.3, 117.4, 115.1, 114.9, 113.6, 56.4. **ESI-HRMS** m/z : found 301.1214, calcd for $\text{C}_{21}\text{H}_{17}\text{O}_2$ $[\text{M}+\text{H}]^+$ 301.1223. $[\alpha]_D^{25} = 39$ ($c = 0.116$; CH_2Cl_2).

S-S-8: To NaH (124 mg, 5.16 mmol) (60% suspension in oil), a solution of *S*-3 (901 mg, 3.0 mmol) in DMF (32 mL) was added at room temperature. After stirring under argon for 60 min, a solution of *S*-(+)-glycidyl nosylate (980 mg; 3.78 mmol) in DMF (8 mL) was added. The mixture was stirred at room temperature under argon for 24 h. Then the reaction was quenched by adding saturated NH_4Cl solution and the resulting mixture was diluted with water and extracted with ethyl acetate. The organic phase was washed with water, dried over anhydrous Na_2SO_4 , filtrated and evaporated. After column chromatography over silica gel (CH_2Cl_2 as eluent), 1.04 g (97 %) *S*-S-8 was obtained as a white solid. $^1\text{H NMR}$ (CD_2Cl_2 , 298K, 500.1 MHz): δ 8.05 (d, $J = 9.1$ Hz, 1H); 8.00 (d, $J = 9.0$ Hz, 1H); 7.93-7.91 (m, 2H); 7.51 (dd, $J = 9.1, 11.4$ Hz, 2H); 7.39-7.33 (m, 2H); 7.27-7.22 (m, 2H); 7.10 (dd, $J = 8.6, 13.7$ Hz, 2H); 4.26 (dd, $J = 2.9, 11.7$ Hz, 1H); 3.97 (dd, $J = 5.4, 11.7$ Hz, 1H); 3.81 (s, 3H); 3.00-2.97 (m, 1H); 2.58 (t, $J = 4.8$ Hz, 1H); 2.34-2.33 (m, 1H). $^{13}\text{C NMR}$ (CD_2Cl_2 , 298K, 125.7 MHz): δ 154.9, 154.1, 134.0, 133.9, 129.6, 129.5, 129.4, 129.1, 128.0, 126.4, 126.3, 125.2, 124.9, 123.9, 123.5, 120.7, 118.9, 116.0, 113.6,

70.3, 56.4, 50.2, 44.0. **ESI-HRMS** m/z: found 379.1296, calcd for C₂₄H₂₀NaO₃ [M+Na]⁺ 379.1305. $[\alpha]_D^{25}$: -62 (c = 0.122; CH₂Cl₂).

S-R-8: The procedure was similar as that of *S-S-8* using the starting materials with the corresponding chirality in 96% yield. ¹H NMR (CD₂Cl₂, 298K, 500.1 MHz): δ 8.05 (d, *J* = 9.1 Hz, 1H); 8.00 (d, *J* = 9.1 Hz, 1H); 7.92-7.91 (m, 2H); 7.52 (d, *J* = 9.1 Hz, 1H); 7.49 (d, *J* = 9.1 Hz, 1H); 7.39-7.33 (m, 2H); 7.27-7.22 (m, 2H); 7.11 (d, *J* = 8.5 Hz, 1H); 7.08 (d, *J* = 8.5 Hz, 1H); 4.21 (dd, *J* = 3.0, 11.6 Hz, 1H); 3.99 (dd, *J* = 5.4, 11.6 Hz, 1H); 3.82 (s, 3H); 2.98-2.95 (m, 1H); 2.60 (t, *J* = 4.8 Hz, 1H); 2.38-2.37 (m, 1H). ¹³C NMR (CD₂Cl₂, 298K, 125.7 MHz): δ 154.9, 154.1, 134.0, 133.9, 129.7, 129.5, 129.4, 129.1, 128.0, 126.4, 126.3, 125.2, 124.9, 123.9, 123.5, 120.7, 118.9, 116.1, 113.7, 70.5, 56.4, 50.1, 44.1. **ESI-HRMS** m/z: found 357.1479, calcd for C₂₄H₂₁O₃ [M+H]⁺ 357.1485. $[\alpha]_D^{25}$: -68 (c = 0.102; CH₂Cl₂).

SSS-SSS-10: To a solution of 7N NH₃ in methanol (36 mL, 252 mmol), compound **6** (300 mg, 0.84 mmol) was added. After stirring at 50 °C for 12 h under argon, the solvent was evaporated. 10 mL pentane was added and evaporated for 3 times to fully remove the residue NH₃. Then 2.0 equivalent of **6** (600 mg, 1.68 mmol) and 70 mL MeOH were added under argon. The solution was stirred at 60 °C for 5 days. After evaporation of the solvent, the crude product was purified by column chromatography over silica gel (first with CH₂Cl₂/AcOEt 1:1, then use CH₂Cl₂/MeOH 100:3), 699 mg (76%) **SSS-SSS-10** was obtained as a white solid. ¹H NMR (CD₂Cl₂, 298K, 500.1 MHz): δ 8.02 (d, *J* = 9.0 Hz, 1H); 7.92 (d, *J* = 8.2 Hz, 1H); 7.83 (d, *J* = 9.1 Hz, 1H); 7.76 (d, *J* = 8.2 Hz, 1H); 7.45 (d, *J* = 9.0 Hz, 1H); 7.37 (t, *J* = 7.2 Hz, 1H); 7.32 (d, *J* = 9.1 Hz, 1H); 7.28-7.24 (m, 2H); 7.17 (t, *J* = 8.5 Hz, 1H); 7.10 (d, *J* = 8.5 Hz, 1H); 7.02 (d, *J* = 8.5 Hz, 1H); 3.95 (dd, *J* = 3.5, 9.9 Hz, 1H); 3.68-3.67 (m, 4H); 3.00-2.99 (m, 1H); 2.69 (bs, 1H); 1.52 (d, *J* = 10.3 Hz, 1H); 1.38 (d, *J* = 10.3 Hz, 1H). ¹³C NMR (CD₂Cl₂, 298K, 125.7 MHz): δ 154.7, 154.1, 133.9, 133.8, 129.5, 129.4, 129.1, 128.0, 127.9, 126.4, 125.1, 124.9, 123.8, 123.5, 120.1, 119.0, 115.5, 113.8, 71.4, 66.3, 56.5, 56.1. **ESI-HRMS** m/z: found 1086.4564, calcd for C₇₂H₆₄NO₉ [M+H]⁺ 1086.4576. $[\alpha]_D^{25}$: -111 (c = 0.115; CH₂Cl₂).

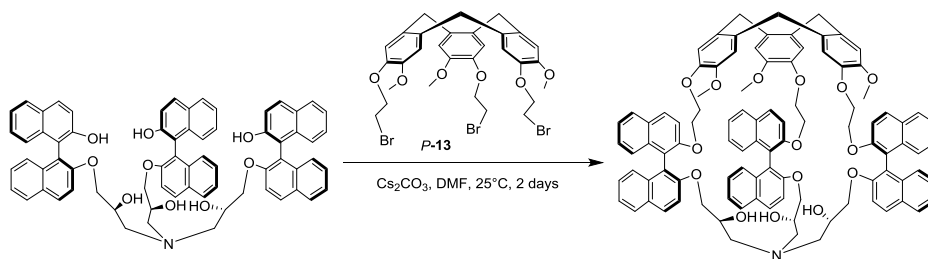
SSS-RRR-10: The procedure was similar as that of *SSS-SSS-10* using the starting materials with the corresponding chirality in 75% yield. ¹H NMR (CD₂Cl₂, 298K, 500.1 MHz): δ 7.99 (d, *J* = 9.0 Hz, 1H); 7.92 (d, *J* = 8.2 Hz, 1H); 7.87 (d, *J* = 9.1 Hz, 1H); 7.75 (d, *J* = 8.1 Hz, 1H); 7.44 (d, *J* = 9.0 Hz, 1H); 7.39-7.36 (m, 2H); 7.26 (t, *J* = 7.6 Hz, 1H); 7.20 (t, *J* = 7.1 Hz, 1H); 7.12-7.10 (m, 2H); 7.03 (d, *J* = 8.5 Hz, 1H); 3.80-3.78 (m, 2H); 3.72 (s, 3H); 3.13-3.12 (m, 1H); 2.71 (bs, 1H); 1.70-1.57 (m, 2 H). ¹³C NMR (CD₂Cl₂, 298K, 125.7 MHz): δ 154.7, 154.1, 133.9, 133.8, 129.6, 129.5, 129.4, 129.1, 128.0, 127.9, 126.4, 126.3, 125.1, 124.9, 123.9, 123.5, 120.3, 119.0, 115.9, 113.6, 71.9, 66.7, 56.7, 56.5. **ESI-HRMS** m/z: found 1086.4555, calcd for C₇₂H₆₄NO₉ [M+H]⁺ 1086.4576. $[\alpha]_D^{25}$: -52 (c = 0.100; CH₂Cl₂).

Preparation of 11 (1M solution in THF): Lithium (600 mg, 86.4 mmol) was added to 10 mL dried THF at room temperature under argon. The mixture was cooled down to 0 °C, and a solution of chlorodiphenylphosphine (3.7 mL, 20.6 mmol) in THF (10 mL) was added dropwise. The mixture was allowed to warm to room temperature and stirred for 2h until it turned red.

SSS-SSS-12: **SSS-SSS-10** (163 mg, 0.15 mmol) was dissolved in THF (1.5 mL) and the solution was stirred at room temperature for 5 min under argon. A 1M solution of lithium

diphenylphosphide **11** in THF (3.6 mL, 3.6 mmol) was added slowly and the mixture was heated at 60°C for 12 h. Afterwards, another 3.6 mL **11** was added and kept the reaction for another 6h. Then, the reaction was cooled to room temperature and a saturated solution of NaHCO₃ was added until a neutral pH was exhibited. CH₂Cl₂ (100 mL) was added and the solution was stirred vigorously for half an hour. The two layers were then separated and the aqueous phase was extracted with CH₂Cl₂ (2×50 mL). The combined organic solutions were washed with water (200 mL), dried over anhydrous Na₂SO₄, filtrated and evaporated. The crude product was purified by column chromatography on silica gel (first with CHCl₃/MeOH 100/1, then use 20/1) to give SSS-SSS-**12** as a beige solid (52 mg, 33%). ¹H NMR (DMSO-*d*₆, 298K, 500.1 MHz): δ 9.27 (s, 1H); 8.03 (d, *J* = 9.1 Hz, 1H); 7.94 (d, *J* = 8.1 Hz, 1H); 7.63 (d, *J* = 8.5 Hz, 2H); 7.56 (d, *J* = 9.1 Hz, 1H); 7.34 (t, *J* = 7.2 Hz, 1H); 7.26-7.22 (m, 2H); 7.16-7.14 (m, 2H); 7.03 (d, *J* = 8.5 Hz, 1H); 6.87-6.85 (m, 1H); 3.96 (s, 1H); 3.87 (dd, *J* = 3.3, 9.9 Hz, 1H); 3.57 (dd, *J* = 3.9, 9.8 Hz, 1H); 2.84 (s, 1H); 1.26 (t, *J* = 12.7 Hz, 1H); 0.92 (d, *J* = 12.2 Hz, 1H). ¹³C NMR (DMSO-*d*₆, 298K, 125.7 MHz): δ 155.1, 153.1, 134.4, 134.0, 129.6, 129.5, 129.3, 128.4, 128.3, 128.2, 126.6, 126.4, 125.3, 124.6, 123.9, 122.7, 120.2, 118.8, 116.7, 115.7, 72.1, 66.0, 57.4. ESI-HRMS *m/z*: found 1044.4064, calcd for C₆₉H₅₈NO₉ [M+H]⁺ 1044.4106. [α]_D²⁵ = -76 (c = 0.096; CH₂Cl₂).

SSS-RRR-12: The procedure was similar as that of SSS-SSS-**12** using the starting materials with the corresponding chirality in 35% yield. ¹H NMR (DMSO-*d*₆, 298K, 500.1 MHz): δ 9.25 (s, 1H); 8.03 (d, *J* = 9.0 Hz, 1H); 7.94 (d, *J* = 8.1 Hz, 1H); 7.68 (d, *J* = 8.8 Hz, 1H); 7.64-7.62 (m, 1H); 7.54 (d, *J* = 9.0 Hz, 1H); 7.34 (t, *J* = 7.3 Hz, 1H); 7.27-7.23 (m, 2H); 7.04-7.01 (m, 3H); 6.84 (d, *J* = 7.3 Hz, 1H); 4.08 (s, 1H); 3.74-3.64 (m, 2H); 3.03 (s, 1H); 1.42 (t, *J* = 11.3 Hz, 1H); 1.26 (d, *J* = 11.7 Hz, 1H). ¹³C NMR (DMSO-*d*₆, 298K, 125.7 MHz): δ 155.1, 153.1, 134.4, 134.0, 129.7, 129.6, 129.3, 128.4, 128.3, 126.6, 126.3, 125.4, 124.6, 124.0, 122.7, 120.5, 118.8, 117.2, 115.6, 72.6, 66.5, 58.1. ESI-HRMS *m/z*: found 1044.4054, calcd for C₆₉H₅₈NO₉ [M+H]⁺ 1044.4106. [α]_D²⁵ = 13.6 (c = 0.090; CH₂Cl₂).



Procedure for [1+1] macrocyclization: A solution of Cs₂CO₃ (187 mg, 574 μmol) and compound SSS-SSS-**12** or SSS-RRR-**12** (100 mg, 96 μmol) in DMF (90 mL) was stirred at 25 °C for 15 min under argon. Then 90 mL DMF solution of enantiopure P-**13** (77 mg, 105 μmol) was added dropwise. The reaction solution was stirred at 25 °C for 48 h. Afterwards, 200 mL CH₂Cl₂ was added to the reaction, followed by washing with brine (100×5) to remove DMF and Cs₂CO₃. The organic phase was dried over anhydrous Na₂SO₄, filtrated and evaporated. The crude product was purified by column chromatography on silica gel to give the corresponding P-SSS-SSS-**1** (37 mg, 25%) (with CH₂Cl₂ as eluent) or P-SSS-RRR-**1** (6.0 mg, 4%) (first with CH₂Cl₂ as eluent, then use CH₂Cl₂/MeOH 80/1).

6.5.3 Absolute configuration assignment

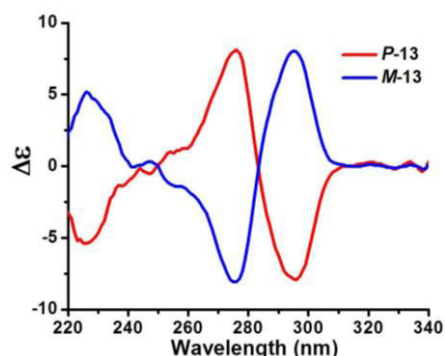


Figure S6.1 Experimental ECD spectra in CH_3CN at 25°C of compound **13**; red: first eluted enantiomer *P*-**13** ($C = 2.39 \times 10^{-4} \text{ M}^{-1}$); red: second eluted enantiomer *M*-**13** ($C = 3.56 \times 10^{-4} \text{ M}^{-1}$).

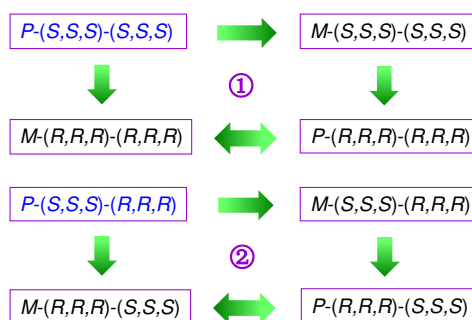


Figure S6.2 A chart showing that with one single chemical correlation experiment, the absolute configuration of four hemicryptophane stereoisomers can be determined.

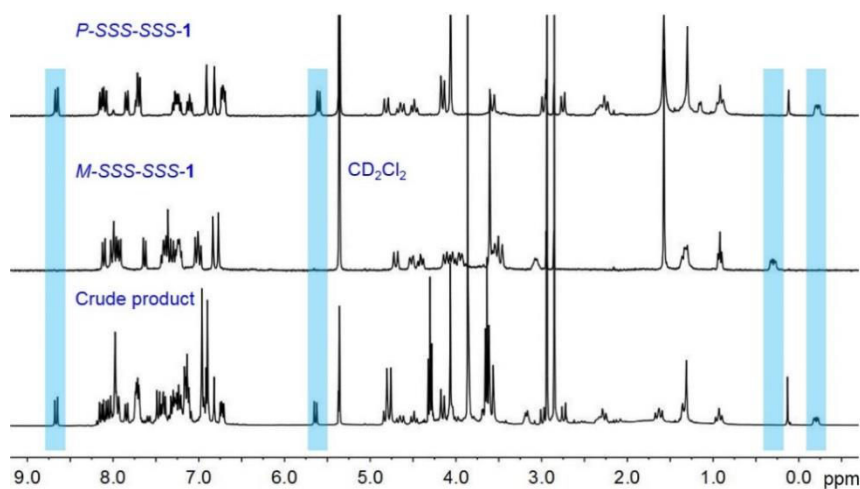


Figure S6.3 ^1H NMR spectra (CD_2Cl_2 , 500.1 MHz, 298K) of *P*-SSS-SSS-**1**, *M*-SSS-SSS-**1** and the crude product obtained by the reaction of *P*-**13** and SSS-SSS-**12**. It can be observed that in the ^1H NMR spectrum of crude product, only the signals of *P*-SSS-SSS-**1** are present.

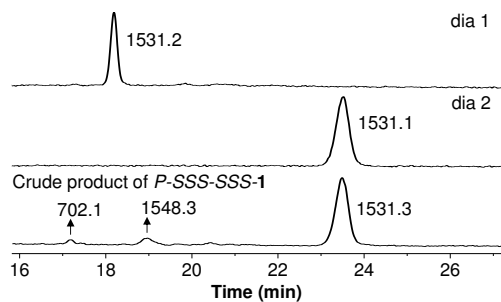


Figure S6.4 Chromatograms of the hemicryptophane diastereomers *P*-SSS-SSS-1 and *M*-SSS-SSS-1, and of the crude product of *P*-SSS-SSS-1 obtained from chemical correlation synthesis; The Mass for each fraction has been indicated. Separation parameters: column: phenomenex-synergi-4 μ -Hydro-RP (250 \times 4.6 mm); eluent: CH₃CN/H₂O, gradient change from 70/30 v/v to 100/0 v/v; flow rate: 0.75 mL/min; UV detection at 250 nm.

6.5.4 ¹H NMR titration

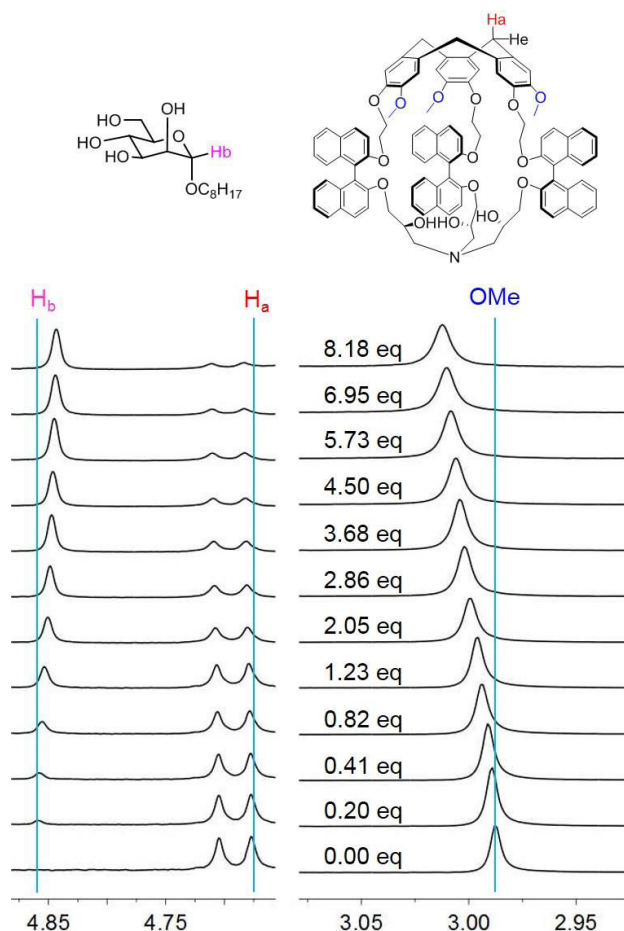


Figure S6.5 Partial ¹H NMR spectra (CDCl₃, 500.1 MHz, 298K) of host *P*-RRR-SSS-1 (1 mM) upon addition of different equiv. of Oct α Man.

¹H NMR titrations: Solutions of hemicryptophane hosts (1.0 mM in CDCl₃, 500 μ L) were titrated in NMR tubes with small aliquots of concentrated solutions (20 mM in CDCl₃) of guests. Complexation induced shifts $\Delta\delta$ of the OMe protons of the host were measured after

each addition and plotted as a function of the guest/host ratio. Mathematical analysis of data and graphic representation of results were performed using the HypNMR 2008 program,¹⁸ handling general host-guest association equilibria under fast exchange regime on the NMR time scale. This allows obtaining the binding constant K_a . Complexation induced shifts were measured on the OMe protons in all these cases because they displayed sharp signals without overlapping region.

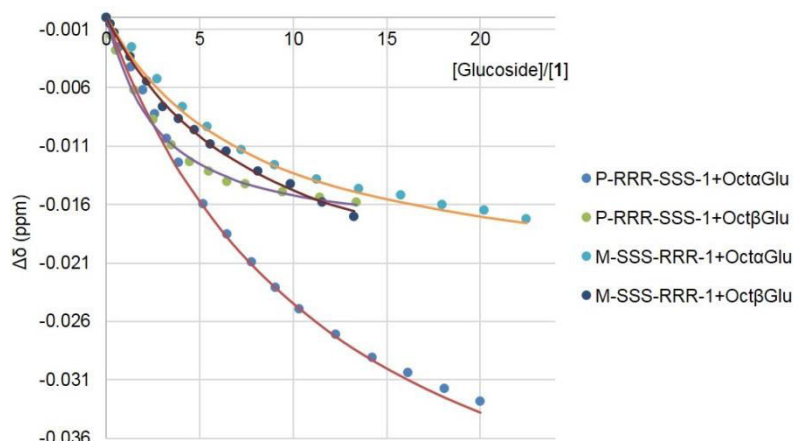


Figure S6.6 ^1H NMR titration curves (CDCl_3 , 500.1 MHz, 298K) for the complexation of glucoside by host **1** (experimental and calculated chemical shifts are shown as points and lines, respectively).

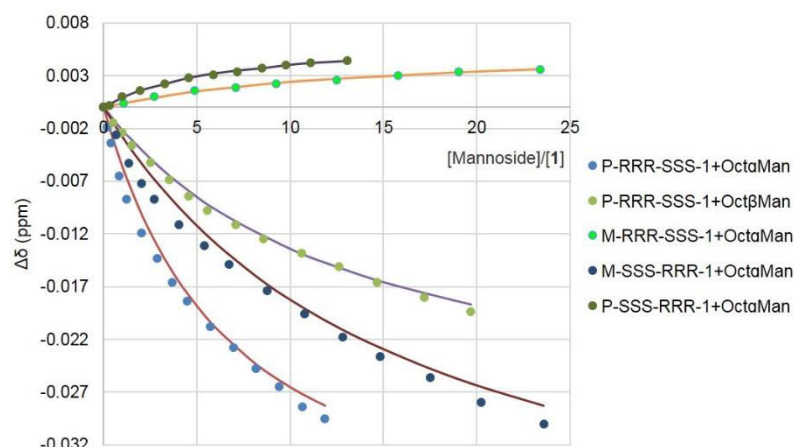


Figure S6.7 ^1H NMR titration curves (CDCl_3 , 500.1 MHz, 298K) for the complexation of mannoside by host **1** (experimental and calculated chemical shifts are shown as points and lines, respectively).

6.5.5 Job plot

The continuous variation method was used for determining the binding stoichiometry.¹⁹ In this method, stock solutions (1.0 mM in CDCl_3) of **1** and of the guest were prepared and mixed in NMR tubes in different ratios. In this way, relative concentrations α were varied continuously but their sum was kept constant (1.0 mM). ^1H NMR spectra were recorded for each sample and values of host's chemical shift δ_{obs} were measured. Job's plots were obtained by plotting $(\delta_{\text{obs}} - \delta_{\text{free}})\alpha$ versus α , where δ_{free} is the chemical shift of the proton in the free host. The stoichiometry of the complexes was obtained from the value of the molar fraction α

which corresponds to the maximum of the curve: a 1:1 complexation is obtained for $\alpha_{\max} = 0.5$.

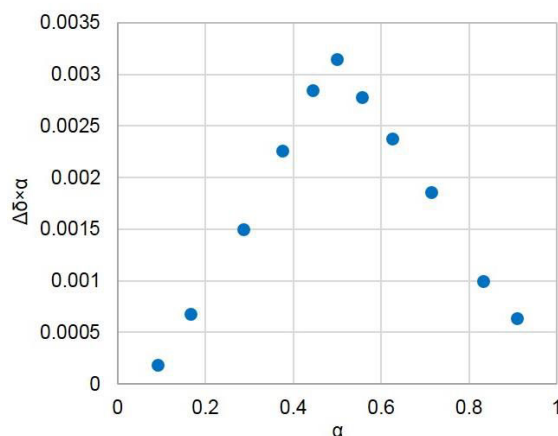


Figure S6.8 Job's plot of *P-RRR-SSS-1* with OctaMan in CDCl_3 .

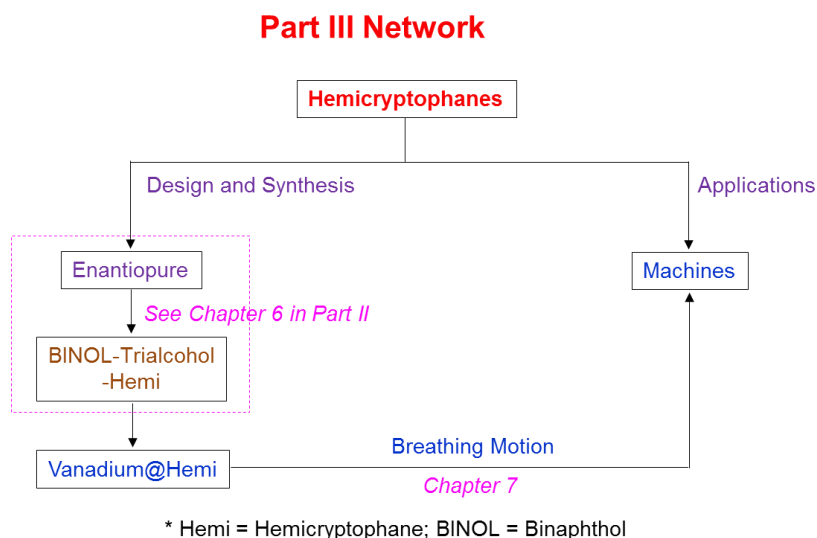
6.6 References

- 1 J. Seyden-Penne, *Chiral Auxiliaries and Ligands in Asymmetric Synthesis*, Wiley and Sons: New York, **1995**.
- 2 G. A. Hembury, V. V. Borovkov, Y. Inoue, *Chem. Rev.* **2008**, *108*, 1.
- 3 a) J. S. Seo, D. Whang, H. Lee, S. I. Jun, J. Oh, Y. J. Jeon, K. Kim, *Nature* **2000**, *404*, 982. b) S. Hoekman, M. O. Kitching, D. A. Leigh, M. Pappmeyer, D. Roke, *J. Am. Chem. Soc.* **2015**, *137*, 7656. c) M. Zurro, S. Asmus, S. Beckendorf, C. Mück-Lichtenfeld, O. G. Mancheño, *J. Am. Chem. Soc.* **2014**, *136*, 13999. d) C. Zhao, Q. F. Sun, W. M. Hart-Cooper, A. G. DiPasquale, F. D. Toste, R. G. Bergman, K. N. Raymond, *J. Am. Chem. Soc.* **2013**, *135*, 18802. e) M. Raynal, P. Ballester, A. Visal-Ferran, P. W. N. M. Van Leeuwen, *Chem. Rev.* **2014**, *43*, 1734. f) S. H. A. M. Leenders, R. Gramage-Doria, B. de Bruin, J. N. H. Reek, *Chem. Soc. Rev.* **2015**, *44*, 433. g) C. Garcia-Simon, R. Gramage-Doria, S. Raoufmoghaddam, T. Parella, M. Costas, X. Ribas, J. N. H. Reek, *J. Am. Chem. Soc.* **2015**, *137*, 2680. h) M. Guitet, P. Zhang, F. Marcelo, C. Tugny, J. Jiménez-Barbero, O. Buriez, C. Amatore, V. Mouries-Mansuy, J.-P. Goddard, L. Fensterbank, Y. Zhang, S. Roland, M. Menand, M. Sollogoub, *Angew. Chem., Int. Ed.* **2013**, *52*, 7213. i) W. Xuan, C. Ye, M. Zhang, Z. Chen, Y. Cui, *Chem. Sci.* **2013**, *4*, 3154.
- 4 a) K. Akagi, G. Piao, S. Kaneko, K. Sakamaki, H. Shirakawa, M. Kyotani, *Science* **1998**, *282*, 1683. b) E. Yashima, K. Maeda, Y. Okamoto, *Nature* **1999**, *399*, 449.
- 5 a) T. Kida, T. Iwamoto, H. Asahara, T. Hinoue, M. Akashi, *J. Am. Chem. Soc.* **2013**, *135*, 3371. b) W. Xuan, M. Zhang, Y. Liu, Z. Chen, Y. Cui, *J. Am. Chem. Soc.* **2012**, *134*, 6904. (c) W.-Z. Zhang, K. Yang, S.-Z. Li, H. Ma, J. Luo, K.-P. Wang, W.-S. Chung, *Eur. J. Org. Chem.* **2015**, 765.
- 6 a) X. Huang, B. H. Rickman, B. Borhan, N. Berova, K. Nakanishi, *J. Am. Chem. Soc.* **1998**, *120*, 6185. b) E. Yashima, T. Matsushima, Y. Okamoto, *J. Am. Chem. Soc.* **1997**, *119*, 6345.
- 7 a) T. Brotin, L. Guy, A. Martinez, J.-P. Dutasta, *Top. Curr. Chem.* **2013**, *341*, 177. b) A. M. Castilla, W. J. Ramsay, J. R. Nitschke, *Acc. Chem. Res.* **2014**, *47*, 2063.
- 8 a) T. Brotin, J.-P. Dutasta, *Chem. Rev.* **2009**, *109*, 88. b) O. Perraud, V. Robert, H. Gornitzka, A. Martinez, J.-P. Dutasta, *Angew. Chem., Int. Ed.* **2012**, *51*, 504. c) A. Martinez,

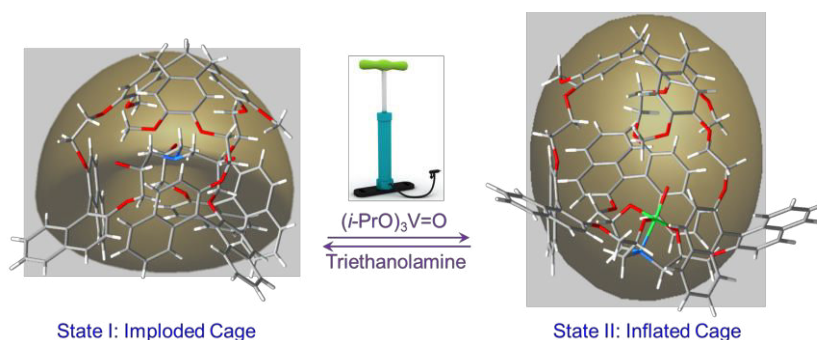
- L. Guy, J.-P. Dutasta, *J. Am. Chem. Soc.*, **2010**, *132*, 16733.
- 9 a) M. J. Hardie, *Chem. Soc. Rev.* **2010**, *39*, 516. b) A. Szumna, *Chem. Soc. Rev.* **2010**, *39*, 4274.
- 10 a) G. Huber, T. Brotin, L. Dubois, H. Desvaux, J.-P. Dutasta, P. Berthault, *J. Am. Chem. Soc.* **2006**, *128*, 6239. b) A. Bouchet, T. Brotin, M. Linares, D. Cavagnat, T. Buffeteau, *J. Org. Chem.* **2011**, *76*, 7816.
- 11 J. R. Cochrane, A. Schmitt, U. Wille, C. A. Hutton, *Chem. Commun.* **2013**, *49*, 8504.
- 12 a) A. Schmitt, B. Chatelet, S. Collin, J.-P. Dutasta, A. Martinez, *Chirality* **2013**, *25*, 475. b) A. Schmitt, V. Robert, J.-P. Dutasta, A. Martinez, *Org. Lett.* **2014**, *16*, 2374.
- 13 a) O. Perraud, A. Martinez, J.-P. Dutasta, *Chem. Commun.* **2011**, *47*, 5861. b) A. Schmitt, B. Chatelet, D. Padula, L. Di Bari, J.-P. Dutasta, A. Martinez, *New J. Chem.* **2015**, *39*, 1749.
- 14 a) A. Gautier, J.-C. Mulatier, J. Crassous, J.-P. Dutasta, *Org. Lett.* **2005**, *7*, 1207. b) B. Chatelet, L. Joucla, D. Padula, L. Di Bari, G. Pilet, V. Robert, V. Dufaud, J.-P. Dutasta, A. Martinez, *Org. Lett.* **2015**, *17*, 500. c) A. Schmitt, O. Perraud, E. Payet, B. Chatelet, B. Bousquet, M. Valls, D. Padula, L. Di Bari, J.-P. Dutasta, A. Martinez, *Org. Biomol. Chem.* **2014**, *12*, 4211.
- 15 B. Chatelet, E. Payet, O. Perraud, P. Dimitrov-Raytchev, L. L. Chapellet, V. Dufaud, A. Martinez, J.-P. Dutasta, *Org. Lett.* **2011**, *13*, 3706.
- 16 S. Lefevre, D. Zhang, E. Godart, M. Jean, N. Vanthuyne, J.-C. Mulatier, J.-P. Dutasta, L. Guy, A. Martinez, *Chem. Eur. J.* **2016**, *22*, 2068.
- 17 a) M. Mazik, *Chem. Soc. Rev.* **2009**, *38*, 935. b) A. P. Davis, *Org. Biomol. Chem.* **2009**, *7*, 3629. c) C. Ke, H. Destecroix, M. P. Crump, A. P. Davis, *Nature Chem.* **2012**, *4*, 718. d) A. P. Davis, R. S. Wareham, *Angew. Chem., Int. Ed.* **1999**, *38*, 2978. e) J. Lippe, M. Mazik, *J. Org. Chem.* **2015**, *80*, 1427. f) O. Francesconi, M. Gentili, C. Nativi, A. Arda, F. J. Canada, J. Jiménez-Barbero, S. Roelens, *Chem. Eur. J.* **2014**, *20*, 6081. g) N. Chandramouli, Y. Ferrand, G. Lautrette, B. Kauffmann, C. D. Mackereth, M. Laguerre, D. Dubreuil, I. Huc, *Nature Chem.* **2015**, *7*, 334. h) T. J. M. Mooibroek, J. M. Casas-Solvas, R. L. Harniman, C. M. Renney, T. S. Carter, M. P. Crump, A. P. Davis, *Nature Chem.* **2016**, *8*, 69. i) S. Rieth, M. R. Miner, C. M. Chang, B. Hurlocker, A. B. Braunschweig, *Chem. Sci.* **2013**, *4*, 357.
- 18 C. Frassinetti, S. Ghelli, P. Gans, A. Sabatini, M. S. Moruzzi, A. Vacca, *Anal. Biochem.* **1995**, *231*, 374.
- 19 P. Job, *Ann. Chim.* **1928**, *9*, 113.
- 20 a) R. P. Bonar-Law, J. K. Sanders, *J. Am. Chem. Soc.* **1995**, *117*, 259. b) M. López de la Paz, G. Ellis, M. Pérez, J. Perkins, J. Jiménez-Barbero, C. Vicent, *Eur. J. Org. Chem.* **2002**, 840.

Part III. Hemicryptophanes in Motion: towards Molecular Machines

Preface



In **Chapter 6** of **Part II**, a series of enantiopure hemicryptophanes bearing three types of chirality have been synthesized, leading to eight stereoisomers, four diastereomeric pairs of enantiomers. Further solution and solid state investigations have shown that these enantiopure cages exhibit a hierarchical implosion between diastereomers. Inspired by this interesting phenomenon, we wonder whether these imploded cages can be inflated by internal coordination of trialcohol unit with vanadium, and whether the resulted vanadium core could be further removed by external coordination. If the bistable states can be switched for several times, the molecule is simulating the behaviour of breathing (see the figure below). Moreover, the binding properties between the imploded and inflated cages should be different. Therefore, **Chapter 7** in **Part III** describes these findings and investigations.



It should be noted that **Chapter 7** is based partially on my publication of *Chemistry – A European Journal* (2017, 23, 6495–6498). The numbers of compounds, figures, schemes and tables have been renumbered compared to the previous chapters, and the numbers of compounds between chapters have no relationship. The Table of Contents in this chapter has been presented in the chapter cover. The cited references are listed at the end of the chapter.

Chapter 7. Breathing Motion of a Modulable Molecular Cavity

This Chapter is based partially on the following manuscript—

Dawei Zhang, James Robert Cochrane, Sebastiano Di Pietro, Laure Guy,
Heinz Gornitzka, Jean-Pierre Dutasta, and Alexandre Martinez

Chem. Eur. J. **2017**, *23*, 6495–6498.

The work in this chapter was carried out at the ENS-Lyon.

Contents

7.1 Abstract	148
7.2 Introduction.....	148
7.3 Results and discussion	148
7.4 Conclusion.....	152
7.5 Experimental section.....	152
7.6 References.....	173

7.1 Abstract

A class of hemicryptophane cages that adopt imploded conformations in solution and in the solid state is described and studied by NMR and X-ray crystallography. We show that the degree of collapse of the molecular cavity can be controlled by changing the stereochemistry of the chiral elements of the hemicryptophanes, leading to a modulation of their physical and chemical properties. Upon the binding of an oxidovanadium unit, the collapsed molecular cavity can inflate to give an expanded conformation. Removal of the vanadium core by an ancillary complexing ligand restores the initial folded structure. Thus coordination/de-coordination of metal ion controls the dynamic motions of the cage leading to a reversible nanomechanical process. This controlled motion between a collapsed and expanded cavity can be seen as that of a breathable molecular cage.

7.2 Introduction

There is an increased interest in the synthesis and development of systems able to perform a defined function at the molecular level.¹ For instance, molecular machines can produce quasi-mechanical movements (output) in response to specific stimuli (input). Currently, synthetic systems mimicking the ability of brakes,^{2a} gears,^{2b} propellers,^{2c} ratchets,^{2d} rotators,^{2e} scissors,^{2f} muscles,^{2g,h} gyroscopes,²ⁱ walkers,^{2j} and motors^{2k-n} have been widely devised and studied. Among them, catenanes and rotaxanes are well known molecular systems that are frequently used as supramolecular forces in the design of molecular devices.^{1,j,k} Remarkable molecular motion of molecular strands from folding to unfolding states has been also achieved using coordination/de-coordination of metal ions.³

Recently, besides the properties of recognition, catalysis, and reactive species stabilization, molecular cages have received a growing interest in constructing molecular machines.⁴ For instance, hemicryptophanes have been used to achieve nanomechanical processes mimicking the function of gyroscopes or molecular propellers.^{2c,4i} Although nice examples of size and shape modifications of molecular cavity in self-assembled or covalent cages have been recently described,⁵ control of the dynamic motion in molecular cages from fully folded to extended states is still a challenge.

We previously reported the synthesis of a new family of enantiopure hemicryptophane cages bearing three types of stereogenic elements, helical, axial and central chirality, which respectively result from the cyclotrimeratrylene (CTV), binaphthol and trialkanolamine moieties, giving rise to four pairs of enantiomers (Figure 7.1a).⁶ Herein, we report how these chiral units modulate the shape and size of the inner cavity and the consequences on their physical and chemical properties. We found that these molecular cages collapse in solution and that the resulting imploded form can re-inflate upon the complexation of an oxidovanadium unit. This conformational change between the collapsed and expanded form is reversible, leading to a synthetic molecule simulating the breathing motion upon the binding-unbinding of an external stimulus.

7.3 Results and discussion

Crystals of *M*-*RRR*-*RRR*-**1**·2(CHCl₃)·0.5(Et₂O) suitable for X-Ray diffraction analysis were obtained by slow evaporation from a concentrated solution of the cage in CHCl₃/Et₂O. The structure of hemicyptophane *M*-*RRR*-*RRR*-**1** exhibits a C₃ symmetry with an unexpected imploded conformation where the trialkanolamine core is collapsed within the CTV unit obstructing the inner cavity (Figures 7.2 and S7.1).⁷ The three OH groups point outward forming hydrogen bonds with the two closest O atoms of the binaphthol groups (O···O distances, 2.77-2.94 Å), whereas the NCH₂ protons, directed toward the CTV unit, interact with the aromatic rings (distances between the axial proton of NCH₂ and the closest CTV aromatic ring, 3.08-3.53 Å).

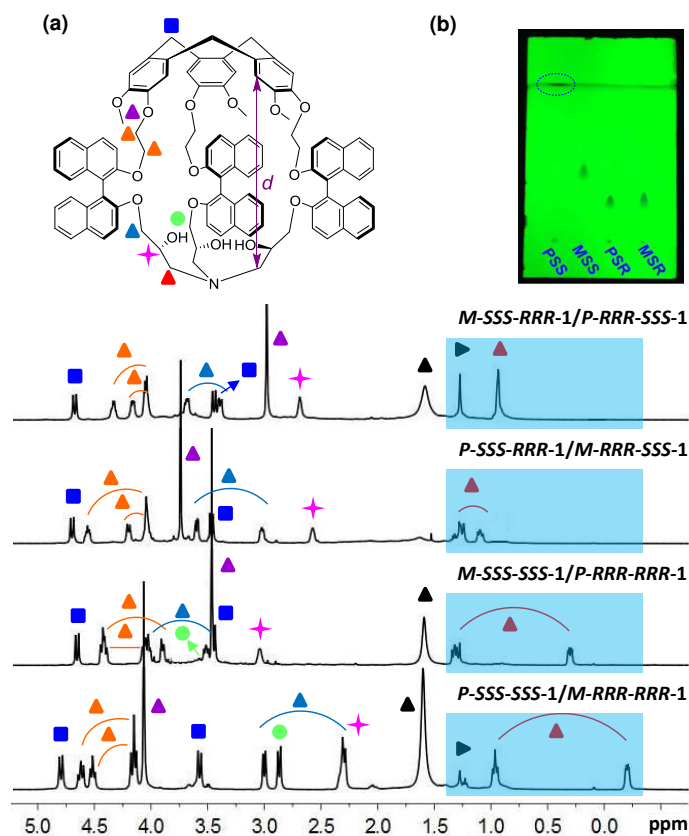


Figure 7.1 (a) Partial ¹H NMR spectra (500.1 MHz, 298 K) of the four diastereomeric pairs of hemicyptophane **1** in CDCl₃ and their protons assignment. ▲ = water; ► = grease. The high-field shifted NCH₂ protons are highlighted. The distance *d* between the more shielded NCH₂ proton and its closest CTV aromatic-H has been illustrated, which is used for the evaluation of the cage collapse degree. (b) TLC migration properties of **1** (silica, eluent: CH₂Cl₂/MeOH = 200/3). The symbolisms used are the abbreviation names of each hemicyptophane isomers, for instance, *PSS* represents *P*-*SSS*-*SSS*-**1**.

Insights into the conformations of the cavities of the four diastereomers of **1** in solution were obtained by ¹H NMR, ¹³C NMR, COSY, HSQC and HMBC experiments (see 7.5.5). In the ¹H NMR spectra, we can observe the high-field shifted signals of the NCH₂ protons (Figures 7.1 and S7.2), with a shielding order *P*-*SSS*-*SSS*-**1** ($\delta = -0.20$ ppm) > *M*-*SSS*-*SSS*-**1** (0.30 ppm) > *M*-*SSS*-*RRR*-**1** (0.97 ppm) \approx *P*-*SSS*-*RRR*-**1** (1.08 ppm). These high-field shifted signals are consistent with imploded conformations as viewed in the crystal structure (Figure 7.2). To

further demonstrate the concave conformation of each cage in solution, ROESY experiments were performed (Figures S7.3-S7.6). Cross-peaks between the protons of the trialkanolamine core and the aromatic and methoxy protons of the CTV unit directly evidence short distances between the two moieties ($< 5 \text{ \AA}$) and are indicative of the imploded conformations of these host molecules in solution. The inter-proton distance between the most shielded NCH_2 proton and its closest CTV aromatic-H (see Figure 7.1a and Experimental section) was calculated, giving a distance for *P*-SSS-SSS-1/*M*-RRR-RRR-1 in the range of 3.03-3.08 \AA , in agreement with that measured from the crystal structure (3.08-3.53 \AA). Moreover, the implosion degree indicated by the calculated $\text{H}\cdots\text{H}$ distances for each cage follows the same trend as that of the chemical shifts of the shielded NCH_2 protons: *P*-SSS-SSS-1 (average: 3.06 \AA) $>$ *M*-SSS-SSS-1 (3.21 \AA) $>$ *P*-SSS-RRR-1 (3.86 \AA). The measurement for *M*-SSS-RRR-1 failed due to peaks overlap of the two NCH_2 signals. These results suggest that the size and shape of the cavity can be modulated by the chirality of its constitutive chiral units. Notably, this imploded conformation is also retained in other solvents such as toluene-*d*₈ and DMSO-*d*₆ and at higher temperature (up to 373 K, Figures S7.7 and S7.8).

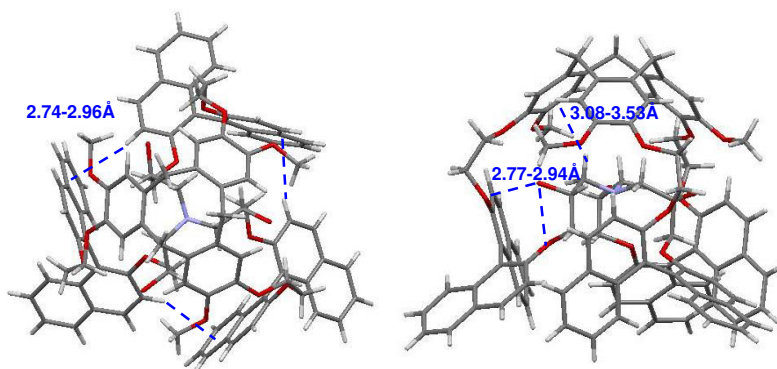


Figure 7.2 Crystal structure of *M*-RRR-RRR-1. Solvent molecules are omitted for clarity. Dashed lines in the left figure represent the distance between the two neighboring binaphthyl groups, and those in the right figure represent the distances between the axial proton on NCH_2 and its closest aromatic-H on CTV or between the O atom on OH and its two closest binaphthyl O atoms.

Several physical properties of these cages are directly related to the hierarchical modulation in the size and shape of their inner cavities. With the increase of the implosion degree from *M*-SSS-RRR-1 to *P*-SSS-SSS-1, (i) the ^1H NMR signal of the alcohol proton becomes sharper and sharper (Figure 7.1a), (ii) their exchange with MeOD reveals increasingly difficult (Figure S7.9), and (iii) the migration properties of these compounds on TLC plates appears easier (R_f equals to 1.00, 0.47, 0.29 and 0.30 for *P*-SSS-SSS-1, *M*-SSS-SSS-1, *P*-SSS-RRR-1 and *M*-SSS-RRR-1, respectively, Figure 7.1b). All these observations indicate that the alkanolamine core of the most imploded cage *P*-SSS-SSS-1, which occupies the inner cavity, is well protected by the CTV shelter, significantly reducing its interaction with the surrounding environment.

Coordination/de-coordination of metal ions can allow for dynamic motions and reversible nanomechanical processes of molecular compounds,³ we thus prepared the oxidovanadium(V)-1 hemicryptophane complexes which were also developed as efficient oxidation catalysts recently (see Chapter 8).⁸ The reaction of each cage diastereomer with 1.0 equiv. of vanadium(V) reagent was carried out at room temperature in CDCl_3 and monitored

by ^1H NMR (Figure S7.10 and S7.11). Interestingly it was found that the reaction rate with the most imploded cage *P*-SSS-SSS-1 is 10-fold slower than those of the other three diastereomers, suggesting a higher energy barrier for the reorganization of the structure for vanadium complexation. In addition, in the ^1H NMR spectrum of the vanadium@*P*-SSS-SSS-1 complex in CDCl_3 , the chemical shifts of the NCH_2 protons are in the region of 1.28-1.78 ppm (Figure S7.12). Compared to those of the free ligand (-0.20 and 0.95 ppm), these protons show an obvious down-field shift. ROESY experiments performed on this complex reveal no NOE correlation between the trialkanolamine unit and the CTV moiety (Figure S7.13). These results are in agreement with strong conformational changes leading to the inflation of the molecular cavity through vanadium complexation (Figure 7.3).

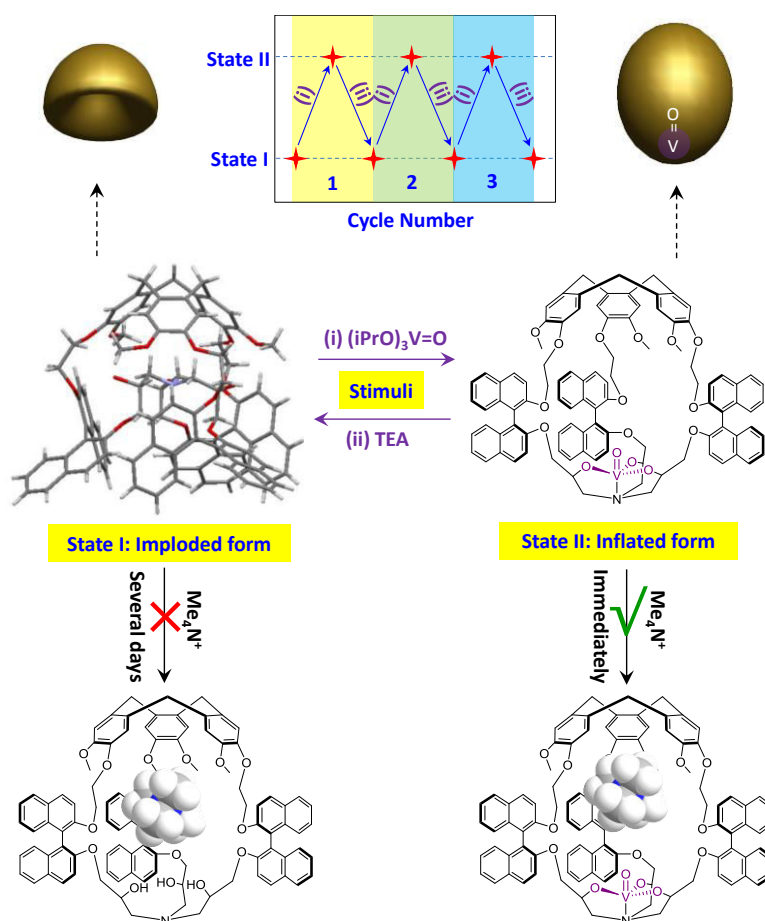


Figure 7.3 Graphical representation of the hemicryptophane cage switching between its bi-stable states, *i.e.* imploded and inflated conformations, with external inputs. This switching can be done at least for three cycles. The new inflated vanadium complex is able to further encapsulate the ammonium guest, while the parent imploded ligand cannot.

Furthermore, tetramethyl ammonium (Me_4N^+) can be efficiently bound by the vanadium@*M*-SSS-RRR-1 cage with a binding constant of 547 M^{-1} (Figure S7.14),⁸ evidencing the presence of a well defined cavity in the complex. An MM3 model of vanadium@*M*-SSS-RRR-1 with Me_4N^+ encapsulated inside the cavity was prepared using SCIGRESS software (Figure S7.15).⁹ Results show that the distance d between the more shielded NCH_2 proton and its closest CTV aromatic-H, as indicated in Figure 7.1, has been

expanded from 3.86 Å to 13.57 Å. In contrast, when similar experiments were performed with Me₄N⁺ and any of the free molecular hosts **1**, no characteristic complex induced shift of the Me₄N⁺ signal was observed, even after several days. These results demonstrate that the inner cavity of the vanadium cage complex is accessible, whereas there is no available molecular cavity in the parent free host. Thus, it appears clearly that the vanadium acts as an inflator to fully inflate the imploded cages.

To test the reversibility of the inflation-deflation dynamic process, we studied the binding-unbinding properties of the hemicyptophanes **1** with vanadium(V) oxytriisopropoxide. To remove the oxidovanadium moiety from the cage ligand, an excess of triethanolamine (TEA) was added to a solution of vanadium@*M*-SSS-SSS-**1** in CDCl₃. The NMR spectrum showed that vanadium was fully de-coordinated from the cage ligand, followed by immediate collapse, proving that the imploded structure of the free ligand is much more stable than its globular form. Subsequent addition to this solution of an excess of vanadium(V) oxytriisopropoxide, recovered the initial shape of the vanadium@hemicyptophane complex. This switch between the imploded and inflated bi-stable states has been performed at least for three cycles in the case of *M*-SSS-RRR-**1** (Figures 7.3 and S7.16). Therefore, through the input of vanadium reagent or TEA as a stimulus, the hemicyptophane cage can artificially breathe.

7.4 Conclusion

In summary, we have described herein a class of imploded hemicyptophane cages. The level of collapse, which can be indicated by the inter-proton distances between the CTV and trialkanolamine units, have been measured based on NOE cross-peaks of the ROESY spectra. It was found that the imploded degree of the cages can be controlled by varying the stereochemistry of the constructing units. Stereomodulation of the inner cavity also results in the regulation of their corresponding physical and chemical properties. For instance, the reaction between vanadium(V) oxytriisopropoxide and the most imploded cage *P*-SSS-SSS-**1** suffers from a slower reaction rate compared to the other three diastereomers. Interestingly, vanadium complexation re-inflates the cage from its imploded conformation to a globular form, and the resulting vanadium core can also be removed from the inner cavity according to external coordination with TEA. Thus, this system is capable of switching between the imploded and expanded bi-stable states via external inputs, leading to a molecular breathing motion. This class of molecular cage is for the first time exploited as a novel mode of switching that is worthy of being explored for potential applications.

7.5 Experimental section

7.5.1 Materials and instrumentation

All solvents used were of commercial grade and were dried prior to use over molecular sieves. ¹H NMR and ¹³C NMR spectra were recorded on a Bruker Avance spectrometer operating at 500.10 MHz and 125.76 MHz for ¹H NMR and ¹³C NMR spectra, respectively. ¹H

NMR chemical shifts (δ) are reported in ppm and referenced to the protonated residual solvent signal. The method for measurement of the interproton distances was proposed by Sebastiano Di Pietro. X-ray data were collected, solved and refined by Heinz Gornitzka.

7.5.2 Crystal data

Table S7.1 Crystal data and refinement for compound *M-RRR-RRR-1*·2(CHCl₃)·(Et₂O).

Empirical formula	C105 H96 Cl6 N O16	
Formula weight	1840.52	
Temperature	173(2) K	
Wavelength	0.71073 Å	
Crystal system	Monoclinic	
Space group	P2 ₁	
Unit cell dimensions	a = 14.9424(6) Å	$\alpha = 90^\circ$.
	b = 17.5525(8) Å	$\beta = 90.028(2)^\circ$.
	c = 17.4344(7) Å	$\gamma = 90^\circ$.
Volume	4572.6(3) Å ³	
Z	2	
Density (calculated)	1.337 Mg/m ³	
Absorption coefficient	0.257 mm ⁻¹	
F(000)	1926	
Crystal size	0.400 x 0.200 x 0.200 mm ³	
Theta range for data collection	1.363 to 27.271°.	
Index ranges	-18 ≤ h ≤ 18, -18 ≤ k ≤ 22, -18 ≤ l ≤ 22	
Reflections collected	42751	
Independent reflections	15741 [R(int) = 0.0320]	
Completeness to theta = 25.242°	96.3 %	
Absorption correction	Semi-empirical from equivalents	
Max. and min. transmission	0.7455 and 0.6729	
Refinement method	Full-matrix least-squares on F ²	
Data / restraints / parameters	15741 / 386 / 1276	
Goodness-of-fit on F ²	1.026	
Final R indices [I > 2σ(I)]	R1 = 0.0589, wR2 = 0.1463	
R indices (all data)	R1 = 0.0832, wR2 = 0.1651	
Absolute structure parameter	0.07(3)	
Extinction coefficient	n/a	
Largest diff. peak and hole	0.513 and -0.433 e.Å ⁻³	

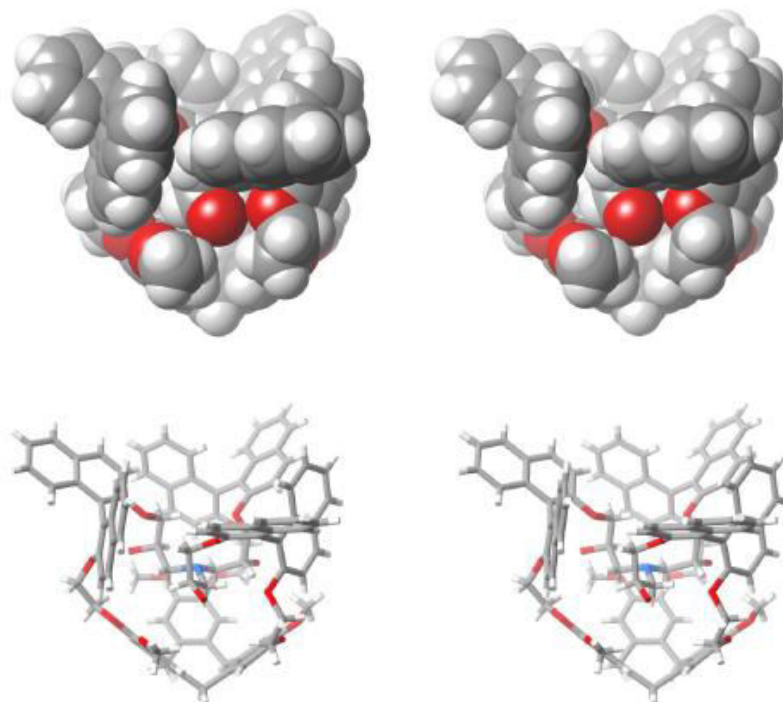


Figure S7.1 Stereo views of crystal structure of *M-RRR-RRR-1*.

7.5.3 Supplementary figures

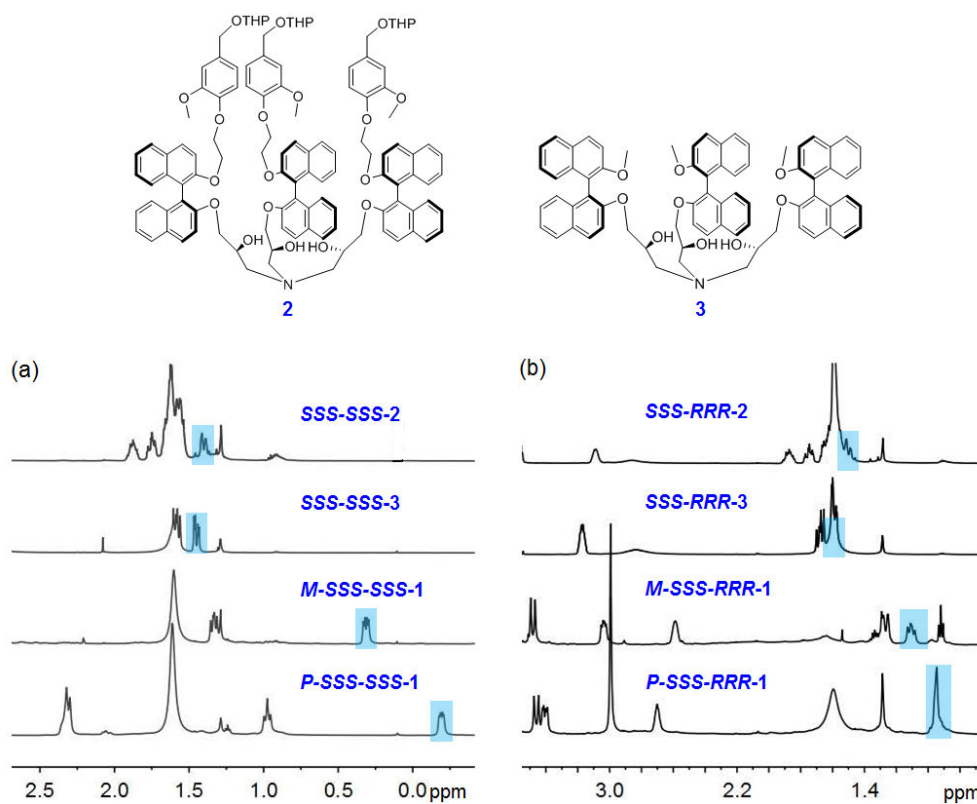


Figure S7.2 A direct comparison of the chemical shifts of NCH_2 in the ^1H NMR spectra (CDCl_3 , 500.1 MHz, 298K) of the cages **1** and the corresponding open structures **2** and **3** (**2** and **3** were synthesized as the previous procedures in Chapter 5)⁶.

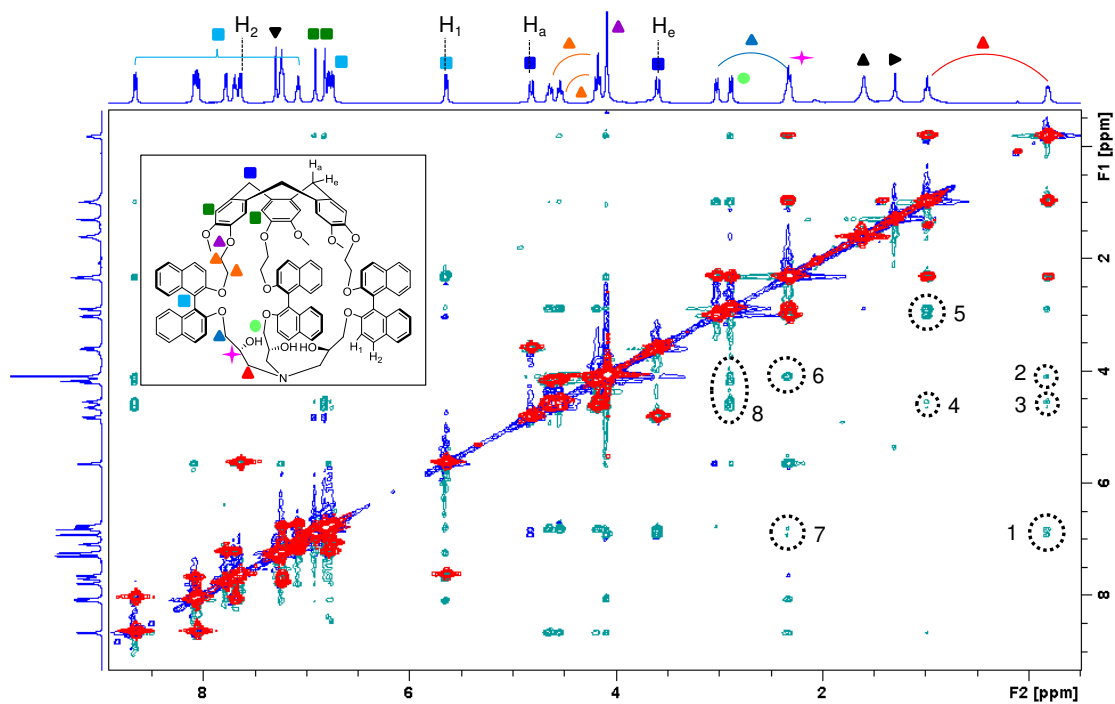


Figure S7.3 An overlap between the full COSY (red) and ROESY (blue and green) spectra of *P*-SSS-SSS-1/*M*-RRR-RRR-1 in CDCl₃ (500.1 MHz, 298 K); Cross-peaks of 1-8 indicate the correlations between the upper and lower parts of the cage, suggesting its imploded conformation.

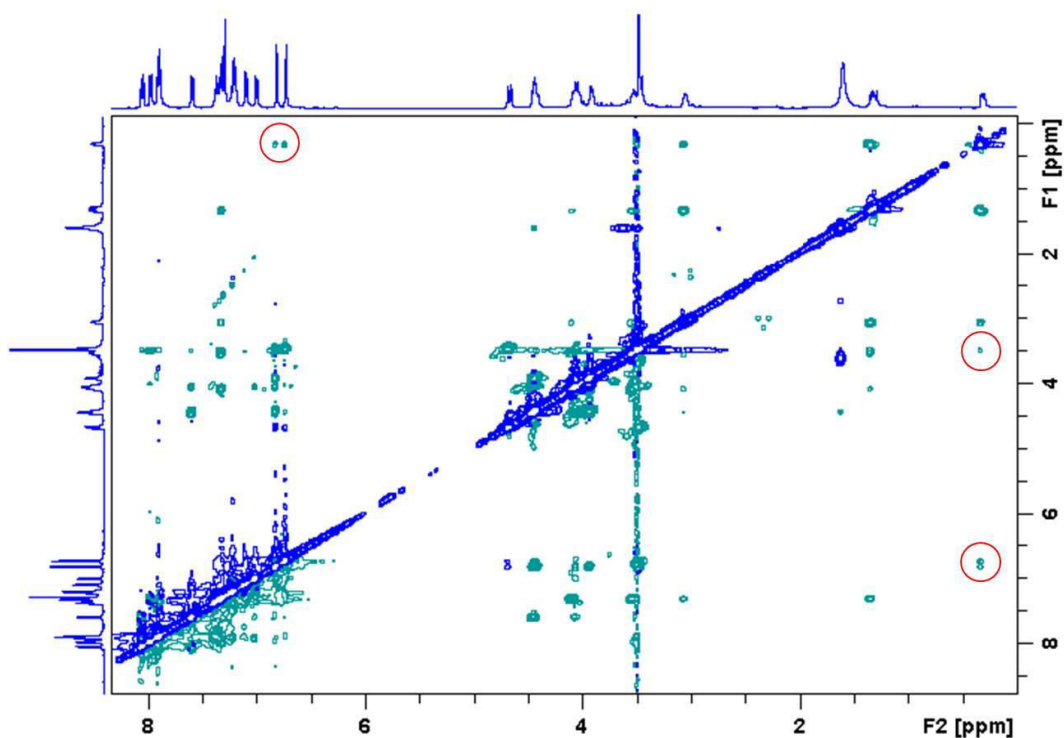


Figure S7.4 ROESY spectrum (CDCl₃, 500.1 MHz, 298K) of *M*-SSS-SSS-1/*P*-RRR-RRR-1; The NOE cross-peaks between the NCH₂ proton of trialkanolamine and benzene-H or OMe on the CTV have been indicated.

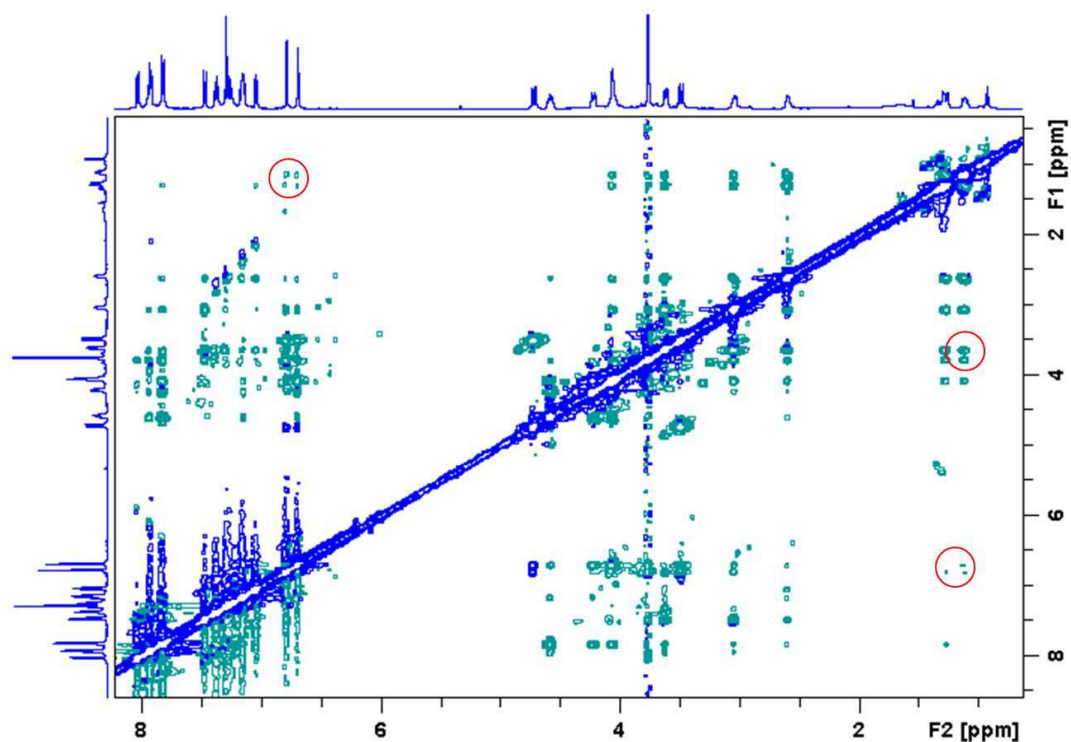


Figure S7.5 ROESY spectrum (CDCl_3 , 500.1 MHz, 298K) of *P*-SSS-RRR-1/*M*-RRR-SSS-1. The NOE cross-peaks between the NCH_2 proton of trialkanolamine and benzene-H or OMe on the CTV have been indicated.

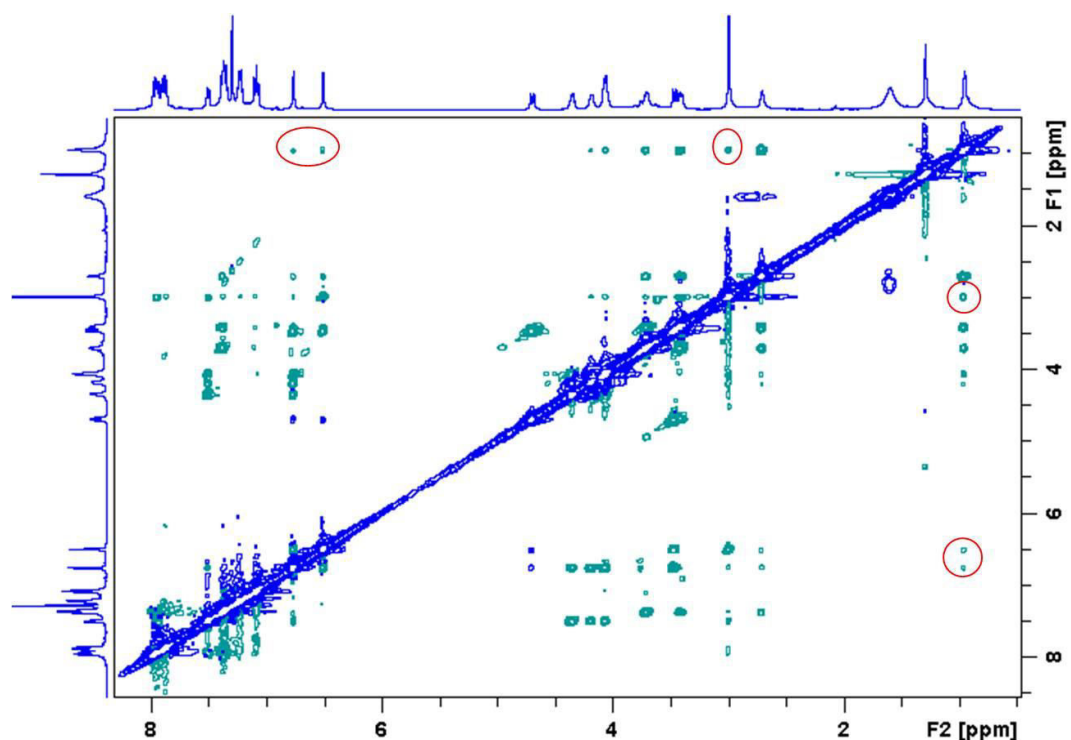


Figure S7.6 ROESY spectrum (CDCl_3 , 500.1 MHz, 298K) of *M*-SSS-RRR-1/*P*-RRR-SSS-1. The NOE cross-peaks between the NCH_2 proton of trialkanolamine and benzene-H or OMe on the CTV have been indicated.

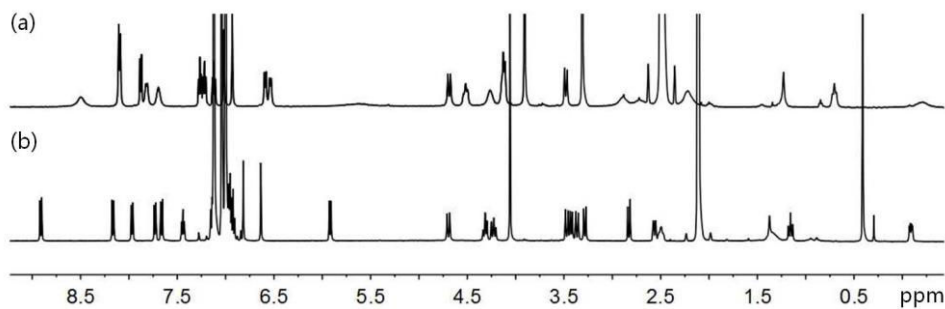


Figure S7.7 ^1H NMR (500.1 MHz, 298K) of *P*-SSS-SSS-1 in (a) $\text{DMSO-}d_6$ and (b) $\text{toluene-}d_8$.

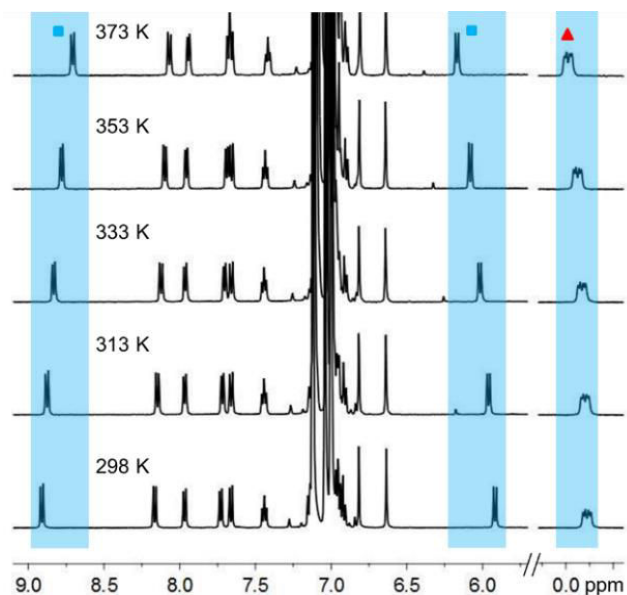


Figure S7.8 ^1H NMR spectra of *P*-SSS-SSS-1 at different temperature in $\text{toluene-}d_8$ (500.1 MHz); ■ and ▲ represent the aromatic binaphthol protons and the axially oriented NCH_2 protons in the cage.

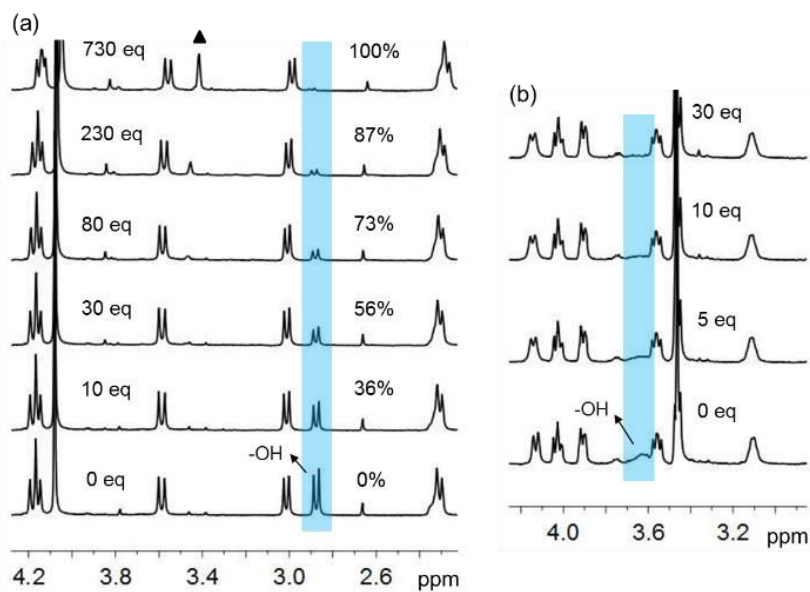


Figure S7.9 ^1H NMR spectra (500.1 MHz, 298 K) of *P*-SSS-SSS-1 (a) and *M*-SSS-SSS-1 (b) upon addition of different equiv. of MeOD. ▲ represents MeOH.

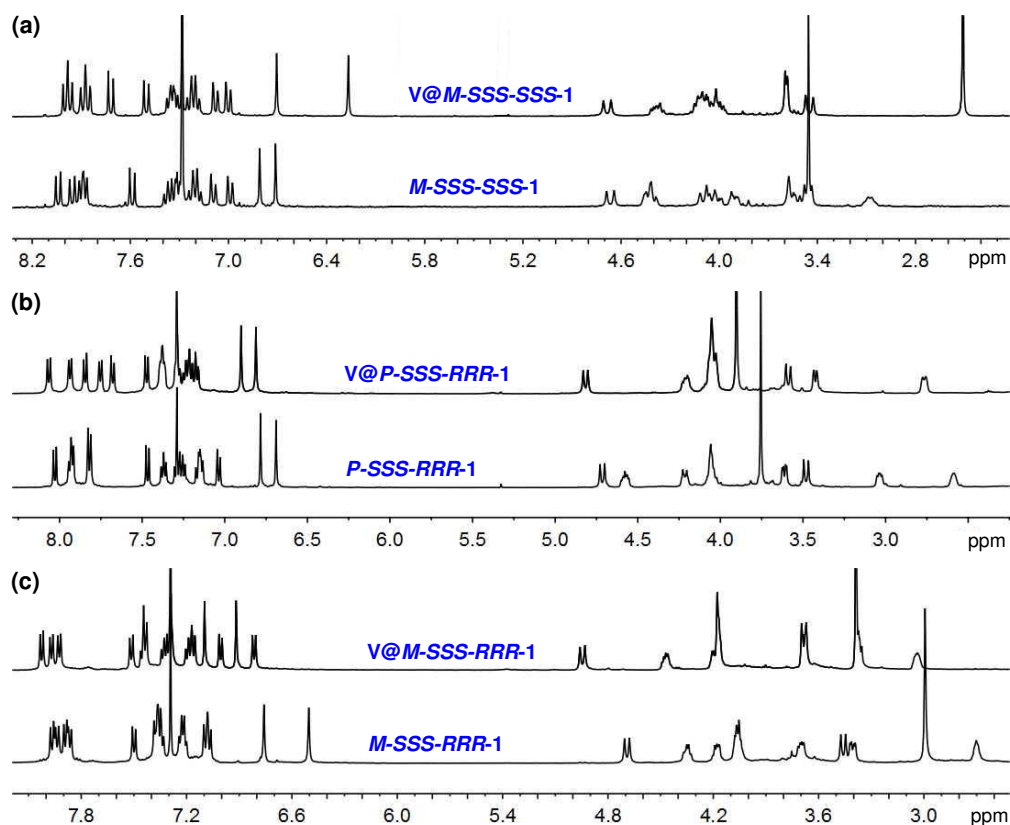


Figure S7.10 ^1H NMR spectra (CDCl₃, 500.1 MHz, 298K) of the hemicryptophane ligands and their corresponding vanadium(V) complexes; Each complex was obtained via the reaction of the ligand with 1.0 equiv. of vanadium(V) oxytriisopropoxide in CDCl₃ for 10 min, followed by evaporation.

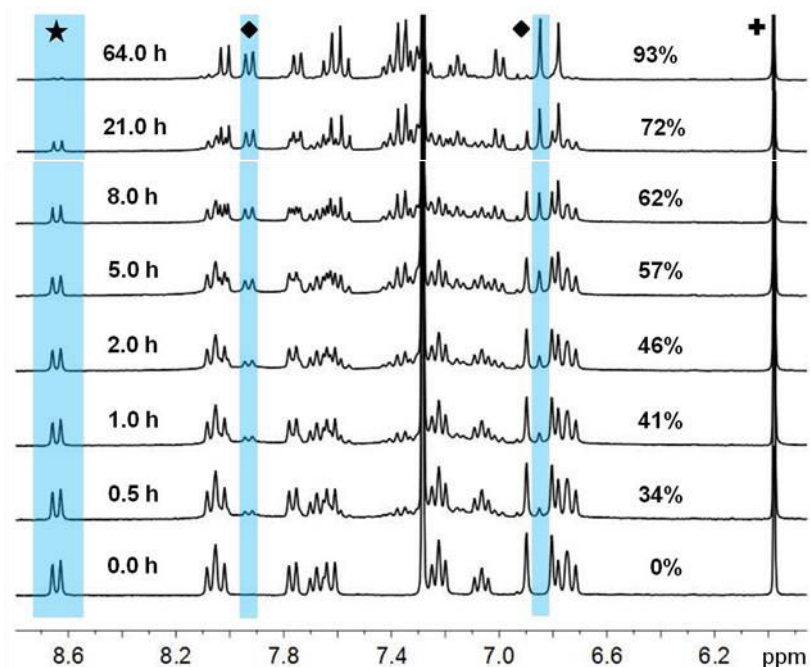


Figure S7.11 Time course of the ^1H NMR spectra (500.1 MHz, 298K) for the reaction of P-SSS-SSS-1 with 1.0 equiv. of vanadium(V) oxytriisopropoxide in CDCl₃ at r.t. ★, ◆ and + represent the species of the ligand, the vanadium(V) complex and the $\text{Cl}_2\text{CHCHCl}_2$, respectively. The intensity of the reference in each spectrum has been adjusted equally. The yield at each time has been indicated.

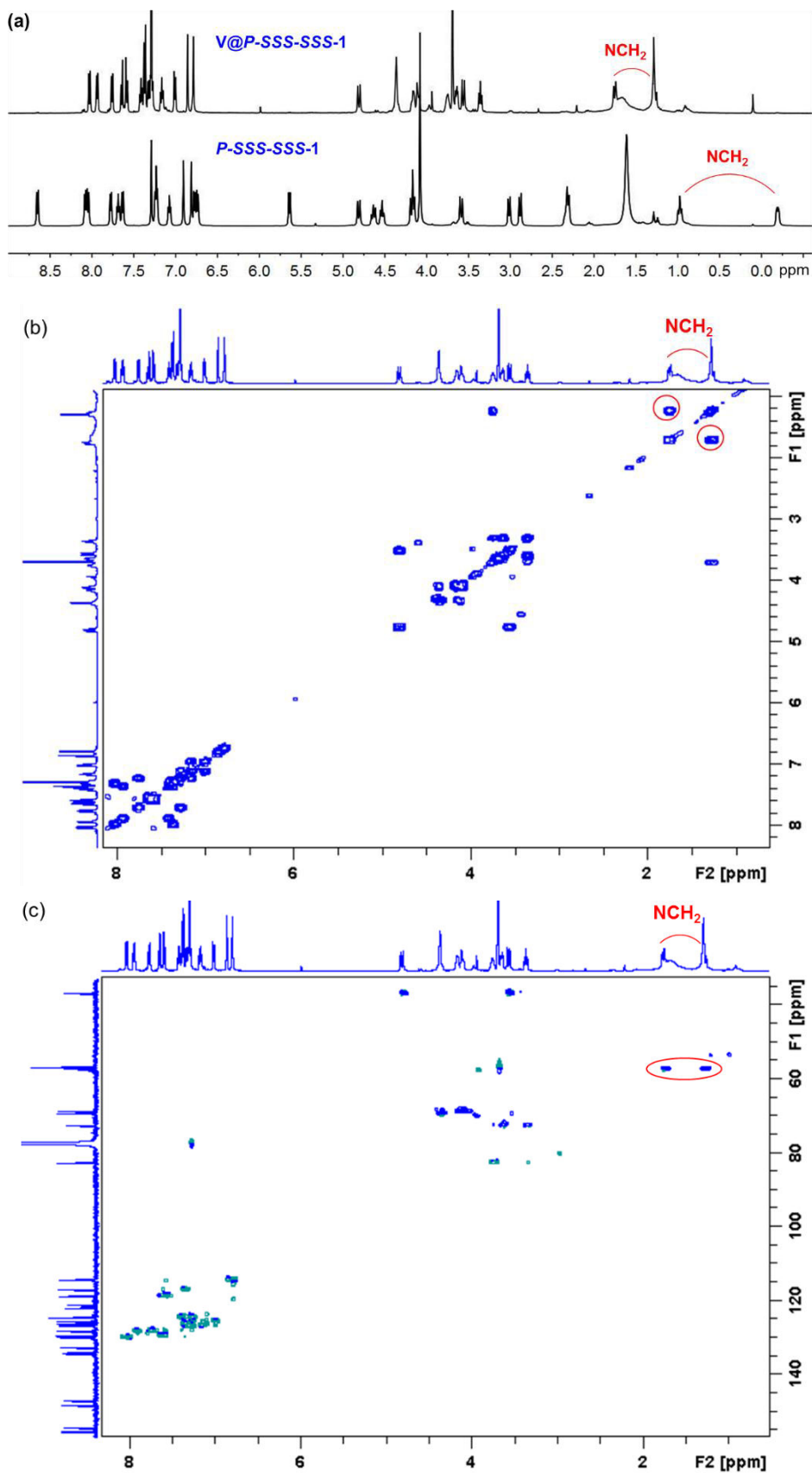


Figure S7.12 (a) ^1H NMR spectra (CDCl_3 , 500.1 MHz, 298K) of P-SSS-SSS-1 and its vanadium(V) complex. (b) COSY spectrum (CDCl_3 , 500.1 MHz, 298K) of V@P-SSS-SSS-1 . (c) HSQC spectrum (CDCl_3 , 500.1 MHz, 298K) of V@P-SSS-SSS-1 .

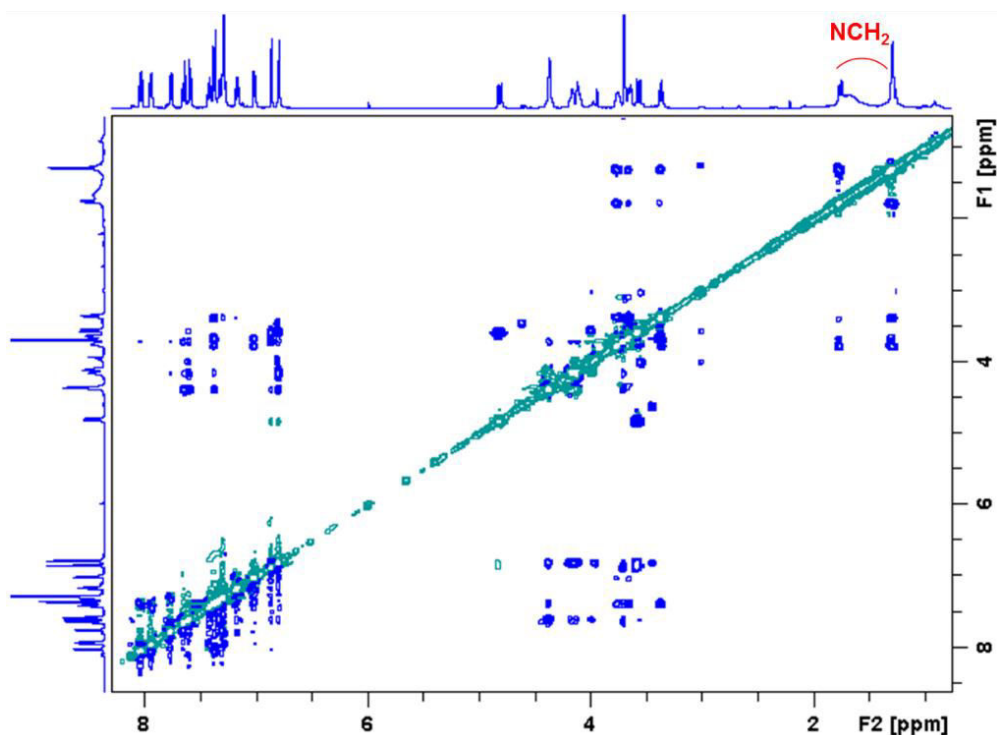


Figure S7.13 ROESY spectra (CDCl_3 , 500.1 MHz, 298K) of V@P-SSS-SSS-1 . No NOE cross-peak between the NCH_2 proton of trialkanolamine and benzene-H or OMe on the CTV was observed.

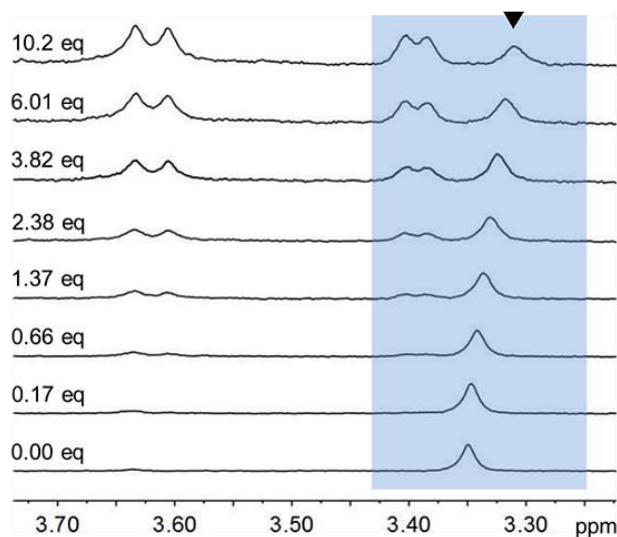


Figure S7.14 ^1H NMR titrations (500.1 MHz, 298 K) of $\text{Me}_4\text{N}^+\text{Pic}^-$ (0.5 mmol/L) in CD_2Cl_2 upon addition of different equiv. of the host V@M-SSS-RRR-1 ; \blacktriangledown represents the signal of Me_4N^+ protons.

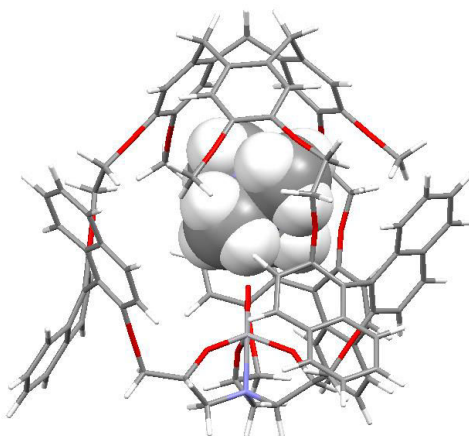


Figure S7.15 MM3-optimized molecular model of vanadium@*M-SSS-RRR-1* with Me₄N⁺ encapsulated inside the cavity.

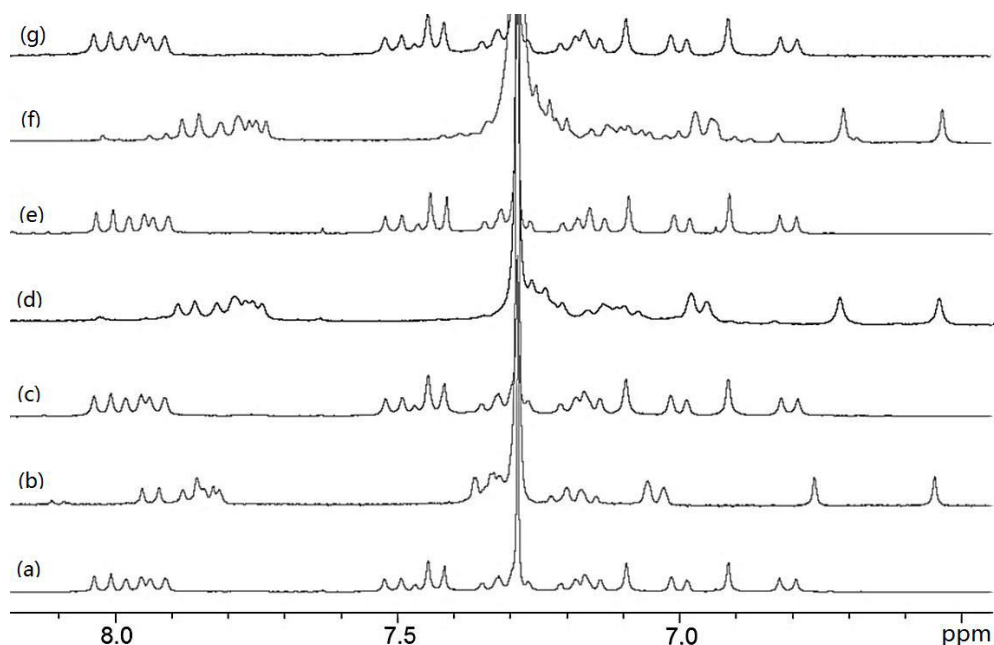


Figure S7.16 ¹H NMR spectra of *M-SSS-RRR-1* or V@*M-SSS-RRR-1* (CDCl₃, 500.1 MHz, 298 K) that illustrate the three cycles between the bi-stable states, *i.e.* the imploded and inflated conformations. (a) Spectra of V@*M-SSS-RRR-1*; (b) Spectra of the ligand *M-SSS-RRR-1* obtained by adding an excess of TEA to (a); (c) Spectra of V@*M-SSS-RRR-1* obtained by adding an excess of vanadium(V) oxytriisopropoxide to (b), followed by the manipulations of filtration, evaporation, dissolution and re-filtration. The purpose of the first filtration is to remove the precipitate formed by TEA and vanadium(V) oxytriisopropoxide, and the second filtration is to remove the vanadium aggregated particles; (d) Spectra of the ligand *M-SSS-RRR-1* obtained by adding an excess of TEA to (c); (e) Spectra of V@*M-SSS-RRR-1* obtained from (d) by the same procedure as that from (b) to (c); (f) Spectra of the ligand *M-SSS-RRR-1* obtained by adding an excess of TEA to (e); and (g) Spectra of V@*M-SSS-RRR-1* obtained from (f) by the same procedure as that from (b) to (c).

7.5.4 Measurement of the interproton distances

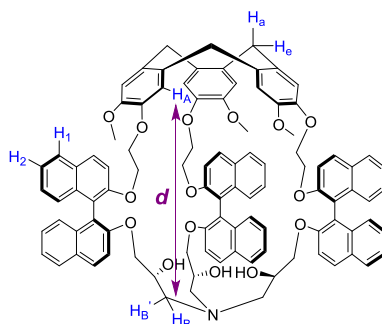
Briefly, for two dipolar coupled nuclei A and B (Scheme S7.1), the rate constant R_{AB} is inversely proportional to the sixth power of their inter-proton distance r_{AB} :

$$R_{AB} = \frac{k}{r_{AB}^6}$$

Where k is a constant which is determined by the parameters of the NMR experiment. If we select another two coupled nuclei C and D in the same cage as the reference, we can exploit the following relationship, since the k value will be cancelled.

$$r_{AB} = r_{cd} \times \sqrt[6]{\frac{R_{CD}}{R_{AB}}}$$

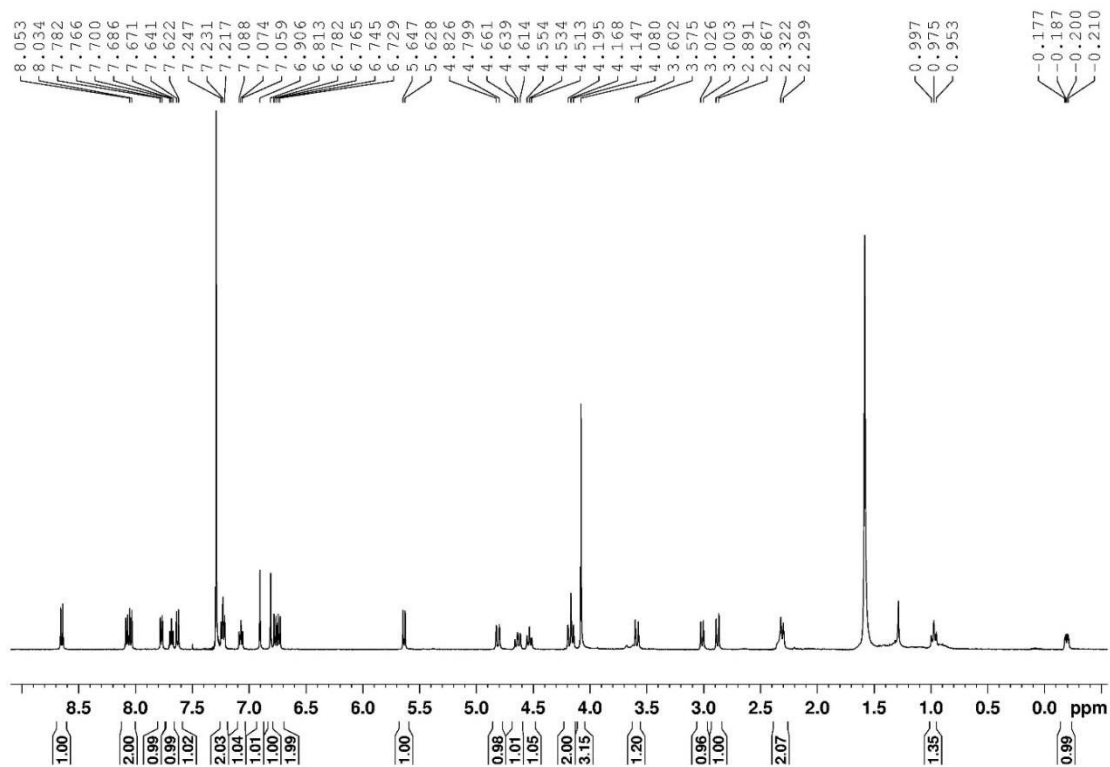
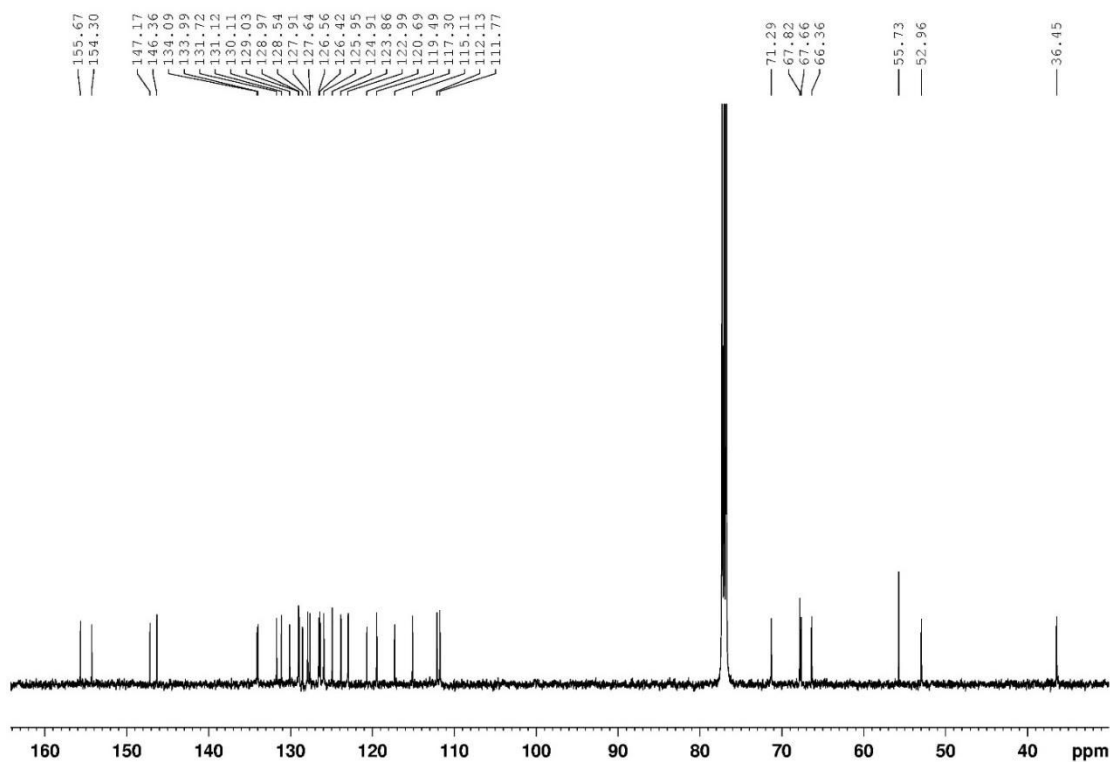
Hence, from this equation, if we determine the rate constants R_{AB} and R_{CD} , and if the reference distance r_{CD} is known, we can calculate the unknown distance r_{AB} . The reference nuclei C and D have to be chosen from the rigid part of the cage to possess an invariable distance, which can be measured directly from the crystal structure. For R_{AB} and R_{CD} , by inputting the relative volumes of both cross and diagonal peaks of the interacting nuclei, the mixing time of the experiment, and the peak volumes of the same couple of nuclei measured at zero mixing time (all the magnetization is in the diagonal peaks), the routine EXSYcalc can output the corresponding rate constant via an eigenvalues eigenvector method.¹⁰



Scheme S7.1 Graphical representation illustrates the desired interproton distance between H_A and H_B , the reference distances between H_1 and H_2 on the binaphthol, and between H_a and H_e on the CTV.

Herein, the distance between H_1 and H_2 on the binaphthol unit (2.29 Å) or that between the diastereotopic H_a and H_e (1.60 Å) on the CTV were chosen as the references (Scheme S7.1).

7.5.5 NMR characterization

Figure S7.17 ^1H NMR spectrum (CDCl_3 , 500.1 MHz, 298K) of *P*-SSS-SSS-1/*M*-RRR-RRR-1.Figure S7.18 ^{13}C NMR spectrum (CDCl_3 , 125.8 MHz, 298K) of *P*-SSS-SSS-1/*M*-RRR-RRR-1.

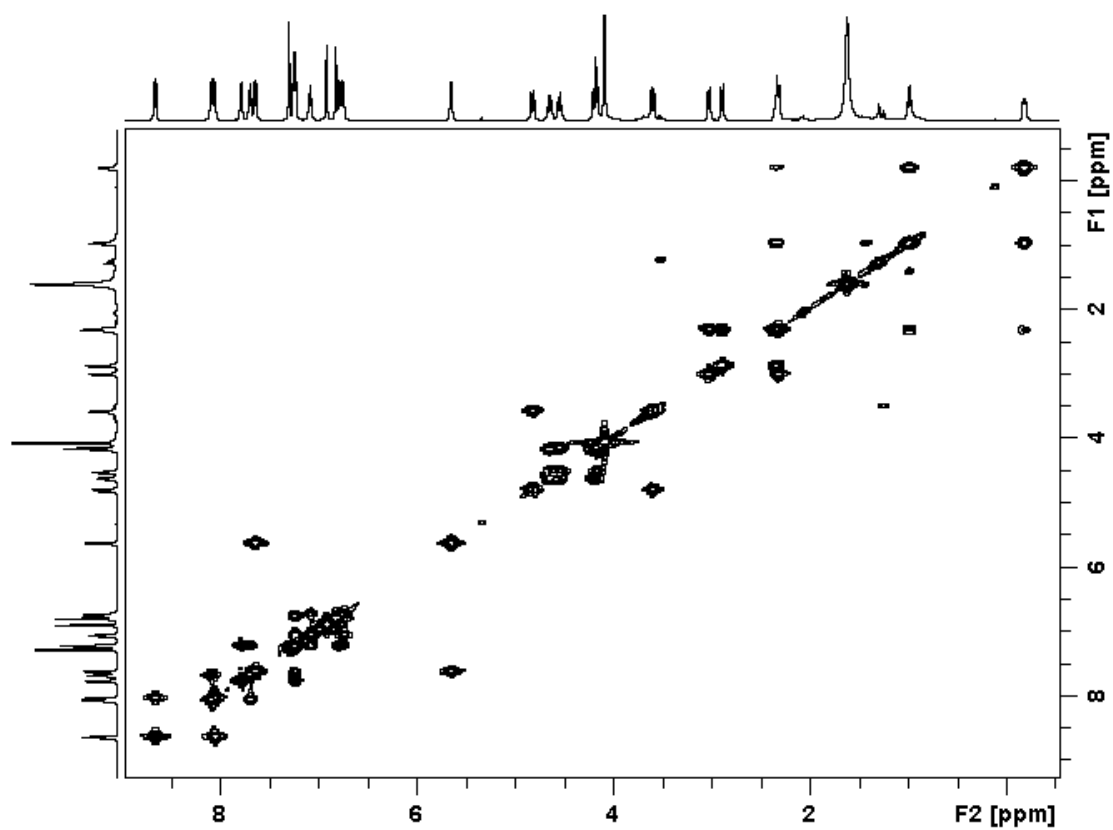


Figure S7.19 COSY spectrum (CDCl_3 , 500.1 MHz, 298K) of *P*-SSS-SSS-1/*M*-RRR-RRR-1.

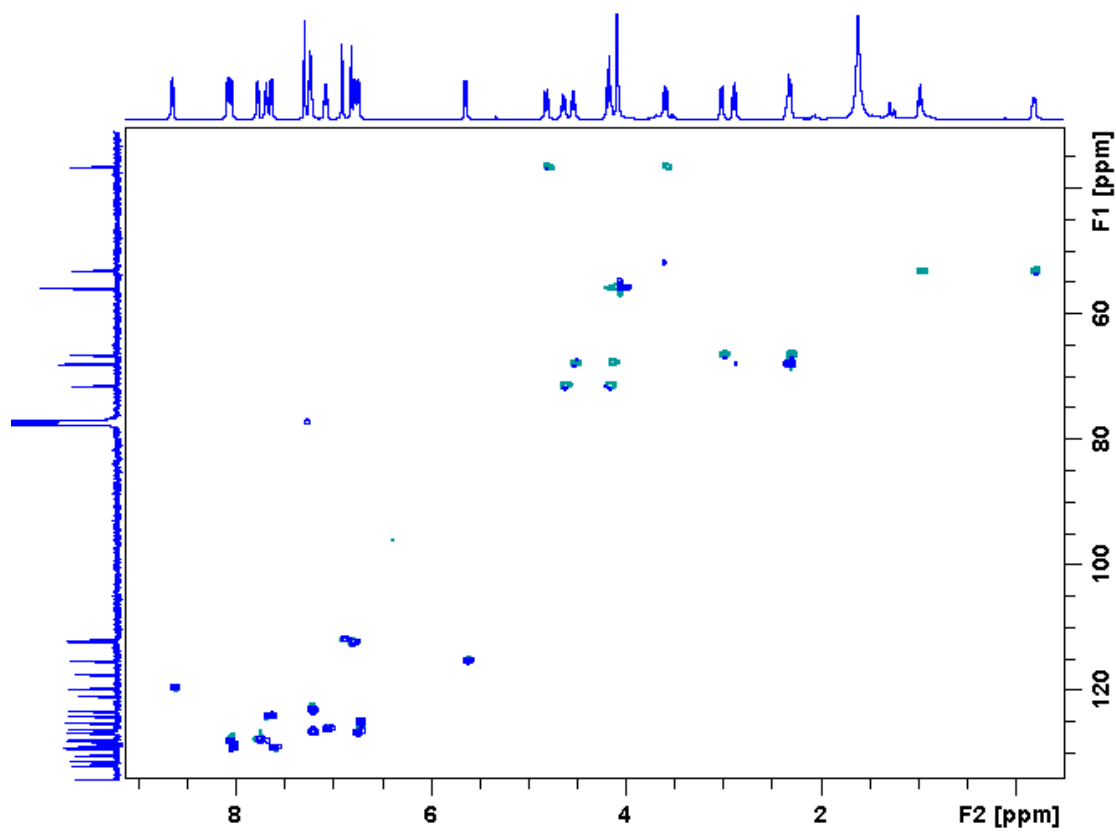


Figure S7.20 HSQC spectrum (CDCl_3 , 500.1 MHz, 298K) of *P*-SSS-SSS-1/*M*-RRR-RRR-1.

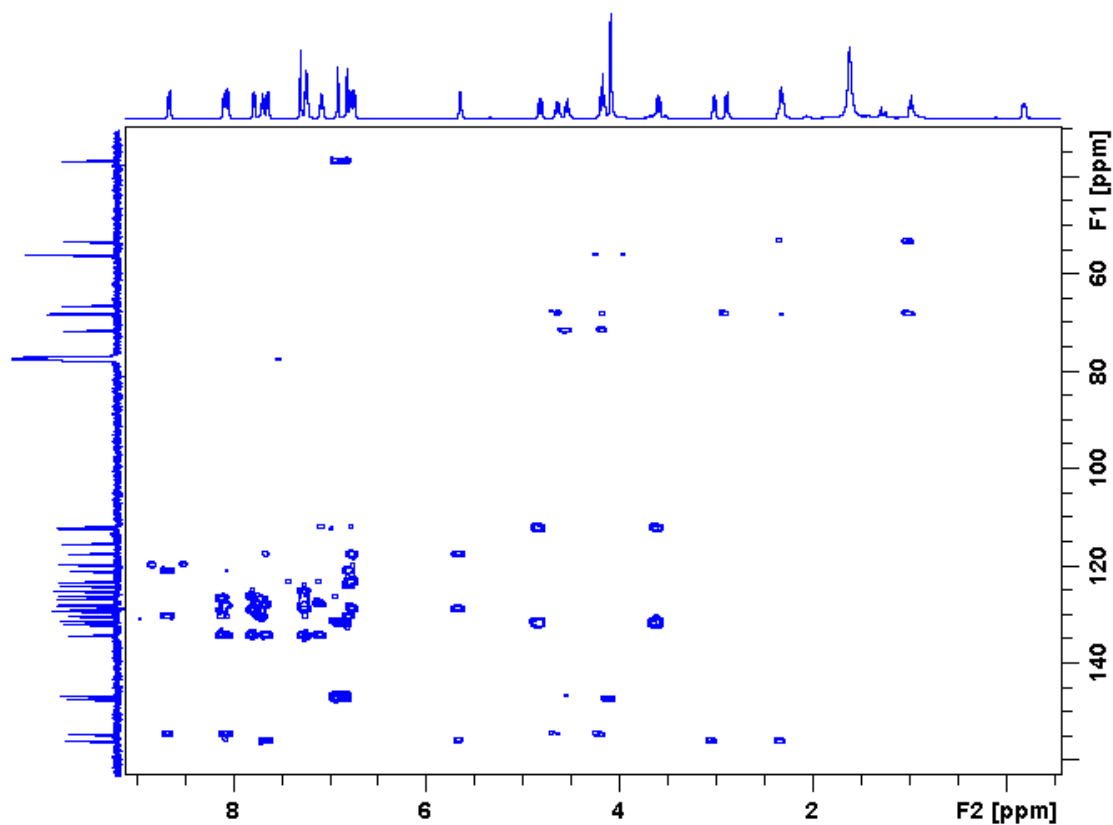


Figure S7.21 HMBC spectrum (CDCl₃, 500.1 MHz, 298K) of *P*-SSS-SSS-1/*M*-RRR-RRR-1.

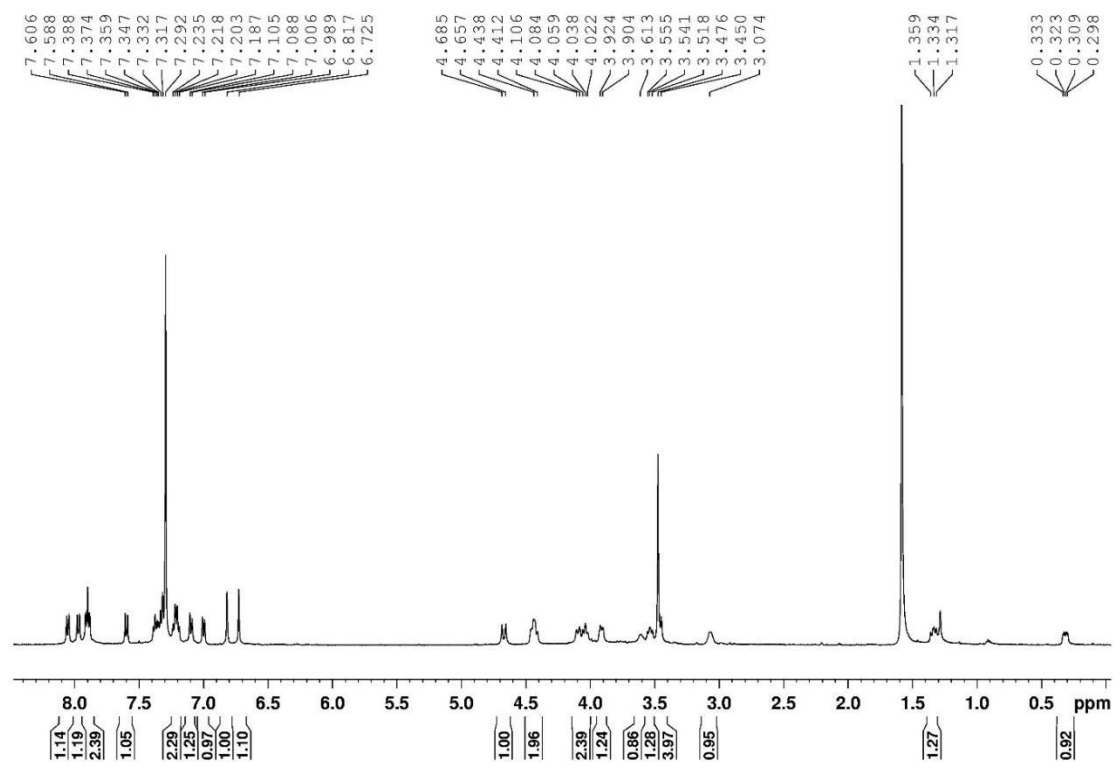


Figure S7.22 ¹H NMR spectrum (CDCl₃, 500.1 MHz, 298K) of *M*-SSS-SSS-1/*P*-RRR-RRR-1.

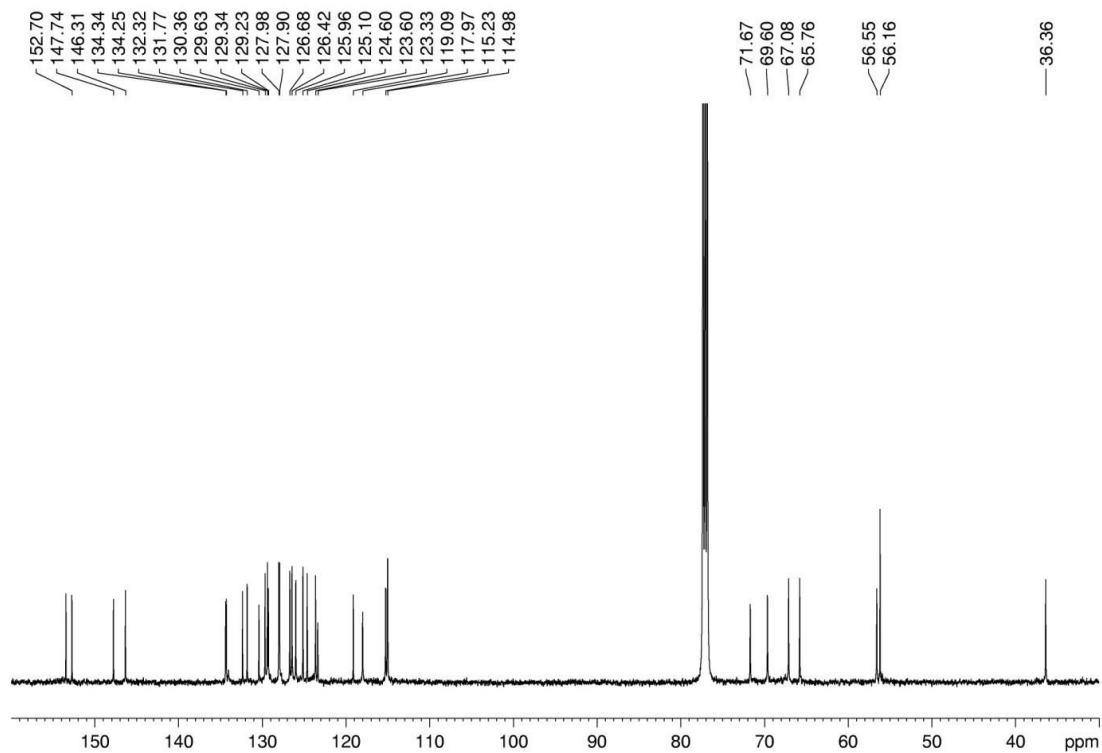


Figure S7.23 ^{13}C NMR spectrum (CDCl_3 , 125.8 MHz, 298K) of *M-SSS-SSS-1/P-RRR-RRR-1*.

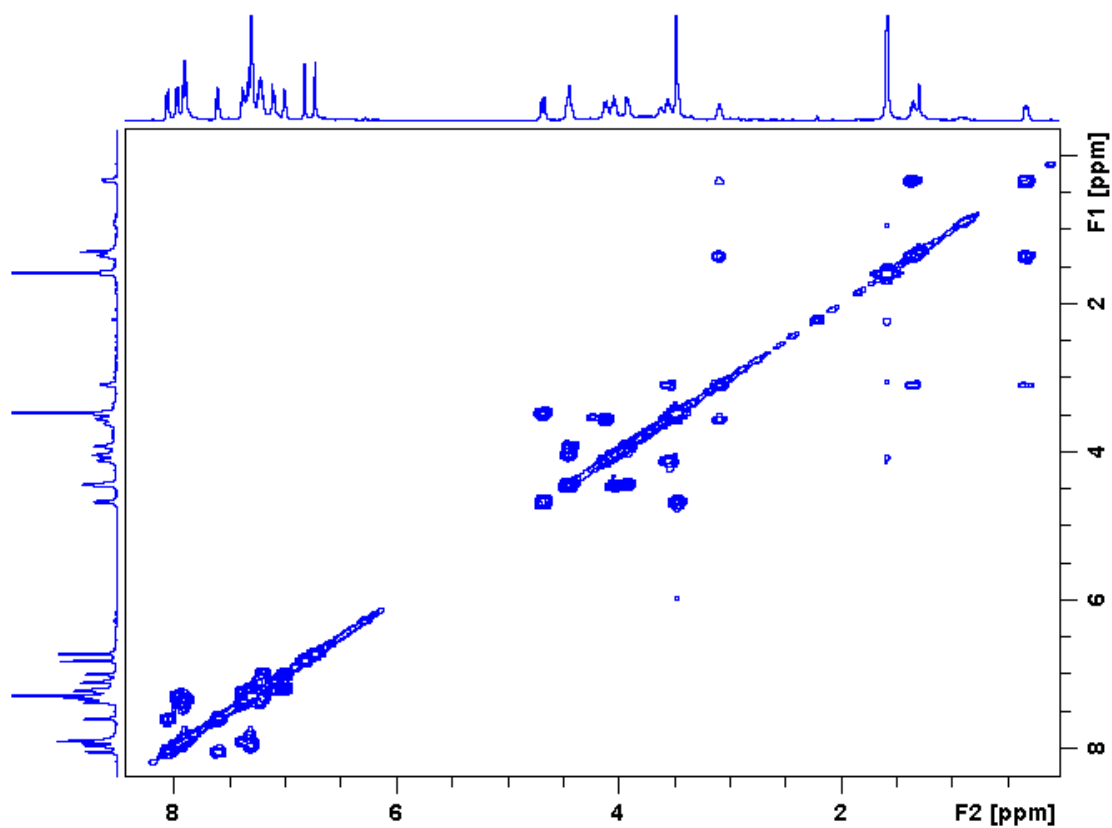


Figure S7.24 COSY spectrum (CDCl_3 , 500.1 MHz, 298K) of *M-SSS-SSS-1/P-RRR-RRR-1*.

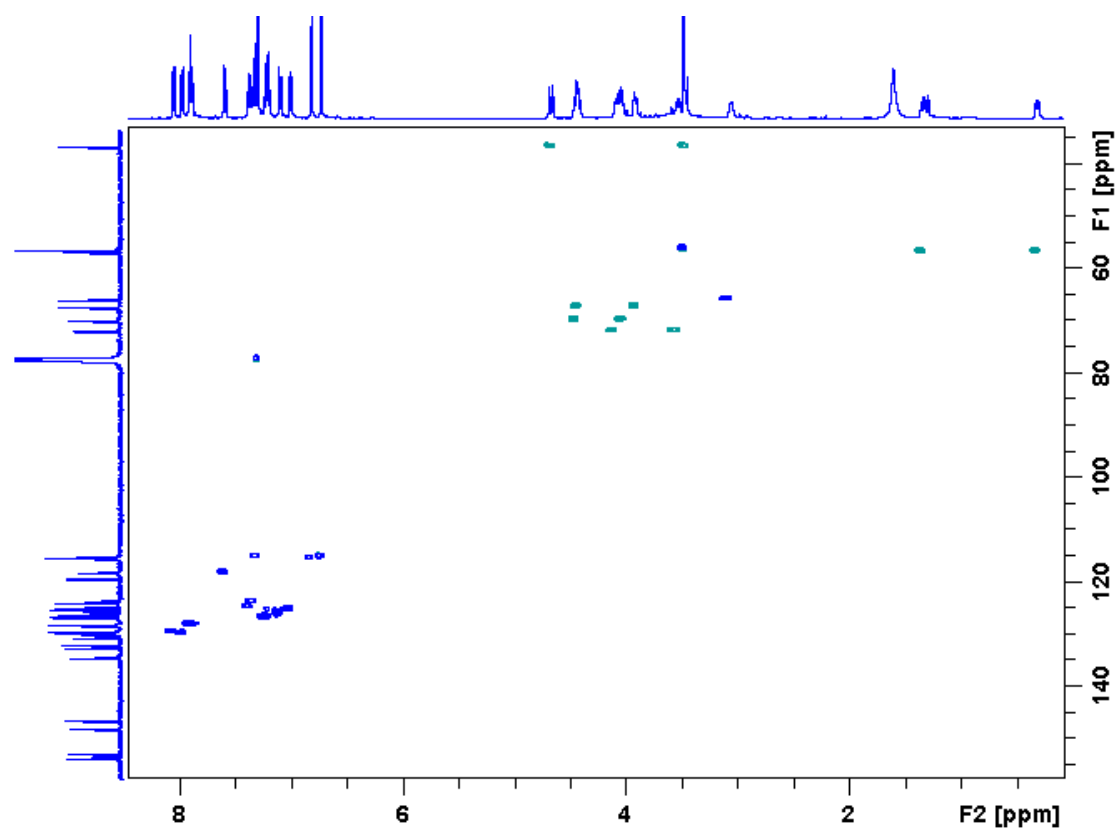


Figure S7.25 HSQC spectrum (CDCl₃, 500.1 MHz, 298K) of *M*-SSS-SSS-1/*P*-RRR-RRR-1.

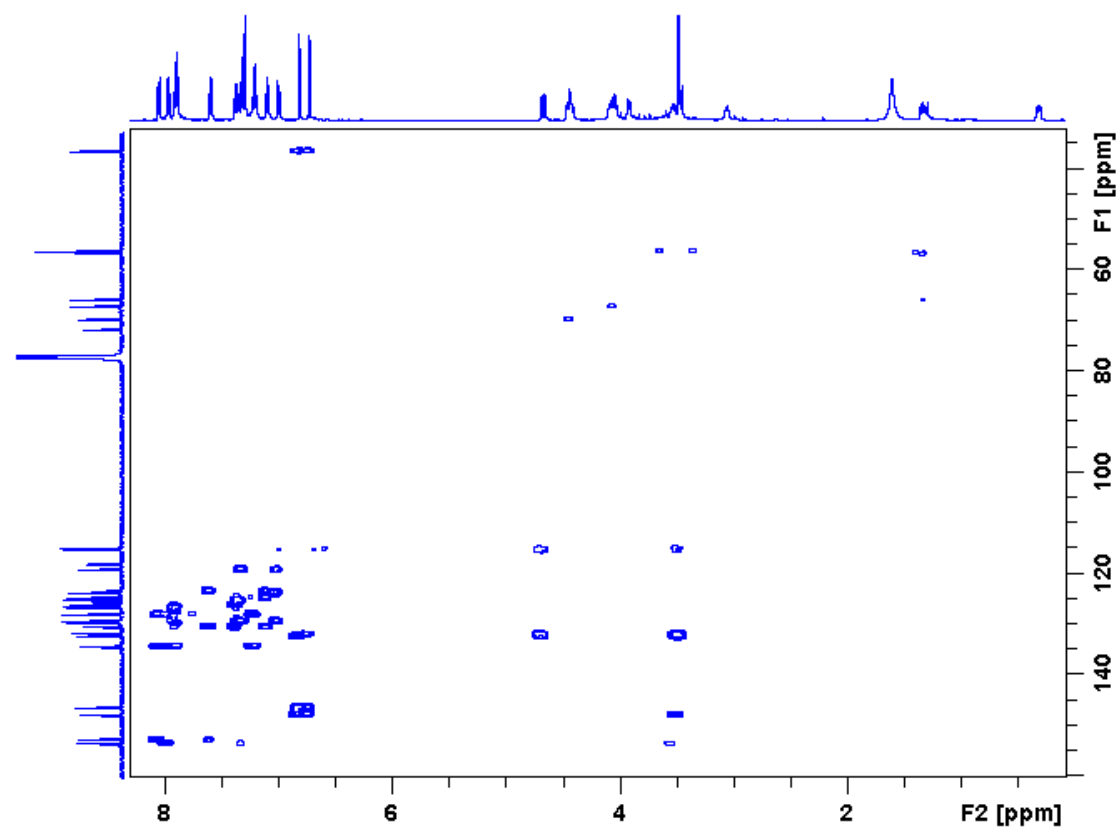


Figure S7.26 HMBC spectrum (CDCl₃, 500.1 MHz, 298K) of *M*-SSS-SSS-1/*P*-RRR-RRR-1.

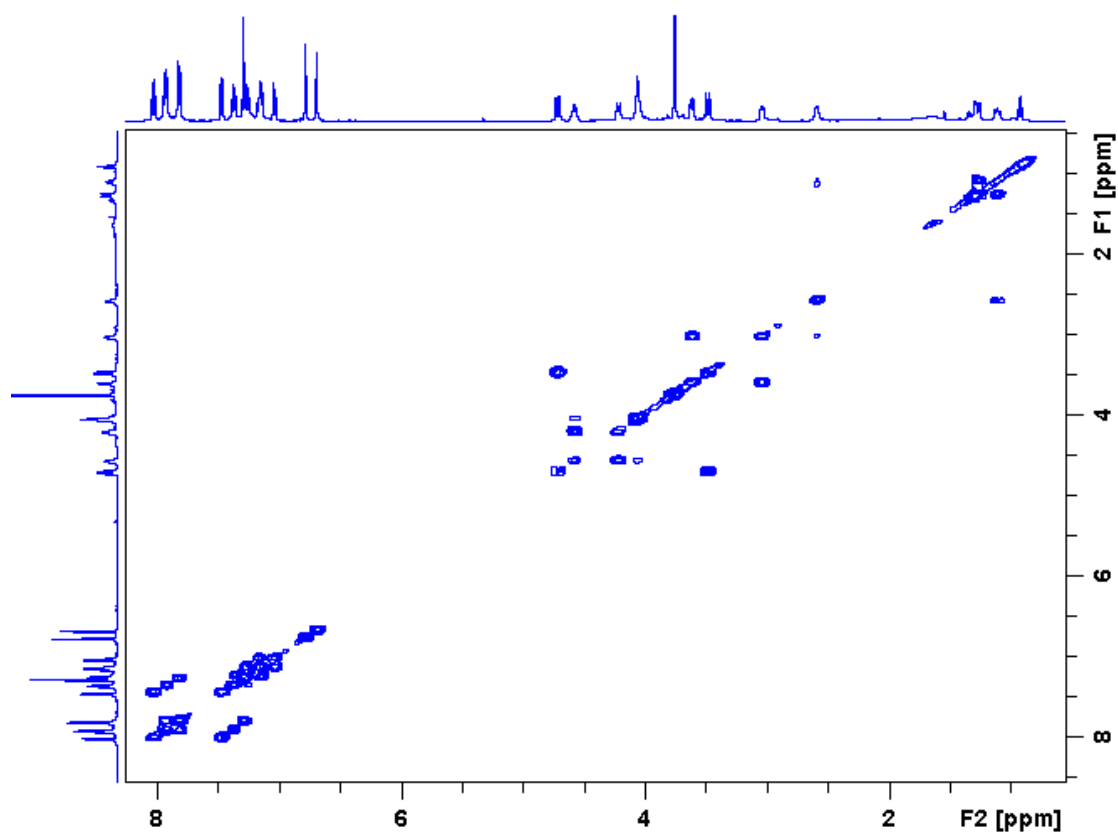


Figure S7.29 COSY spectrum (CDCl₃, 500.1 MHz, 298K) of *P-SSS-RRR-1/M-RRR-SSS-1*.

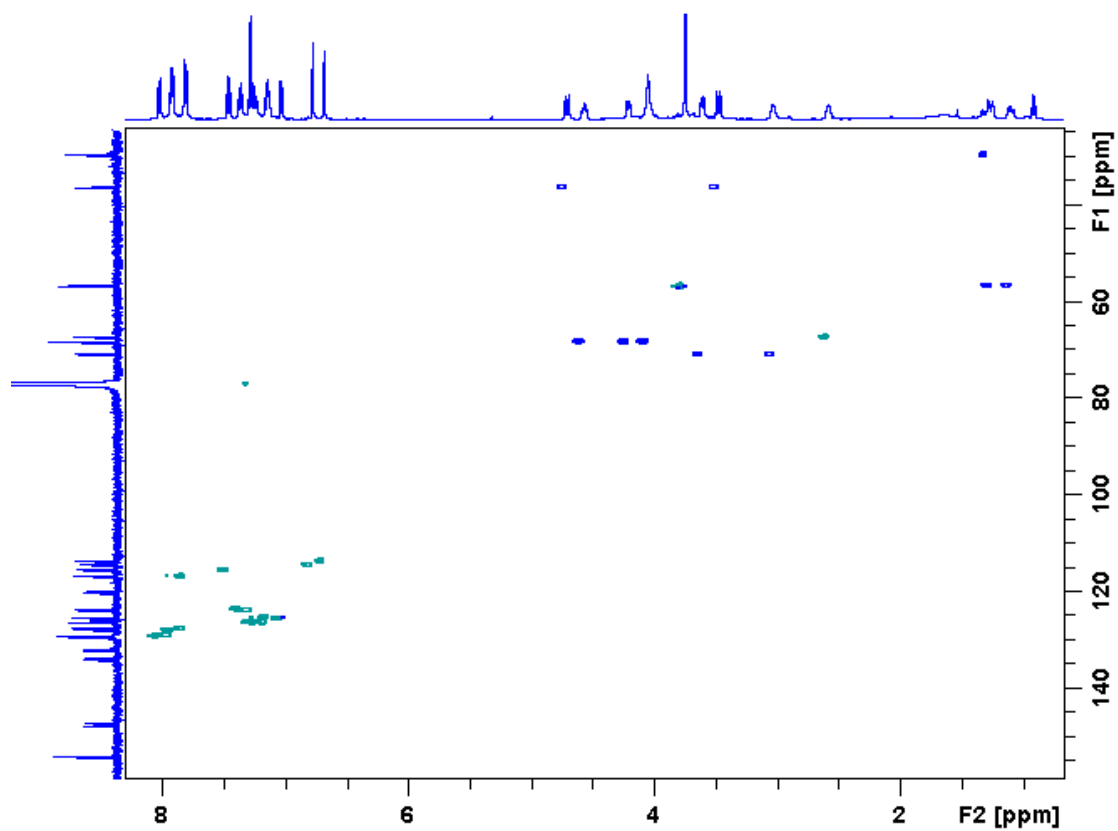


Figure S7.30 HSQC spectrum (CDCl₃, 500.1 MHz, 298K) of *P-SSS-RRR-1/M-RRR-SSS-1*.

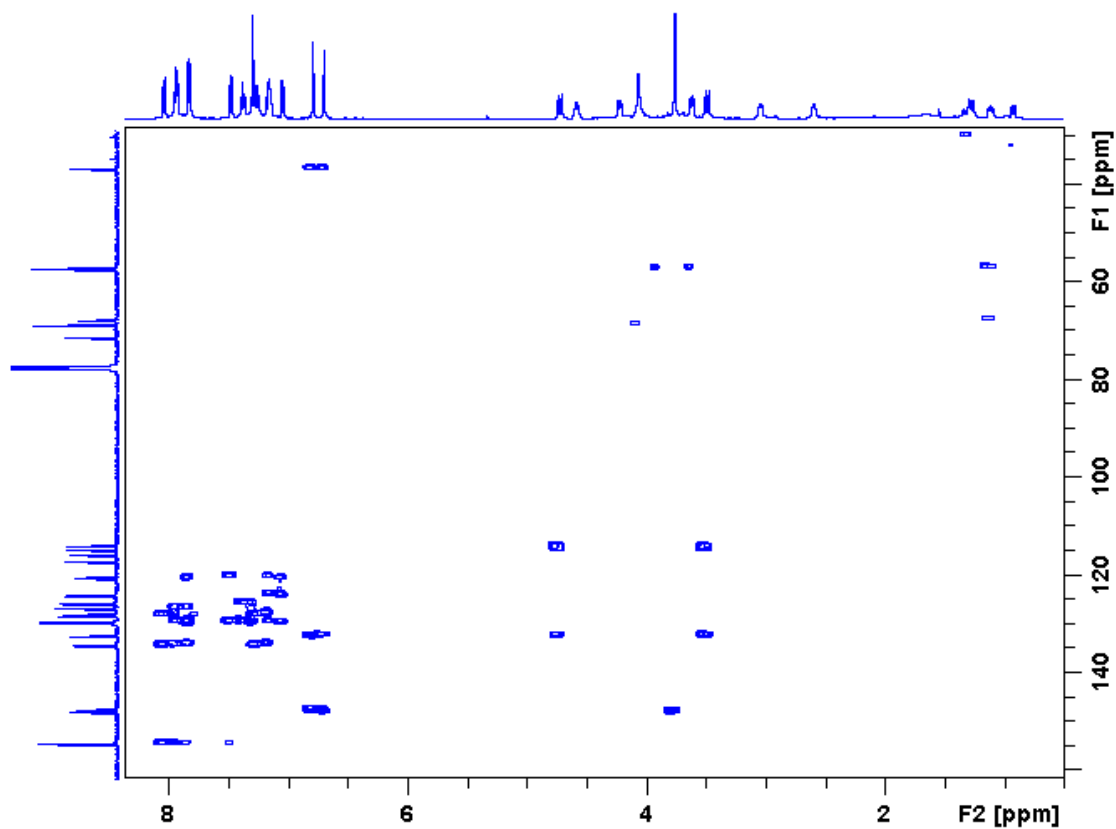


Figure S7.31 HMBC spectrum (CDCl_3 , 500.1 MHz, 298K) of *P*-SSS-RRR-1/*M*-RRR-SSS-1.

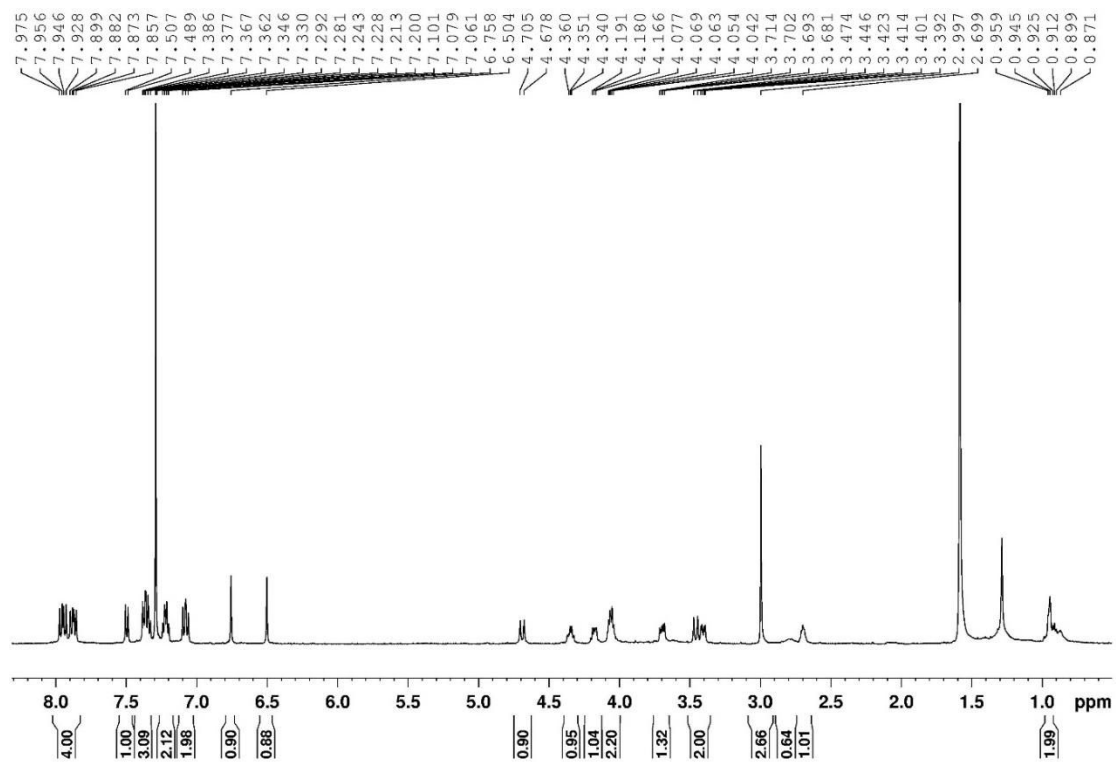


Figure S7.32 ^1H NMR spectrum (CDCl_3 , 500.1 MHz, 298K) of *M*-SSS-RRR-1/*P*-RRR-SSS-1.

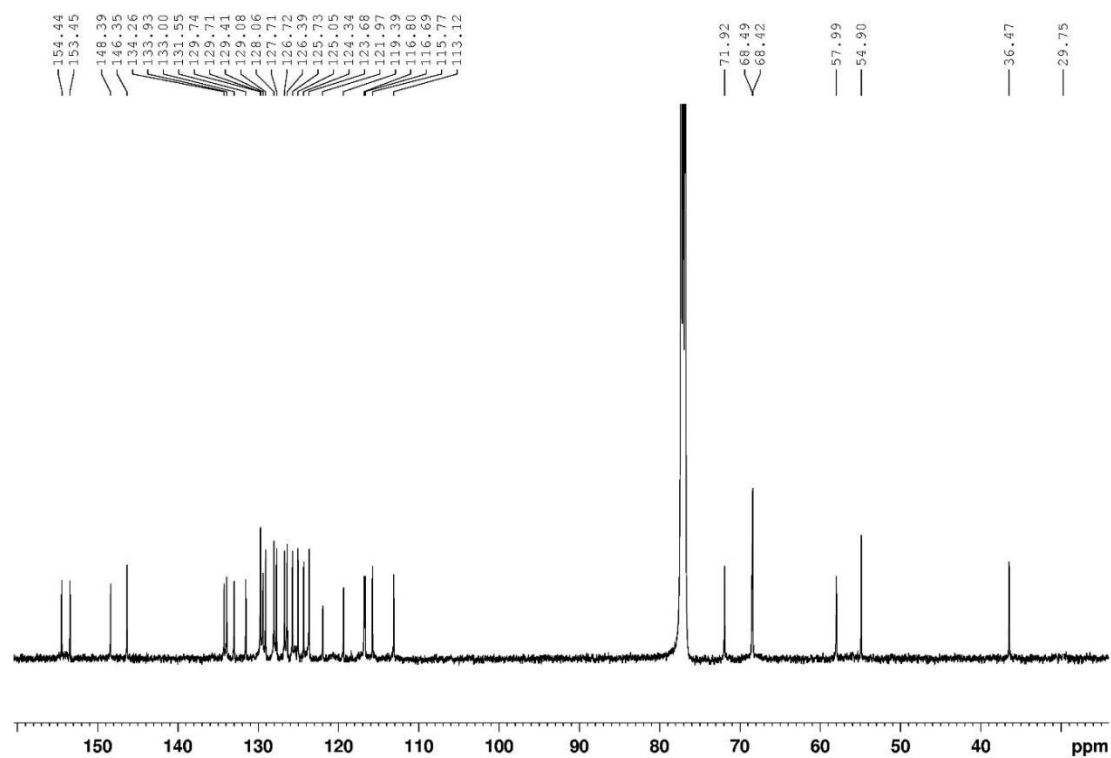


Figure S7.33 ^{13}C NMR spectrum (CDCl_3 , 125.8 MHz, 298K) of *M-SSS-RRR-1/P-RRR-SSS-1*.

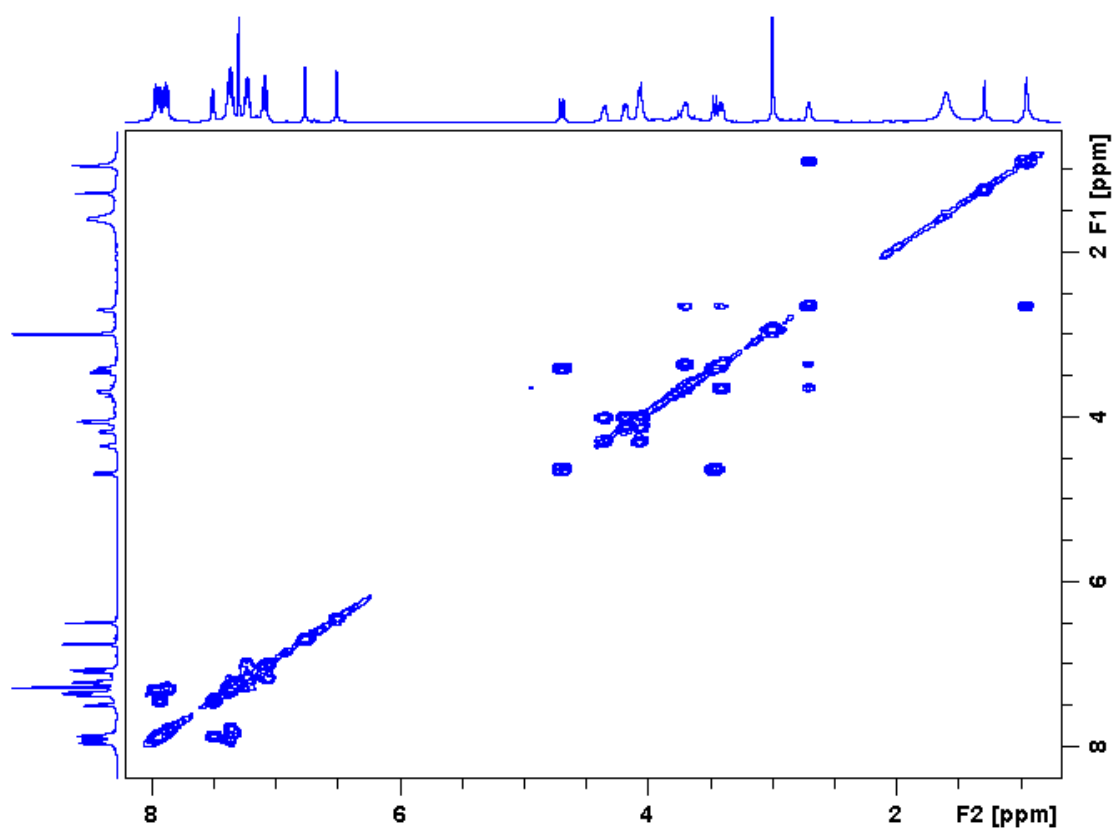


Figure S7.34 COSY spectrum (CDCl_3 , 500.1 MHz, 298K) of *M-SSS-RRR-1/P-RRR-SSS-1*.

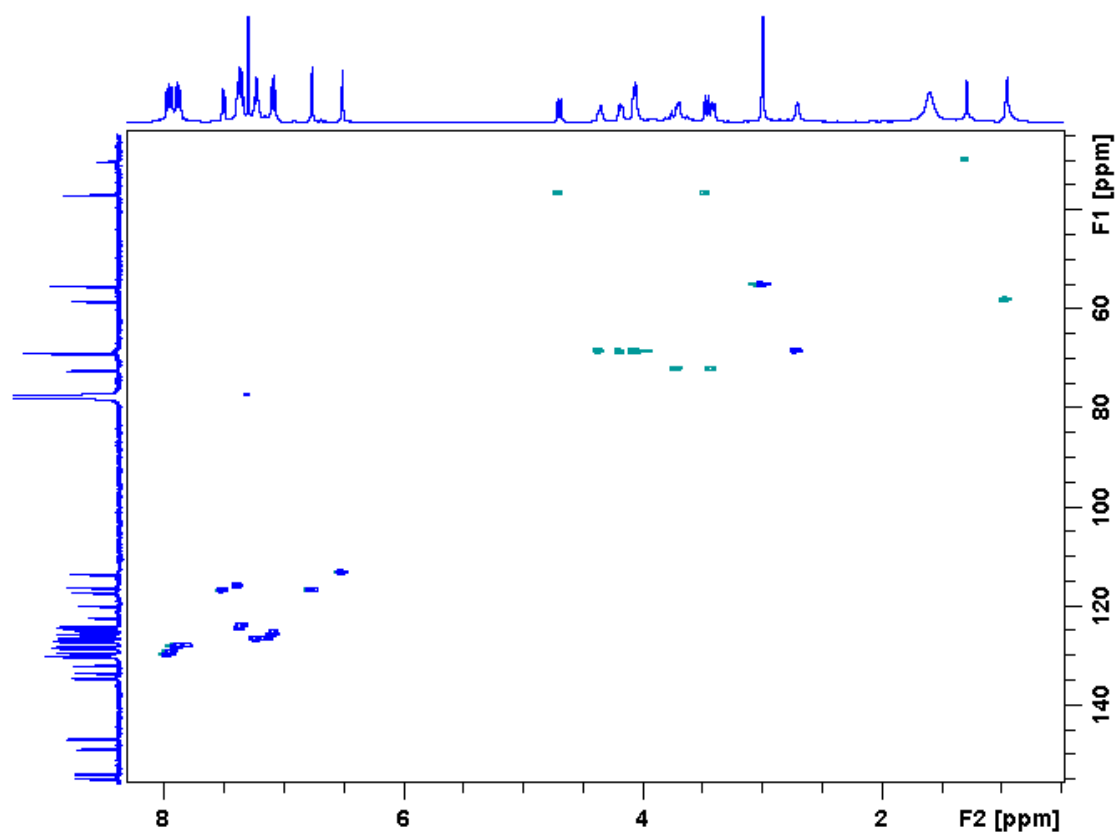


Figure S7.35 HSQC spectrum (CDCl₃, 500.1 MHz, 298K) of *M*-SSS-RRR-1/*P*-RRR-SSS-1.

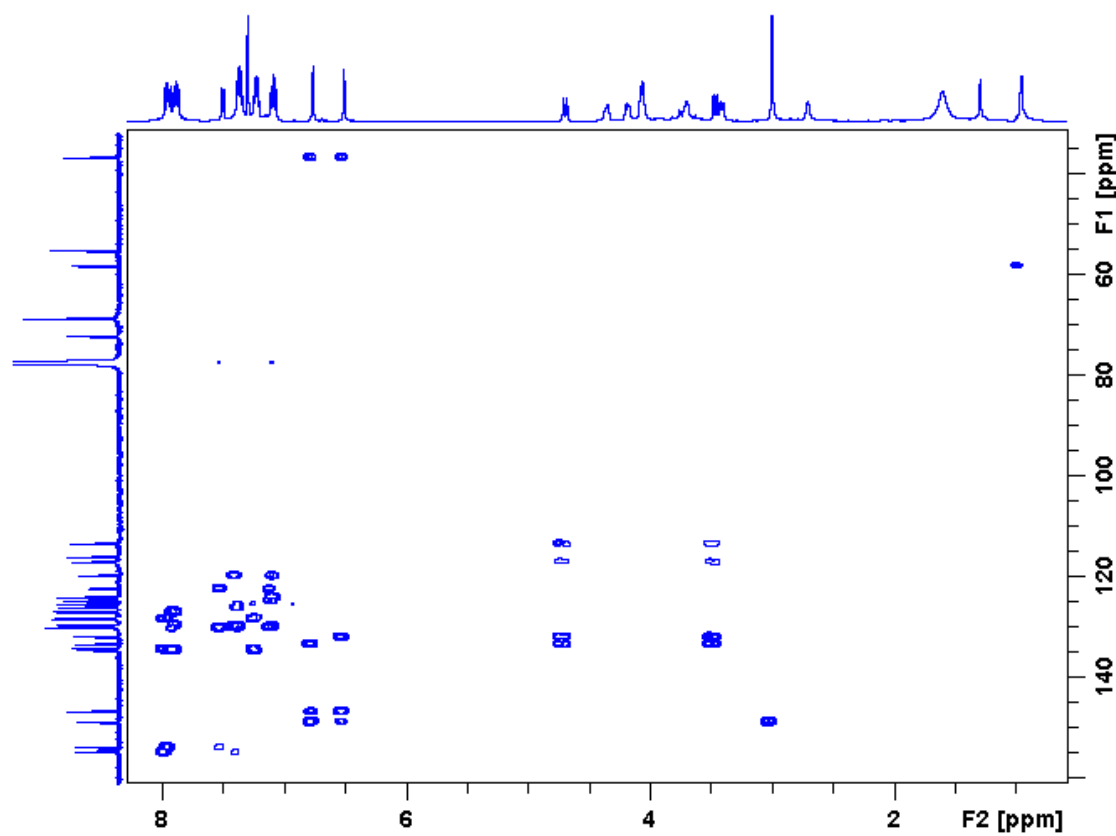


Figure S7.36 HMBC spectrum (CDCl₃, 500.1 MHz, 298K) of *M*-SSS-RRR-1/*P*-RRR-SSS-1.

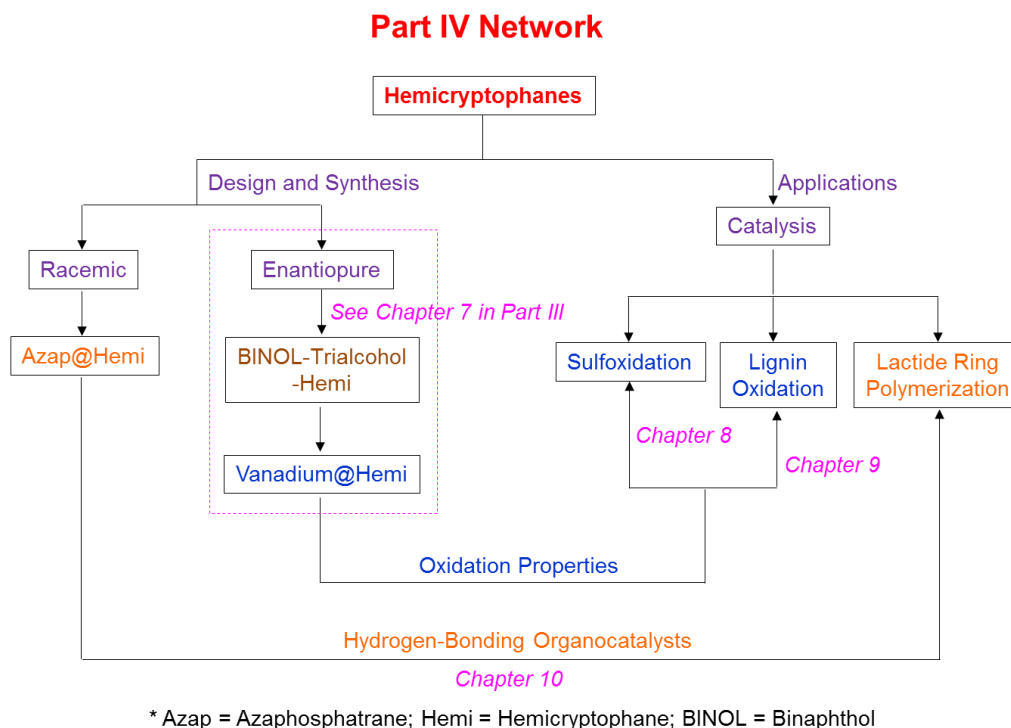
7.6 References

1. a) V. Balzani, A. Credi, F. M. Raymo, J. F. Stoddart, *Angew. Chem., Int. Ed.* **2000**, *39*, 3348-3391. b) S. Erbas-Cakmak, D. A. Leigh, C. T. McTernan, A. L. Nussbaumer, *Chem. Rev.* **2015**, *115*, 10081-10206. c) C. J. Brunns, J. F. Stoddart, *Acc. Chem. Res.* **2014**, *47*, 2186-2199. d) E. C. Harvey, B. L. Feringa, J. G. Vos, W. R. Browne, M. T. Pryce, *Coord. Chem. Rev.* **2015**, *282*, 77-86. e) J. W. Canary, *Chem. Soc. Rev.* **2009**, *38*, 747-756. f) C. A. Schalley, K. Beizai, F. Vögtle, *Acc. Chem. Res.* **2001**, *34*, 465-476. g) E. R. Kay, D. A. Leigh, F. Zerbetto, *Angew. Chem., Int. Ed.* **2007**, *46*, 72-191. h) J. H. Jordan, B. C. Gibb, *Chem. Soc. Rev.* **2015**, *44*, 547-585. i) R. Kay, D. A. Leigh, *Angew. Chem., Int. Ed.* **2015**, *54*, 10080-10088. j) J.-C. Chambron, J.-P. Sauvage, *New. J. Chem.* **2013**, *37*, 49-57. k) J.-P. Sauvage, C. Dietrich-Buchecker, *Molecular Catenanes, Rotaxanes and Knots: A Journey through the World of Molecular Topology*, ed. Wiley-VCH: Weinheim, **1999**. l) W. Wang, Y.-X. Wang, H.-B. Yang, *Chem. Soc. Rev.*, **2016**, *45*, 2656-2693.
2. a) B. E. Dial, P. J. Pellechia, M. D. Smith, K. D. Shimizu, *J. Am. Chem. Soc.* **2012**, *134*, 3675-3678. b) Y. Tian, C. D. Mao, *J. Am. Chem. Soc.* **2004**, *126*, 11410-11411. c) A. Martinez, L. Guy, J.-P. Dutasta, *J. Am. Chem. Soc.* **2010**, *132*, 16733-16734. d) T. R. Kelly, I. Tellitu, J. P. Sestelo, *Angew. Chem., Int. Ed.* **1997**, *36*, 1866-1868. e) M. Hughes, M. Jimenez, S. Khan, M. A. Garcia-Garibay, *J. Org. Chem.* **2013**, *78*, 5293-5302. f) T. Muraoka, K. Kinbara, Y. Kobayashi, T. Aida, *J. Am. Chem. Soc.* **2003**, *125*, 5612-5613. g) M. C. Jimenez, C. Dietrich-Buchecker, J.-P. Sauvage, *Angew. Chem., Int. Ed.* **2000**, *39*, 3284-3287. h) Y. Liu, A. H. Flood, P. A. Bonvallett, S. A. Vignon, B. H. Northrop, H.-R. Tseng, J. O. Jeppesen, T. J. Huang, B. Brough, M. Baller, S. Magonov, S. D. Solares, W. A. Goddard, C.-M. Ho, J. F. Stoddart, *J. Am. Chem. Soc.* **2005**, *127*, 9745-9759. i) T. Shima, F. Hampel, J. Gladysz, *Angew. Chem., Int. Ed.* **2004**, *43*, 5537-5540. j) M. J. Barrell, A. G. Campana, M. von Delius, E. M. Geertsema, D. A. Leigh, *Angew. Chem., Int. Ed.* **2011**, *50*, 285-290. k) P. Kovaricek, J.-M. Lehn, *Chem. Eur. J.* **2015**, *21*, 9380-9384. l) L. Greb, J.-M. Lehn, *J. Am. Chem. Soc.* **2014**, *136*, 13114-13117. m) N. Koumura, R. W. J. Zijlstra, R. A. van Delden, N. Harada, B. L. Feringa, *Nature* **1999**, *401*, 152-155. n) T.-C. Lee, M. Alarcon-Correa, C. Miksch, K. Hahn, J. G. Gibbs, P. Fischer, *Nano Lett.* **2014**, *14*, 2407-2412.
3. M. Barboiu, A.-M. Stadler, J.-M. Lehn, *Angew. Chem., Int. Ed.* **2016**, *55*, 4130-4154.
4. a) D. Ajami, L. Liu, J. Rebek Jr., *Chem. Soc. Rev.* **2015**, *44*, 490-499. b) K. I. Assaf, W. M. Nau, *Chem. Soc. Rev.* **2015**, *44*, 394-418. c) S. Zarra, D. M. Wood, D. A. Roberts, J. R. Nitschke, *Chem. Soc. Rev.* **2015**, *44*, 419-432. d) K. Kobayashi, M. Yamanaka, *Chem. Soc. Rev.* **2015**, *44*, 449-466. e) C. J. Brown, F. D. Toste, R. G. Bergman, K. N. Raymond, *Chem. Rev.* **2015**, *115*, 3012-3035. f) M. Raynal, P. Ballester, A. Vidal-Ferran, P. W. van Leeuwen, *Chem. Soc. Rev.* **2014**, *43*, 1660-1733. g) M. Yoshizawa, J. K. Klosterman, M. Fujita, *Angew. Chem., Int. Ed.* **2009**, *48*, 3418-3438. h) T. Brotin, J.-P. Dutasta, *Chem. Rev.* **2009**, *109*, 88-130.

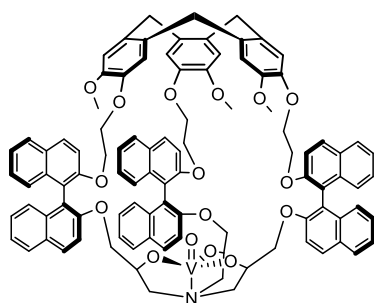
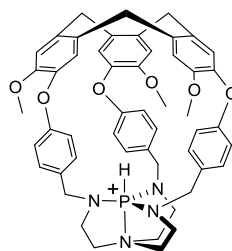
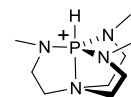
- i) N. S. Khan, J. M. Perez-Aguilar, T. Kaufmann, P. A. Hill, O. Taratula, O.-S. Lee, P. J. Carroll, J. G. Saven, I. J. Dmochowski, *J. Org. Chem.* **2011**, *76*, 1418-1424.
5. a) S. Wang, T. Sawada, K. Ohara, K. Yamaguchi, M. Fujita, *Angew. Chem., Int. Ed.* **2016**, *55*, 2103-2106. b) F. A. Arroyave, P. Ballester, *J. Org. Chem.*, **2015**, *80*, 10866-10873.
6. D. Zhang, J.-C. Mulatier, J. R. Cochrane, L. Guy, G. Gao, J.-P. Dutasta, A. Martinez, *Chem. Eur. J.* **2016**, *22*, 8038-8042.
7. a) O. Taratula, P. A. Hill, N. S. Khan, P. J. Carroll, I. J. Dmochowski, *Nat. Commun.* **2010**, *1*, 148. b) S. T. Mough, J. C. Goeltz, K. T. Holman, *Angew. Chem., Int. Ed.* **2004**, *43*, 5631-5635. c) G. Huber, T. Brotin, L. Dubois, H. Desvaux, J.-P. Dutasta, P. Berthault, *J. Am. Chem. Soc.* **2006**, *128*, 6239-6246.
8. D. Zhang, K. Jamieson, L. Guy, G. Gao, J.-P. Dutasta, A. Martinez, *Chem. Sci.* **2017**, *8*, 789-794.
9. M. Kieffer, B. S. Pilgrim, T. K. Ronson, D. A. Roberts, M. Aleksanyan, J. R. Nitschke, *J. Am. Chem. Soc.* **2016**, *138*, 6813-6821.
10. a) J. C. Cobas, M. Martin-Pastor, *EXSYCalc*, version 1.0; **2004**. b) A. Rotondo, E. Rotondo, G. A. Casella, G. Grasso, *Dalton Trans.* **2008**, 596. c) A. Lends, E. Olszewska, S. Belyakov, N. Erchak, E. Liepinsh, *Heteroat. Chem.* **2015**, *26*, 12.

Part IV. Hemicryptophanes as Supramolecular Catalysts

Preface



In **Chapter 7** of **Part III**, a series of vanadium(V)@hemicryptophane complexes bearing binaphthol groups as linkers have been prepared leading to a breathing motion at the molecular level. We notice that these vanadium@hemicryptophane complexes bearing inflated cavities are interesting supramolecular catalysts due to the oxidation properties of vanadium(V) as well as the well-defined hydrophobic cavities above the metal centers. Therefore, **Chapter 8** describes the utilization of these vanadium complexes as supramolecular catalysts for sulfoxidation. Moreover, in collaboration with Prof. R. Tom Baker at the University of Ottawa, these vanadium complexes were also used for the oxidation of lignin models, as the results discussed in **Chapter 9**.

Catalyst in **Chapters 8** and **9**Previous catalyst for CO₂ activationCatalyst in **Chapter 10**

Previously our group reported several azaphosphatrane-based hemicryptophanes, such as the one above, and they were found to be efficient catalysts for CO₂ conversion benefiting from the hydrogen-bonding donor ability of ⁺P–H group (Section 1.6.1.2). We propose that this unit might be also efficient hydrogen-bonding organocatalysts for activation of carbonyl

groups. Therefore, in collaboration with Dr. Brigitte Bibal at the University of Bordeaux, we also tested the catalytic properties of the azaphosphatrane-based hemicryptophanes for lactide ring-opening polymerization. Interestingly, a low reactivity with hemicryptophane catalysts was observed probably because the steric hindrance induced by the cage prevents the three reactants simultaneously close to the catalytic site. Instead, the model catalysts without cavities show good catalytic behavior. Hence, **Chapter 10** only describes the catalytic properties of the model catalysts for lactide ring-opening polymerization.

It should be noted that **Chapters 8** and **10** are respectively based partially on the following publications: *Chemical Sciences* (2017, 8, 789–794) and *European Journal of Organic Chemistry* (2016, 1619–1624). The work in **Chapter 9** is being prepared for submission. The numbers of compounds, figures, schemes and tables have been renumbered in each chapter from the beginning, and the numbers of compounds between chapters have no relationship. The Table of Contents in each chapter has been presented in the corresponding chapter cover. The cited references are listed at the end of each chapter.

Chapter 8. Tailored Oxido-Vanadium(V) Cage Complexes for Selective Sulfoxidation in Confined Spaces

This Chapter is based partially on the following manuscript—

Dawei Zhang, Kelsey Jamieson, Laure Guy, Guohua Gao, Jean-Pierre Dutasta,
Alexandre Martinez

Chem. Sci., **2017**, *8*, 789–794.

The work in this chapter was carried out at the ENS-Lyon.

Contents

8.1 Abstract	180
8.2 Introduction.....	180
8.3 Results and discussion	182
8.4 Conclusion.....	187
8.5 Experimental section.....	188
8.6 References.....	197

8.1 Abstract

Five sets of oxido-vanadium(V) complexes, including both cages and open structures, were prepared and tested in catalytic oxidation of sulfides. It was found that the hemicryptophane complexes comprising simultaneously cyclotrimeratrylene (CTV), binaphthol and oxido-vanadium(V) moieties are the most efficient supramolecular catalysts. The specific shape of the confined hydrophobic space above the metal center leads to a strong improvement of the yield, the selectivity and the rate of the reaction, compared to the other catalysts investigated herein. A remarkable turnover number (TON) of 10000 was obtained, which can be attributed both to the high reactivity and to the stability of the catalyst. Similar as enzymes, kinetic analysis shows that the mechanism of oxidation with the supramolecular catalysts obeys the Michaelis-Menten model, with initial rate saturation upon increasing substrate concentration. This enzyme-like behavior is also supported by the competitive inhibition and substrate size-selectivity observed, underlining the crucial role played by the cavity.

8.2 Introduction

Molecular cages, bearing a well-defined cavity with suitable endohedral functionalities, are very attractive since they can mimic biological systems, such as enzymes, to realize supramolecular catalysis of various reactions in their confined space.¹ These cage catalysts are capable of surrounding the surfaces of the reactants imposing specific orientation and conformation of the substrate in the vicinity of the catalytic site, leading to new and original reactivity.² Importantly, the goal of using such systems as true synthetic analogues of enzymes requires not only a high selectivity but also the enhancement of the reaction rates, like in enzymatic reactions.³ However, product inhibition using supramolecular catalysts is commonly observed, since the high affinity of the product with the cavity can prevent further catalytic cycles.⁴ Consequently, relatively large catalyst loadings are frequently required and low turnover numbers (TONs) are usually obtained. This issue has become one of the biggest challenges in supramolecular catalysis.^{4a} A pioneering work presenting high-turnover catalysis with supramolecular catalysts was reported by Raymond and Bergman groups in 2011.⁵ They incorporated a ruthenium(II) cation into a supramolecular assembly, which was active in the isomerization of allyl alcohols with turnovers reaching 1070. Recently, using the same assembly, high TONs (> 300) were also reached in alkyl-alkyl reductive elimination catalyzed by the encapsulated gold(III) or platinum(IV) complex.^{2j}

Although tremendous advances have been made in the development of self-assembled hosts for guest encapsulation and transformation, it should be noted that covalent cages present several advantages, such as their stability and easier endohedral functionalization.^{2n-p,6} Among the covalent cage compounds, hemicryptophanes, which are constructed from a cyclotrimeratrylene (CTV) moiety and another different C₃ symmetrical unit, have recently received a growing interest. The endohedral functionalization of their cavities via covalent bonds is versatile, giving rise to various excellent supramolecular catalysts presenting improved selectivity, reactivity, TON and/or stability compared to the

related model catalysts which lack a cavity.⁷ For instance, an oxido-vanadium(V) active site was attached inside the hydrophobic cavity of hemicyptophanes (complexes in Set III, Figure 8.1), which were efficient in oxidation of the hydrophobic sulfide substrate into the hydrophilic sulfoxide product with 180 turnovers.^{7e}

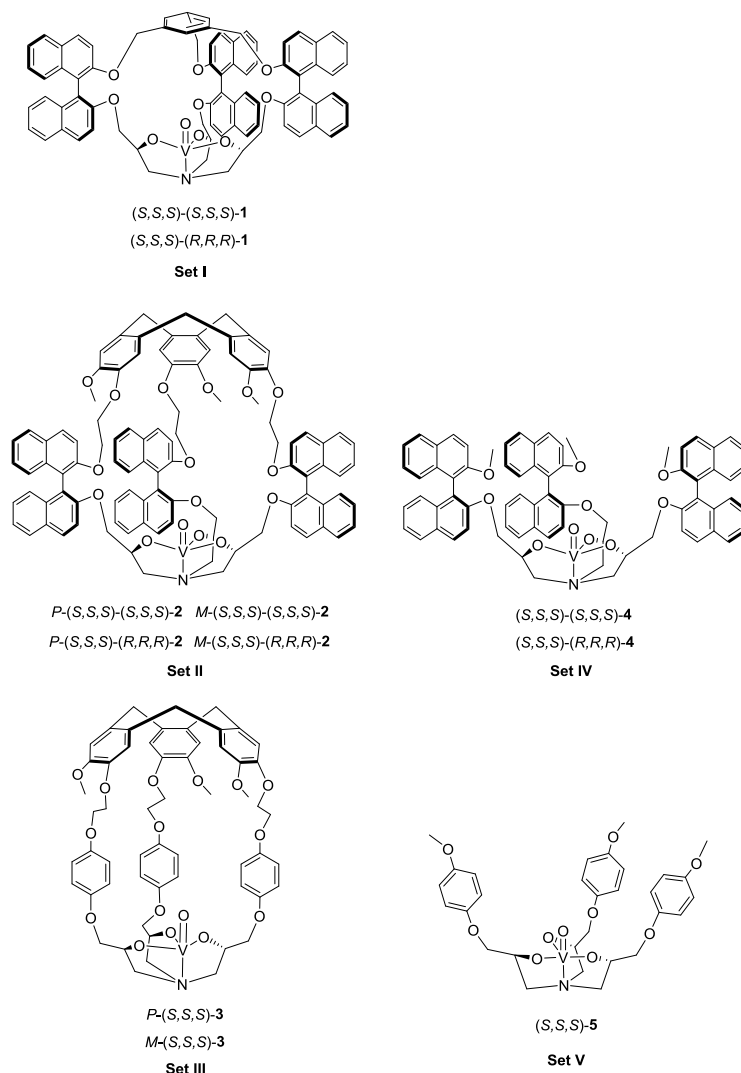


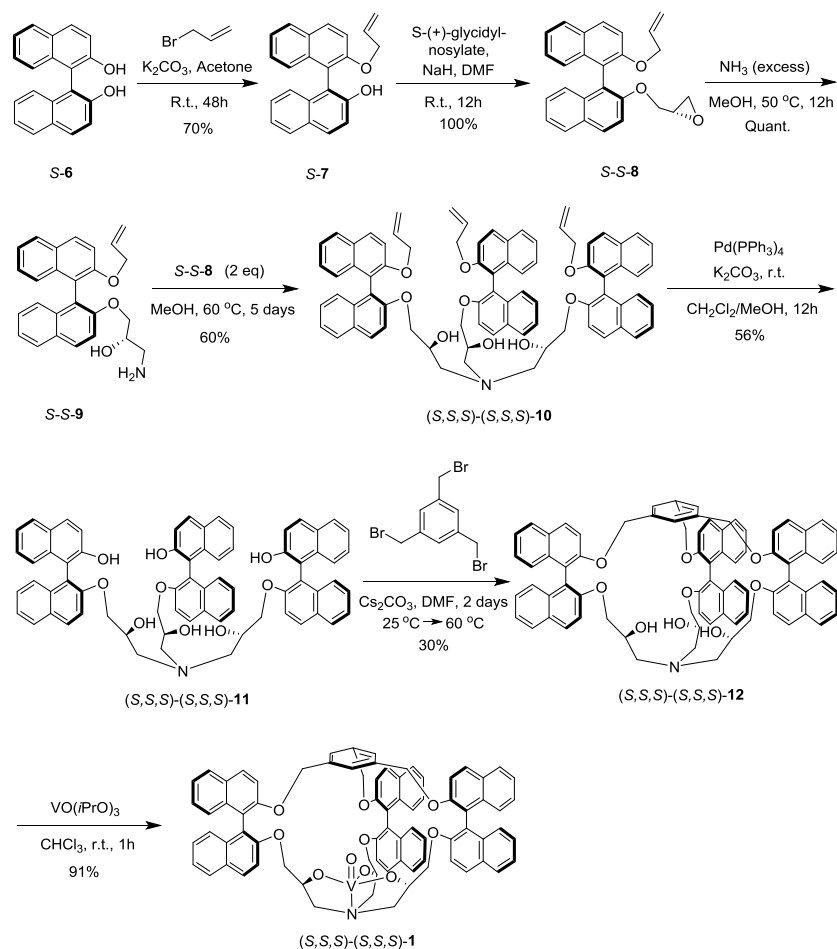
Figure 8.1 Structures of the five sets of oxido-vanadium(V) complexes.

In the present work, we have designed hemicyptophane derivatives containing binaphthol moieties (complexes in Set II, Figure 8.1), aiming at constructing more hydrophobic cavities. In addition, compared with the catalysts in Set III, the location of the bulky binaphthol units in the linkers can isolate more efficiently the heart of the cavity from the bulk solution, thus the effect of the confinement in stabilizing a transition state should be more pronounced. We have also prepared the oxido-vanadium(V) complexes of the related open structure (complexes in Set IV and V) and of cages with smaller cavity size (cage complexes in Set I) to demonstrate the necessity of having a cavity and the essential role of its size. Sulfoxidation, an important oxidation reaction due to the importance of sulfoxides in the synthesis of pharmaceutical and agrochemical products,⁸ was chosen as the model reaction. It was found that the new hemicyptophane complexes (Set II) combining both a CTM moiety and binaphthol units are most efficient for the oxidation of thioanisole, exhibiting a TON of 10000,

a remarkable TON for a supramolecular cage catalyst. Mechanism studies show that the catalytic behaviors exhibit the Michaelis-Menten kinetics, competitive inhibition and substrate size-selectivity, suggesting that the reaction occurs inside the cavity of the hemicryptophanes.

8.3 Results and discussion

8.3.1 Design and synthesis



Scheme 8.1 Synthesis of the complex (S,S,S)-(S,S,S)-1.

The synthesis of the oxido-vanadium complexes **3** and **5** have been previously reported.^{7e,9} Complexes **2** and **4** were obtained from the corresponding stereoisomers¹⁰ by reaction with vanadium(V)-oxytriisopropoxide in CHCl_3 at room temperature (r.t.) with excellent yields (> 90%). The ^1H NMR spectra of each isomer of complexes **2** and **4** are consistent with a C_3 symmetry. The synthetic route for the vanadium complexes in set I, such as (S,S,S)-(S,S,S)-**1**, is shown in Scheme 8.1. Firstly, the enantiopure binaphthol **6** was mono-protected with an allyl group via the reaction of S-6 with 1 equiv. of allyl bromide in acetone in the presence of K_2CO_3 to give S-7. The enantiopure epoxide (S,S)-**8** was obtained by a regioselective nucleophilic substitution reaction of S-7 on commercially available (S)-(+)-glycidyl nosylate in DMF. An excess of ammonia in methanol was then reacted with (S,S)-**8** to give the primary

amine (*S,S*)-**9**. The C_3 symmetrical allyl-protected trialkanolamine (*S,S,S*)-(*S,S,S*)-**10** was obtained by a trimerization reaction of **9** with 2 equiv. of **8** in MeOH for 5 days. Compound **10** was subsequently deprotected to generate the phenol derivative (*S,S,S*)-(*S,S,S*)-**11**, followed by a [1+1] reaction with 1,3,5-tris(bromomethyl)benzene in DMF under high dilution conditions to give the cage (*S,S,S*)-(*S,S,S*)-**12**. Compared to our previously reported synthesis of compound **11** based on the deprotection of methoxy groups,¹⁰ this new pathway gives higher yield (56% vs. 33%) and displays an easier purification step. Finally, the oxido-vanadium complex (*S,S,S*)-(*S,S,S*)-**1** was obtained by the reaction of **12** with 1.0 equiv. of vanadium(V)-oxytriisopropoxide in $CHCl_3$. Derivative (*S,S,S*)-(*R,R,R*)-**12** was obtained following the same procedure starting from enantiopure binaphthol *S*-**6** and (*R*)-(-)-glycidyl nosylate. However, the subsequent complexation of vanadium failed to give the desired complex, even in the presence of an excess of vanadium(V)-oxytriisopropoxide, probably because of the more hindered conformation of the cavity.

8.3.2 Catalytic properties

These complexes were first tested in the oxidation of thioanisole into sulfoxide, using cumene hydroperoxide (CHP) as terminal oxidant with 1.5 mol% of catalyst loading in CH_2Cl_2 at 0 °C. The results at 180 min and their kinetics are shown in Table 8.1 and Figure S8.1, respectively. It can be seen that (i) with CHP as oxidant, all the supramolecular complexes in Set II are very efficient giving rise to high yields from 85% (*P*-(*S,S,S*)-(*R,R,R*)-**2**) to 93% (*P*-(*S,S,S*)-(*S,S,S*)-**2**) (Table 8.1, entries 2-5). The excellent selectivity is (> 91%) evidenced by the typical kinetic curves of both yield and conversion of *P*-(*S,S,S*)-(*S,S,S*)-**2** that are almost identical (Figure S8.2). (ii) In addition, the yields obtained with hemicryptophane catalysts **2** (entries 2-5) are also significantly higher than those obtained with the corresponding model catalysts **4**, which lack a cavity (entries 8 and 9), and the performances of catalysts **4** and **5** are very close, indicating that the cage structure is essential for efficient sulfoxidation. (iii) Noticeably, the hemicryptophane catalysts **2** are more effective than the smaller cage catalyst **1** (entry 1), highlighting the important role of the cavity size. (iv) Furthermore, the yields with the new hemicryptophane catalysts in Set II are much higher than those with the previous hemicryptophane catalysts in Set III (entries 6 and 7). The improvement of the hydrophobicity and the more pronounced confinement effect induced by these specific bulky binaphthol linkages could account for the enhancement of the reaction rates and yields. (v) It is also interesting to note that the kinetic curves, monitoring the yields as a function of time, are very close to each other among the catalysts in each set (Figure S8.1). Using *tert*-butyl hydroperoxide (TBHP) as a terminal oxidant led to similar trends in reactivity (Figure S8.3). Therefore, the order of the catalytic activity, *i.e.* Set II > Set I > Set III > Set IV ≈ Set V, emphasizes that only the cages containing simultaneously CTV, binaphthol and oxido-vanadium moieties can serve as highly efficient supramolecular catalysts. The specific shape of the confined hydrophobic space above the metal center efficiently isolates the substrate from the surrounding solvent and expels the hydrophilic product, leading to a strong improvement of the activity.² Moreover, the stabilization of the transition state with catalysts **2** may also account for this improvement since the oxygen transfer will give a partial positive charge on the sulfur atom in the transition state which can be better stabilized by the

numerous aromatic rings of the cage.

Table 8.1 Oxidation of thioanisol with CHP in the presence of catalyst.^a

Entry	Catalyst	Yield (%) ^b	Selectivity (%) ^b	
1	Set I (<i>S,S,S</i>)-(<i>S,S,S</i>)- 1	74	93	
2	<i>P</i> -(<i>S,S,S</i>)-(<i>S,S,S</i>)- 2	93	97	
3	Set II <i>M</i> -(<i>S,S,S</i>)-(<i>S,S,S</i>)- 2	88	94	
4		<i>P</i> -(<i>S,S,S</i>)-(<i>R,R,R</i>)- 2	85	91
5		<i>M</i> -(<i>S,S,S</i>)-(<i>R,R,R</i>)- 2	91	97
6	Set III <i>M</i> -(<i>S,S,S</i>)- 3	40	90	
7		<i>P</i> -(<i>S,S,S</i>)- 3	39	90
8	Set IV (<i>S,S,S</i>)-(<i>R,R,R</i>)- 4	16	64	
9		(<i>S,S,S</i>)-(<i>S,S,S</i>)- 4	15	50
10	Set V (<i>S,S,S</i>)- 5	16	89	

^a Conditions: 1.5 mol% catalyst, 1.0 equiv. of CHP, CH₂Cl₂, 0 °C, 180 min. ^b Yield and selectivity were determined by HPLC with benzophenone as internal standard. Selectivity is defined as the yield/conversion ratio.

To have more accurate evaluation on the ratio of the kinetic constants, the catalyst amount was decreased to 1.0 mol% while keeping other conditions identical and using CHP as oxygen source. As shown in Figure 8.2, the reaction rate with *P*-(*S,S,S*)-(*S,S,S*)-**2** is much faster than with other catalysts, and 91% yield has been reached within 120 min. Based on the initial rate, the kinetic constant with *P*-(*S,S,S*)-(*S,S,S*)-**2** was estimated to be 3-, 5- and 33-fold higher than with (*S,S,S*)-(*S,S,S*)-**1**, *M*-(*S,S,S*)-**3** and (*S,S,S*)-(*S,S,S*)-**4**, respectively, again emphasizing the efficiency of the new hemicryptophane complexes.

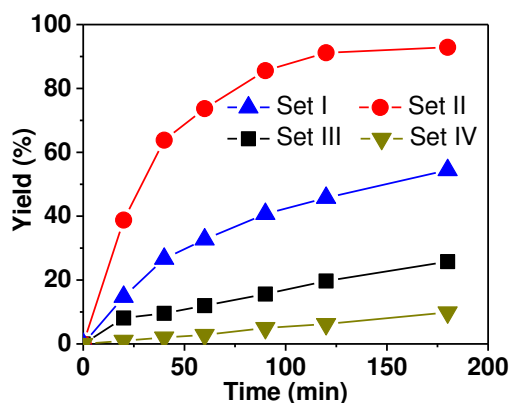


Figure 8.2 Oxidation of thioanisol with four typical catalysts: (*S,S,S*)-(*S,S,S*)-**1** in Set I, *P*-(*S,S,S*)-(*S,S,S*)-**2** in Set II, *M*-(*S,S,S*)-**3** in Set III and (*S,S,S*)-(*S,S,S*)-**4** in Set IV (1.0 mol% catalyst, 1.0 equiv. of CHP, 0 °C, CH₂Cl₂).

As the confinement can strongly improve the reaction rate and no product inhibition effect was exhibited, we wonder if the new hemicryptophane complexes in Set II can overcome the issue of low TON which is commonly observed in supramolecular catalysis.⁵ Thus, the oxidation of thioanisol was carried out with *M*-(*S,S,S*)-(*R,R,R*)-**2** at a low loading (0.01%) at r.t. As shown in Figure 8.3, a yield of 85% was obtained within 10 h, and a rarely observed remarkable TON up to 10000 was reached after 13 h. A turnover frequency (TOF) of 1200 h⁻¹ further indicates the high catalytic activity of this family of confined catalysts. Albeit the catalyst loading is extremely low, the high selectivity for the reaction was also retained (> 90%), suggesting the stability of the catalyst. To further evaluate this stability, catalytic cycles using the same catalyst (0.1 mol%) for oxidation of thioanisol in CH₂Cl₂ at room temperature was performed. It was found that no noticeable alteration in catalytic activity over four-cycle experiments was observed (Figure S8.4), emphasizing the high stability of the encaged catalyst. Obviously, the constraint cage structure protects the metal active site from degradation as we, and also other groups, have previously reported.^{5,7d}

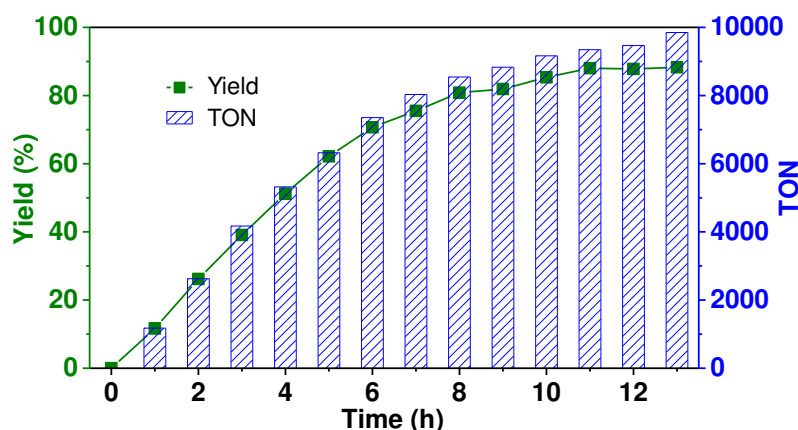


Figure 8.3 Oxidation of thioanisol catalyzed by catalyst *M*-(*S,S,S*)-(*R,R,R*)-**2** (0.01 mol% catalyst, 1.0 equiv. of CHP, r.t., CH₂Cl₂).

8.3.3 Mechanism investigation.

To understand whether the reaction catalyzed by hemicryptophane catalysts is similar to enzymatic catalysis, more detailed investigations, Michaelis-Menten kinetics, were explored. In enzymatic reactions, a substrate and enzyme typically participate in a reversible equilibrium with an enzyme-substrate complex, and usually rate saturation at high substrate concentrations can be observed.²⁸ As shown in Figure 8.4a, when the substrate concentration was increased while maintaining constant amounts of hemicryptophane catalyst *M*-(*S,S,S*)-(*R,R,R*)-**2** and oxidant, initial rate saturation was observed, consistent with the Michaelis-Menten rate profile. Strict compliance was further confirmed by re-plotting the data to give the Lineweaver-Bruck plot in Figure 8.4b with an excellent fit ($R^2 = 0.99$). The slope and y -intercept gave $K_m = 18.72$ mM and $V_{max} = 4.08 \times 10^{-2}$ mM s⁻¹. The latter value was used to calculate a turnover rate, K_{cat} ($V_{max}/[\text{Catalyst}]$), of 3.71×10^{-2} s⁻¹. To determine the rate enhancement, K_{cat}/K_{uncat} , the background experiment, the oxidation of thioanisol by CHP under the same conditions without any catalyst, was performed. It was observed that after 7 days, the conversion is < 2%, giving rise to a K_{uncat} of $< 3.3 \times 10^{-9}$ s⁻¹. Therefore, it can be

evaluated that the rate acceleration, $K_{\text{cat}}/K_{\text{uncat}}$, is larger than 1.12×10^7 , being an enzyme-like remarkable value.

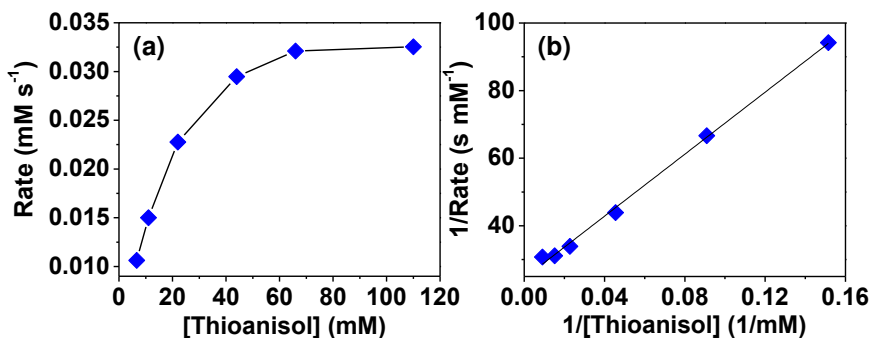


Figure 8.4 (a) Initial rate dependence on the concentration of thioanisol in CH₂Cl₂ with 1.1 mM hemicryptophane catalyst *M*-(*S,S,S*)-(R,R,R)-**2** and 110 mM CHP at 0 °C. (b) The corresponding Lineweaver-Burke line plotted by 1/rate as a function of 1/[Thioanisol].

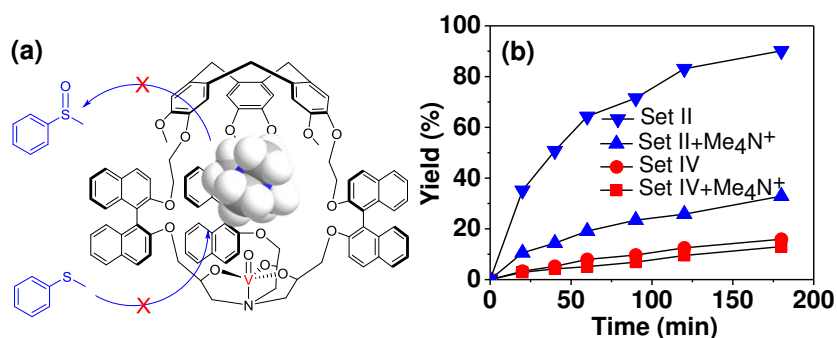


Figure 8.5 (a) Graphical representation of catalysis inhibition by Me₄N⁺. (b) Oxidation of thioanisol in the absence or presence of Me₄N⁺ catalyzed by *M*-(*S,S,S*)-(R,R,R)-**2** of Set II or (*S,S,S*)-(R,R,R)-**4** of Set IV (1.5 mol% catalyst, 1.0 equiv. of CHP, 0 °C, CH₂Cl₂).

Another characteristic aspect of enzymatic catalysis is the possible inhibition of the enzyme active site with a suitable nonreactive molecule. A bound inhibitor can exclude substrate from the cavity, thereby inhibiting the activity of the enzyme. The Me₄N⁺ cation was expected to be encapsulated by the hemicryptophane cage because of the possible cation- π interactions between this cationic guest and the numerous aromatic rings of the cage.¹¹ As shown in Figure S8.5, upon progressive addition of a concentrated solution of the host *M*-(*S,S,S*)-(R,R,R)-**2** to a solution of guest Me₄NPic in CD₂Cl₂, the ¹H NMR signals of the protons of Me₄N⁺ display up-field shifts, which can be attributed to the shielding effect induced by guest encapsulation. Modelling the titration curve with HypNMR2008 afforded a binding constant of 547 M⁻¹ for the 1:1 host-guest complex (Figure S8.5).¹² Hence Me₄N⁺ was considered as the competitive inhibitor, and oxidation of thioanisol in the presence of Me₄N⁺ catalyzed by either the cage *M*-(*S,S,S*)-(R,R,R)-**2** or the model (*S,S,S*)-(R,R,R)-**4** catalyst was carried out. Me₄N⁺Pic⁻ (1.33 catalyst equiv.) was added to the reaction mixture since this concentration corresponds to its solubility limit in CH₂Cl₂ at r.t., and also, based on the binding constant, on average more than half of the cavities can be occupied by the Me₄N⁺ guest. As expected, the catalytic activity of the cage *M*-(*S,S,S*)-(R,R,R)-**2** strongly decreased in the presence of Me₄N⁺, whereas that of the model compound (*S,S,S*)-(R,R,R)-**4** almost remained constant (Figure 8.5). Indeed, the reaction rate became 3.5-fold slower in the

presence of 1.33 equiv. of Me_4N^+ when the cage $M\text{-(}S,S,S\text{)-(}R,R,R\text{)-}2$ was used as the catalyst, while no obvious change was observed with the open model catalyst. These results evidence the crucial role played by the cavity and also indicate that the catalytic process occurs inside the cavity. Once the cavity is blocked, the benefit induced by the hydrophobic confinement is lost, hence the catalytic activity of the cage complex drops significantly.

To further elucidate the significant role of the cavity on the catalysis, catalytic oxidation of larger substrates, such as benzylphenyl sulfide (**B**) and naphthylmethyl phenyl sulfide (**C**), were performed to explore the substrate size-selectivity (Figure 8.6). Under the same conditions used for thioanisol (**A**), the new hemicyptophane complexes in Set II are still the most efficient catalysts for both substrates (**B** and **C**) displaying high yield and selectivity (Figures S8.6-S8.9). Interestingly, it was found that the reaction rate catalyzed by the smaller cage $(S,S,S)\text{-(}S,S,S\text{)-}1$ continually decreased with the substrate size increased (Figure 8.6). In contrast, the reactivity of $M\text{-(}S,S,S\text{)-(}R,R,R\text{)-}2$ first increased when changing the substrate from thioanisol (**A**) to benzylphenyl sulfide (**B**), followed by a remarkable drop for the oxidation of the largest naphthylmethyl phenyl sulfide (**C**) (Figure 8.6). Moreover, Michaelis-Menten kinetics for **B** and **C** with catalyst $M\text{-(}S,S,S\text{)-(}R,R,R\text{)-}2$ were also investigated (Figure S8.10-S8.11), and it was found that the values of K_{cat} are $3.71 \times 10^{-2} \text{ s}^{-1}$, $4.89 \times 10^{-2} \text{ s}^{-1}$ and $3.78 \times 10^{-2} \text{ s}^{-1}$ for substrates **A**, **B** and **C**, respectively, with a K_{m} of 18.72 mM, 17.13 mM and 18.33 mM. The smaller K_{m} of substrate **B** suggests a better binding of **B** by the cage **2** compared with those of **A** and **C**.³ Therefore, all these results indicate that benzylphenyl sulfide and naphthylmethyl phenyl sulfide are too sterically demanding to fully access the cavity of $(S,S,S)\text{-(}S,S,S\text{)-}1$, while the size of benzylphenyl sulfide is suitable and complementary for the cavity of $M\text{-(}S,S,S\text{)-(}R,R,R\text{)-}2$. This substrate size-dependent behavior further evidences that the cavity of the supramolecular catalysts plays an essential role for efficient catalysis mimicking enzymatic functions.

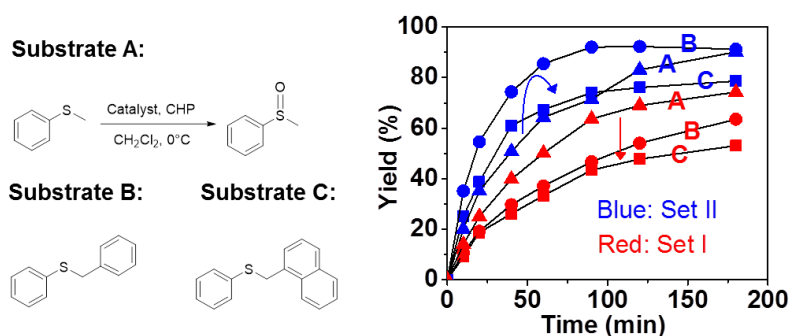


Figure 8.6 Oxidation of thioanisol (substrate **A**), benzylphenyl sulfide (substrate **B**), or naphthylmethyl phenyl sulfide (substrate **C**) with catalyst $M\text{-(}S,S,S\text{)-(}R,R,R\text{)-}2$ in Set II or $(S,S,S)\text{-(}S,S,S\text{)-}1$ in Set I (1.5 mol% catalyst, 1.0 equiv. of CHP, 0°C , CH_2Cl_2).

8.4 Conclusion

In summary, using the oxidation of sulfide as a model reaction, we have described herein five sets of oxido-vanadium(V) complexes, including both cages (Sets I-III) and open (Sets IV and V) structures. It was found that the complexes (Set II) simultaneously holding CTV, binaphthol and oxido-vanadium groups are the most efficient catalysts because of the

construction of the hydrophobic cavity with the right size, which is suitable to accommodate and convert the sulfide substrates, and to expel the product from the inner cavity. The oxidation of thioanisole, using the catalysts of Set II, displayed reaction rates 3-, 5- and 33-fold faster than those obtained with catalysts of Sets I, III and IV, respectively. The specific shape of the confined hydrophobic space above the metal center induced by the bulky binaphthol linkages, leads to strong improvement of the yield, the selectivity and also the catalytic activity. Hence, the present case constitutes a rare example of supramolecular catalysts that exhibit extremely high levels of efficiency with 10000 turnovers. The catalytic reaction obeys the Michaelis-Menten model of enzyme kinetics, and competitive inhibition of this reaction was observed using Me_4N^+ as an inhibitor. The substrate size-selectivity of the cage catalysts further indicate that the reaction occurs inside the cavity of the hemicryptophane hosts mimicking enzymatic functions. Catalytic activities of these new supramolecular catalysts toward other reactions benefiting from the encapsulated vanadium(V) active sites, like oxidation of lignin models, are in progress in our laboratory.

8.5 Experimental section

8.5.1 Materials and instrumentation

All solvents used were of commercial grade and were dried prior to use over molecular sieves. ^1H NMR and ^{13}C NMR spectra were recorded on a Bruker Avance spectrometer operating at 500.10 MHz and 125.76 MHz for ^1H NMR and ^{13}C NMR spectra, respectively. ^1H NMR chemical shifts (δ) are reported in ppm and referenced to the protonated residual solvent signal. Mass spectra were recorded by the Centre de Spectrométrie de Masse, Lyon. HPLC analyses were performed on an Agilent-1100 apparatus (binary pump, autosampler, column, thermostat, and diode array detector) using Chiralpack IC (0.46 × 25 cm) column.

8.5.2 Synthesis and characterization

S-7/R-7: A solution of K_2CO_3 (3.7 g, 27 mmol) and (*S*)-(-)-1,1'-Bi(2-naphthol) (6.0 g, 20.9 mmol) in acetone (45 mL) was stirred at room temperature for 1 h under argon. Then 5 mL acetone solution of allyl bromide (2.8 g, 23 mmol) was added in one portion. After reflux under argon for 48 h, the solvent was evaporated. The mixture was then dissolved in CH_2Cl_2 , and washed with distilled water for 3 times. The organic phase was dried over anhydrous Na_2SO_4 , filtrated and evaporated. After column chromatography over silica gel (CH_2Cl_2 /petroleum ether 3:2), 4.8 g (70%) *S*-7 was obtained as a white solid. ^1H NMR (CD_2Cl_2 , 298K, 500.1 MHz): δ 8.08 (d, J = 9.1 Hz, 1H); 7.94 (d, J = 8.8 Hz, 2H); 7.90 (d, J = 8.1 Hz, 1H); 7.50 (d, J = 9.1 Hz, 1H); 7.41 (t, J = 7.4 Hz, 1H); 7.36-7.29 (m, 3H); 7.24 (t, J = 8.5 Hz, 1H); 7.16 (d, J = 8.5 Hz, 1H); 7.05 (d, J = 8.4 Hz, 1H); 5.86-5.80 (m, 1H); 5.12-5.08 (m, 2H); 5.03 (s, 1H); 4.63-4.61 (m, 2H). ^{13}C NMR (CD_2Cl_2 , 298K, 125.7 MHz): δ 155.0, 151.3, 134.0, 133.8, 133.2, 130.8, 129.7, 129.6, 129.1, 128.2, 128.1, 127.1, 126.4, 124.6(9), 124.6(5), 124.2, 123.2, 117.4, 116.9, 116.0, 115.4, 115.1, 69.8. **ESI-HRMS** m/z : found 349.1196, calcd for $\text{C}_{23}\text{H}_{18}\text{NaO}_2$ [$\text{M}+\text{Na}$] $^+$ 349.1199.

S-S-8: To NaH (131 mg, 3.28 mmol) (60% suspension in oil), a solution of *S*-7 (622 mg, 1.91

mmol) in DMF (22 mL) was added at room temperature. After stirring under argon for 60 min, a solution of *S*-(+)-glycidyl nosylate (621 mg, 2.40 mmol) in DMF (8 mL) was added. The mixture was stirred at room temperature under argon for 24 h. Then the reaction was quenched by adding saturated NH₄Cl solution and the resulting mixture was diluted with water and extracted with ethyl acetate. The organic phase was washed with water, dried over anhydrous Na₂SO₄, filtrated and evaporated. After column chromatography over silica gel (CH₂Cl₂ as eluent), 730 mg (100 %) *S*-*S*-**8** was obtained as a white solid. ¹H NMR (CD₂Cl₂, 298K, 500.1 MHz): δ 8.01 (d, *J* = 9.0 Hz, 2H); 7.92 (d, *J* = 8.2 Hz, 2H); 7.50 (d, *J* = 9.1 Hz, 1H); 7.47 (d, *J* = 9.1 Hz, 1H); 7.36 (q, *J* = 6.7 Hz, 2H); 7.25 (t, *J* = 8.1 Hz, 2H); 7.12 (t, *J* = 8.3 Hz, 2H); 5.85-5.79 (m, 1H); 5.07-5.04 (m, 2H); 4.59-4.58 (m, 2H); 4.26 (dd, *J* = 2.6, 11.6 Hz, 1H); 3.98 (dd, *J* = 5.4, 11.6 Hz, 1H); 3.0 (bs, 1H); 2.59 (t, *J* = 4.7 Hz, 1H); 2.34 (dd, *J* = 2.5, 4.8 Hz, 1H). ¹³C NMR (CD₂Cl₂, 298K, 125.7 MHz): δ 154.0(3), 153.9(8), 133.9(8), 133.9(5), 133.7, 129.6, 129.4, 129.3(0), 129.2(5), 127.9, 126.3, 125.2, 125.0, 123.8, 123.6, 120.5, 119.6, 116.3, 115.8, 115.3, 70.2, 69.8, 50.2, 44.0. **ESI-HRMS** *m/z*: found 405.1455, calcd for C₂₆H₂₂NaO₃ [M+Na]⁺ 405.1461.

S*-*R*-**8*: The procedure was similar as that of *S*-*S*-**8** using the starting materials with the corresponding chirality in 90% yield. ¹H NMR (CD₂Cl₂, 298K, 500.1 MHz): δ 8.02 (d, *J* = 8.9 Hz, 2H); 7.93 (d, *J* = 8.0 Hz, 2H); 7.50 (t, *J* = 9.0 Hz, 2H); 7.38 (q, *J* = 7.1 Hz, 2H); 7.26 (bs, 2H); 7.16-7.12 (m, 2H); 5.87-5.81 (m, 1H); 5.10-5.06 (m, 2H); 4.61 (bs, 2H); 4.23 (d, *J* = 11.4 Hz, 1H); 4.00 (dd, *J* = 5.3, 11.4 Hz, 1H); 2.99 (bs, 1H); 2.60 (bs, 1H); 2.39 (bs, 1H). ¹³C NMR (CD₂Cl₂, 298K, 125.7 MHz): δ 154.1, 154.0, 134.0(0), 133.9(8), 133.7, 129.6, 129.4, 129.3(3), 129.3(0), 128.0, 126.3(4), 126.3(1), 125.3, 125.1, 123.9, 123.6, 120.6, 119.7, 116.4, 115.9, 115.3, 70.4, 69.8, 50.1, 44.1. **ESI-HRMS** *m/z*: found 405.1456, calcd for C₂₆H₂₂NaO₃ [M+Na]⁺ 405.1461.

(*S,S,S*)-(*S,S,S*)-10****: To a solution of 7N NH₃ in methanol (75 mL, 525 mmol), (*S,S,S*)-(*S,S,S*)-**8** (450 mg, 1.18 mmol) was added. After stirring at 50 °C for 12 h under argon, the solvent was evaporated. 10 mL pentane was added and evaporated, which was repeated for 3 times to fully remove the residue NH₃. Then 2.0 equiv. of (*S,S,S*)-(*S,S,S*)-**8** (900 mg, 2.35 mmol) and 150 mL MeOH were added under argon. The solution was stirred at 60 °C for 5 days. After evaporation of the solvent, the crude product was purified by column chromatography over silica gel (CH₂Cl₂/MeOH 200:3), 820 mg (60%) (*S,S,S*)-(*S,S,S*)-**10** was obtained as a white solid. ¹H NMR (CD₂Cl₂, 298K, 500.1 MHz): δ 8.02 (d, *J* = 9.0 Hz, 3H); 7.93 (d, *J* = 8.1 Hz, 3H); 7.79 (d, *J* = 9.0 Hz, 3H); 7.75 (d, *J* = 8.1 Hz, 3H); 7.45 (d, *J* = 9.0 Hz, 3H); 7.37 (t, *J* = 7.1 Hz, 3H); 7.30 (d, *J* = 9.1 Hz, 3H); 7.26 (q, *J* = 7.6 Hz, 6H); 7.17 (t, *J* = 7.4 Hz, 3H); 7.12 (d, *J* = 8.4 Hz, 3H); 7.04 (d, *J* = 8.5 Hz, 3H); 5.76-5.68 (m, 3H); 4.99-4.95 (m, 6H); 4.51-4.43 (m, 6H); 3.96 (dd, *J* = 3.6, 9.8 Hz, 3H); 3.68 (dd, *J* = 4.4, 9.8 Hz, 3H); 3.00-2.97 (m, 3H); 1.51 (s, 3H); 1.38 (dd, *J* = 2.9, 13.4 Hz, 3H). ¹³C NMR (CD₂Cl₂, 298K, 125.7 MHz): δ 154.1, 153.8, 133.9(2), 133.8(9), 133.5, 129.5, 129.4, 129.3, 129.2, 128.0, 127.9, 126.3(4), 126.3(2), 125.1(5), 125.0(6), 123.7(3), 123.6(9), 120.0, 119.9, 116.6, 115.7, 115.3, 71.2, 70.0, 66.3, 56.2. **ESI-HRMS** *m/z*: found 1064.5011, calcd for C₇₈H₇₀NO₉ [M+H]⁺ 1164.5045.

(*S,S,S*)-(*R,R,R*)-10****: The procedure was similar as that of (*S,S,S*)-(*S,S,S*)-**10** using the starting materials with the corresponding chirality in 64% yield. ¹H NMR (CD₂Cl₂, 298K, 500.1 MHz): δ 8.01 (d, *J* = 9.0 Hz, 3H); 7.93 (d, *J* = 8.2 Hz, 3H); 7.83 (d, *J* = 9.1 Hz, 3H); 7.75 (d, *J* = 8.1 Hz, 3H); 7.44 (d, *J* = 9.1 Hz, 3H); 7.37 (t, *J* = 7.1 Hz, 3H); 7.33 (d, *J* = 9.0 Hz, 3H); 7.26 (t, *J* = 7.4 Hz, 3H); 7.21 (t, *J* = 7.2 Hz, 3H); 7.14-7.05 (m, 9H); 5.78-5.70 (m, 3H); 5.00-4.97 (m, 6H); 4.53-4.45 (m, 6H);

3.79 (d, $J = 4.8$ Hz, 6H); 3.12-3.10 (m, 3H); 1.70-1.59 (m, 6H). ^{13}C NMR (CD_2Cl_2 , 298K, 125.7 MHz): δ 154.1, 153.7, 134.0, 133.9, 133.5, 129.5(2), 129.4(5), 129.3(2), 129.2(9), 128.0, 127.9, 126.4, 126.3, 125.2, 125.1, 123.8, 123.7, 120.2, 119.9, 116.5, 115.7, 115.4, 71.9, 69.9, 66.7, 56.7. **ESI-HRMS** m/z : found 1064.5006, calcd for $\text{C}_{78}\text{H}_{70}\text{NO}_9$ $[\text{M}+\text{H}]^+$ 1164.5045.

(S,S,S)-(S,S,S)-11: To a mixture solution of CH_2Cl_2 and MeOH (1/1), **(S,S,S)-(S,S,S)-10** (800 mg, 0.69 mmol), $\text{Pd}(\text{PPh}_3)_4$ (794 mg, 0.69 mmol) and K_2CO_3 (950 mg, 6.87 mmol) were added. The mixture was stirred at room temperature for 1 night under argon. After evaporation of the solvent, CH_2Cl_2 and distilled water were added to the mixture. The two layers were then separated and the aqueous phase was extracted with CH_2Cl_2 (1×100 mL), and the organic phase was washed with distilled water (2×50 mL). The combined organic solutions were dried over anhydrous Na_2SO_4 , filtrated and evaporated. The crude product was purified by column chromatography on silica gel (first with $\text{CH}_2\text{Cl}_2/\text{MeOH}$ 40/1, then use 200/9) to give **(S,S,S)-(S,S,S)-11** as a beige solid (402 mg, 56%). ^1H NMR ($\text{DMSO}-d_6$, 298K, 500.1 MHz): δ 9.27 (s, 3H); 8.03 (d, $J = 9.1$ Hz, 3H); 7.94 (d, $J = 8.1$ Hz, 3H); 7.63 (d, $J = 8.5$ Hz, 6H); 7.56 (d, $J = 9.1$ Hz, 3H); 7.34 (t, $J = 7.2$ Hz, 3H); 7.26-7.22 (m, 6H); 7.16-7.14 (m, 6H); 7.03 (d, $J = 8.5$ Hz, 3H); 6.87-6.85 (m, 3H); 3.96 (s, 3H); 3.87 (dd, $J = 3.3, 9.9$ Hz, 3H); 3.57 (dd, $J = 3.9, 9.8$ Hz, 3H); 2.84 (s, 3H); 1.26 (t, $J = 12.7$ Hz, 3H); 0.92 (d, $J = 12.2$ Hz, 3H). ^{13}C NMR ($\text{DMSO}-d_6$, 298K, 125.7 MHz): δ 155.1, 153.1, 134.4, 134.0, 129.6, 129.5, 129.3, 128.4, 128.3, 128.2, 126.6, 126.4, 125.3, 124.6, 123.9, 122.7, 120.2, 118.8, 116.7, 115.7, 72.1, 66.0, 57.4. **ESI-HRMS** m/z : found 1044.4064, calcd for $\text{C}_{69}\text{H}_{58}\text{NO}_9$ $[\text{M}+\text{H}]^+$ 1044.4106.

(S,S,S)-(R,R,R)-11: The procedure was similar as that of **(S,S,S)-(S,S,S)-11** using the starting materials with the corresponding chirality in 55% yield. ^1H NMR ($\text{DMSO}-d_6$, 298K, 500.1 MHz): δ 9.25 (s, 3H); 8.03 (d, $J = 9.0$ Hz, 3H); 7.94 (d, $J = 8.1$ Hz, 3H); 7.68 (d, $J = 8.8$ Hz, 3H); 7.64-7.62 (m, 3H); 7.54 (d, $J = 9.0$ Hz, 3H); 7.34 (t, $J = 7.3$ Hz, 3H); 7.27-7.23 (m, 6H); 7.04-7.01 (m, 9H); 6.84 (d, $J = 7.3$ Hz, 3H); 4.08 (s, 3H); 3.74-3.64 (m, 6H); 3.03 (s, 3H); 1.42 (t, $J = 11.3$ Hz, 3H); 1.26 (d, $J = 11.7$ Hz, 3H). ^{13}C NMR ($\text{DMSO}-d_6$, 298K, 125.7 MHz): δ 155.1, 153.1, 134.4, 134.0, 129.7, 129.6, 129.3, 128.4, 128.3, 126.6, 126.3, 125.4, 124.6, 124.0, 122.7, 120.5, 118.8, 117.2, 115.6, 72.6, 66.5, 58.1. **ESI-HRMS** m/z : found 1044.4054, calcd for $\text{C}_{69}\text{H}_{58}\text{NO}_9$ $[\text{M}+\text{H}]^+$ 1044.4106.

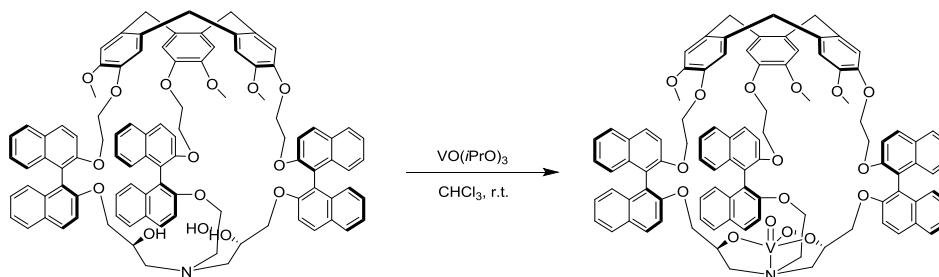
(S,S,S)-(S,S,S)-12: A solution of Cs_2CO_3 (300 mg, 919 μmol) and **(S,S,S)-(S,S,S)-11** (160 mg, 153 μmol) in DMF (140 mL) was stirred at 25 °C for 15 min under argon. Then 140 mL DMF solution of tris(bromomethyl)benzene (60 mg, 169 μmol) was added dropwise. The reaction solution was stirred at 25 °C for 48 h. Afterwards, 200 mL CH_2Cl_2 was added to the reaction, followed by washing with brine (100×5) to remove DMF and Cs_2CO_3 . The organic phase was dried over anhydrous Na_2SO_4 , filtrated and evaporated. The crude product was purified by column chromatography on silica gel (first with $\text{CH}_2\text{Cl}_2/\text{MeOH}$ 200/1, then use 200/3) to give **(S,S,S)-(S,S,S)-12** (53 mg, 30%) as a white solid. ^1H NMR (CD_2Cl_2 , 298K, 500.1 MHz): δ 8.31 (d, $J = 9.1$ Hz, 3H); 8.24 (d, $J = 8.8$ Hz, 3H); 8.13 (d, $J = 8.2$ Hz, 3H); 8.06 (d, $J = 8.1$ Hz, 3H); 7.73 (d, $J = 8.8$ Hz, 3H); 7.62 (d, $J = 9.2$ Hz, 3H); 7.50-7.47 (m, 3H); 7.39 (t, $J = 7.3$ Hz, 3H); 7.34 (t, $J = 8.1$ Hz, 3H); 7.28 (d, $J = 8.4$ Hz, 3H); 7.21 (t, $J = 7.6$ Hz, 3H); 7.06 (d, $J = 8.6$ Hz, 3H); 5.26 (s, 3H); 4.48 (d, $J = 10.5$ Hz, 3H); 4.30 (d, $J = 12.2$ Hz, 3H); 4.25 (d, $J = 10.5$ Hz, 3H); 3.59 (t, $J = 10.1$ Hz, 3H); 3.38 (bs, 6H); 2.45-2.42 (m, 6H). ^{13}C NMR (CD_2Cl_2 , 298K, 125.7 MHz): δ 153.8, 136.1, 134.3, 134.1, 130.6, 129.8, 129.3, 129.2, 128.3, 127.9, 126.8, 126.7, 125.7, 125.5, 124.9, 124.7, 123.9, 123.2, 119.8, 118.1, 114.6, 73.2, 71.5, 70.5, 62.2. **ESI-HRMS** m/z : found 1158.4547, calcd for $\text{C}_{78}\text{H}_{64}\text{NO}_9$

$[M+H]^+$ 1158.4576.

(S,S,S)-(R,R,R)-12: The procedure was similar as that of (S,S,S)-(S,S,S)-12 using the starting materials with the corresponding chirality in 43% yield. $^1\text{H NMR}$ (CD_2Cl_2 , 298K, 500.1 MHz): δ 8.31 (d, $J = 9.0$ Hz, 3H); 8.24 (d, $J = 9.0$ Hz, 3H); 8.06 (t, $J = 8.7$ Hz, 6H); 7.78 (d, $J = 9.1$ Hz, 3H); 7.62 (d, $J = 9.0$ Hz, 3H); 7.48-7.43 (m, 6H); 7.30 (q, $J = 8.7$ Hz, 6H); 7.15 (d, $J = 8.6$ Hz, 3H); 7.12 (d, $J = 8.5$ Hz, 3H); 6.44 (s, 3H); 6.22 (s, 3H); 4.85 (d, $J = 11.9$ Hz, 3H); 4.61 (d, $J = 11.9$ Hz, 3H); 4.21 (dd, $J = 4.1, 10.5$ Hz, 3H); 4.08-4.07 (m, 3H); 3.83-3.80 (m, 3H); 2.65 (t, $J = 12.7$ Hz, 3H); 2.15 (d, $J = 12.7$ Hz, 3H). $^{13}\text{C NMR}$ (CD_2Cl_2 , 298K, 125.7 MHz): δ 153.7, 153.4, 137.5, 134.3, 134.2, 129.9(3), 129.8(9), 129.8, 128.1(1), 128.0(6), 126.9, 126.7, 125.4, 125.2, 124.5, 124.3, 121.2, 120.7, 116.0, 115.6, 72.2, 71.1, 66.6, 64.3. **ESI-HRMS** m/z : found 1158.4543, calcd for $\text{C}_{78}\text{H}_{64}\text{NO}_9$ $[M+H]^+$ 1158.4576.

(S,S,S)-(S,S,S)-1: To 15 mL CHCl_3 , (S,S,S)-(S,S,S)-12 (70 mg, 60.4 μmol) was added. The solution was stirred at room temperature for 5 min. Then vanadium(V) oxytriisopropoxide (14.2 μL , 60.4 μmol) was added to the solution, which was further stirred for 1 h. After evaporation of the solvent, the mixture was dissolved in 10 mL CH_2Cl_2 . The solution was filtered by syringe filter (pore size: 0.45 μm), followed by evaporation to give the complex (S,S,S)-(S,S,S)-1 (67 mg, 91%) as a dark green solid. $^1\text{H NMR}$ (CD_2Cl_2 , 298K, 500.1 MHz): δ 8.24 (t, $J = 8.3$ Hz, 6H); 8.17 (d, $J = 8.2$ Hz, 3H); 8.04 (d, $J = 8.1$ Hz, 3H); 7.60 (d, $J = 8.9$ Hz, 3H); 7.54 (d, $J = 9.2$ Hz, 3H); 7.48-7.44 (m, 6H); 7.33-7.27 (m, 6H); 7.18-7.13 (m, 6H); 5.57 (s, 3H); 4.44 (q, $J = 12.6$ Hz, 6H); 4.36-4.35 (m, 3H); 4.16 (t, $J = 11.1$ Hz, 3H); 3.89 (dd, $J = 4.3, 11.5$ Hz, 3H); 2.09 (dd, $J = 3.6, 12.8$ Hz, 3H); 1.83 (t, $J = 11.5$ Hz, 3H). $^{13}\text{C NMR}$ (CD_2Cl_2 , 298K, 125.7 MHz): δ 154.0, 153.3, 136.8, 134.4, 134.0, 129.9, 129.8, 129.5, 129.3, 128.1, 127.9, 127.0, 126.8, 126.4, 125.2, 125.1, 124.4(2), 124.3(6), 121.4, 120.7, 116.5, 114.2, 83.1, 71.6, 69.3, 57.1. **ESI-HRMS** m/z : found 1244.3526, calcd for $\text{C}_{78}\text{H}_{60}\text{NNaO}_{10}\text{V}$ $[M+\text{Na}]^+$ 1244.3549.

(S,S,S)-(R,R,R)-1: A similar procedure as that of (S,S,S)-(S,S,S)-1 has been used for the synthesis of (S,S,S)-(R,R,S)-1 using the corresponding ligand. However, the reaction failed to give the desired complex as the $^1\text{H NMR}$ spectrum is too complicated to analyze. The different behavior from the synthesis of (S,S,S)-(S,S,S)-1 probably because of its more hindered conformation of the cavity.



Scheme S8.1 Synthesis of the oxido-vanadium(V) hemicryptophane complexes **2**.

P-(S,S,S)-(S,S,S)-2: The ligand of *P*-(S,S,S)-(S,S,S)-2 complex was synthesized according to our previous procedure.¹⁰ To 3 mL CHCl_3 , the ligand of *P*-(S,S,S)-(S,S,S)-2 (10 mg, 6.5 μmol) was added. The solution was stirred at room temperature for 5 min. Then vanadium(V) oxytriisopropoxide (4.8 μL , 19.6 μmol) was added to the solution, which was further stirred for 1 h. After evaporation of the solvent, the mixture was dissolved in 5 mL CH_2Cl_2 . The solution was filtered by syringe filter (pore size: 0.45 μm), followed by evaporation to give the

complex *P*-(*S,S,S*)-(*S,S,S*)-**2** (10 mg, 96%) as a dark green solid. $^1\text{H NMR}$ (C_6D_6 , 298K, 500.1 MHz): δ 8.42 (d, $J = 9.2$ Hz, 3H); 7.84-7.78 (m 12H); 7.50 (d, $J = 8.5$ Hz, 3H); 7.31-7.17 (m, 12H); 7.02-6.98 (m, 6H); 6.60 (s, 3H); 6.57 (s, 3H); 4.70 (d, $J = 13.7$ Hz, 3H); 4.23 (t, $J = 11.2$ Hz, 3H); 4.02 (t, $J = 10.2$ Hz, 3H); 3.78-3.75 (m, 6H); 3.45-3.40 (m, 9H); 3.04-2.98 (m, 12H); 0.72 (dd, $J = 3.8$, 13.3 Hz, 3H); 0.23 (t, $J = 12.6$ Hz, 3H). $^{13}\text{C NMR}$ (C_6D_6 , 298K, 125.7 MHz): δ 156.3, 154.3, 147.7, 146.6, 134.4, 133.8, 131.8, 131.2, 130.2, 130.0, 129.5, 129.2, 128.2, 127.2, 126.5, 126.3, 125.7, 125.3, 124.4, 123.8, 121.1, 121.0, 119.9, 116.1, 112.3, 111.9, 81.4, 72.5, 70.0, 67.2, 56.0, 53.8, 36.7. **ESI-HRMS** m/z : found 1617.5128, calcd for $\text{C}_{99}\text{H}_{84}\text{NNaO}_{16}\text{V} [\text{M}+\text{Na}]^+$ 1616.5122.

M-(*S,S,S*)-(*S,S,S*)-**2**, *P*-(*S,S,S*)-(*R,R,R*)-**2** and *M*-(*S,S,S*)-(*R,R,R*)-**2**: The procedure for each of the complexes from their corresponding ligands was similar as that of *P*-(*S,S,S*)-(*S,S,S*)-**2** except that only 1.0 equiv. of vanadium(V) oxytriisopropoxide instead of 3 equivalents was used. The reason for this difference is because the ligand of *P*-(*S,S,S*)-(*S,S,S*)-**2** shows an extremely imploded conformation, which suffers from a slow vanadium chemical complexation kinetics. For all the complexes, the yields are higher than 90%.

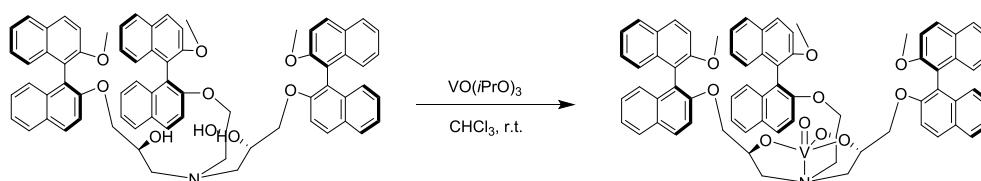
M-(*S,S,S*)-(*S,S,S*)-**2**: $^1\text{H NMR}$ (C_6D_6 , 298K, 500.1 MHz): δ 8.13 (d, $J = 9.1$ Hz, 3H); 7.73 (d, $J = 9.1$ Hz, 3H); 7.69 (d, $J = 9.1$ Hz, 3H); 7.63 (dd, $J = 8.2$, 13.2 Hz, 6H); 7.50 (d, $J = 9.1$ Hz, 3H); 7.26 (d, $J = 8.5$ Hz, 3H); 7.19 (d, $J = 8.6$ Hz, 3H); 7.10 (d, $J = 7.1$ Hz, 3H); 7.05-6.98 (m, 6H); 6.88 (t, $J = 8.2$ Hz, 3H); 6.75 (s, 3H); 6.23 (s, 3H); 4.37 (d, $J = 13.6$ Hz, 6H); 4.06-4.02 (m, 3H); 3.94-3.91 (m, 3H); 3.80-3.77 (m, 3H); 3.70-3.66 (m, 3H); 3.59-3.53 (m, 6H); 3.20 (d, $J = 13.6$ Hz, 3H); 2.40 (s, 9H); 1.94 (t, $J = 12.2$ Hz, 3H); 0.90 (dd, $J = 3.7$, 12.9 Hz, 3H). $^{13}\text{C NMR}$ (C_6D_6 , 298K, 125.7 MHz): δ 155.4, 153.4, 148.8, 146.0, 134.5, 133.7, 133.6, 131.7, 130.3, 130.1, 129.6, 129.0, 128.1, 127.8, 126.9, 126.3, 125.7, 125.2, 124.4, 124.1, 122.0, 121.0, 119.4, 118.3, 116.8, 112.7, 83.7, 73.9, 69.1, 67.3, 54.3, 54.2, 36.4. **ESI-HRMS** m/z : found 1616.5109, calcd for $\text{C}_{99}\text{H}_{84}\text{NNaO}_{16}\text{V} [\text{M}+\text{Na}]^+$ 1616.5122.

P-(*S,S,S*)-(*R,R,R*)-**2**: $^1\text{H NMR}$ (C_6D_6 , 298K, 500.1 MHz): δ 7.95 (d, $J = 8.4$ Hz, 3H); 7.78 (d, $J = 8.1$ Hz, 3H); 7.74 (d, $J = 9.0$ Hz, 3H); 7.65 (d, $J = 8.2$ Hz, 3H); 7.39-7.34 (m, 6H); 7.30-7.28 (m, 6H); 7.21 (d, $J = 8.5$ Hz, 3H); 7.07 (t, $J = 7.7$ Hz, 3H); 7.03 (d, $J = 9.0$ Hz, 3H); 6.93 (t, $J = 8.0$ Hz, 3H); 6.59(2) (s, 3H); 6.58(9) (s, 3H); 4.66 (d, $J = 13.7$ Hz, 3H); 4.24 (dd, $J = 5.7$, 12.1 Hz, 3H); 3.92-3.84 (m, 6H); 3.78-3.70 (m, 9H); 3.37 (d, $J = 13.8$ Hz, 3H); 3.25-3.20 (m, 3H); 3.06 (s, 9H); 1.04 (dd, $J = 3.7$, 13.2 Hz, 3H); 0.79 (dd, $J = 10.6$, 12.7 Hz, 3H). $^{13}\text{C NMR}$ (CDCl_3 , 298K, 125.7 MHz): δ 155.3, 153.6, 148.3, 147.0, 133.9, 133.5, 132.0, 131.7, 129.6, 129.3, 128.8, 128.0, 126.8, 126.6, 126.5, 126.3, 125.2, 124.7, 123.8, 121.7, 119.9, 119.7, 114.5, 114.0, 113.7, 81.6, 71.0, 69.6, 68.9, 56.5, 54.6, 36.3. **ESI-HRMS** m/z : found 1616.5066, calcd for $\text{C}_{99}\text{H}_{84}\text{NNaO}_{16}\text{V} [\text{M}+\text{Na}]^+$ 1616.5122.

M-(*S,S,S*)-(*R,R,R*)-**2**: $^1\text{H NMR}$ (CDCl_3 , 298K, 500.1 MHz): δ 8.03 (d, $J = 9.0$ Hz, 3H); 7.97 (d, $J = 8.1$ Hz, 3H); 7.93 (d, $J = 8.2$ Hz, 3H); 7.51 (d, $J = 9.1$ Hz, 3H); 7.46-7.43 (m, 6H); 7.35-7.33 (m, 6H); 7.21-7.15 (m, 6H); 7.10 (s, 3H); 7.01 (d, $J = 8.5$ Hz, 3H); 6.92 (s, 3H); 6.81 (d, $J = 8.9$ Hz, 3H); 4.95 (d, $J = 13.8$ Hz, 3H); 4.50-4.45 (m, 3H); 4.21-4.17 (m, 9H); 3.70-3.67 (m, 6H); 3.38-3.35 (m, 12H); 3.05-3.04 (m, 3H); 0.95 (dd, $J = 3.8$, 13.1 Hz, 3H); 0.62 (t, $J = 11.3$ Hz, 3H). $^{13}\text{C NMR}$ (CDCl_3 , 298K, 125.7 MHz): δ 154.6, 153.3, 148.7, 145.9, 134.3, 133.9, 133.4, 132.0, 130.3, 130.1, 129.9, 129.6, 128.8, 128.4, 126.9, 126.6, 125.3, 125.0, 124.7, 124.3, 123.2, 122.0, 118.7, 118.6, 116.5, 113.0, 81.9, 72.4, 69.0, 66.7, 55.1, 54.4, 36.7. **ESI-HRMS** m/z : found 1616.5090, calcd for $\text{C}_{99}\text{H}_{84}\text{NNaO}_{16}\text{V} [\text{M}+\text{Na}]^+$ 1616.5122.

(*S,S,S*)-(*S,S,S*)-**4**: The ligand of (*S,S,S*)-(*S,S,S*)-**4** complex was synthesized according to our

previous procedure.^[1] To 30 mL CHCl₃, the ligand of (*S,S,S*)-(*S,S,S*)-**4** (300 mg, 276 μmol) was added. The solution was stirred at room temperature for 5 min. Then vanadium(V) oxytriisopropoxide (64.8 μL, 276 μmol) was added to the solution, which was further stirred for 1 h. After evaporation of the solvent, the mixture was dissolved in 15 mL CH₂Cl₂. The solution was filtered by syringe filter (pore size: 0.45 μm), followed by evaporation to give the complex (*S,S,S*)-(*S,S,S*)-**4** (318 mg, 100%) as a yellow solid. ¹H NMR (CD₂Cl₂, 298K, 500.1 MHz): δ 8.06 (d, *J* = 9.0 Hz, 3H); 7.94 (d, *J* = 8.2 Hz, 3H); 7.82 (d, *J* = 9.1 Hz, 3H); 7.74 (d, *J* = 8.1 Hz, 3H); 7.49 (d, *J* = 9.0 Hz, 3H); 7.41-7.36 (m, 6H); 7.30-7.23 (m, 9H); 7.11 (d, *J* = 8.4 Hz, 3H); 7.06 (d, *J* = 8.4 Hz, 3H); 4.07 (dd, *J* = 3.2, 9.8 Hz, 3H); 3.74 (s, 9H); 3.65-3.59 (m, 3H); 3.53-3.52 (m, 3H); 1.48 (t, *J* = 12.1 Hz, 3H); 1.24 (dd, *J* = 3.5, 12.8 Hz, 3H). ¹³C NMR (CD₂Cl₂, 298K, 125.7 MHz): δ 155.2, 153.9, 133.9, 133.8, 129.7, 129.6, 129.0, 128.9, 128.0, 127.8, 126.5, 126.4, 125.0, 124.9, 124.0, 123.5, 120.4, 119.0, 115.7, 114.1, 82.2, 70.3, 56.6, 54.1. **ESI-HRMS** *m/z*: found 1172.3518, calcd for C₇₂H₆₀NNaO₁₀V [M+Na]⁺ 1172.3549. (*S,S,S*)-(*R,R,R*)-**4**: The procedure was similar as that of (*S,S,S*)-(*S,S,S*)-**4** using the corresponding ligand in 94% yield. ¹H NMR (CD₂Cl₂, 298K, 500.1 MHz): δ 8.03 (d, *J* = 9.0 Hz, 3H); 7.95 (t, *J* = 9.3 Hz, 6H); 7.76 (d, *J* = 8.1 Hz, 3H); 7.49 (d, *J* = 9.1 Hz, 3H); 7.46 (d, *J* = 9.0 Hz, 3H); 7.40 (t, *J* = 7.3 Hz, 3H); 7.28 (t, *J* = 7.9 Hz, 3H); 7.21-7.13 (m, 9H); 7.05 (d, *J* = 8.4 Hz, 3H); 3.87 (s, 9H); 3.74-3.67 (m, 6H); 3.64-3.61 (m, 3H); 1.46 (t, *J* = 12.5 Hz, 3H); 1.37 (dd, *J* = 3.8, 12.8 Hz, 3H). ¹³C NMR (CD₂Cl₂, 298K, 125.7 MHz): δ 154.7, 154.0, 134.1, 133.8, 130.0, 129.7, 129.5, 129.0, 128.1, 127.8, 126.6, 126.5, 125.2, 125.1, 124.2, 123.7, 121.1, 119.2, 116.9, 113.4, 82.1, 71.3, 56.4, 54.9. **ESI-HRMS** *m/z*: found 1172.3535, calcd for C₇₂H₆₀NNaO₁₀V [M+Na]⁺ 1172.3549.



Scheme S8.2 Synthesis of the oxido-vanadium(V) complexes **4**.

8.5.3 Supplementary figures

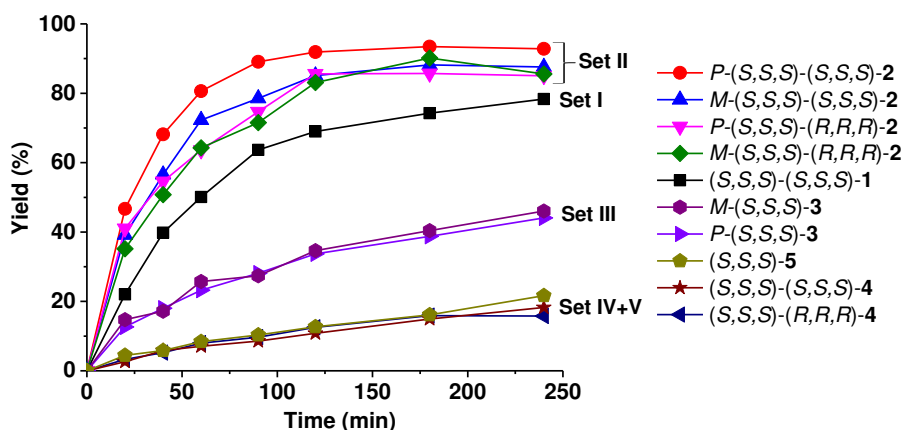


Figure S8.1 Time course of oxidation of thioanisol with catalysts in different sets (conditions: 1.5 mol% catalyst, 1.0 equiv. of CHP, 0 °C, CH₂Cl₂).

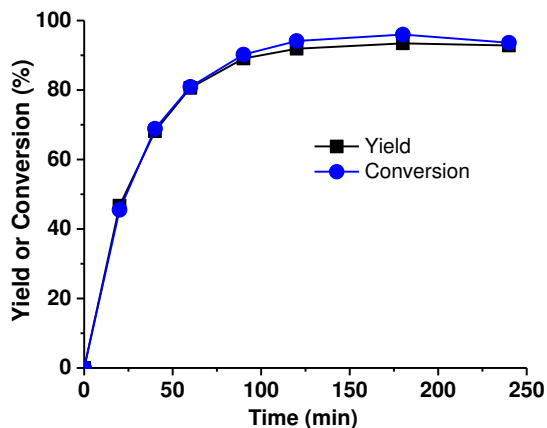


Figure S8.2 Time course of oxidation of thioanisol with hemicyptophane catalyst *P*-(*S,S,S*)-(*S,S,S*)-2 (conditions: 1.5 mol% catalyst, 1.0 equiv. of CHP, 0 °C, CH₂Cl₂).

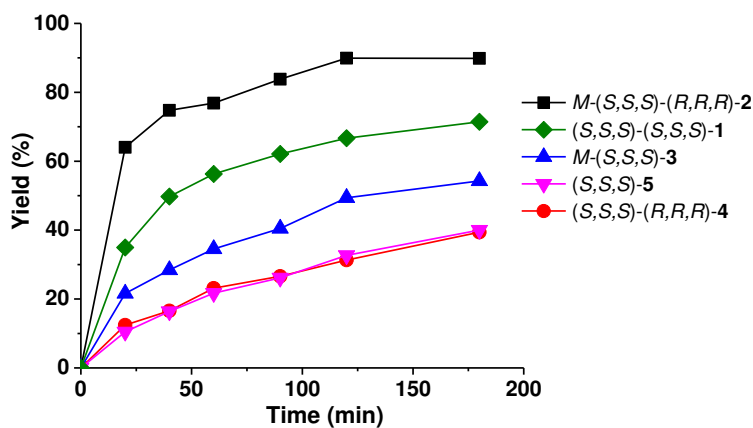


Figure S8.3 Time course of oxidation of thioanisol with typical catalysts in different sets (conditions: 1.5 mol% catalyst, 1.0 equiv. of TBHP, 0 °C, CH₂Cl₂).

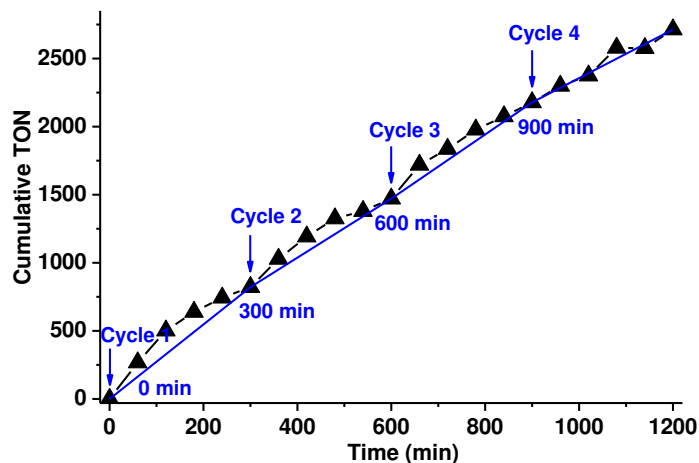


Figure S8.4 Changes of the cumulative TON over four-cycle experiments catalyzed by *M*-(*S,S,S*)-(*R,R,R*)-2 with the development of time (conditions: 0.1 mol% catalyst, 1.0 equiv. of CHP, r.t., CH₂Cl₂; after each cycle, 1.0 equiv. of reaction substrate and CHP were reloaded; TON was calculated from the yield).

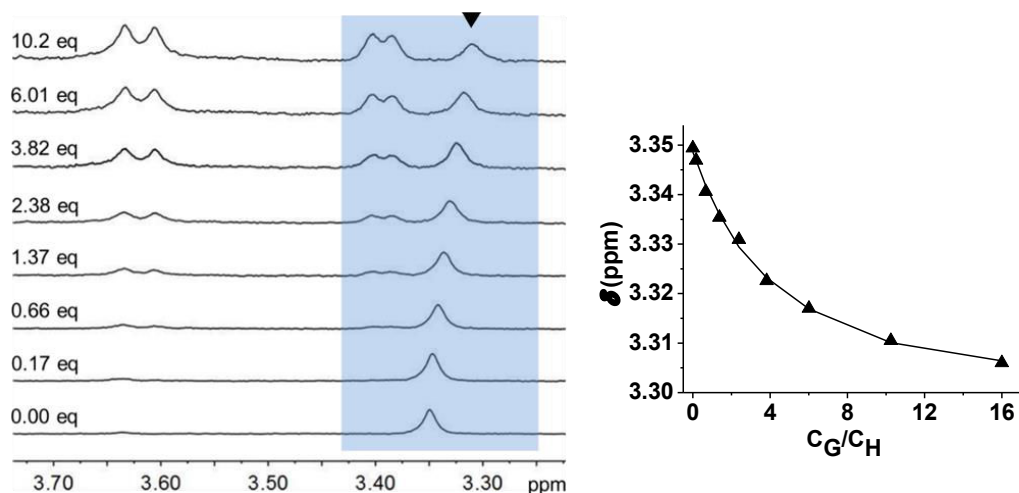


Figure S8.5 ^1H NMR spectra (500 MHz, 298 K) of $\text{Me}_4\text{N}^+\text{Pic}^-$ (▼) in CD_2Cl_2 upon progressive addition of different equivalents of the host $M\text{-(S,S,S)-(R,R,R)-2}$ (left side) and its titration curve fitted by HypNMR2008 (right side).

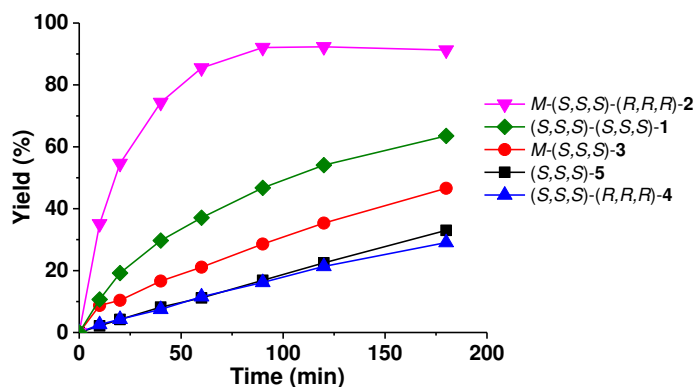


Figure S8.6 Time course of oxidation of benzylphenyl sulfide with typical catalysts (conditions: 1.5 mol% catalyst, 1.0 equiv. of CHP, 0 °C, CH_2Cl_2).

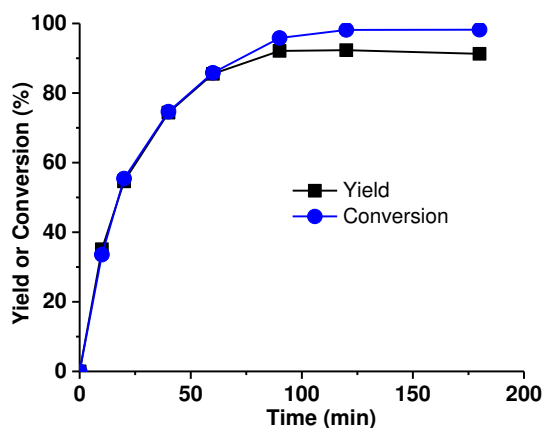


Figure S8.7 Time course of oxidation of benzylphenyl sulfide with hemicryptophane catalyst $M\text{-(S,S,S)-(R,R,R)-2}$ (conditions: 1.5 mol% catalyst, 1.0 equiv. of CHP, 0 °C, CH_2Cl_2).

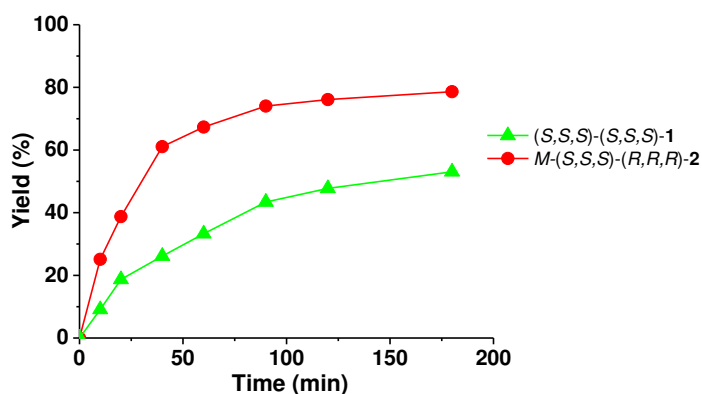


Figure S8.8 Time course of oxidation of naphthylmethyl phenyl sulfide with typical catalysts (conditions: 1.5 mol% catalyst, 1.0 equiv. of CHP, 0 °C, CH₂Cl₂).

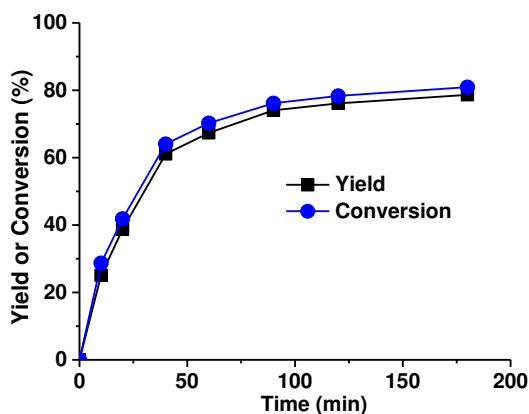


Figure S8.9 Time course of oxidation of naphthylmethyl phenyl sulfide with hemicryptophane catalyst *M*-(*S,S,S*)-(*R,R,R*)-**2** (conditions: 1.5 mol% catalyst, 1.0 equiv. of CHP, 0 °C, CH₂Cl₂).

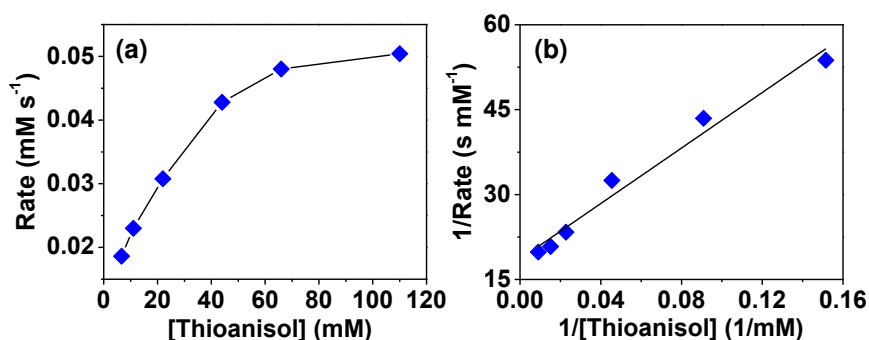


Figure S8.10 (a) Initial rate dependence on the concentration of benzylphenyl sulfide in CH₂Cl₂ with 1.1 mM hemicryptophane catalyst *M*-(*S,S,S*)-(*R,R,R*)-**2** and 110 mM CHP at 0 °C. (b) The corresponding Lineweaver-Burke line plotted by 1/rate as a function of 1/[benzylphenyl sulfide].

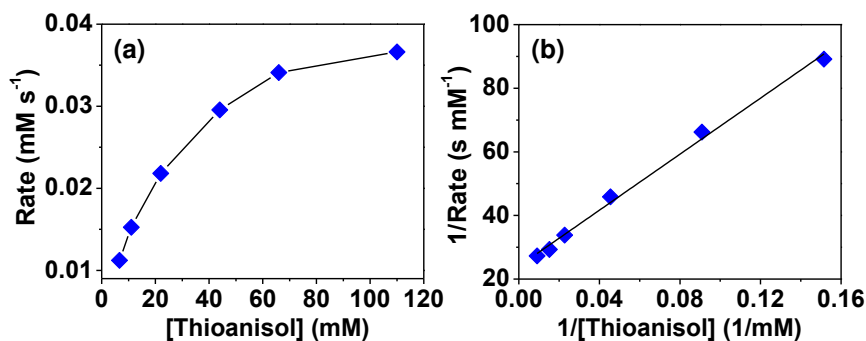


Figure S8.11 (a) Initial rate dependence on the concentration of naphthylmethyl phenyl sulfide in CH₂Cl₂ with 1.1 mM catalyst *M*-(*S,S,S*)-(*R,R,R*)-**2** and 110 mM CHP at 0 °C. (b) The corresponding Lineweaver-Burke line plotted by 1/rate as a function of 1/[naphthylmethyl phenyl sulfide].

8.6 References

- (a) M. Raynal, P. Ballester, A. Vidal-Ferran and P. W. N. M. Van Leeuwen, *Chem. Soc. Rev.*, 2014, **43**, 1660; (b) M. Raynal, P. Ballester, A. Vidal-Ferran and P. W. N. M. Van Leeuwen, *Chem. Soc. Rev.*, 2014, **43**, 1734; (c) C. J. Brown, F. D. Toste, R. G. Bergman and K. N. Raymond, *Chem. Rev.*, 2015, **115**, 3012; (d) M. D. Pluth, R. G. Bergman and K. N. Raymond, *Acc. Chem. Res.*, 2009, **42**, 1650; (e) S. H. A. M. Leenders, R. Gramage-Doria, B. de Bruin and J. N. H. Reek, *Chem. Soc. Rev.*, 2015, **44**, 433; (f) B. Breiner, J. K. Clegg and J. R. Nitschke, *Chem. Sci.*, 2011, **2**, 51; (g) T. K. Hyster, L. Knörr, T. R. Ward and T. Rovis, *Science*, 2012, **338**, 500; (h) T. Heinisch, M. Pellizzoni, M. Dürrenberger, C. E. Tinberg, V. Köhler, J. Klehr, T. Schirmer, D. Baker and T. R. Ward, *J. Am. Chem. Soc.*, 2015, **137**, 10414; (i) M. W. Hosseini, J. -M. Lehn, K. C. Jones, K. E. Plute, K. B. Mertes and M. P. Mertes, *J. Am. Chem. Soc.*, 1989, **111**, 6330.
- (a) Y. Kohyama, T. Murase and M. Fujita, *J. Am. Chem. Soc.*, 2014, **136**, 2966; (b) S. Horiuchi, T. Murase and M. Fujita, *Angew. Chem., Int. Ed.*, 2012, **51**, 12029; (c) K. Ikemoto, Y. Inokuma and M. Fujita, *J. Am. Chem. Soc.*, 2011, **133**, 16806; (d) Y. Nishioka, T. Yamaguchi, M. Kawano and M. Fujita, *J. Am. Chem. Soc.*, 2008, **130**, 8160; (e) Z. J. Wang, K. N. Clary, R. G. Bergman, K. N. Raymond and F. D. Toste, *Nature Chem.*, 2013, **5**, 100; (f) W. M. Hart-Cooper, K. N. Clary, F. D. Toste, R. G. Bergman and K. N. Raymond, *J. Am. Chem. Soc.*, 2012, **134**, 17873; (g) C. J. Hastings, D. Fiedler, R. G. Bergman and K. N. Raymond, *J. Am. Chem. Soc.*, 2008, **130**, 10977; (h) Z. J. Wang, C. J. Brown, R. G. Bergman, K. N. Raymond and F. D. Toste, *J. Am. Chem. Soc.*, 2011, **133**, 7358; (i) M. D. Pluth, R. G. Bergman and K. N. Raymond, *Science*, 2007, **316**, 85; (j) D. M. Kaphan, M. D. Levin, R. G. Bergman, K. N. Raymond and F. D. Toste, *Science*, 2015, **350**, 1235; (k) S. R. Shenoy, F. R. P. Crisostomo, T. Iwasawa and J. Jr. Rebeck, *J. Am. Chem. Soc.*, 2008, **130**, 5658; (l) M. M. J. Smulders and J. R. Nitschke, *Chem. Sci.*, 2012, **3**, 785; (m) R. Gramage-Doria, J. Hessels, S. H. A. M. Leenders, O. Tröppner, M. Dürr, I. Ivanović-Burmazović and J. N. H. Reek, *Angew. Chem., Int. Ed.*, 2014, **53**, 13380; (n) B. Kersting, *Z. Anorg. Allg. Chem.*, 2004, **630**, 765; (o) S. Käss, T. Gregor and B. Kersting, *Angew. Chem., Int. Ed.*, 2006, **45**, 101; (p) G.

- Steinfeld, V. Lozan and B. Kersting, *Angew. Chem., Int. Ed.*, 2003, **42**, 2261; (q) S. Di Stefano, R. Cacciapaglia and L. Mandolini, *Eur. J. Org. Chem.*, 2014, 7304; (r) E. A. Kataev and C. Müller, *Tetrahedron*, 2014, **70**, 137.
- 3 (a) Z. J. Wang, C. J. Brown, R. G. Bergman, K. N. Raymond and F. D. Toste, *J. Am. Chem. Soc.*, 2011, **133**, 7358. (b) C. J. Hastings, R. G. Bergman and K. N. Raymond, *Chem. Eur. J.*, 2014, **20**, 3966; (c) C. J. Hastings, M. D. Pluth, R. G. Bergman and K. N. Raymond, *J. Am. Chem. Soc.*, 2010, **132**, 6938; (d) S. Kopilevich, A. Muller and I. A. Weinstock, *J. Am. Chem. Soc.*, 2015, **137**, 12740.
- 4 (a) R. J. Hooley, *Nature Chem.*, 2016, **8**, 202; (b) Q. -Q. Wang, S. Gonell, S. H. A. M. Leenders, M. Dürr, I. Ivanović-Burmazović and J. N. H. Reek. *Nature Chem.*, 2016, **8**, 225; (c) W. Cullen, M. C. Misuraca, C. A. Hunter, N. H. Williams and M. D. Ward, *Nature Chem.*, 2016, **8**, 231; (d) J. K. Sanders, *Chem. Eur. J.*, 1998, **4**, 1378; (e) M. Yoshizawa, M. Tamura and M. Fujita, *Science*, 2006, **312**, 251. (f) J. Kang and J. Jr. Rebek, *Nature*, 1997, **385**, 50; (g) S. Mosca, Y. Yu, J. V. Gavette, K. -D. Zhang and J. Jr. Rebek, *J. Am. Chem. Soc.*, 2015, **137**, 14582.
- 5 C. J. Brown, G. M. Miller, M. W. Johnson, R. G. Bergman and K. N. Raymond, *J. Am. Chem. Soc.*, 2011, **133**, 11964.
- 6 (a) K. I. Assaf and W. M. Nau, *Chem. Soc. Rev.*, 2015, **44**, 394; (b) K. I. Assaf, M. S. Ural, F. Pan, T. Georgiev, S. Simova, K. Rissanen, D. Gabel and W. M. Nau, *Angew. Chem. Int. Ed.*, 2015, **54**, 6852; (c) H. S. El-Sheshtawy, B. S. Bassil, K. I. Assaf, U. Kortz and W. M. Nau, *J. Am. Chem. Soc.*, 2012, **134**, 19935; (d) S. J. Barrow, S. Kasera, M. J. Rowland, J. del Barrio and O. A. Scherman, *Chem. Rev.*, 2015, **115**, 12320; (e) F. Liu, R. C. Helgeson and K. N. Houk, *Acc. Chem. Res.*, 2014, **47**, 2168; (f) I. Pochorovski and F. Diederich, *Acc. Chem. Res.*, 2014, **47**, 2096; (g) D. S. Kim and J. L. Sessler, *Chem. Soc. Rev.*, 2015, **44**, 532.
- 7 (a) P. D. Raytchev, A. Martinez, H. Gornitzka and J. -P. Dutasta, *J. Am. Chem. Soc.*, 2011, **133**, 2157; (b) B. Chatelet, H. Gornitzka, V. Dufaud, E. Jeanneau, J. -P. Dutasta and A. Martinez, *J. Am. Chem. Soc.*, 2013, **135**, 18659; (c) B. Chatelet, V. Dufaud, J. -P. Dutasta and A. Martinez, *J. Org. Chem.*, 2014, **79**, 8684; (d) B. Chatelet, L. Joucla, J. -P. Dutasta, A. Martinez and V. Dufaud, *Chem. Eur. J.*, 2014, **20**, 8571; (e) A. Martinez and J. -P. Dutasta, *J. Catal.*, 2009, **267**, 188; (f) Y. Makita, K. Sugimoto, K. Furuyoshi, K. Ikeda, S. I. Fujiwara and T. Shin-ike, *Inorg. Chem.*, 2010, **49**, 7220; (g) O. Perraud, A. B. Sorokin, J. -P. Dutasta and A. Martinez, *Chem. Commun.* 2013, **49**, 1288.
- 8 S. S. Negi, K. Sivaranjani, A. P. Singh and C. S. Gopinath, *Appl. Catal. A-Gen.*, 2013, **452**, 132.
- 9 A. Gautier, J. -C. Mulatier, J. Crassous and J. -P. Dutasta, *Org. Lett.*, 2005, **7**, 1207.
- 10 D. Zhang, J. -C. Mulatier, J. R. Cochrane, L. Guy, G. Gao, J. -P. Dutasta and A. Martinez. *Chem. Eur. J.*, 2016, **22**, 8038.
- 11 (a) O. Perraud, V. Robert, A. Martinez and J. -P. Dutasta, *Chem. Eur. J.*, 2011, **17**, 4177. (b) L. Garel, B. Lozach, J. -P. Dutasta and A. Collet, *J. Am. Chem. Soc.*, 1993, **115**, 11652.
- 12 C. Frassinetti, S. Ghelli, P. Gans, A. Sabatini, M. S. Moruzzi and A. Vacca, *Anal. Biochem.*, 1995, **231**, 374.

Chapter 9. Merging Aerobic Oxidation of Lignin Model Compounds with Supramolecular Catalysis

This Chapter is based partially on the following manuscript—

Dawei Zhang, Christian Díaz-Urrutia, R. Tom Baker, Alexandre Martinez

2017, *In preparation*.

The work in this chapter was carried out at the University of Ottawa.

Contents

9.1 Abstract	200
9.2 Introduction.....	200
9.3 Results and discussion	201
9.4 Conclusion.....	203
9.5 Experimental section.....	203
9.6 References.....	206

9.1 Abstract

Development of new catalytic processes for valorization of nonfood biomass polymers to chemicals and fuels is of great interest. In this communication, we have the first time demonstrated the aerobic oxidation of lignin model by a supramolecular cage catalyst, constructed by a hemicyptophane framework incorporated with an oxido-vanadium site inside the cavity. Compared to the model catalyst with an open structure, the cage catalyst exhibited an improvement of the catalytic activity without product inhibition phenomena. A diastereoselective conversion for a mixture of chiral lignin substrates has been observed, indicating either a diastereoselective recognition between the substrates and the cage catalyst or stabilization of the transition states.

9.2 Introduction

The confinement of catalytic sites in well-defined cavities arises a growing interest since it can mimic the binding pocket of enzyme and thus induce new reactivities and selectivities.¹ Among the hosts presenting a well-defined cavity and capable of metal complexation, hemicyptophanes combining a cyclotritylene (CTV) moiety with another C_3 symmetrical unit, constitute a novel class of supramolecular catalysts.² Indeed, depending on the catalytic sites encaged in the molecular cavity, improvement of the stability of the catalyst, rate and selectivity of the reaction can be observed.³ For instance, encapsulation of an oxido-vanadium site in a hemicyptophane core led to supramolecular catalyst **1** (Figure 9.1) for the oxidation of sulfide into sulfoxide: a strong improvement of the catalytic activity was achieved when compared to the model catalyst **2** which lacks a cavity.⁴

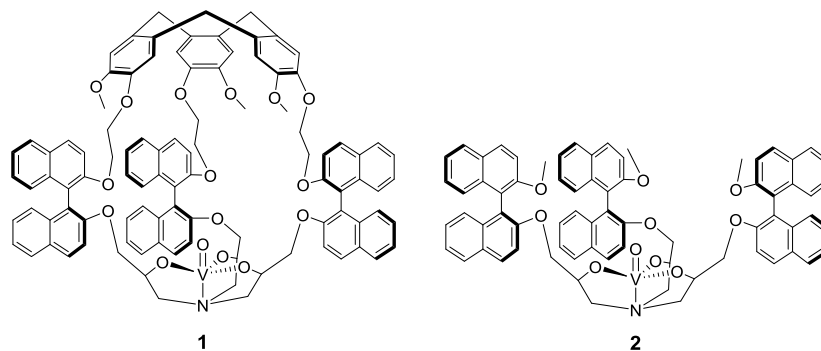


Figure 9.1 Structures of the cage and model complexes **1** and **2**.

Furthermore, we have recently showed that such oxido-vanadium model complex, similar as **2**, exhibits good activity in the oxidation of lignin model, and an original two-electron-process was evidenced both experimentally and theoretically.⁵ Such development of new catalytic processes for valorization of nonfood biomass polymers to chemicals and fuels is of great interest.⁶ Indeed, Lignin is a nonfood biomass polymer composed by an irregular polymer presenting methoxy-substituted phenolic subunits.⁷ However, this polymer is relatively complex and the different linkages are difficult to chemically breakdown.⁸ Among the strategies that have been used,⁹ the aerobic oxidation of this robust bio-polymer appears particularly promising.¹⁰ Thus, considering the effect of

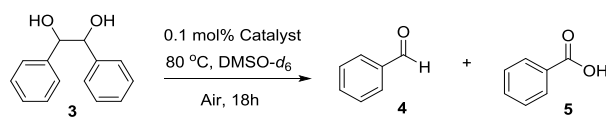
confinement on the catalytic activity of oxido-vandium in the oxidation of sulfide,⁴ and the good activity of this oxido-vanadium model in the oxidation of lignin,¹⁰ we decided to examine the catalytic activities of the engaged vanadium complex **1** for the valorization of nonfood biopolymers. Merging supramolecular catalysis and lignin oxidation was expected to give rise to original complex systems with improved catalytic activity and/or selectivity.

Herein, we report the use of the cage complex **1** as a supramolecular catalyst for aerobic oxidation of lignin models. The encapsulation was found to improve the catalytic activity of the trapped vanadium site associated with the phenomenon of diastereoselective conversion of chiral substrates.

9.3 Results and discussion

We first tested the catalytic activity of the cage and model catalysts for aerobic oxidation of a simple diol substrate **3** (Table 9.1). Although this substrate cannot be considered as a lignin model, we chose this reaction in order to investigate the ability of the confined catalyst to perform such reaction on an easier oxidable compound and to have a preliminary result on the comparative efficiency of these systems. Reactions were carried out at 80°C in DMSO-*d*₆ using 0.1 mol % of a catalyst. The yield and conversion were determined by ¹H NMR using mesitylene as an internal standard (Figure S9.1). We observed that after 18h, a conversion of 61% was reached with the cage catalyst **1**, corresponding to a TON of 610. This represents a relatively high TON for a supramolecular catalyst considering the product inhibition frequently observed in supramolecular catalysis (Table 9.1).¹¹ A good selectivity was also achieved with this encapsulated complex, similar to that of the model one: over-oxidation was avoided since the aldehyde was obtained as a major product with an aldehyde/acid ratio of 10/1.3. Moreover, the engaged catalyst **1** displays a better catalytic activity than the mode **2**, with conversions of 61% and 44%, respectively. Thus, it appears that for this simple diol substrate **3**, the confinement has improved the reactivity and also retained the selectivity of the catalyst. This encourages us to examine the catalytic activity of this complex for substrate **6**, which is usually employed as a lignin model.^{10a}

Table 9.1. Oxidation of **3** by catalysts **1** and **2**.



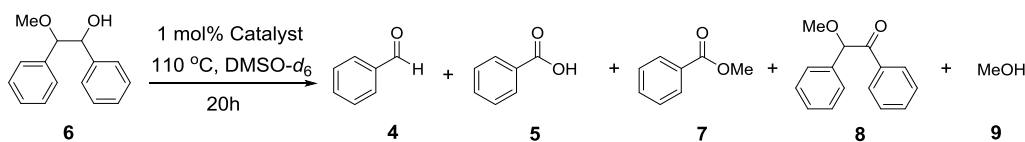
Catalyst	Conversion (%) ^a	Yield (%) ^a	
		4	5
1	61	44	6
2	44	34	4

^a Determined by ¹H NMR using mesitylene as an internal standard.

We then tested the catalytic properties of the hemicryptophane catalyst **1** and the model

catalyst **2** for the aerobic oxidation of **6**. Yields and conversions were first determined by ^1H NMR spectroscopy using mesitylene as an internal standard (Figure S9.2). Reactions were performed in $\text{DMSO-}d_6$ at 110°C with 1 mol % of a catalyst loading for 20 h (optimized conditions). Lowering the reaction time to 5 h at 110°C or the temperature to 100°C for 13 h decreased significantly the conversion (with each catalyst for either condition, conversions < 15%). Almost no catalytic activity was observed in CD_3CN under reflux for 20h. We were pleased to observe that under the optimized conditions, the cage complex **1** gave better yields in products **4** and **7** (37% and 20%, respectively) than its model **2** (28% and 15%, respectively) (Table 9.2), again indicating that the confinement improved the reaction rate. However, because of signals overlap, this NMR method does not allow an accurate measurement of the yield of product **5** as well as the conversion. Thus we turn our attention in GC method to study more accurately the cage effect.

Table 9.2 Oxidation of **6** by catalysts **1** and **2**.



Catalyst	Method	Conversion (%)	Yield (%) ^a				
			4	5	7	8	9
1	$^1\text{H NMR}^b$	— ^a	37	— ^a	20	14	3
	GC ^c	87	38	15	17	12	— ^a
2	$^1\text{H NMR}^b$	— ^a	28	— ^a	15	12	2
	GC ^c	67	30	12	13	12	— ^a

^a Cannot be accurately determined. ^b Determined by ^1H NMR using mesitylene as an internal standard. ^c Determined by GC using mesitylene as an internal standard.

Full assignment of the signals of **4-8** in the GC chromatogram was successfully achieved, allowing obtaining the yield of each product as well as the conversion (Figure S9.3). This GC analysis is consistent with the NMR data: the cage catalyst **1** give a better conversion than the model **2** (87% and 67%, respectively), as a consequence, better yields in products **4** and **7** were achieved: 38% and 17% respectively with the former *vs* 30% and 13% with the latter. Thus it appears that the supramolecular catalyst **1** does not suffer from product inhibition, as the observation for oxidation of **3**, and a good conversion can be reached with a low loading for a cage catalyst.

As the substrate **6** was used as a 1/3.5 mixture of two diastereomers which can be distinguished by GC chromatogram showing two separate peaks, and the catalyst **1** is used as a single isomer, we expected that diastereoselective conversion of the substrates may be observed.¹² The GC analysis reveals that with the model catalyst **2**, the initial ratio was almost retained at the end of the reaction (from 1/3.5 to 1/3.4), showing that the reaction rates are very similar for the two diastereomers (Figure S9.4). In contrast, this ratio changed to 1:1.4

with the cage complex **1**, evidencing that the rate for one diastereomer is faster than for the other. The different catalytic behaviors of catalysts **1** and **2** may also reflect the fact that diastereoselective host-guest combination between the substrates and the cage catalyst may have occurred that can affect the catalytic rate.¹² Thus, it appears that the cage structure induced an improvement of the diastereoselectivity of the reaction, as previously observed with engaged Verkade superbases in a hemicryptophane core when used as catalyst in a Diels-Dalder basico-catalyzed reaction.

9.4 Conclusion

In conclusion, an oxido-vanadium complex trapped inside a hemicryptophane cavity has been used as a supramolecular catalyst for the aerobic oxidation of lignin model. Compared to the model catalyst with an open structure, an improvement of the catalytic activity associated with a diastereomerically selective conversion has been observed. Good TON was reached considering the supramolecular feature of catalyst **1**. This underlines that this class of supramolecular catalysts benefits from its flexibility to prevent product inhibition, as previously observed for other hemicryptophane catalytic systems. Following this communication, our future work will seek to expand the scope of lignin substrates with the hemicryptophane catalyst to comprehensively understand the confinement effect.

9.5 Experimental section

9.5.1 Materials and instrumentation

Unless specified otherwise, all reactions were carried out under nitrogen using Schlenk techniques. Deuterated solvents were purchased from Cambridge Isotope Laboratories. ¹H NMR spectra were obtained at room temperature on a Bruker AVANCE 300 spectrometer, with chemical shifts referenced to the residual solvent signals. GC-MS analysis was performed using a Hewlett-Packard 6890 GC system equipped with a HewlettPackard 5973 mass selective detector.

9.5.2 Catalytic procedure

Catalytic oxidation of substrate 3. In a 25 mL Schlenk flask, substrate **3** (23.5 mg, 0.110 mmol), and 0.1 mol % **1** (0.18 mg, 1.10×10^{-4} mmol) or **2** (0.13 mg, 1.10×10^{-4} mmol) were dissolved in 0.8 mL of DMSO-*d*₆. The reaction was heated to 80 °C with constant stirring for 18 h. At the end of the reaction, the Schlenk flask was cooled down to room temperature. 0.4 mL of DMSO-*d*₆ containing 1,3,5-trimethylbenzene (6.0 μL, 0.043 mmol) as an internal standard was added. The reaction mixture was transferred to a NMR tube and ¹H NMR spectrum was recorded. The yields of **4** and **5**, and the conversion of **3** were calculated based on the corresponding integration against that of the internal standard.

Catalytic oxidation of substrate 6. In a 25 mL Schlenk flask, substrate **6** (25.0 mg, 0.110 mmol), and 1 mol % **1** (1.75 mg, 1.10×10^{-4} mmol) or **2** (1.28 mg, 1.10×10^{-4} mmol) were

dissolved in 0.8 mL of DMSO-*d*₆. The reaction was heated to 120 °C with constant stirring for 20 h. At the end of the reaction, the Schlenk flask was cooled down to room temperature. 0.4 mL of DMSO-*d*₆ containing 1,3,5-trimethylbenzene (6.0 uL, 0.043 mmol) as an internal standard was added. The reaction mixture was transferred to a NMR tube and ¹H NMR spectrum was recorded. The yields of **7**, **8**, **10** and **11** were calculated based on the corresponding integration against that of the internal standard. The yield of **9** and the conversion of **6** cannot be determined due to signals overlap.

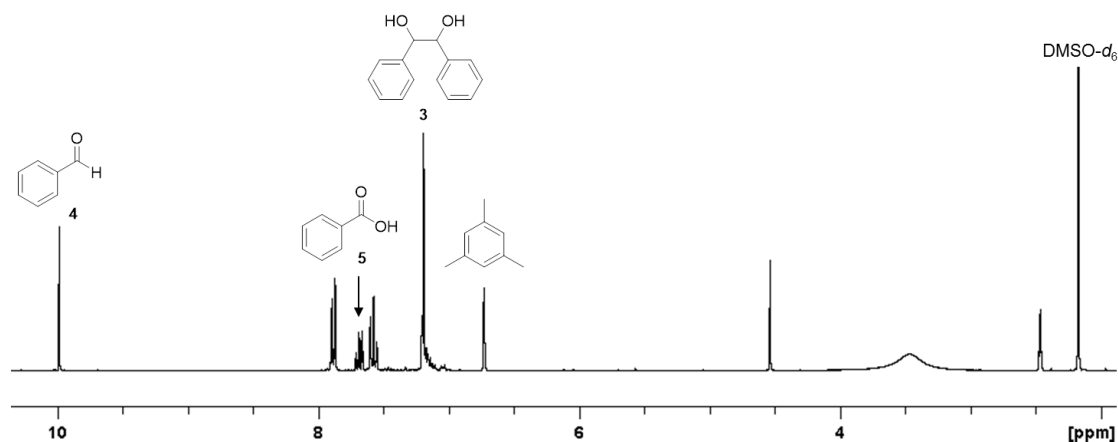


Figure S9.1 ¹H NMR spectrum (DMSO-*d*₆, 300 MHz, 298K) of the reaction mixture of catalytic oxidation of **3** by the cage catalyst **1** at 80 °C in DMSO-*d*₆ for 18 h. The yields of **4** and **5**, and the conversion of **3** were calculated based on the integrations against that of the internal standard. Similar spectrum with different integration ratios was obtained for the same substrate catalyzed by the model catalyst **2** under the same conditions.

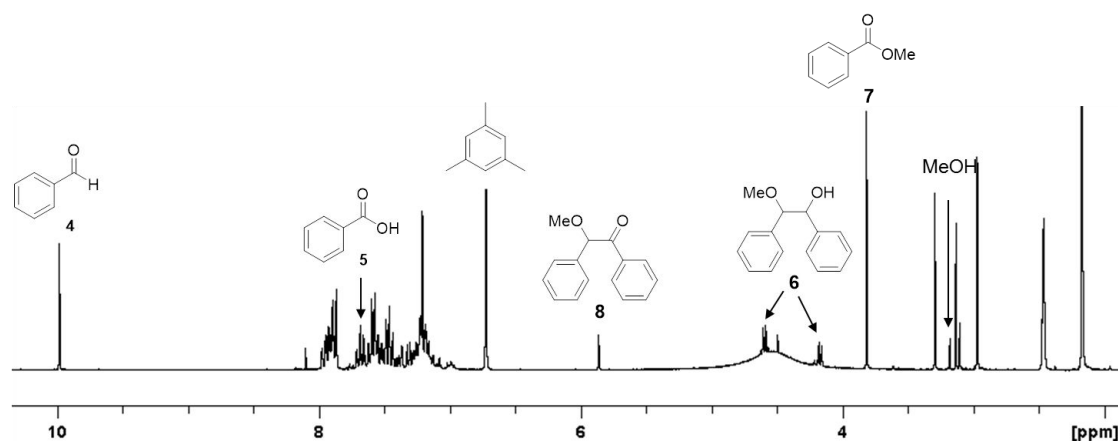


Figure S9.2 ¹H NMR spectrum (DMSO-*d*₆, 300 MHz, 298K) of the reaction mixture of catalytic oxidation of **6** by the cage catalyst **1** at 110 °C in DMSO-*d*₆ for 20 h. The yields of **4**, **7**, **8** and MeOH (**9**) were calculated based on the integrations against that of the internal standard. Due to signals overlap, the yield of **5** and the conversion of **6** cannot be determined. Similar spectrum with different integration ratios was obtained for the same substrate catalyzed by the model catalyst **2** under the same conditions.

9.5.3 GC analysis

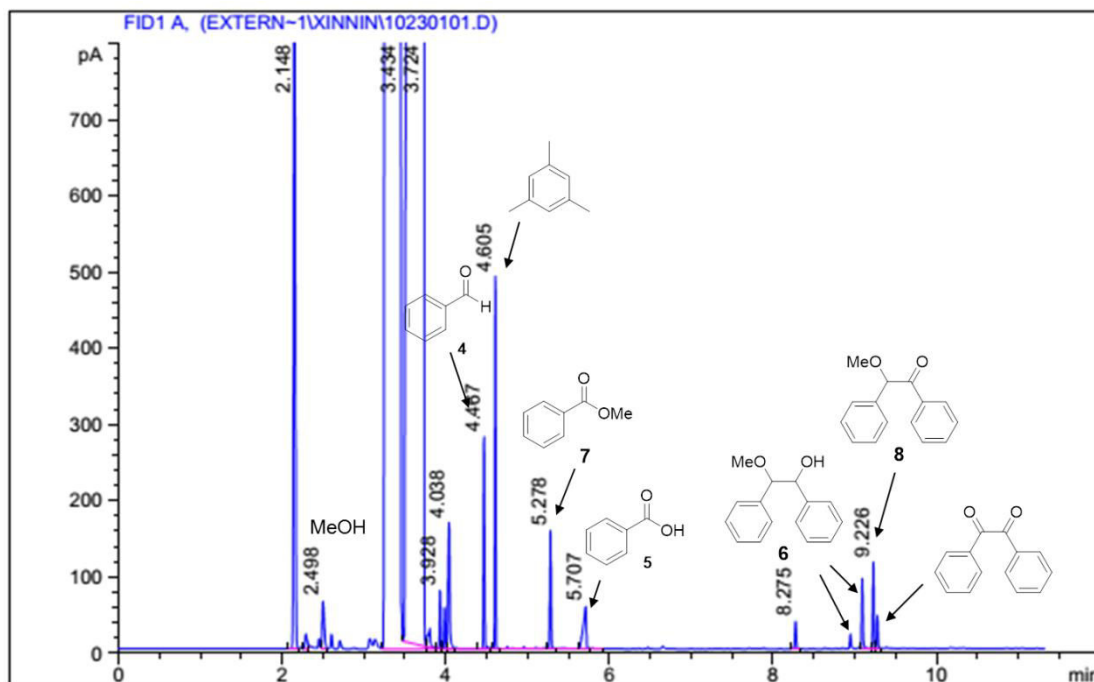


Figure S9.3 GC analytical spectrum of the reaction mixture of catalytic oxidation of **6** by the cage catalyst **1** at 110 °C in DMSO- d_6 for 20 h, with the full assignment of all the signals of **4-8**.

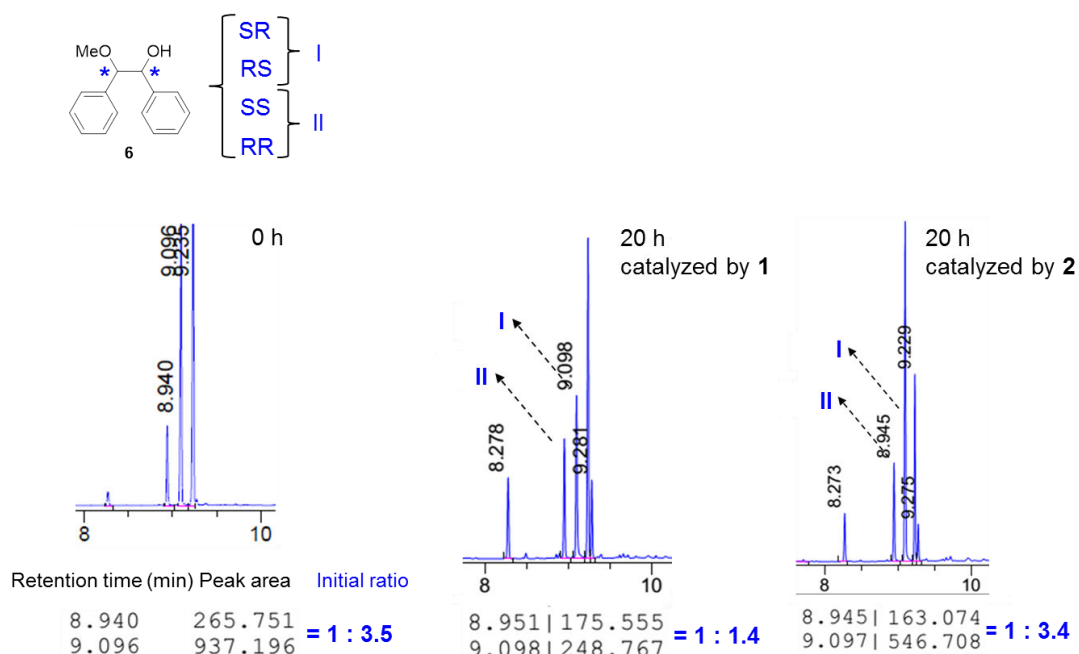


Figure S9.4 GC analysis showing that after 20 h of catalytic oxidation of **6** catalyzed by the cage catalyst **1**, obvious variation in the ratio between the two diastereomeric pairs of enantiomers has been observed (from 1:3.5 to 1:1.4); while when catalyzed by the model catalyst **2**, no obvious change occurred (from 1:3.5 to 1:3.4).

9.6 References

- (a) Raynal, M.; Ballester, P.; Vidal-Ferran, A.; van Leeuwen, P. W. N. M. *Chem. Soc. Rev.* **2014**, *43*, 1660. (b) Raynal, M.; Ballester, P.; Vidal-Ferran, A.; van Leeuwen, P. W. N. M. *Chem. Soc. Rev.* **2014**, *43*, 1734. (c) Brown, C. J.; Toste, F. D.; Bergman, R. G.; Raymond, K. N. *Chem. Rev.* **2015**, *115*, 3012. (d) Leenders, S. H. A. M.; Gramage-Doria, R.; de Bruin, B.; Reek, J. N. H. *Chem. Soc. Rev.* **2015**, *44*, 433. (e) Hyster, T. K.; Knorr, L.; Ward, T. R.; Rovis, T. *Science* **2012**, *338*, 500. (f) Hosseini, M. W.; Lehn, J. M.; Jones, K. C.; Plute, K. E.; Mertes, K. B.; Mertes, M. P. J. *Am. Chem. Soc.* **1989**, *111*, 6330.
- Zhang, D.; Matinez, A.; Dutasta, J.-P. *Chem. Rev.* **2017**, *Accepted*.
- (a) Chatelet, B.; Joucla, L.; Dutasta, J. P.; Martinez, A.; Dufaud, V. *Chem. Eur. J.* **2014**, *20*, 8571. (b) Martinez, A.; Dutasta, J. P. *J. Catal.* **2009**, *267*, 188. (c) Makita, Y.; Sugimoto, K.; Furuyoshi, K.; Ikeda, K.; Fujiwara, S.; Shin-ike, T.; Ogawa, A. *Inorg. Chem.* **2010**, *49*, 7220. (d) Makita, Y.; Ikeda, K.; Sugimoto, K.; Fujita, T.; Danno, T.; Bobuatong, K.; Ehara, M.; Fujiwara, S.; Ogawa, A. *J. Organomet. Chem.* **2012**, *706*, 26.
- Zhang, D. W.; Jamieson, K.; Guy, L.; Gao, G. H.; Dutasta, J. P.; Martinez, A. *Chem. Sci.* **2017**, *8*, 789.
- Unpublished results*.
- (a) Wyman, C. E. *Biotechnol. Progr.* **2003**, *19*, 254. (b) Corma, A.; Iborra, S.; Velty, A. *Chem. Rev.* **2007**, *107*, 2411. (c) Li, C. Z.; Zhao, X. C.; Wang, A. Q.; Huber, G. W.; Zhang, T. *Chem. Rev.* **2015**, *115*, 11559.
- Rencoret, J.; Gutierrez, A.; Nieto, L.; Jimenez-Barbero, J.; Faulds, C. B.; Kim, H.; Ralph, J.; Martinez, A. T.; del Rio, J. C. *Plant Physiol.* **2011**, *155*, 667.
- Sannigrahi, P.; Pu, Y. Q.; Ragauskas, A. *Curr. Opin. Env. Sust.* **2010**, *2*, 383.
- (a) Zakzeski, J.; Bruijninx, P. C. A.; Jongerius, A. L.; Weckhuysen, B. M. *Chem. Rev.* **2010**, *110*, 3552. (b) Zakzeski, J.; Bruijninx, P. C. A.; Weckhuysen, B. M. *Green. Chem.* **2011**, *13*, 671. (c) Deng, H. B.; Lin, L.; Liu, S. J. *Energ. Fuel.* **2010**, *24*, 4797. (d) Cho, D. W.; Parthasarathi, R.; Pimentel, A. S.; Maestas, G. D.; Park, H. J.; Yoon, U. C.; Dunaway-Mariano, D.; Gnanakaran, S.; Langan, P.; Mariano, P. S. *J. Org. Chem.* **2010**, *75*, 6549. (e) Cho, D. W.; Latham, J. A.; Park, H. J.; Yoon, U. C.; Langan, P.; Dunaway-Mariano, D.; Mariano, P. S. *J. Org. Chem.* **2011**, *76*, 2840.
- (a) Hanson, S. K.; Baker, R. T. *Acc. Chem. Res.* **2015**, *48*, 2037. (b) Jiang, Y. Y.; Yan, L.; Yu, H. Z.; Zhang, Q.; Fu, Y. *Acs Catal.* **2016**, *6*, 4399. (c) Son, S.; Toste, F. D. *Angew. Chem., Int. Edit.* **2010**, *49*, 3791. (d) Diaz-Urrutia, C.; Sedai, B.; Leckett, K. C.; Baker, R. T.; Hanson, S. K. *Acs Sustain. Chem. Eng.* **2016**, *4*, 6244.
- Hooley, R. J. *Nat. Chem.* **2016**, *8*, 202.
- Zhang, D. W.; Mulatier, J. C.; Cochrane, J. R.; Guy, L.; Gao, G. H.; Dutasta, J. P.; Martinez, A. *Chem. Eur. J.* **2016**, *22*, 8038.

Chapter 10. Azaphosphatranes as Hydrogen-Bonding Organocatalysts for the Activation of Carbonyl Groups: Investigation of Lactide Ring-Opening Polymerization

This Chapter is based partially on the following manuscript—

Dawei Zhang, Damien Jardel, Frédéric Peruch, Nathalie Calin, Véronique Dufaud, Jean-Pierre Dutasta, Alexandre Martinez, Brigitte Bibal

Eur. J. Org. Chem. **2016**, 1619–1624.

The work in this chapter was carried out at the ENS-Lyon.

Contents

10.1 Abstract.....	208
10.2 Introduction.....	208
10.3 Results and discussion	209
10.4 Conclusion	214
10.5 Experimental section.....	214
10.6 References.....	216

10.1 Abstract

The hydrogen-bonding activation of C=O bonds by azaphosphatranes was explored in a model reaction, *i.e.*, the ring-opening polymerization of lactide. The polymerization process was controlled, and allowed the preparation of poly lactides with narrow dispersity under mild conditions (20 °C, 24 h, 10 mol% catalyst loading). Interestingly, the steric hindrance of azaphosphatranes, as globular rigid structures, prevents any undesired interaction with the tertiary amine cocatalysts, as shown by X-ray analysis and semi-empirical calculations. In contrast to their organocatalytic activity in the CO₂/epoxide reaction, all of the phosphonium derivatives tested were found to be efficient catalysts in this ROP benchmark reaction.

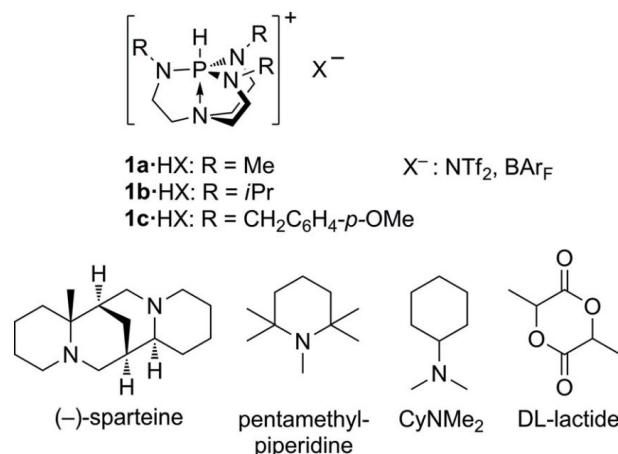
10.2 Introduction

Proazaphosphatranes, first described by Verkade and coworkers more than 20 years ago, show remarkable properties as basic or nucleophilic catalysts in numerous reactions.¹⁻³ Compared to these Verkade's superbases, their azaphosphatrane conjugate acids, resulting from protonation at the phosphorus atom of the proazaphosphatrane, have received little attention. Nevertheless, protonated azaphosphatranes have several interesting features as potential catalysts for various reactions related to their charge, the relative ease and modular character of their syntheses, their robustness, and the positively polarized proton located on the phosphorus atom. Two synthetic applications of these molecules have been reported by Verkade's group: one involves their use as procatalysts in the conversion of bromo-alkanes to alkenes under the action of sodium hydride,⁴ the second one involves their ability to act as promoters of the Michael and Strecker reactions.⁵ Martinez *et al.* have also reported the use of these azaphosphatranes as highly active and robust phase-transfer catalysts, and as organocatalysts for the synthesis of cyclic carbonates from CO₂ and epoxides.⁶⁻¹⁰ In the latter reaction, the mechanism was shown to involve an initial activation step of the epoxide through formation of a hydrogen bond with the ⁺P-H group of the azaphosphatrane. This recent result encouraged us to further explore the use of this original cation as an organocatalyst in the activation of C=O groups.

Indeed, the activation of carbonyl bonds by hydrogen-bond donor compounds is still a blossoming field of research, as a result of current challenges in asymmetric catalysis and ring opening polymerization (ROP).¹¹ Notably, the organocatalyzed ROP of cyclic esters by a hydrogen-bonding system (donor + acceptor) has become a model reaction to evaluate the activity of new hydrogen-bond-donor catalysts, and test their ability to activate C=O bonds, even in the presence of a hydrogen-bond acceptor (HBA) cocatalyst.¹² Since the pioneering work of Hedrick *et al.* based on the Takemoto's catalyst,¹³ hydrogen-bond donor catalysts such as thiourea derivatives,¹⁴ fluorinated alcohols,¹⁵ phosphoric acids,¹⁶ sulfonamides,¹⁷ amides,¹⁸ thiazolines,¹⁹ and phenols,²⁰ as well as protonated amines²¹ and quaternary ammonium compounds²² have been evaluated in the ROP of lactide (LA) as a model monomer.

These hydrogen-bonding systems can be either bifunctional or dual systems, as the hydrogen-bond donor is used in the presence of a tertiary amine – which acts as a

hydrogen-bond acceptor (cocatalyst) – such as (-)-sparteine (Sp),¹⁴ pentamethylpiperidine (PMP),²³ or CyNMe₂ (Scheme 10.1). As shown by Bibal *et al.*, the choice of cocatalyst should be adjusted depending on the hydrogen-bond donor to avoid inhibition of the desired transformation by a strong interaction between the cocatalysts.^{18b}



Scheme 10.1 Azaphosphatranes [**1a–1c·H**]⁺·X⁻ (X: NTf₂, BAr_F) and hydrogen-bond acceptors [(–)-sparteine, pentamethylpiperidine, and CyNMe₂] involved in the ring opening of DL-lactide.

To address the scope of the azaphosphatranes as hydrogen bonding moieties, their ability to activate C=O bonds was first evaluated in the model reaction of lactide ROP. Indeed, as the pK_a values of azaphosphatranes are larger than 32 in CH₃CN,²⁴ their corresponding protonated azaphosphatranane salts are very weak acids. As a consequence, the latter can be used in partnership with basic cocatalysts such as Sp, PMP, or CyNMe₂ (pK_a < 22 in CH₃CN),²⁵ without any proton exchange.

The effect of phosphonium substituents (R: Me, *i*Pr, CH₂C₆H₄-*p*-OMe) was screened using protonated Verkade's bases [**1a–1c·H**]⁺·X⁻ (Scheme 10.1). In addition, two hindered and lipophilic anions, bis(trifluoromethane)sulfonimide (X: NTf₂⁻) and tetrakis[3,5-bis(trifluoromethyl)phenyl]borate (X: BAr_F⁻), were used as non-coordinating counterions to ensure the solubility of the cationic catalysts in dichloromethane, and to favour their interactions with the monomer.

10.3 Results and discussion

10.3.1 Synthesis

New azaphosphatranes [**1a–1c·H**]⁺·Cl⁻ (Scheme 10.1) were obtained according to a two-step published procedure.^{26–28} A triple reductive amination of the appropriate aldehyde with tris(2-aminoethyl)amine (tren) gave the desired substituted tren ligands. These then reacted with PCl(NMe₂)₂ in acetonitrile. Anion-metathesis reactions were then carried out by mixing azaphosphatranane chloride salts and NaBAr_F or LiNTf₂ salts in ethanol/water mixtures. Precipitation of the resulting azaphosphatranane salts gave the six catalysts (*i.e.*, [**1a–1c·H**]⁺·NTf₂⁻ and [**1a–1c·H**]⁺·BAr_F⁻) in yields of 76–100 %. The ¹H spectra, recorded in CDCl₃ at 298 K, are consistent with C₃-symmetrical structures for the azaphosphatranane units. One doublet due to

the acidic proton could be observed between 5.27 and 5.85 ppm, with a J constant between 491 and 502 Hz. The ^{31}P NMR spectra show the characteristic signal of an azaphosphatrane, with chemical shifts varying between -9.0 and -11.6 ppm, similar to their chloride analogues.

10.3.2 X-ray diffraction

Crystallographic structures of azaphosphatranes with different aliphatic R substituents and different anions have been reported since the late 1980s.^{1,29} These structures unambiguously show the hybridization of the phosphorus and nitrogen atoms within these rigid globular compounds. Monocrystals of $[\mathbf{1b}\cdot\text{H}]^+\cdot\text{NTf}_2^-$ and $[\mathbf{1b}\cdot\text{H}]^+\cdot\text{BARf}^-$ were grown by slow evaporation from methanol solutions. The bond lengths and bond angles of these two compounds were found to be similar to those obtained for $[\mathbf{1b}\cdot\text{H}]^+\cdot\text{aluminatrane}^-$.^{29d} Detailed bond lengths and close contacts are listed in the Experimental section of this Chapter and summarized in Table 10.1. In particular, the $^+\text{P}\text{-H}$ bond length is 1.300 Å for $[\mathbf{1b}\cdot\text{H}]^+\cdot\text{NTf}_2^-$, and 1.277 Å for $[\mathbf{1b}\cdot\text{H}]^+\cdot\text{BARf}^-$. The phosphorus atom is also surrounded by three sp^2 -hybridized N_{eq} atoms ($^+\text{P}\text{-N}_{\text{eq}}$ bond lengths of $1.658\text{--}1.681$ Å), and a fourth sp^3 -hybridized nitrogen atom N_{ax} ($^+\text{P}\text{-N}_{\text{ax}}$ bond length of 1.981 Å for both crystals).

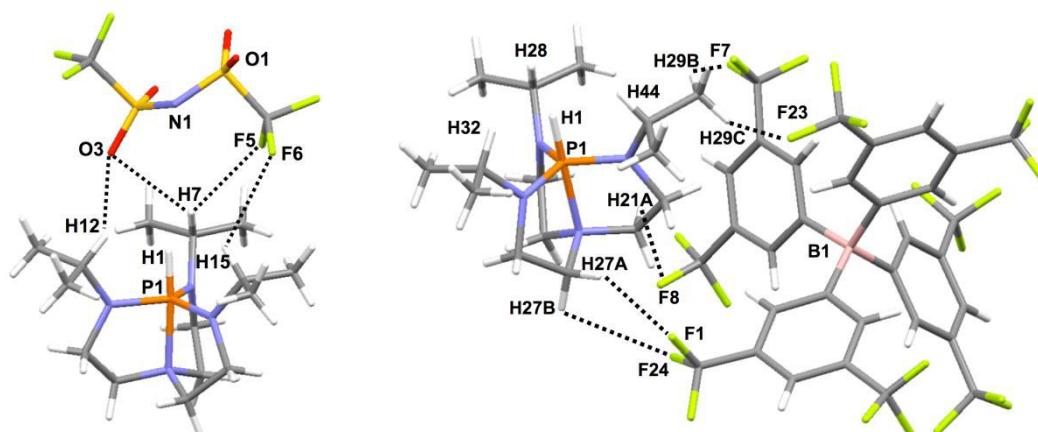


Figure 10.1 Selected contacts in crystal cells: $[\mathbf{1b}\cdot\text{H}]^+\cdot\text{NTf}_2^-$ (left) and $[\mathbf{1b}\cdot\text{H}]^+\cdot\text{BARf}^-$ (right).

For the $[\mathbf{1b}\cdot\text{H}]^+\cdot\text{NTf}_2^-$ crystal (Figure 10.1, left), each cation is mainly in close contact with its NTf_2^- anion through $\text{C}\text{-H}\cdots\text{F}\text{-C}$ ($2.567\text{--}2.85$ Å), $\text{C}\text{-H}\cdots\text{O}=\text{S}$ ($2.517\text{--}2.90$ Å), and $\text{C}\text{-H}\cdots\text{N}^-$ (2.601 Å) interactions. The anions also experienced $\text{C}\text{-F}\cdots\text{F}\text{-C}$ interactions ($2.84\text{--}3.09$ Å). Remarkably, the $^+\text{P}\text{-H}$ bonds are located near their benzylic substituents [$^+\text{P}\text{-H}\cdots\text{H}\text{-C}$ distances: 1.928 (H12), 2.042 (H7), and 2.130 (H15) Å], and embedded into a hydrophobic cavity with no other close contacts.

In the $[\mathbf{1b}\cdot\text{H}]^+\cdot\text{BARf}^-$ crystal (Figure 10.1, right), each cation is surrounded by other azaphosphatranes (intercation distances $2.503\text{--}2.829$ Å), and by several BARf^- anions through numerous $\text{C}\text{-H}\cdots\text{F}\text{-C}$ close contacts ($2.53\text{--}2.80$ Å). The latter anions also interact with each other through short $\text{C}\text{-F}\cdots\text{F}\text{-C}$ contacts ($2.81\text{--}3.10$ Å). Again, the $^+\text{P}\text{-H}$ bond is embedded into a hydrophobic cavity, and is only in close contact with its three nearby $\text{C}\text{-H}$ substituents [$^+\text{P}\text{-H}\cdots\text{H}\text{-C}$ distances: 2.044 (H44), 2.052 (H28), and 2.060 (H32) Å].

Thus, the inspection of these two azaphosphatranes in the solid state showed that the

globular rigid structures can provide a ^+P-H group as a main hydrogen-bond donor, possibly assisted by the three surrounding C–H bonds from the aliphatic substituents R.

Table 10.1 Main short contacts (\AA) in $[\mathbf{1b}\cdot\text{H}]^+\cdot\text{NTf}_2^-$ and $[\mathbf{1b}\cdot\text{H}]^+\cdot\text{BArF}_6^-$ monocrystals.

	Distance ^+P-H to $H-C_{\text{Nsubstituent}}$ (\AA)	Cation-anion Contacts (\AA)	Other close contacts (\AA)
$[\mathbf{1b}\cdot\text{H}]^+\cdot\text{N Tf}_2^-$	1.928, 2.042, 2.130	2.57-2.85 (C-H \cdots F-C), 2.601 (N \cdots H-C), 2.52-2.77 (C-H \cdots O-S)	2.84-3.09 (C-F \cdots F-C), 2.52-2.77 (C-H \cdots H-C)
$[\mathbf{1b}\cdot\text{H}]^+\cdot\text{BArF}_6^-$	2.044, 2.052, 2.060	2.53-2.85 (C-H \cdots F-C)	2.81-3.00 (C-F \cdots F-C), 2.50-2.83 (C-H \cdots H-C)

10.3.3 Intermolecular hydrogen-bonds

The accepted mechanism for the ring-opening polymerization of cyclic esters promoted by hydrogen bonding relies on the simultaneous formation of two distinct hydrogen-bonded complexes (Figure 10.2) in both initiation and propagation steps.^{12,13} Indeed, when the carbonyl group of the monomer is interacting with the hydrogen-bond-donor catalyst (*i.e.*, azaphosphatranes $[\mathbf{1a-c}\cdot\text{H}]^+\cdot\text{X}^-$), and at the same time the hydrogen-bond-acceptor catalyst (*i.e.*, a tertiary amine) is also hydrogen bonded to the initiator or the end of the growing chain (both alcohols), then both the nucleophile and the electrophile are activated, and could react at room temperature.

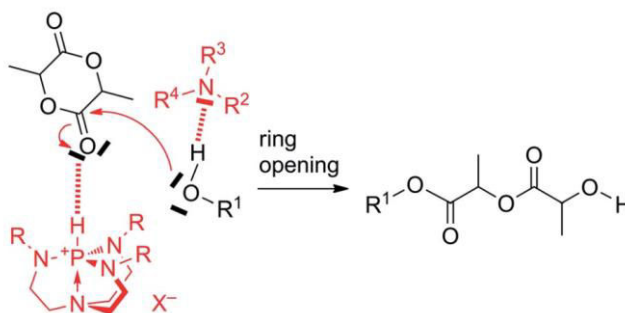


Figure 10.2 Proposed H-bonding activation using the $[\mathbf{1a-c}\cdot\text{H}]^+\cdot\text{X}^-$ and tertiary amine ($\text{NR}^2\text{R}^3\text{R}^4$) couple catalysts for the consensual ROP mechanism (R^1OH as the initiator or the growing chain).

This mechanism requires the formation of specific hydrogen bonds between the desired partners. If stronger hydrogen bonds can form between other partners (*e.g.*, between the two catalysts), then the efficiency of the catalysis can be dramatically reduced.^{18b}

To evaluate the hydrogen bonding between partners, and the ability of different catalyst combinations to promote the ROP reaction, geometry optimizations at the PM3 level were undertaken on a mixture of $[\mathbf{1b}\cdot\text{H}]^+$ with ι -lactide (desired hydrogen bonds), and on mixtures of $[\mathbf{1b}\cdot\text{H}]^+$ with the different cocatalysts (undesired hydrogen bonds) (see Figure 10.3, right). A hydrogen bond between the P^+-H bond and the carbonyl group of lactide (O-1–P-1: 2.75 \AA) was observed, without any steric hindrance between the two partners (Figure 10.3, left). In contrast, the formation of a hydrogen-bonded complex between CyNMe_2 and $[\mathbf{1b}\cdot\text{H}]^+$ is prevented by strong steric hindrance between the aliphatic substituents of the two partners. The bulkier tertiary amines, *i.e.*, PMP and (–)-sparteine, cannot form hydrogen bonds between

their nitrogen atom and the P-H bond (see Experimental section in this chapter). Based on semi-empirical calculations, the chosen azaphosphatranes and tertiary amines should not inhibit the catalytic reaction through undesired hydrogen bonding between the catalyst molecules. However, in the key step of the mechanism, two hydrogen-bonded complexes are formed in close proximity. So the bulkiness of all of the partners could play a role in the efficiency of the initiation and propagation steps. This point will be considered in the following reactivity section.

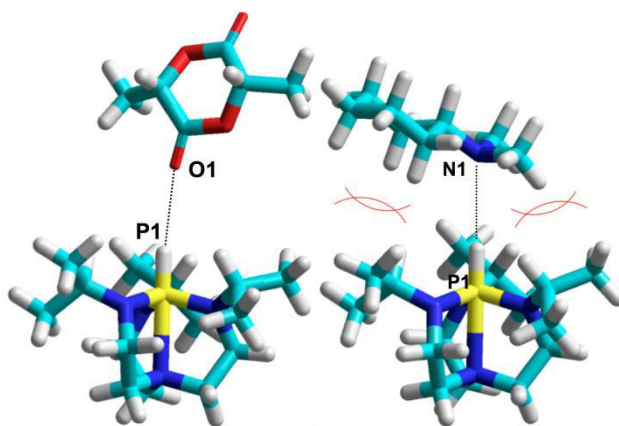


Figure 10.3 Energy-minimized structures (PM3 level, HyperChem 8.0) between $[\mathbf{1b-H}]^+$ and: (i) L-lactide (left) and (ii) CyNMe_2 (right).

10.3.4 Catalytic properties in the ROP of lactide

The organocatalyzed ROP of DL-lactide was carried out in dry dichloromethane under the usual conditions (20 °C, 24 h, 4 Å molecular sieves,³⁰ $[\text{LA}] = 1 \text{ M}$), in the presence of the hydrogen-bonding systems (donor + acceptor; 5 or 10 mol%), and 4-biphenylmethanol (BMP) as the initiator (5 or 10 mol%).¹² Due to its known efficiency in the ROP of LA, (-)-sparteine (Sp) was systematically used as the hydrogen-bond acceptor catalyst, while pentamethylpiperidine (PMP) and CyNMe_2 were tested with some of the azaphosphatranes. Preliminary experiments indicated that each component of the catalytic system [azaphosphatrane, tertiary amine, initiator, or molecular sieves (4 Å)] did not trigger the ROP independently. Only Sp gave a conversion of about 10% in the presence of the initiator and in the absence of a hydrogen-bond donor.^{18b}

The reaction mixtures were analysed by ^1H NMR spectroscopy to establish the percentage conversion. The crude polyesters were analysed by size-exclusion chromatography (SEC) to determine the molar mass (M_n) and dispersity (D), and by mass spectrometry to establish the chain-end fidelity and distribution (see Experimental section). In accordance with a living-like mechanism through H-bonds, the average molar masses were close to the theoretical ones, and the dispersity was narrow ($D = 1.03\text{--}1.09$). MALDI-TOF analysis confirmed these data, and showed that the side-reaction of polyester transesterification was very limited

The conversion ranged from 40 to 53% when the catalytic systems were at 5 mol%, and it reached 74–81% when the hydrogen-bonding systems were used at 10 mol% catalyst loading

(Table 10.2). Compared to the leading system (thiourea + Sp)¹⁴ which gives 100% conversion, the catalytic efficiency of these combinations is somewhat lower. Two hypotheses can be proposed: either the hydrogen-bond donor properties of azaphosphatranes towards C=O are moderate, or the steric hindrance of the azaphosphatranes can preclude their approach towards the (alcohol/hydrogen-bond acceptor) complex, a crucial step for the propagation. Concerning the strength of the hydrogen bond between lactide and the azaphosphatranes, titrations monitored by ¹H and ³¹P NMR spectroscopy (CDCl₃) revealed changes in chemical shift that were too small for the corresponding binding constants to be determined accurately. This fact also indicates that the hydrogen bonding between the two species is weak ($K < 1 \text{ M}^{-1}$), and weaker than previously reported.^{14,18b,18c,20a} So both moderate hydrogen-bond activation of the C=O group and steric hindrance from the azaphosphatranes can account for the conversions being 74–81% after 24 h.

Table 10.2 Catalytic properties of H-bond donors [**1a–c**·H]⁺·X[−] in presence of acceptors, in the ROP of lactide.^{a,b}

HB Donor Catalyst	HB Acceptor Catalyst	Catalysts Loading (mol%)	% conv. ^c
[1a·H]⁺·NTf₂[−]	Sp	5, 10	53, 74
	PMP	5	14
	CyNMe ₂	5	17
[1a·H]⁺·BAr_F[−]	Sp	5, 10	50, 75
[1b·H]⁺·NTf₂[−]	Sp	5, 10	45, 77
[1b·H]⁺·BAr_F[−]	Sp	5, 10	40, 75
[1c·H]⁺·NTf₂[−]	Sp	5, 10	42, 81
	PMP	5	16
	CyNMe ₂	5	16
[1c·H]⁺·BAr_F[−]	Sp	5, 10	32, 76

^a Conditions: DL-Lactide 1 M in CH₂Cl₂, biphenylmethanol as initiator (same loading as catalysts), [**1a–c**·H]⁺·X[−] and HB acceptor catalysts (1:1, 5 or 10 mol%), 4 Å molecular sieves, 20 °C, 24 h. ^b Poly(lactides) were analysed by ¹H NMR and size exclusion chromatography. ^c Determined by ¹H NMR.

It is interesting that for each cation we tested in these ROP reactions, the nature of the

phosphonium counterion (X^- : NTf₂⁻ or BArF⁻) had no impact on the conversion. This might be due to the noncoordination of the ion pairs in each case. Furthermore, variation of the phosphonium substituents (R: Me, *i*Pr, CH₂C₆H₄-*p*-OMe) has no noticeable effect, as conversions are similar in all entries of Table 10.2. This is in sharp contrast with our previous results related to the use of azaphosphatranes as phase-transfer catalysts or organocatalysts for CO₂ conversion.^{6–10} In both these previous cases, [1a·H]⁺·Cl⁻ was found to be a much less efficient catalyst than its aromatic or neopentylsubstituted counterparts, steric hindrance accounting for the higher stability of these latter two. Thus, the mild conditions used here in this ROP reaction allow the simplest system (*i.e.*, [1a·H]⁺·X⁻) to show catalytic activity comparable to that of more hindered systems, paving the way for the use of this easily accessible compound in other reactions involving C=O activation. However, when the azaphosphatrane-based hemicyptophane cage (Figure 10.4) was used as catalysts (conditions: 5 mol% catalyst, BArF⁻ counterion, Sp, 5 mol% BMP, DL-Lactide 1 M in CH₂Cl₂, 20 °C, 24 h), only 10% of conversion was observed, indicating that the steric hindrance induced by the cage is too significant, which prevents the three reactants simultaneously close to the catalytic site to afford the catalytic reaction.

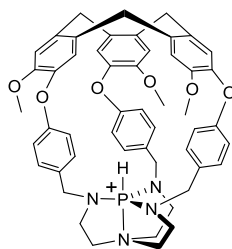


Figure 10.4 Structure of the azaphosphatrane-based hemicyptophane catalyst.

10.4 Conclusion

New azaphosphatranes with lipophilic hindered anions (NTf₂⁻ or BArF⁻) were synthesized. Crystallographic analysis and semiempirical calculations revealed that the phosphonium group is located in a hydrophobic cavity on top of a globular structure. Thus, the ⁺P–H bond can interact with the C=O group of lactide, but undesired hydrogen bonding with the tertiary amine cocatalysts does not take place, due to steric hindrance. The ability of azaphosphatranes to activate C=O groups in the ring-opening polymerization of lactide is promising, as the conversion reached 74–81% under classical conditions, even with the simplest azaphosphatrane catalyst. Again, this ROP model reaction offered a wealth of learning opportunities for the further exploration of azaphosphatranes in hydrogen-bonding catalysis. Future modifications of the azaphosphatrane structures should improve their ability to promote other transformations through the formation of multiple hydrogen bonds.

10.5 Experimental section

10.5.1 Materials and instrumentation

DL-Lactide was recrystallized three times in toluene and freshly sublimated. Dichloromethane was dried over calcium hydride and distilled. 4-biphenylmethanol was purified by precipitation in pentane. Commercially available Proazaphosphatranes, (-)-sparteine, PMP, CyNMe₂, LiNTf₂ and NaBARf were used as received. The synthesis of azaphosphatranes [1a-1c·H]⁺Cl⁻ was achieved according to the literature.²⁶⁻²⁸ The anion exchanges were adapted from our previously published procedure.²²

10.5.2 Synthesis and characterization

Synthesis of Azaphosphatranes [1a-1c·H]⁺NTf₂⁻: The corresponding phosphonium chloride [1a-1c·H]⁺Cl⁻ (400 mg) was dissolved in deionized water/ethanol (1:1; 2 mL), and a solution of LiNTf₂ (1.1 equiv.) in deionized water/ethanol (1:1; 2 mL) was added dropwise. A white precipitate was formed instantaneously. The reaction mixture was stirred for 1 h at room temperature. The solid was then collected by filtration, washed with deionized water (3 × 1 mL) and water/ethanol (1:1; 3 × 1 mL), and dried under vacuum, yield 81–100 %.

[1a·H]⁺NTf₂⁻: ¹H NMR (CDCl₃, 298K, 500.1 MHz): δ 5.30 (d, ¹J_{P-H} = 491.25 Hz, 1H, P-H); 3.26 (m, 6H, N(CH₂)₂N); 3.10 (m, 6H, N(CH₂)₂N); 2.69 (d, ³J_{P-H} = 17.45 Hz, 9H, NCH₃). ¹³C NMR (CDCl₃, 298K, 125.7 MHz): δ 119.9 (q, ¹J_{F-C} = 320.54 Hz, CF₃); 47.4 (d, ²J_{P-C} = 7.54 Hz, N(CH₂)₂N); 41.3 (d, ²J_{P-C} = 5.03 Hz, N(CH₂)₂N); 34.6 (d, ²J_{P-C} = 15.08 Hz, NCH₃). ³¹P NMR (CDCl₃, 298K, 202.4 MHz): δ -10.43. **ESI-HRMS** m/z: calcd for C₉H₂₂N₄P (M⁺) 217.1577, found 217.1584; calcd for C₂F₆NO₄S₂ (A⁻) 279.9178, found 279.9186.

[1b·H]⁺NTf₂⁻: ¹H NMR (CDCl₃, 298K, 500.1 MHz): δ 5.59 (d, ¹J_{P-H} = 497.80 Hz, 1H, P-H); 3.58 (m, 3H, NCH(CH₃)₂); 3.25 (m, 6H, N(CH₂)₂N); 3.07 (m, 6H, N(CH₂)₂N); 1.18 (d, ³J_{H-H} = 6.60 Hz, 18H, NCH(CH₃)₂). ¹³C NMR (CDCl₃, 298K, 125.7 MHz): δ 119.9 (q, ¹J_{F-C} = 321.79 Hz, CF₃); 47.1 (d, ²J_{P-C} = 15.08 Hz, NCH(CH₃)₂); 46.7 (d, ²J_{P-C} = 8.80 Hz, N(CH₂)₂N); 32.6 (d, ²J_{P-C} = 6.29 Hz, N(CH₂)₂N); 21.2 (d, ³J_{P-C} = 5.03 Hz, NCH(CH₃)₂). ³¹P NMR (CDCl₃, 298K, 202.4 MHz): δ -11.30. **ESI-HRMS** m/z: calcd for C₁₅H₃₄N₄P (M⁺) 301.2516, found 301.2522; calcd for C₂F₆NO₄S₂ (A⁻) 279.9178, found 279.9185.

[1c·H]⁺NTf₂⁻: ¹H NMR (CDCl₃, 298K, 500.1 MHz): δ 7.12 (d, ³J_{H-H} = 8.00 Hz, 6H, ArH); 6.91 (d, ³J_{H-H} = 8.00 Hz, 6H, ArH); 5.89 (d, ¹J_{P-H} = 496.65 Hz, 1H, P-H); 4.15 (d, ³J_{P-H} = 17.00 Hz, 6H, ArCH₂); 3.85 (s, 9H, OCH₃); 3.31 (m, 6H, N(CH₂)₂N); 3.10 (m, 6H, N(CH₂)₂N). ¹³C NMR (CDCl₃, 298K, 125.7 MHz): δ 159.4 (s, C_{Ar}); 128.9 (d, ³J_{P-C} = 5.03 Hz, C_{Ar}); 128.8 (s, C_{Ar}); 119.9 (q, ¹J_{F-C} = 321.79 Hz, CF₃); 114.4 (s, C_{Ar}); 55.4 (s, OCH₃); 50.9 (d, ²J_{P-C} = 15.08 Hz, ArCH₂); 47.0 (d, ²J_{P-C} = 7.54 Hz, N(CH₂)₂N); 38.9 (d, ²J_{P-C} = 5.03 Hz, N(CH₂)₂N). ³¹P NMR (CDCl₃, 298K, 202.4 MHz): δ -11.59. **ESI-HRMS** m/z: calcd for C₃₀H₄₀N₄O₃P (M⁺) 535.2833, found 535.2818; calcd for C₂F₆NO₄S₂ (A⁻) 279.9178, found 279.9188.

Synthesis of Azaphosphatranes [1a-1c·H]⁺BARf⁻: The corresponding phosphonium chloride [1a-1c·H]⁺Cl⁻ (400 mg) was dissolved in deionized water/ethanol (1:1; 2 mL), and a solution of NaBARf (1.1 equiv.) in deionized water/ethanol (1:1; 2 mL) was added dropwise. A white precipitate was formed instantaneously. The reaction mixture was stirred for 1 h at room temperature. The solid was then collected by filtration, washed with deionized water (3 × 1 mL) and water/ethanol (1:1; 3 × 1 mL), and dried under vacuum, yield 76–100 %.

[1a·H]⁺·BA_{rr}⁻: ¹H NMR (CDCl₃, 298K, 500.1 MHz): δ 7.72 (s, 8H, ArH); 7.58 (s, 4H, ArH); 5.27 (d, ¹J_{P-H} = 495.85 Hz, 1H, P-H); 2.92 (m, 12H, N(CH₂)₂N); 2.61 (d, ³J_{P-H} = 17.55 Hz, 9H, NCH₃). ¹³C NMR (CDCl₃, 298K, 125.7 MHz): δ 161.7 (q, ²J_{F-C} = 49.02 Hz, C_{Ar}); 134.77 (s, C_{Ar}); 129.0 (q, ³J_{F-C} = 31.40 Hz, C_{Ar}); 124.53 (q, ¹J_{F-C} = 272.8 Hz, CF₃); 117.6 (s, C_{Ar}); 47.3 (d, ²J_{P-C} = 6.29 Hz, N(CH₂)₂N); 40.9 (d, ²J_{P-C} = 3.77 Hz, N(CH₂)₂N); 34.6 (d, ²J_{P-C} = 16.34 Hz, NCH₃). ³¹P NMR (CDCl₃, 298K, 202.4 MHz): δ -8.99. **ESI-HRMS** m/z: calcd for C₉H₂₂N₄P (M⁺) 217.1577, found 217.1573; calcd for C₃₂H₁₂BF₂₄ (A⁻) 863.0660, found 863.0651.

[1b·H]⁺·BA_{rr}⁻: ¹H NMR (CDCl₃, 298K, 500.1 MHz): δ 7.73 (s, 8H, ArH); 7.57 (s, 4H, ArH); 5.59 (d, ¹J_{P-H} = 501.60 Hz, 1H, P-H); 3.56 (m, 3H, NCH(CH₃)₂); 2.94 (m, 6H, N(CH₂)₂N); 2.87 (m, 6H, N(CH₂)₂N); 1.13 (d, ³J_{H-H} = 6.60 Hz, 18H, NCH(CH₃)₂). ¹³C NMR (CDCl₃, 298K, 125.7 MHz): δ 161.7 (q, ²J_{F-C} = 50.28 Hz, C_{Ar}); 134.8 (s, C_{Ar}); 129.0 (q, ³J_{F-C} = 30.17 Hz, C_{Ar}); 124.5 (q, ¹J_{F-C} = 271.51 Hz, CF₃); 117.5 (s, C_{Ar}); 47.5 (d, ²J_{P-C} = 16.34 Hz, NCH(CH₃)₂); 46.8 (d, ²J_{P-C} = 8.80 Hz, N(CH₂)₂N); 32.4 (d, ²J_{P-C} = 5.03 Hz, N(CH₂)₂N); 21.0 (d, ³J_{P-C} = 5.03 Hz, NCH(CH₃)₂). ³¹P NMR (CDCl₃, 298K, 202.4 MHz): δ -9.62. **ESI-HRMS** m/z: calcd for C₁₅H₃₄N₄P (M⁺) 301.2516, found 301.2520; calcd for C₃₂H₁₂BF₂₄ (A⁻) 863.0660, found 863.0687.

[1c·H]⁺·BA_{rr}⁻: ¹H NMR (CDCl₃, 298K, 500.1 MHz): δ 7.71 (s, 8H, ArH); 7.55 (s, 4H, ArH); 7.07 (d, ³J_{H-H} = 8.25 Hz, 6H, ArH); 6.91 (d, ³J_{H-H} = 8.25 Hz, 6H, ArH); 5.95 (d, ¹J_{P-H} = 501.25 Hz, 1H, P-H); 4.15 (d, ³J_{P-H} = 17.00 Hz, 6H, ArCH₂); 3.84 (s, 9H, OCH₃); 2.96 (m, 6H, N(CH₂)₂N); 2.87 (m, 6H, N(CH₂)₂N). ¹³C NMR (CDCl₃, 298K, 125.7 MHz): δ 161.7 (q, ²J_{F-C} = 49.82 Hz, C_{Ar}); 159.7 (s, C_{Ar}); 134.8 (s, C_{Ar}); 129.0 (q, ³J_{F-C} = 32.13 Hz, C_{Ar}); 128.8 (s, C_{Ar}); 127.9 (d, ³J_{P-C} = 4.88 Hz, C_{Ar}); 124.6 (q, ¹J_{F-C} = 272.54 Hz, CF₃); 117.5 (s, C_{Ar}); 114.6 (s, C_{Ar}); 55.3 (s, OCH₃); 51.3 (d, ³J_{P-C} = 15.42 Hz, ArCH₂); 47.0 (d, ³J_{P-C} = 7.42 Hz, N(CH₂)₂N); 38.6 (d, ³J_{P-C} = 4.47 Hz, N(CH₂)₂N). ³¹P NMR (CDCl₃, 298K, 202.4 MHz): δ -10.60. **ESI-HRMS** m/z: calcd for C₃₀H₄₀N₄O₃P (M⁺) 535.2833, found 535.2819; calcd for C₃₂H₁₂BF₂₄ (A⁻) 863.0660, found 863.0657.

10.5.3 Procedure for ring-opening polymerization

Dry dichloromethane (1 mL), DL-lactide (1 mmol), azaphosphatrane [1-2·H]⁺·X⁻ (5 or 10 mol-%), the hydrogen-bond-acceptor cocatalyst (Sp, PMP, or CyNMe₂; 5 or 10 mol-%), 4-biphenylmethanol (5 or 10 mol-%), and molecular sieves (4 Å; 5 beads) were successively introduced into a dry Schlenk tube under nitrogen. The reaction mixture was stirred at 20 °C under nitrogen for 24 h. The reaction was quenched by the addition of water (50 μL), and the reaction mixture was filtered, and concentrated in vacuo. The conversion was determined by ¹H NMR spectroscopy, integrating the signals of the methane proton (adjacent to the carbonyl group) in both the residual monomer and the polymer. Molar masses and dispersity of the crude products were measured by size-exclusion chromatography (SEC) when the conversion was greater than 70 %.

10.6 References

- 1 C. Lensink, S. K. Xi, L. M. Daniels, J. G. Verkade, *J. Am. Chem. Soc.* **1989**, *111*, 3478–3479.
- 2 a) P. B. Kisanga, J. G. Verkade, *Tetrahedron* **2003**, *59*, 7819–7858; b) P. B. Kisanga, J. G. Verkade, *Aldrichim. Acta* **2004**, *37*, 3–14.

- 3 P. B. Kisanga, J. G. Verkade, R. Schwesinger, *J. Org. Chem.* **2000**, *65*, 5431–5432.
- 4 X. Liu, J. G. Verkade, *J. Org. Chem.* **1999**, *64*, 4840–4843.
- 5 B. M. Fetterly, N. K. Jana, J. G. Verkade, *Tetrahedron* **2006**, *62*, 440–456.
- 6 P. Dimitrov-Raytchev, J.-P. Dutasta, A. Martinez, *ChemCatChem* **2012**, *4*, 2045–2049.
- 7 B. Chatelet, L. Joucla, J.-P. Dutasta, A. Martinez, K. C. Szeto, V. Dufaud, *J. Am. Chem. Soc.* **2013**, *135*, 5348–5351.
- 8 B. Chatelet, L. Joucla, J.-P. Dutasta, A. Martinez, V. Dufaud, *Chem. Eur. J.* **2014**, *20*, 8571–8574.
- 9 B. Chatelet, E. Jeanneau, J.-P. Dutasta, V. Robert, A. Martinez, V. Dufaud, *Catal. Commun.* **2014**, *52*, 26–30.
- 10 B. Chatelet, L. Joucla, J.-P. Dutasta, A. Martinez, V. Dufaud, *J. Mater. Chem. A* **2014**, *2*, 14164–14172.
- 11 a) P. R. Schreiner, *Chem. Soc. Rev.* **2003**, *32*, 289–296; b) P. M. Pihko, *Angew. Chem. Int. Ed.* **2004**, *43*, 2062–2064; *Angew. Chem.* **2004**, *116*, 2110–2113; c) M. S. Taylor, E. N. Jacobsen, *Angew. Chem. Int. Ed.* **2006**, *45*, 1520–1543; *Angew. Chem.* **2006**, *118*, 1550–1573; d) X. Yu, W. Wang, *Chem. Asian J.* **2008**, *3*, 516–532; e) P. M. Pihko (Ed.), *Hydrogen Bonding in Organic Synthesis* **2009**, Wiley-VCH, Weinheim, Germany; f) K. EtzenbachEffers, A. Berkessel, *Top. Curr. Chem.* **2010**, *291*, 1–27; g) F. Giacalone, M. Gruttadauria, P. Agrigento, R. Noto, *Chem. Soc. Rev.* **2012**, *41*, 2406–2447.
- 12 a) N. E. Kamber, W. Jeong, R. M. Waymouth, R. C. Pratt, B. G. G. Lohmeijer, J. L. Hedrick, *Chem. Rev.* **2007**, *107*, 5813–5840; b) D. Bourissou, S. MoebsSanchez, B. Martin-Vaca, *C. R. Chim.* **2007**, *10*, 775–794; c) M. K. Kiesewetter, E. J. Shin, J. L. Hedrick, R. M. Waymouth, *Macromolecules* **2010**, *43*, 2093–2107; d) A. P. Dove, *ACS Macro Lett.* **2012**, *1*, 1409–1412; e) C. Thomas, B. Bibal, *Green Chem.* **2014**, *16*, 1687–1699.
- 13 A. P. Dove, R. C. Pratt, B. G. G. Lohmeijer, R. M. Waymouth, J. L. Hedrick, *J. Am. Chem. Soc.* **2005**, *127*, 13798–13799.
- 14 B. G. G. Lohmeijer, R. C. Pratt, F. Leibfarth, J. W. Logan, D. A. Long, A. P. Dove, F. Nederberg, J. Choi, C. Wade, R. M. Waymouth, J. L. Hedrick, *Macromolecules* **2006**, *39*, 8574–8583.
- 15 O. Coulembier, D. P. Sanders, A. Nelson, A. N. Hollenbeck, H. W. Horn, J. E. Rice, M. Fujiwara, P. Dubois, J. L. Hedrick, *Angew. Chem. Int. Ed.* **2009**, *48*, 5170–5173; *Angew. Chem.* **2009**, *121*, 5272–5275.
- 16 a) K. Makiguchi, T. Satoh, T. Kakuchi, *Macromolecules* **2011**, *44*, 1999–2005; b) D. Delcroix, A. Couffin, N. Susperregui, C. Navarro, L. Maron, B. Martin-Vaca, D. Bourissou, *Polym. Chem.* **2011**, *2*, 2249–2256.
- 17 a) A. Alba, A. Schopp, A.-P. De Souza Delgado, R. Cherif-Cheikh, B. MartinVaca, D. Bourissou, *J. Polym. Sci., Part A* **2010**, *48*, 959–965; b) C. Thomas, F. Peruch, B. Bibal, *All Res. J. Chem.* **2012**, *3*, 7–11.
- 18 a) S. Koeller, J. Kadota, A. Deffieux, F. Peruch, S. Massip, J.-M. Léger, J.-P. Desvergne, B. Bibal, *J. Am. Chem. Soc.* **2009**, *131*, 15088–15089; b) S. Koeller, J. Kadota, F. Peruch, A. Deffieux, N. Pinaud, I. Pianet, S. Massip, J.-M. Leger, J.-P. Desvergne, B. Bibal, *Chem. Eur. J.* **2010**, *16*, 4196–4205; c) S. Koeller, C. Thomas, F. Peruch, A. Deffieux, S. Massip, J.-M. Léger, J.-P. Desvergne, A. Milet, B. Bibal, *Chem. Eur. J.* **2014**, *20*, 2849–2859.

- 19 J. M. Becker, S. Tempelaar, M. J. Stanford, R. J. Pounder, J. A. Covington, A. P. Dove, *Chem. Eur. J.* **2010**, *16*, 6099–6105.
- 20 a) C. Thomas, F. Peruch, A. Deffieux, A. Milet, J.-P. Desvergne, B. Bibal, *Adv. Synth. Catal.* **2011**, *353*, 1049–1054; b) C. Thomas, F. Peruch, B. Bibal, *RSC Adv.* **2012**, *2*, 12851–12856.
- 21 a) J. Kadota, D. Pavlovic, J.-P. Desvergne, B. Bibal, F. Peruch, A. Deffieux, *Macromolecules* **2010**, *43*, 8874–8879; b) D. J. Coady, K. Fukushima, H. W. Horn, J. E. Rice, J. L. Hedrick, *Chem. Commun.* **2011**, *47*, 3105–3107; c) O. Coulembier, T. Josse, B. Guillermin, P. Gerbaux, P. Dubois, *Chem. Commun.* **2012**, *48*, 11695–11697; d) Y. Miao, N. Stanley, A. Favrelle, T. Bousquet, M. Bria, A. Mortreux, P. Zinck, *J. Polym. Sci., Part A* **2015**, *53*, 659–664.
- 22 C. Thomas, A. Milet, F. Peruch, B. Bibal, *Polym. Chem.* **2013**, *4*, 3491–3498.
- 23 a) E. Piedra-Arroni, P. Brignou, A. Amgoune, S. M. Guillaume, J.-F. Carpentier, D. Bourissou, *Chem. Commun.* **2001**, *47*, 9828–9830; b) C. Thomas, J. A. Gladysz, *ACS Catal.* **2014**, *4*, 1134–1138.
- 24 pKa (CH₃CN) for azaphosphatranes: 32.9, 33.63, and 31.14 for **1a**, **1b**, and **1c**, respectively. For reference, see: a) P. B. Kisanga, J. G. Verkade, R. Schwesinger, *J. Org. Chem.* **2000**, *65*, 5431–5432; b) P. Dimitrov Raytchev, A. Martinez, H. Gornitzka, J.-P. Dutasta, *J. Am. Chem. Soc.* **2011**, *133*, 2157–2159.
- 25 pKa (CH₃CN) for basic cocatalysts: 21.66 (Sp), 18.62 (PMP), and ca. 18 (CyNMe₂). For reference, see: C. F. Lemaire, J. J. Aerts, S. Voccia, L. C. Libert, F. Mercier, D. Goblet, A. R. Plenevaux, A. J. Luxen, *Angew. Chem., Int. Ed.* **2010**, *49*, 3161–3164; *Angew. Chem.* **2010**, *122*, 3229–3232.
- 26 P. Kisanga, J. G. Verkade, *Tetrahedron* **2001**, *57*, 467–475.
- 27 H. Schmidt, C. Lensink, S. K. Xi, J. G. Verkade, *Z. Anorg. Allg. Chem.* **1989**, *578*, 75–80.
- 28 P. Dimitrov Raytchev, A. Martinez, H. Gornitzka, J.-P. Dutasta, *J. Am. Chem. Soc.* **2011**, *133*, 2157–2159.
- 29 a) K. Ishihara, Y. Karumi, S. Kondo, H. Yamamoto, *J. Org. Chem.* **1998**, *63*, 5692–5695; b) X. Liu, P. Ilankumaran, I. A. Guzei, J. G. Verkade, *J. Org. Chem.* **2000**, *65*, 701–706; c) J. V. Kingston, J. G. Verkade, *Inorg. Chem. Commun.* **2005**, *8*, 643–646; d) W. Su, Y. Kim, A. Ellern, I. A. Guzei, J. G. Verkade, *J. Am. Chem. Soc.* **2006**, *128*, 13727–13735; e) V. R. Chintareddy, A. Ellern, J. G. Verkade, *J. Org. Chem.* **2010**, *75*, 7166–7174; f) W. C. Ewing, A. Marchione, D. W. Himmelberger, P. J. Carroll, L. G. Sneddon, *J. Am. Chem. Soc.* **2011**, *133*, 17093–17099; g) J. Lee, Y. Kim, *Acta Crystallogr., Sect. E* **2012**, *68*, o3317.
- 30 Molecular sieves (4 Å) were used with the aim of removing residual water molecules from the reaction mixture (introduced by reactants and reagents), as water is a strong hydrogen-bonding competitor with the catalysts.

Part V. Beyond Hemicryptophanes: Cages Constructed by Self-Assembly

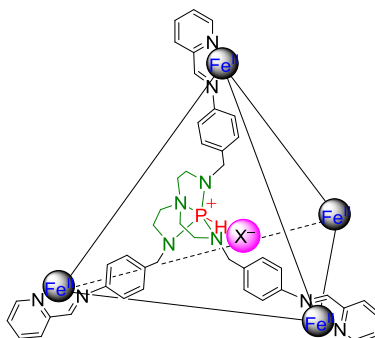
Preface

Part V Network



* Hemi = Hemicryptophane

In the last part of this PhD thesis, my attention is not limited to the hemicryptophane cages, we intend to open a more perspective view to prepare self-assembled cages. In this area, the group of Prof. Jonathan R. Nitschke at the University of Cambridge has achieved significant progress in the preparation and investigation of assembled cages by subcomponent self-assembly. Subcomponent self-assembly is a process, in which the building blocks (generally aldehydes and amines) spontaneously self-assemble around templates leading to simultaneous dynamic-covalent (C=N) and coordinative (N → metal) bonds formation, allowing the generation of complex architectures from simple building blocks (*Acc. Chem. Res.* **2014**, *47*, 2063–2073). This method has been successfully used to construct well-defined metal-organic macrocycles, helicates, catenanes, rotaxanes, grids, and cages. On the other hand, in **Chapter 10** of **Part IV**, we have developed the azaphosphatrane units as hydrogen-bonding organocatalysts for lactide ring-opening polymerization. We notice that the azaphosphatrane unit should be attractive functional moiety for incorporation into the faces of tetrahedral cages built by subcomponent self-assembly. The four acidic $+P-H$ groups on the faces of tetrahedron pointing inside should allow the cage as an efficient anion binder (see the figure below). Therefore, **Chapter 11** describes these investigations and findings conducted in collaboration with Prof. Jonathan R. Nitschke.



It is worth mentioning that the work in **Chapter 11** is based partially on my publication of *Journal of the American Chemical Society* (**2017**, *139*, 6574–6577). The numbers of compounds, figures, schemes and tables have been renumbered compared to the previous chapters, and the numbers of compounds between chapters have no relationship. The Table of Contents in this chapter has been presented in the chapter cover. The cited references are listed at the end of the chapter.

Chapter 11. Anion Binding in Water Drives Structural Adaptation in an Azaphosphatrane-Functionalized $\text{Fe}^{\text{II}}_4\text{L}_4$ Tetrahedron

This Chapter is based partially on the following manuscript—

Dawei Zhang, Tanya K. Ronson, Jesús Mosquera, Alexandre Martinez, Laure Guy, and Jonathan R. Nitschke

J. Am. Chem. Soc. **2017**, *139*, 6574–6577.

The work in this chapter was carried out at the University of Cambridge.

Contents

11.1 Abstract.....	224
11.2 Introduction.....	224
11.3 Results and discussion	225
11.4 Conclusion	229
11.5 Experimental section.....	230
11.6 References.....	272

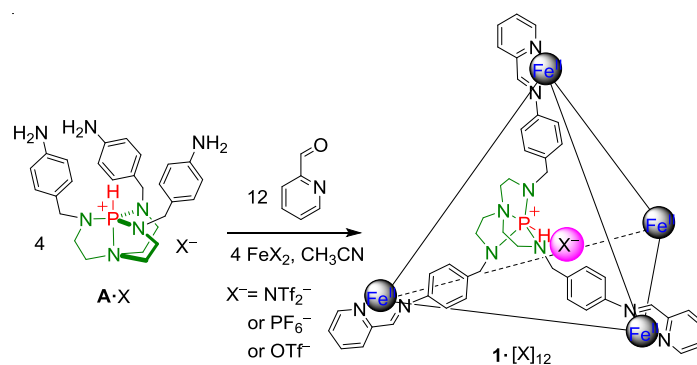
11.1 Abstract

Anion binding in water templated the self-assembly of an endohedrally functionalized $\text{Fe}^{\text{II}}\text{L}_4$ tetrahedron from azaphosphatrane-based subcomponents. This new water-soluble cage is flexible and able to encapsulate anions with volumes ranging from 35 to 219 Å³ *via* hydrogen bonding and electrostatic interactions. It structurally adapts in response to the size and shape of the template anions, adopting a conformation either where all four azaphosphatrane $^+\text{P-H}$ vectors point inward or else in which one points outward and the other three inward. The two cage isomers coexist in solution in some cases and interconvert. A shape memory phenomenon was observed during guest displacement due to its faster kinetics relative to those of structural reconfiguration.

11.2 Introduction

Self-assembly is an efficient tool for the construction of diverse functional architectures.¹ One subset of these, metal–organic polyhedral complexes, have proven useful in a range of applications, including molecular recognition,² chirality sensing,³ gas separation,⁴ stabilization of reactive species,⁵ and catalysis.⁶ The strategy of subcomponent self-assembly⁷ allows the preparation of a variety of capsules with different shapes and sizes, which bind a diverse collection of guests.⁸ Most such capsules contain cavities surrounded by aromatic panels.^{7a-d} The elaboration of the cavity microenvironment, through incorporation of functional moieties,^{7e,7f} represents an attractive means by which specific substrate encapsulation might be achieved.

Azaphosphatranes, the conjugate acids of Verkade superbases,⁹ are attractive functional moieties for incorporation into the faces of tetrahedral capsules. Their polarized $^+\text{P-H}$ groups enable them to be employed as catalysts for CO_2 activation and lactide ring-opening polymerization.¹⁰ Although both of these applications benefit from the hydrogen-bond donor ability of the $^+\text{P-H}$ group, their use as anion receptors has not been reported. Importantly, these cationic species can be rendered water-soluble *via* selection of a suitable counterion, potentially enabling their use as anion binders in water, the development of which has been identified as a key challenge in supramolecular chemistry.¹¹



Scheme 11.1 Subcomponent self-assembly of cage **1** in acetonitrile.

Here we report a new azaphosphatrane-functionalized tetrahedron **1**, (Scheme 11.1)

assembled from cationic triamine subcomponent **A**. The design of **1** was based on the following four principles. First, the cationic nature of the azaphosphatranes together with the metal ions provide an overall +12 charge, offering a strong electrostatic driving force for anion binding. Second, the cationic framework also inductively increases the affinity of the ^+P-H hydrogen bond donor for anionic species.¹² Third, the counterion SO_4^{2-} was chosen to maximize the water solubility of **1**. Fourth, methylene groups between the phenyl rings and azaphosphatrane nitrogen atoms were introduced to enhance cage flexibility, enabling the cavity to adapt to fit a diverse array of anions.

11.3 Results and discussion

We first prepared cage **1** as the bis(trifluoromethanesulfonyl)imide (triflimide, NTf_2), hexafluorophosphate (PF_6^-) and trifluoromethanesulfonate (triflate, OTf^-) salts, all of which were soluble in acetonitrile (Scheme 11.1). Subcomponent **A**·Cl was obtained in four steps from commercially available starting materials (Scheme S11.1). The Cl^- counterion of **A** readily exchanged with NTf_2^- , PF_6^- or OTf^- *via* anion metathesis. The reaction of **A**·X (4 equiv) with the corresponding FeX_2 salt (4 equiv) and 2-formylpyridine (12 equiv) in acetonitrile gave a single product with one azaphosphatrane capping each face. The products were characterized by NMR and mass spectrometry (Figures S11.1-S11.36). ^{19}F NMR spectra (Figures S11.5, S11.17 and S11.29) indicated the encapsulation of one anion inside the cavity, in slow exchange on the NMR timescale with the external anions.

Single-crystal X-ray diffraction confirmed the structure of **1** in the solid state. As shown in Figure 11.1, **1** has a face-capped tetrahedral framework with approximate *T*-symmetry. Both enantiomers ($\Delta\Delta\Delta\Delta$ and $\Lambda\Lambda\Lambda\Lambda$) are present in the unit cell. The ^+P-H groups of the azaphosphatrane units point inward into cavity, where a disordered triflate anion is encapsulated. The Fe^{II} centers are separated by an average of 14.7 Å, and the volume of the central cavity approximates 166 Å³ (51% occupancy for OTf^- , Figure S11.70).

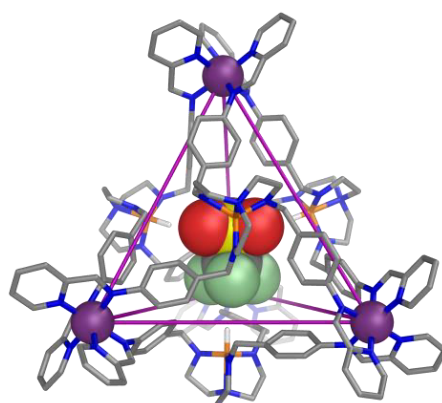


Figure 11.1 Crystal structure of $OTf^- \subset \mathbf{1}$, which shows a *T*-symmetric cage. Disorder, unbound counterions, nonacidic hydrogen atoms, and solvents are omitted for clarity.

We then attempted the preparation of a water-soluble cage by employing SO_4^{2-} counterions.¹³ The Cl^- of **A** was exchanged to SO_4^{2-} (Scheme S11.2). However, the subsequent reaction of **A**· $[SO_4]_{0.5}$ (4 equiv) with $FeSO_4$ (4 equiv) and 2-formylpyridine (12 equiv) failed to give the expected cage complex (Figure S11.37). We infer that the hydrophilic character of

SO_4^{2-} prevents it acting as a template for the formation of **1**.¹⁴ Therefore, a series of other anions with different shapes and volumes, listed in Figure 11.2, were added to the aqueous reaction mixture to investigate their template effects (1 equiv of anion was added in each case with regard to the final cage).

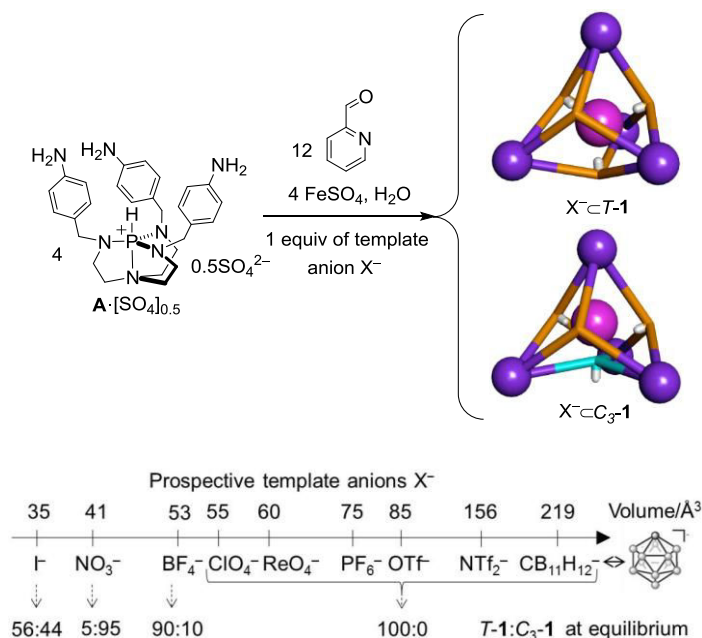


Figure 11.2 Schematic representation of the two cage isomers $X^- \subset T-1$ and $X^- \subset C_3-1$ obtained by self-assembly in water driven by 1 equiv of template anion. The tripods colored orange in the faces of the tetrahedra represent *endo*-azaphosphatrane ligands with the $^+\text{P-H}$ oriented inward, while the one colored cyan represents *exo* $^+\text{P-H}$.

All of the anions listed in Figure 11.2, with volumes ranging from 35 \AA^3 (I^-) to 219 \AA^3 ($\text{CB}_{11}\text{H}_{12}^-$), were observed to serve as competent templates for **1**, indicating that its cavity adapted readily to guests having different sizes and shapes. In particular, cage **1** manifested this adaptability in a novel way: for the smaller template anions with volumes $\leq 53 \text{ \AA}^3$, part of the population of **1** consisted of a C_3 -symmetric isomer (C_3-1) in which one of the azaphosphatrane $^+\text{P-H}$ groups was oriented away from the inner cavity (defined as *exo*) with the other three pointed inward (defined as *endo*); while a T -symmetric isomer ($T-1$) constructed by four *endo* $^+\text{P-H}$ groups constituted the other part of the population. For the larger anionic templates with volumes $\geq 55 \text{ \AA}^3$, the T -symmetric isomer ($T-1$) was observed exclusively.

The ^1H NMR spectra of **1** templated by BF_4^- , NO_3^- or I^- in water show five sets of ligand signals (Figures S11.49), in which one set belongs to $T-1$, while the other four sets in a 1:1:1:1 integrated ratio belong to C_3-1 (for full structural assignment, see Figure S11.53). The corresponding ^{31}P NMR spectra exhibit three peaks, one for $T-1$ and two in a 3:1 ratio for C_3-1 (Figures S11.52, S11.62 and S11.65). The two cage isomers were observed to interconvert taking at least two weeks at 298 K to reach equilibrium, which was monitored by both ^1H and ^{31}P NMR. For instance, for the self-assembly with NO_3^- as a template, a gradual conversion from $T-1$ to C_3-1 was observed with the ratio changing from 58:42 at 24 h to 10:90 at 215 h (Figure 11.3, S11.50 and S11.52). This indicates that $\text{NO}_3^- \subset T-1$ is kinetically metastable while

$\text{NO}_3^- \text{C}_3\text{-1}$ is thermodynamically favorable. After two weeks at 298 K, the ratio of $\text{NO}_3^- \text{C}_3\text{-1}:\text{NO}_3^- \text{C}_3\text{-1}$ became constant with a value of 5:95. This value remained unchanged on varying the initial concentration. The free energy of activation for interconversion was then determined from ^1H NMR experiments, and calculated to be 105 kJ mol^{-1} at 298 K from $\text{NO}_3^- \text{C}_3\text{-1}$ to $\text{NO}_3^- \text{C}_3\text{-1}$ with a rate constant of $(2.95 \pm 0.08) \times 10^{-6} \text{ s}^{-1}$ (Figure S11.67).

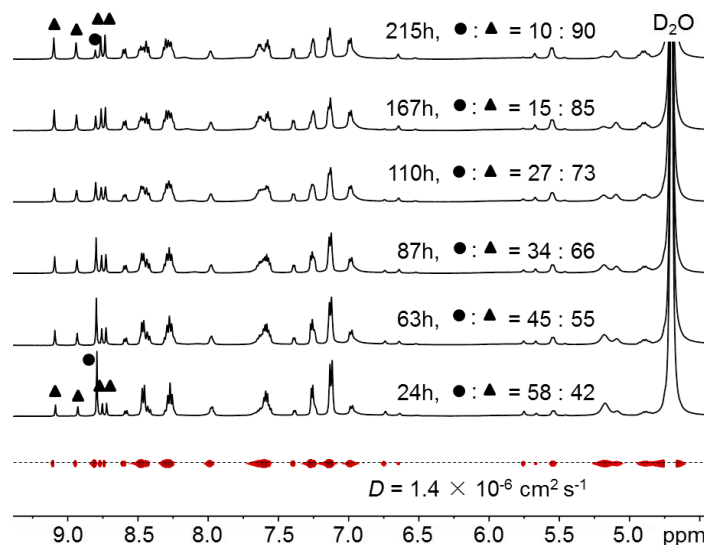


Figure 11.3 Time evolution of the ratio between $\text{NO}_3^- \text{C}_3\text{-1} \cdot [\text{SO}_4]_{5.5}$ (●) and $\text{NO}_3^- \text{C}_3\text{-1} \cdot [\text{SO}_4]_{5.5}$ (▲) at 298 K by monitoring the integration of the corresponding imine peaks in the ^1H NMR spectra (D_2O , 500 MHz, 298 K). DOSY shows that the two species give the same diffusion coefficient.

In the cases of BF_4^- and I^- (Figures S11.61, S11.62, S11.64 and S11.65), $\text{BF}_4^- \text{C}_3\text{-1}$ and $\text{I}^- \text{C}_3\text{-1}$ were observed to be both kinetically and thermodynamically favored products compared to $\text{BF}_4^- \text{C}_3\text{-1}$ and $\text{I}^- \text{C}_3\text{-1}$, respectively, giving ratios of 90:10 and 56:44 at equilibrium after two weeks. The free energies of activation at 298 K for the conversion from $\text{X}^- \text{C}_3\text{-1}$ to $\text{X}^- \text{C}_3\text{-1}$ ($\text{X}^- = \text{BF}_4^-$ or I^-) are 105 kJ mol^{-1} and 106 kJ mol^{-1} , respectively (Figures S11.68 and S11.69), similar to the value in the case of NO_3^- . Considering these values are very close to the previously reported energy barriers of interconversion between homochiral and heterochiral M_4L_6 tetrahedral isomers (around 102 kJ mol^{-1})¹⁵ and noting that no disassembled products were observed during the conversion, we infer that the cage transformation occurs *via* a partial reconfiguration mechanism, which is also the pathway with the minimum energy barrier: only one azaphosphatrane face among the four is (partially) released followed by inversion and reassembly; during the whole process, the cage framework maintains a degree of structural integrity.¹⁶

Based on the crystal structure of $\text{OTf}^- \text{C}_3\text{-1}$ in Figure 11.1, we prepared an MM3 model of $\text{NO}_3^- \text{C}_3\text{-1}$ using SCIGRESS software (Figure 11.4).¹⁷ The modelling studies support a configuration where all Fe^{II} centers maintain the same Δ or Λ stereochemistry. The trigonal planar NO_3^- is located in the plane formed by the three *endo* $^+\text{P-H}$ groups with hydrogen bonding interactions. The bulky methylene groups of the *exo*-azaphosphatrane occupy the rest of the cavity. Consequently, its $^+\text{P-H}$ is also available to form hydrogen bonds with the surrounding water. The volume of the preorganized planar cavity approximates 59 \AA^3 (69% occupancy for NO_3^- , Figure S11.70), significantly smaller than that of $\text{OTf}^- \text{C}_3\text{-1}$ (166 \AA^3). This modelling also emphasizes why the assembled cage driven by NO_3^- , rather than BF_4^- (Figure

S11.63) or I⁻ (Figure S11.66), predominantly favors the C₃-isomeric conformation.

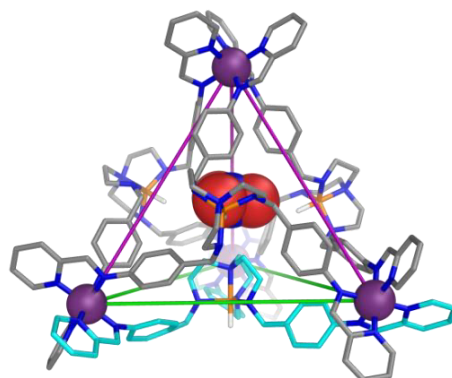


Figure 11.4 MM3-optimized molecular model of NO₃⁻⊂C₃-1, based on the crystal structure of OTf⁻⊂1 in Figure 11.1. Nonacidic hydrogen atoms are omitted for clarity. The *exo*-azaphosphatrane ligand is colored cyan.

¹H NMR spectra of **1** templated by ClO₄⁻, ReO₄⁻, PF₆⁻, OTf⁻, NTf₂⁻ or CB₁₁H₁₂⁻ in water show only one set of ligand signals (Figure S11.38 and S11.39), indicating the exclusive formation of the *T*-cage. This is also consistent with the highly symmetric ¹³C and ³¹P NMR spectra (Figure S11.40 and S11.41) as well as 2D NMR spectra (Figure S11.43-S11.48). Especially, the ¹H-¹⁹F HOESY spectra of OTf⁻/PF₆⁻⊂T-1·[SO₄]_{5.5} exhibit strong NOE correlations between the F atoms of the encapsulated guest and the ⁺P-H of the azaphosphatranes, underlining the hydrogen bonding interactions (Figures S11.42, S11.47 and S11.48).

Although the cage is unstable in the absence of a template anion, competitive guest exchange offers a way of measuring the relative binding affinities of the different anions. We first chose the ¹⁹F NMR spectrum of OTf⁻⊂1·[SO₄]_{5.5} as the reference and monitored the decrease of the encapsulated OTf⁻ and increase of the free OTf⁻ upon addition of a competitive anion. Results show that the binding affinities of PF₆⁻, ReO₄⁻ and ClO₄⁻ are 17, 1.9 and 0.03-fold relative to that of OTf⁻, respectively (Figures S11.71-S11.73). No obvious OTf⁻ displacement was observed upon addition of NO₃⁻, BF₄⁻, I⁻, NTf₂⁻ or CB₁₁H₁₂⁻.¹⁸ We then chose the ¹H NMR spectrum of NTf₂⁻⊂1·[SO₄]_{5.5} as the reference to classify the relative binding affinities of these latter anions. It was observed that 1.7 equiv of CB₁₁H₁₂⁻ completely displaced the encapsulated NTf₂⁻, (Figure S11.74), while a larger excess of BF₄⁻ or I⁻ was needed, with BF₄⁻ binding stronger than I⁻ (Figure S11.75 and S11.76). NO₃⁻ was unable to displace the bound NTf₂⁻. Combining all these results, we can establish the following anion binding hierarchy: PF₆⁻ > ReO₄⁻ > OTf⁻ > ClO₄⁻ > CB₁₁H₁₂⁻ > NTf₂⁻ > BF₄⁻ > I⁻ > NO₃⁻. This hierarchy cannot be rationalized by Rebek's 55% rule due to the flexibility of the cavity.¹⁹ Moreover, it can be noted that the binding affinity for ReO₄⁻ is higher than those for most of other anions, indicating that the cage may be a promising receptor for perrhenate or the physicochemically similar pertechnetate in water, which is useful in the context of radiopharmaceuticals and nuclear waste treatment.^{11d}

Despite the BF₄⁻ templated assembly existing in two distinct cage isomers in equilibrium (T-1 ⇌ C₃-1), it was noted that during the titration of BF₄⁻ into NTf₂⁻⊂T-1, only BF₄⁻⊂T-1 was observed within 5 h, while BF₄⁻⊂C₃-1 appeared thereafter, indicating a short-term shape

memory effect (Figure 11.5). Further experiments showed that after addition of 2 equiv of BF_4^- to the solution containing a 5:95 ratio of $\text{NO}_3^- \text{C-T-1}:\text{NO}_3^- \text{C}_3\text{-1}$, a 5:95 ratio of $\text{BF}_4^- \text{C-T-1}:\text{BF}_4^- \text{C}_3\text{-1}$ was observed immediately following the competitive anion displacement (Figure S11.77). Over time, $\text{BF}_4^- \text{C}_3\text{-1}$ gradually converted to $\text{BF}_4^- \text{C-T-1}$ to reach equilibrium. These results indicate that two successive processes have occurred: the fast kinetics of the direct guest displacement giving a shape memory phenomenon followed by the slow kinetics of BF_4^- templated isomeric reconfiguration. Importantly, benefiting from the larger population of $\text{BF}_4^- \text{C}_3\text{-1}$ (95%) after anion exchange from $\text{NO}_3^- \text{C}_3\text{-1}$, we clearly observed NOE correlations between the bound BF_4^- and the methylene protons of the *exo*-azaphosphatrane of $\text{BF}_4^- \text{C}_3\text{-1}$ in the $^1\text{H}-^{19}\text{F}$ HOESY spectrum (Figure S11.78), which we were unable to observe directly in the BF_4^- -driven assembly (population of $\text{BF}_4^- \text{C}_3\text{-1} < 25\%$), further verifying the accuracy of the assigned structure.

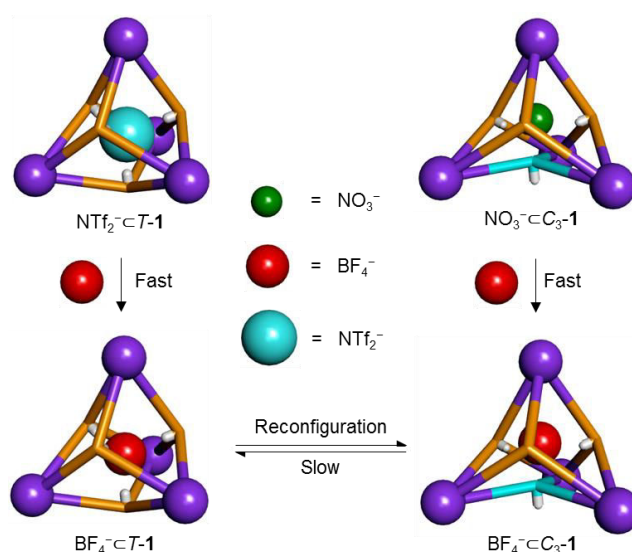


Figure 11.5 Schematic representation of two successive processes: fast kinetics of guest displacement of NTf_2^- or NO_3^- by BF_4^- giving shape memory phenomena followed by slow kinetics of isomeric reconfiguration.

11.4 Conclusion

In summary, this study has demonstrated the feasibility of introducing azaphosphatranes into polyhedral complexes using subcomponent self-assembly, and also proved for the first time the utility of azaphosphatranes as anion binding moieties. Due to the designed flexibility, the assembled tetrahedron with acidic protons located inside encapsulates various anions in water with volumes ranging from 35 to 219 \AA^3 via hydrogen bonding and electrostatic interactions. Moreover, structural adaptation was observed during cage formation in response to the size and shape of the external template anions exhibiting a X-C-T -cage or a X-C_3 -cage. The two cage isomers may coexist in solution and interconvert. Shape memory phenomena were observed during guest displacement due to its faster kinetics compared to that of isomeric reconfiguration. Future work will seek to use this tailored cage as an organocatalyst in supramolecular catalysis benefiting from the azaphosphatrane catalytic sites, for instance for CO_2 conversion.

11.5 Experimental section

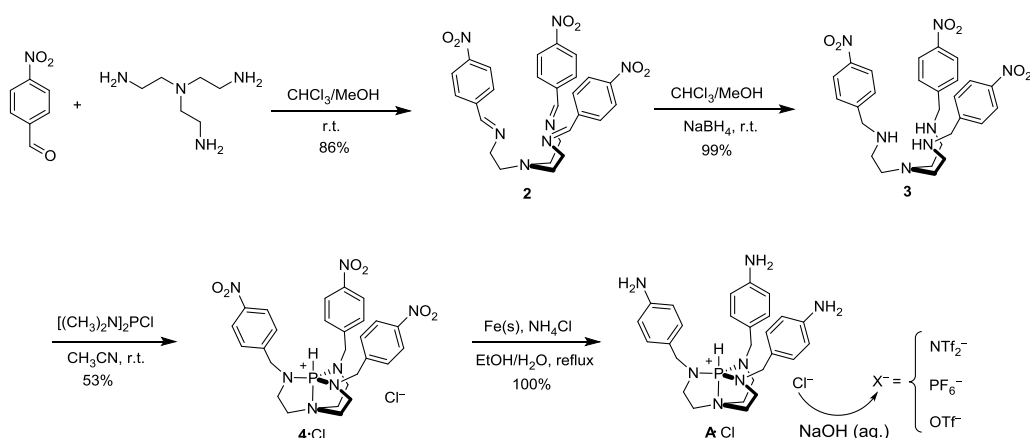
11.5.1 Materials and instrumentation

Unless otherwise specified, all reagents were purchased from commercial sources and used as received. NMR spectra were recorded using a Bruker 400 MHz Avance III HD Smart Probe (routine ^1H NMR), DCH 500 MHz dual cryoprobe (high-resolution ^{13}C), and DPX S5 500 MHz BB ATM (^1H , ^{13}C , ^{19}F and ^{31}P NMR and 2D experiments). Chemical shifts for ^1H , ^{13}C , ^{19}F and ^{31}P NMR are reported in ppm on the δ scale. DOSY experiments were performed on a Bruker DPX S5 500 MHz BB ATM spectrometer. Maximum gradient strength was 6.57 G/cmA. The standard Bruker pulse program, ledbpgp2s, employing a stimulated echo and longitudinal eddy-current delay (LED) using bipolar gradient pulses for diffusion was utilized. Rectangular gradients were used with a total duration of 1.5 ms. Gradient recovery delays were 1200 μs . Individual rows of the S4 quasi-2D diffusion databases were phased and baseline corrected. X-ray data were collected, solved and refined by Tanya K. Ronson.

Flash column chromatography was performed using Silica Gel high purity grade (pore size 60 Å, 230-400 mesh particle size, Sigma-Aldrich). TLC analyses were performed on Merck TLC Silica Gel 60 F254 Glass plates. Product spots were visualized under UV light ($\lambda_{\text{max}} = 254$ nm). All anhydrous reactions were carried out in oven-dried glassware and under an inert atmosphere of nitrogen. All reactions were stirred with magnetic followers. Centrifugation of samples was carried out using a Grant-Bio LMC-3000 low speed benchtop centrifuge. Low resolution electrospray ionization mass spectrometry was undertaken on a Micromass Quattro LC mass spectrometer (cone voltage 10-30 eV; desolvation temp. 313 K; S4 ionization temp. 313 K) infused from a Harvard syringe pump at a rate of 10 $\mu\text{L}/\text{min}$. High-resolution mass spectra were acquired using a Thermofisher LTQ Orbitrap XL.

11.5.2 Synthesis and characterization

11.5.2.1 Synthesis of subcomponents A·NTf₂, A·PF₆ and A·OTf



Scheme S11.1 Synthetic route for the preparation of azaphosphatrane-based subcomponents A·NTf₂, A·PF₆ and A·OTf.

Compound 2: In a 250 mL round bottom flask, tris(2-aminoethyl)amine (tren) (2.178 g; 14.90 mmol) was dissolved in a 1:1 mixture of chloroform/methanol (60 mL) cooled in an ice-bath. Then, a solution of 4-nitrobenzaldehyde (9.00 g; 59.6 mmol) in a 1:1 mixture of chloroform/methanol (90 mL) was added drop-wise. The reaction was slowly warmed to room temperature, and a large amount of yellow precipitate gradually appeared. After one night, the precipitate was filtrated off and washed with methanol, the yellow solid was dried under vacuum (7.00g, 86% yield). $^1\text{H NMR}$ (CD_2Cl_2 , 298K, 500.1 MHz): δ 8.27 (s, 1H); 8.20 (d, $J = 8.8$ Hz, 2H); 7.78 (d, $J = 8.8$ Hz, 2H); 3.76 (t, $J = 6.1$ Hz, 2H); 2.99 (t, $J = 6.4$ Hz, 2H) ppm. $^{13}\text{C NMR}$ (CD_2Cl_2 , 298K, 125.7 MHz): δ 160.0, 149.7, 142.7, 129.3, 124.6, 61.0, 56.0 ppm. **ESI-HRMS** m/z: found 568.1924, calcd for $\text{C}_{27}\text{H}_{27}\text{N}_7\text{NaO}_6$ $[\text{M}+\text{Na}]^+$ 568.1915.

Compound 3: In a 2 L round bottom flask, compound 2 (6.40 g; 11.7 mmol) was dissolved in a 1:1 mixture of chloroform/methanol (1.2 L) cooled with an ice-bath. Subsequent portions of NaBH_4 (6.22 g; 165 mmol) were added over a thirty minutes period. The reaction was slowly warmed to room temperature. After 4 h, the solvents were evaporated. A solution of 10% NaOH in water was added (300 mL), and the resulting mixture was extracted with CH_2Cl_2 (3 \times 300 mL). The organic layers were dried over Na_2SO_4 , filtrated, and the solvent was removed under reduced pressure to give a yellow solid product (6.40 g, 99% yield). $^1\text{H NMR}$ (CD_2Cl_2 , 298K, 500.1 MHz): δ 8.10 (d, $J = 8.6$ Hz, 2H); 7.47 (d, $J = 8.6$ Hz, 2H); 3.86 (s, 2H); 2.68 (t, $J = 5.7$ Hz, 2H); 2.61 (t, $J = 5.7$ Hz, 2H) ppm. $^{13}\text{C NMR}$ (CD_2Cl_2 , 298K, 125.7 MHz): δ 149.6, 147.7, 129.2, 124.2, 54.9, 53.9, 48.0 ppm. **ESI-HRMS** m/z: found 574.2386, calcd for $\text{C}_{27}\text{H}_{33}\text{N}_7\text{NaO}_6$ $[\text{M}+\text{Na}]^+$ 574.2385.

Compound 4·Cl: In an ice-bath cooled round bottom flask (100 mL), tris(dimethylamino)phosphine (0.776 mL, 4.26 mmol) was dissolved in acetonitrile (40 mL). Phosphorus trichloride (0.184 mL, 2.12 mmol) was then added. The reaction mixture was vigorously stirred at 0 °C for 0.5 h, and a solution of compound 3 (3.2 g; 5.8 mmol) in acetonitrile (16 mL) was added drop-wise. The reaction mixture was then stirred for 2 days at room temperature. The solvent was removed under reduced pressure and the resulting yellow oil was purified by column chromatography eluting with 15:5 dichloromethane/methanol solution to give pure 4·Cl as a yellow powder (1.90 g; 53% yield). $^1\text{H NMR}$ (CD_3CN , 298K, 500.1 MHz): δ 8.16 (d, $J = 8.6$ Hz, 6H); 7.47 (d, $J = 8.6$ Hz, 6H); 5.78 (d, $J = 503.9$ Hz, 1H); 4.35 (d, $J = 17.9$ Hz, 6H); 3.33 (q, $J = 5.8$ Hz, 6H); 3.15 (dt, $J = 10.0, 6.2$ Hz, 6H) ppm. $^{13}\text{C NMR}$ (CD_3CN , 298K, 125.7 MHz): δ 148.2, 146.8, 129.2, 124.6, 50.9, 48.1, 39.8 ppm. $^{31}\text{P NMR}$ (CD_3CN , 298K, 202.4 MHz): δ -11.8 ppm. **ESI-HRMS** m/z: found 580.2071, calcd for $\text{C}_{27}\text{H}_{31}\text{N}_7\text{O}_6\text{P}$ $[\text{M}]^+$ 580.2068.

Compound A·Cl: In a round bottom flask (250 mL), compound 4·Cl (750 mg; 1.22 mmol), Fe powder (1.47 g; 26.3 mmol), and NH_4Cl (156 mg; 2.92 mmol) were respectively added to a 5:1 mixture of ethanol/water (85 mL). The reaction mixture was vigorously stirred under reflux for 4 h. After completion, the reaction solution was filtered to remove the residual iron powder, followed by evaporation under reduced pressure to quantitatively give a dark yellow solid. The solid was the protonated form of compound A·Cl, which was used directly in the next anion exchange step without further purification.

Compounds A·NTf₂, A·PF₆ and A·OTf: Compound A·Cl was dissolved in 5% NaOH

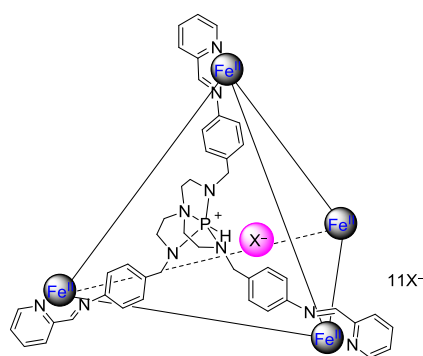
aqueous solution and an excess of LiNTf₂, KPF₆ or NaOTf (around 5 equiv) was added directly. A white precipitate formed. The reaction mixture was stirred for 1 h at room temperature. After filtration and washing with deionized water, the solid was dried under vacuum (Yields: > 90%).

Compound A·NTf₂: ¹H NMR (CD₃CN, 298K, 500.1 MHz): δ 6.99 (d, *J* = 8.3 Hz, 6H); 6.62 (d, *J* = 8.4 Hz, 6H); 5.88 (d, *J* = 503.1 Hz, 1H); 4.15 (s, 6H); 4.06 (d, *J* = 16.7 Hz, 6H); 3.06 (q, *J* = 5.6 Hz, 6H); 2.94 (dt, *J* = 10.3, 6.2 Hz, 6H) ppm. ¹³C NMR (CD₃CN, 298K, 125.7 MHz): 148.3, 129.7, 127.2, 120.8, 115.3, 51.4, 47.6, 39.3 ppm. ³¹P NMR (CD₃CN, 298K, 202.4 MHz): δ -11.2 ppm. ¹⁹F NMR (470.4 MHz, 298 K, CD₃CN): δ -80.4 ppm. **ESI-HRMS** *m/z*: found 490.2844, calcd for C₂₇H₃₁N₇O₆P [M]⁺ 490.2843.

Compound A·PF₆: ¹H NMR (CD₃CN, 298K, 500.1 MHz): δ 6.99 (d, *J* = 8.3 Hz, 6H); 6.62 (d, *J* = 8.4 Hz, 6H); 5.88 (d, *J* = 503.1 Hz, 1H); 4.15 (s, 6H); 4.06 (d, *J* = 16.9 Hz, 6H); 3.06 (q, *J* = 5.6 Hz, 6H); 2.94 (dt, *J* = 10.3, 6.2 Hz, 6H) ppm. ¹³C NMR (CD₃CN, 298K, 125.7 MHz): 148.3, 129.7, 127.2, 115.3, 51.4, 47.6, 39.3 ppm. ³¹P NMR (CD₃CN, 298K, 202.4 MHz): δ -11.2, -144.6 ppm. ¹⁹F NMR (470.4 MHz, 298 K, CD₃CN): δ -73.1 ppm. **ESI-HRMS** *m/z*: found 490.2847, calcd for C₂₇H₃₁N₇O₆P [M]⁺ 490.2843.

Compound A·OTf: ¹H NMR (CD₃CN, 298K, 500.1 MHz): δ 6.99 (d, *J* = 8.3 Hz, 6H); 6.62 (d, *J* = 8.4 Hz, 6H); 5.88 (d, *J* = 503.1 Hz, 1H); 4.16 (s, 6H); 4.06 (d, *J* = 16.9 Hz, 6H); 3.06 (q, *J* = 5.6 Hz, 6H); 2.94 (dt, *J* = 10.3, 6.2 Hz, 6H) ppm. ¹³C NMR (CD₃CN, 298K, 125.7 MHz): 148.3, 129.7, 127.2, 115.3, 51.4, 47.6, 39.3 ppm. ³¹P NMR (CD₃CN, 298K, 202.4 MHz): δ -11.2 ppm. ¹⁹F NMR (470.4 MHz, 298 K, CD₃CN): δ -79.5 ppm. **ESI-HRMS** *m/z*: found 490.2853, calcd for C₂₇H₃₁N₇O₆P [M]⁺ 490.2843.

11.5.2.2 Preparation of 1·[NTf₂]₁₂, 1·[PF₆]₁₂ and 1·[OTf]₁₂ in acetonitrile



A·NTf₂ (48.5 mg, 62.9 μmol, 4 equiv), A·PF₆ (40.0 mg, 62.9 μmol, 4 equiv), or A·OTf (40.2 mg, 62.9 μmol, 4 equiv) was dissolved in acetonitrile (4 mL) together with the corresponding Fe(NTf₂)₂(H₂O)₄ (42.0 mg, 62.9 μmol, 4 equiv), Fe(CH₃CN)₆(PF₆)₂ (37.3 mg, 62.9 μmol, 4 equiv), or Fe(OTf)₂ (22.3 mg, 62.9 μmol, 4 equiv), and 2-formylpyridine (20.2 mg, 189 μmol, 12 equiv). The reaction was kept at r.t. overnight under nitrogen. Diethyl ether (20 mL) was added. The purple microcrystalline powder was precipitated, collected by centrifugation, and dried under reduced pressure. The yields of 1·[NTf₂]₁₂, 1·[PF₆]₁₂ and 1·[OTf]₁₂ were 84%, 82% and 90%, respectively.

Cage 1·[NTf₂]₁₂: ¹H NMR (CD₃CN, 298K, 500.1 MHz): δ 8.99 (s, 12H, H_a); 8.60 (d, *J* = 7.7 Hz, 12H, H_b); 8.38 (t, *J* = 7.7 Hz, 12H, H_c); 7.81 (t, *J* = 6.4 Hz, 12H, H_d); 7.49 (d, *J* = 5.0 Hz, 12H, H_e); 7.17 (d, *J* = 8.0 Hz, 24H, H_g); 6.07 (d, *J* = 508.6 Hz, 4H, H_k); 5.42 (d, *J* = 8.0 Hz, 24H, H_f); 4.52 (t, *J* = 15.9 Hz, 12H, H_h); 3.58 (t, *J* = 13.4 Hz, 12H, H_i); 2.84-2.60 (m, 48H, H_{i,j}) ppm. ¹³C NMR (CD₃CN, 298K, 125.7 MHz): 173.9 (C_a), 157.6 (C_n), 155.8 (C_e), 150.3 (C_i), 139.7 (C_c), 137.9 (C_m), 131.5 (C_b), 130.5 (C_d), 130.3 (C_g), 121.4 (C_f), 49.4 (C_h), 45.6, 37.9 (C_i and _j) ppm. ³¹P NMR (CD₃CN, 298K,

202.4 MHz): δ -12.6 (*P-H_k) ppm. ^{19}F NMR (470.4 MHz, 298 K, CD_3CN): δ -75.6 (encapsulated NTf_2^-), -80.2 (free NTf_2^-) ppm. ESI-MS m/z 546.6 $[\text{M}+4\text{NTf}_2^-]^+$, 664.7 $[\text{M}+5\text{NTf}_2^-]^+$, 822.1 $[\text{M}+6\text{NTf}_2^-]^+$, 1042.5 $[\text{M}+7\text{NTf}_2^-]^+$, 1373.1 $[\text{M}+8\text{NTf}_2^-]^+$.

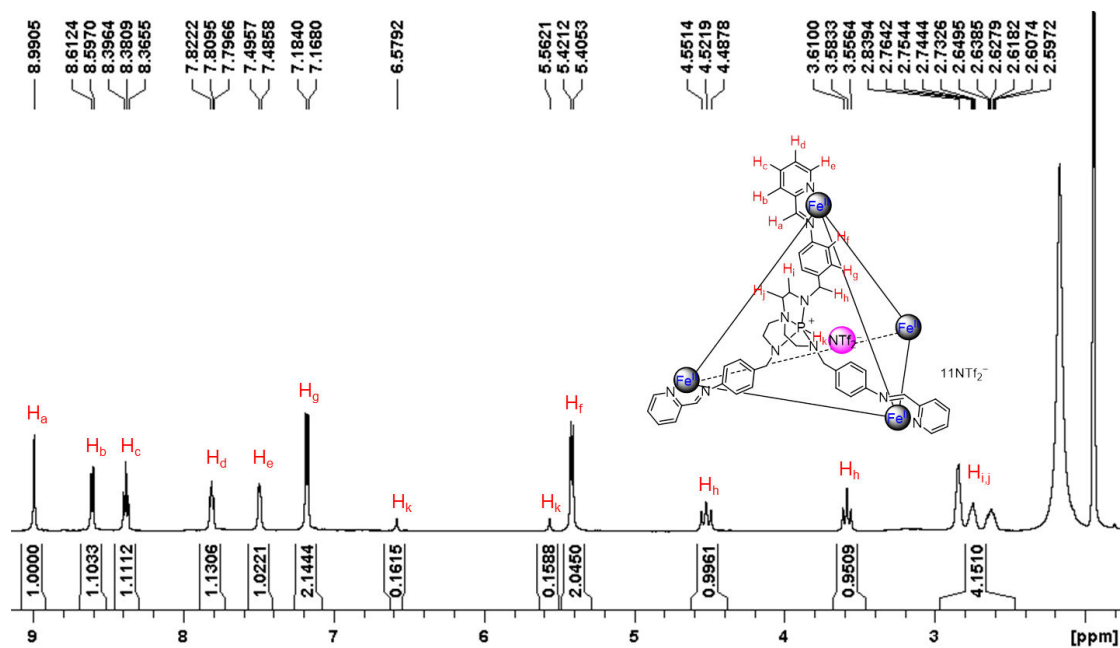


Figure S11.1 ^1H NMR (CD_3CN , 500 MHz, 298 K) spectrum of $\mathbf{1}\cdot[\text{NTf}_2]_{12}$.

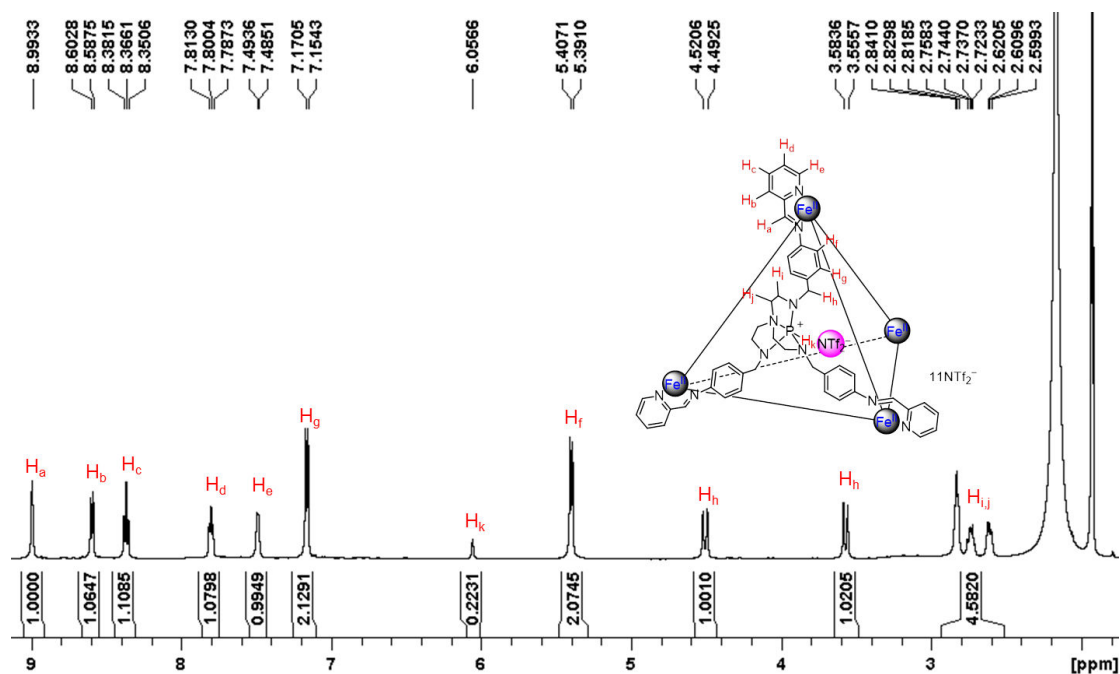


Figure S11.2 ^{31}P -decoupled ^1H NMR (CD_3CN , 500 MHz, 298 K) spectrum of $\mathbf{1}\cdot[\text{NTf}_2]_{12}$.

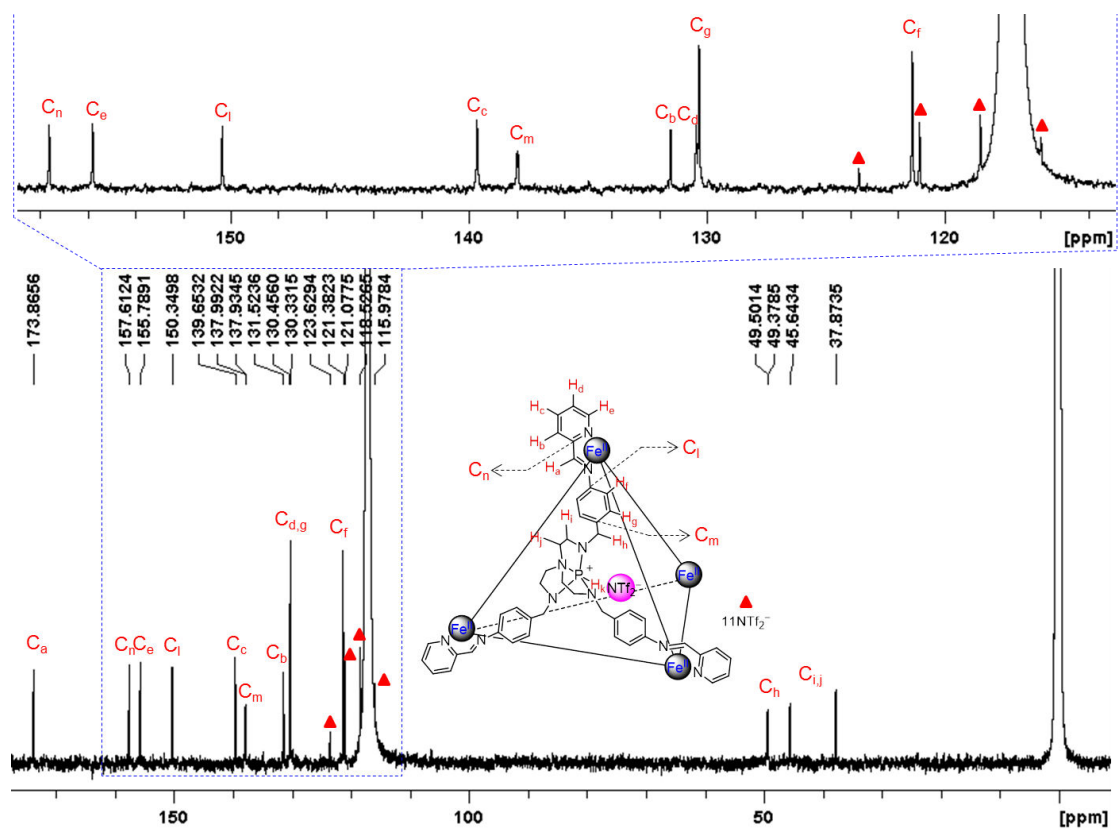


Figure S11.3 ^{13}C NMR spectrum (CD_3CN , 125.8 MHz, 298K) of $1 \cdot [\text{NTf}_2]_{12}$.

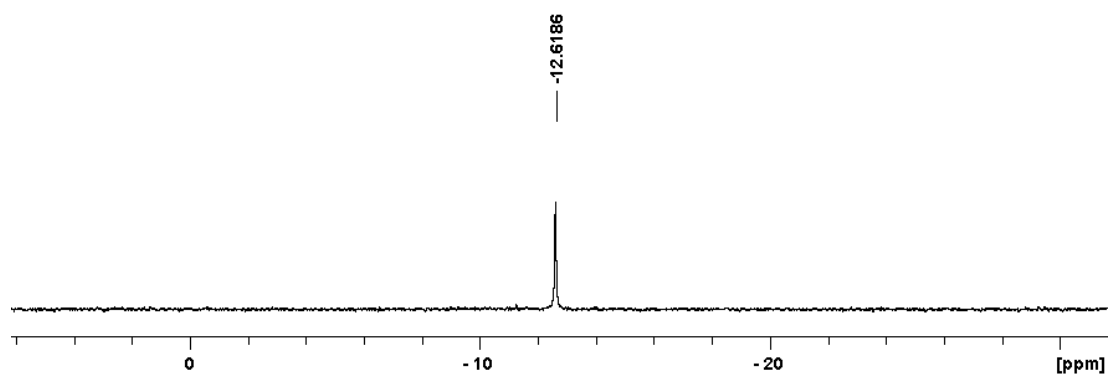


Figure S11.4 ^1H -decoupled ^{31}P NMR spectrum (CD_3CN , 202.4 MHz, 298K) of $1 \cdot [\text{NTf}_2]_{12}$.

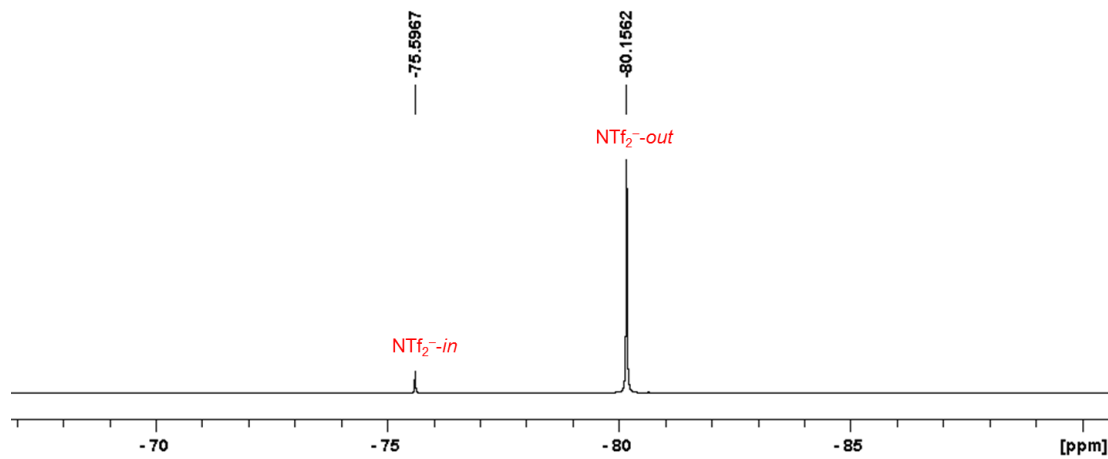


Figure S11.5 ^{19}F NMR spectrum (CD_3CN , 470.4 MHz, 298K) of $1 \cdot [\text{NTf}_2]_{12}$.

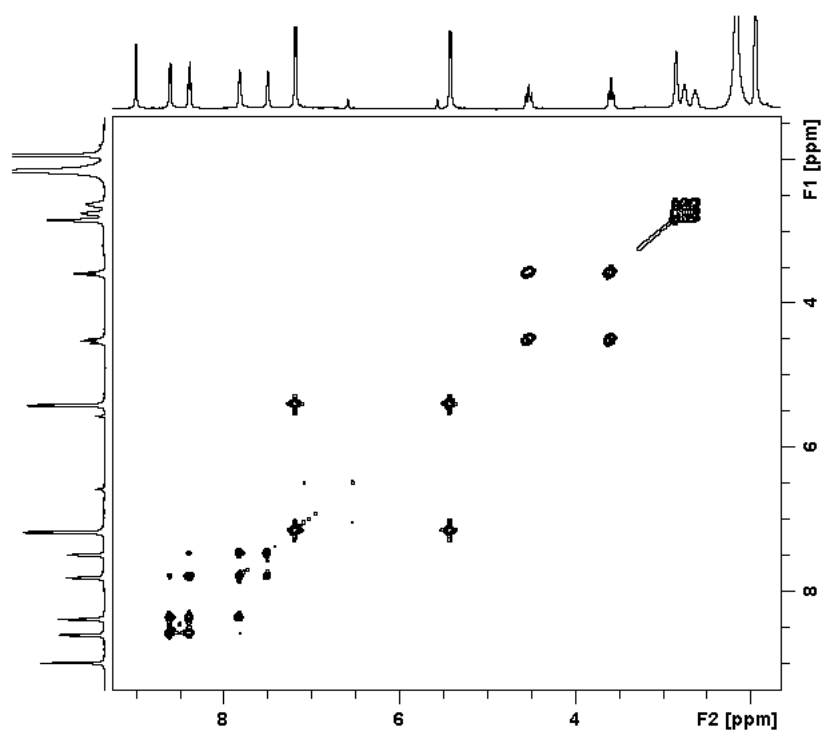


Figure S11.6 ^1H - ^1H COSY spectrum (CD_3CN , 500 MHz, 298K) of $1 \cdot [\text{NTf}_2]_{12}$.

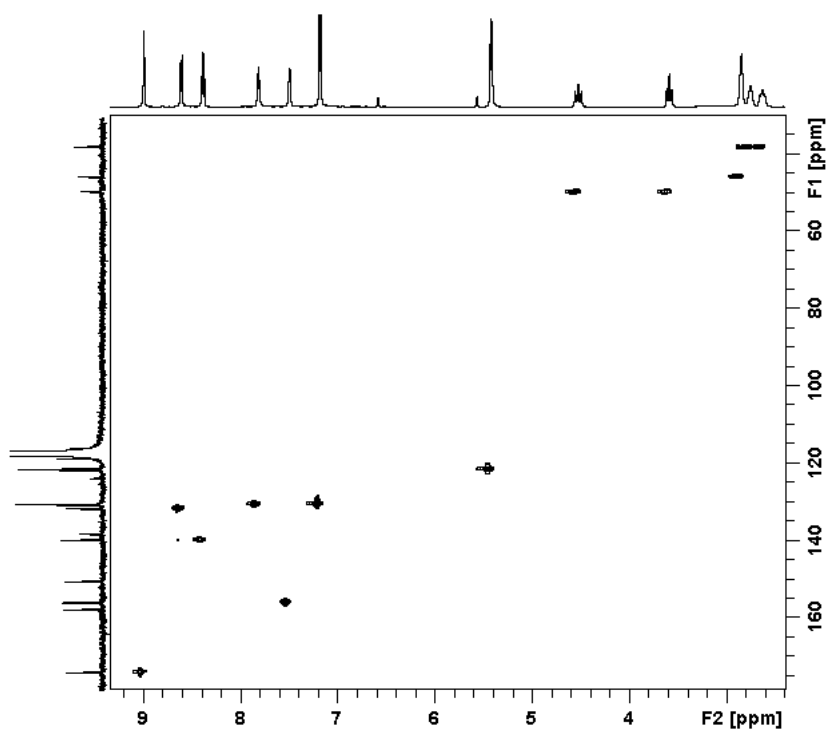


Figure S11.7 ^1H - ^{13}C HSQC spectrum (CD_3CN , 500 MHz, 298K) of $1 \cdot [\text{NTf}_2]_{12}$.

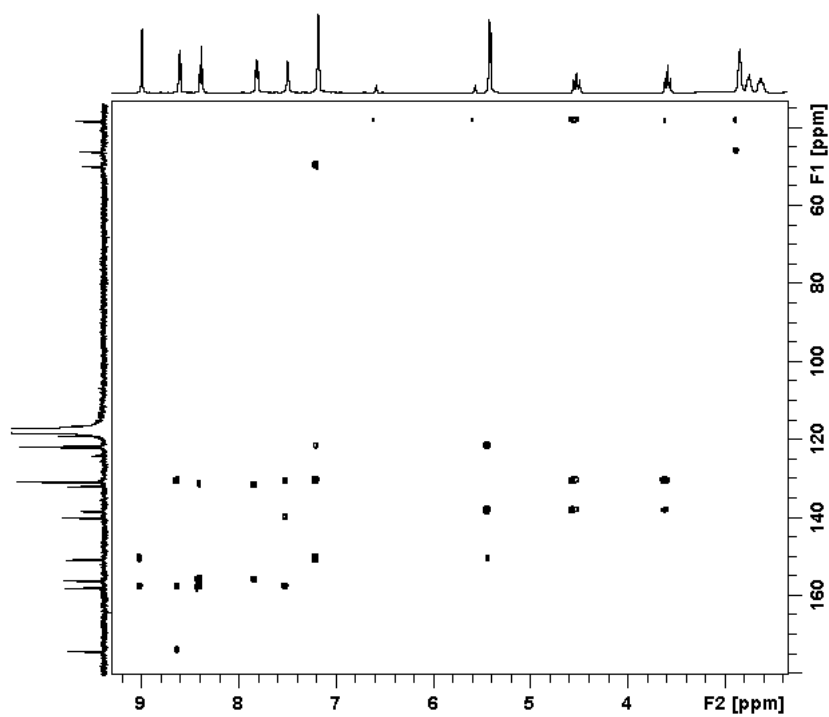


Figure S11.8 ^1H - ^{13}C HMBC spectrum (CD_3CN , 500 MHz, 298K) of $1 \cdot [\text{NTf}_2]_{12}$.

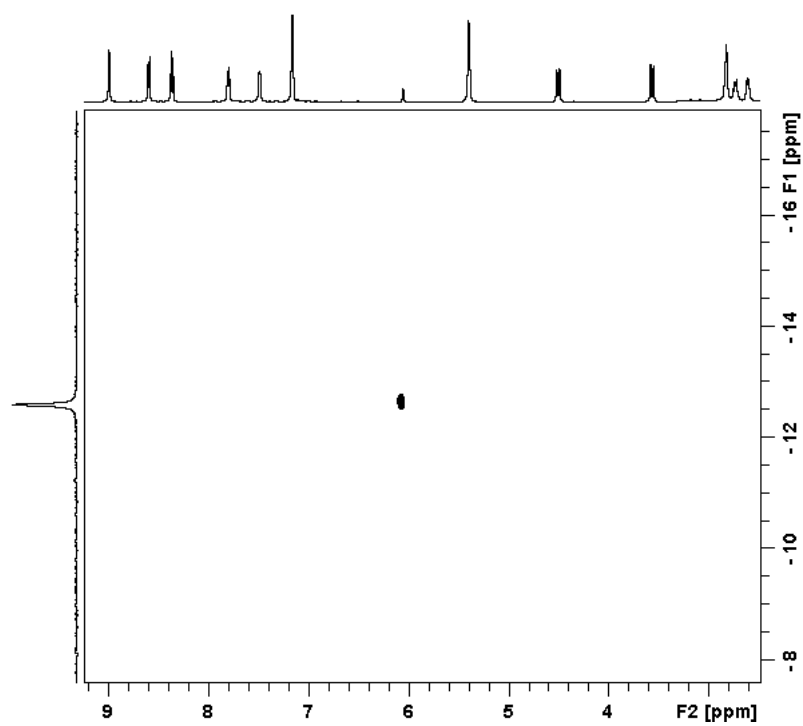


Figure S11.9 ^1H - ^{31}P HSQC spectrum (CD_3CN , 500 MHz, 298K) of $1 \cdot [\text{NTf}_2]_{12}$.

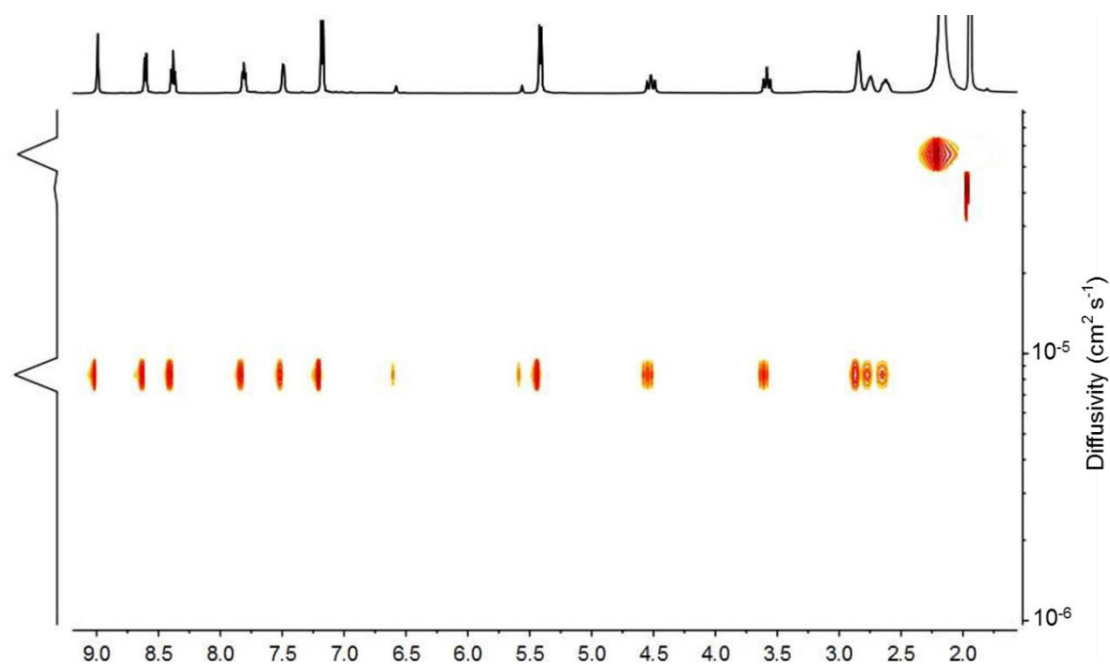


Figure S11.10 ^1H DOSY spectrum (CD_3CN , 500 MHz, 298K) of $1\cdot[\text{NTf}_2]_{12}$. The diffusion coefficient of $1\cdot[\text{NTf}_2]_{12}$ in CD_3CN was measured to be $8.25 \times 10^{-6} \text{ cm}^2 \text{ s}^{-1}$.

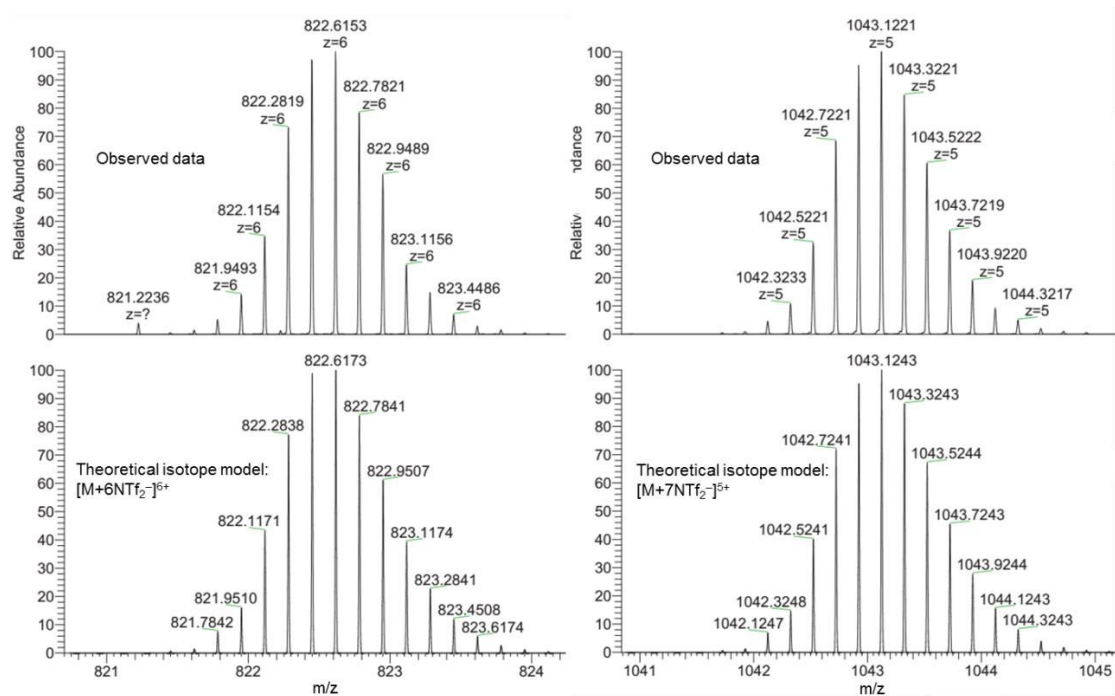


Figure S11.11 High-resolution ESI-mass analysis of $1\cdot[\text{NTf}_2]_{12}$ showing the +6 and +5 peaks.

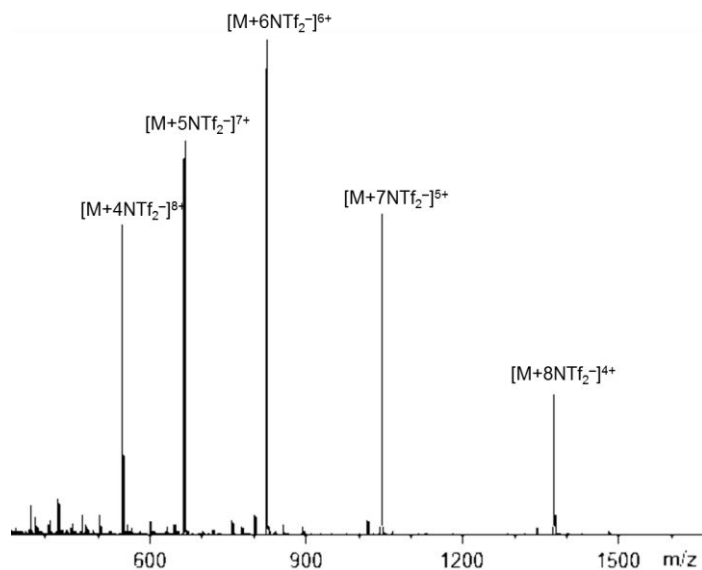


Figure S11.12 Low-resolution ESI-mass spectrum of $1 \cdot [NTf_2]_{12}$.

Cage 1·[PF₆]₁₂: 1H NMR (CD₃CN, 298K, 500.1 MHz): δ 8.85 (s, 12H, H_a); 8.52 (d, $J = 7.5$ Hz, 12H, H_b); 8.38 (t, $J = 7.6$ Hz, 12H, H_c); 7.73 (t, $J = 6.3$ Hz, 12H, H_d); 7.36 (d, $J = 5.3$ Hz, 12H, H_e); 7.13 (d, $J = 7.5$ Hz, 24H, H_g); 6.30 (d, $J = 494.8$ Hz, 4H, H_k); 5.06 (bs, 24H, H_f); 4.71 (t, $J = 13.9$ Hz, 12H, H_h); 3.70 (dd, $J = 33.8, 14.5$ Hz, 12H, H_h); 2.69-2.35 (m, 48H, H_{i,j}) ppm. ^{13}C NMR (CD₃CN, 298K, 125.7 MHz): 175.3 (C_a), 159.0 (C_n), 156.6 (C_e), 150.3 (C_l), 140.4 (C_c), 137.6 (C_m), 131.9 (C_b), 131.0 (C_g), 130.5 (C_d), 122.2 (C_f), 50.7 (C_h), 46.1, 38.5 (C_i and _j) ppm. ^{31}P NMR (CD₃CN, 298K, 202.4 MHz): δ -18.9 ($^+P-H_k$), -142.6 (encapsulated PF₆⁻), -144.5 (free PF₆⁻) ppm. ^{19}F NMR (470.4 MHz, 298 K, CD₃CN): δ -71.2 (encapsulated PF₆⁻), -72.4 (free PF₆⁻) ppm. **ESI-MS** m/z 479.1 [M+4PF₆⁻]⁺⁸, 568.3 [M+5PF₆⁻]⁺⁷, 687.2 [M+6PF₆⁻]⁺⁶, 853.6 [M+7PF₆⁻]⁺⁵, 1103.2 [M+8PF₆⁻]⁺⁴, 1519.3 [M+9PF₆⁻]⁺³.

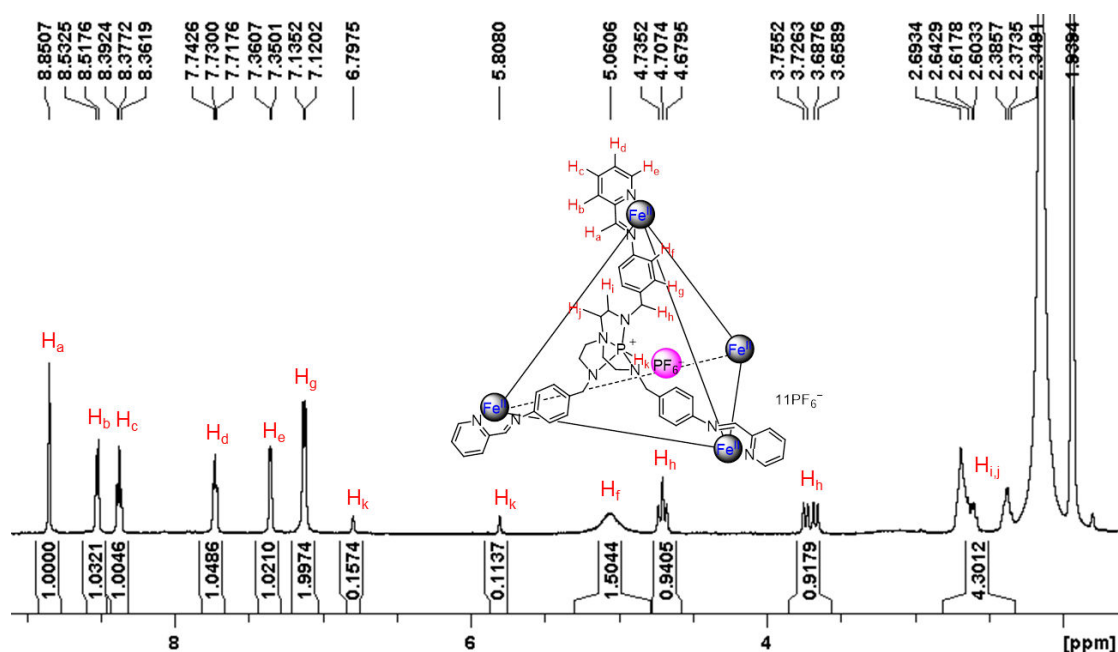
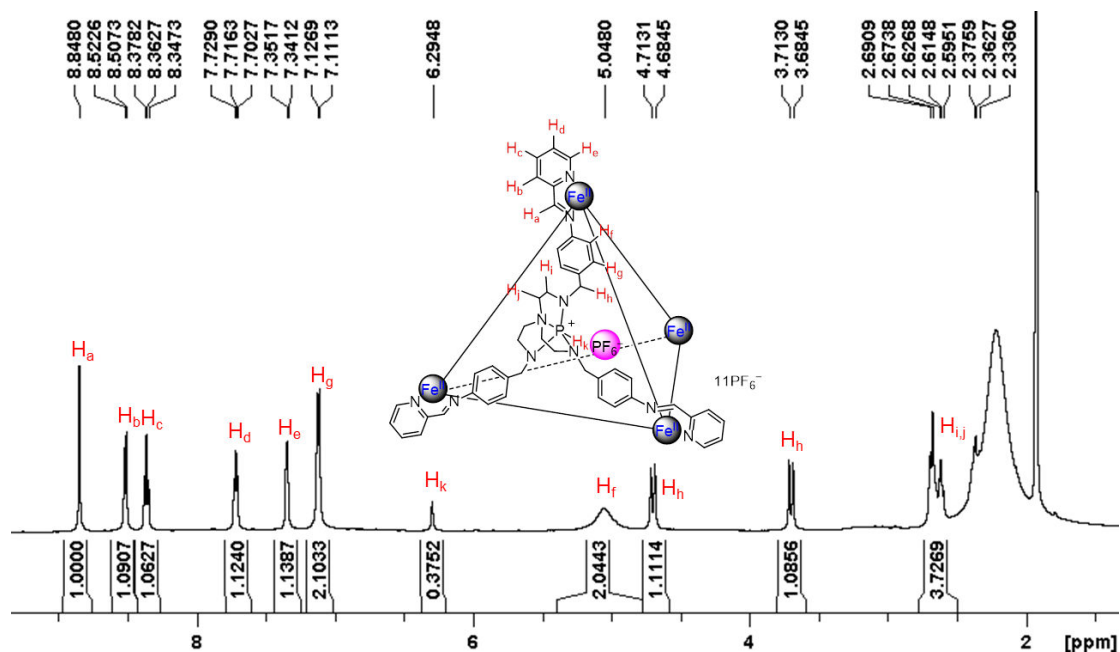
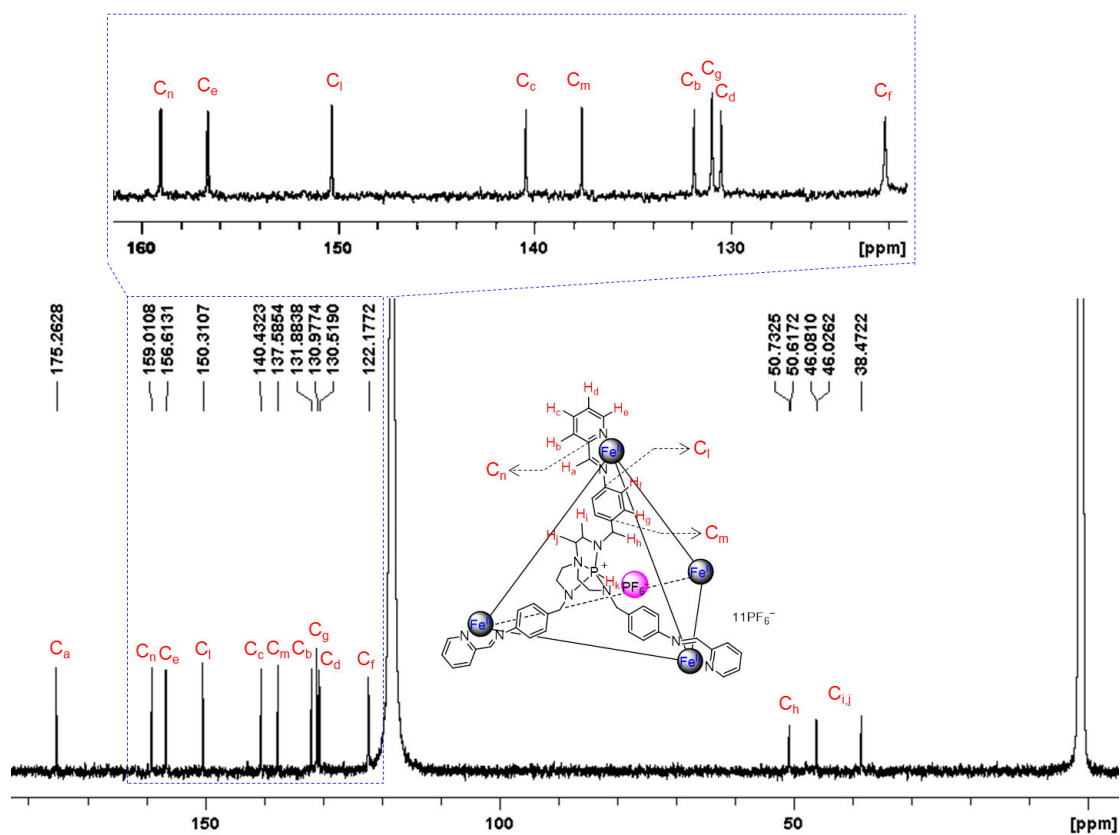


Figure S11.13 1H NMR (CD₃CN, 500 MHz, 298 K) spectrum of $1 \cdot [PF_6]_{12}$.

Figure S11.14 ^{31}P -decoupled ^1H NMR (CD_3CN , 500 MHz, 298 K) spectrum of $\mathbf{1}\cdot[\text{PF}_6]_{12}$.Figure S11.15 ^{13}C NMR spectrum (CD_3CN , 125.8 MHz, 298K) of $\mathbf{1}\cdot[\text{PF}_6]_{12}$.

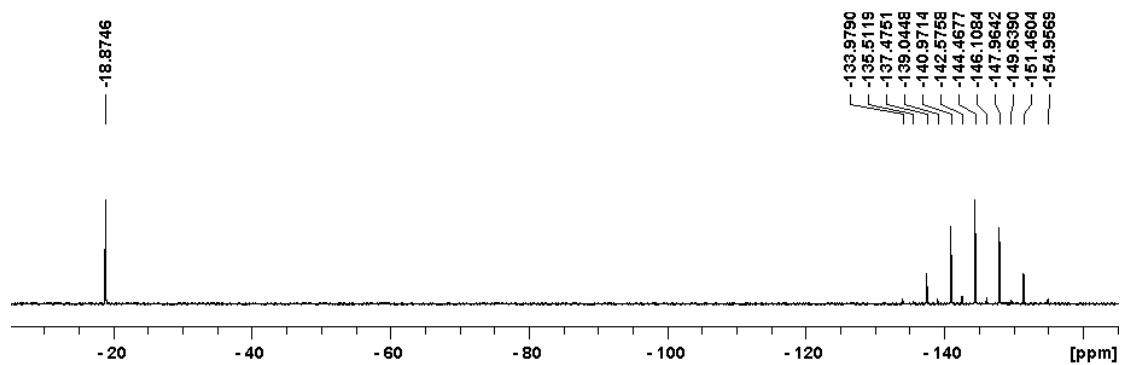


Figure S11.16 ^1H -decoupled ^{31}P NMR spectrum (CD_3CN , 202.4 MHz, 298K) of $1\cdot[\text{PF}_6]_{12}$.

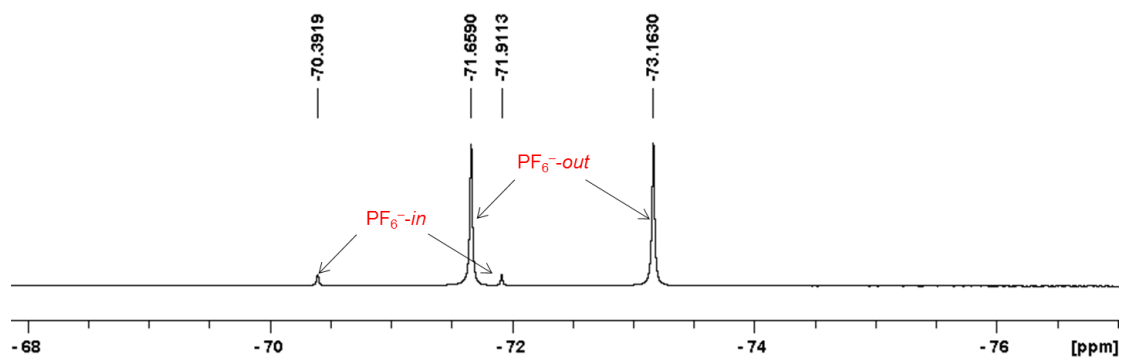


Figure S11.17 ^{19}F NMR spectrum (CD_3CN , 470.4 MHz, 298K) of $1\cdot[\text{PF}_6]_{12}$.

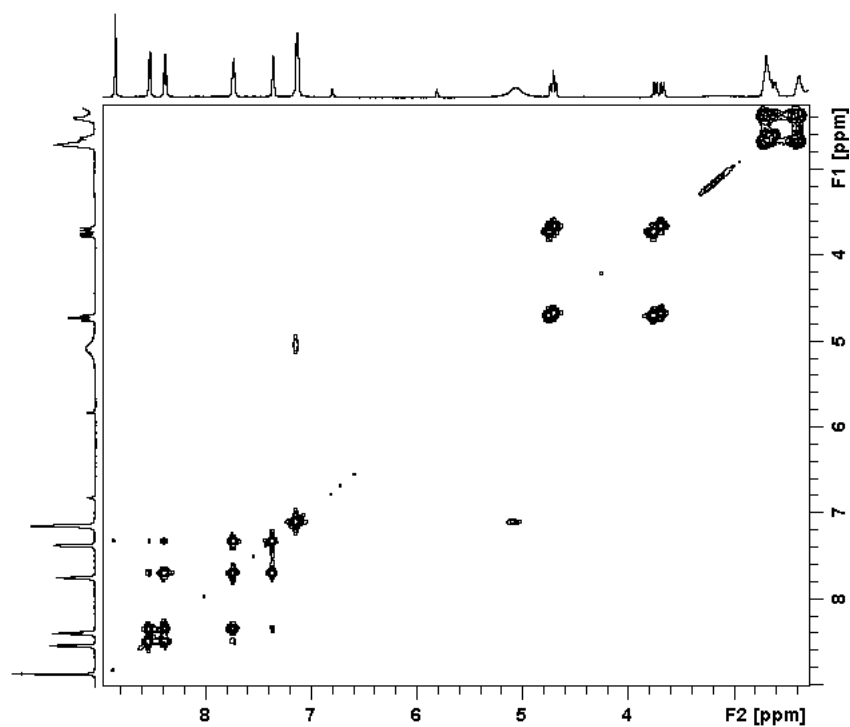


Figure S11.18 ^1H - ^1H COSY spectrum (CD_3CN , 500 MHz, 298K) of $1\cdot[\text{PF}_6]_{12}$.

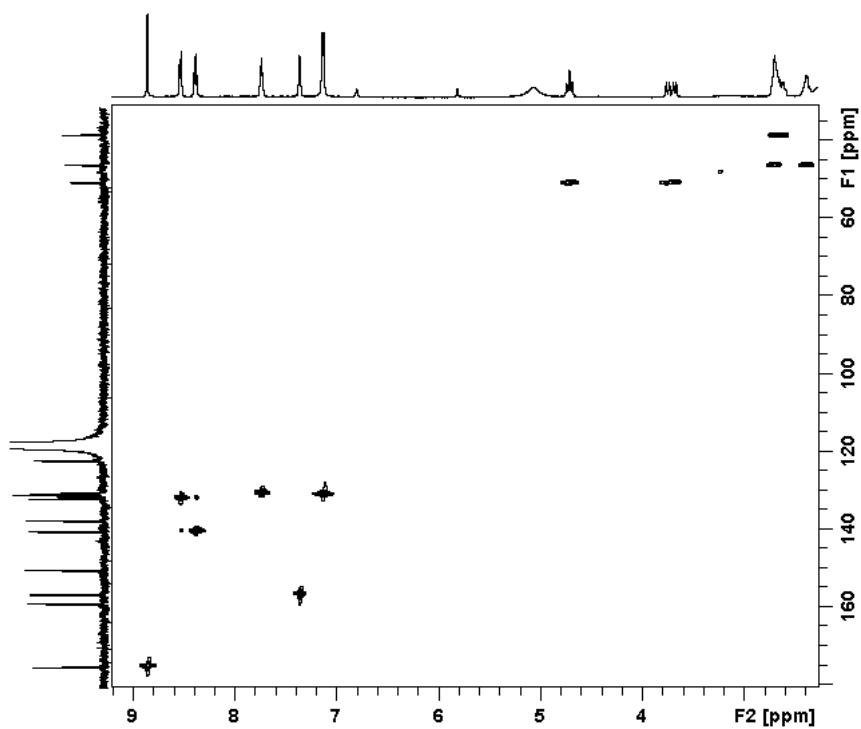


Figure S11.19 ^1H - ^{13}C HSQC spectrum (CD_3CN , 500 MHz, 298K) of $1\cdot[\text{PF}_6]_{12}$.

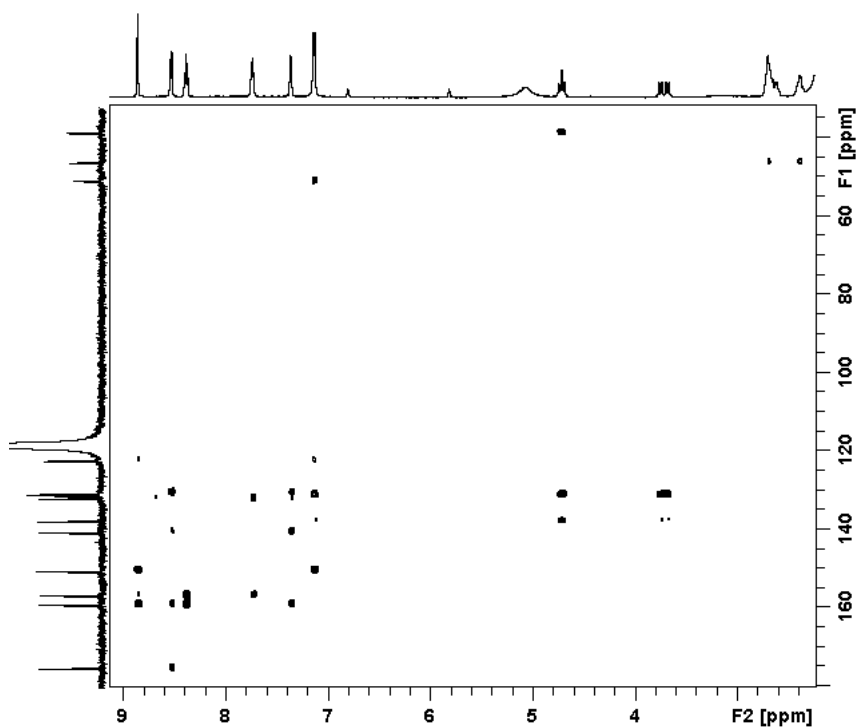


Figure S11.20 ^1H - ^{13}C HMBC spectrum (CD_3CN , 500 MHz, 298K) of $1\cdot[\text{PF}_6]_{12}$.

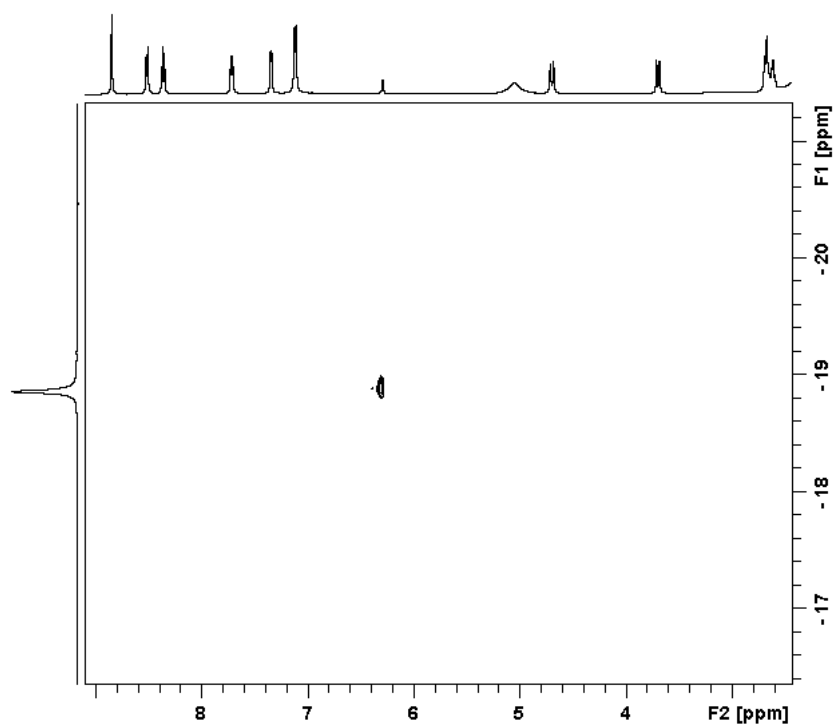


Figure S11.21 ¹H-³¹P HSQC spectrum (CD₃CN, 500 MHz, 298K) of **1**·[PF₆]₁₂.

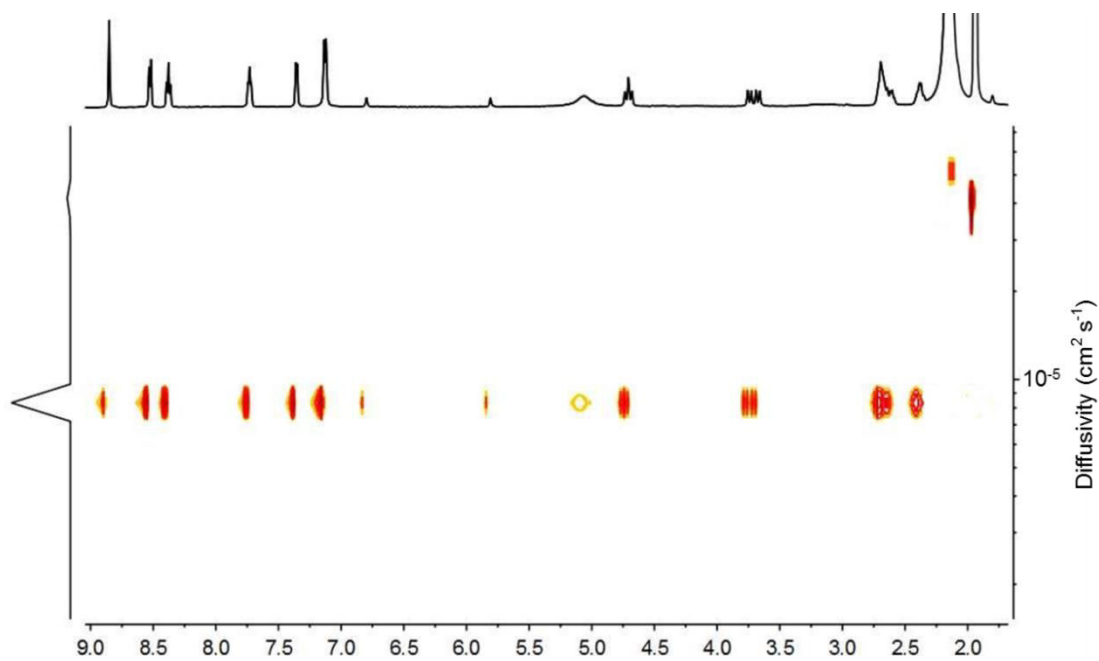


Figure S11.22 ¹H DOSY spectrum (CD₃CN, 500 MHz, 298K) of **1**·[PF₆]₁₂. The diffusion coefficient of **1**·[PF₆]₁₂ in CD₃CN was measured to be $8.35 \times 10^{-6} \text{ cm}^2 \text{ s}^{-1}$.

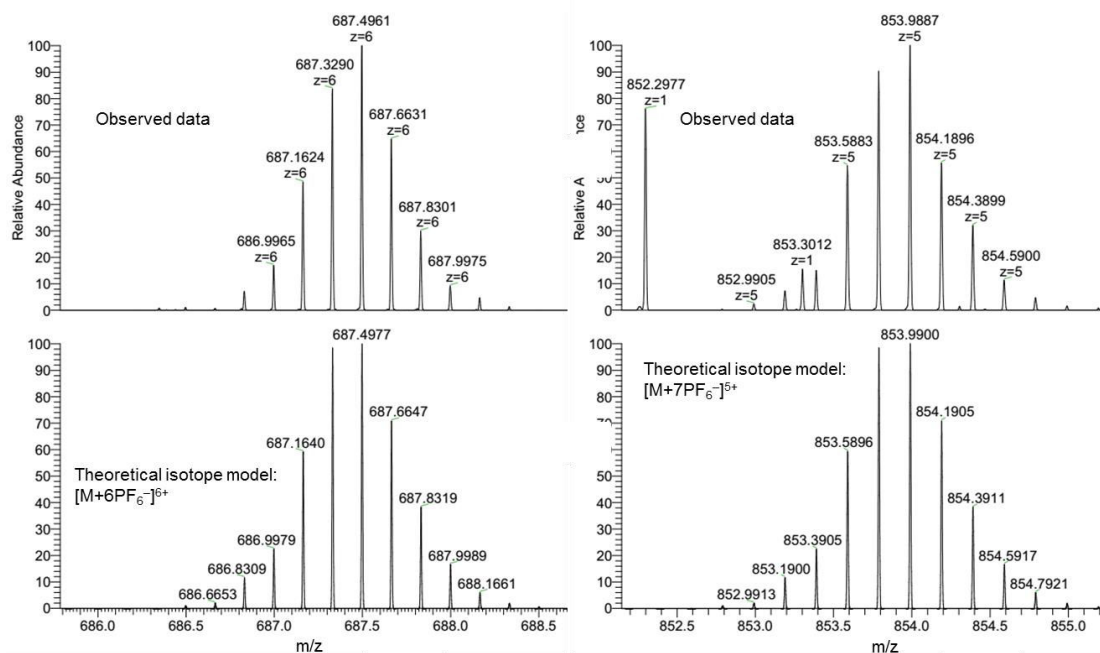


Figure S11.23 High-resolution ESI-mass analysis of $1 \cdot [PF_6]_{12}$ showing the +6 and +5 peaks.

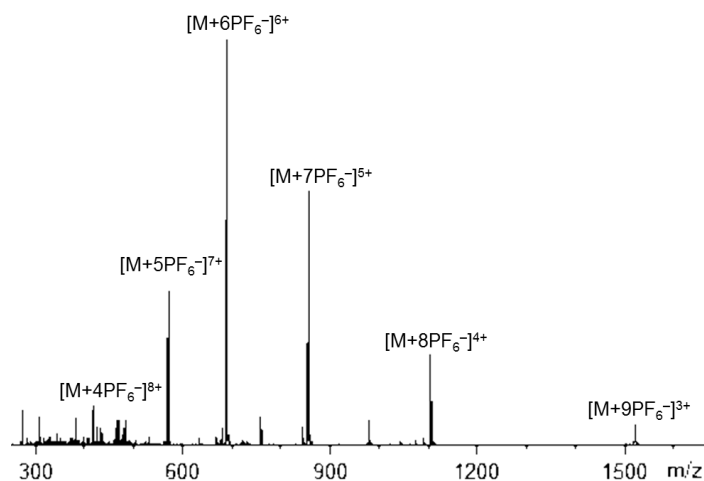
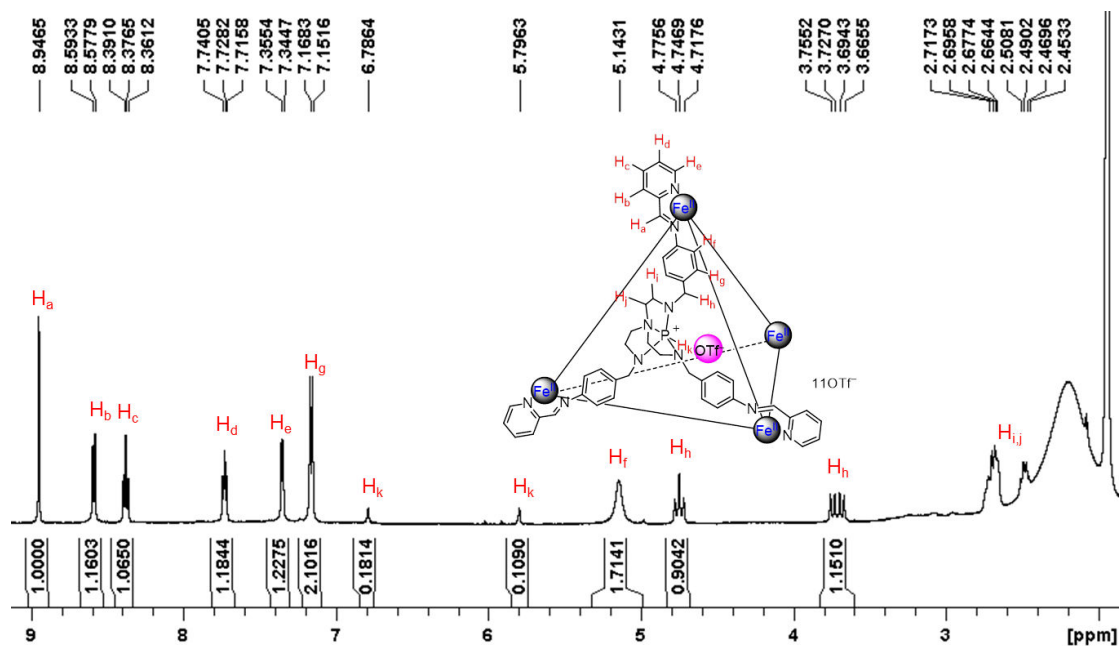
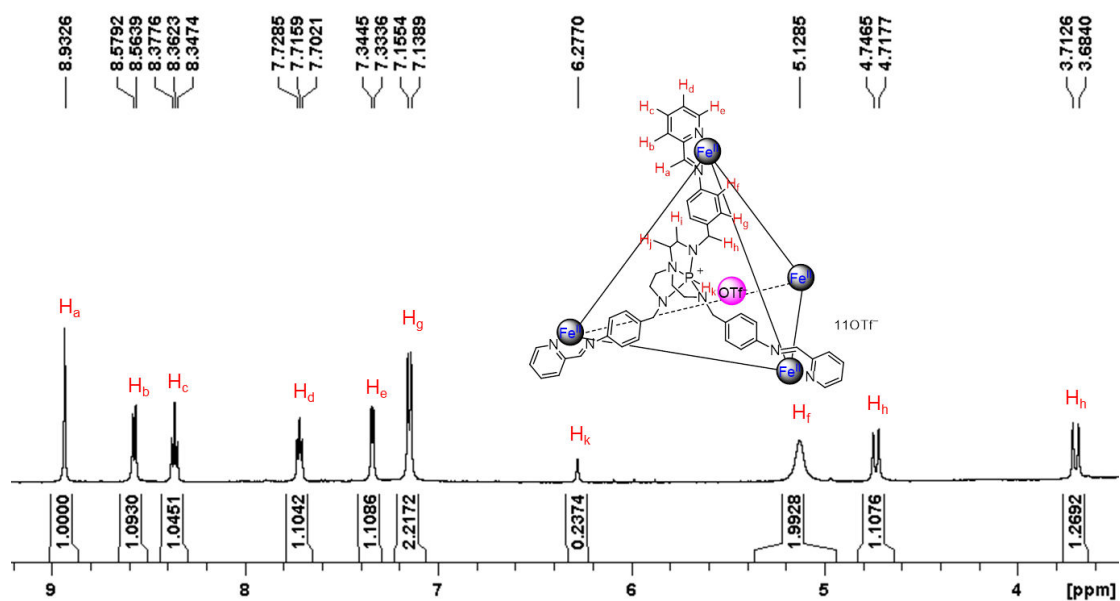


Figure S11.24 Low-resolution ESI-mass spectrum of $1 \cdot [PF_6]_{12}$.

Cage $1 \cdot [OTf]_{12}$: 1H NMR (CD_3CN , 298K, 500.1 MHz): δ 8.95 (s, 12H, H_a); 8.58 (d, $J = 7.7$ Hz, 12H, H_b); 8.38 (t, $J = 7.5$ Hz, 12H, H_c); 7.73 (t, $J = 6.2$ Hz, 12H, H_d); 7.36 (d, $J = 5.4$ Hz, 12H, H_e); 7.16 (d, $J = 8.4$ Hz, 24H, H_g); 6.29 (d, $J = 495.1$ Hz, 4H, H_k); 5.14 (bs, 24H, H_i); 4.75 (t, $J = 14.5$ Hz, 12H, H_h); 3.71 (dd, $J = 30.45, 14.1$ Hz, 12H, H_n); 2.72-2.45 (m, 48H, $H_{i,j}$) ppm. ^{13}C NMR (CD_3CN , 298K, 125.7 MHz): 174.7 (C_a), 158.3 (C_n), 155.8 (C_e), 149.5 (C_l), 139.6 (C_c), 137.2 (C_m), 131.2 (C_b), 130.2 (C_g), 129.7 (C_d), 121.4 (C_f), 49.8 (C_h), 45.6, 37.8 (C_i and j) ppm. ^{31}P NMR (CD_3CN , 298K, 202.4 MHz): δ -17.9 ($^+P-H_k$) ppm. ^{19}F NMR (470.4 MHz, 298 K, CD_3CN): δ -77.0 (encapsulated OTf^-), -78.2 (free OTf^-) ppm. **ESI-MS** m/z 411.1 $[M+3OTf]^{+9}$, 481.1 $[M+4OTf]^{+8}$, 571.1 $[M+5OTf]^{+7}$, 691.2 $[M+6OTf]^{+6}$, 859.2 $[M+7OTf]^{+5}$, 1111.2 $[M+8OTf]^{+4}$, 1531.3 $[M+9OTf]^{+3}$.

Figure S11.25 ¹H NMR (CD₃CN, 500 MHz, 298 K) spectrum of 1·[OTf]₁₂.Figure S11.26 ³¹P-decoupled ¹H NMR (CD₃CN, 500 MHz, 298 K) spectrum of 1·[OTf]₁₂.

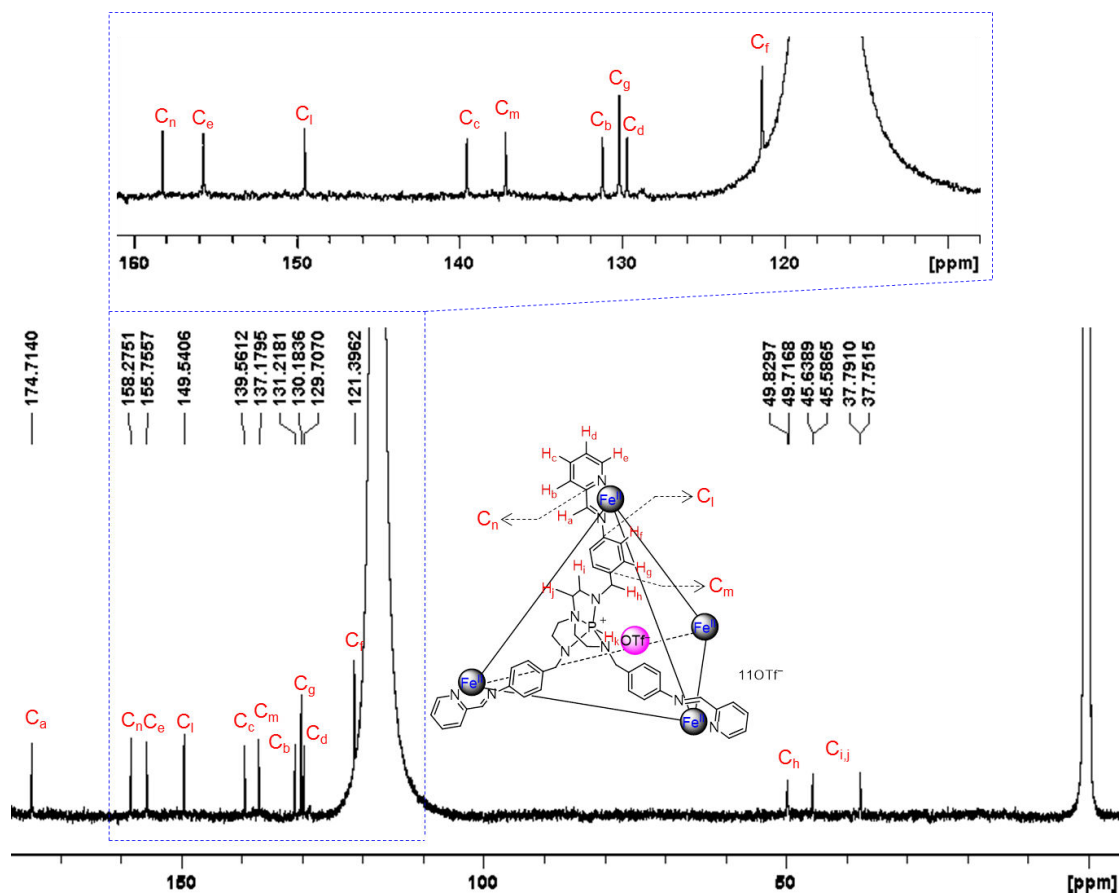


Figure S11.27 ^{13}C NMR spectrum (CD_3CN , 125.8 MHz, 298K) of $1 \cdot [\text{OTf}]_{12}$.

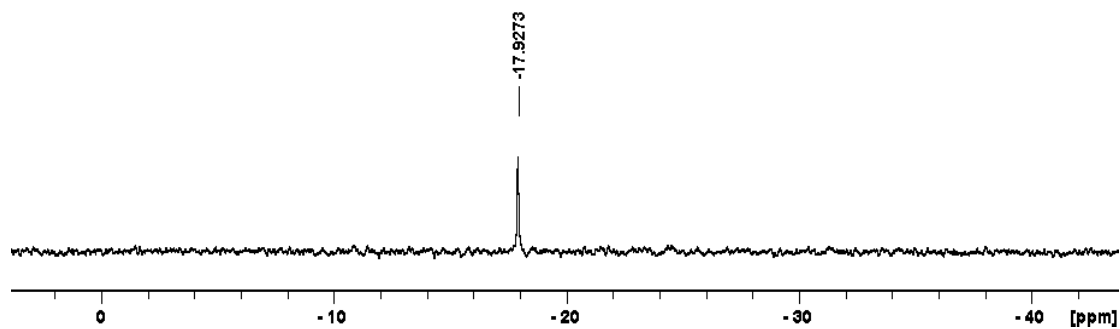


Figure S11.28 ^{31}P NMR spectrum (CD_3CN , 202.4 MHz, 298K) of $1 \cdot [\text{OTf}]_{12}$.

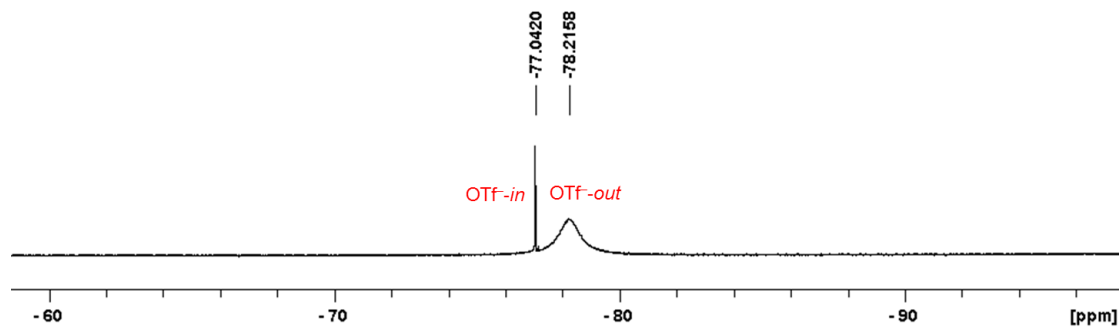


Figure S11.29 ^{19}F NMR spectrum (CD_3CN , 470.4 MHz, 298K) of $1 \cdot [\text{OTf}]_{12}$.

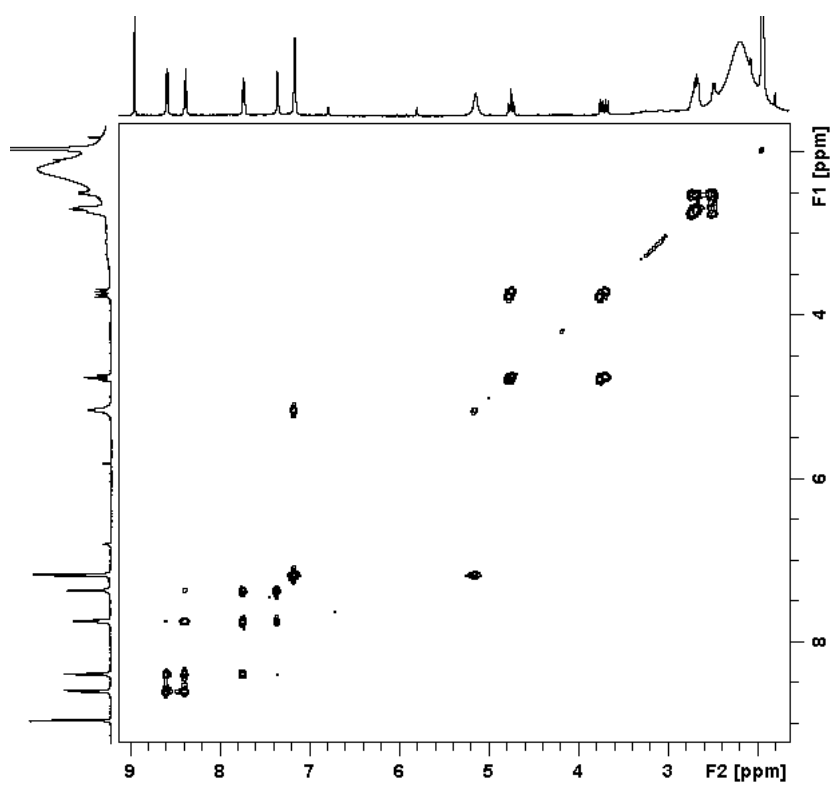


Figure S11.30 ^1H - ^1H COSY spectrum (CD_3CN , 500 MHz, 298K) of $1\cdot[\text{OTf}]_{12}$.

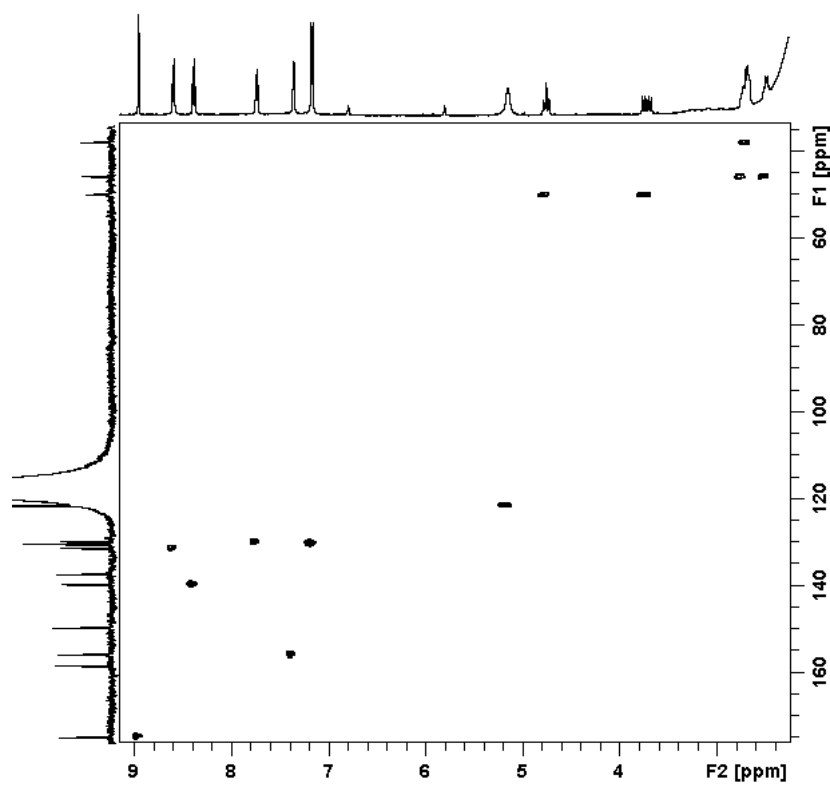


Figure S11.31 ^1H - ^{13}C HSQC spectrum (CD_3CN , 500 MHz, 298K) of $1\cdot[\text{OTf}]_{12}$.

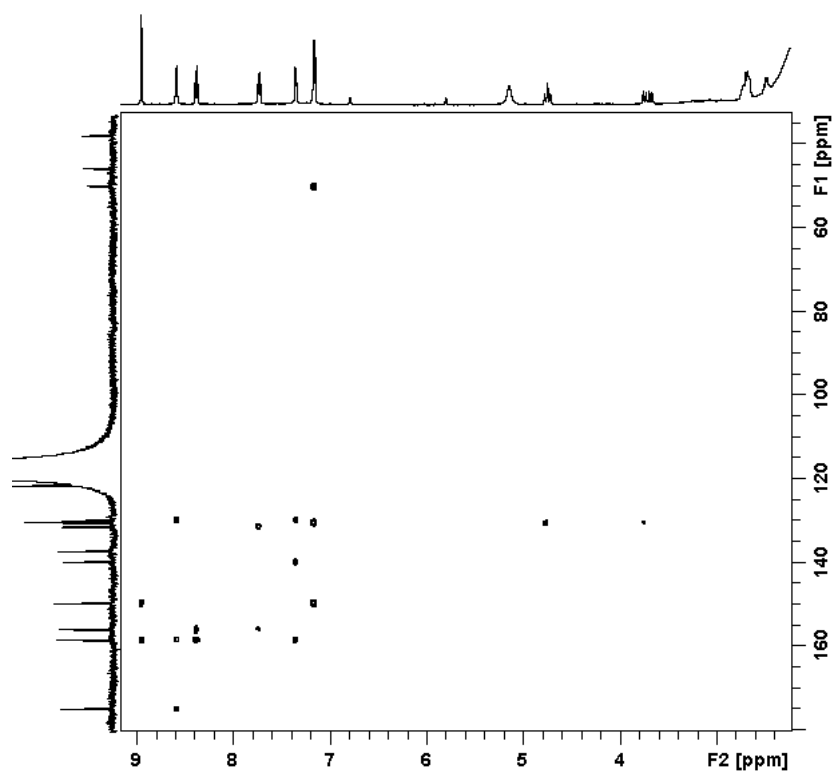


Figure S11.32 ^1H - ^{13}C HMBC spectrum (CD_3CN , 500 MHz, 298K) of $1\cdot[\text{OTf}]_{12}$.

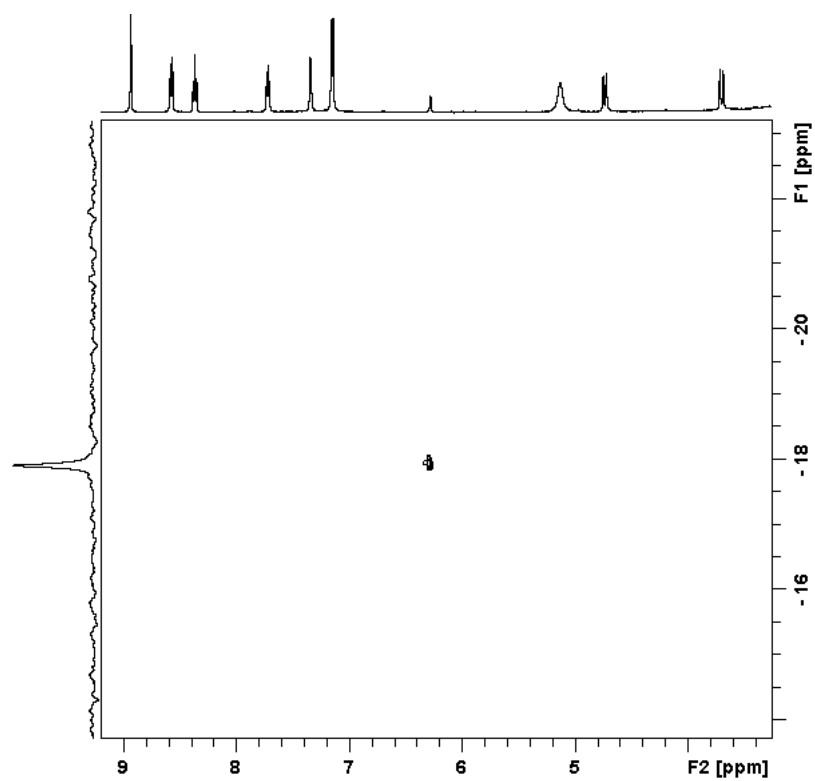


Figure S11.33 ^1H - ^{31}P HSQC spectrum (CD_3CN , 500 MHz, 298K) of $1\cdot[\text{OTf}]_{12}$.

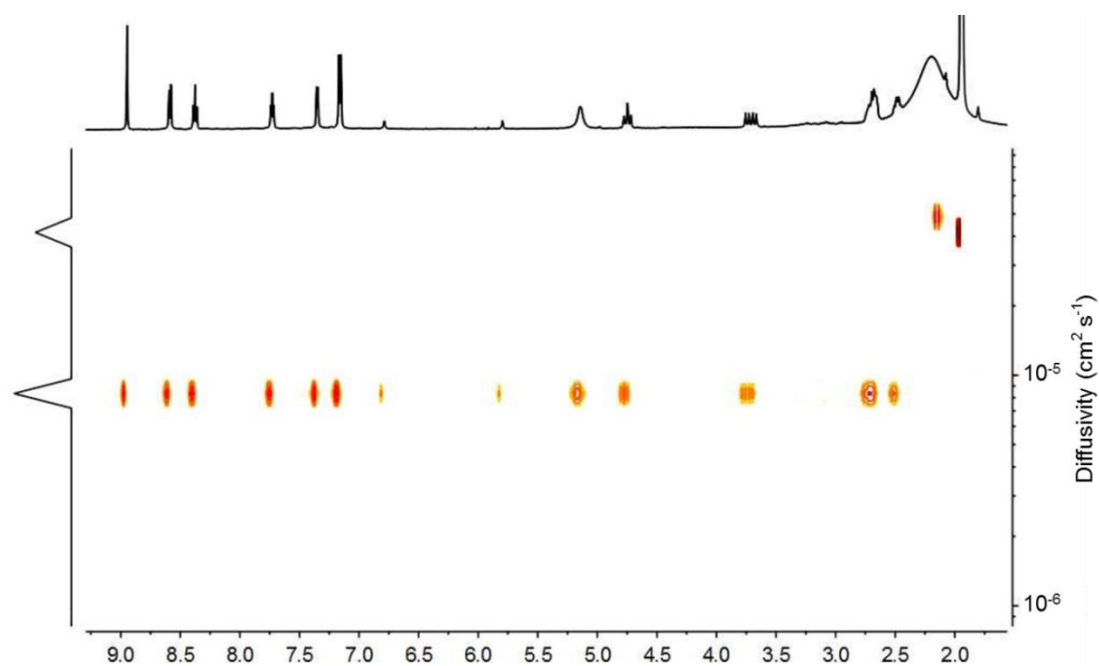


Figure S11.34 ^1H DOSY spectrum (CD_3CN , 500 MHz, 298K) of $1 \cdot [\text{OTf}]_{12}$. The diffusion coefficient of $1 \cdot [\text{OTf}]_{12}$ in CD_3CN was measured to be $8.25 \times 10^{-6} \text{ cm}^2 \text{ s}^{-1}$.

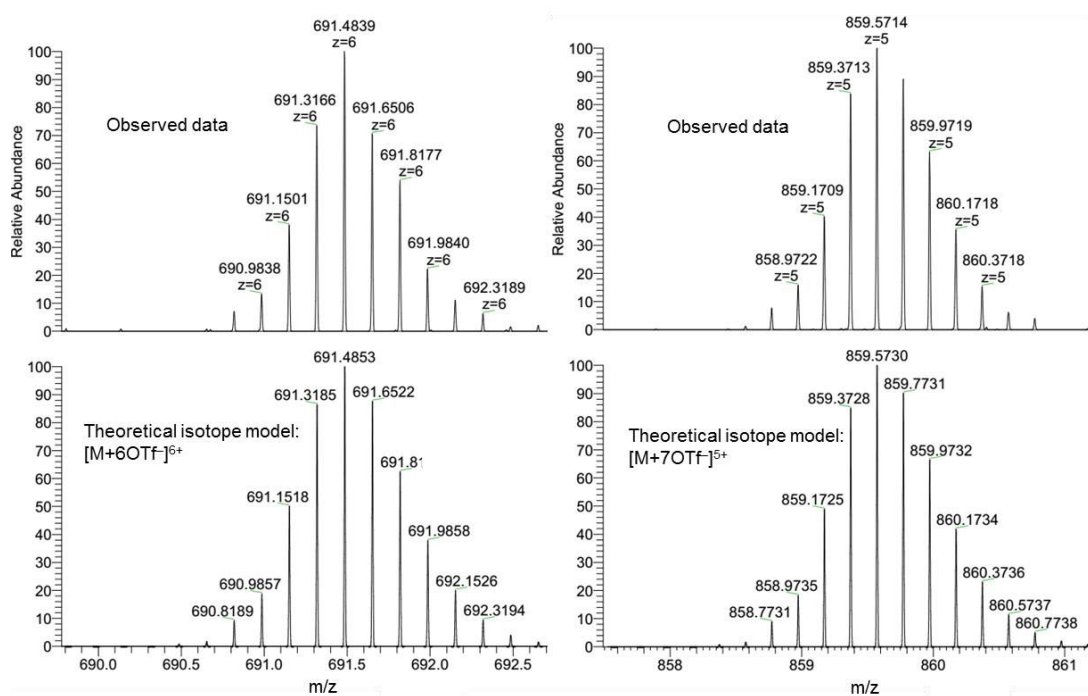
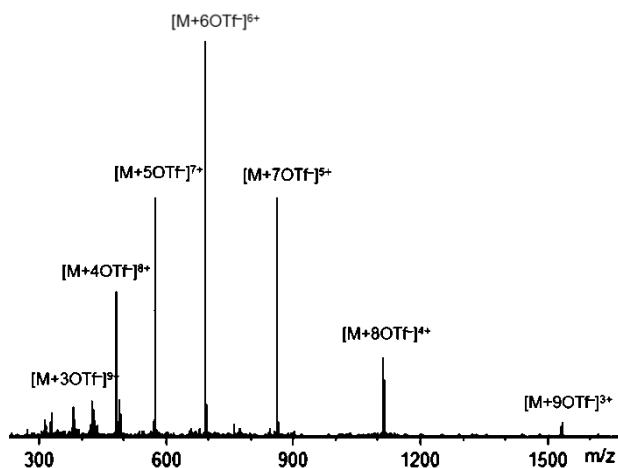
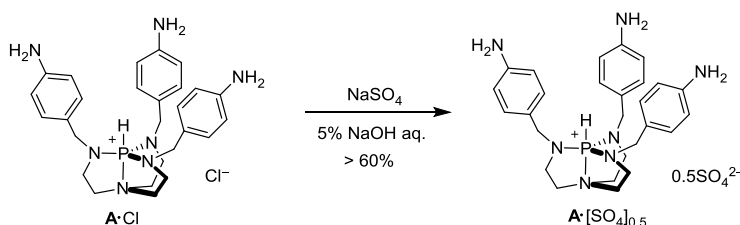


Figure S11.35 High-resolution ESI-mass analysis of $1 \cdot [\text{OTf}]_{12}$ showing the +6 and +5 peaks.

Figure S11.36 Low-resolution ESI-mass spectrum of $1 \cdot [\text{OTf}]_{12}$.

11.5.2.3 Synthesis of subcomponent $\mathbf{A} \cdot [\text{SO}_4]_{0.5}$

Scheme S11.2 Synthetic route for the azaphosphatrane-based subcomponent $\mathbf{A} \cdot [\text{SO}_4]_{0.5}$.

Compound $\mathbf{A} \cdot \text{Cl}$ was dissolved in 5% NaOH aqueous solution and a large excess of Na_2SO_4 (around 60 equiv) was added directly. A light yellow precipitate was instantaneously formed, which was collected by filtration. The solid was dried under vacuum (Yield: > 60%). $^1\text{H NMR}$ (D_2O , 298K, 500 MHz): δ 6.93 (d, $J = 8.2$ Hz, 6H); 6.68 (d, $J = 8.2$ Hz, 6H); 5.59 (d, $J = 499.1$ Hz, 1H); 3.90 (d, $J = 18.1$ Hz, 6H); 3.02 (q, $J = 5.0$ Hz, 6H); 2.92–2.88 (m, 6H) ppm. $^{13}\text{C NMR}$ (D_2O , 298K, 125.7 MHz): 146.4, 129.9, 129.6, 117.3, 51.0, 47.5, 39.3. $^{31}\text{P NMR}$ (D_2O , 298K, 202.4 MHz): δ -12.0 ppm. **ESI-HRMS** m/z : found 490.2842, calcd for $\text{C}_{27}\text{H}_{31}\text{N}_7\text{O}_6\text{P} [\text{M}]^+$ 490.2843.

11.5.2.4 Preparation of cage $\mathbf{X}^- \cdot \mathbf{1} \cdot [\text{SO}_4]_{5.5}$ in water

$\mathbf{A} \cdot [\text{SO}_4]_{0.5}$ (25.9 mg, 48.0 μmol , 4 equiv.), $\text{FeSO}_4(\text{H}_2\text{O})_7$ (13.3 mg, 48.0 μmol , 4 equiv.) and 2-formylpyridine (15.4 mg, 144 μmol , 12 equiv.) were dissolved in D_2O (4 mL). Then 1 equiv of template anion (12 μmol) from the salt of NaBF_4 , KNO_3 , KI , KClO_4 , NaReO_4 , KPF_6 , NaOTf , LiNTf_2 or $\text{CsCB}_{11}\text{H}_{12}$, was added. The reaction mixture was kept at 25 $^\circ\text{C}$ under nitrogen. The resulting purple solution of $\mathbf{X}^- \cdot \mathbf{1} \cdot [\text{SO}_4]_{5.5}$ was used directly for the following anion displacement and shape memory phenomena.

It was found that for the assembly of the cage without additional template anions, no cage was formed. When using the template anions with volumes $\geq 55 \text{ \AA}^3$, such as ClO_4^- , ReO_4^- , PF_6^- , OTf^- , NTf_2^- or $\text{CB}_{11}\text{H}_{12}^-$, $\mathbf{X}^- \cdot \mathbf{T} \cdot \mathbf{1} \cdot [\text{SO}_4]_{5.5}$ was formed after one night. However when using the template anion with volumes $\leq 53 \text{ \AA}^3$, such as BF_4^- , NO_3^- or I^- , both $\mathbf{X}^- \cdot \mathbf{T} \cdot \mathbf{1} \cdot [\text{SO}_4]_{5.5}$ and $\mathbf{X}^- \cdot \mathbf{C}_3 \cdot \mathbf{1} \cdot [\text{SO}_4]_{5.5}$ were observed after one night. The two species then slowly interconverted taking almost 2 weeks to reach equilibrium.

Cage formation without additional template anions

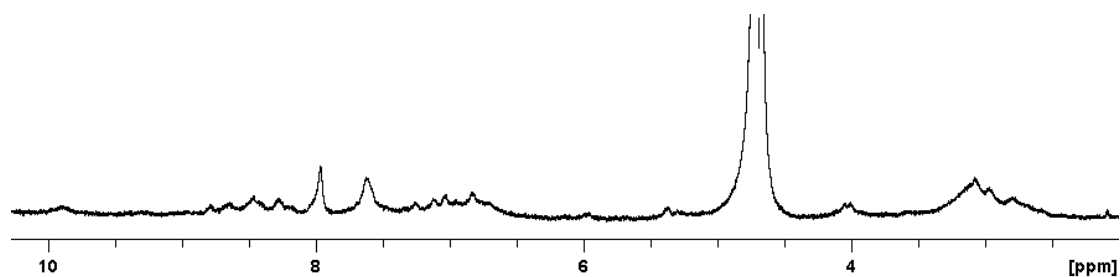


Figure S11.37 ^1H NMR (D_2O , 500 MHz, 298 K) spectrum of the assembly of $1\cdot[\text{SO}_4]_6$ without additional template anions.

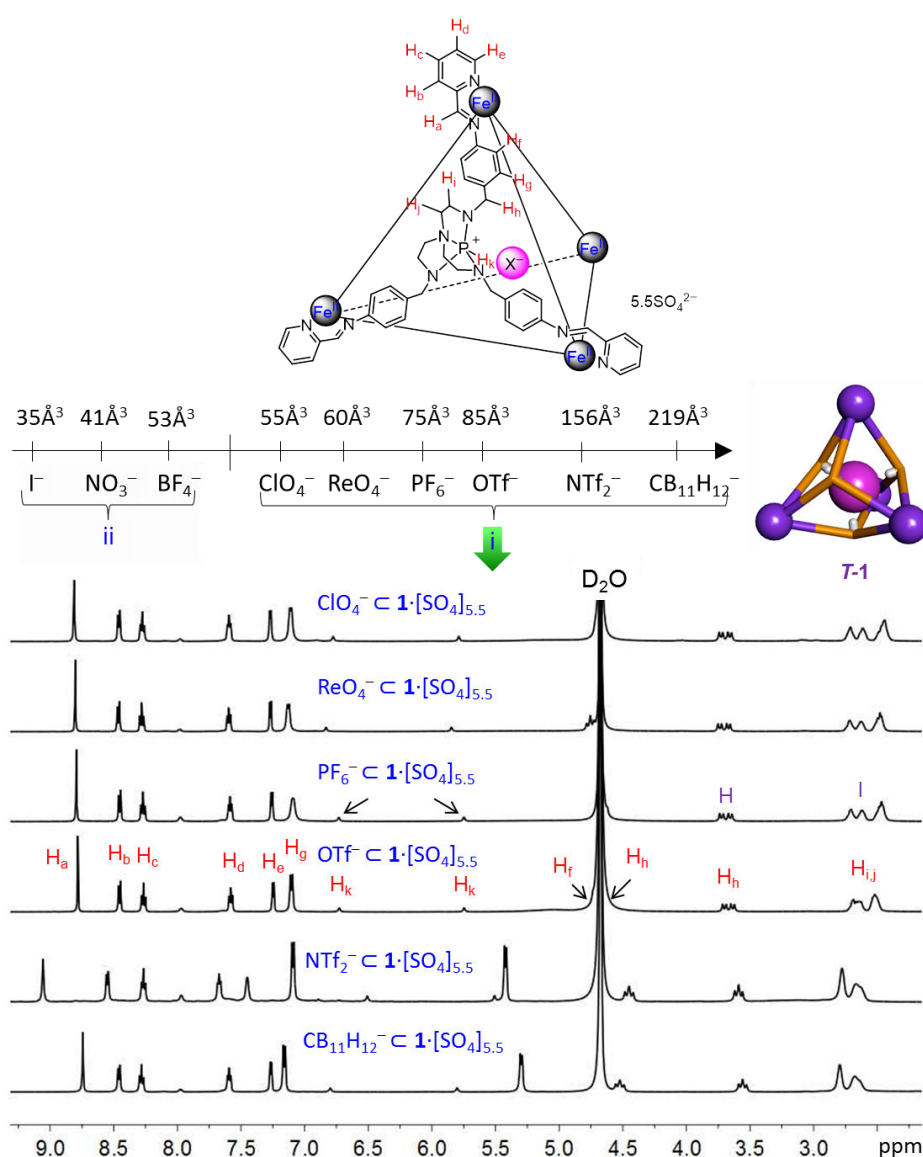
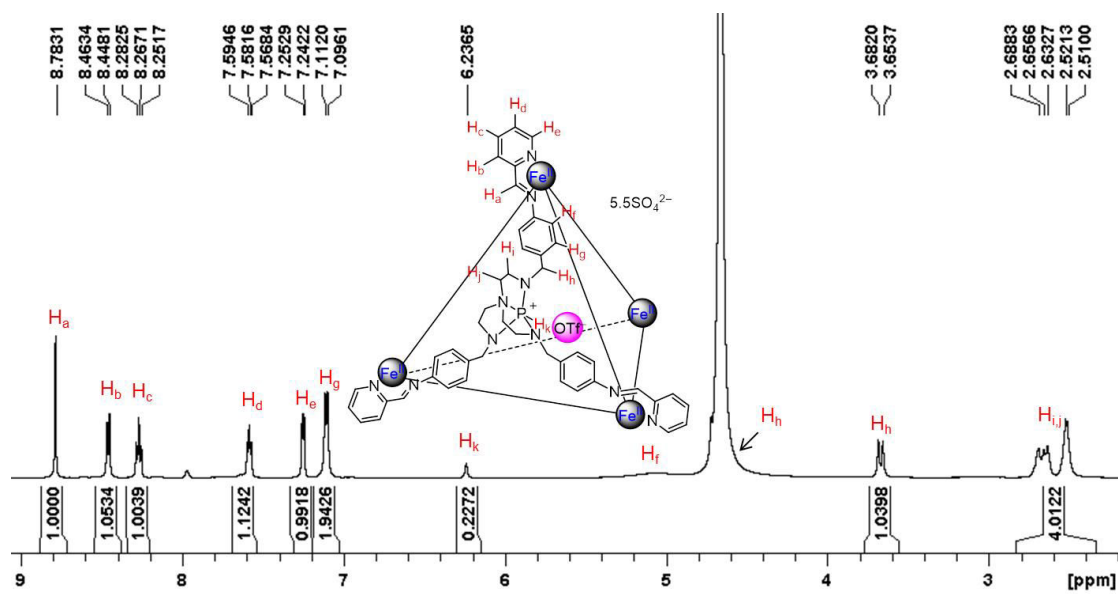
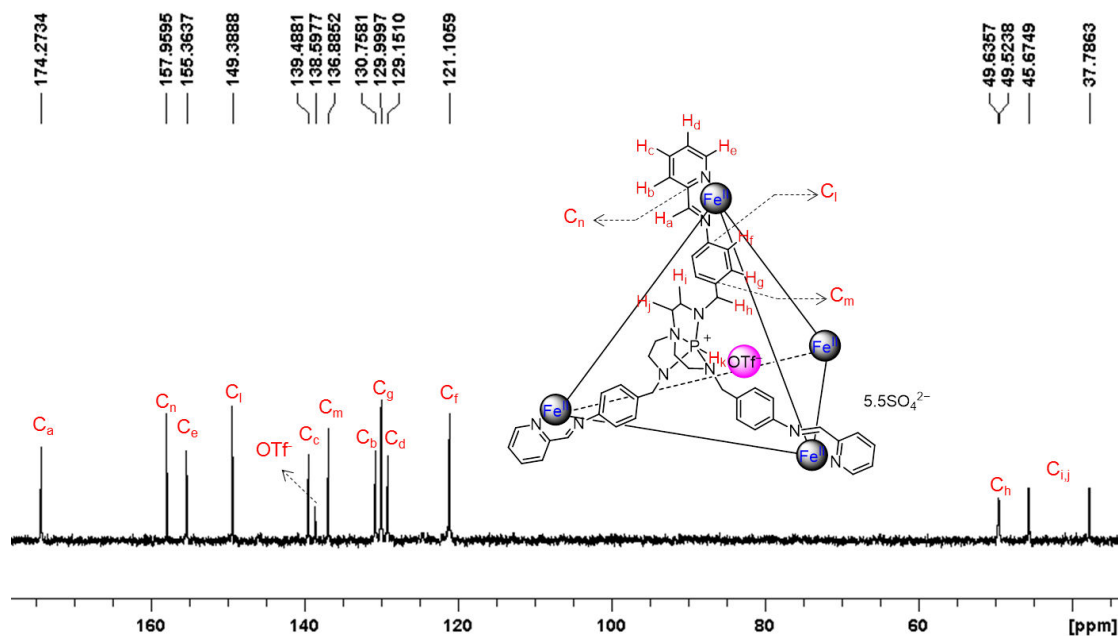
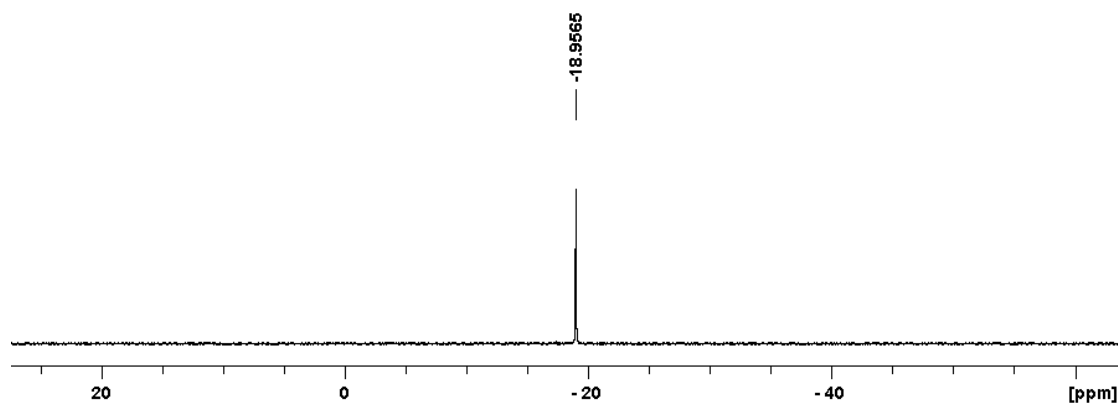
Cage formation driven by template anions with volumes $\geq 55 \text{ \AA}^3$ 

Figure S11.38 ^1H NMR (D_2O , 500 MHz, 298 K) spectra of the assembly of $\text{X}^- \cdot \text{T-1} \cdot [\text{SO}_4]_{5.5}$ after one night ($\text{X}^- = \text{ClO}_4^-, \text{ReO}_4^-, \text{PF}_6^-, \text{OTf}^-, \text{NTf}_2^-$ or $\text{CB}_{11}\text{H}_{12}^-$). The volume of each anion, which was reported previously,²⁰⁻²² has been provided; Protons of $\text{OTf}^- \cdot \text{T-1} \cdot [\text{SO}_4]_{5.5}$ have been assigned; the protons assignments for cages driven by other template anions are similar and have been omitted.

Figure S11.39 ³¹P-decoupled ¹H NMR (D₂O, 500 MHz, 298 K) spectrum of OTf-c-T-1·[SO₄]_{5.5}.Figure S11.40 ¹³C NMR (D₂O, 125.8 MHz, 298 K) spectrum of OTf-c-T-1·[SO₄]_{5.5}.Figure S11.41 ¹H-decoupled ³¹P NMR spectrum (D₂O, 202.4 MHz, 298K) of OTf-c-T-1·[SO₄]_{5.5}.

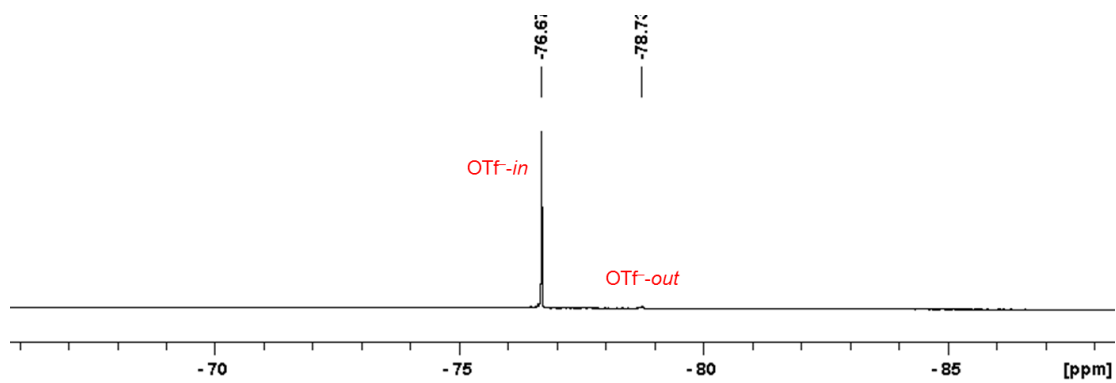


Figure S11.42 ^{19}F NMR spectrum (D_2O , 470.4 MHz, 298K) of $\text{OTf}^- \cdot \text{cT-1} \cdot [\text{SO}_4]_{5.5}$.

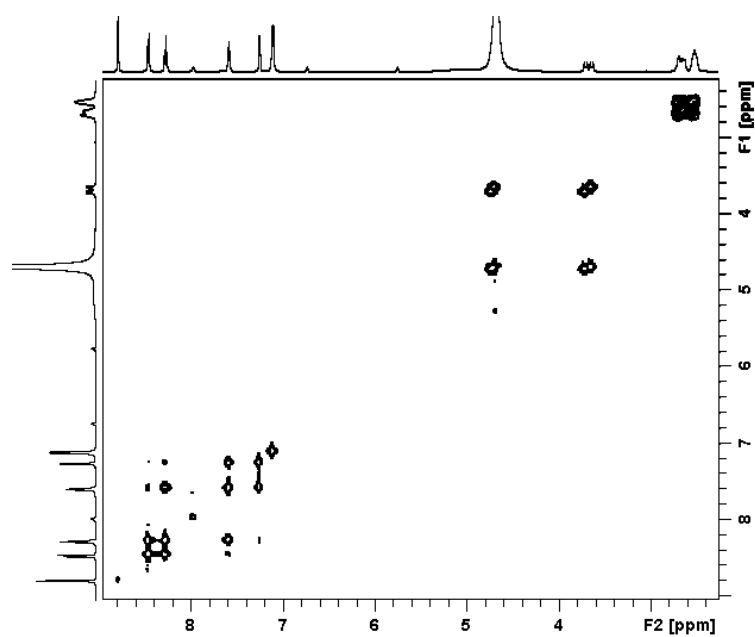


Figure S11.43 ^1H - ^1H COSY spectrum (D_2O , 500 MHz, 298K) of $\text{OTf}^- \cdot \text{cT-1} \cdot [\text{SO}_4]_{5.5}$.

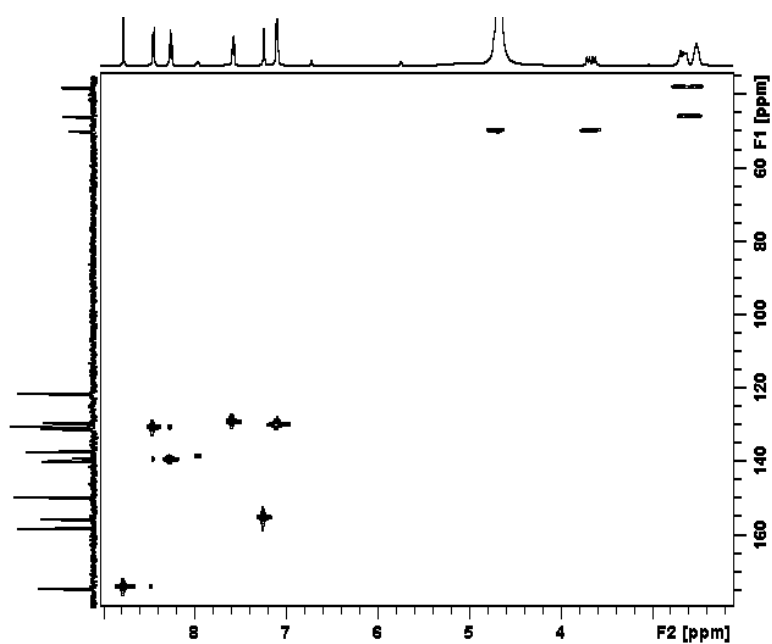


Figure S11.44 ^1H - ^{13}C HSQC spectrum (D_2O , 500 MHz, 298K) of $\text{OTf}^- \cdot \text{cT-1} \cdot [\text{SO}_4]_{5.5}$.

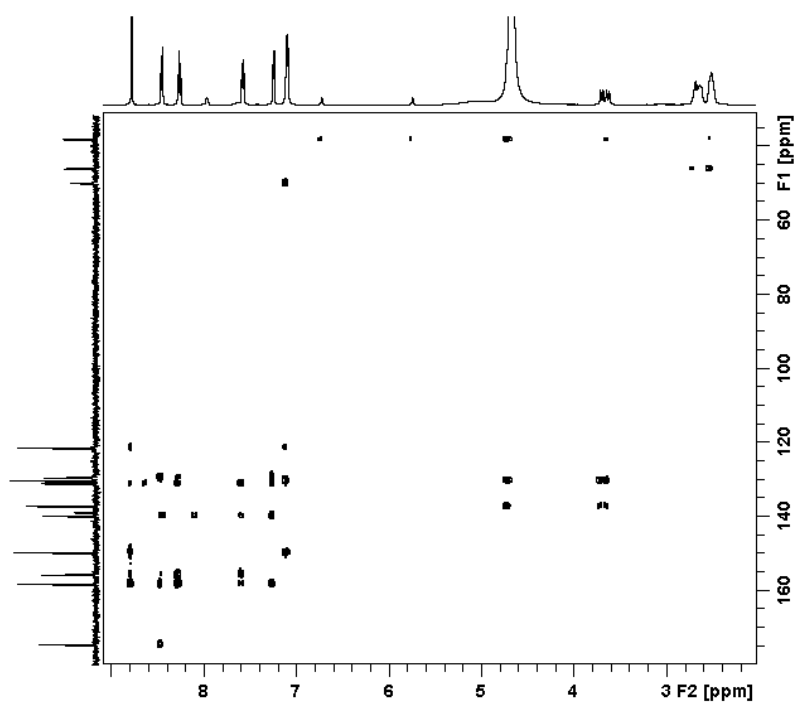


Figure S11.45 ^1H - ^{13}C HMBC spectrum (D_2O , 500 MHz, 298K) of $\text{OTf}^- \cdot \text{T-1} \cdot [\text{SO}_4]_{5.5}$.

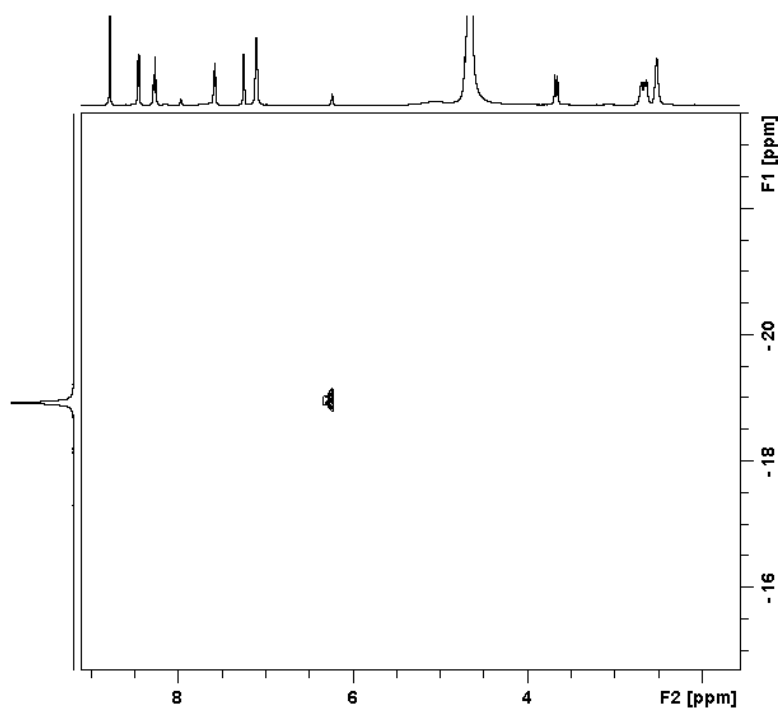


Figure S11.46 ^1H - ^{31}P HSQC spectrum (D_2O , 500 MHz, 298K) of $\text{OTf}^- \cdot \text{T-1} \cdot [\text{SO}_4]_{5.5}$.

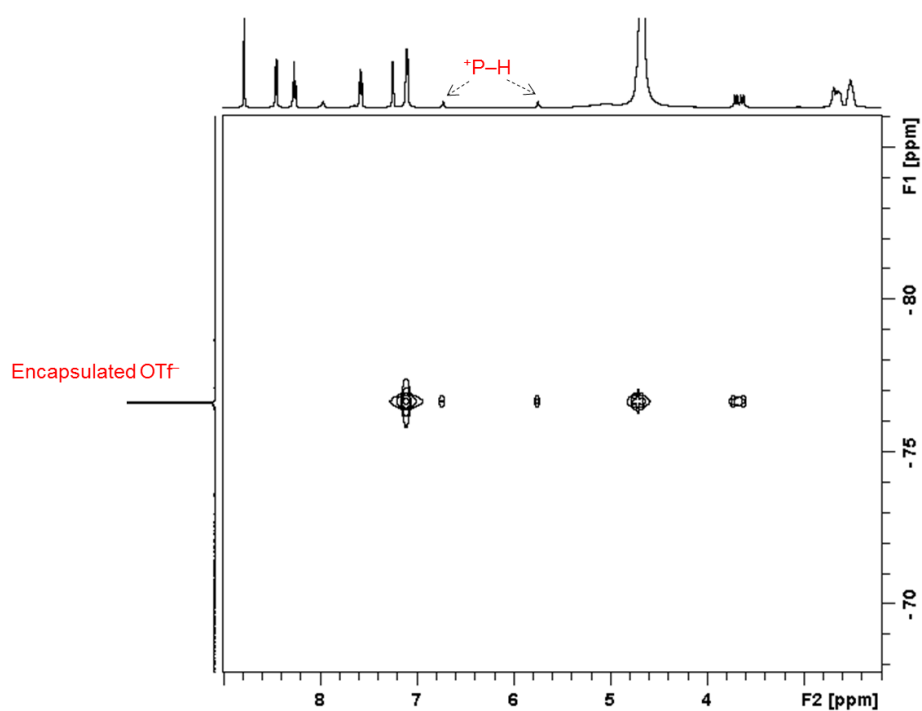


Figure S11.47 ^1H - ^{31}F HOESY spectrum (D_2O , 500 MHz, 298K) of $\text{OTf}^- \cdot \text{CT-1} \cdot [\text{SO}_4]_{5.5}$.

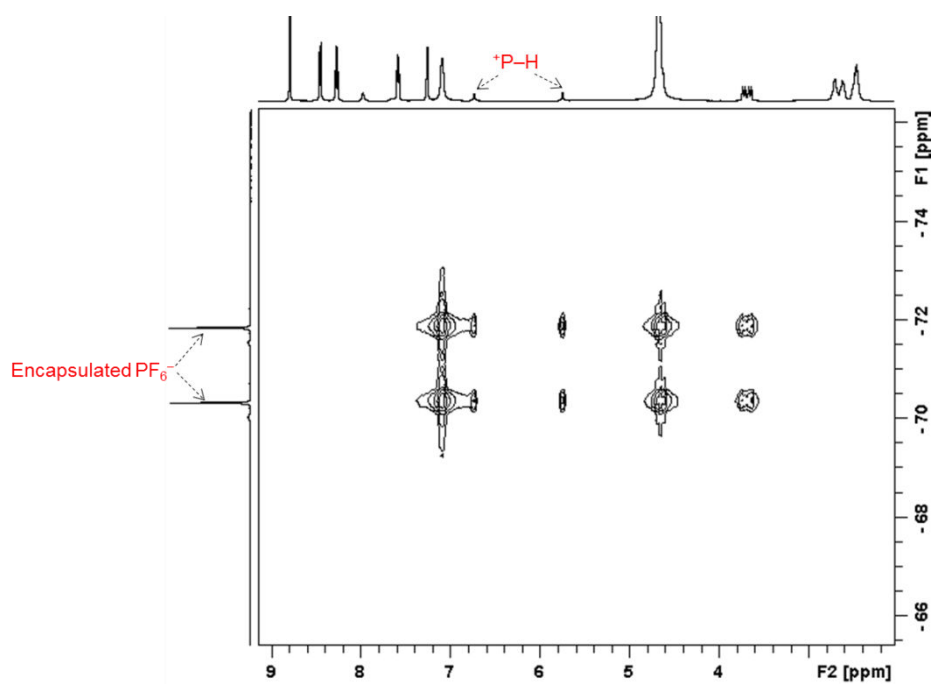


Figure S11.48 ^1H - ^{31}F HOESY spectrum (D_2O , 500 MHz, 298K) of $\text{PF}_6^- \cdot \text{CT-1} \cdot [\text{SO}_4]_{5.5}$.

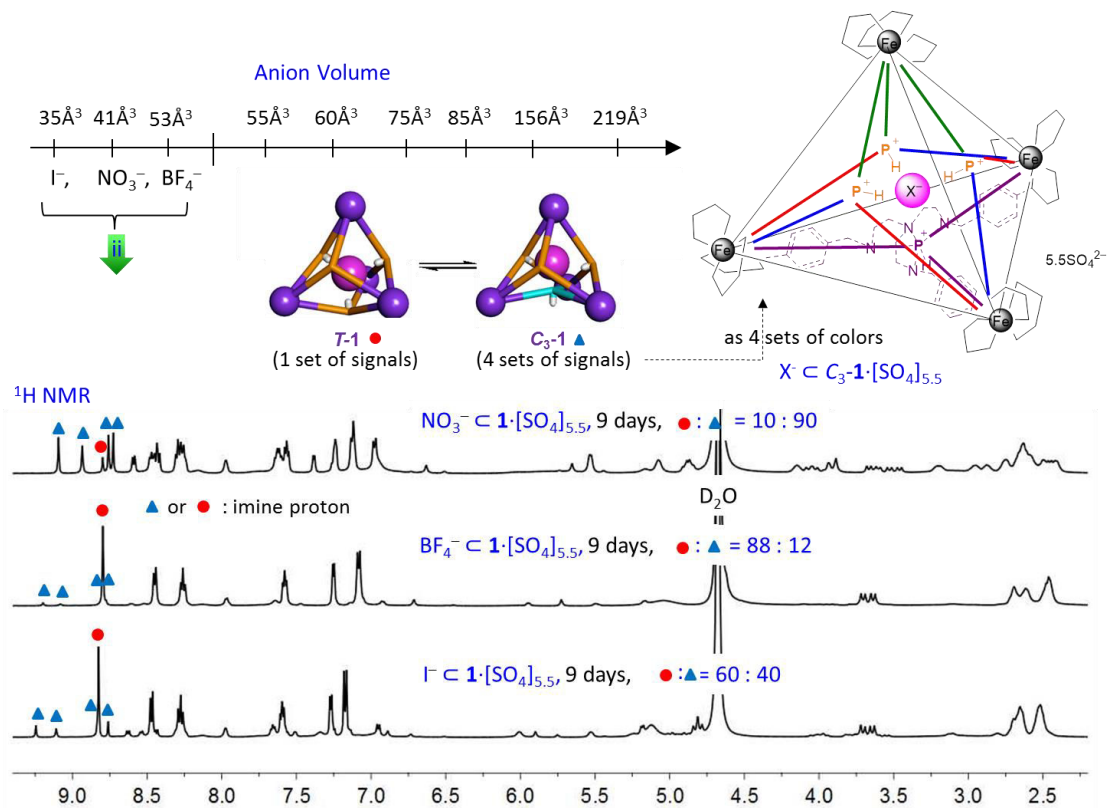
Cage formation driven by template anions with volumes $\leq 53 \text{ \AA}^3$ 

Figure S11.49 ^1H NMR (D_2O , 500 MHz, 298 K) spectra of the assembly of $\text{X}^- \subset \mathbf{1} \cdot [\text{SO}_4]_{5.5}$ after 9 days ($\text{X}^- = \text{NO}_3^-, \text{BF}_4^-, \text{or } \text{I}^-$). Two cage isomers $\text{X}^- \subset \mathbf{T-1} \cdot [\text{SO}_4]_{5.5}$ and $\text{X}^- \subset \mathbf{C}_3\text{-1} \cdot [\text{SO}_4]_{5.5}$ were observed in solution. The schematic inset with four sets of colors on the four faces of the tetrahedron illustrates the four sets of signals in the ^1H NMR spectra of $\text{X}^- \subset \mathbf{C}_3\text{-1} \cdot [\text{SO}_4]_{5.5}$.

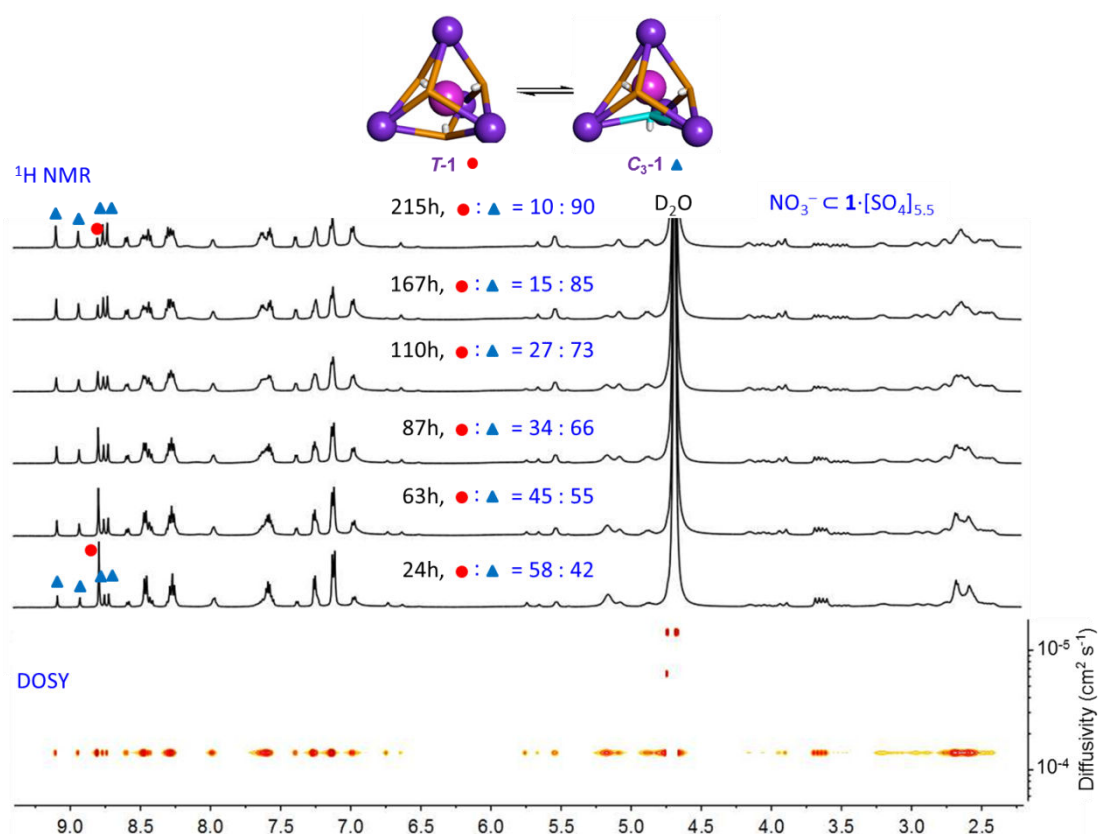


Figure S11.50 Time evolution of the ratio between $\text{NO}_3^- \subset T\text{-1} \cdot [\text{SO}_4]_{5,5}$ (●) and $\text{NO}_3^- \subset C_3\text{-1} \cdot [\text{SO}_4]_{5,5}$ (▲) at 298 K monitored by ^1H NMR spectroscopy (D_2O , 500 MHz, 298 K). Imine protons have been labelled in the spectra. DOSY spectrum shows that the two species give the same diffusion coefficient ($1.4 \times 10^{-6} \text{ cm}^2 \text{ s}^{-1}$).

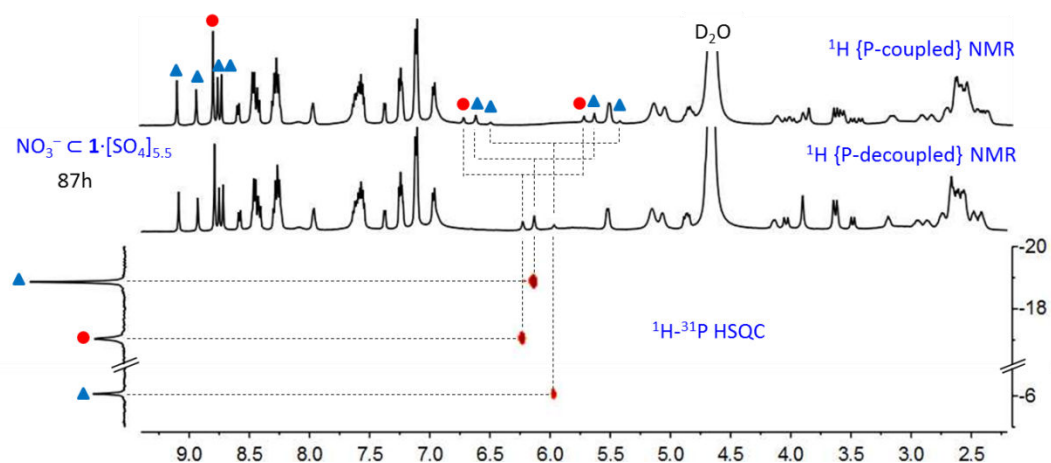


Figure S11.51 ^{31}P coupled/decoupled ^1H NMR (D_2O , 500 MHz, 298 K) spectrum of the assembly of $\text{NO}_3^- \subset \mathbf{1} \cdot [\text{SO}_4]_{5,5}$ after 87 h in D_2O , giving two isomeric cage species of $\text{NO}_3^- \subset T\text{-1} \cdot [\text{SO}_4]_{5,5}$ (●) and $\text{NO}_3^- \subset C_3\text{-1} \cdot [\text{SO}_4]_{5,5}$ (▲), and the corresponding $^1\text{H}\text{-}^{31}\text{P}$ HSQC (D_2O , 500 MHz, 298K) spectrum.

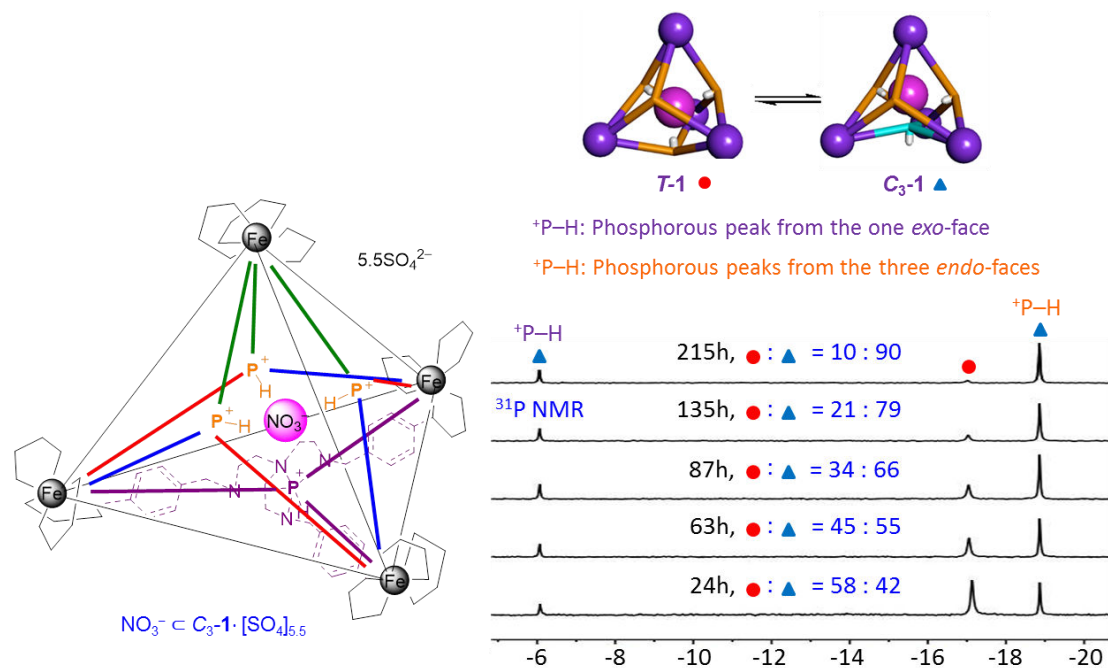


Figure S11.52. Time evolution of the ratio between $\text{NO}_3^- \cdot T\text{-1} \cdot [\text{SO}_4]_{5.5}$ (●) and $\text{NO}_3^- \cdot C_3\text{-1} \cdot [\text{SO}_4]_{5.5}$ (▲) at 298 K monitored by ^{31}P NMR spectroscopy (D_2O , 202.4 MHz, 298 K). Phosphorous peaks have been assigned in the spectra. The schematic inset at the left with two types of colors of $^+\text{P-H}$ (orange and purple) on the four faces of the tetrahedron illustrates the two sets of signals in the ^{31}P NMR spectra of $\text{NO}_3^- \cdot C_3\text{-1} \cdot [\text{SO}_4]_{5.5}$.

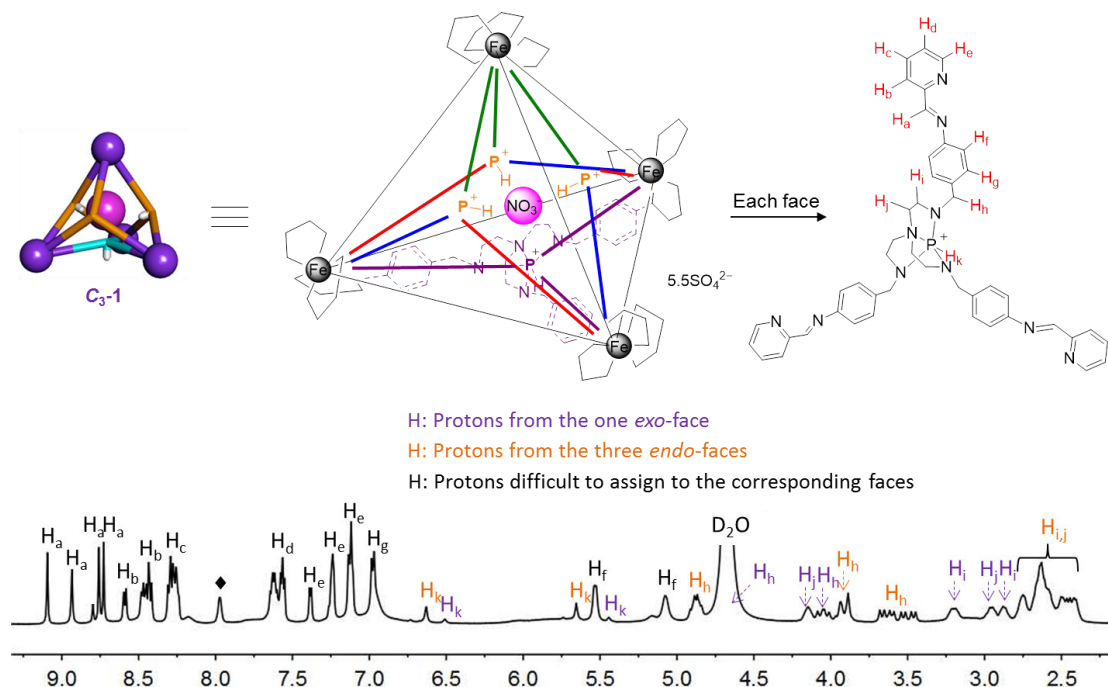


Figure S11.53 ^1H NMR (D_2O , 500 MHz, 298 K) spectrum of the assembly of $\text{NO}_3^- \cdot C_3\text{-1} \cdot [\text{SO}_4]_{5.5}$ in D_2O after 2 weeks which shows the percentage of $\text{NO}_3^- \cdot C_3\text{-1} \cdot [\text{SO}_4]_{5.5}$ among the two cage isomers is 95%.

The protons of $\text{NO}_3^- \cdot C_3\text{-1} \cdot [\text{SO}_4]_{5.5}$ have been labelled and assigned in the spectrum; ♦ represents impurity.

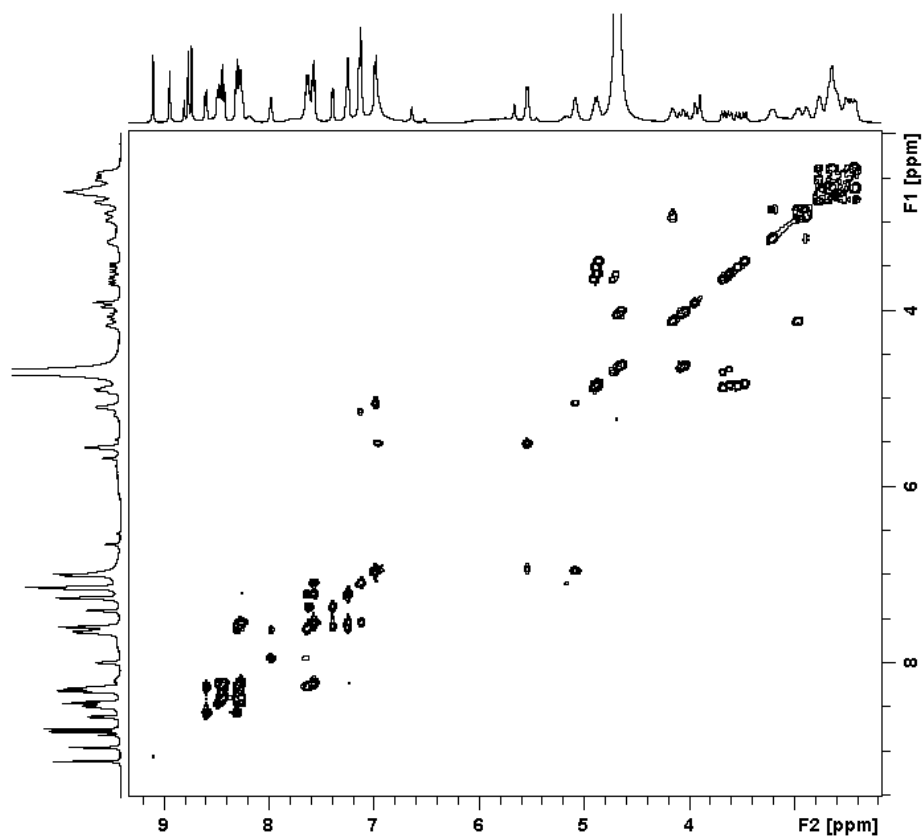


Figure S11.54 ^1H - ^1H COSY spectrum (D_2O , 500 MHz, 298K) of the assembly of $\text{NO}_3^- \text{C}_1\text{-[SO}_4\text{]}_{5.5}$ in D_2O after 2 weeks with the ratio of $\text{NO}_3^- \text{C}_1\text{-[SO}_4\text{]}_{5.5} : \text{NO}_3^- \text{C}_3\text{-[SO}_4\text{]}_{5.5} = 5 : 95$.

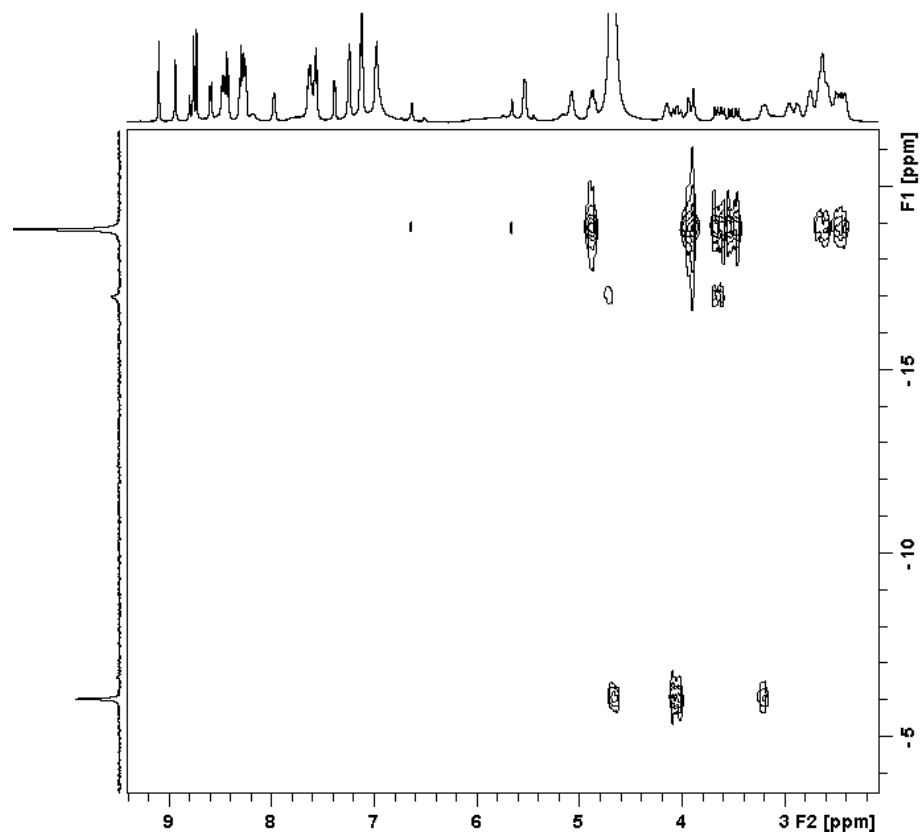


Figure S11.55 ^1H - ^{31}P HMBC spectrum (D_2O , 500 MHz, 298K) of the assembly of $\text{NO}_3^- \text{C}_1\text{-[SO}_4\text{]}_{5.5}$ in D_2O after 2 weeks with the ratio of $\text{NO}_3^- \text{C}_1\text{-[SO}_4\text{]}_{5.5} : \text{NO}_3^- \text{C}_3\text{-[SO}_4\text{]}_{5.5} = 5 : 95$.

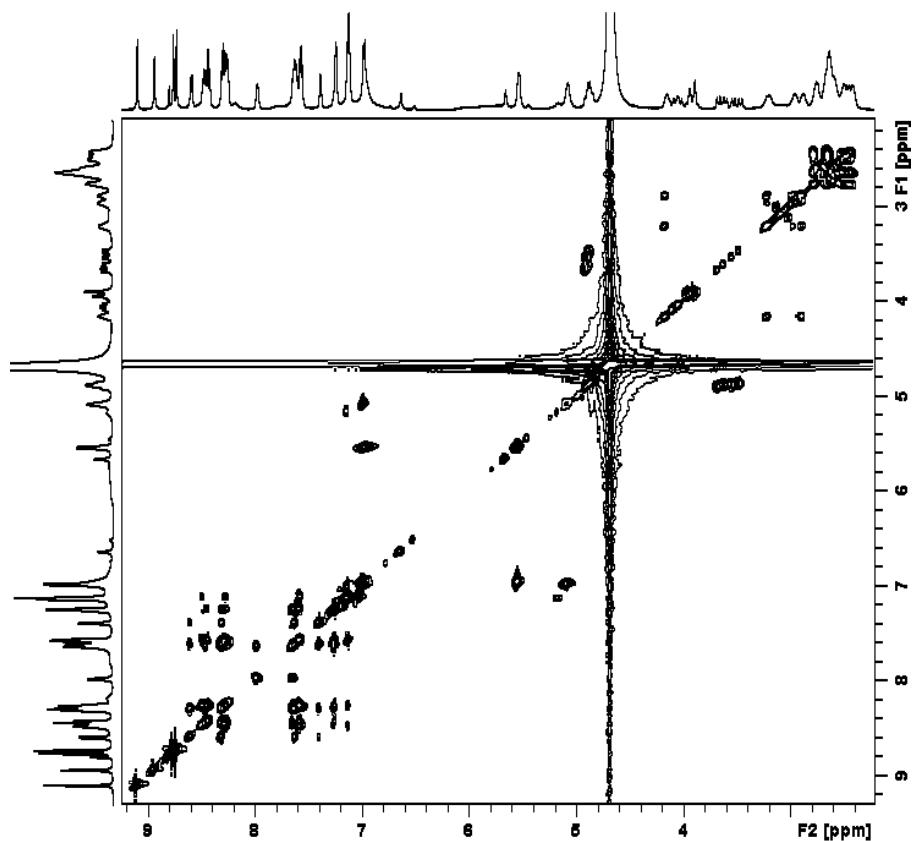


Figure S11.56 TOCSY spectrum (D₂O, 500 MHz, 298K, mixing time: 50 ms) of the assembly of NO₃⁻·C₁·[SO₄]_{5.5} in D₂O after 2 weeks with the ratio of NO₃⁻·C₁·[SO₄]_{5.5} : NO₃⁻·C₃-1·[SO₄]_{5.5} = 5 : 95.

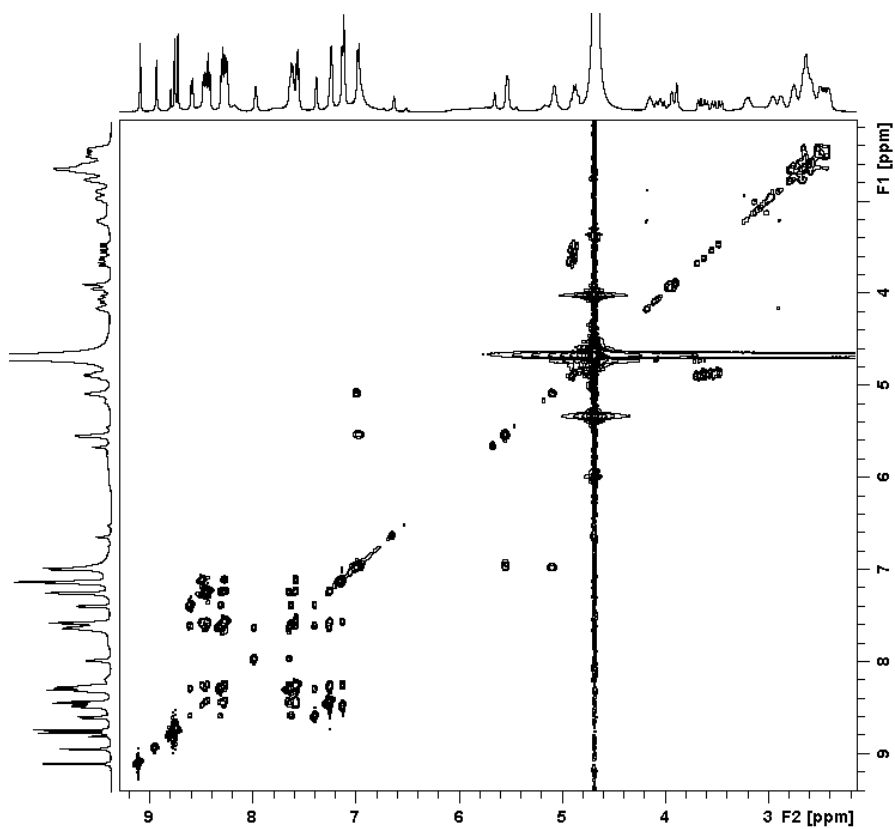


Figure S11.57 TOCSY (D₂O, 500 MHz, 298K, mixing time: 100 ms) of the assembly of NO₃⁻·C₁·[SO₄]_{5.5} in D₂O after 2 weeks with the ratio of NO₃⁻·C₁·[SO₄]_{5.5} : NO₃⁻·C₃-1·[SO₄]_{5.5} = 5 : 95.

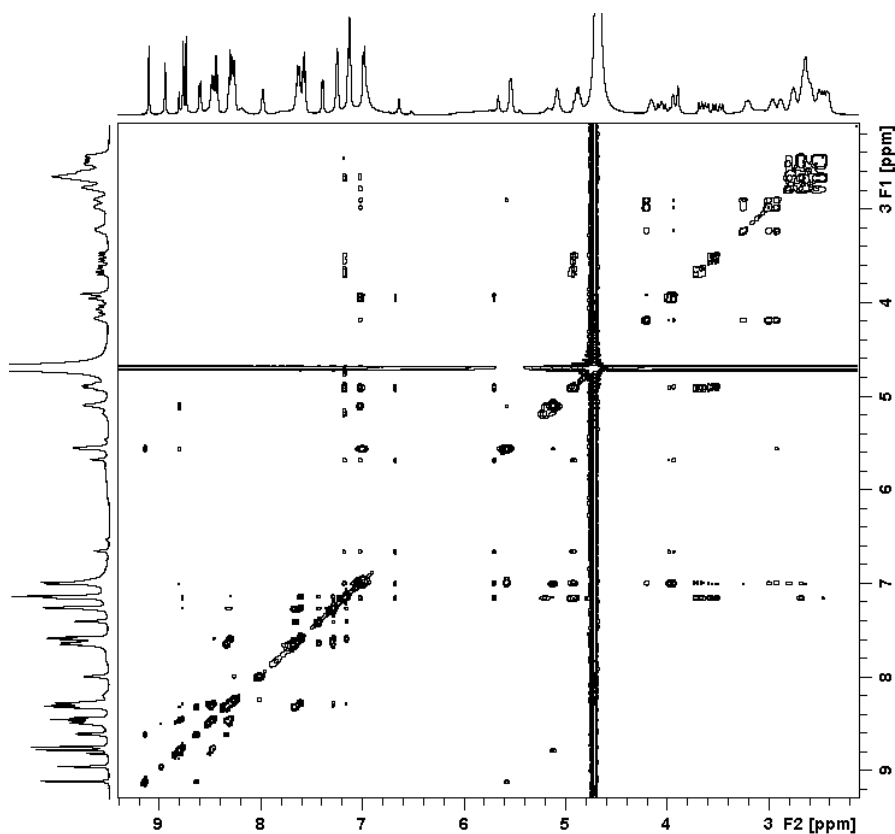


Figure S11.58 NOESY spectrum (D₂O, 500 MHz, 298K) of the assembly of NO₃⁻·C₁·[SO₄]_{5.5} in D₂O after 2 weeks with the ratio of NO₃⁻·C_T-**1**·[SO₄]_{5.5} : NO₃⁻·C₃-**1**·[SO₄]_{5.5} = 5 : 95.

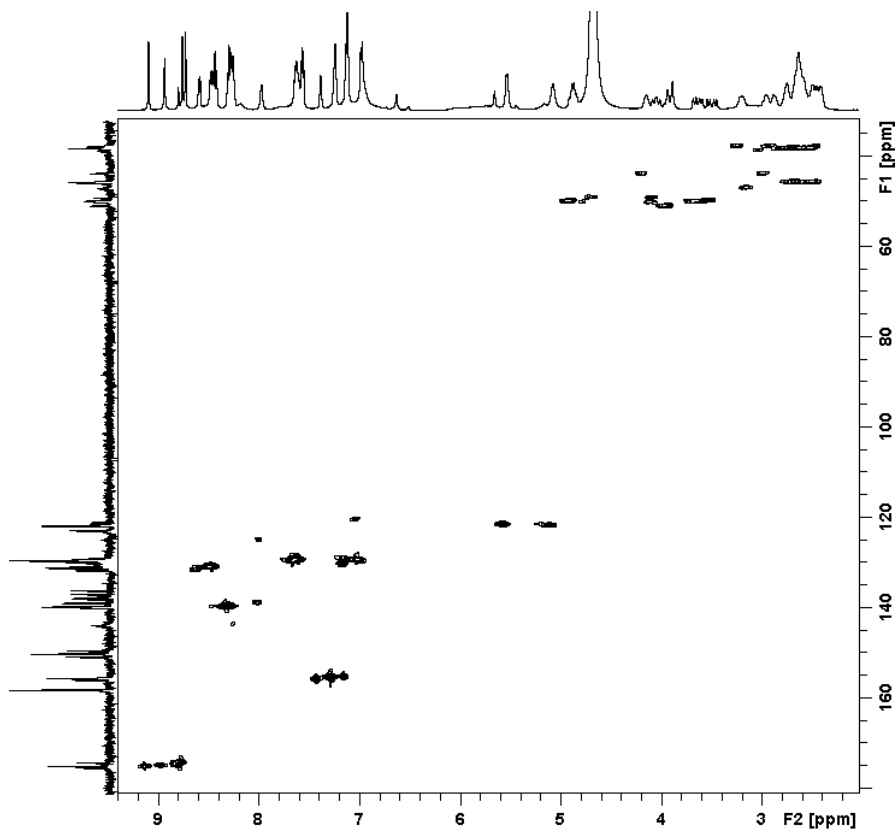


Figure S11.59 ¹H-¹³C HSQC spectrum (D₂O, 500 MHz, 298K) of the assembly of NO₃⁻·C₁·[SO₄]_{5.5} in D₂O after 2 weeks with the ratio of NO₃⁻·C_T-**1**·[SO₄]_{5.5} : NO₃⁻·C₃-**1**·[SO₄]_{5.5} = 5 : 95.

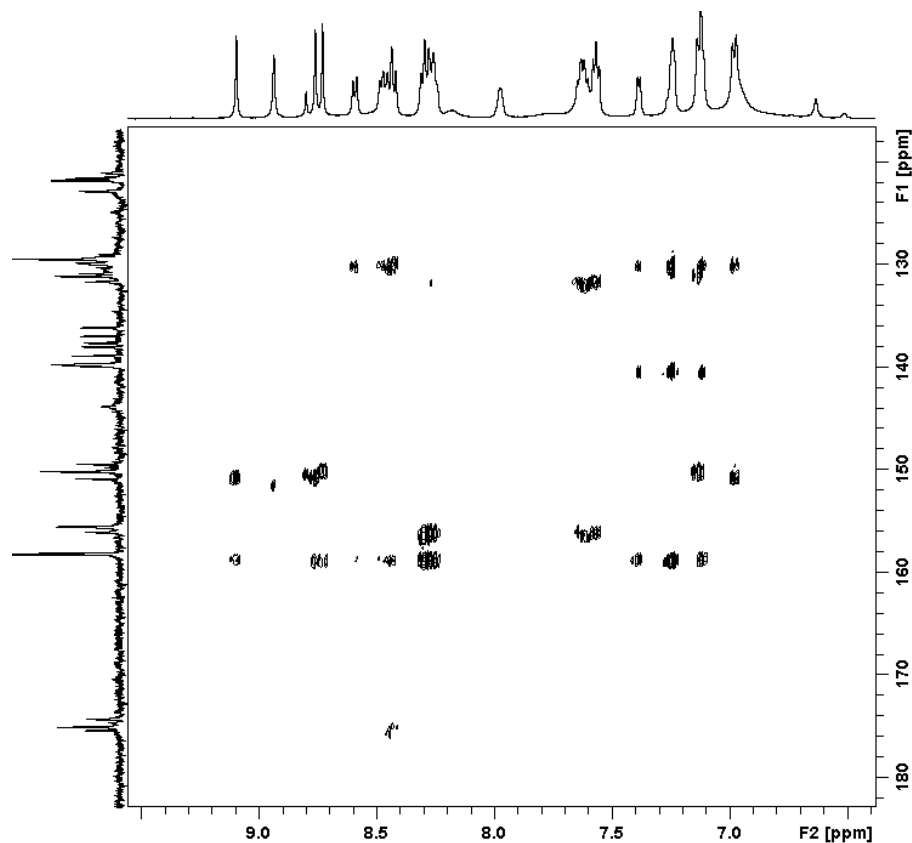


Figure S11.60 Aromatic region of ^1H - ^{13}C HMBC (D_2O , 500 MHz, 298K) of the assembly of $\text{NO}_3^- \cdot \text{C}_1 \cdot [\text{SO}_4]_{5.5}$ in D_2O after 2 weeks with the ratio of $\text{NO}_3^- \cdot \text{T-1} \cdot [\text{SO}_4]_{5.5} : \text{NO}_3^- \cdot \text{C}_3\text{-1} \cdot [\text{SO}_4]_{5.5} = 5 : 95$.

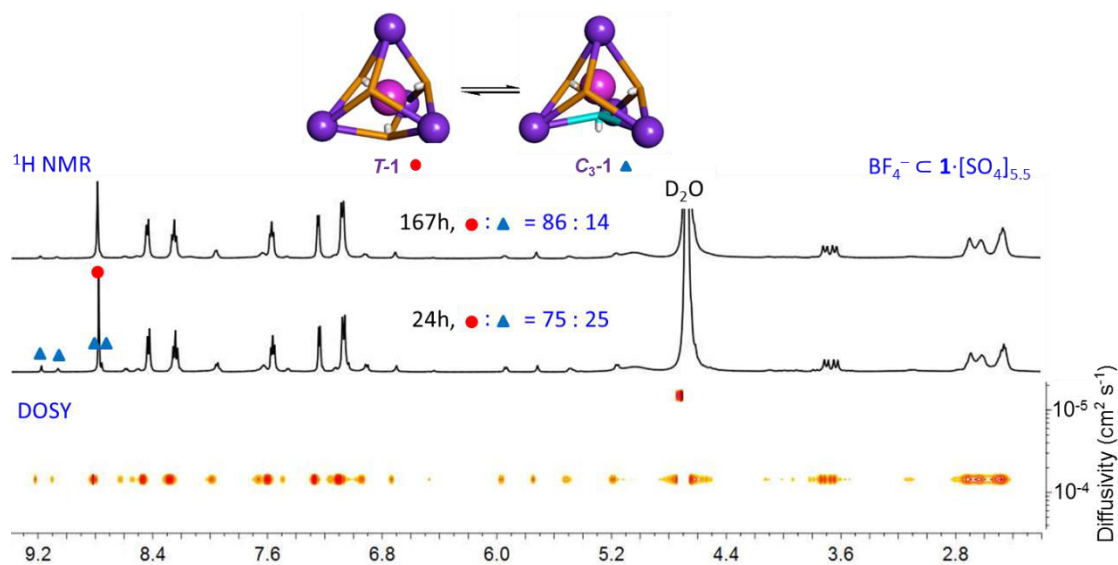


Figure S11.61 Time evolution of the ratio between $\text{BF}_4^- \cdot \text{T-1} \cdot [\text{SO}_4]_{5.5}$ (●) and $\text{BF}_4^- \cdot \text{C}_3\text{-1} \cdot [\text{SO}_4]_{5.5}$ (▲) at 298 K monitored by ^1H NMR spectroscopy (D_2O , 500 MHz, 298 K). Imine protons have been labelled in the spectra. DOSY spectrum shows that the two species give the same diffusion coefficient ($1.4 \times 10^{-6} \text{ cm}^2 \text{ s}^{-1}$).

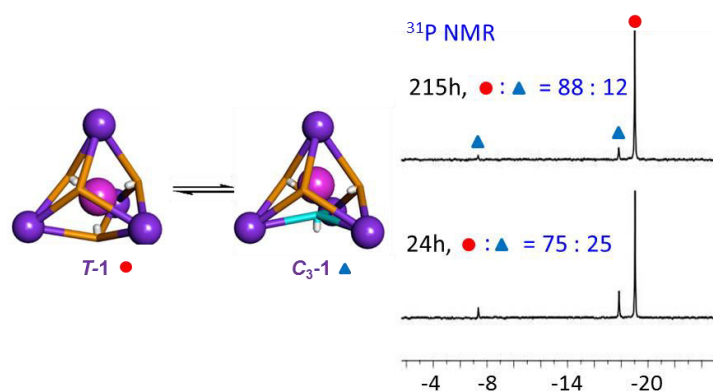


Figure S11.62 Time evolution of the ratio between $\text{BF}_4^- \cdot \text{T-1} \cdot [\text{SO}_4]_{5.5}$ (●) and $\text{BF}_4^- \cdot \text{C}_3\text{-1} \cdot [\text{SO}_4]_{5.5}$ (▲) at 298 K monitored by ^{31}P NMR spectroscopy (D_2O , 202.4 MHz, 298 K). Phosphorous peaks have been assigned.

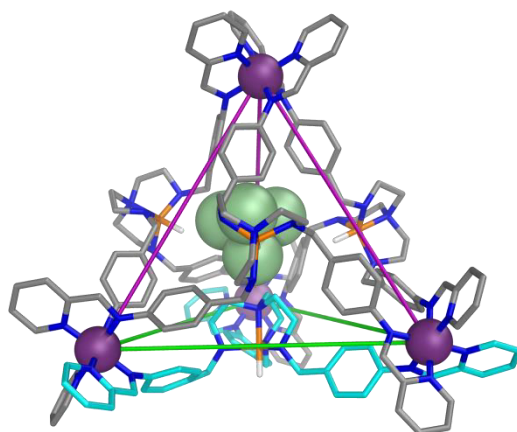


Figure S11.63 MM3-optimized molecular model of $\text{BF}_4^- \cdot \text{C}_3\text{-1}$, based on the single-crystal X-ray structure of $\text{OTf}^- \cdot \text{T-1}$. Nonacidic hydrogen atoms are omitted for clarity. The *exo*-azaphosphatane is colored cyan.

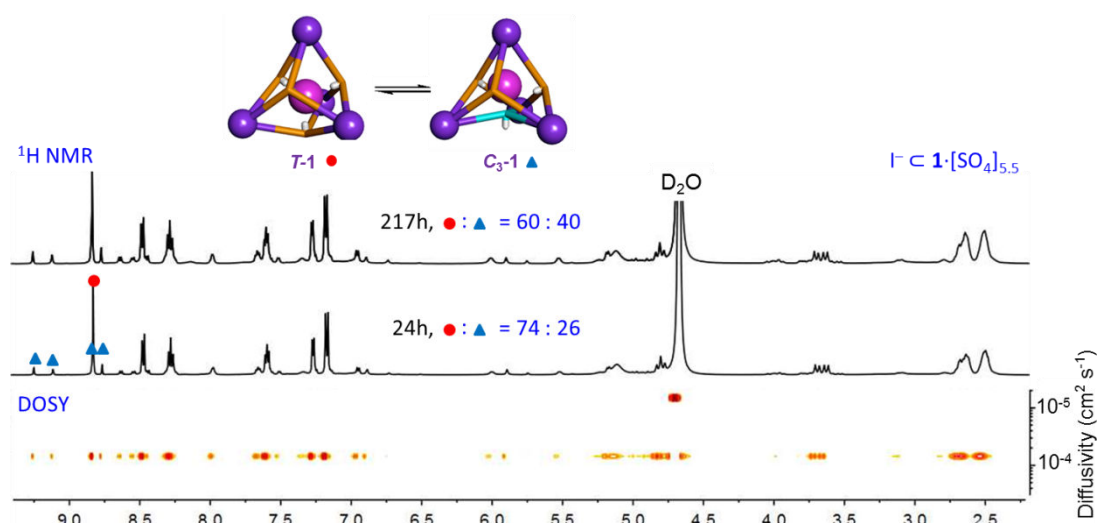


Figure S11.64 Time evolution of the ratio between $\text{I}^- \cdot \text{T-1} \cdot [\text{SO}_4]_{5.5}$ (●) and $\text{I}^- \cdot \text{C}_3\text{-1} \cdot [\text{SO}_4]_{5.5}$ (▲) at 298 K monitored by ^1H NMR (D_2O , 500 MHz, 298 K). Imine protons have been labelled in the spectra. DOSY spectrum shows that the two species give the same diffusion coefficient ($1.4 \times 10^{-6} \text{ cm}^2 \text{ s}^{-1}$).

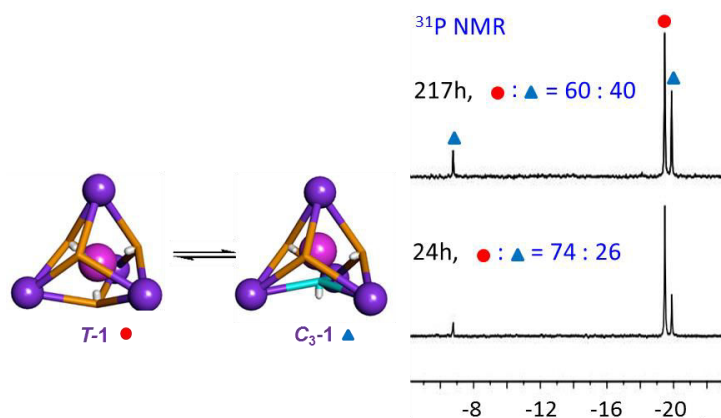


Figure S11.65 Time evolution of the ratio between $\Gamma\text{-}T\text{-}1\cdot[\text{SO}_4]_{5.5}$ (●) and $\Gamma\text{-}C_3\text{-}1\cdot[\text{SO}_4]_{5.5}$ (▲) at 298 K monitored by ^{31}P NMR spectroscopy (D_2O , 202.4 MHz, 298 K). Phosphorous peaks have been assigned.

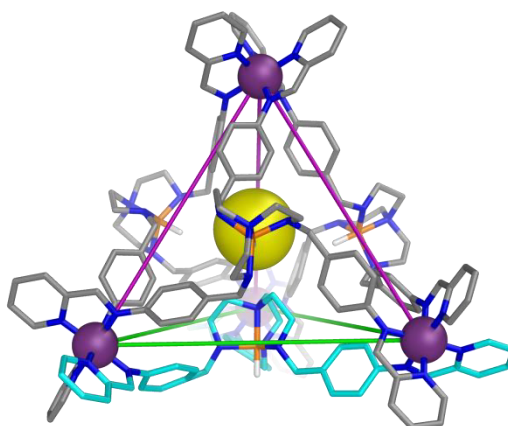
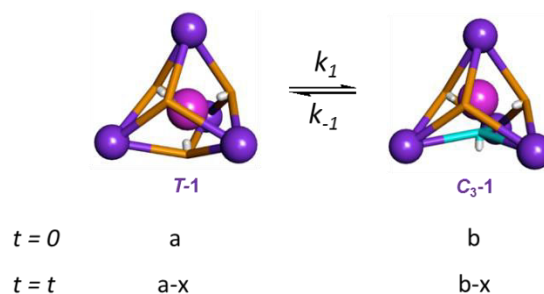


Figure S11.66 MM3-optimized molecular model of $\Gamma\text{-}C_3\text{-}1$, based on the single-crystal X-ray structure of $\text{OTf}\text{-}T\text{-}1$. Nonacidic hydrogen atoms are omitted for clarity. The *exo*-azaphosphatane is colored cyan and the central iodide is yellow.

Kinetic study on cage isomeric interconversion



After complete formation of the cage by self-assembly (set $t = 0$), the concentrations of $T\text{-}1$ and $C_3\text{-}1$ are “ a ” and “ b ”, respectively. “ k_1 ” and “ k_{-1} ” are the rate constants for the following interconversion. At any time “ t ”, the concentration change, x , can be monitored by ^1H NMR spectroscopy. $t\text{-BuOH}$ was used as the internal standard. Based on the reference,²³ the

following equation can be obtained:

$$k_1 t = -\frac{1}{1 + \frac{1}{K^0}} \ln \left(1 - \frac{x \left(1 + \frac{1}{K^0} \right)}{a - \frac{b}{K^0}} \right) \quad \text{Eq 1}$$

$$K^0 = \frac{[B]^{eq}}{[A]^{eq}} = \frac{k_1}{k_{-1}} \quad \text{Eq 2}$$

Here “[A]^{eq}” and “[B]^{eq}” in Eq 2 are the concentrations of two cage isomers at the equilibrium, which can be determined by ¹H NMR spectroscopy. Therefore, at different time “*t*”, the corresponding value of “*k*₁*t*” can be calculated based on the right part of Eq 1. If we establish *Y* = *k*₁*t*, Then *k*₁ can be determined by linear fit between *Y* and *t*. Based on Eq 2, *k*₋₁ could be also calculated from *k*₁ and *K*⁰.

From Eyring equation, the free activation energy Δ*G*[‡] can be calculated as follows:

$$\Delta G^\ddagger = -RT \ln \frac{k_1 h}{k_B T} \quad \text{Eq 3}$$

Here *T* is 298 K. Therefore, according to the values of *k*₁ and *k*₋₁, the corresponding activation energies of Δ*G*₁[‡] and Δ*G*₋₁[‡] for interconversion can be determined.

It should be noted that Δ*G*₁[‡] is the free energy of activation for the conversion from *T*-1 to *C*₃-1, and *k*₁ is the corresponding rate constant; while Δ*G*₋₁[‡] is the free energy of activation for the conversion from *C*₃-1 to *T*-1, and *k*₋₁ is the corresponding rate constant.

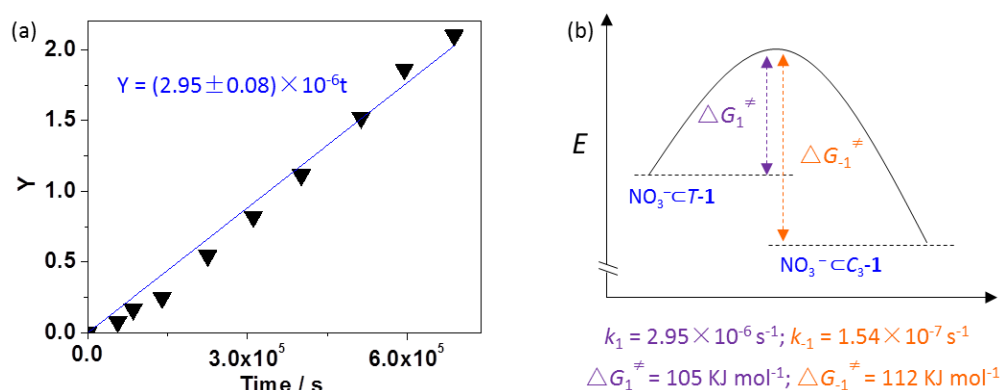


Figure S11.67 Kinetic study of interconversion of $\text{NO}_3^- \text{C-T-1} \cdot [\text{SO}_4]_{5.5} \rightleftharpoons \text{NO}_3^- \text{C-C}_3\text{-1} \cdot [\text{SO}_4]_{5.5}$. (a) The plot between *Y* and the time *t*, where *Y* is calculated by Eq 1 at the right part; the corresponding slope is the rate constant *k*₁, as indicated in Figure S67b; the time after 24 h of assembly was chosen as “*t* = 0”; *k*₋₁, Δ*G*₁[‡] and Δ*G*₋₁[‡] were determined by either Eq 2 or Eq 3. (b) Activation energy diagram of $\text{NO}_3^- \text{C-T-1} \rightleftharpoons \text{NO}_3^- \text{C-C}_3\text{-1}$.

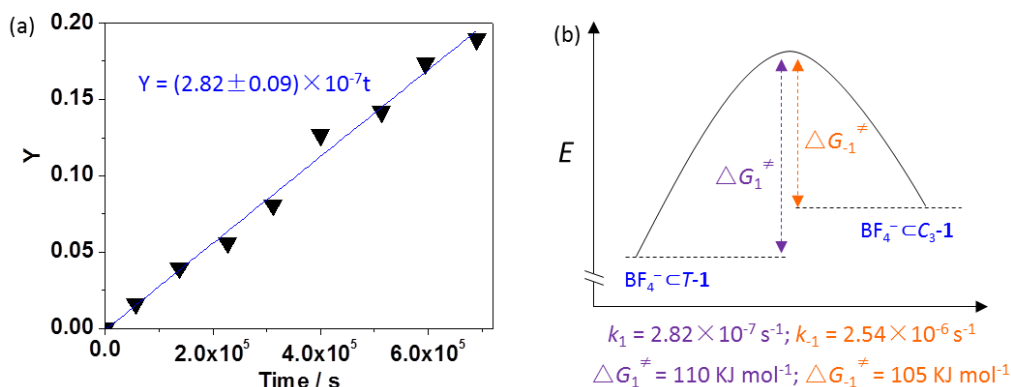


Figure S11.68 Kinetic study of interconversion of $\text{BF}_4^- \text{c-T-1} \cdot [\text{SO}_4]_{5.5} \rightleftharpoons \text{BF}_4^- \text{c-C}_3\text{-1} \cdot [\text{SO}_4]_{5.5}$. (a) The plot between Y and the time t , where Y is calculated by **Eq 1** at the right part; the corresponding slope is the rate constant k_1 , as indicated in Figure S68b; the time after 24 h of assembly was chosen as “ $t = 0$ ”; k_1 , ΔG_1^\ddagger and ΔG_{-1}^\ddagger were determined by either **Eq 2** or **Eq 3**. (b) Activation energy diagram of $\text{BF}_4^- \text{c-T-1} \rightleftharpoons \text{BF}_4^- \text{c-C}_3\text{-1}$.

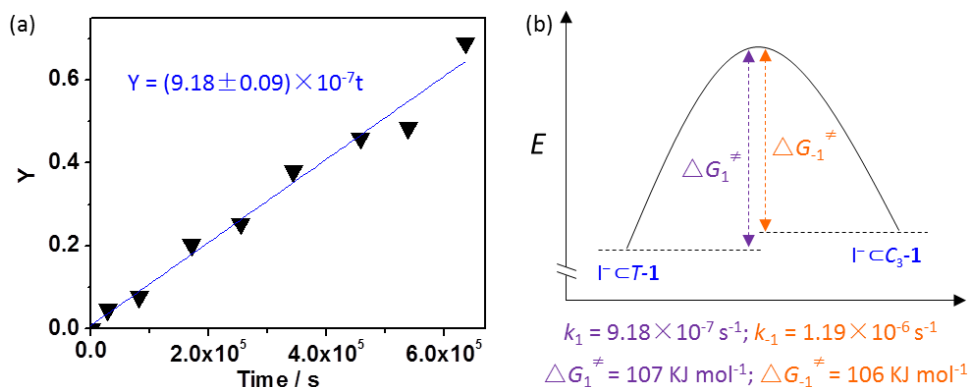


Figure S11.69 Kinetic study of interconversion of $\text{I}^- \text{c-T-1} \cdot [\text{SO}_4]_{5.5} \rightleftharpoons \text{I}^- \text{c-C}_3\text{-1} \cdot [\text{SO}_4]_{5.5}$. (a) The plot between Y and the time t , where Y is calculated by **Eq 1** at the right part; the corresponding slope is the rate constant k_1 , as indicated in Figure S69b; the time after 40 h of assembly was chosen as “ $t = 0$ ”; k_1 , ΔG_1^\ddagger and ΔG_{-1}^\ddagger were determined by either **Eq 2** or **Eq 3**. (b) Activation energy diagram of $\text{I}^- \text{c-T-1} \cdot [\text{SO}_4]_{5.5} \rightleftharpoons \text{I}^- \text{c-C}_3\text{-1} \cdot [\text{SO}_4]_{5.5}$.

11.5.3 X-ray crystallography

Data were collected using a Bruker D8 VENTURE equipped with high-brilliance $\text{I}\mu\text{S}$ Cu-K α radiation (1.54178 Å), with ω and ψ scans at 180(2) K. Data integration and reduction were undertaken with SAINT and XPREP.²⁴ Subsequent computations were carried out using the WinGX-32 graphical user interface.²⁵ Multi-scan empirical absorption corrections were applied to the data using SADABS.²⁴ Structures were solved by direct methods using SHELXT²⁶ then refined and extended with SHELXL-2013.²⁶ In general, non-hydrogen atoms with occupancies greater than 0.5 were refined anisotropically. Carbon-bound hydrogen atoms were included in idealized positions and refined using a riding model. Phosphorus-bound hydrogen atoms were first located in the difference Fourier map before

refinement. Disorder was modelled using standard crystallographic methods including constraints, restraints and rigid bodies where necessary. Crystallographic data along with specific details pertaining to the refinement follow. Crystallographic data have been deposited with the CCDC (CCDC 1529220).

1·[PF₆]_{1.5}·[OTf]_{10.5}

1·[PF₆]_{1.5}·[OTf]_{10.5}

Formula C_{190.50}H₁₈₄F_{40.50}Fe₄N₄₀O_{31.50}P_{5.50}S_{10.50}, *M* 5037.63, Orthorhombic, space group F d d d (#70), *a* 18.6629(8), *b* 64.266(3), *c* 85.271(4) Å³, *V* 102273(8) Å³, *D_c* 1.309 g cm⁻³, *Z* 16, crystal size 0.210 by 0.170 by 0.080 mm, colour purple, habit block, temperature 180(2) Kelvin, λ(CuKα) 1.54178 Å, μ(CuKα) 3.746 mm⁻¹, *T*(SADABS)_{min,max} 0.5665, 0.7488, 2θ_{max} 89.05, *hkl* range -16 16, -43 58, -77 72, *N* 53746, *N*_{ind} 10071 (*R*_{merge} 0.0349), *N*_{obs} 8700 (*I* > 2σ(*I*)), *N*_{var} 1652, residuals* *R*1(*F*) 0.1078, *wR*2(*F*²) 0.2780, GoF(all) 1.085, Δρ_{min,max} -0.644, 0.937 e⁻ Å⁻³.

**R*1 = Σ||*F*_o| - |*F*_c||/Σ|*F*_o| for *F*_o > 2σ(*F*_o); *wR*2 = (Σ*w*(*F*_o² - *F*_c²)/Σ(*wF*_c²))^{1/2} all reflections

w = 1/[σ²(*F*_o²) + (0.1114*P*)² + 3339.7393*P*] where *P* = (*F*_o² + 2*F*_c²)/3

Specific refinement details:

Crystals of 1·[PF₆]_{1.5}·[OTf]_{10.5} were grown by diffusion of diethyl ether into an acetonitrile solution of a mixture of 1·[OTf]₁₂ and 1·[PF₆]₁₂. The crystals employed immediately lost solvent after removal from the mother liquor and rapid handling prior to flash cooling in the cryostream was required to collect data. Despite these measures and the use of a high intensity laboratory source few reflections at greater than 1.1 Å resolution were observed. Nevertheless, the quality of the data is far more than sufficient to establish the connectivity of the structure. The asymmetric unit was found to contain one half of a Fe₄L₄ assembly and associated counterions and solvent molecules. Due to the less than ideal resolution, bond lengths and angles within the two crystallographically unique organic ligands were restrained to be similar to each other and thermal parameter restraints (SIMU, RIGU) were applied to all atoms except for iron.

The anions within the structure show evidence of substantial disorder. Three triflimide anions were modelled as disordered over two or three locations and several anions were modelled with partial occupancies. The encapsulated triflate was disordered around a symmetry position and modelled as a rigid group. Substantial bond length and thermal parameter restraints were applied to facilitate a reasonable refinement of the disordered anions.

Further reflecting the solvent loss and poor diffraction properties there is a significant amount of void volume in the lattice containing smeared electron density from disordered solvent and 3.7 unresolved anions per Fe₄L₄ complex (included as triflate in the formula). Consequently the SQUEEZE²⁷ function of PLATON²⁸ was employed to remove the contribution of the electron density associated with these remaining anions and further highly disordered solvent.

11.5.4 Volume calculations

In order to determine the available void space within **1** in the complex OTf⁻·**T-1**, VOIDOO calculations²⁹ based on the crystal structure were performed. The volume of **1** within NO₃⁻·**C₃-1** was similarly calculated from the MM3 model. In both cases a virtual probe with a radius of 1.4 Å (set by default, water-sized) was employed, and the standard parameters tabulated below were used, following the previously published procedure.³⁰

Maximum number of volume-refinement cycles:	30
Minimum size of secondary grid:	3
Grid for plot files:	0.1
Primary grid spacing:	0.1

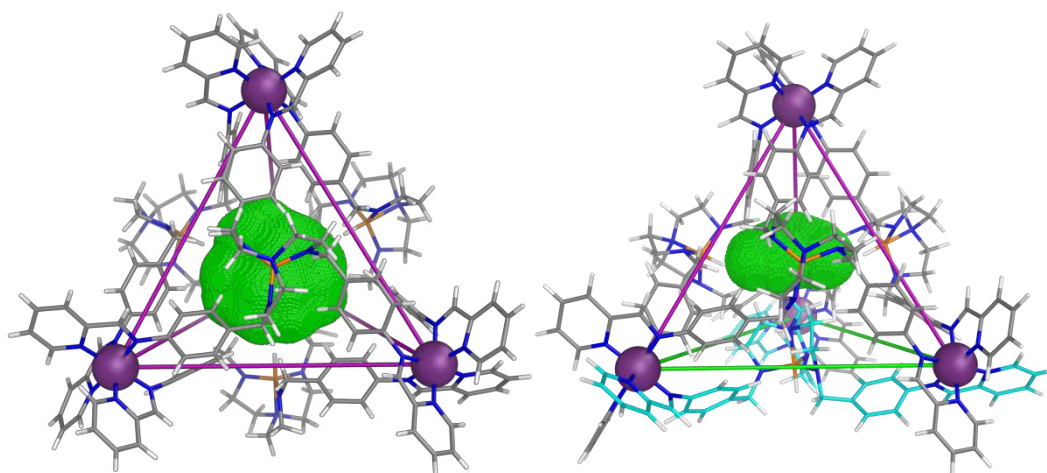
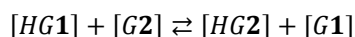


Figure S11.70 VOIDOO-calculated void space as shown (green mesh) within the crystal structure of OTf⁻·**T-1** (left) and within the MM3-optimized structure of NO₃⁻·**C₃-1** (right) in the absence of the encapsulated anions.

11.5.5 Competitive binding studies

A 3.0 mM stock solution of the templated cage OTf⁻/NTf₂⁻·**C₁**·[SO₄]_{5.5} in D₂O was prepared through the procedures described in Section 11.5.2.4 in this Chapter. Then its concentration was adjusted to be around 1.0 mM through dilution with D₂O, using *t*-BuOH as the internal standard. This solution was used directly for probing the relative binding strength of anions inside the cavity relative to OTf⁻ or NTf₂⁻ by recording ¹⁹F NMR or ¹H NMR spectra. For each anionic guest, different equivalents were added to the reference solution in order to obtain an accurate average relative binding affinity. After each addition of the guest anion to the reference, the mixture was kept at 298 K for at least 12 h prior to recording the spectra to make sure the exchange between anions had reached the equilibrium.

In solution, there is the following equilibrium:



The relative binding constant (K_{rel}) is calculated by the following equation:

$$K_{rel} = \frac{K_a^2}{K_a^1} = \frac{[HG2]}{[HG1]} \times \frac{[G1]}{[G2]}$$

Here K_{rel} is the relative binding constant; K_a^2 is the binding constant for guest **2** and K_a^1 is the binding constant for guest **1**. In the ^{19}F NMR spectra after addition of a competitive anion, the concentration of the encapsulated OTf⁻ is $[HG1]$; The concentration of the free OTf⁻ is $[G1]$; $[HG1]$ and $[G1]$ can be calculated from the concentration of the internal standard; $[HG2]$ can be obtained by a subtraction between $[G1]$ and $[G1]_0$, where $[G1]_0$ is the concentration of the initial free OTf⁻; $[G2]$ is equal to the subtraction between $[G2]_{add}$ and $[HG2]$, where $[G2]_{add}$ is the concentration of added G2. Hence based on the above four concentrations, the relative binding constant K_{rel} can be determined by ^{19}F NMR spectroscopy. Different equivalents of competitive guests were added, and an average value of relative binding constant was calculated.

11.5.5.1 Binding affinity relative to OTf⁻·C1·[SO₄]_{5.5}

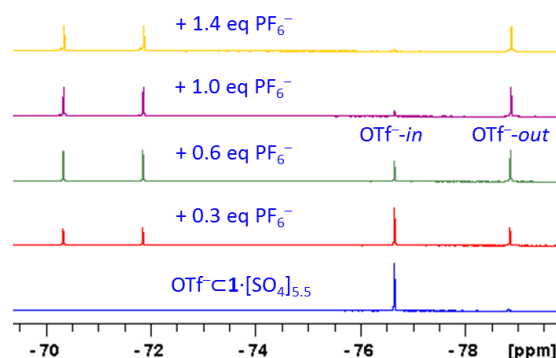


Figure S11.71 Competitive titration of PF_6^- into a solution of $\text{OTf}^- \cdot \text{C1} \cdot [\text{SO}_4]_{5.5}$ in D_2O monitored by ^{19}F NMR spectroscopy (D_2O , 470.4 MHz, 298K). Each spectrum was recorded after 12 h since the addition of PF_6^- to the solution to reach equilibrium. The relative binding constant for PF_6^- versus OTf^- was calculated to be 17.

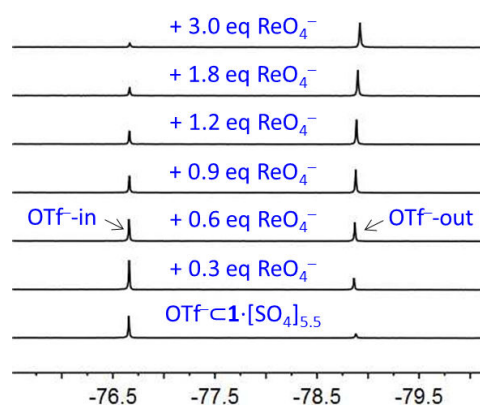


Figure S11.72 Competitive titration of ReO_4^- into a solution of $\text{OTf}^- \cdot \text{C1} \cdot [\text{SO}_4]_{5.5}$ in D_2O monitored by ^{19}F NMR spectroscopy (D_2O , 470.4 MHz, 298K). Each spectrum was measured after 12 h since the addition of ReO_4^- to the solution to reach equilibrium. The relative binding constant for ReO_4^- versus OTf^- was calculated to be 1.9.

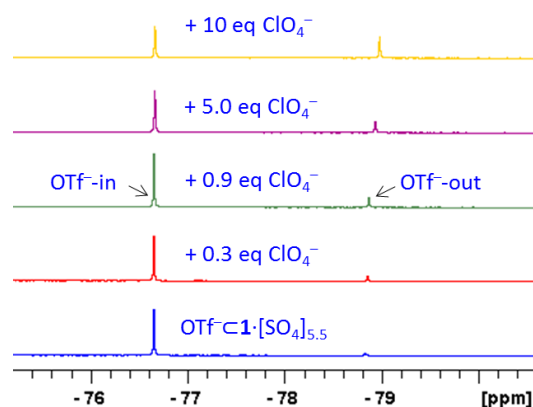


Figure S11.73 Competitive titration of ClO_4^- into a solution of $\text{OTf}^- \cdot \mathbf{1} \cdot [\text{SO}_4]_{5.5}$ in D_2O monitored by ^{19}F NMR spectroscopy (D_2O , 470.4 MHz, 298K). Each spectrum was measured after 12 h since the addition of ClO_4^- to the solution to reach equilibrium. The relative binding constant for ClO_4^- versus OTf^- was calculated to be 0.03.

11.5.5.2 Binding affinity relative to $\text{NTf}_2^- \cdot \mathbf{1} \cdot [\text{SO}_4]_{5.5}$

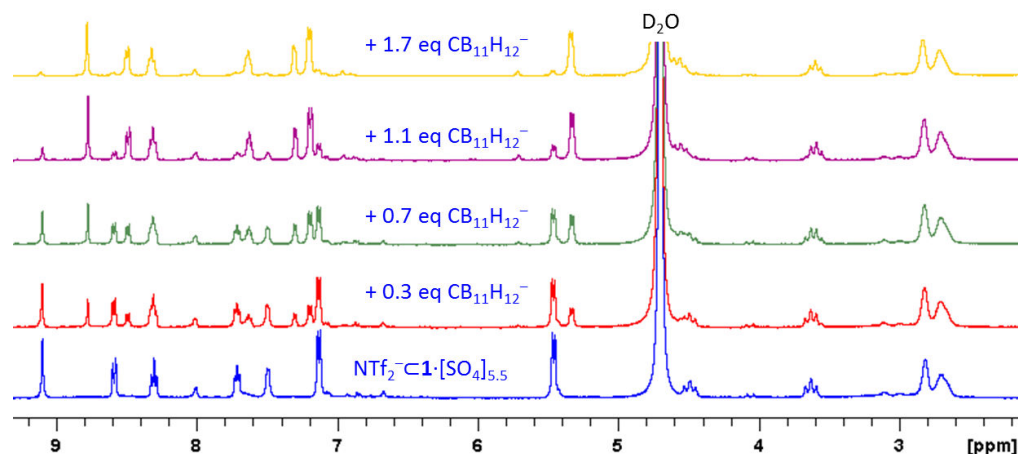


Figure S11.74 Competitive titration of $\text{CB}_{11}\text{H}_{12}^-$ into a solution of $\text{NTf}_2^- \cdot \mathbf{1} \cdot [\text{SO}_4]_{5.5}$ in D_2O monitored by ^1H NMR spectroscopy (D_2O , 400 MHz, 298K). Each spectrum was measured after 12 h since adding $\text{CB}_{11}\text{H}_{12}^-$ to the solution to reach equilibrium. Results show that 1.7 equiv of $\text{CB}_{11}\text{H}_{12}^-$ could quantitatively displace the encapsulated NTf_2^- , indicating the stronger binding of $\text{CB}_{11}\text{H}_{12}^-$ than that of NTf_2^- , but weaker than that of PF_6^- , ReO_4^- , OTf^- or ClO_4^- .

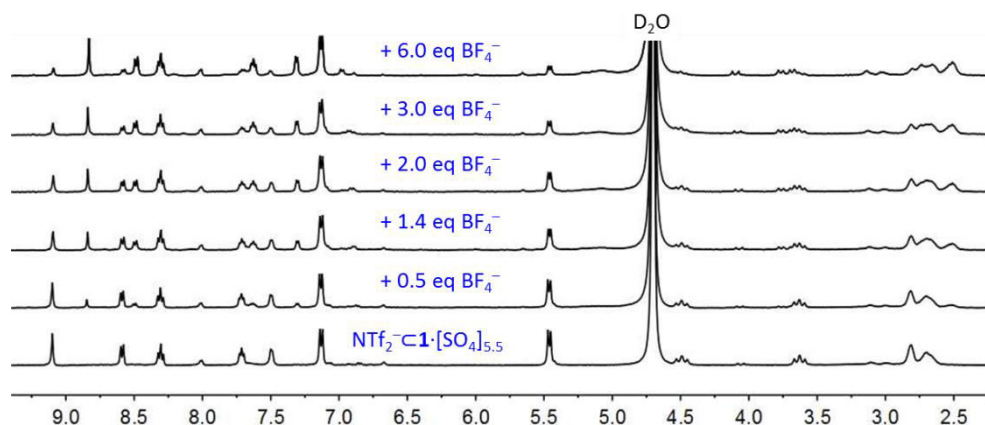


Figure S11.75 Competitive titration of BF_4^- into a solution of $\text{NTf}_2^- \cdot \mathbf{1} \cdot [\text{SO}_4]_{5.5}$ in D_2O monitored by ^1H NMR spectroscopy (D_2O , 400 MHz, 298K). Each spectrum was measured after 12 h since adding BF_4^- to the solution to reach equilibrium. Results show that 6.0 equiv of BF_4^- are not enough to fully displace the encapsulated NTf_2^- , indicating the weaker binding of BF_4^- than that of NTf_2^- .

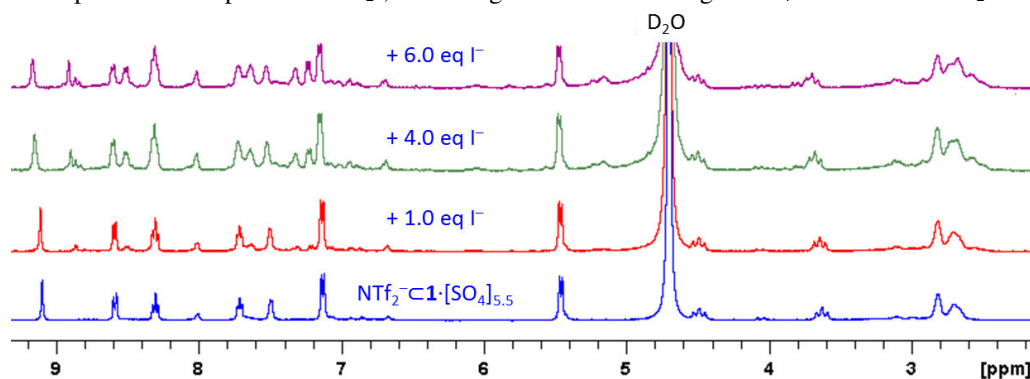


Figure S11.76 Competitive titration of I^- into a solution of $\text{NTf}_2^- \cdot \mathbf{1} \cdot [\text{SO}_4]_{5.5}$ in D_2O monitored by ^1H NMR spectroscopy (D_2O , 400 MHz, 298K). Each spectrum was measured after 12 h since adding I^- to the solution to reach equilibrium. Results show that the binding of I^- relative to NTf_2^- is much weaker than that of BF_4^- .

11.5.6 Shape memory phenomenon

NO_3^- -driven assembled cages were used to investigate the shape memory phenomena by addition of the competitive anion BF_4^- in D_2O . As described above, two weeks after initial mixture of the building blocks, the assembly driven by NO_3^- gave two cage isomers of $\text{NO}_3^- \cdot \mathbf{T-1}$ and $\text{NO}_3^- \cdot \mathbf{C3-1}$ in a ratio of 5 : 95, as shown in the ^1H NMR spectrum (i) of Figure S11.77a. After addition of BF_4^- to the solution, the ^1H NMR spectrum changed immediately, giving a spectrum corresponding to the mixture of $\text{BF}_4^- \cdot \mathbf{T-1}$ and $\text{BF}_4^- \cdot \mathbf{C3-1}$ in a ratio of 5 : 95. This indicates that guest displacement is relatively rapid. Afterwards, it was observed that in time, the concentration of $\text{BF}_4^- \cdot \mathbf{T-1}$ gradually increased while that of $\text{BF}_4^- \cdot \mathbf{C3-1}$ decreased. This interconversion from $\text{BF}_4^- \cdot \mathbf{C3-1}$ to $\text{BF}_4^- \cdot \mathbf{T-1}$ suggests that after anion displacement, the assembly follows the kinetics of BF_4^- -driven assembly, rather than that driven by NO_3^- . The observed behavior occurs also because the kinetics of guest displacement are faster than the kinetics of cage isomer reconfiguration. Therefore during the whole process, we first observed the shape memory phenomenon induced by guest displacement, followed by the BF_4^- -driven cage isomeric interconversion.

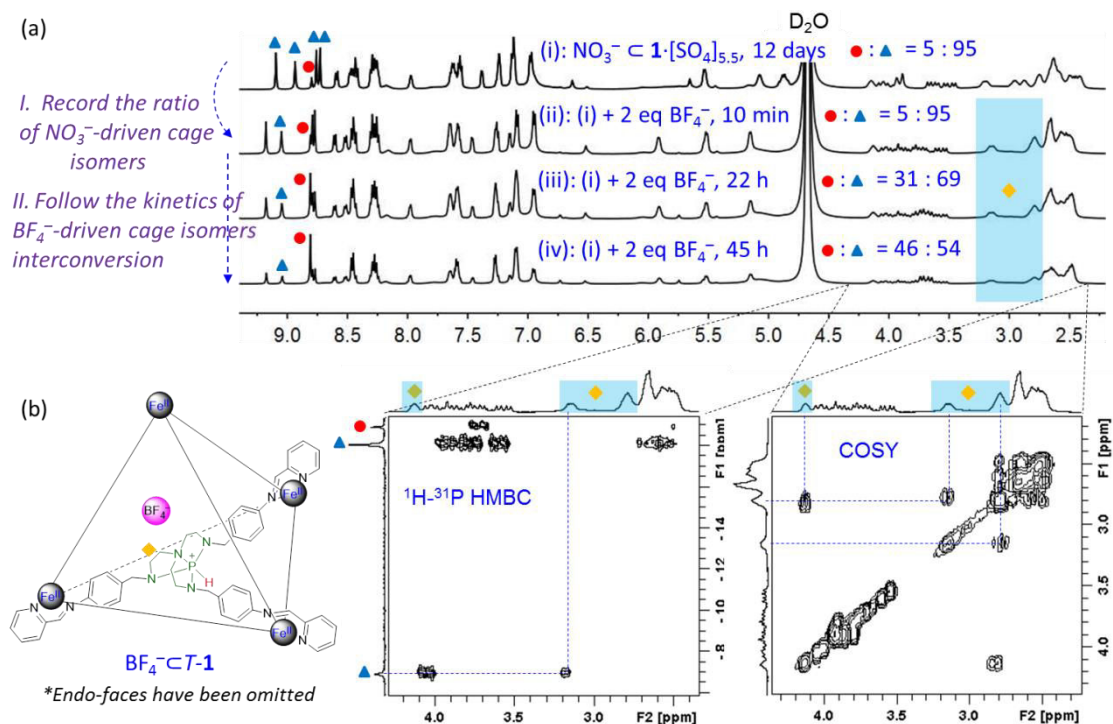


Figure S11.77 (a) Shape memory phenomena observed by ^1H NMR spectroscopy (D₂O, 500 MHz, 298K). (b) Assignment of the methylene protons of the *exo*-azaphosphatrane in cage $\text{BF}_4^- \subset \mathbf{1} \cdot [\text{SO}_4]_{5.5}$ to its ^1H NMR spectrum by (b) partial ^1H - ^{31}P HMBC and ^1H - ^1H COSY experiments.

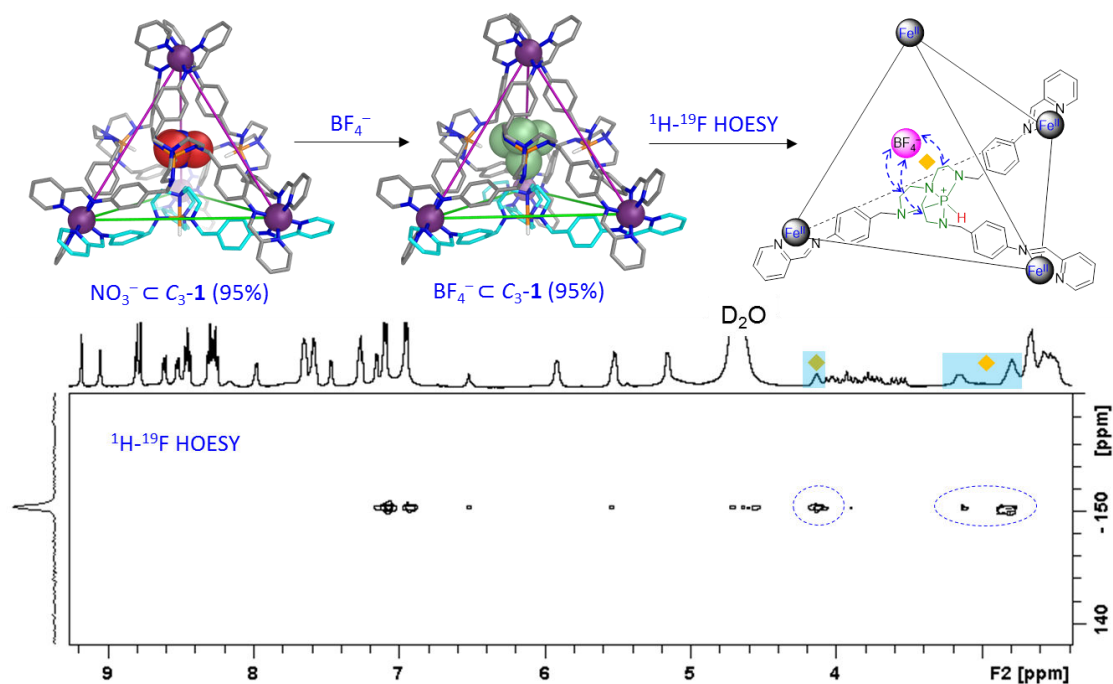


Figure S11.78 ^1H - ^{19}F HOESY (D₂O, 500 MHz, 298K) spectrum of $\text{BF}_4^- \subset \mathbf{1} \cdot [\text{SO}_4]_{5.5}$ (95% population) obtained by competitive anion displacement from 95% $\text{NO}_3^- \subset \mathbf{1} \cdot [\text{SO}_4]_{5.5}$ solution. Clear NOE correlations have been observed between BF_4^- and the methylene protons of the *exo*-azaphosphatrane in the spectrum.

In order to assign the $\mathbf{C}_3\text{-1}$ structure induced by NO_3^- , BF_4^- or I^- , we investigated by ^1H - ^{19}F

HOESY spectra of $\text{BF}_4^- \subset \text{C}_3\text{-1}$ to observe the NOE correlations between the F atoms of the encapsulated BF_4^- and the methylene groups of the *exo*-azaphosphatrane. However, with the solution assembled directly by BF_4^- , we could not observe these NOE correlations because the population of $\text{BF}_4^- \subset \text{C}_3\text{-1}$ was too small compared to that of $\text{BF}_4^- \subset \text{T-1}$ (the population of $\text{BF}_4^- \subset \text{C}_3\text{-1}$ during assembly changed from 25% at 24 h to 14% at 167 h, Figure S11.61). Benefiting from the higher population of $\text{BF}_4^- \subset \text{C}_3\text{-1}$ (95%) obtained by guest displacement from $\text{NO}_3^- \subset \text{C}_3\text{-1}$ (95%) solution, however, we could clearly observe the expected NOE correlations. We first used ^1H - ^{31}P HMBC and ^1H - ^1H COSY experiments to assign the methylene protons of the *exo*-azaphosphatrane in $\text{BF}_4^- \subset \text{C}_3\text{-1}$ (Figure S11.77b), then the ^1H - ^{19}F HOESY experiment was carried out to this solution (Figure S11.78).

11.6 References

- (a) Wang, W.; Wang, Y. X.; Yang, H. B. *Chem. Soc. Rev.* **2016**, *45*, 2656. (b) Cook, T. R.; Stang, P. J. *Chem. Rev.* **2015**, *115*, 7001. (c) Krieg, E.; Bastings, M. M. C.; Besenius, P.; Rybtchinski, B. *Chem. Rev.* **2016**, *116*, 2414. (d) He, Z. F.; Jiang, W.; Schalley, C. A. *Chem. Soc. Rev.* **2015**, *44*, 779. (e) Mauro, M.; Aliprandi, A.; Septiadi, D.; Kehra, N. S.; De Cola, L. *Chem. Soc. Rev.* **2014**, *43*, 4144. (f) Yang, L. L.; Tan, X. X.; Wang, Z. Q.; Zhang, X. *Chem. Rev.* **2015**, *115*, 7196. (g) Yu, G. C.; Jie, K. C.; Huang, F. H. *Chem. Rev.* **2015**, *115*, 7240.
- (a) Chan, A. K. W.; Lam, W. H.; Tanaka, Y.; Wong, K. M. C.; Yam, V. W. W. *P. Natl. Acad. Sci. USA* **2015**, *112*, 690. (b) Bloch, W. M.; Abe, Y.; Holstein, J. J.; Wandtke, C. M.; Dittrich, B.; Clever, G. H. *J. Am. Chem. Soc.* **2016**, *138*, 13750. (c) Zhang, Z.; Kim, D. S.; Lin, C. Y.; Zhang, H. C.; Lammer, A. D.; Lynch, V. M.; Popov, I.; Miljanic, O. S.; Anslyn, E. V.; Sessler, J. L. *J. Am. Chem. Soc.* **2015**, *137*, 7769. (d) Custelcean, R.; Bonnesen, P. V.; Duncan, N. C.; Zhang, X. H.; Watson, L. A.; Van Berkel, G.; Parson, W. B.; Hay, B. P. *J. Am. Chem. Soc.* **2012**, *134*, 8525. (e) Samanta, S. K.; Moncelet, D.; Briken, V.; Isaacs, L. *J. Am. Chem. Soc.* **2016**, *138*, 14488. (f) Bruns, C. J.; Fujita, D.; Hoshino, M.; Sato, S.; Stoddart, J. F.; Fujita, M. *J. Am. Chem. Soc.* **2014**, *136*, 12027.
- (a) You, L.; Berman, J. S.; Anslyn, E. V. *Nat. Chem.* **2011**, *3*, 943. (b) Albrecht, M.; Isaak, E.; Baumert, M.; Gossen, V.; Raabe, G.; Frohlich, R. *Angew. Chem., Int. Edit.* **2011**, *50*, 2850.
- (a) Wu, Y.; Zhou, X. P.; Yang, J. R.; Li, D. *Chem. Commun.* **2013**, *49*, 3413. (b) Chen, T. H.; Popov, I.; Kaveevivitchai, W.; Chuang, Y. C.; Chen, Y. S.; Daugulis, O.; Jacobson, A. J.; Miljanic, O. S. *Nat. Commun.* **2014**, *5*.
- Ren, H. F.; Huang, Z. H.; Yang, H.; Xu, H. P.; Zhang, X. *ChemPhysChem* **2015**, *16*, 523.
- (a) Yoshizawa, M.; Tamura, M.; Fujita, M. *Science* **2006**, *312*, 251. (b) Cakmak, Y.; Erbas-Cakmak, S.; Leigh, D. A. *J. Am. Chem. Soc.* **2016**, *138*, 1749. (c) Kaphan, D. M.; Levin, M. D.; Bergman, R. G.; Raymond, K. N.; Toste, F. D. *Science* **2015**, *350*, 1235. (d) Omagari, T.; Suzuki, A.; Akita, M.; Yoshizawa, M. *J. Am. Chem. Soc.* **2016**, *138*, 499. (e) Cullen, W.; Misuraca, M. C.; Hunter, C. A.; Williams, N. H.; Ward, M. D. *Nat. Chem.* **2016**, *8*, 231.
- (a) Ronson, T. K.; Zarra, S.; Black, S. P.; Nitschke, J. R. *Chem. Commun.* **2013**, *49*, 2476. (b) Zhou, X. P.; Wu, Y.; Li, D. *J. Am. Chem. Soc.* **2013**, *135*, 16062. (c) Sham, K. C.; Yiu, S. M.; Kwong, H. L. *Inorg. Chem.* **2013**, *52*, 5648. (d) Ren, D. H.; Qiu, D.; Pang, C. Y.; Li, Z. J.; Gu, Z. G. *Chem. Commun.* **2015**, *51*, 788. (e) Yi, S.; Brega, V.; Captain, B.; Kaifer, A. E. *Chem. Commun.* **2012**, *48*, 10295. (f) Young, M. C.; Holloway, L. R.; Johnson, A. M.; Hooley, R. J.

- Angew. Chem., Int. Edit.* **2014**, *53*, 9832. (g) Bunzen, H.; Nonappa; Kalenius, E.; Hietala, S.; Kolehmainen, E. *Chem. Eur. J.* **2013**, *19*, 12978. (h) Domer, J.; Slootweg, J. C.; Hupka, F.; Lammertsma, K.; Hahn, F. E. *Angew. Chem., Int. Edit.* **2010**, *49*, 6430. (i) Lewing, D.; Koppetz, H.; Hahn, F. E. *Inorg. Chem.* **2015**, *54*, 7653.
- 8 (a) Frischmann, P. D.; Kunz, V.; Wurthner, F. *Angew. Chem., Int. Edit.* **2015**, *54*, 7285. (b) Roukala, J.; Zhu, J. F.; Giri, C.; Rissanen, K.; Lantto, P.; Telkki, V. V. *J. Am. Chem. Soc.* **2015**, *137*, 2464. (c) Luo, D.; Zhou, X. P.; Li, D. *Angew. Chem., Int. Edit.* **2015**, *54*, 6190.
- 9 Lensink, C.; Xi, S. K.; Daniels, L. M.; Verkade, J. G. *J. Am. Chem. Soc.* **1989**, *111*, 3478.
- 10 (a) Chatelet, B.; Joucla, L.; Dutasta, J. P.; Martinez, A.; Szeto, K. C.; Dufaud, V. *J. Am. Chem. Soc.* **2013**, *135*, 5348. (b) Zhang, D. W.; Jardel, D.; Peruch, F.; Calin, N.; Dufaud, V.; Dutasta, J. P.; Martinez, A.; Bibal, B. *Eur. J. Org. Chem.* **2016**, 1619.
- 11 (a) Busschaert, N.; Caltagirone, C.; Van Rossom, W.; Gale, P. A. *Chem. Rev.* **2015**, *115*, 8038. (b) Ballester, P. *Chem. Soc. Rev.* **2010**, *39*, 3810. (c) Zhou, Y.; Zhang, J. F.; Yoon, J. *Chem. Rev.* **2014**, *114*, 5511. (d) Katayev, E. A.; Kolesnikov, G. V.; Sessler, J. L. *Chem. Soc. Rev.* **2009**, *38*, 1572. (e) Sokkalingam, P.; Shraberg, J.; Rick, S. W.; Gibb, B. C. *J. Am. Chem. Soc.* **2016**, *138*, 48. (f) Langton, M. J.; Serpell, C. J.; Beer, P. D. *Angew. Chem., Int. Edit.* **2016**, *55*, 4629. (g) Kang, S. O.; Llinares, J. M.; Day, V. W.; Bowman-James, K. *Chem. Soc. Rev.* **2010**, *39*, 3980. (h) Jo, J.; Olsasz, A.; Chen, C. H.; Lee, D. *J. Am. Chem. Soc.* **2013**, *135*, 3620. (i) Kubik, S. *Chem. Soc. Rev.* **2010**, *39*, 3648.
- 12 Ayme, J. F.; Beves, J. E.; Campbell, C. J.; Gil-Ramirez, G.; Leigh, D. A.; Stephens, A. J. *J. Am. Chem. Soc.* **2015**, *137*, 9812.
- 13 Bolliger, J. L.; Ronson, T. K.; Ogawa, M.; Nitschke, J. R. *J. Am. Chem. Soc.* **2014**, *136*, 14545.
- 14 (a) Custelcean, R. *Chem. Commun.* **2013**, *49*, 2173. (b) Pandurangan, K.; Kitchen, J. A.; Blasco, S.; Boyle, E. M.; Fitzpatrick, B.; Feeney, M.; Kruger, P. E.; Gunnlaugsson, T. *Angew. Chem., Int. Edit.* **2015**, *54*, 4566.
- 15 Meng, W.; Clegg, J. K.; Thoburn, J. D.; Nitschke, J. R. *J. Am. Chem. Soc.* **2011**, *133*, 13652.
- 16 Castilla, A. M.; Ousaka, N.; Bilbeisi, R. A.; Valeri, E.; Ronson, T. K.; Nitschke, J. R. *J. Am. Chem. Soc.* **2013**, *135*, 17999.
- 17 Stewart, J. J. P. SCIGRESS, Version 2.9.0, Fujitsu Limited, United States, **2009**.
- 18 It was observed that addition of NTf₂⁻ and CB₁₁H₁₂⁻ resulted in precipitation of the cage without changing the ratio of ¹⁹F-out/¹⁹F-in and 1 equiv of NTf₂⁻ precipitates about 9% of the cage.
- 19 Mecozzi, S.; Rebek, J. *Chem. Eur. J.* **1998**, *4*, 1016.
- 20 J. K. Clegg, J. Cremers, A. J. Hogben, B. Breiner, M. M. J. Smulders, J. D. Thoburn and J. R. Nitschke, *Chem. Sci.*, 2013, **4**, 68-76.
- 21 A. M. Castilla, T. K. Ronson and J. R. Nitschke, *J. Am. Chem. Soc.*, 2016, **138**, 2342-2351.
- 22 F. J. Rizzuto, W.-Y. Wu, T. K. Ronson and J. R. Nitschke, *Angew. Chem. Int. Ed.*, 2016, **55**, 7958-7962.
- 23 A. Martinez, V. Robert, H. Gornitzka and J.-P. Dutasta, *Chem. Eur. J.*, 2010, **16**, 520-527.
- 24 Bruker-Nonius, APEX, SAINT and XPREP, Bruker AXS Inc., Madison, Wisconsin, USA, 2013.
- 25 L. Farrugia, *J. Appl. Crystallogr.*, 2012, **45**, 849-854.
- 26 G. Sheldrick, *Acta Cryst.*, 2008, **A64**, 112-122.
- 27 P. van der Sluis and A. L. Spek, *Acta Cryst.*, 1990, **A46**, 194-201.

- 28 A. L. Spek, *PLATON: A Multipurpose Crystallographic Tool*, Utrecht University, Utrecht, The Netherlands, 2008.
- 29 G. J. Kleywegt and T. A. Jones, *Acta Cryst.*, 1994, **D50**, 178-185.
- 30 Y. R. Hristova, M. M. J. Smulders, J. K. Clegg, B. Breiner and J. R. Nitschke, *Chem. Sci.*, 2011, **2**, 638-641.

Part VI. Conclusion

In this PhD thesis, the advances in hemicryptophane chemistry have been thoroughly reviewed in **Chapter 1**. A brief history about its development is first given in the introduction part. Then synthetic methods and applications in recognition, molecular machines and supramolecular catalysis are successively described. Based on the inborn advantages of hemicryptophanes compared to other cages that were widely used in supramolecular chemistry as well as the limitation in the current development, in **Chapter 2**, we have proposed the objectives of this thesis. The major mission of this PhD work is to design and synthesize new hemicryptophane cages to either broaden their applications or to make the existing utilization more efficient. The final goal is to enhance the fundamental knowledge of hemicryptophanes in order to realize the targeted-function-directed molecular design, and apply them to other relevant cage hosts. These include the preparation of a series of new heteroditopic hemicryptophanes bearing new building blocks, the synthesis of enantiopure cages having up to three types of chirality, and the preparation of metal@hemicryptophane complexes and self-assembled molecular capsules, all of which have been designed as recognition receptors, molecular machines, or supramolecular catalysts. These two chapters constitute the first part of this thesis (**Part I**).

The works in **Part II** mainly focus on the host-guest chemistry of hemicryptophanes. This begins with a fluorescent hemicryptophane cage combining a CTV unit and a Zn(II) metal center, as described in **Chapter 3**. This fluorescent hemicryptophane was developed as the first fluorescent sensor for a zwitterion, choline phosphate, in competitive media. The heteroditopic character of the host towards the guest was thoroughly investigated by both fluorescence and NMR spectroscopy. The exact binding mode has been examined by DFT calculations. In **Chapter 4**, two new hemicryptophane hosts bearing fluorinated aromatic linkers were synthesized to investigate their complexation properties of ion pairs. The introduction of fluorine atoms around the aromatic linkers was expected to improve the anion binding abilities of the host, therefore affecting their ion pair binding performance. The binding affinity toward anions was found to strongly rely on the location of the fluorine atoms on the linkers, highlighting the complexity of anion- π interactions. The cooperativity involved in the recognition of ion pairs was found to be able to modulate from positive to negative by this chemical engineering. These observations have been supported by CASSCF/CASPT2 calculations. Encouraged by the two efficient heteroditopic hemicryptophanes in the recognition of zwitterions and ion pairs, in **Chapter 5**, two new heteroditopic hemicryptophanes bearing TPA units were synthesized: one with phenyl rings as linkers and the other with naphthalene rings. As TPA unit is able to complex various metals, these hemicryptophanes are chemical platforms available for various purposes and applications. The naphthalene linkers in one cage also confer fluorescence properties to the host structure, and gram-scale synthesis of the other cage was also achieved. The racemate of each hemicryptophane was finally resolved by chiral HPLC, and their enantiopure versions have been obtained. We anticipate their promising applications, for instance for heteroditopic recognition of chiral zwitterions. Due to the strong interest in chirality as well as the consideration of their importance, in **Chapter 6**, eight enantiopure cages were designed and

synthesized combining three classes of chirality on seven stereogenic units: the helical chirality of the CTV unit, the axial chirality of the binaphthol linkages, and the central chirality of the asymmetric carbons on the triol unit. Albeit the multiple chirality in the engineered structure makes difficult the assignment of the absolute configuration of CTV with conventional methods, a chemical correlation strategy was developed, to successfully determine the configuration of the eight hemicyptophane stereoisomers. The stereoselective recognition properties toward glucose and mannose derivatives with these new enantiopure cages were investigated, and from moderate to exclusive guest diastereo- and enantio-discrimination were observed.

As described in Section 1.5, hemicyptophanes have also been developed as molecular machines, which include only two examples. Despite this area in hemicyptophane chemistry is not fruitful, in **Chapter 7 (Part III)**, the breathing motion of a series of enantiopure cages was explored. In fact, we observed that the cages obtained in **Chapter 6** adopt imploded conformation in both solution and solid states and a hierarchical imploded degree between the four cage diastereomers was exhibited. The hierarchical implosion also results in the regulation of their corresponding physical and chemical properties. For instance, the reaction between vanadium(V) oxytriisopropoxide and the most imploded cage suffers from a slower reaction rate compared to the other three diastereomers. Interestingly, vanadium complexation re-inflates the cage from its imploded conformation to a globular form, and the resulting vanadium core can also be removed from the inner cavity according to external coordination with TEA. Thus, this system is capable of switching between the imploded and expanded bistable states via external inputs, leading to the molecular breathing motion.

In **Part IV**, three works related to the supramolecular catalysis with functionalized hemicyptophanes have been discussed. Benefiting from the obtained vanadium(V) complexes in **Chapter 7**, using the oxidation of sulfide as a model reaction, in **Chapter 8**, we described in total five sets of oxido-vanadium(V) complexes, including both cages and open structures. It was found that the complexes simultaneously holding CTV, binaphthol and oxido-vanadium groups are the most efficient catalysts because of the construction of the hydrophobic cavity with the size appropriate to accommodate and convert the sulfide substrates, and to expel the products from the inner cavity. This case constitutes a rare example of supramolecular catalysts that exhibit extremely high levels of efficiency with 10000 turnovers. The catalytic reaction obeys the Michaelis-Menten model of enzyme kinetics, and competitive inhibition was observed using Me_4N^+ as an inhibitor. The substrate size-selectivity of the cage catalysts further indicate that the reaction occurs inside the cavity of the hemicyptophane hosts mimicking enzymatic functions. In **Chapter 9**, we further tested the catalytic lignin oxidation properties of these developed vanadium(V) hemicyptophane catalysts in collaboration with the group of Prof. R. Tom Baker at the University of Ottawa. This would be the first example of lignin oxidation by supramolecular catalysts. Compared to the model catalyst with an open structure, an improvement of the catalytic activity associated with a diastereo-selective conversion has been observed. Good turnover number was also reached considering the supramolecular feature of the catalyst. In **Chapter 10**, in collaboration with the group of Dr. Brigitte Bibal at the University of Bordeaux, we attempted to develop the azaphosphatane-functionalized hemicyptophanes as hydrogen-bonding

organocatalysts for the ring-opening polymerization of lactide. Although we observed a low reactivity with hemicryptophane cages, it was found that the model catalysts with lipophilic hindered counteranions (NTf₂⁻ or BArF⁻) show good catalytic behavior. Crystallographic analysis and semiempirical calculations revealed that the phosphonium group is located in a hydrophobic cavity on top of a globular structure. Thus, the ⁺P-H bond can interact with the C=O group of lactide, but undesired hydrogen bonding with the tertiary amine cocatalysts is unable to take place due to steric hindrance. The ability of azaphosphatranes to activate C=O groups in the ring-opening polymerization of lactide is promising, as the conversion reached 74–81% under classical conditions.

In this PhD thesis, my goal is not limited to the hemicryptophane cages, a more prospective view focusing on cages constructed by self-assembly has been opened, as described in **Chapter 11 (Part V)**. In collaboration with Prof. Jonathan R. Nitschke at the University of Cambridge, we have demonstrated the feasibility of introducing azaphosphatranes into tetrahedron complexes using subcomponent self-assembly, and also proved for the first time the utility of azaphosphatranes as anion binding moieties. Due to the designed flexibility, the assembled tetrahedron is able to encapsulate various anions in water with volumes ranging from 35 to 219 Å³ *via* hydrogen bonding and electrostatic interactions. Moreover, structural adaptation was observed during cage formation in response to the size and shape of the external template anions exhibiting a X⁻⊂T-cage or a X⁻⊂C₃-cage. The two cage isomers may coexist in solution and interconvert. Shape memory phenomena were finally observed during guest displacement due to its faster kinetics compared to that of isomeric reconfiguration. We believe that this endohedrally functionalized assembled cage will have the great potential in supramolecular catalysis.